University of Southampton

Faculty of Engineering and Physical Sciences

Energy Technology Research Group

Reaction Kinetics Mechanisms of Novel Intensified Transesterification Methods via Microturbulence and Micro-level Diffusion for Biodiesel Production

by

Kang Yao Wong

ORCID ID: 0000-0001-5211-8420

Thesis for the degree of Doctor of Philosophy

January 2021

University of Southampton

Abstract

Faculty of Engineering and the Physical Sciences

Energy Technology Research Group

Thesis for the degree of Doctor of Philosophy

Reaction Kinetics Mechanisms of Novel Intensified Transesterification Methods via Microturbulence and Micro-level Diffusion for Biodiesel Production

by

Kang Yao Wong

In recent years, biodiesel has proven to become a feasible alternative source of energy, due to its attractive benefits such as reduced emissions, renewability, and energy sustainability. The conventional techniques implemented to produce biodiesel vary but aim to address production challenges such as the natural mass transfer limitation of reactants and the governing reaction kinetics prediction of transesterification. In this study, the processing methodologies for novel biodiesel reactors such as Reticulated Vitreous Carbon (RVC) batch reactor and microchannel reactor are extensively evaluated, particularly the kinetic mechanisms and theories of the intensification approaches. The kinetic mechanisms was identified for the RVC reactor and microchannel reactor, along with constructing the mass transfer and glyceride prediction models. These reactors are then benchmarked against the conventional stirred tank reactor to evaluate their respective performances in reaction kinetics, mass transfer, and biodiesel yield. Optical analyses such as thermal imaging and digital microscopy were performed for the RVC reactor and microchannel reactor, respectively. In addition to the qualitative approach for analysis, statistical models such as Pareto, factorial, and response surface methodology were also implemented to characterise the reactors quantitatively. The physical-limiting regime for the benchmark batch reactor was found to be in the range of 0s to 270s, where intensification is significant for yield before transitioning into a reactant-limiting regime. However, the low porosity RVC (20–30 ppi) combined with high agitation speed (400 rpm) can achieve a high biodiesel yield of 74% within 3 minutes. The physical-limiting regime (0–180 s) for the RVC reactor was found to be shorten by 10–20 s against benchmark reactor due to more substantial agitation capabilities caused by micro-turbulences induced from the reticulated surfaces. The microchannel reactor utilises micro-level diffusion and internal circulation to promote mass transfer in transesterification. Higher reaction temperature causes slug flow to transit into an annular flow, resulting in an overall increase in specific interfacial area. The mass fractions of the slug and annular flows change over time due to the production of biodiesel. The magnitude of the volumetric mass transfer coefficients and first-order kinetic constants are in the increasing order of microchannel, benchmark, and RVC reactors. An increase in reaction temperature from 30°C to 45°C shows an improvement of 157.9% and 63.2% for mass transfer using microchannel and RVC reactors, respectively. In contrast, an improvement of 90.0% and 149.9% was observed for kinetic rates in microchannel and RVC reactors, respectively. Overarching insights indicate that the RVC reactor has higher mass transfer and kinetic rates for transesterification reaction, while microchannel reactors are more sensitive to improvement from increasing reaction temperature. The reaction kinetic models discussed in this study provides additional mechanisms to the conventional first-order, second-order kinetics to improve conventional model adequacies.

I dedicate this work to my mother, MeeYean Leong,

to my aunt, BeeLan Leong,

and to my uncle, Ang

Mit Hilfe dieser Theorie werden aIle Bestrebungen nach einem rationellen Warmemotor eine einheitliche Richtung annehmen, anstatt sich zu zersplittern, und es ist zu hoffen, dass ein theoretisch vollkommener Motor recht bald die bisherigen, sehr unvollkommenen Warmekraftmaschinen ersetzen wird. Die Ausführung eines solchen vollkommenen Motors ist nicht einmal besonders schwierig;

Diesel, R., 1893.

Theorie und Konstruktion eines rationellen Wärmemotors. p. 46.

Table of Contents

Table of Tables

Table of Tables

Table of Tables

Table of Figures

Table of Figures

Table of Figures

Table of Figures

Table of Figures

Table of Figures

List of Publications

Published articles

1. K. Y. Wong, J.-H. Ng, C. T. Chong, S. S. Lam and W. T. Chong, 2019. Biodiesel process intensification through catalytic enhancement and emerging reactor designs: A critical review. Renewable and Sustainable Energy Reviews, 116, p.109399.
2. K. Y. Wong, J.-H. Ng, C. T. Chong. A Full Factorial Analysis on One-Way Transient Transesterification Interactions Affecting Palm Biodiesel for Batch Reactor. Chemical Engineering Transactions, 72, 349-354.
3. J.-H. Ng, J. X. The, K. Y. Wong, K. H. Wu and C.T. Chong (2017) A Techno-Economical and Automotive Emissions Impact Study of Global Biodiesel Usage in Diesel Engines. Journal of the Society of Automotive Engineers Malaysia, 1(2): 124-136.

Articles in progress

1. K. Y. Wong, J.-H. Ng, C. T. Chong, S. S. Lam, W. T. Chong. Pareto-Hierarchical Clustering Framework for Biodiesel Transesterification. Submitted to Sustainable Energy Technologies and Assessments (Rebuttal stage).
2. K. Y. Wong, J.-H. Ng, C. T. Chong, S. S. Lam, W. T. Chong. Microturbulence-assisted Biodiesel Transesterification with the use of Reticulated Vitreous Carbon. The manuscript will be submitted to Carbon.

Conference proceedings

1. K. Y. Wong, J.-H. Ng, C. T. Chong, W. T. Chong. A Full Factorial Analysis on One-Way Transient Transesterification Interactions Affecting Palm Biodiesel for Batch Reactor. The 4th International Conference on Low Carbon Asia (ICLCA), October 2018.
2. K. Y. Wong, J.-H. Ng, C. T. Chong, W. T. Chong. Microturbulence-assisted Biodiesel Transesterification with the use of Reticulated Vitreous Carbon. Energy System Conference (ENER) June 2018.
3. K. Y. Wong, J.-H. Ng, A. J. Cruden. Microturbulence-Assisted Biodiesel Transesterification with the use of Reticulated Vitreous Carbon. 2018 Mechanical Engineering Postgraduate Conference of the Engineering Sciences Academic Unit, Southampton, UK. pp. 38.

4. J.-H. Ng, K. Y. Wong, C. T. Chong, S. Rajoo. Integrated 1D-Chemical Kinetics Model of a Diesel and Biodiesel Fuelled Light-Duty Diesel Engine. 2017 3rd International Conference on Power Generation Systems and Renewable Energy Technologies (PGSRET), Johor, Malaysia. pp. 89-94.

Posters

1. Biodiesel Production: A Transient Pareto Approach. University of Reading Malaysia Research Annual Assembly, November 21, 2018. Johor, Malaysia.
2. Microturbulence-Assisted Biodiesel Transesterification with the use of Reticulated Vitreous Carbon. 2018 Mechanical Engineering Postgraduate Conference of the Engineering Sciences Academic Unit, January 16th, 2018. Southampton, UK.
3. Microturbulence-assisted chemical reaction with Reticulated Vitreous Carbon (RVC) for biodiesel transesterification. Royal Society of Chemistry Twitter Poster Conference, March 20, 2017.

Research Thesis: Declaration of Authorship

Print name:	**Kang Yao Wong**

Title of thesis:	**Reaction Kinetics Mechanisms of Novel Intensified Transesterification Methods for Biodiesel Production**

I declare that this thesis and the work presented in it are my own and has been generated by me as the result of my own original research.

I confirm that:

1. This work was done wholly or mainly while in candidature for a research degree at this University;
2. Where any part of this thesis has previously been submitted for a degree or any other qualification at this University or any other institution, this has been clearly stated;
3. Where I have consulted the published work of others, this is always clearly attributed;
4. Where I have quoted from the work of others, the source is always given. With the exception of such quotations, this thesis is entirely my own work;
5. I have acknowledged all main sources of help;
6. Where the thesis is based on work done by myself jointly with others, I have made clear exactly what was done by others and what I have contributed myself;
7. Parts of this work have been submitted for publication as:

    1. K. Y. Wong, J.-H. Ng, C. T. Chong, S. S. Lam and W. T. Chong, 2019. Biodiesel process intensification through catalytic enhancement and emerging reactor designs: A critical review. Renewable and Sustainable Energy Reviews, 116, p.109399.
    2. K. Y. Wong, J.-H. Ng, C. T. Chong. A Full Factorial Analysis on One-Way Transient Transesterification Interactions Affecting Palm Biodiesel for Batch Reactor. Chemical Engineering Transactions, 72, 349-354.
    3. K. Y. Wong, J.-H. Ng, C. T. Chong, S. S. Lam, W. T. Chong. Pareto-Hierarchical Clustering Framework for Biodiesel Transesterification. Submitted to Sustainable Energy Technologies and Assessments (Rebuttal stage).

4. K. Y. Wong, J.-H. Ng, C. T. Chong, S. S. Lam, W. T. Chong. Microturbulence-assisted Biodiesel Transesterification with the use of Reticulated Vitreous Carbon. The manuscript will be submitted to Carbon.

Signature: **Date:** **29th January 2021**

Acknowledgements

I would like to express my sincere gratitude to my supervisor, Dr Jo-Han Ng, for his continuous guidance and invaluable advice during the course of this PhD, and more importantly, for his mentorship and friendship. It is my pleasure to study under his tutoring since my undergraduate days as his passion and ethos for science truly inspired me. Dr Jo-Han has provided me with a generous amount of liberty and resources in my journey in science where research creativity is advocated. He has always encouraged me to pursue opportunities and make the most out of my PhD, which has moulded me into the young scientist that I am today.

I would also like to extend my appreciation to my co-supervisors, Professor Neil Stephen and Professor Andy Cruden. They provided me with constructive advice, networks, and resources to support my PhD work.

Special thanks to Dr Cheng Tung Chong from Shanghai Jiao Tong University and Dr William Chong from Universiti Teknologi Malaysia. They have shared many of their professional experiences to me which I found useful. Their commitment to science and vast knowledge have also greatly influenced many of my perspectives in science.

My sincere appreciation also goes to Gus Gilliam, technical specialist who have provided many constructive insights for my experiments through his expertise. Additionally, the professional IT support provided by Ian Black has proved to be practical and useful.

I would like to thank my friends and colleague for all the great moments we spent which has made this PhD enjoyable and fun. In special, I would like to mention Dr Ivan Ling, Brandon Goh, Horacio Figueredo, Luis Fernando. Our research group and office, Cassandra Wong, Tao Zhu, Peng Jiang, James Bailey, Nicholas Hernandez, Rachel McKerracher, and many more in the university.

I am also grateful for my country, Malaysia, for financially supporting me through the Fundamental Research Grant Scheme (FRGS) provided by the Ministry of Education. I would not have had the opportunity to pursue a PhD if I had not met these brilliant teachers. In particular, my A-level physics teacher, Mr Lim and my coach Mr Philip Tan. I wish to thank all my former teachers and supervisors for their efforts to educate and motivate me in my education journey.

Above all, I would like to thank my family for all the support, love, and sacrifice. This was a longer journey than I thought, where I've discovered more about the world and myself. Life is so beautiful, and each day is a gift.

Definitions and Abbreviations

Abbreviation	Meaning
ACO	Ant colony optimisation
ACT	Acetone
AN	Acetonitrile
ANN	Artificial neural network
ANOVA	Analysis of variance
ASTM	American society for testing materials
CBN	Dichlorobenzene
CFD	Computational fluid dynamics
CN	Cetane number
CO	Carbon monoxide
CSTR	Continuous-stirred tank reactor
DEE	Diethyl ether
DMC	Dimethyl Carbonate
DOE	Design of experiments
EGA-MS	Evolved gas analysis by mass spectrometry
EN	European standard
FAME	Fatty acid methyl ester
FFA	Free fatty acid
FID	Flame ionisation detector
GC	Gas chromatography
HCL	Hydrochloric acid
HDPE	High-density polyethylene

ICE	Internal combustion engine
IPA	Isopropyl alcohol
IV	Iodine value
NO	Nitrogen oxides
OFAT	One-factor-at-a-time
PID	Proportional integral differential
PME	Palm methyl ester
ppi	Pores per inch
PSO	Particle swarm optimisation
PVC	Polyvinyl chloride
RBD	Refined bleached deodorised
RGB	Red green blue
RIMM	Rectangular interdigital micromixer
RMSE	Root mean square error
RPM	Revolution per minute
RSM	Response surface methodology
RVC	Reticulated vitreous carbon
SCMH	Simultaneous cooling and microwave heating
SIMM	Slit interdigital micromixer
THF	Tetrahydrofuran
UHC	Unburned hydrocarbon
WCO	Waste cooking oil
XRD	X-ray diffraction

Symbol	Meaning	Units
a	Specific interfacial area	mm^{-1}
A	Pre-exponential factor	min^{-1}
A_{EI}	Peak area corresponding to methyl heptadecanoate	m^2
C_{EI}	Concentration of methyl heptadecanoate solution	$kg\ cm^{-1}$
d_h	Hydraulic diameter	m
J	Energy	$kg\ m^2\ s^{-2}$
K	reciprocal value of the equilibrium constant for the overall methanolysis reaction	1
m	Mass of sample, synthesised biodiesel	kg
M	initial molar ratio of TG to methanol ($=c_{Ao}/\ c_{Bo}$) = 1/6	1
p	Local pressure	Pa
p_v	Vaporising pressure	Pa
P_D	Power dissipated	$kg\ m^2\ s^{-3}$
U_g	Superficial velocity	$m\ s^{-1}$
U_l	Superficial coordinates	$m\ s^{-1}$
v	Velocity of fluid flow	$m\ s^{-1}$
V_0	Volumetric flow rate	$m^3\ s^{-1}$
V_{EI}	Volume of the methyl heptadecanoate solution	m^3

Dimensionless correlations

Ca	Cavitation number	Dimensionless
We	Weber number	Dimensionless

Symbol	Meaning	Units
Greek letters		
α	Total flow area on plate	m^{-1}
β	Hole diameter on orifice to pipe diameter	Dimensionless
β_0	Total flow area on orifice plate to the cross-sectional flow area of pipe	Dimensionless
Δ	$4 \bullet 3M(1-K) - (1+3M)^2 < 0$	1
ΔP	Pressure drop	Pa
ε'	Dielectric constant	Dimensionless
ε''	Dielectric loss	dimensionless
μ	Dynamic viscosity	kg m^{-1} s^{-1}
v	Kinematic viscosity	m^2 s^{-1}
ρ	Density	kg m^{-3}

Chapter 1 Introduction

Conventional energy are usually sourced from the combustion of fossil fuels such as coal, crude oil, and natural gas which are both non-renewable and non-sustainable. By estimation, non-sustainable fossil fuel reserves such as petroleum are consumed at an average rate of 94.1 billion barrels per day globally in 2020 [1]. World energy consumption is projected to increase from 575 quadrillions Btu to 736 quadrillions Btu between 2015 and 2040, representing a total energy consumption rise of 28%. Most of the increases are expected to be contributed by the non-OECD countries with a share of 41% in contrast to a 9% increment for OECD countries [2]. Mitigation obligations such as the Kyoto Protocol in 1997 and the Paris Agreement in 2015, have fostered the growth of renewable energy usage due to the pressing fossil fuel depletion conundrum. Under these treaties and agreements, countries are required to meet their emissions target through national measures to deal with mitigation of greenhouse gases. For example, recently the Paris Agreement rulebook has been finalised during the COP24 (Conference of Parties) organised by UNFCCC (United Nations Framework Convention on Climate Change) in Katowice, Poland, such that countries set out to keep global warming to well below 2°C above pre-industrial levels by 2100; and to limit the increase to 1.5°C [3].

Biodiesel has always been one of the primary alternative energy sources to overcome the fossil fuel depletion crisis, due to its attractive properties such as reduced emissions, renewability, and sustainability. Additionally, biodiesel can also be produced from renewable sources that are obtained naturally, such as plant oil, animal fat, and microorganism, which makes it a promising fuel from a sustainability perspective. Biodiesel is also proven to be more environmentally friendly, due to the reduced emissions during combustion and superior biodegradability when compared with fossil fuel [4,5].

According to the American Society for Testing and Materials (ASTM), biodiesel can be volumetrically blended with commercial fossil diesel up to 5% (B5), for combustion within an internal combustion engine (ICE) [6]. Alternatively, blends that consist of 6% to 20% biodiesel are popular choices. They represent a good balance of fuel performance and cost, which complies to the prescribed standards as specified by ASTM D7467 [7,8]. Blending allows biodiesel to be combusted in an ICE with minimal or without modification, hence reducing the consumption and dependency on fossil oil. Studies have also shown signs of a reduction in tailpipe emissions such as carbon monoxides (CO), nitrogen oxides (NO), unburned hydrocarbon (UHC), and soot via the usage of biodiesel-diesel blends [9,10].

1.1 Biodiesel as Renewable Fuel

Biodiesel is a viable candidate as an alternative fuel because it can be produced by renewable sources. First-generation feedstocks are usually derived from edible agriculture plants such as palm, soy, canola, corn, coconut, and sometimes animal fats [11,12]. The food versus fuel debate argues that the first generation feedstock introduces direct competition between the food industry and biodiesel production [13,14]. On the other hand, majority of the feedstocks for producing biodiesel production globally remains to be edible oil, due to greater accessibility and maturity of the processing technologies. On the other hand, second and third-generation feedstocks have only recently been popularised, as it is sourced from non-edible oil and microorganism lipid, respectively. They are designed to be cultivated in marginal, as well as barren lands which require lesser maintenance [14–16]. Moreover, since these plants do not directly compete with food, the use of non-edible oil in biodiesel production would relieve some of the environmental-social problems caused by the use of arable land [14–16]. Figure 1-1 shows the average edible oil crop production per capita for years 2000 to 2019.

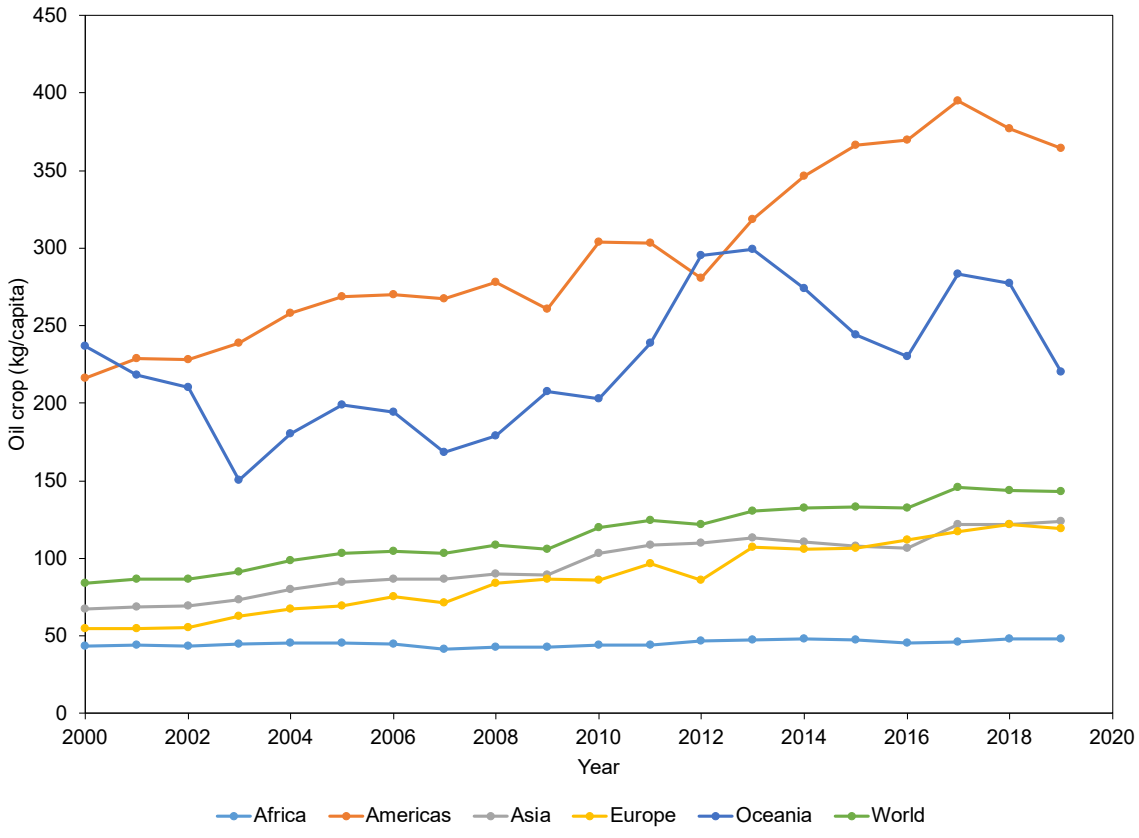

Figure 1-1. Worldwide oil crop production per capita from 2000 to 2019. Adapted and compiled from FAOSTAT [17].

The leading oil crop production continents are the Americas and Oceania, while the highest biodiesel producers are from the Americas, as shown in Figure 1-2. Additionally, biodiesel production for the Americas is more than that for both Asia and Europe combined in 2019. There is a positive correlation for the oil crop producers and biodiesel producing continents. This shows that oil crop in these continents is not used only for food, but also for potential biodiesel production. Overall, the worldwide oil crop production per capita has shown a progressive increase since the year 2000, which indicates that biodiesel production is still in demand.

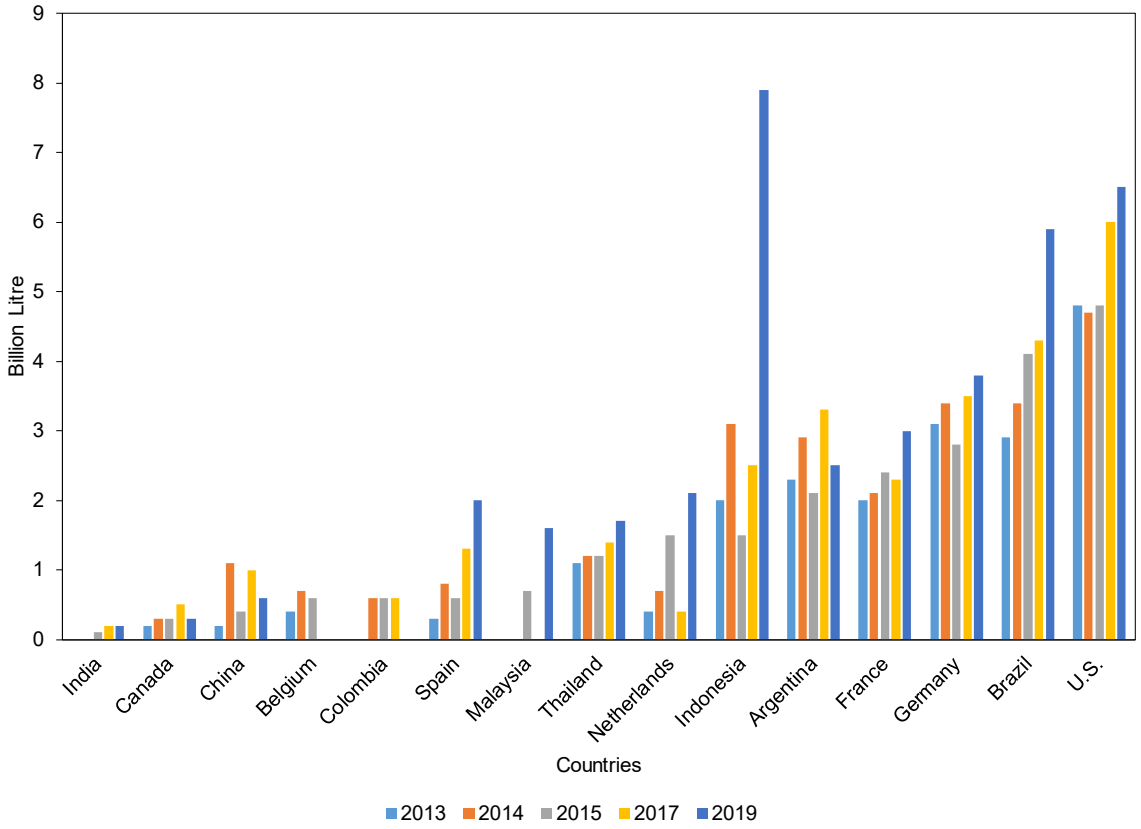

Figure 1-2. The largest biodiesel producers for the years 2013 to 2019.

For example, the Oceanian countries, such as Australia, New Zealand and Fiji, have passed legislation for mandatory biodiesel blending. For instance, in 2015 several local councils in Australia, namely, Townsville, Adelaide, Sydney, Newcastle City are operating at a higher blending ratio of B20 [18]. Similarly, in 2007, New Zealand introduced a Biofuel Bill which has resulted in a 3.35% obligated biodiesel blending [18]. Furthermore, a NZ$36 million Biodiesel Grants Scheme was introduced to encourage biodiesel production from the years of 2009 to 2012 [19].

1.2 Research Challenges

To date, biodiesel has been widely accepted as an alternative fuel for modern engines. Biodiesel production is presently dominated by batch-type reactor transesterification process. However, the influence of batch-type reactor conditions is often concluded based on the steady-state yield rates. Furthermore, the critical issue regarding the mass transfer of biodiesel transesterification and its kinetic rates have not been studied in-depth, lacking consideration from a transient reaction kinetics perspective that can potentially solve biodiesel's mass transfer issue in transesterification. The design of a novel reactor used for biodiesel production needs to quantify and benchmark in yield, conversion, and reaction kinetics. Besides, other design parameters such as the operating condition limitations, mass transfer coefficient, and kinetic models of the individual reactors have to be considered to justify a holistic comparison.

1.3 Scope, Scientific Question and Research Hypothesis

This study features the design and characterisation of traditional and novel biodiesel reactors (reticulated vitreous carbon and microchannel) to convert vegetable lipids to biodiesel. The study was aimed to establish an in-depth study of transesterification process with its respective operating conditions for the biodiesel reactors, combined with the investigation of the production performance of using novel materials as reactor agitator while utilising fluid dynamics principles (microturbulence and micro-level diffusion). The characterisation of biodiesel yield content and its glycerides enables estimating the chemical kinetics rates under the transient-state of transesterification, allowing a holistic comparison of different reactor designs. The outcome of these studies are then used to identify the potential stages of transesterification that has room for improvement, hence optimisation of the reactor's operating condition can be performed at different stages of transesterification.

Additionally, the scope of this study can be used to develop better practices in transesterification, particularly for stirred tank reactor which is widely used for research and industry, as well as reviewing other state-of-the-art biodiesel processing technologies and benchmarked them against stirred tank reactors.

The main scientific questions in the present study are stated as follows:

- How do factors perform at different stages of transesterification in batch processing?
- How do individual factors interact with each other from transient to steady-state in batch processing?
- How does RVC promote mass transport for biodiesel processing in batch processing?

- What is the chemical kinetics of RVC-assisted stirred tank reactor as compared to traditional reactors?
- What are the physical flow patterns and chemical interactions of biodiesel reactants in a microfluidics biodiesel reactor?
- How does a methanol droplet affect an in-situ biodiesel transesterification through the use of microfluidics biodiesel reactor?

The research hypotheses of this study are stated as follows:

- 'Pareto analysis can be used in a transient manner to identify the evolving effects of the operating condition in a standardised and comparable setting throughout transesterification.'
- 'Microturbulence generated by the reticulated and porous surfaces of the RVC agitator can promote mass transfer in transesterification of biodiesel.'
- 'Droplets of methanol in the stream of oil increases the contact surface between reactants, hence promoting mass transfer in transesterification through the use of microfluidics and peristaltic pumps.

1.4 Research Objectives

This study aims to investigate the mass transport issue in transesterification of biodiesel and strategies to increase the overall performance and reaction kinetics of novel and traditional biodiesel reactor.

Accordingly, the research study has the following specific objectives:

- To identify the limiting stages of the transesterification from the transient to steady-state.
- To evaluate the performance of transesterification factors from the beginning to the end of a process in a comparable manner.
- To study the interaction of a novel RVC-assisted stirred tank reactor using microturbulence to enhance mass transport of biodiesel production.
- To characterise the RVC reactor in terms of mass transfer and reaction kinetics.
- To study the physicochemical performance of microfluidics-assisted biodiesel reactor using optical and chemical analytics.
- To characterise the chemical kinetics using microfluidic-assisted biodiesel reactor through a transient approach.

1.5 Thesis Content

Several tasks were carried out for this research study, each discussed as individual chapters in this thesis. An overview of the study outline and the research publication outcome is, as shown in Figure 1-3.

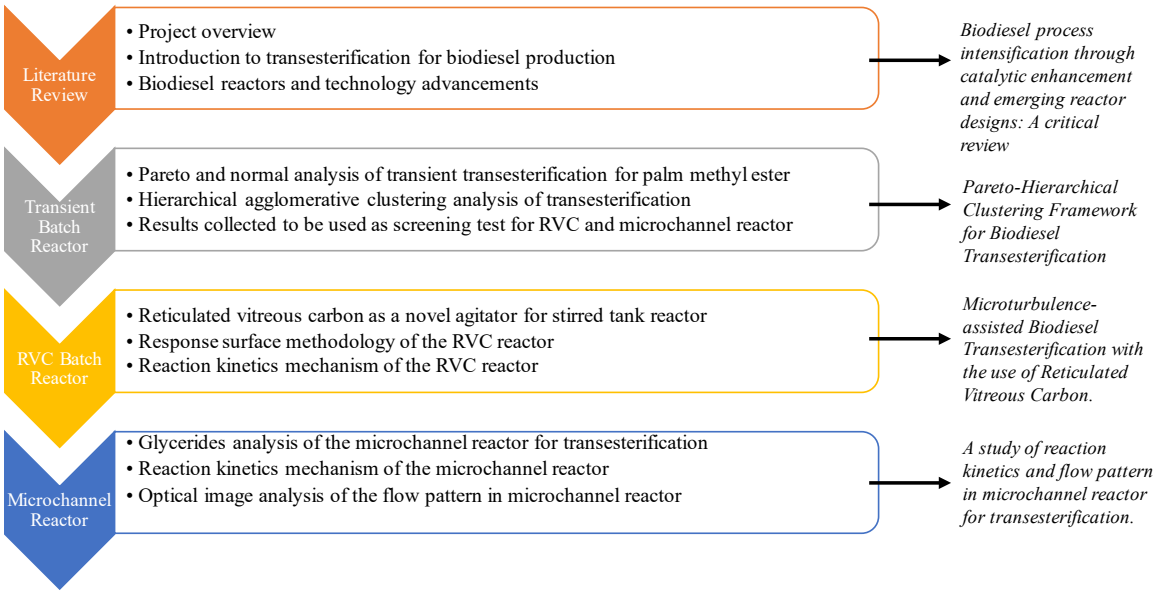

Figure 1-3. Structure of thesis chapters and publication outcome.

In this chapter, biodiesel's current research background as renewable energy is explained with the recent research challenges. Key objectives of this study are identified based on the research question and hypothesis proposed for individual work packages for the study. The novelty of the research is also addressed in the original contribution section to highlight the research outcome of this study.

In the second chapter, a comprehensive literature study was done to summarise the biodiesel processing technologies, which are employed currently including traditional and novel biodiesel reactors. Four different transesterification types were also discussed, namely, homogeneous base, homogeneous acid, heterogeneous base, and heterogeneous acid. Biodiesel properties, worldwide regulations and standards are reviewed and then compared to highlight their differences.

In the third chapter, a full factorial biodiesel experiment with 4 factors and 3 levels was carried out to study the transesterification process in a transient perspective. The 81 unique experiments combined with ten independent sampling intervals for data points were conducted to identify the significance of operating conditions throughout transesterification. The results were analysed using a combination of novel methodologies such as transient Pareto, hierarchical, and normal to draw quantitative and qualitative insights.

In the fourth chapter, microturbulence-assisted transesterification is demonstrated by integrating Reticulated Vitreous Carbon (RVC) agitator in a stirred tank reactor. The interaction of RVC and the mass transport of transesterification is characterised via (i) transient biodiesel yield from experiments at intervals to track the evolution of the reaction, (ii) the study of operating conditions such as temperature, RVC pores per inch, the rotational speed of perturbation, catalyst loading, and methanol to oil molar ratio at different levels to understand how the use of RVC impacts high-shear for enhanced mass transport. Additionally, a conventional stirred-tank reactor is used to benchmark against the RVC reactor's results to compare their respective performances from transient to steady-state of the transesterification process. The pseudo first-order and pseudo second-order kinetic models are tested for RVC reactor's transesterification feasibility while prediction models using glycerides concentration are constructed. Thermal imaging is used to analyse the heat transfer of the RVC reactor to identify how the change in temperature affects the transesterification process at different stages of the reaction.

In the fifth chapter, transesterification in the microchannel reactor is discussed. The main objective is to evaluate the feasibility of using a pseudo first-order prediction model for the glycerides of the transesterification. Optical image analysis is also included to evaluate how the flow pattern can alter the interaction of the liquid-liquid interface of methanol and oil and the yield of the biodiesel. The mass transfer coefficients of the reactor are evaluated and benchmarked against the batch-type reactor to understand their respective advantages and disadvantages.

In the sixth chapter, remarks and conclusion were discussed for individual chapters from above. This leads to a discussion of future work for each work package, as a form of continuation in the series to the working chapters.

1.6 Original Contributions

Significant contributions to the biodiesel research field are:

- Demonstrated the feasibility of implementing a quantitative transient-based analysis for the experiments where results are presented with qualitative insights.
- Identified the mass transfer limitation for biodiesel transesterification in a stirred tank reactor using hierarchical clustering at the physical-limiting and reaction-limiting stage.
- Outline the reactor operating condition's limitations using RVC as an agitator for mass transport enhancement in stirred tank reactor through factorial and response surface analysis.
- Identified the range of optimal pores per inch using RVC in biodiesel transesterification for agitation through microturbulence for physical-limiting and reactant-limiting stage.

- Integrated optical studies into conventional microfluidics biodiesel transesterification to determine the relationship of flow pattern with biodiesel yield.
- Identified the mass transfer and kinetic rates limitation for microchannel reactor for the reaction temperature range of 30°C to 60°C.

Chapter 2 Literature Review

2.1 Introduction

Transesterification is a popular approach for biodiesel production because it is straightforward as compared to the other production methods such as microemulsion of oil, pyrolysis, and fractional cracking [4]. Rudolf Diesel, the pioneer of diesel engine conducted experiments with straight vegetable peanut oil in diesel engine in the late 1890s. However, straight vegetable oil in diesel engines is deemed too viscous for combustion, which can cause huge variation in the ignition delay, causing inconsistency during the ignition cycle that leads to engine damage.

The aim of transesterification is to reduce the overall viscosity, without trading off the calorific value of fuel, since vegetable oil is less suitable to be used in an unmodified diesel engine [20]. Transesterification uses the triglycerides in oil or fat to react with alcohols such as methanol or ethanol in the presence of a catalyst. The conversion consists of three consecutive reversible reactions in series, each further breaking down the glycerides into a simpler form, forming a methyl ester group. Thus, at the end of the transesterification, three molecules of methyl esters and one molecule of glycerol are produced. In general, glycerol is produced as a by-product. However, glycerol can be refined to a higher purity due to its commercial value in the pharmaceutical, food, and cosmetic industries. The summary of the chemical reaction process is shown in Eq. 2-1 [4], and the overview of the transesterification production chain is shown in Figure 2-1. Conventional biodiesel production. Adapted from [21,22]..

$$\begin{array}{c} CH_2-OOC-R_1 \\ | \\ CH-OOC-R_2 \\ | \\ CH_2-OOC-R_3 \\ Triglycerides \end{array} + \underset{Alcohol}{3R_4OH} \overset{catalyst}{\longleftrightarrow} \begin{array}{c} R_1-COO-R_4 \\ R_2-COO-R_4 \\ R_3-COO-R_4 \\ Ester \end{array} + \begin{array}{c} CH_2-OH \\ | \\ CH-OH \\ | \\ CH_2-OH \\ Glycerol \end{array} \qquad \text{Eq. 2-1}$$

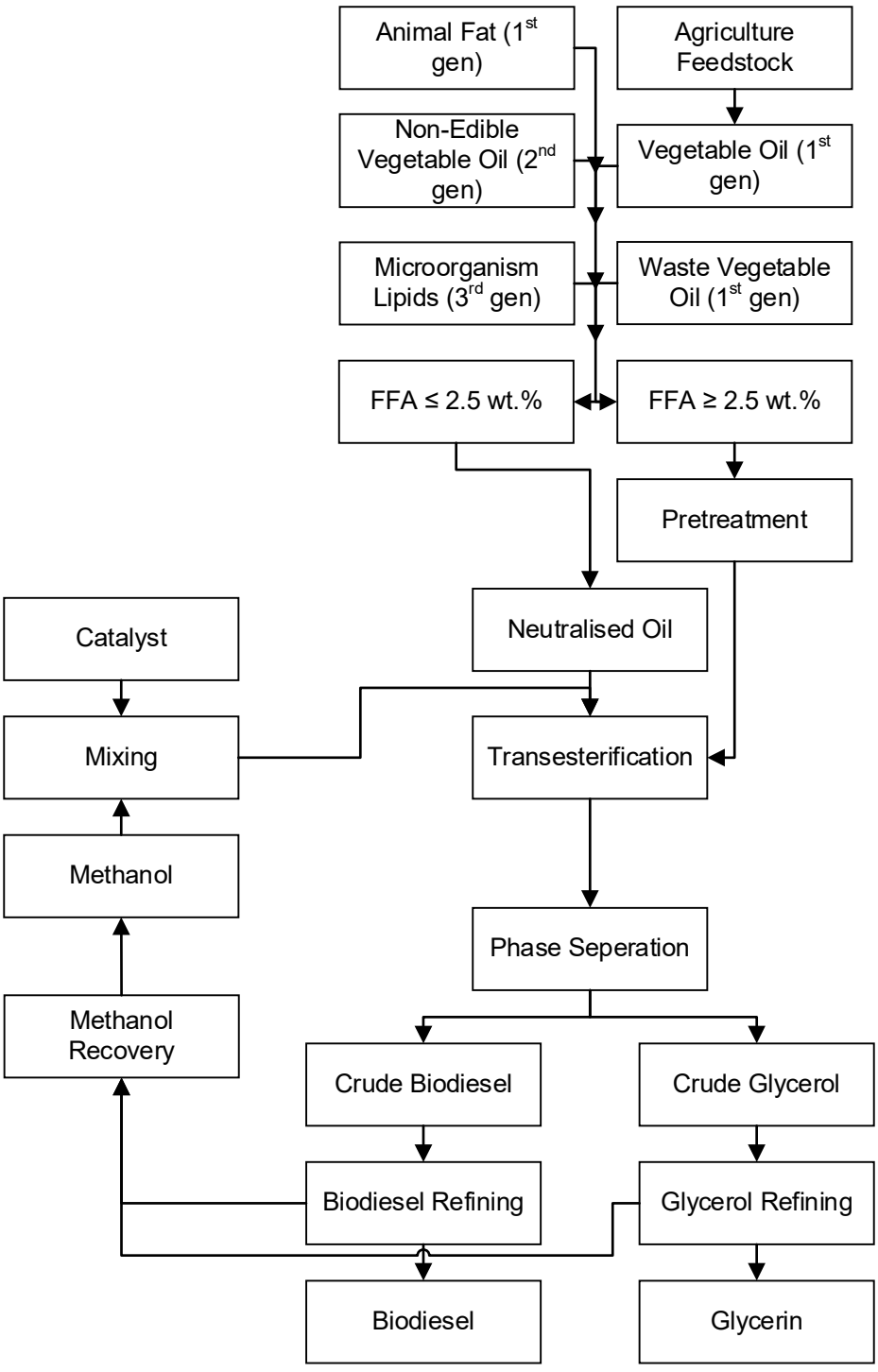

Figure 2-1. Conventional biodiesel production. Adapted from [21,22].

2.2 Biodiesel properties and fuel standards

Biodiesel is made of various saturated and unsaturated fatty acid methyl esters (FAME), such as lauric (saturated), palmitic (saturated), stearic (saturated), oleic (monounsaturated), and linoleic (polyunsaturated) as compared to fossil diesel which only consists of various hydrocarbons [23].

Biodiesel's quality has to be controlled during production to ensure it conforms to the standards specified by international bodies. The standards are designed to provide specifications for the physicochemical characteristics of the biodiesel. The two major international biodiesel standards are the American Standards for Testing Materials (ASTM D6751) and the European Standards (EN14214). The properties of biodiesel and fossil diesel are tabulated in Table 2-1.

Table 2-1. Technical properties of biodiesel, ASTM and EN standards Diesel No.2 (adapted from [4,24,25]).

Common name	**Biodiesel (EN 14214)**	**ASTMD975 Diesel No.2**	**EN 590:2004 Diesel**
Common chemical name	Fatty acid (m)ethyl ester	Mixture of various hydrocarbon	Mixture of various hydrocarbon
Chemical formula range	C_{14}-C_{24} methyl esters or $C_{15-25}H_{28-48}O_2$	$C_{12}H_{23}$ / $C_{10-15}H_{20-28}$	$C_{12}H_{23}$ / $C_{10-15}H_{20-28}$
Kinematic viscosity (mm^2/s at 313 K)	3.3-5.2	1.9-4.1	2.0-4.5
Density range (kg/m^3 at 288K)	860-894	850	820-845
Boiling point (K)	>475	453-613	-
Flash point (K)	420-450	>325	>328
Distillation (K)	470-600	422-644	523-633
Cetane number	48-65	40-55	>49

Table 2-1 shows that biodiesel's selected properties are used to define the physical and chemical makeup of the fuel. These properties are density, kinematic viscosity, cetane number, flash point,

oxidation stability, and iodine value. The selected parameters have also shown differences in the collection of standards from different regions.

2.2.1 Biodiesel policy, standards and emissions analysis

Biodiesel made from vegetable oil or animal fat has long-chain alkyl from either methyl, ethyl, or propyl esters. Often, waste cooking oil is post-processed to be used as a feedstock for biodiesel production derived from both vegetable and animal fat, hence the variance in the feedstock quality can be quite significant. As such, biodiesel's quality has to be controlled during production to ensure it conforms to the standards specified by international bodies.

Some biodiesel producing countries adopt the specification guidelines from ASTM and EN to define their biodiesel standards. The biodiesel standards mandated in the United States (ASTM), the Europe Union (EN), Malaysia, Australia, India (IS), Japan (JIS), Brazil (ANP), and South Africa (SANS) are tabulated in Table 2-2.

Typically, biodiesel standards have localised context to favour the predominant feedstock used in the production, storage, and usage of the biofuel for the countries. For example, the nature of Malaysia’s tropical climate requires a higher average storage temperature, hence a more stringent requirement for fuel flashpoint, as shown in Table 2-2. This helped in allaying fears in Malaysia when the country is planning to implement a mandatory blending of 20% biodiesel for fossil diesel by June 2021 [26], to exploit the country's potential to reduce unexported crude palm oil and improve energy security [27].

Table 2-2. Biodiesel standards for various countries [28–35].

Property	**Units**	**EN 14214:2008**	**ASTM D6751-12**	**Malaysia PME Standards 2014**	**Australia Biodiesel Standards 2003**	**India IS 15607:2005**	**Japan JIS K2390:2016**	**Brazil ANP 42**	**South Africa SANS 1935**
Ester content	%(m/m)	>96.5	-	>96.5	>96.5	>96.5	>96.5	-	>96.5
Density at 15°C	kg/m³	860-900	-	860-900	860-890	860-900	860-900	-	860-900
Viscosity at 40°C	mm²/s	3.5-5.0	1.9-6.0	3.5-5.0	3.5-5.0	2.5-6.0	2.0-5.0	Report[a]	3.5-5.0
Flash point	°C	> 101	>93	>120	>120	>120	>100	>100	>120
Cloud point	°C	-	Report[a]	-	-	-	-	-	-
Pour point	°C	-	-	-	-	-	-	-	-
Cold filter plugging point	°C	-	-	<15	-	-	Report[a]	-	(-)4/ (+)3[b]
Sulfur content	mg/kg	<10	<15 ppm[c] <0.05%[d]	<10	<10	<50	<10	<10	<10

Carbon residue (on 10% distillation residue)	%(m/m)	<0.3	<0.050 (100% sample)	-	<0.3	<0.05(100% sample)	<0.3	<0.05(100% sample)	<0.3
Acid value	mg KOH/g	<0.5	<0.5		<0.8	<0.5	<0.5	<0.8	<0.5
Sulfated ash content	%(m/m)	<0.02	<0.02	<0.02	<0.02	<0.02	<0.02	<0.02	<0.02
Water content	mg/kg	<500	<500	<500	<500	<500	<500	<500	<500
Total contamination	mg/kg	<24	-	<24	<24	<24	<24	Report[a]	<24
Cetane number	-	>51	>47	>51	>51	>51	>51	>45	>51
Copper strip corrosion (3hr at 50°C)	rating	Class 1	<No. 3	Class 1	No.3 or Class 1[e]	No. 1	No. 1	No. 1	No. 1
Oxidation stability, 110°C	hr	>8	>3	>10	>6	>6	>10	>6	>6
Iodine value	g iodine/100g	<120	-	<110	-	Report[a]	Report[a]	Report[a]	<140

Linolenic acid methyl ester	%(m/m)	<12	-	<12	-	-	<12	-	<12
Polyunsaturated (≥ 4 double bonds) methyl esters	%(m/m)	<1	-	<1	-	-	-	-	<1
Methanol content	%(m/m)	<0.2	<0.2	<0.2	<0.2	<0.2	<0.2	<0.5	<0.2
Monoglycerides content	%(m/m)	<0.7	<0.4	<0.7	-	-	<0.7	<1.0	<0.8
Diglycerides content	%(m/m)	<0.2	-	<0.2	-	-	<0.2	<0.25	<0.2
Triglycerides content	%(m/m)	<0.2	-	<0.2	-	-	<0.2	<0.25	<0.2
Free glycerol	%(m/m)	<0.02	<0.02	<0.02	<0.02	<0.02	<0.02	<0.02	<0.02
Total glycerol	%(m/m)	<0.25	<0.24	<0.25	<0.25	<0.25	<0.25	<0.38	<0.25
Phosphorus content	mg/kg	<4	<0.001% wt.	<4	<10	<10	<4	<10	<10
Group I metals (Na+K)	mg/kg	<5	<5	<5	<5	Report[a]	<5	<10	<5
Group II metals (Ca+Mg)	mg/kg	<5	<5	<5	<5	Report[a]	<5	Report[a]	<5

Distillation temperature, 90% recovered (T90)	°C	-	<360	-	<360	-	-	<360	-	

[a] Report as measured.

[b] For winter/summer.

[c] For S15.

[d] For S500.

[e] For <10 mg/kg sulfur.

2.2.2 Density

The density of biodiesel is measured via EN ISO 3675/12185 or ASTM D1298. The average biodiesel density is at 880 kg/m^{3,} which is roughly 7% greater than that of fossil diesel. The higher density of biodiesel is proven to be useful in fuel combustion as fuel injection is volumetric based. Thus, effectively higher fuel mass is injected to compensate for the lack of calorific value as compared to fossil diesel [9]. Generally, biodiesel has a 9% [36] lower mass calorific value than diesel due to its higher oxygen content [37]. However, when density is taken into account, biodiesel delivers 80.9-96.2% of fuel energy for each injection cycle, when compared with fossil diesel's fuel calorific value.

2.2.3 Kinematic viscosity

Kinematic viscosity is the measure of fluid flow property and plays a significant role in liquid fuel, as it affects the fuel spray atomisation from the fuel injection system [38]. Overall, a fuel with high kinematic viscosity is not suitable in diesel engine, as it will raise problems from an injection point of view such as clogging and contributes to poorer fuel spray atomisation [39]. The standards characterisation process is done by EN ISO 3104/14105 or ASTM D445. The viscosity of biodiesel is about 10-15 times greater than that of fossil diesel [40], because it has larger molecular mass and longer carbon chain length [41]. These issues are magnified under low environmental temperature, as viscosity is a temperature-dependent property which increases with the decrease in temperature. Table 2-2 shows that some countries like India and Japan have about twice as large an acceptable range as compared to other biodiesel viscosity standards. This suggests that more tolerance is given to viscosity since biodiesel is eventually blended with fossil diesel at low proportion, hence overall viscosity increment is negligible [31,33]. Recent advancement in the fuel injection system can also allow a greater tolerance of biodiesel blends in fossil diesel, accompanied by a higher fuel viscosity [42]. Additionally, the improvement in the fuel injection technology should also be considered for future biodiesel standards, in terms of setting a higher kinematic viscosity limit.

2.2.4 Flash point

Flash point is the measure of fuel flammability and is affected by chemical components of the fuel, such as the number of double bonds and carbon chain length [43]. The measuring procedure can be done by using EN ISO 2719/3679 or ASTM D93. Biodiesel is essentially non-flammable under sea-level atmospheric condition. The flash point is roughly 100 K higher than that of fossil diesel, which proves to be safer for storage and handling purposes. From Table 2-2, countries which include Malaysia, Australia, India shows a higher flash point limit (>120 °C) when compared with ASTM (>93 °C) and EN (>101 °C). This can be directly linked to the geographical influence since these countries are closer to the equator, hence the average atmospheric temperature of the countries are also higher.

2.2.5 Cetane number

Cetane number (CN) has an arbitrary scale because it was defined from the combustion qualities of hexadecane and 2,2,4,4,6,8,8,-heptamethylnonane cetane numbers of 100 and 15, respectively [38]. The EN ISO 5165 and ASTM D613 are used to determine the CN of a fuel. Higher CN represents better fuel ignition quality for diesel engine usage, which indicates shorter ignition delay after fuel injection [44]. On the contrary, fuels with lower CN can impede the cold start ability of an ICE, which will contribute to problems related to noise, vibration and harshness (NVH) [45]. The use of a low CN fuel is also accompanied by an increase in engine noise and exhaust emissions of hydrocarbons, particulate matters (PM), and nitrogen oxides (NO_x) [45]. Different feedstock produces biodiesel with a different CN as the high level of saturated fatty acid promotes higher CN [38]–[40]. The CN specifications are slightly lower for the American and Brazilian standards, at 47 and 45, respectively, as opposed to other countries at 51. The differences in limits are related to vehicle certification and emissions standards from their respective region [46,47]. Similarly, the improvement in fuel injection technology can also reduce the dependency of using fuel with higher CN, hence reducing its significance in determining the biodiesel standards [36], [38].

2.2.6 Oxidative stability

Oxidative stability determines the tendency of biodiesel to react with oxygen, which is usually tied to the quality of fuel since poor stability often leads to fuel deterioration. The general oxidative stability is measured via the Rancimat method specified by EN ISO 14112. The largest contribution to oxygen reactivity is the degree of unsaturation in methyl ester as they consist of highly reactive double bonds that are more susceptible to free radical attacks [48,49]. In contrast, biodiesel which contains a high proportion of saturated fatty acid will have better oxidative stability. Thus,

antioxidant treatment is not required. Therefore, a high percentage of linoleic and linolenic acids in vegetable oil such as soybean, sunflower and grape seed tends to cause poor oxidative stability. However, oxidative stability for the saturated fatty acid-rich palm, olive, and almond methyl ester, are generally better [23]. Among all the aforementioned biodiesel standards, ASTM has the least stringent limit of oxidative stability of 3 hours induction. On the other hand, major biodiesel feedstock exporter such as Malaysia, have started to increase the limit to 10 hours enabling storage under prolonged period.

2.2.7 Iodine values

Biodiesel with a high level of unsaturated fatty acid chains is accompanied by high iodine value (IV) [47]. Iodine does not react completely with the double conjugate bonds C18:3, a minor fatty acid constituent [50]. Thus, IV reflects the tendency of biodiesel to oxidise, hence biodiesel with high IV is more susceptible to oxidative degradation [23]. The conventional method to determine IV is through EN ISO 14111 in which IV is defined as grams of iodine that reacts with 100 g of the respective sample when iodine is added to the fatty acids [23]. Knothe *et al.*, Murphy *et al.*, and Serdari *et al.* [51–53] reported increasing unsaturation from fatty acids chain such as stearic, oleic, and linoleic acid is confirmed to reduce the CN and increase IV. Figure 2-2 shows that CN and IV against the degree of unsaturation.

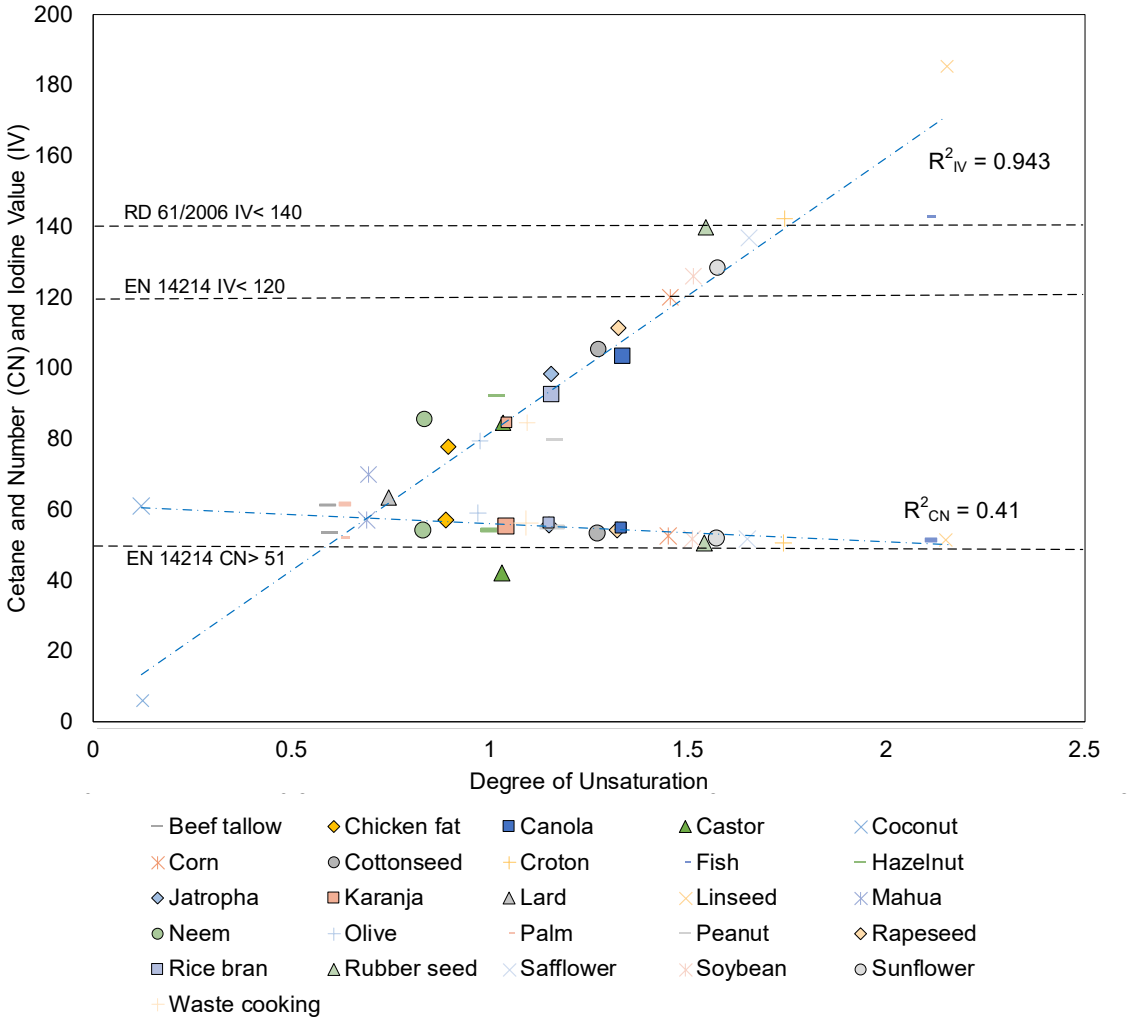

Figure 2-2. Cetane number and iodine value of biodiesels against the degree of unsaturation (adapted from [23,54]).

Based on the European Standards limit for IV and CN in Figure 2-2, biodiesel from various feedstocks will need to be within the upper limits of 120 and lower limits of 51 for IV and CN, respectively, to conform to the specifications. Therefore, lower IV indirectly indicates better ignition property since CN will be greater. Although some feedstocks which includes grapeseed, sunflower, and soybean are out of the defined limits for both IV and CN of EN standards, these feedstocks still comply with the RD 61/2006 standards.

2.3 Biodiesel processing methodologies

Currently, a collection of methodologies such as continuous stirred tank, microtubular mixer, microwave technique, and cavitation intensification has been reported to enhance biodiesel production through transesterification of vegetable feedstocks [55]. The process usually utilises the presence of a catalyst, either in homogeneous or heterogeneous forms to improve the rate of reactions [56]. These catalysts can cause huge environment impacts as they are often organic acids and bases that require downstream post-processing. To date, the number of catalysts discovered for biodiesel transesterification has increased significantly since the classification of homogeneous, heterogeneous, and enzymatic catalysts which draw attention away from physical intensifying methodologies. The main challenges in biodiesel transesterification remains with the mass transfer limit due to the reactants being immiscible by nature [57]. Consequently, transesterification process is also a reversible process which obeys the Le Châtelier's principle of chemical equilibrium therefore limiting the biodiesel yield.

2.3.1 Homogeneous base transesterification

Biodiesel can be produced with the aid of a base-type catalyst. Base-catalysed transesterification methods are widely used as they are relatively cheap, highly reactive, and effective at mild reacting conditions [58]. However, presence of water content and free fatty acid (FFA) in the feedstocks will encourage other chemical pathways such as esterification and saponification [59]. Base type catalysts promote the saponification process in biodiesel feedstock with the presence of FFA [58,60,61]. Eq. 2-2 shows the chemical pathway of saponification, where FFA reacts with hydroxide ion to form soap, leading to reduction in catalyst activity.

$$FFA + OH^- \rightarrow Soap + H_2O \qquad \text{Eq. 2-2}$$

Thus, transesterification with base catalyst are prone to soap formation for either high FFA content, or high catalyst loading, which ultimately leads to a decrease in biodiesel yield. Therefore, the prerequisite of using base-catalysed transesterification is to ensure biodiesel feedstocks have a FFA level of less than 2%, through refinement or pre-treatment resulting in production cost increase [62,63].

Table 2-3 tabulates the base catalyst transesterification of other published work with suggested FFA for the different feedstocks, organised by year. From it, it is observed that the FFA requirement has become more flexible, with an increase from less than a percent to more than or equal to three percent over the years. The observation can be explained by the heavy transition from the use of first generation feedstocks to second generation feedstocks, which are naturally high in FFA content. The use of high FFA feedstock are known to introduce complications when conventional base-catalysed

transesterification are used, as the FFA will react with the catalyst to produce soap as a by-product, which makes biodiesel and glycerine increasingly difficult to separate [12].

Table 2-3. Recommended level of FFA for homogeneous base type transesterification. Adapted from [58].

Feedstocks	**Feedstock Generation**	**Recommended FFA (wt. %)**	**Reference**	**Year**
Soybean	First	< 1	Freedman *et al.* [64]	1984
Edible oil and fats	First	< 0.05	Ma and Hanna [65]	1999
Review of edible oil and animal fat	First	< 1	Canakci and Van Gerpen [66]	2001
Review		< 0.5	Zhang *et al.* [67]	2003
Rubber seed oil	Second	2	Ramadhas *et al.* [62]	2005
Jatropha oil	Second	< 1	Kumar Tiwari *et al.* [68]	2007
Polanga oil	Second	≤ 2	Sahoo *et al.* [63]	2007
Karanja oil	Second	≤ 3	Sharma and Singh [20,69]	2008
Polanga oil	Second	≤ 2	Ong *et al.* [70]	2014

Besides, an additional separation process is required to remove the homogeneous base from the end product, usually through neutralisation of acids where trace amount of water is produced. This causes problems to the purification process. The drawbacks of using a homogeneous base catalyst in transesterification seems to be significant. However, this method is still preferred on an industrial scale production, because of its consistency in production and economic viability.

Table 2-4 summarised the homogeneous base type catalyst used in transesterification from the year of 2000 to 2018. In a study by Darnoko and Cheryan [71], transesterification of refined, bleached and deodorised (RBD) palm oil is carried out with KOH and methanol:oil ratio of 6:1 in a continuous-stirred tank reactor (CSTR), at a temperature 60 °C for 90 minutes. The fatty acid methyl ester (FAME) concentration (wt. %) varies from 80% to 90% when KOH catalyst loading from 0.5 to 1.2 wt. % is used, with the maximum FAME concentration at 1.0 wt. % catalyst. In another report by Dias *et al.* [72], transesterification of soybean, sunflower, and waste cooking oil (WCO) studied

using bases such as NaOH, KOH, and CH_3ONa. However, biodiesel yield suffered a decrease from 99.4% to below 96.5% when 1.2 wt. % of catalytic loading was used for all the mentioned catalysts, as compared to 0.8 wt. %. The observations are potentially due to the competing reaction of saponification producing soap as unwanted by-product. On the other hand, the catalyst type causes insignificant differences for biodiesel yield when the optimised loading was used.

Transesterification of animal fat such as duck tallow has been studied by Chung *et al.* using CSTR at 600 rpm with catalyst such as KOH, NaOH, and $NaOCH_3$, with KOH being the most effective [73]. Although the biodiesel conversion is relatively high, measured at 97% FAME content, the complete transesterification took 3 hours for the reaction to achieve chemical equilibrium. The operating parameters are KOH catalytic loading of 1 wt. %, 65°C reaction temperature, and 6:1 methanol to oil molar ratio.

Table 2-4. Homogeneous base catalysts for biodiesel transesterification.

Feedstock	Reactor parameters	Oil quantity	Catalyst	Loading (wt. %)	Alcohol	Alcohol:Oil molar ratio	Temperature (°C)	Time (min)	Yield (%)	Ref.	Year
Palm	Magnetic stirrer	500 g	KOH	1.0	Methanol	6:1	60	90	97.0	[71]	2000
Palm	Static mixer at 350 rpm	-	CH_3ONa	0.125[a]	Methanol	10:1	70	1	99.0	[74]	2004
Palm	Static mixer at 300 rpm	-	NaOH	0.2[a]	Methanol	6:1	70	1	99.0	[74]	2004
Rapeseed	Static mixer at 600 rpm	500 g	CH_3OK	1.0	Methanol	6:1	65	120	96.0	[75]	2008
Rapeseed	Static mixer at 600 rpm	500 g	CH_3ONa	1.0	Methanol	6:1	65	120	73.0	[75]	2008
Soybean	Magnetic stirrer	200 g	CH_3ONa	0.4	Methanol	6:1	60	60	93.0	[72]	2008
Sunflower	Magnetic stirrer	200 g	CH_3ONa	0.4	Methanol	6:1	60	60	95.0	[72]	2008
Waste cooking oil	Magnetic stirrer	200 g	CH_3ONa	0.4	Methanol	6:1	60	60	92.0	[72]	2008
Rapeseed	Static mixer at 600 rpm	500 g	KOH	1.0	Methanol	6:1	65	120	96.0	[75]	2008
Soybean	Magnetic stirrer	200 g	KOH	0.4	Methanol	6:1	60	60	94.0	[72]	2008
Sunflower	Magnetic stirrer	200 g	KOH	1.0	Methanol	6:1	60	60	93.0	[72]	2008
Waste cooking oil	Magnetic stirrer	200 g	KOH	0.8	Methanol	6:1	60	60	90.0	[72]	2008
Rapeseed	Static mixer at 600 rpm	500 g	NaOH	1.0	Methanol	6:1	65	120	82.0	[75]	2008
Soybean	Magnetic stirrer	200 g	NaOH	0.4	Methanol	6:1	60	60	97.0	[72]	2008

Sunflower	Magnetic stirrer	200 g	NaOH	0.4	Methanol		6:1	60	60	96.0	[72] 2008
Waste cooking oil	Magnetic stirrer	200g	NaOH	1.0	Methanol		6:1	60	60	90.0	[72] 2008
Duck Tallow	Static stirrer at 600 rpm	-	KOH	1.0	Methanol		6:1	65	180	97.0	[73] 2009
Palm	Constant total volume, with magnetic stirrer	303 ml	KOH	8.5	Dimethyl (DMC)	Carbonate	9:1	75	480	96.2	[76] 2010
Palm	Static mixer at max speed	-	Activated carbon/ CaO	5.5	Methanol		15:1	190	81	81.0	[77] 2011
Waste cooking oil	Magnetic stirrer at 600 rpm	-	NaOH	0.5	Methanol		7.5:1	50	30	96.0	[78] 2012
Fish oil	Magnetic stirrer at 600 rpm	50 g	KOH	0.5	Methanol		6:1	32	60	96.0	[79] 2013
Rapeseed	Preheated oil with magnetic starrier at 600 rpm	6 g	KOH	1.0	Methanol		6:1	60	60	91.0	[60] 2014
Palm	Magnetic stirring at 600 rpm	-	CH_3ONa	0.32	Methanol		5.48:1	55	40	85.0	[80] 2017
Waste rapeseed oil	5.5% FFA and 3 wt. % Water content with static mixer at 600 rpm	40 ml	CH_3ONa	3.0	Methanol		18:1	60	5	97.0	[61] 2018

[a] Catalyst loading in mol/kg.

2.3.2 Homogeneous acid transesterification/esterification

The main chemical pathway of biodiesel production with base type catalyst is through transesterification of triglycerides in vegetable oil. However, acid type catalyst can convert feedstocks to biodiesel via esterification of free fatty acids and transesterification of triglycerides concurrently. Eq. 2-1 and Eq. 2-3 show examples of esterification chemical processes of FFA-triglycerides-methanol to produce water, ester and glycerol.

$$\underset{FFA}{R-COOH} + \underset{Alcohol}{R_4OH} \overset{catalyst}{\longleftrightarrow} \underset{Water}{H_2O} + \underset{Ester}{R-COOH_2CR_4} \qquad \text{Eq. 2-3}$$

The acid catalysed biodiesel production avoids the saponification process which leads to soap formation and complicated downstream processing, hence increasing the final yield of biodiesel and reducing production cost [81]. This process allows cheaper feedstocks such as waste cooking oil, which is high in FFA content to be used for biodiesel conversion without pre-treatment. Additionally, feedstocks from edible oil such as palm, sunflower, and soybean; feedstocks from non-edible oils such as *Jatropha curcas*, and *Pongamia pinnata* (Karanja) which are high in FFA contents (>2%) in nature will also benefit from using acid catalyst [82,83].

Table 2-5 summarises the homogeneous acid type catalyst in biodiesel transesterification. Farag *et al.* [84] reported using a model oil which consist of 50% sunflower oil and 50% soybean oil to simulate the direct esterification of FFA. The effect of different acid catalyst type was found to be significant, with the percentage of FFA conversion in the decreasing order of H_2SO_4, HCl, AlCl3, $FeSO_4$, and $SnCl.H_2O$. In the optimum conditions, a 96.6% FFA conversion can be achieved at 6:1 methanol to oil molar ratio, temperature of 60 °C, H_2SO_4 catalytic loading at 2.5% w/w, agitation speed at 300 rpm, and reaction time of 60 minutes. The optimised conditions were replicated on home and restaurant cooking oil to compare the FFA conversion. Home domestic oil was observed to have virtually no conversion in the first 30 minutes reaction, while restaurant domestic oil is able to achieve more than 80% conversion at 90 minutes into the transesterification process. From it, waste cooking oil produced by restaurant seems to be more efficient to be used as a biodiesel feedstock when compared with home domestic oil, as the former are produced at a larger scale.

Aranda *et al.* [85] compared the use of four different homogeneous type acid catalysts, with methanesulfonic (CH_4O_3S) and sulfuric acid, (H_2SO_4) outperforming the rest in the esterification of palm oil by approximately 60% in yield difference. Although a 3:1 methanol to oil molar ratio was implemented, a conversion higher than 90% was able to be achieved, due to higher FFA proportion in palm oil, and esterification being the primary chemical reaction. Non-catalytic conditions were

also compared, where a small amount of H_2SO_4 catalyst at 0.01 wt. %, was able to promote from 30% to more than 70%.

Fauzi and Amin [86] reported using acidic ionic liquid, particularly 1-buthyl-3-methylimidazolium hydrogen sulfate ([BMIM][HSO_4]) for oleic acid esterification. The ionic liquid catalyst was used as a greener alternative as compared to conventional acid catalyst such as H_2SO_4, due to its reusable properties. Additionally, the post-processing does not produce acidic wastewater. The recyclability of catalyst was tested, with results showing that the ionic liquid can be recycled up to five times before the conversion reduces. Catalytic performance of ionic liquid as acid catalyst shows a conversion of 80.4% after optimisation, which is still relatively lower than those of conventional acid and base catalyst. The optimised transesterification parameters are reaction temperature of 87.3 °C, reaction time of 5.2 hours, methanol-oleic acid molar ratio of 8.6:1 and 0.063 mol catalyst loading.

Table 2-5. Homogeneous acid catalysts for biodiesel esterification.

Feedstock	Reactor parameters	Oil Quantity	Catalyst	Loading (wt. %)	Alcohol	Alcohol: Oil molar ratio	Temperature (°C)	Time (min)	FFA (%)	Conversion	Ref	Year
Palm	Static mixer at 500 rpm	307 g	H_2SO_4	0.1	Methanol	3:1	130	60		90	[85]	2008
Palm	Static mixer at 500 rpm	307 g	CH_4O_3S	1.0	Methanol	3:1	130	60		90	[85]	2008
Sunflower/soybean	Static mixer at 300 rpm	100 g	H_2SO_4	2.5	Methanol	6:1	60	90		96.6	[84]	2010
Sunflower/soybean	Static mixer at 300 rpm	100 g	HCl	2.5	Methanol	6:1	60	180		87.9	[84]	2010
Sunflower/soybean	Static mixer at 300 rpm	100 g	$AlCl_3$	2.5	Methanol	6:1	60	180		88	[84]	2010
Palm/rubber seed	Static mixer at 360 rpm	-	H_2SO_4	0.5	Methanol	15:1	65	180		95	[87]	2010
Oleic acid	Constant stirring rate	15.8 ml	1-butyl-3-methylimidazolium hydrogen sulfate (BMIM HSO_4)	0.063[a]	Methanol	9:1	87	312		80.6	[86]	2013

[a] Catalyst loading in terms of mol.

2.3.3 Heterogeneous base transesterification

Heterogeneous catalysts are viable candidates to replace homogeneous-type catalysts, as they are potentially more sustainable than the aforementioned homogeneous catalysts [88]. Biodiesel are generally produced by the homogeneous catalyst at a larger scale due to cheap and readily available catalyst such as NaOH, KOH, HCl, and H_2SO_4. However, the post-processing of homogeneous catalyst transesterification/esterification involves considerable amount of energy during the purification stage, owing to the need for catalyst removal [89]. Nonetheless, the disposal of wastewater generated have augmented the overall processing expenses [90]. Additionally, the catalysts often diffuse into the glycerol layer, reducing the quality of glycerol and reusability of catalyst.

As a result, heterogeneous catalysts are developed to take advantage of the ease of separation and reusability. The base solid catalysts are generally derived from the alkaline earth metals. The catalyst are oxides of elements such as Mg, Ca, Sr, and Ba which exhibit strong basic properties at their active sites, when used as a catalyst in biodiesel production. For example, the CaO alkali solid catalyst can be found in natural occurring resources, such as limestones, egg shells, and oyster shells which makes it a primary candidate in heterogeneous catalysed transesterification due to its cost effectiveness [91,92].

Table 2-6 summarises studies on heterogeneous basic type catalyst for biodiesel transesterification. Granados *et al.* [93], studied the deterioration of catalytic performance via air contact and reusability of catalyst, through characterisation technique such as X-ray diffraction (XRD), and evolved gas analysis by mass spectrometry (EGA-MS). The CaO catalyst was reported to be sensitive to H_2O and CO_2 in the atmosphere, and results indicate that fresh solid CaO are susceptible to hydration to form $Ca(OH)_2$ and carbonation to form $CaCO_3$, reducing the catalytic activity of CaO in transesterification. As a result, evacuation of hydrated and carbonated CaO at elevated temperature is able to reactivate the catalyst, hence improving the biodiesel yield in the transesterification process. The CaO catalyst treated at 700 °C is able to achieve a yield of 94% for biodiesel, and retains an 81% conversion after eight consecutive uses. However, it was discovered that active species from solid catalyst has a tendency to leach into the reactants, resulting in a performance decline after several transesterification cycles.

Table 2-6. Heterogeneous basic catalysts for biodiesel transesterification.

Feedstock	Reactor parameters	Oil Quantity	Catalyst	Calcination Method	Loading (wt. %)	Alcohol	Alcohol: Oil molar ratio	Temperature (°C)	Time (min)	Yield %	Ref	Year
Canola	50 ml pressurised batch reactor	-	MgO	500 °C	3	Methanol	20:3	190	120	82.8	[94]	2003
Canola	50 ml pressurised batch reactor	-	t-MgO	PDMS-PEO, 500 °C	3	Methanol	20:3	190	120	98.2	[94]	2003
Sunflower	Static mixer at 1000 rpm	50 g	CaO	700 °C	1	Methanol	13:1	60	90	60.0	[93]	2007
Sunflower	Static mixer at 1000 rpm	50 g	CaO	700 °C	1	Methanol	13:1	60	90	>90.0	[93]	2007
Soybean	Static mixer	100 ml	$CaCO_3$	He gas at 900 °C	0.8	Methanol	12:1	-	120	93.0	[95]	2008
Soybean	Microwave 1100 W	15 g	SrO	-	1.84	Methanol	3.7:1	60	0.67	97.0	[96]	2011
Waste cooking oil	Microwave 1100 W	15 g	SrO	-	1.84	Methanol	3.7:1	60	0.67	99.0	[96]	2011
Waste cooking oil	Microwave (2.45 GHz) and Ultrasound irradiations (25kHz) (100W/100W)	-	BaO	-	0.75	Methanol	6:1	73.6	2	94.7	[97]	2014

Another improved version of the CaO catalyst was done by co-precipitation method of a lanthanum-based calcium oxide ($CaO\text{-}La_2O_3$) [98], resulting in a mixed solid oxide which was demonstrated to be feasible for solid base transesterification, using crude jatropha oil as a feedstock. Catalytic performance of the Ca-La catalyst was measured through studying the reaction conditions, which enable the results to characterise the physico-chemical properties of the catalyst. Results of the transesterification activity using different Ca:La atomic ratios of the $CaO\text{-}La_2O_3$ catalyst showed that pure LaO_2O_3 catalyst has zero effect on transesterification. However, further increment of CaO loading from 2 wt. % to 4 wt. % showed that the CaO active phase enhances FAME yield from 52% to 82% due to an increase in basicity, which is directly correlated to catalyst activity. Subsequently, the reusability and regeneration of catalyst can be done by a simpler alkali solution washing, without significant leaching of catalyst, hence retaining majority of its catalytic performance.

Jeon *et al.* [94] used magnesium oxide, (MgO) to perform base-catalysed transesterification. In this study, it was reported the synthesis of a mesoporous MgO using an amphiphilic comb-like copolymer, PDMS-PEO to alter the morphological structure of MgO, hence creating a templated MgO (t-MgO). The canola oil transesterification process via t-MgO is then compared to the non-templated MgO (nt-MgO). The structural differences in pores and surface area were also observed using SEM imaging and TEM analysis, with the t-MgO exhibiting high level of interconnected porous structure with bimodal pore distribution. This results in improved mass transport to the surface of active catalytic site on t-MgO. Transesterification results from t-MgO shows that a maximum biodiesel yield of 98.2% is obtained after 2 hours of reaction at a temperature of 190 °C, using a methanol to oil molar ratio of 20:3, and a 3.0 wt. % catalytic loading.

2.3.4 Heterogeneous acid transesterification

Despite all of the advantages of using homogeneous-type catalysts in transesterification, it is costly to separate and complicated to recover the liquid catalysts when they form a single phase with the end products. On the contrary, solid acid catalysts are superior, as compared to homogeneous catalysts and base type catalysts. This is because they are easier to be separated from the end products, which leads to better reusability and recovery of the solid catalyst, hence effectively lowering the processing cost [99].

There are several prerequisites for the selection of a strong heterogeneous acid catalyst. These are properties that favour the esterification process, as tabulated in Table 2-7. Examples of typical heterogeneous acid catalyst are shown in Figure 2-3.

Table 2-7. Criteria, advantages, and disadvantages of an ideal solid acid catalyst.

Criteria of an ideal solid acid catalyst	Advantages of an ideal solid acid catalyst	Disadvantages of an ideal solid acid catalyst
• Strong Brønsted acid group that are highly polarised hydroxyl group, at the surface of catalyst.	• Insensitive to free fatty acid and moisture which enables the use of a lower grade oil.	• Catalytic activity of solid base is greater than solid acid, hence operating conditions such as reaction temperature and pressure for using a solid acid catalyst are usually higher.
• Strong Lewis acid group which are actively promoting transesterification, provided that the active sites are not poisoned by water.	• One-step process where esterification and transesterification can simultaneously take place.	• The tendency of acid leaching into the end product, particularly the sulfate group, H_2SO_4, into reactant, promoting homogenous catalytic activity that interferes with the measurement.
• Unique interconnected large pore structure and texture.	• Eliminates the need of washing for the biodiesel, while reducing potential corrosion issue downstream of production.	

• A hydrophobic catalytic surface.	• Easier separation of catalyst with the end product, hence more efficient for the recovery process of catalyst that also allows for extensive reusability. • For the continuous flow-type reactor, the end products separation and purification costs can be minimised. • Avoid deactivation, poisoning and leaching of acid sites.

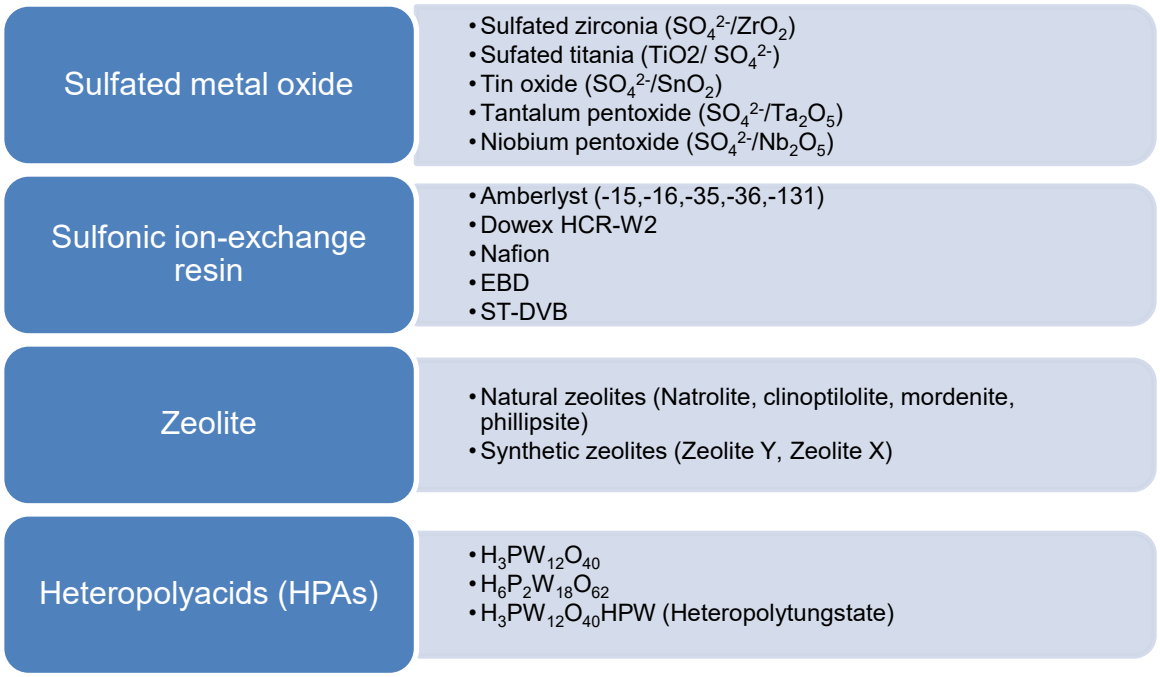

Figure 2-3. Typical heterogeneous acid catalysts families for biodiesel esterification and transesterification.

Table 2-8 summarises the experimental studies using heterogeneous acid in the transesterification process. Sulfated metal oxide is one of the most popular solid acid catalysts, as it is classified as a superacid which heavily favours the transesterification process. Superacids of such are more environmentally friendly when used for esterification of biodiesel and can be obtained easily [100]. Zirconium oxide (ZrO_2) as a support for catalytic scaffolding has also been studied under the sulfated metal oxide group. Positive influence was observed from its acidic catalytic behaviour, with simultaneous oxidising and reducing properties on the surfaces [101]. Zirconium oxides are generally impregnated with sulfuric acid to be converted into sulfated zirconia, SO_4^{2-}/ZrO_2. Alternatively, the surface acidity can also be modified through the introduction of other metal oxides such as sulfate or tungstate to provide greater catalytic activity.

Table 2-8. Heterogeneous acid catalysts for biodiesel transesterification.

Feedstock	Reactor parameters	Oil quantity (ml)	Catalyst	Catalyst preparation	Loading (wt. %)	Alcohol	Alcohol: Oil molar ratio	Temperature (°C)	Time (hr)	Yield %	Ref	Year
Soybean	Sealed capillary tubes in preheated furnace	0.3	ETS-10 zeolite	Calcined at 500 °C in flowing air at a heating rate of 4 °C/min and held for 10 hr.	0.03[a]	Methanol	6:1	120	24	94.6	[102]	2004
Waste cooking oil	Magnetic stirrer at 1500 rpm	-	Amberlyst-15 (ion-exchange resins)	Wet form resins dried in oven for 12 hr at 110 °C. Amberlyst-15 with high crosslinking, catalyst surface area of 53 m^2/g, 33% porosity, average pore diameter of 30 nm.	2.0	Methanol	20[b]	60	3	45.7%[c]	[103]	2008
Waste cooking oil	High temperature and pressure in an autoclave	-	Sulfated zirconia (SO_4^{2-}/ZrO_2)	Zirconium hydroxide powder with H_2SO_4, dried at 110 °C then calcined at 600 °C.	3.0	Methanol	9:1	120	4	93.6	[101]	2008
Waste cooking oil	Stainless steel batch reactor with magnetic stirrer	300	Sulfated tin oxide SO_4^{2-}/SnO_2)	Amorphous tin oxide in H_2SO_4 solution for 6 hr, then calcined at 300 °C for 2 hr.	3.0	Methanol	15:1	150	3	92.3	[104]	2009
Sunflower	Mechanical stirrer	100	Fly-ash Na-X zeolite	Ion exchange with potassium acetate, dried at 110 °C for 2 hr, then calcined at 500 °C for 2 hr.	3.0	Methanol	6:1	65	8	83.5	[105]	2012
RBD Palm	Continuous stirring at 500 rpm	125	Natural zeolite	Zeolite impregnation with KOH for 24 hr, dried at 110 °C for 24 hr, calcined at 450 °C for 4 hr.	3.0	Methanol	7:1	60	4	95.01	[106]	2013
Oleic acid	Batch reactor with magnetic stirrer	100	Sulfated zirconia (SO_4^{2-}/ZrO_2)	Hydrated zirconia with aqueous ammonia solution dried at 100 °C, then calcined at 600 °C for 4 hr.	0.5[a]	Methanol	40:1	60	12	90.0	[107]	2013

Rapeseed/oleic acid mix	Sealed pressure endurance tubes with stirring	-	ST-DVB (cation-exchange resin)	Resin ball swelled in dichloroethane at 60 °C, then mixed with H_2SO_4. Catalyst surface area of 185 m^2/g, average pore diameter of 9.7 nm.	10.0	Methanol	15:1	100	3	97.8%[c]	[108]	2015
Oleic acid	Batch reactor with continuous stirring	50	HY kaolin zeolite	NaY zeolite in ammonium nitrate at 100 °C for 4 hr, dried at 100 °C for 6 hr, stirred in oxalic acid for 8 hr, dried again at 100 °C , then calcined at 550 °C for 5 hr.	5.0	Ethanol	6:1	70	1	85.0	[109]	2016

[a] Catalyst loading in grams.

[b] Percentage of volume (vol. %).

[c] Percentage in terms of oil conversion.

Patel *et al.* [107] investigated the synthesis of sulfated zirconia and the biodiesel conversion of oleic acid, which is used to simulate the esterification process of free fatty acids. Catalytic loading of sulfated zirconia has been observed to have a positive correlation with biodiesel yield. For the concentration of 1.0 N SO_4^{2-}/ZrO_2 (0.1 g), an initial yield of 18% was achieved. Using the same operation condition, further improvement on the catalyst was done by using a second stage calcination process at 600 °C for an extended 4 hours, which improved the esterification yield to 40%. However, the reaction rates of the esterification process is considered to be relatively poor, even when extreme operating conditions are implemented, such as using an alcohol to oil molar ratio of 40:1, at a reaction temperature of 60 °C, and 4 hours of reaction time. The esterification process was optimised through parametric study of reaction time and catalyst loading, which leads to an optimised operating condition of 0.5 g catalytic loading at 12 hours reaction time, achieving 90% yield. The catalyst is then regenerated to determine its reusability in the esterification process. A reduction of 3% yield for one-cycle esterification on oleic acid was observed. The calcined SO_4^{2-}/ZrO_2 was also used to study the effect of the simultaneous esterification and transesterification process in waste cooking oil and jatropha oil, resulting in a conversion of 82% and 80%, respectively. This proves that SO_4^{2-}/ZrO_2 can be useful in esterification, transesterification, and even simple regeneration process without significant loss in catalytic strength. In all, catalytic activity for heterogeneous acid catalysts are still relatively weaker when compared with its homogeneous counterparts.

Doyle *et al*. [109] proposed the synthesis of zeolite catalysts with kaolin clay, which can be used in the esterification process. This is a favourable catalyst candidate because of its low cost, and also structural advantage of having both mesoporous [110] and microporous [111] frameworks. Zeolite Y was prepared as a scaffold, and then impregnated with ammonium nitrate to form HY zeolite to be used as a catalyst for esterification. A maximum yield of 85% was achieved by using an operating condition of 1-hour reaction time, 6:1 molar ratio of ethanol/oleic acid, and 70 °C reaction temperature. The reusability study of the catalyst showed a decrease in conversion from 85% to 77% after a single cycle. The catalytic performance reduction is speculated to be related to the adsorption of water at the active site of the catalyst. The esterification process using the HY zeolite produced from kaolin clay was then compared against a commercially sourced HY zeolite catalyst. The HY kaolin zeolite was able to perform better at the first hour of the reaction, but the conversion reduces to the same as compared to the commercial sample after two hours. The unique low Si/Al ratio of HY kaolin zeolite catalyst contributed to a higher catalytic activity at an earlier stage of free fatty acid esterification, due to the higher density of acid sites and greater Brønsted acid strength.

Ion-exchange resin catalysts are also heterogeneous acid catalysts that are proven to be effective in biodiesel production, due to their strong cross-linked structures which exhibit acidic active sites that are used in esterification and transesterification reactions [112]. Additionally, these resins swell under the presence of polar components, leading to a change in the magnitude of cross-links that will determine the rigidity of the resins [103]. High swelling capacity is also correlated to lower crosslinking [90-91], which indicates an improvement in the surface area and pore diameter of the resins. This will result in a higher density of acid sites for the resin to facilitate the esterification process.

Shibasaki-Kitakawa *et al.* [114] studied the use of Diaion PK208LH, which is a cation-exchange resin with low crosslinking density. The resin was used to study the conversion of biodiesel, using waste rice bran acid oil as feedstock. Since esterification of FFA in the acidic oil produces moisture as a by-product, the concentration of water and the reaction rates of conversion were first correlated. The results showed that the use of resin catalyst with a water concentration of less than 20 wt. % does not change the FFA conversion and FAME formation rates. The moisture is not required to be completely removed for the pre-treatment of catalyst, since 20 wt. % is a relatively high upper limit for water content.

2.4 Biodiesel reactors and technology advancements

2.4.1 Continuous stirred tank reactor (CSTR)

Continuous stirred tank reactor (CSTR) is an extension of the batch-type reactors, which has a similar fundamental agitation mechanism. Batch processing is one of the most commonly available type of reactors, which enables biodiesel to be produced in a single batch over a period of time [71,72,74,84]. However, through the use of CSTR, continuous production of biodiesel can be achievable using a simple setup. Nevertheless, large scale production of biodiesel that utilises batch processing technique requires large reactor volumes, which increases capital investment, making it less economically viable. Furthermore, the batch-to-batch variation is also a common issue in biodiesel batch processing, since the quality of biodiesel tends to differ slightly for every processing batches. The CSTR technology is straightforward to scale up as compared to other types of reactors. All variation of CSTR shares similar concepts of utilising physical disruption through mechanical stirring. The mechanical stirrer is physically attached to a motor externally to provide adequate mixing and energy input to the system. The reactants and products are simultaneously added and removed, to maintain a steady-state continuous system in a CSTR. The system should achieve chemical equilibrium in the steady-state condition, where there is no net change in the concentration of the oil-methanol-biodiesel-glycerol mixture, which is done by constant monitoring and maintaining the operating parameters. Table 2-9 summarises the continuous stirred tank system, with varying designs and operating conditions.

Table 2-9. Continuous stirred tank reactor for biodiesel production.

Feedstock	Reactor parameters	Catalyst	Catalytic Loading (wt. %)	Alcohol	Alcohol: Oil molar ratio	Temperature (°C)	Reaction time (min)	Yield (%)	Ref	Year
Palm	CSTR is activated when steady-state is achieved, using 500 g oil with 20 vol. replacement.	KOH	1	Methanol	6:1	60	60	97.3	[115]	2000
Palm	CSTR with 6-stages at 300 rpm and production rate of 17.3 l/h, using a power consumption of 0.6 kW/m^3.	NaOH	1	Methanol	6:1	60	6	97.6	[116]	2008
Palm	CSTR with 4-stages (303-706 rpm) and production rate of 8.3 l/h.	H_2SO_4	1.7[a]	Methanol	3:1	60	20	83.7	[117]	2009
Sunflower	Single stage CSTR at 800 rpm, oil feed at 1.8 ml/min	Immobilised lipase enzyme	40[b]	Methanol-buffer solution	0.6[c]	30	275	81.0	[118]	2017

[a] Catalyst loading in percentage of volume (vol. %).

[b] Catalyst loading in grams.

[c] Alcohol feed at 0.6 ml/min continuously.

Typically, CSTR involves more than a single stage, where the configuration of the system consists of a reactor and a phase separator as shown in Figure 2-4. In the beginning stage of the reactor, alcohol and triglycerides are allowed to be partially converted into biodiesel. This is then followed by a glycerol removal step for the reacted mixture in the second stage of CSTR, which is used to promote the forward reaction of transesterification through shifting of the chemical equilibrium. The multi-stage reactor is able to ensure the complete conversion of oil through the highly efficient production and separation system.

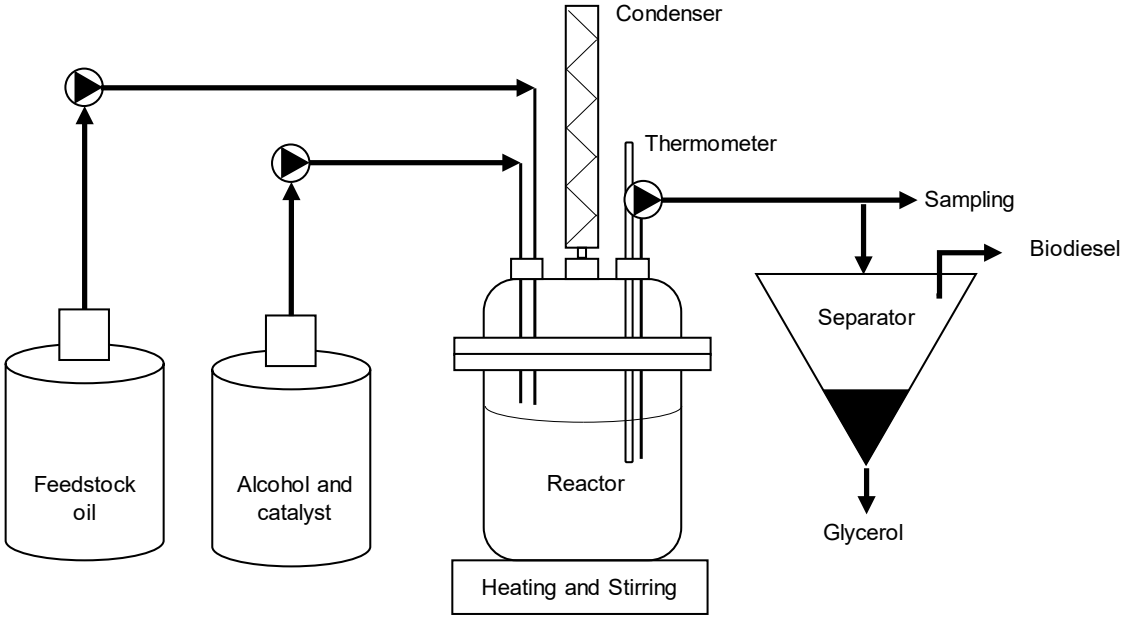

Figure 2-4. Schematic drawing of a single reactor CSTR. Adapted from [115].

Darnoko and Cheryan [115] produced biodiesel through a two-stage CSTR system with RBD palm oil. The second stage of the prototype developed is a separator which is used for glycerol removal. The operation of the CSTR requires the batch mode to be enabled over a residence time of 40 minutes during the initialisation. This is then followed by activating the feed pumps to deliver the feedstocks and methanol at a consistent rate. Another feed pump is then used to move the mixture to the separator, where glycerol is later removed through phase separation. During the initialisation stage, 82.7% biodiesel yield was achieved. However, the final yield suffered a significant drop, only achieving a 58.8% yield after a steady-state of five volume replacement cycles in the continuous mode. Optimisation was also performed by changing the residence time during batch mode, and increasing the number of volume replacements to allow better stability in the continuous transesterification system. A maximum yield of 97.3% is achieved in steady-state, after using the optimal conditions of 20 volume replacement at a residence time of 60 minutes, 6:1 methanol to oil molar ratio, using a 1 wt. % catalyst loading, and 60 °C reaction temperature.

A multi-stage CSTR system was studied by Leevijit *et al.* [116] at a larger scale, involving a 6-stage CSTR with a capacity of 2.272 L. Initially, the feed pumps were allowed to fill the reactor, and the flow rates were adjusted until the desired biodiesel yield were achieved. The residence time of the reaction was controlled by the combined flow rates of feedstock oil and methanol, whereby residence time range of 3 to 12 minutes was tested, with a stirring speed that varied between 100 and 800 rpm. The result suggests that the biodiesel yield can be improved with higher residence time and stirring speed. The lower limit of biodiesel yield can be increased with increasing residence time, while increasing stirring speed showed diminishing influence towards yield as reaction time progresses. The highest stirring speed of 800 rpm negatively impacts the biodiesel yield, reducing the average yield from 97.5% to 96.2%. For the residence times between 6 and 12 minutes, biodiesel yield was able to achieve 97.5–99.2% with a production capacity of 8.5–17.3 L/hr. The power consumption of each stirrer is rated at 0.2, 0.6, 2.8 kW/m^3 for stirrer speeds of 200, 300, and 500 rpm, respectively.

Prateepchaikul *et al.* [117] used a CSTR system with a series of four CSTR reactors stacked together. The CSTR each has a six-bladed turbine attached, as shown in Figure 2-5.

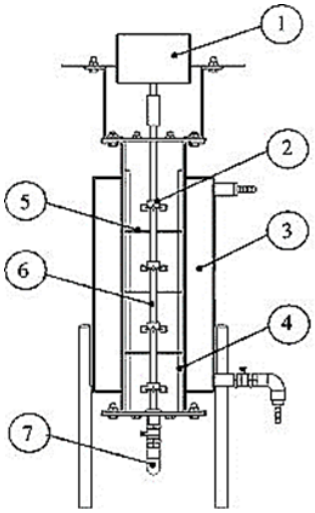

No.	Apparatus
1	Motor
2	6-blade turbine
3	Jacket
4	Baffle
5	Separate tank plate
6	Axle
7	Feeding hole

Figure 2-5. Schematic of CSTR impellers in series. Adapted from[117].

The stacked CSTR has a smaller reactor footprint as compared to the CSTR in multiple stages. They are also relatively easier to be integrated into the feed pump system, since pressure drop is reduced as compared to a multiple stage CSTR. The internal baffles are used to enhance the mixing process to prevent dead volume which can be generated by vortex, hence reducing mixing efficiency. Additionally, the disk turbine is also capable of producing larger turbulent using radial flow, by inducing a high shear force at its edge. Raw, un-degummed, mixed crude palm oil which contains 8–12% FFA was used as feedstock. Acid-catalysed esterification process was used to produce the biodiesel. During the esterification with the FFA, significant amount of water is produced as a by-

product which interferes with the conversion of biodiesel. Therefore, gravity separation is required after the extraction of product from CSTR to remove the water content. The esterified oil and acidified water obtained from the gravity separator is found to be at 83.7 and 16.3 vol. %, respectively. However, if scaling up is done for the stacked CSTR set up, a gravity separator of a much larger scale will also be required. This would result in an increased processing time for the gravity separator. Alternative, a centrifugal separator can be employed to significantly improve the separation process.

2.4.2 Microchannel reactor

Transesterification reaction often suffered from issues such as low mass transfer and low effective surface area of reactants, which lead to lowered reaction rates. Microchannel reactors or sometimes as known as microreactors, are designed to overcome the issues of CSTR [119]. Microreactors are intensively researched and can be categorised as, microtubular reactors, zig-zag microchannel reactors, etched microchannel reactors, and microfluidic laminated lab chip. Microchannel reactors utilise a meso or micro scale geometry for their reacting channels, which can have different hydraulic diameters in the range of 10–1,000 μm. The narrow channel enables a high surface-to-volume ratio transesterification process, which effectively decreases the diffusion length of reactants, hence increasing the mass transfer to promote reaction rates. Microreactors typically have approximately a 10,000–50,000 m^2/m^3 surface-to-volume ratio, which are quoted to be 10–50 and 100–500 times greater when compared with conventional laboratory vessels of 1,000 m^2/m^3 and production vessel of 100 m^2/m^3, respectively [120]. Thus, microchannel reactors are often selectively operated under milder conditions, since they have superior rates of reaction, which reduce the energy requirement for the transesterification process.

In general, microchannel reactors have relatively smaller footprints, as compared to other types of biodiesel reactors. Microchannel reactors utilise microfluidic devices, such as a micromixer for its agitation process. Since most of the chemical reaction for microreactors involve mixing of two or more fluids, the use of a micromixer can enhance the mixing efficiency at microscale [121]. Micromixer can be either active or static type mixer of various geometries. Active mixing actuators are usually powered externally by electric or magnetic excitation, whereby static mixers involve passive mixing through the use of pressure differences. Both type of mixers utilise different mixing principles, defined by their operations at different ranges of production capacities and mixing speeds [122]. Two types of intensification can occur in the micromixer [122], (i) heterogeneous mixing created by convection, (ii) homogeneous mixing at the molecular level which is driven by diffusion of adjacent domains. The common types of micromixer are namely the T-junction, J-junction, Y-junction, and cross-junction as shown in Figure 2-6. These mixers are used to direct the flow of

reactants into the main reacting channel, where mixing will occur through the aforementioned intensification methods. A summary of microreactor research using various feedstock accompanied with their performances is tabulated in Table 2-10.

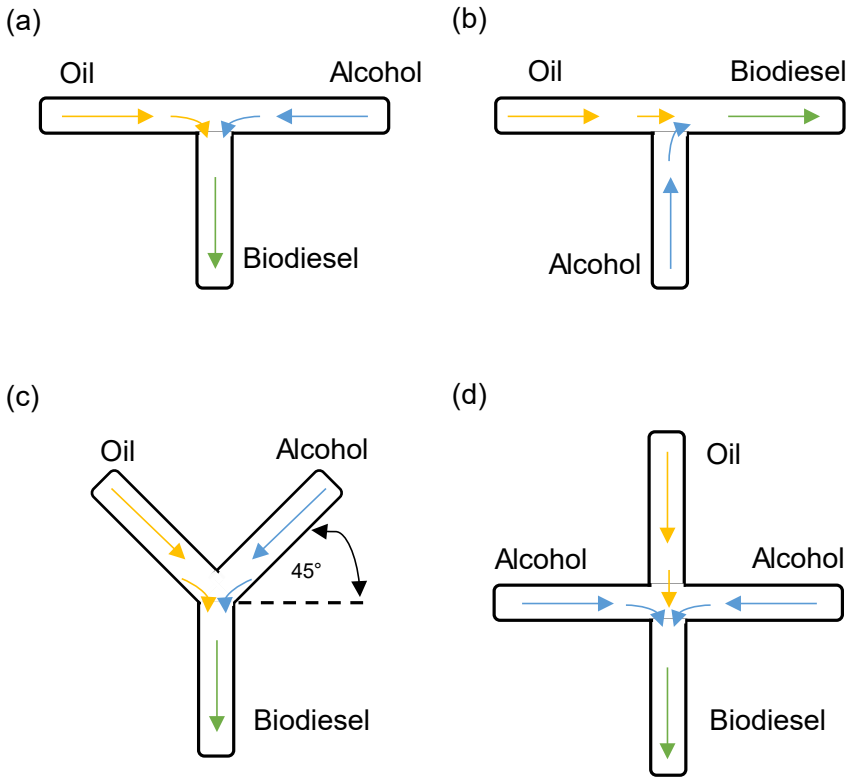

Figure 2-6. Micromixers with (a) T-junction, (b) J-junction, (c) Y-junction, (d) cross-junction.

Table 2-10. Microchannel reactors for biodiesel transesterification.

Feedstock	Mixer type	Internal diameter (mm)	Flow rate (ml/hr)	Catalyst	Loading (wt. %)	Alcohol	Alcohol: Oil molar ratio	Temperature (°C)	Residence time (s)	Yield (%)	Ref	Year
Soybean	T-junction	0.240[a]	16.1	NaOH	1.2	Methanol	6:1	56	18	97.3	[123]	2009
Cottonseed	Rectangular interdigital micromixer	0.600	150	KOH	1.0	Methanol	8:1	70	44	94.8	[124]	2010
WCO	T-junction	0.508	175.2	H_2SO_4	1	Methanol	9:1	65	5	91.76	[125]	2013
Pork lard	T-junction	0.508	175	KOH	1.3	Methanol	6:1	65	5	95.41	[126]	2014
Soybean	T-junction	0.900	-	KOH	1.2	Methanol	9:1	60	180	97.5	[127]	2016
Palm	T-junction	0.667[a]	-	CaO	30 mg powder	Methanol	24:1	65	534	99.0	[128]	2017

[a] Hydraulic diameter

Sun *et al.* [124] studied four different types of static micromixers, namely, a T-junction, J-junction, rectangular interdigital micromixer (RIMM), and a slit interdigital micromixer (SIMM). Interdigital type micromixers have alternating feed channels to periodically create liquid lamellae, which are used to study the hydrodynamics for mixing two different liquid streams [129]. In their work, the outlet of the micromixer are connected to a transparent polytetrafluoroethylene (PTFE) tube of 1.2 mm internal diameter, to observe the formation of oil droplets and flow patterns. Stainless steel Dixon rings, are filter rings with massive surface-to-volume ratio were packed in the reacting channel to avoid the phase separation during the transesterification process, as shown in Figure 2-7. Overall, the multilamination micromixer, RIMM and SIMM are superior micromixers which can achieve approximately double in the biodiesel yield when compared with than the T- and J-junction passive micromixers. The result shows significant improvement to biodiesel yield with the use of the interdigital micromixers, mainly because of the enhanced contact area between the methanol and oil. The optimised operating condition at operating conditions of 8:1 methanol to oil molar ratio, with a residence time of 17 s, under reaction temperature of 70 °C, and a biodiesel throughput of 10 ml/min combined with the Dixon rings-packed PTFE tube, allows a biodiesel yield of 99.5% to be achieved.

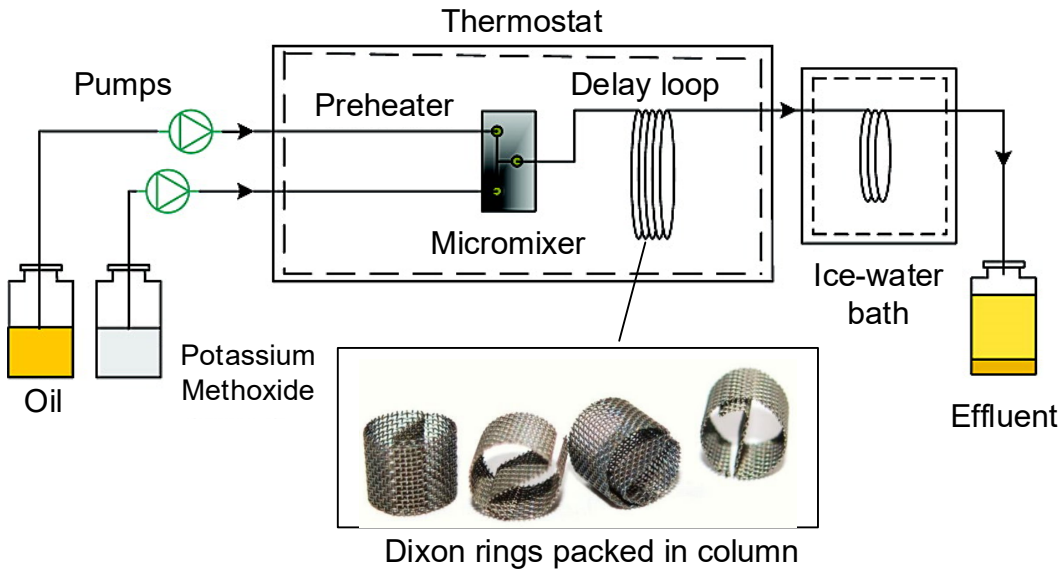

Figure 2-7. Micromixer reactor setup with delay loop packed with Dixon ring. Adapted from [124,130].

The larger interfacial surface area allows the feedstock oil and alcohol, which are both immiscible in nature to mix homogeneously, as oil droplets are formed in the stream of alcohol shown in Figure 2-8. The degree of mixing and size of droplets formed are highly dependent on the angle of impact from the micromixer. For instance, T-junction, J-junction, Y-junction, and cross-junction micromixer has an angle of impact of 180°, 90°, less than 90°, and 90°, respectively. Another important factor which controls the droplet size in microreactors is the residence time, which is defined as the average length of time that the reactants spend in the microchannel, from the beginning of the micromixer to the output. The residence time is usually controlled by varying the channel length and also combined flow rates of oil and alcohol. As the channel length increases, the mixture flow will suffer from a pressure drop, hence effectively decreasing the flow rates and mixing potential.

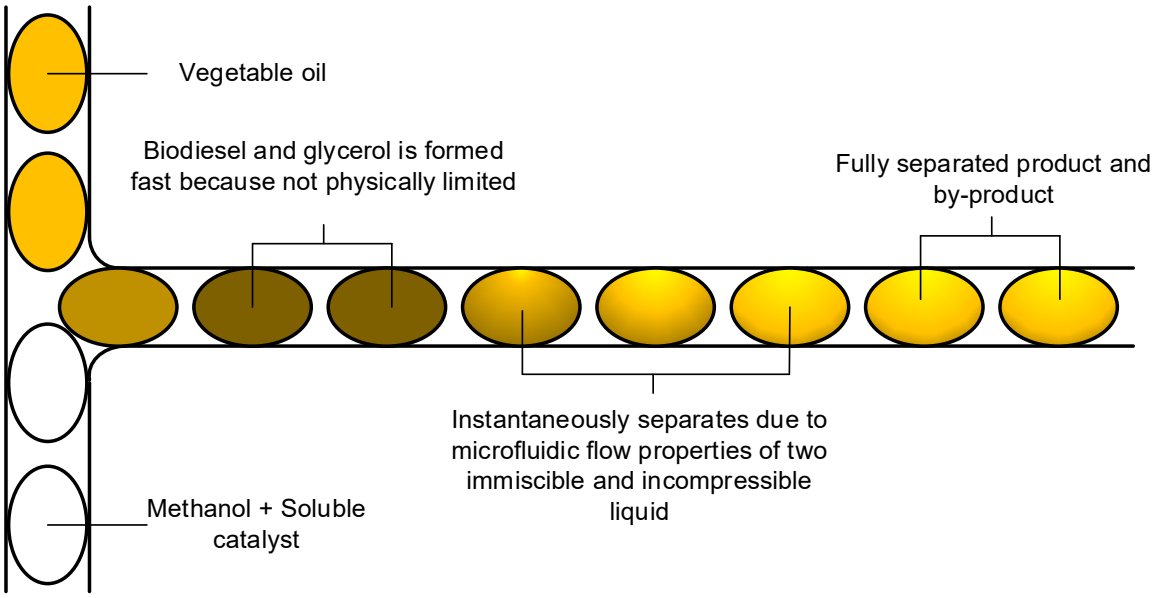

Figure 2-8. Formation of biodiesel in a T-junction mixer of microchannel reactors.

A study conducted by Kaewchada *et al.* [127] shows the effects of micromixer types and residence time on the biodiesel yield. Two types of static micromixers were tested namely, the T- and J-junction, where the T-junction outperforms the J type for the range of 5 to 20 seconds. The flow rate is observed to decrease when channel length is kept constant, which resulted in pressure drop across the reaction channel, leading to a significant drop in biodiesel yield from 97.14 to 91.43 %. On the other hand, prolonged residence time can cause the droplet size to increase, hence effectively allowing less interfacial area for the oil and methanol during mixing. Figure 2-9 shows the oil droplet size for two types of micromixer at various residence times. The optimal biodiesel yield of 97.14% is achieved with catalyst loading of 1 wt. %, operating at reaction temperature of 60 °C, using methanol to oil molar ratio of 6:1, and a residence time of 5s.

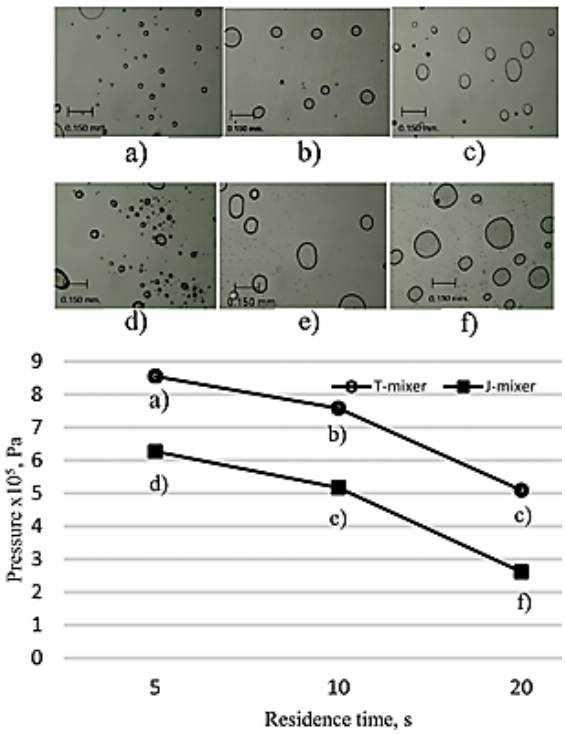

Figure 2-9. Effect of residence time on pressure for T- and J-junction: (a) 5 s, T-junction; (b) 10 s, T-junction; (c) 20 s, T-junction; (d) 5 s, J-junction; (e) 10 s, J-junction; (f) 20 s, J-junction (10 mg/g KOH, methanol-to-oil molar ratio 6:1, and 60 °C) [127].

Wen *et al.* [123] used a zigzag microreactor to intensify the biodiesel transesterification process. The microreactor features a zigzag patterned reaction channel. Extensive study was done by correlating the hydraulic diameter (240–500 μm) and numbers of turn (10–350), with the oil droplet size and biodiesel yield. Results suggest positive relationship with the increasing number of turns and decreasing channel sizes, for the final biodiesel yield point. The optimised zigzag microchannel has a hydraulic diameter of 240 μm and 350 number of turns, which also shows strong influence on decreasing the mean droplet size by decreasing the channel size. For the 350 turn's configuration, decreasing the hydraulic diameter from 900 to 240 μm decreases the mean droplet diameter from 5.41 to 1.93 μm, representing a 64% reduction. Additionally, higher number of turns also improves the passive mixing and intensification process. Batch stirred reactor was used to provide benchmark with the microreactor's results, where for the same yield of 97%, the zigzag microreactor is about 21 times more energy efficient (0.175 W as compared to 3.7 W), while only requiring 0.7% of the reaction time (28s as compared to 1 hour).

Many researchers have reported a decrease in reaction rates when higher operating temperatures of 70 °C and above for biodiesel production were implemented. This is because the reaction temperature used is above the methanol boiling point of 64.7 °C. This consequently results in creating a gas-liquid mixture within the reacting channel, forming a layer of vapour that insulates the oil-alcohol interface. Thus, the specific interfacial surface reduces and therefore biodiesel yield decreases. The results are in accordance with from past research [123,124,127,128]. However, Sun *et al.* [124]

observed the pressure drop in the reaction system, suggesting a change in the methanol boiling point as calculated by the Antoine equation. Therefore, this allows a higher reacting temperature to be used without completely boiling the methanol. This also suggest that the induced pressure drop can have a significant effect on improving the rates of reaction, for the limited operating temperature of microreactors which tends to be lower than the boiling point of alcohol used.

Further intensification can be done by packing the microchannel with device that can either improve the passive mixing or increase the surface-to-volume ratio to allow greater mass transfer. Aghel *et al.* [126] used a wire coil insert to change the geometric properties of the reactor, which performs the same role of a micromixer. This is done to provide more convectional mixing throughout the reacting channel as compared to using micromixers. Wire coils of different geometries were used, with parameters such as wire coil length and wire pitch length, as shown in Figure 2-10. Response surface methodology (RSM) is used to optimise the independent operating conditions for the transesterification process. The largest improvement was observed when the methanol to oil molar ratio was increased from 6 to 9, where the wire coil microreactor is capable of achieving a 94% biodiesel yield, as compared to a biodiesel yield of less than 90% without the wire coil. However, when excessive methanol to oil molar ratio of 12:1 is used, the yield decreases due to the reversible reaction of transesterification. Overall, the wire coil insert demonstrated an improvement in all aspect for the operating condition as compared to non-wire coil experiments. Results showed that a long wire coil (30 cm) with a shorter pitch length (0.5 mm) can improve the biodiesel yield by 6%, as compared to the ordinary wire coil due to intensified mixing which promotes mass transfer.

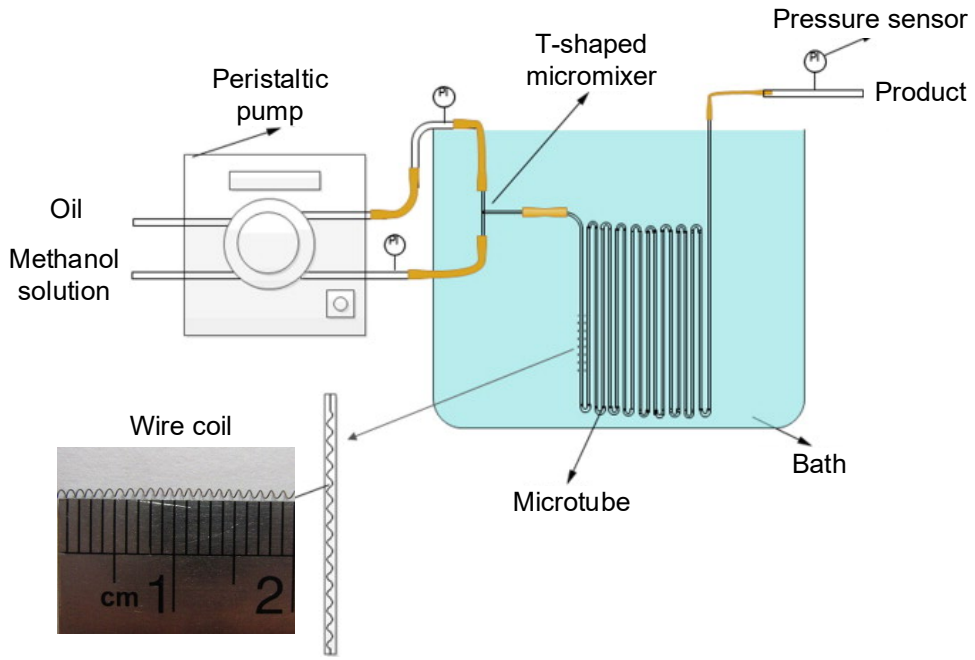

Figure 2-10. Schematic of microreactor with wire coil of 1 mm pitch length [126].

2.4.3 Cavitation reactor

The discovery of the cavitation phenomena can be traced back to 1754, first mentioned by Leonhard Euler in the theory of turbines. However, the use of cavitation only started to gain attention after approximately a century later. Cavitation occurs in flowing liquid systems when the liquid experiences a sudden change of pressure to below its vapour pressure, where bubble cavities are formed and quickly implodes as it reaches a high pressure area [131]. The collapsing cavities releases enormous amount of energy, causing high local temperature and local pressure of few thousand Kelvin and atmospheres, respectively [132]. Cavitation are used not just in application such as chemical reactor design, but also found in submerged rotating propeller of ships, control valves, pumps, which causes significant wear damages. There are four different types of cavitations, namely, acoustic, hydrodynamic, optical and particle [133]. Figure 2-11 summarises each of the categories and the cause of the phenomena. Sonification and hydrodynamic cavitations are preferred for chemical reactor application due to its favourable intensification effect [134].

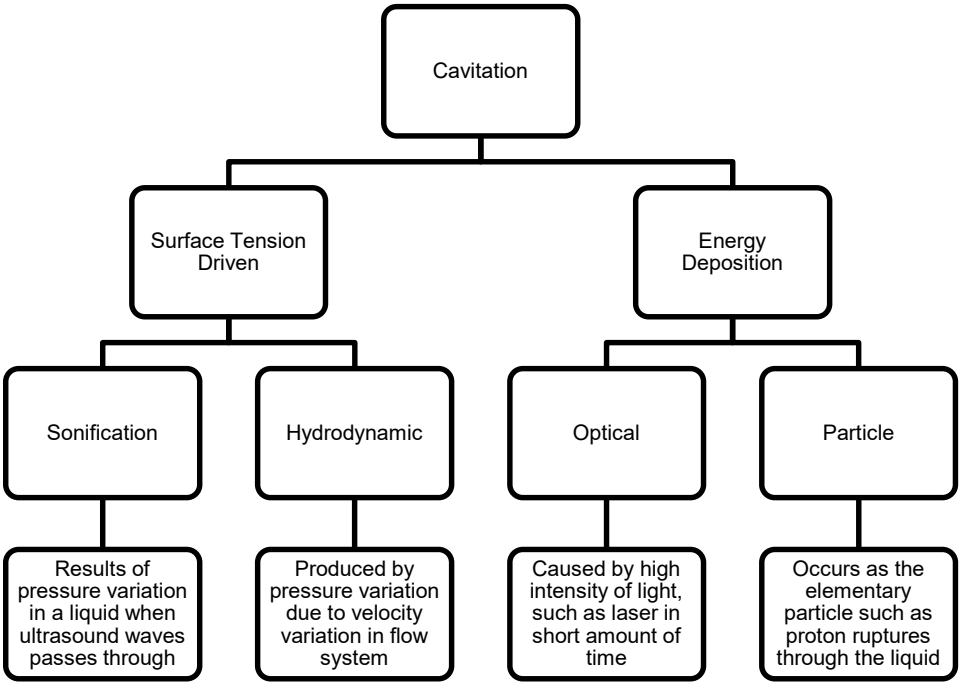

Figure 2-11. Cavitation classifications.

2.4.3.1 Sonification

Sonochemical reactors can be classified into indirect and direct cavitation. The former involves generating and applying ultrasound waves to reactants through a vessel or flask, which are immersed in a bath of liquid. This type of indirect irradiation is often utilised for cleaning rather than promoting chemical reaction. For the latter, an ultrasonic probe, usually known as an ultrasound horn is used for generating the oscillation from an ultrasonic transducer. Figure 2-12 shows a typical setup for ultrasonic chemical reactor using direct cavitation with an immersed horn.

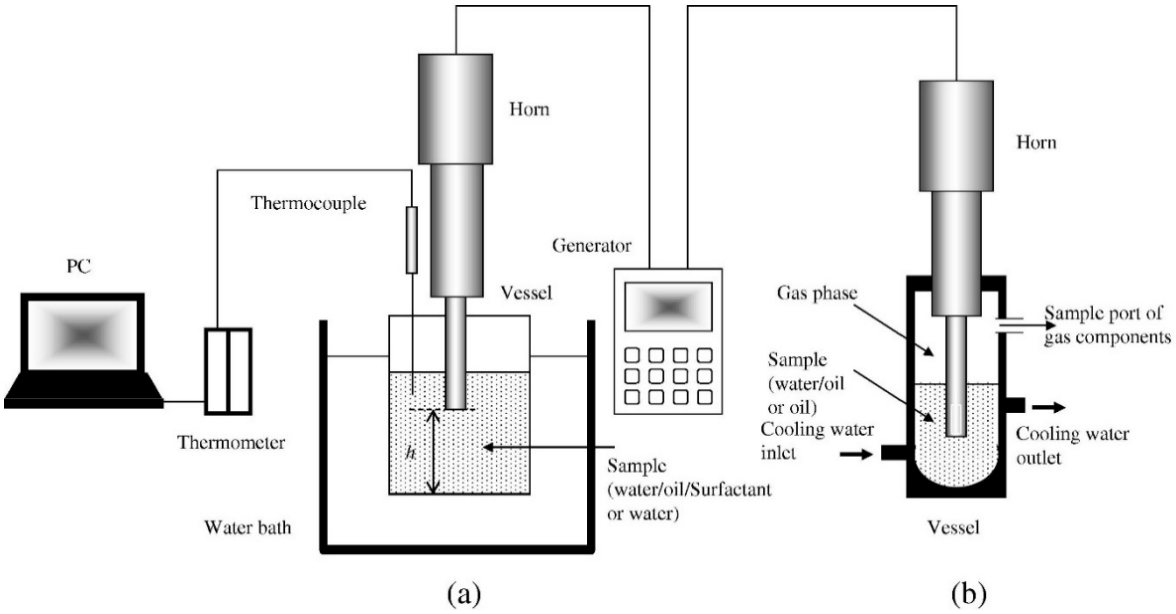

Figure 2-12. Schematic diagram of ultrasonic system setup used for the preparation of emulsion fuel and cracking of diesel oil [135].

Typically, the low and high frequency ranges are defined as 20–100 kHz and 2–10 MHz, respectively [136]. The high frequency ultrasound is usually coupled with low power application, useful for medical scanning and analytical chemistry. On the contrary, low frequency operation is generally used with higher power output, which is suitable for ultrasonic cleaning bath and process intensification of chemical reactions, especially for increasing the mass transfer across non-miscible reactants [136,137]. The use of high frequency in ultrasonic intensification for biodiesel production is not suitable, as the energy released from the imploding bubbles are weaker than the impingement of the reactants [138]. Table 2-11 summarises the sonication reactor studies that are used for biodiesel transesterification process.

Table 2-11. Sonification reactor for biodiesel production.

Feedstock	Reacting parameters	Oil quantity	Catalyst	Loading (wt. %)	Alcohol	Alcohol to oil molar ratio	Temperature (°C)	Reaction time (min)	Yield (wt. %)	Frequency (kHz)	Power (W)	Power density	Ref.	Year
Soybean	Submerged ultrasonic horn at 2 cm	1,000 g	KOH	1.0	Methanol	6:1	45	15	100	19.7	150	900 J/g	[139]	2006
Palm	Continuous flow reactor (constant residence time) at 6 volume replacement	-	KOH	-	Methanol	6:1	48	20	96.0	45	600	274.809 kJ/L	[140]	2007
Soybean	-	450 ml[a]	KOH	0.5	Methanol	6:1	45	30	99.0	611	139	556 kJ/L	[141]	2009
Palm	-	250 ml[a]	SrO	3.0	Methanol	9:1	65	60	95.2	20	100	-	[142]	2010
Canola	Continuous flow reactor at 8 L/min	-	KOH	0.7	Methanol	5:1	35	50	99.0	20	2,000	-	[143]	2010
WCO	Ultrasonic water bath (50% duty cycle) with static mixer at 100 rpm	-	Novazym 435	10	Dimethyl carbonate	6:1	60	240	86.61	25	200	-	[144]	2013
WCO	Continuous flow reactor (50 ml/min)	-	KOH	1.0	Methanol	6:1	45	-	91.6	24	102.8	124.3 kJ/L	[145]	2015
WCO	Ultrasonic horn submerged (2 cm), 60% duty cycle	-	Lipase enzyme	3.0	Methyl Acetate	9:1	40	180	96.1	20	80	-	[146]	2016
Canola oil	Probe diameter at 3.5 cm with 150 rpm shaker agitation	-	Lipase enzyme	0.23	Methanol	5:1	-	90	99.0[b]	20	40	2 W/cm^3	[147]	2017

[a] Volume of total reactants.

[b] Conversion of feedstock oil.

Mahamuni and Adewuyi [141] have studied the use of a multifrequency ultrasonic reactor, which operates at frequencies of 323 kHz, 581 kHz, 611 kHz, and 1300 kHz, and power input settings of 13 to 223 W. At the optimum frequency, an increase in input power generally raises the final biodiesel yield, albeit with diminishing improvements. Increased frequency reduces the critical size of the cavities, hence also decreases the imploding interval of the cavities. [141]. Additionally, the use of higher frequency also promotes smaller cavitation bubbles with increased transport activities. Similarly, as cavitation bubbles reduces in size, the energy released locally during cavities implosion are further reduced, limiting significant reactions to some extent. Therefore, there is an optimum point between operating frequency of ultrasound and rate of bubble cavities collapsing, for maximum reaction rates. It was also proposed that the 611 kHz and 139 W frequency-power combination form the optimum parameters for maximum possible micro-level mixing. As such, increasing operating frequency has positive effects on reaction kinetics as it leads to a decrease in overall volume and implosion time of bubbles.

According to Ji *et al.* [139], low frequency operation at 19.7 kHz is implemented to achieve a faster reaction rates and higher biodiesel yield. The factors affecting biodiesel yield are in the ascending order of oil to alcohol molar ratio, temperature, pulse frequency, and power. At the power output of 200 W, biodiesel yield is reduced due to formation of bubble mass from methanol gasification. This layer of bubble hinders the transesterification process at the liquid-liquid interface of oil and methanol, hence reducing mass transfer and kinetic rate. This shows that higher power output does not always lead to enhanced reaction, hence the degree of emulsification is more important to define the reaction rates when utilising acoustic cavitation.

In a study from Mostafaei *et al.* [145], probe diameter, ultrasonic amplitude, vibration pulse, and irradiation distance were extensively studied. Flow patterns of ultrasound in the reactor can be associated with probe diameters, where larger probe leads to higher reaction rate. Whereas smaller probe can have higher intensity concentrated at the tip area, resulting in an inhomogeneous ultrasonic field. The amplitude and pulse have similar roles in affecting the energy input to the reaction medium. An increase in amplitude is followed by increasing ultrasonic power, then reaction enhancement. However, overcommitting with high power induces secondary reaction of biodiesel, further cracking it into fractions of shorter-chained organic compound, and oxidising the biodiesel into ketones and aldehydes. Figure 2-13 summarises the effects of increasing frequency and power operation in ultrasonic chemical reactor.

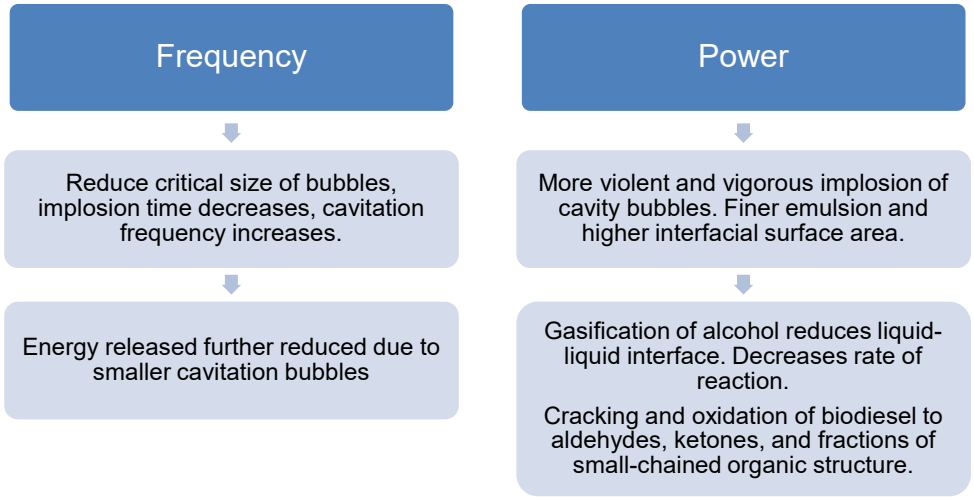

Figure 2-13. Effects of increasing frequency and power operation in ultrasonic cavitation reactor.

Ultrasonic-induced cavitation can be also integrated into a continuous transesterification system to efficiently produce biodiesel. The implementation of continuously-synthesised biodiesel can achieve greater energy efficiency and reduce processing cost for the transesterification process, hence it is more economically feasible for larger scale production. In a work by Stavarache *et al.* [140], an ultrasonic reactor with a working volume of 2.62 litre is used to produce biodiesel continuously from RBD palm oil, with a biodiesel yield up to 95% as compared to a larger working volume of 6.35 litre, which achieves less than 90% yield. The ultrasonic reactor was operated at a frequency of 45 kHz and a maximum power of 600 W. Residence time is defined as the time spent by reactants in ultrasonic irradiation, and are tested at a total residence time of 10, 20, and 30 minutes. On the occasion of 30 minutes residence time, biodiesel yield reduces, which is counter-intuitive, possibly due to the accumulation of glycerol layer at bottom of reactor trapping the methanol in glycerol phase. This essentially reduces the effective molar ratio since the reactor has a bottom to top configured outlet.

Mostafaei *et al.* [145] utilises waste cooking oil to produce biodiesel continuously with an ultrasonic reactor. The waste cooking oil is first pretreated as the excess FFA and water content in the oil can reduce the efficacy of transesterification process. Micro-emulsion can be achieved by using the ultrasonic to cause micro-streaming, which is a rapid oscillatory of fluid motion to provide intense micro-level mixing in the reactants for enhanced biodiesel conversion. Regression model was used to optimise the continuous reactor, leading to an optimised operating condition of 50 ml/min flow rate, irradiation distance of 75 mm, probe diameter of 28 mm, vibration pulse at 62%, and ultrasonic amplitude of 56%. The biodiesel yield converges to 91.12% experimentally, which concurs with the model prediction of 91.6%. Figure 2-14 shows the schematic of an ultrasonic-assisted reactor for continuous biodiesel production. In the reported experiment, the optimised flow rate is relatively

high when compared with the reactor's working volume of 350 ml, hence the accumulation of glycerol phase is negligible.

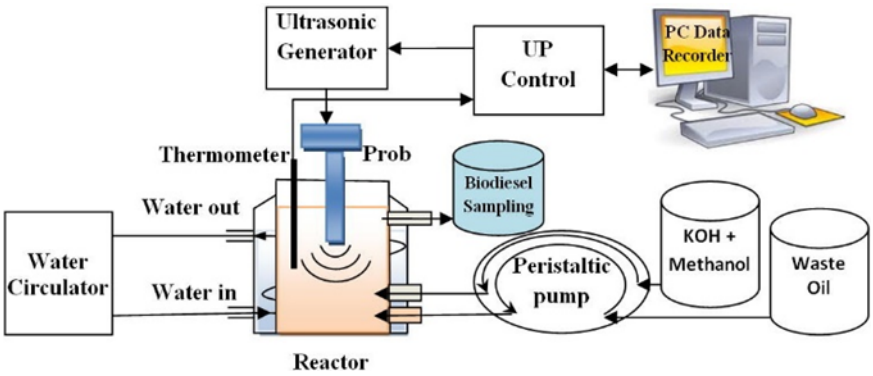

Figure 2-14. Schematic diagram of experimental setup for ultrasonic assisted continuous biodiesel production [145].

2.4.3.2 Hydrodynamic

According to Bernoulli's effect, an incompressible fluid undergoes velocity variation in a constriction, the pressure will also change conversely to obey the energy conservation principle of flowing fluids [148]. The Bernoulli's effect allows the fluid in the chemical reactor to achieve vapour pressure as it accelerates through these constrictions, creating a local boiling effect which aids in agitating the mixture as a whole, often known as hydrodynamic cavitation [149]. Hydrodynamic cavitation reactor has similar underlying principle of operation when compared with its sonificator reactors counterpart, where both reactor utilises the formation, growth, and implosion of cavity bubbles to achieve high intensity of micro-emulsion and high level of micro-mixing in multiphase reactants [150]. However, hydrodynamic reactors are often packaged as a static mixing reactor. Mixture of reactants are allowed to flow through a series of orifices, valves, or throttles in an open or closed-loop system to achieve uniform mixing of contents through the manipulation of pressure difference. Table 2-12 shows the cavitation reactors that are used for biodiesel production.

Table 2-12. Hydrodynamic cavitation reactor for biodiesel production.

Feedstock	Reacting parameters	Operating pressure (MPa)	Catalyst	Loading (wt. %)	Alcohol	Alcohol to oil molar ratio	Temperature (°C)	Reaction time (min)	Yield (wt. %)	Cavitational yield (mg/J)	Ref.	Year
Soybean	Single orifice with 1,000g oil	0.7	KOH	1.0	Methanol	6:1	45	60	97.0	2.58[a]	[139]	2006
Sunflower and palm	Single orifice plate	-	H_2SO_4	1.0	Methanol	10:1	28	90	92.0[b]	0.17	[151]	2008
Thumba	Orifice plate	-	NaOH	1.0	Methanol	4.5:1	45-55	30	80.0	-	[152]	2010
WCO	Single 10 mm orifice	0.3	KOH	1.0	Methanol	6:1	60	60	95.0	1.28	[153]	2013
WCO	Single slit venturi	0.3	Potassium methoxide	1.0	Methyl acetate	12:1	<57.1[c]	60	89.2	1.22	[154]	2014
WCO	Plate with 21 hole at 1mm diameter each	0.2	KOH	1.0	Methanol	6:1	60	15	98.1	1.25	[155]	2015
Rubber seed	Plate with 21 hole at 1mm diameter each	0.3	KOH	1.0	Methanol	6:1	55	18	97.0	0.91	[156]	2016

[a] Calculated values, where soybean methyl ester molecular weight is assumed as 292.2 g/mol.

[b] Yield in percentage of mol.

[c] Below boiling point of methyl acetate.

Cavitation number (Ca) is a dimensionless number used in hydraulic devices and flow systems. It characterises the potential of flow cavitation by drawing relationship between the difference of a local absolute pressure from the vapour pressure and kinetic energy per volume, as shown in Eq. 2-4 below [157].

$$Ca = \frac{p - p_v}{\frac{1}{2}\rho v^2} \qquad \text{Eq. 2-4}$$

where ρ is the density of the fluid, p is the local pressure, p_v is the vaporising pressure, and v is the velocity of the fluid flow.

In a research from Maddikeri *et al.* [154], biodiesel intensification is investigated by manipulating cavitation number using inlet pressure from 1 to 5 bar for the hydrodynamic cavitation reactor. The effect of inlet pressure on cavitation number using three cavitation devices of varying geometries is shown in Figure 2-15. It is noticeable that the decrease in cavitation number is associated with the increase in device inlet pressure, which is likely due to an increase in velocity at the throat of venture leading to a higher cavitation activity.

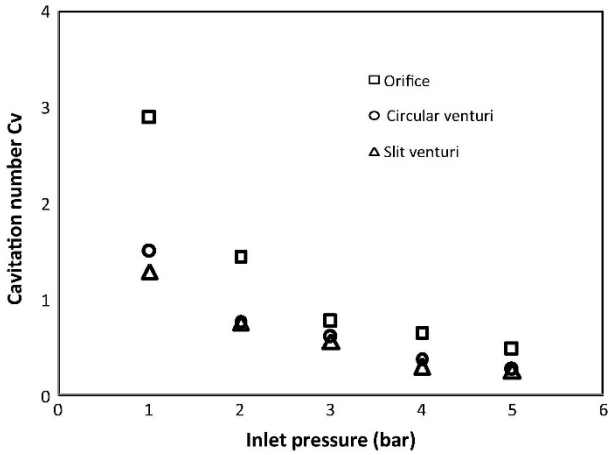

Figure 2-15. Cavitation number produced by different inlet pressure of different cavitation devices [154].

There are considerable differences in the upstream pressure from 1 to 2 bar in terms of the changes in cavitation number. However, beyond 3 bar the improvement for individual cavitation devices reduces. The observation can be justified by choked cavitation, due to mass transfer resistance being insignificant at a higher flow rate, therefore the inherent reaction kinetics becomes rate limiting [120]. Overall, slit venturi has the lowest cavitation numbers as compared to orifice and circular venture, as it has the highest volumetric flow rate resulting in a greater mass transfer across the constriction.

As such, the frequency of cavitation increases. The power dissipation from hydrodynamic cavitation can be measured according to the Eq. 2-5 using pressure drop and volumetric flow [154].

$$P_D = \Delta P \times V_0 \quad \text{Eq. 2-5}$$

where P_D is the power dissipated into the system in J/s, ΔP is the pressure drop across the cavitation device in Pa, and V_0 is the volumetric flow rate through the cavitation device in m^3/s.

Slit venturi which has the lowest cavitation number is able to produce the highest power, at approximately 1.1 times and 1.5 times higher than those of circular venturi and orifice, respectively. The results for biodiesel yield are also dependent on the power input of the devices, with slit venturi, circular venturi, and orifice having yields of 89%, 82%, and 64%, respectively. The operating condition of the hydrodynamic cavitation reactor utilises a catalytic loading of 1 wt. %, at 12:1 alcohol to oil molar ratio, and an inlet pressure of 3 bar.

Cavitational yield is a generalised parameter to enable comparison to be made between cavitational reactors [151], and equated by,

$$Cavitational\ yield = \frac{Amount\ of\ methyl\ ester\ (g)}{Energy\ supplied\ (J)} \quad \text{Eq. 2-6}$$

The equation above provides a measure of efficiency based of the energy supplied from the reactor and the amount of biodiesel produced. This can also be easily extrapolated to other type of biodiesel reactors to allow a cross-reactor comparison regardless of reactor category.

Furthermore, Ghayal *et al.* [153] studied the relationships between operating pressure of a hydrodynamic cavitation reactor and flow geometries such as hole size, number of holes, and total perimeter of holes on a orifice plate. This allows the characterisation of the cavitation activities in biodiesel transesterification using a hydrodynamic reactor. The results show similar trends to that of Maddikeri *et al*. [154], where the improvements in cavitation and rate of reaction were observed when upstream pressure increases. However, increasing pumping liquid flow rate had diminishing returns in terms of improvement. This work extensively correlates the cavitation effects to flow geometries of orifice plates, such as the ratio of total perimeter of holes to total flow area on plate, α, the ratio of hole diameter on orifice to pipe diameter, β, and the ratio of total flow area on orifice plate to the cross-sectional flow area of pipe, β_0. Higher biodiesel yield is achieved with increasing values of α, β, β_0 for orifice plates, which are physically represented by greater number of holes and smaller hole size of the orifice. These flow geometry properties contribute to more cavity generating spots, allowing greater shear layer area to exist, hence mass transfer is further enhanced through better emulsification of multiphase reactants.

Chuah *et al.* [155] utilised an optimised orifice plate to demonstrate large scale biodiesel transesterification via a hydrodynamic cavitation system with a 50 litre capacity. The reactor is assisted by a double diaphragm pump in their pilot biodiesel plant as shown in Figure 2-16.

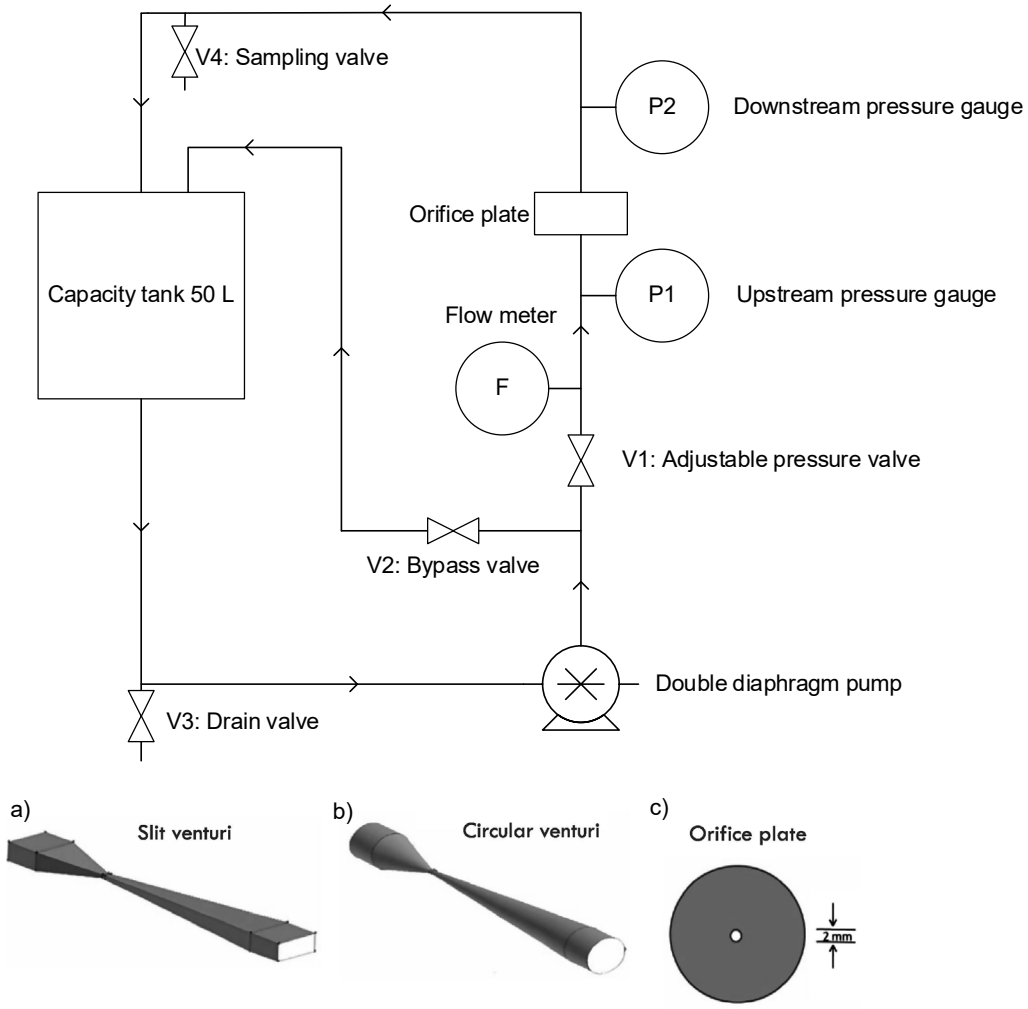

Figure 2-16. Schematic of a 50 L capacity hydrodynamic cavitation reactor for biodiesel production, and hydrodynamic cavitation devices (a) slit venturi, (b) circular venturi, and (c) orifice plate [154,155].

Waste cooking oil is used as the feedstock of choice because of its low cost and abundance in availability. The optimised operating parameters of the biodiesel plant was able to produce biodiesel of more than 96.5% yield in 15 minutes of reaction time. Thus, the biodiesel produced complies with the minimum yield criteria of the international biodiesel standards of American standards, ASTM D 6751 and British standards, EN 14214. Effects of methanol to oil molar ratio were investigated from 4:1 to 7:1, where only the 6:1 and 7:1 ratio resulted in achieving high biodiesel yields. Molar ratio with lower level of methanol is insufficient when diffusion of methanol into glycerol layer is taken into account. In contrast, high methanol to oil molar ratio level also decreases conversion slightly, as

the dilution of oil with methanol occurs. The study with catalyst loading of 1.0 wt. % performs better as compared to 1.25 wt. %, where the latter was observed to promote saponification reaction to form soap, contributing to biodiesel conversion inefficiency. Besides, operating temperatures of 50 °C and 65 °C are optimal for biodiesel transesterification in a hydrodynamic cavitation reactor, since higher temperature promotes solubility between oil and methanol, increasing the interfacial contact surface of two reactants, for better mass transfer [158].

However, there are limited amount of studies in continuous biodiesel production using a hydrodynamic cavitation reactor, with an open-loop flow system. Most of the setup is based on a closed-loop recirculation of reactants via a pump, through constriction devices to induce cavitation over certain amount of time. The biggest issue of hydrodynamic cavitation is the static mixing of reactants, which requires a significant amount of pressure differences, usually above 1 bar upstream pressure for the inlet cavitation device [153,154,156]. This allows the fluid to reach a desired velocity change, hence achieving vaporising pressure for the cavitation process to take place. Therefore, as the volumetric flow increases, closed-loop systems are favourable as they take up less space. Continuous hydrodynamic reactor for biodiesel transesterification is viable by implementing a series of constriction devices to increase the cavitation zone. Subsequently, the down-scaling of reactor's total capacity is recommended to compensate for the long flow pathway of an open-loop system.

2.4.4 Microwave reactor

Microwaves are in fact not micro in size, instead, they have wavelengths ranging from millimetre to meter scale. The common frequencies of a microwave are between 300 MHz (100 cm) and 300 GHz (0.1 cm) [159]. In the electromagnetic spectrum, microwave is situated between infrared and radio wavelength, hence it is a considerably large wave as compared to other type of electromagnetic radiation.

The main application of microwaves is the generation of heat, often in household microwave oven operating at 2.45 GHz specifically to avoid interference with telecommunications. Fundamentally, the microwave produced by a magnetron, is carrying both electric and electromagnetic fields that are directly perpendicular, and travelling at the speed of light. The fields interact with dielectrics such as polar molecules and ions, to continuously realign them along the field's direction of propagation. Heat energy is then generated from the rapid oscillation of rotating polar molecules with its surrounding molecule via frictional forces. Large ions can also contribute to the heating of liquid media when the electric field changes in direction, as a result of kinetic energy dissipation in the form of heat [160]. Microwave irradiation heating is more efficient as compared to conventional conduction and convection within material as it does not depend on the material properties, such as thermal conductivity, specific heat capacity, and density of material [161].

Biodiesel transesterification reaction involves reactions such as lipids and alcohol which are good microwave absorbers as they contain high level of dielectrics. Thus, microwave-assisted transesterification allows reaction intensification using alternative heating method, rather than the less efficient conduction from water bath or heating element. Table 2-13 tabulates the microwave reactors that are used for biodiesel production from different studies.

Table 2-13. Microwave reactor for biodiesel production and their respective operating conditions.

Feedstock	Reacting parameters	Catalyst	Loading (wt. %)	Alcohol	Alcohol to oil molar ratio	Temperature (°C)	Reaction time (min)	Power output (W)	Yield (wt. %)	Energy efficiency	Ref.	Year
WCO	Continuous microwave reactor at 7.2 L/min	KOH	1.0	Methanol	6:1	50	4.5	1600	94.6	26 kJ/L	[162]	2007
WCO	Continuous microwave reactor mixed via T-junction	NaOH	3.0	Methanol	12:1	78	0.5	800	97.0	74.8 Wh/L	[163]	2008
Soybean	Batch microwave reactor with magnetic stirrer using 1L of oil	KOH	1.0	1-Butanol	6:1	120	1.0	1600	93.0	-	[164]	2008
Castor	Microwave reactor with static mixing at 600 rpm using 20 g of oil	H_2SO_4/C	5.0	Methanol	12:1	65	60	200	94.0	-	[165]	2009
Yellow horn seed	Microwave batch reactor with 10 g of oil	H_2SO_4	1.0	Methanol	20:1	90	30	500	95.2	-	[166]	2010
Yellow horn seed	Microwave batch reactor with 10 g of oil	Heteropolyacid ($Cs_{2.5}H_{0.5}PW_{12}O_{40}$)	1.0	Methanol	12:1	60	10	500	96.2	-	[166]	2010
Dry algae (*Nannochloropsis*)	Dry algae biomass of 2g, simultaneous lipid extraction and transesterification via microwave irradiation	KOH	2.0	Methanol	12:1	60-64	4-5	400	80.13	-	[167]	2011
Jatropha curcas	Continuous recycling flow in microwave reactor at 8 ml/min	CaO	3.17	Methanol	8.42:1	60	67.9	800	97.1	-	[168]	2013
Palm	-	CH_3ONa	0.75	Methanol	6:1	-	3	750	99.5	-	[169]	2014
WCO	Microwave and static mixer at 300 rpm with total reactant volume of 80 ml.	KOH	1.0	Methanol	6:1	60	8	300	91.3	-	[170]	2014

Palm	Reactant premixed by static stirrer, then feed into microwave reactor continuously	NaOH	1.0	Methanol	12:1	70	1.75	400	99.4	0.1167 kWh/L	[171]	2015

Although microwave can heat up reactant rapidly, it is only restricted to a small volume of fluid due to the limited penetrating depth of microwave. According to Grant and Halstead [172], penetrating depth is a function of reactant's temperature. For example, microwaves have a penetration depth of 0.76 cm in methanol at 20 °C, and 1.4 cm at 60 °C. Therefore, external agitation or stirring is still required for uniform heating of the bulk fluid. Thus, the scaling ability of microwave-assisted transesterification is fairly poor as compared to other processing techniques.

Nevertheless, many research have claimed that high biodiesel yields can be obtained in a short amount of time, through the use of microwave irradiation. Lin *et al.* [169] reported that microwave heating system was used to improve the palm biodiesel's yield. The microwave reactor can simultaneously reduce both reaction time and energy consumption of biodiesel production, as compared to conventional heating system. When the process is optimised, a 99.5% biodiesel yield was achievable in 3 minutes through microwave irradiation at total energy consumption of 486 kJ, combined with mechanical stirring from a magnetic stirrer. This represents up to a total of 30 times reduction in reaction time and 22 times reduction in total energy consumption, when compared with conventional heating which uses energy in the range from 3,000 kJ to 11,000 kJ. Besides, using a higher methanol to oil molar ratio decreases the biodiesel yield, which is due to the dilution of heat dissipation from the microwaves, since methanol is a better microwave absorber as compared to oil. The optimised operating parameter runs on 750 W microwave power output, with 6:1 methanol to oil molar ratio, using a Ch_3ONa catalyst loading of 0.75 wt. %.

In a research conducted by Mazubert *et al.* [170], the reaction temperature was monitored via fibre optic probe in the reaction medium directly to ensure accuracy of measurements. Typically, temperature measurement methodologies such as thermometers and thermocouples are implemented in microwave reactors with poor choices of probing locations, hence leading to false interpretation of the reactor's conditions. Active feedback is used to control the microwave power as temperature is monitored with the probe, in order to heat up the reactants to desired set point. The experiments were repeated with an infrared temperature sensor, where underestimation of 10 to 20 °C in temperature was observed as compared to the fibre optic sensor. The discrepancy from the infrared sensor will affect the transesterification kinetics representation from the results. This meant that thermal heating of microwave irradiation is the main contribution to improvement of reaction rates, instead of non-thermal microwave effect. The dielectric constant, $\mathcal{E}'$ characterises how well a dielectric compound absorbs microwaves and stores energy, while dielectric loss $\mathcal{E}''$, represents the ability of compound to convert absorbed energy into heat [170]. When microwave heating system is used in biodiesel transesterification, the selection of alcohol is important, as it holds a significant volume proportion of the mixture. However, the selection of oil is less significant since the dielectric constant is between the value of 3 and 5 [173]. Alcohol with high dielectric constant and dielectric loss is favourable since it is a better microwave absorber. In theory, methanol will outperform the other primary alcohols as a solvent for microwave irradiation as the dielectric constants for methanol,

ethanol, and propanol are, 32.7, 24.5, and 17.9, respectively [173]. Yuan *et al.* [165] reported that the effect of methanol is greater as compared to ethanol for the transesterification process, which suggest that more energy is transferred into the oil-methanol system. Other researcher such as Barnard *et al.* [162], Lertsathapornsuk *et al.* [163], and Leadbeater *et al.* [164], have used methanol, ethanol, and butanol, to obtain biodiesel yield of 99.0%, 97.0%, and 93.0%, respectively.

Microwave heating has good synergy with heterogeneous catalyst, especially those with high microwave absorption characteristic. Since catalytic effect takes place on the active site of solid catalyst, reactants adsorb on the external and internal surface which will be acting as microwave hot spots, promoting rate of reaction for biodiesel transesterification [165]. Yuan *et al.* [165] used activated carbon as heterogeneous catalyst carrier, as it has a high volume to surface area and strong microwave radiation absorbing characteristics. The highly polar sulfuric acid (H_2SO_4) is also used as a loading catalyst combined with activated carbon (H_2SO_4/C). This combination further enhances the microwave absorption properties. The experiment compares the effect between homogeneous (H_2SO_4) and heterogeneous (H_2SO_4/C) type of catalyst, under the heating influence of microwave irradiation. Sulfuric acid concentration is controlled to be identical for both cases, with the H_2SO_4/C reaching reaction equilibrium faster, hence a biodiesel yield of more than 90% is achieved as compared to 40% when H_2SO_4 is used as catalyst for the same reaction time.

In the recent years, microwave heating has captured more attention in 3rd generation biodiesel feedstock processing. The high cost of downstream treatments which involves harvesting, drying, extraction, separation, and transesterification of 3rd generation feedstocks such as microalgae is not economically favourable for upscale production [174]. Thus, microwave technologies are used in attempts to (i) provide efficient heating, (ii) reduce number of intermediate process by combining stages, (iii) provide better extraction of lipids from feedstocks. Loong *et al.* [174] developed a one-step transesterification using simultaneous cooling and microwave heating (SCMH), where cell disruption and transesterification of wet microalgae (*Nannochloropsis sp.*) was performed simultaneously in a single step. The mixture of concentrated microalgae (20% water content) and methanol with sodium hydroxide catalyst was added to the reactor, which was first cooled at 15 °C with a chiller. Conventional microwave workstation was then used to control the microwave power output to 800 W, at 50 °C for 10 minutes. The one-step SCMH was able to achieve a 75.0% biodiesel production level, as compared to water bath heating of 13.46%, and one-step microwave heating of 15.39%. The cooling stage promotes the microwave absorption properties of molecules, hence improving the penetration of microwave irradiation, subsequently promoting the microalgae lipid extraction and transesterification yield.

Continuous flow microwave reactor system for biodiesel production are also reviewed as reported by Choedkiatsakul *et al.* [171]. Commercially available microwave system can streamline the reactor setup and design. However, the size of these systems still restricts the biodiesel production to be performed within laboratory scale. The Figure 2-17 shows the configuration of the continuous biodiesel production microwave system. The use of thin coiled tubing in the microwave system is advantageous for the efficient transfer of energy. Since there is no mechanical stirrer in a continuous microwave system, homogeneous heating can only be done via full penetration of microwave to reactants. The microwave system is able to achieve a biodiesel yield of 99.4%, in 105 seconds of residence time. The operating conditions entail a methanol to oil ratio of 12:1, a NaOH catalyst loading of 1.0 wt. %, under a microwave power output of 400 W at 70 °C reacting temperature. The measured energy consumption using the system is 0.1167 kWh/L, which is half of the requirement for conventional heating process.

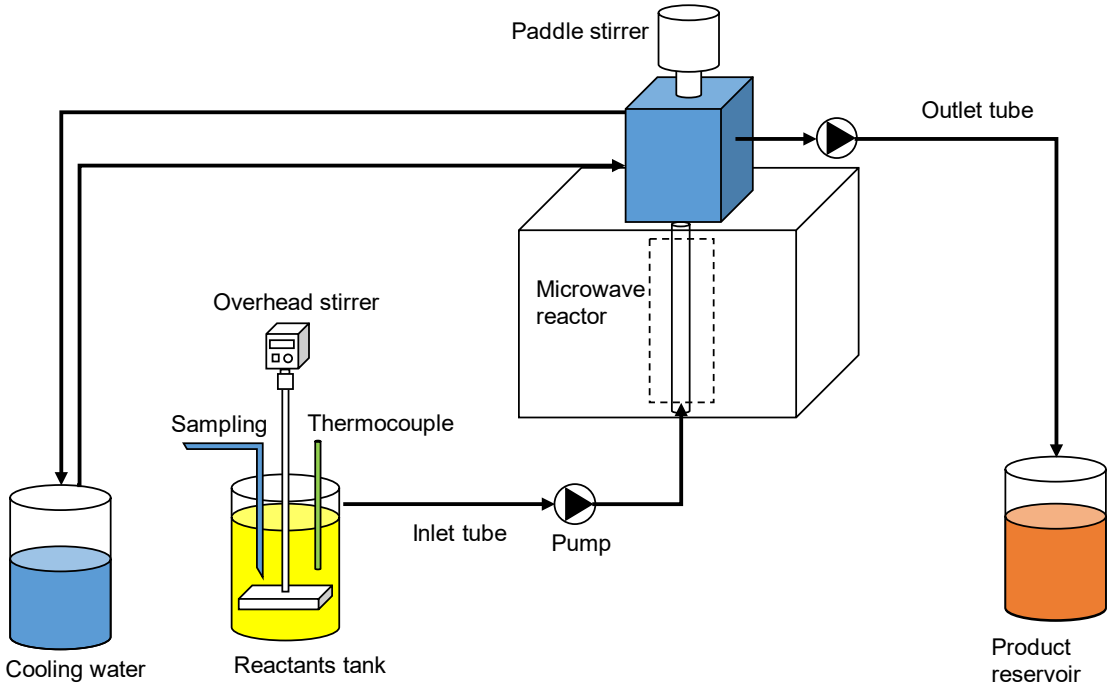

Figure 2-17. Schematic of continuous flow microwave reactor for biodiesel production. Adapted from [171].

2.4.5 Cosolvent-assisted transesterification

Cosolvent is usually a secondary solvent used in a reaction that does not react with the primary solvent and be involved in the primary reaction pathway. Instead, the use of a cosolvent is to amplify the magnitude of effectiveness in trace quantities, prior to the primary solvent. In the context of biodiesel transesterification, the cosolvent used for the process should be inert towards the reaction of transesterification, hence does not cause inactivation of the catalyst [5].

Biodiesel transesterification uses oil, which mainly consists of triglycerides that are nonpolar and hydrophobic. The oil is used to react with alcohol which is polar and hydrophilic, hence using the analogy of 'like dissolve like', oil and alcohol are immiscible in nature. Therefore, when oil and alcohol are mixed together, the transesterification process only occurs on the contact surfaces of oil and alcohol, resulting in the formation of a two-phase system.

The cosolvent used for biodiesel production should be soluble in both fluids, acting as an interface solvent between oil and alcohol. This encourages the formation of a single-phase system. Biodiesel transesterification has been proven to achieve higher yield by using cosolvent such as Acetone (ACT), Tetrahydrofuran (THF), diethyl ether (DEE), and FAME [175–177]. The solubility of some solvents and organic solvents are compared with transesterification compound, shown in Table 2-14, while biodiesel transesterification yield through different alcohol and base type catalyst loading are shown in Table 2-15.

Table 2-14. Dissolution of reactants and products in organic solvents at 20 °C [178].

Solvents	**Organic Solvents**							
Compounds	H_2O	CH_3OH	ACT	THF	IPA	AN	DEE	FAME
Triglycerides	X	X	◎	◎	◎	X	◎	◎
FAME	X	X	◎	◎	◎	◎	◎	◎
Glycerol	◎	◎	X	X	◎	X	X	X
CH_3OH	◎	◎	◎	◎	◎	◎	◎	X
Oleic acid[a]	X	◎	◎	◎	◎	X	◎	◎
Stearic acid[b]	X	X	X	◎	X	X	X	X
Soap	◎	◎	◎	◎	◎	Δ	Δ	Δ

◎: Miscible

Δ: Partially miscible

X: Immiscible

[a]Melting points of oleic acid is 16.3 °C.

[a]Melting points of stearic acid is 69.9 °C.

Organic solvent used: Methanol (CH_3OH), Acetone (ACT), Tetrahydrofuran (THF), Isopropyl alcohol (IPA), Acetonitrile (AN), Diethyl ether (DEE), Fatty acid methyl ester (FAME).

Table 2-15. Biodiesel transesterification yield through different alcohol and base type catalyst loading [179].

Catalyst	Catalyst Loading (%)	Biodiesel yield (%)												
		Methanol				Ethanol			Isopropanol			Butanol		
		Time (min)				Time (min)			Time (min)			Time (min)		
		10	20	40	60	10	20	60	10	20	60	20	40	>60
NaOH	0.5	-	-	-	80	-	79	-	78	-	-	-	-	83
	1.0	91	-	-	-	-	40	-	47	-	-	-	90	-
	1.5	35	-	-	-	47	-	-	79	-	-	89	-	-
KOH	0.5	-	-	-	86	-	55	-	76	-	-	-	-	91
	1.0	-	-	85	-	-	57	-	60	-	-	-	91	-
	1.5	-	83	-	-	44	-	-	29	-	-	97	-	-

Table 2-16 summarises the cosolvent-assisted biodiesel transesterification studies. Alhassan *et al.* [177] demonstrated the production of biodiesel from cotton seed oil by using commercially available cosolvent such as, DEE, Dichlorobenzene (CBN), and ACT, to produce a cosolvent system with mixtures of methanol at different levels of concentration. Under the reaction temperature of 60 °C, methanol to oil molar ratio of 6:1, and catalyst concentration of 0.75%, the biodiesel yield achieved exceeded 90% conversion in the first 10 minutes with 10 vol. % cosolvent, as compared to non-cosolvent transesterification observed at below 70% yield. The experimental results suggest that the reaction proceeds as soon as phase equilibrium between solvent and oil established in the first few minutes. All of the different cosolvent systems produce at least 90% biodiesel yield performance in the first 10 minutes except for DEE which resulted lower yield. The findings also agree to the results reported by Luu *et al.* [175], where non-solvent system has a slower reaction rate. This is reflected by a maximum difference of 15% biodiesel yield at the 100th minute point of the transesterification process (<100 min), as compared to cosolvent used such as Diethyl Ketone, Ethyl Methyl Ketone, AN, and Ethyl Acetate.

Table 2-16. Cosolvent-assisted biodiesel production process and their respective operating conditions.

Feedstock	Reacting parameters	Cosolvent	Cosolvent loading (wt. %)	Catalyst	Catalyst loading (wt. %)	Alcohol	Alcohol to oil molar ratio	Temperature (°C)	Reaction time (min)	Yield (wt. %)	Ref.	Year
Soybean	Tetrahydrofuran to methanol volume ratio of 1.6	Tetrahydrofuran	38.4	NaOH/	1.0	Methanol	6:1	20	10	87[b]	[180]	1996
Corn	Cosolvent pressurised at 500 kPa, reactor in oil bath and shaker with 2.6 Hz shaking speed.	Dimethyl ether	0.57[a]	p-toluenesulfonic acid	4.0	Methanol	6:1	80	120	97.1	[181]	2009
WCO, Canola, Catfish, *Jatropha curcas*	Acetone premixed with 40g of oil by magnetic stirrer until homogeneous before transesterification	Acetone	25	KOH	1.0	Methanol	4.5:1	25	30	98.1[c], 98.3[c], 97.0[c], 97.9[c]	[176]	2013
Jatropha curcas	Acetone premixed with 30g of oil	Acetone	20	KOH	1.0	Methanol	6:1	40	30	99.0	[175]	2014
Cotton seed	Magnetic stirring at 350 rpm	Dichlorobenzene and Acetone	10[d]	KOH	0.75	Methanol	6:1	55	10	96.85	[177]	2014
Microalgae	Wet algae of 0.75 g reacted in sealed tube with no agitation.	Ethyl acetate	6.67[e]	H_2SO_4	4.06 M	Ethyl acetate	6.67[f]	114	120	97.8	[182]	2017
Linseed	Linseed in-situ transesterification at 700 rpm agitation rate	Tetrahydrofuran	30	KOH	6.8	Methanol	10:1[g]	40	90	93.15	[183]	2018

[a] DME to methanol ratio.

[b] Estimation from results.

[c] Yield are according in the order of feedstocks; Catfish oil's reaction temperature at 35 °C.

[d] Cosolvent loading in percentage of volume (vol. %).

[e] Cosolvent loading in ml/g.

[f] 6.67 ml Ethyl acetate per gram of dried algae.

[g] Alcohol to oil molar ratio in percentage of weight (wt. %).

Another study from Maeda *et al.* showed that biodiesel can be produced using a milder reaction condition when homogeneous cosolvent system is implemented, as lower energy consumption is required [178]. The transesterification process of canola, cat fish, *Jatropha curcas* oil was studied, at a pilot plant scale of 300 L/batch capacity with the operating conditions of 4.5:1 methanol to oil molar ratio, a KOH catalyst loading of 0.5 wt. %, and a reaction temperature of 25 °C. Effects of cosolvent was also studied using various cosolvent such as, ACT, Isopropyl alcohol, THF, and AN at cosolvent to oil ratio of 25 wt. %. Biodiesel yield above 90% was achieved with the homogeneous system within 10 minutes of reaction time, while heterogeneous system without cosolvent barely reaching 70% biodiesel yield. The use of cosolvent allows reduction in methanol, temperature, and catalyst loading as compared to a conventional transesterification process, which is likely due to enhanced mass transfer led by the molecular scale reaction [178].

Furthermore, the separation time of glycerol from biodiesel production is also extensively studied by Thanh *et al.* [176]. It was observed that after a 60-minute transesterification, the glycerol separation times require 37, 30, and 50 minutes using acetone at 20, 25, 30 wt. % of oil, respectively. However, without cosolvent the phase separation requires a significant longer time of 4 hours. The addition of cosolvent allows to increase (i) the difference in specific gravity and (ii) difference in relative viscosity between the two phases [178]. As a result, glycerol can be separated from the reacted system and precipitated within minute scale, because of the large differences in specific gravity and similar viscosities between the two components. For the case of using acetone concentration at 30 wt. %, the increase in phase separation time can be pointed towards the relationship between the relative concentrations of glycerol and methanol to the overall mixture. When the acetone concentration increases, the relative proportion of excess methanol-glycerol decreases in the overall system, hence they will be less likely to merge and form a single phase that separates from the biodiesel layer.

The specific gravities and viscosities of FAME and potential cosolvent for transesterification are tabulated in Table 2-17, with the FAME-isopropanol system separating the fastest and dimethyl ether the slowest for glycerol.

Table 2-17. Specific density, relative viscosity, and yield of FAME with cosolvent via mixing ratio of 2:1 ratio wt. % at 15 °C [178].

Mixture	**Density (g.cm-^{3})**	**Relative viscosity[a]**	**Biodiesel yield[b] (%)**
Water	1.0000	1.000	-
FAME + isopropanol	0.8456	4.130	99
FAME + tetrahydrofuran	0.8797	2.630	93
FAME + acetonitrile	0.8311	2.020	90
FAME + acetone	0.8395	1.830	99
FAME + dimethyl ether	0.8202	1.690	93
FAME	0.8797	0.885	88

[a] Relative viscosity to water.

[b] Based on reaction condition of molar ratio methanol to canola oil, 4.5:1; cosolvent to oil, 25 wt. %.; KOH catalyst loading, 0.5 wt. %; Temperature, 20 °C; Reaction time, 60 minutes. Yield is an estimation from data points extracted from graph [178].

2.5 Trends and perspectives

Biodiesel reactors have also been tailored specifically to tackle the challenges mentioned above. The amounts of reactor design and biodiesel-related research have shown positive correlations with respect to the fluctuation of crude oil prices as shown in Figure 2-18. The patent search in Figure 2-18 for biodiesel reactor designs was based on the World Intellectual Property Organization (WIPO) [184], whereas the published scientific articles related to biodiesel reactors are derived from the Scopus database [185], this is also represented in Table 2-18.

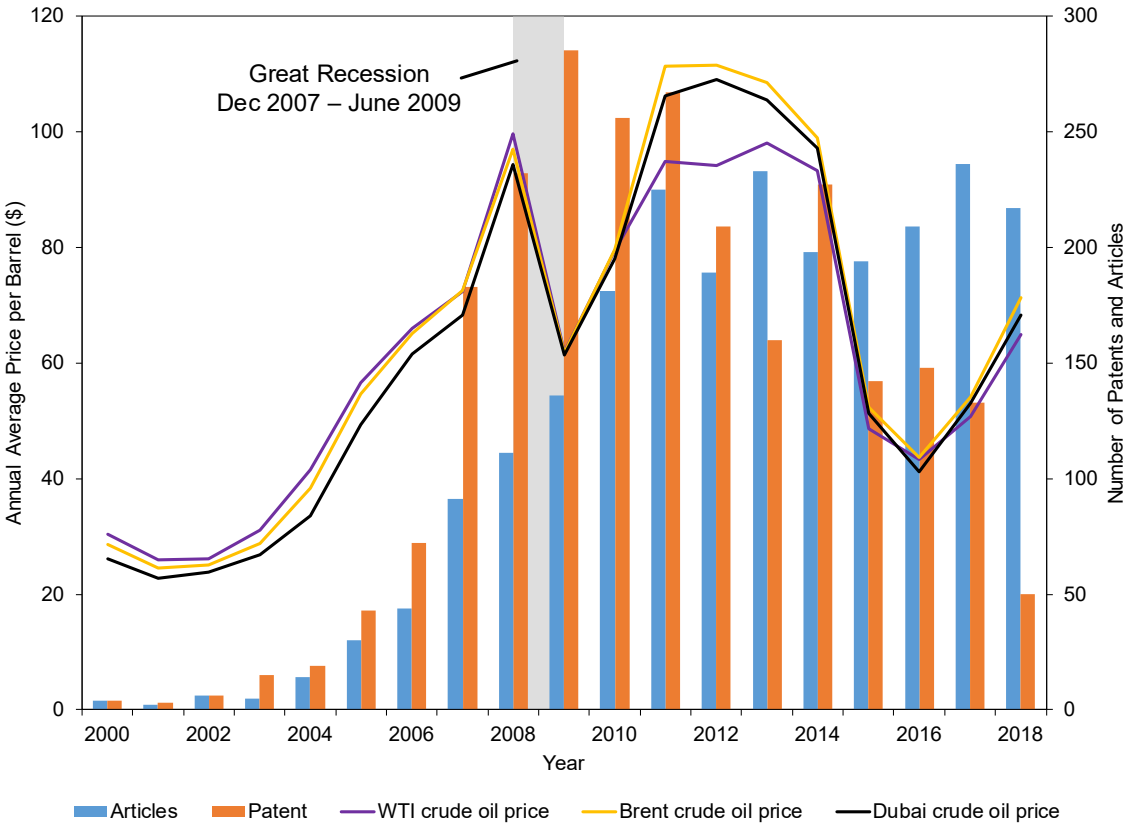

Figure 2-18. Crude oil prices, biodiesel research articles and patents for years 2000-2018.

Table 2-18. Sum of biodiesel reactor patent from the year 2000 to 2018, sourced from WIPO [184].

Sum of Patent Countries	**Year 20**																			
	00	01	02	03	04	05	06	07	08	09	10	11	12	13	14	15	16	17	18	Grand Total
Australia	2	1	1	2	4	1	1	6	7	10	8	8	7	3	1	4	2	3	2	73
Bulgaria								1				1			1					3
Canada		1		1	1	4	5	14	14	11	9	13	6	2	3	3	2	5		94
China				1	2	2	10	58	68	84	69	76	69	32	99	66	86	80	2	804
Denmark										1	1	1	1	3	2		2		1	12
Egypt								1						1						2
France						1					1	1								3
Germany			1		3				2	2	1			1						10
India						3	2	7	13	16	9	16	16	13	12	6	6	7	8	134
Indonesia															1	1		1	1	4
Israel									1	1	1		1							4
Japan						1	2	4	9	8	7	5	5	4	1	1	2			49
Malaysia			1		1	3	1	7	9	7	9	9	7	5	3	4	3	4		73
Mexico					1	2	2	1	7	10	9	13	6	5	5	2	1	6	6	76
Portugal										1		2		1					1	5
Republic of Korea							9	9	5	14	13	4	7	18	11	10	4	2	5	111

Romania									1					2		2					5
Russian Federation										2	3	2	2	1	1	1	1	4	4		21
Singapore									1	1		1	2	2	1						8
South Africa							1	1		2	1										5
Spain						1						1	2	4	3	1	2				14
Tunisia													1								1
United Kingdom						1	1	2	2	3			1		1	1		1			13
United States	1	1	1	5	4	13	18	26	26	47	50	48	29	27	43	21	19	9	6		394
Patent Offices [a]	1		2	6	3	11	20	46	67	65	65	66	47	36	39	19	18	11	14		536
Grand Total	4	3	6	15	19	43	72	183	232	285	256	267	209	160	227	142	148	133	50		2454

[a] Collection of patents from European Patent Office and Patent Cooperation Treaty.

The number of scientific literatures covering the period of January 2000 to December 2018 for this particular topic was 2325, while the total number of patents filed from the year 2000 to 2018 was 2454. The WTI and Brent crude oil price data was compiled from the U.S. Energy Information Administration [186], while the Dubai crude oil price for the same period was source from World Bank Open Data [187].

From Figure 2-18, it is observable that the average WTI, Brent and Dubai crude oil prices directly influence both the patents filed and scientific articles published, as the latter two clearly lag behind the fluctuation trends of crude oil prices. The grey shaded area represents the Great Recession which has led to a diminishing demand for energy between December 2007 and June 2009, causing the crude oil prices to collapse. From it, crude oil prices have fallen more than 36% over a year, followed by the declination of biodiesel-related patents by 10% and 16% in 2010 and 2012, respectively. Similarly, biodiesel-related research fell by 16% in 2012, which corresponds to a lag of 3 years from the effect of the Great Recession. Thus, the series of cascading effects from the global economic downturn show that scientific studies are less responsive to the fluctuation of crude oil economies in terms of time, as compared to patent work. Another noticeable trend between the years 2014-2016 was observed, when the average crude oil prices fell by approximately 50% of its price in 2014, due to a combination of factors. This is due to the increase of supply from new sources, such as shale oil and shale gas, in addition to oil producers maintaining the level of crude oil production. At the same time, the decrease in growth rate causes a shrink in global demand of energy, which led to a global overproduction of crude oil. Thus, biodiesel-related technologies have plummeted immediately in tandem with crude oil prices, while the numbers of research articles remain at a steady output. Current research approaches towards biodiesel production still heavily relies on the usage of catalyst and type of biodiesel reactor. According to Chuah *et al*. [55], new and cleaner biodiesel intensification technologies are in demand, which should be more environmental friendly from an operating condition perspective while maintaining high yield.

Thus, the purpose of this section is to critically review the development of current biodiesel production technologies and also to study the trend of emerging techniques for biodiesel intensification such as continuous stirred tank, microchannel, cavitation, microwave, and cosolvent while assessing the novelty and maturity of these technologies. The techno-economical perspective of biodiesel production on a global level is also addressed to highlight several high potential biodiesel producing country. Besides, a comprehensive analysis of biodiesel standards variations is also discussed to elucidate the differences of specifications from the major biodiesel producing countries.

2.5.1 Techno-economic analysis

The current biodiesel production volume as shown in Figure 2-19 illustrates that there are only a few countries that contribute more than a billion litres of biodiesel volume production annually, such as United States of America (USA), Brazil, Argentina, Germany, France, Spain, Poland, Indonesia, Thailand and China. The cumulative production of the aforementioned countries are 25.6 billion litres, equivalent to 74.8% of the total world production.

Figure 2-19. Worldwide leading biodiesel production in 2017, by continent (in billion litres).

The versatility of biodiesel feedstock allows many other countries across the continent to yield great potential for larger volume of biodiesel production. Thus, a data-driven predictive model was used to estimate the maximum biodiesel production volume of 155 countries as shown in Figure 2-20 [173]. The model is supported with primary sources of data obtained from the Food and Agriculture Organization of the United Nations Statistics Division [174], Index Mundi [175] and US Energy Information Administration [176]. In addition to the previously mentioned country, eight other countries such as, Malaysia, Ukraine, Canada, Netherlands, Russia, Belgium, Philippines, and Colombia have immense potential for biodiesel production volume exceeding a billion litres annually. The Southeast Asian nations such as Malaysia and Indonesia have the capacity to produce up to 16.3 and 30.3 billion litres of biodiesel per year, due to the excess availability of palm feedstock.

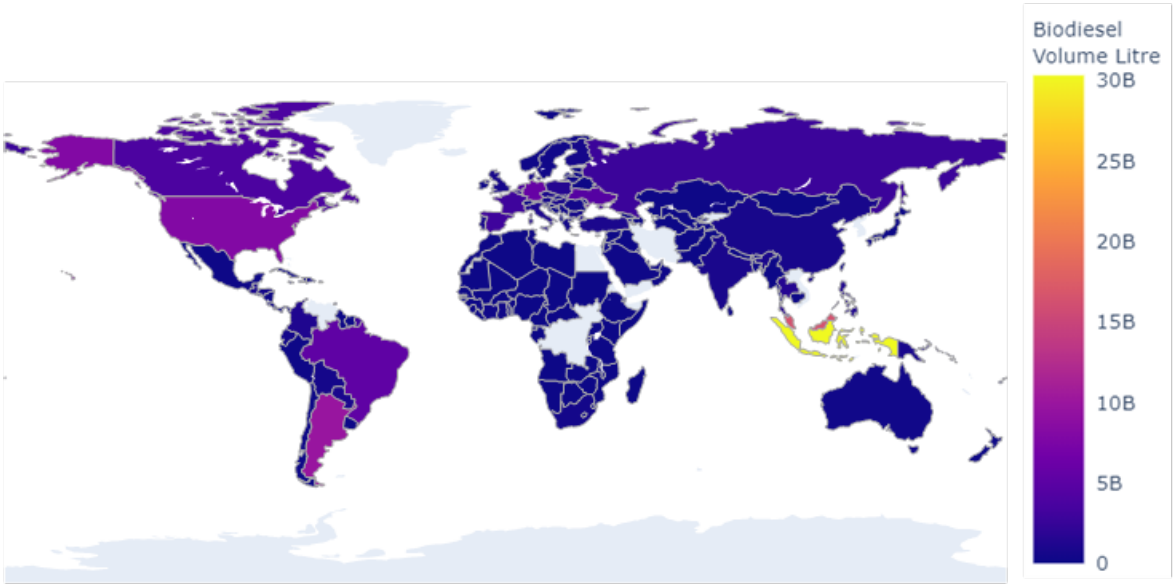

Figure 2-20. Maximum biodiesel production volume (in billion litres).

Figure 2-20 shows the maximum biodiesel blend levels that is achievable for the 155 countries, with respect to their level of diesel consumption. It is indicated that biodiesel can potentially replace all the diesel fuel consumption (B100) for only one country, namely, Malaysia, provided that the economic climate is viable for biodiesel production. There are other countries situated between the red and black lines in Figure 2-21 that have the potential to implement B10 to B100, while countries suitable for B1 to B10 blends are in between the black and blue lines, and countries not having potential above B1 are below the blue line.

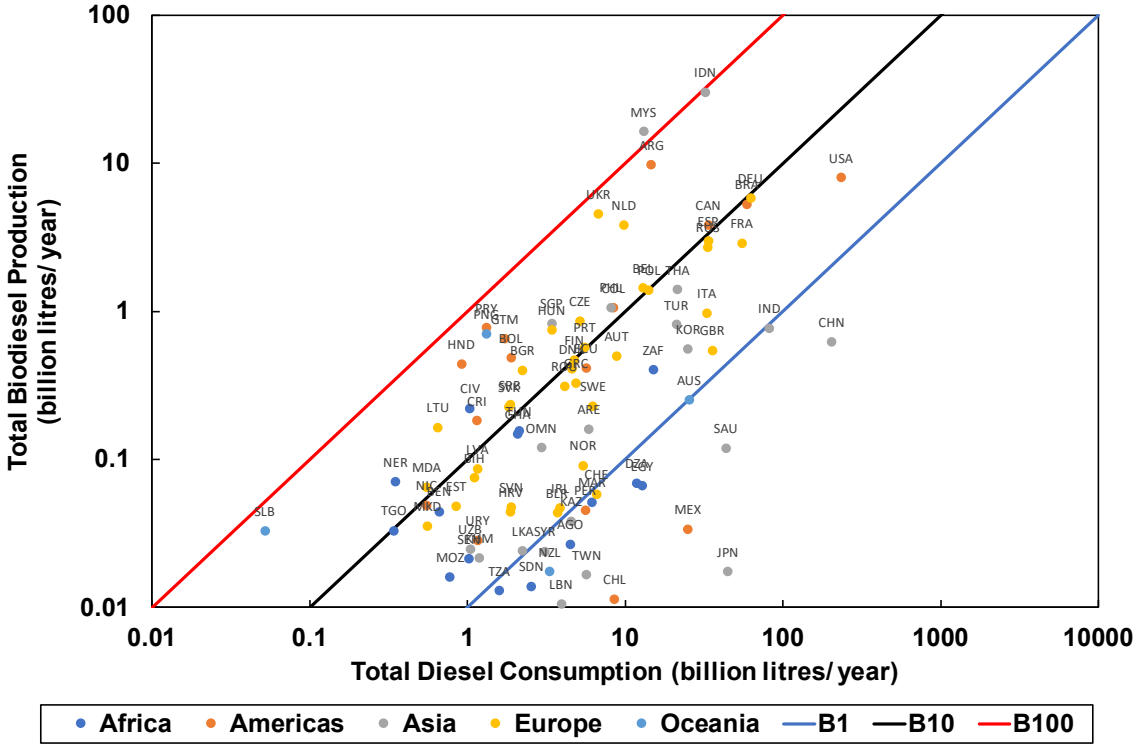

Figure 2-21. Maximum biodiesel blend levels achievable for each country.

There are 25, 41, and 23 countries that are able to volumetrically replace 10–100%, 1–10% and below 1% biodiesel blend in diesel, respectively. The large volume of diesel consumption in countries such as China, Indonesia, and Japan have made it less feasible for their economies to implement a higher blending ratio of biodiesel solely with the locally available feedstock.

2.6 Conclusion

The prevailing batch-type reactor is used as a benchmark against other types of biodiesel processing reactors. However, the comparison made is often unfair as the biodiesel yield and reaction time are the only factors to be compared. As such, other more important factors such as the processing capacity, energy efficiency, and scalability of technology have to be taken into consideration for a holistic comparison. In terms of the stirred-tank reactor, many reactors are designed to achieve homogeneous reactants via various methods of agitation. However, there are no well-defined approaches to measure the homogeneity of reactants throughout the transesterification process, as well as how the effect of agitation interacts with the other operating conditions. Furthermore, the limitations from the effect of agitation are also not addressed in different stage of transesterification, which is important to provide insights on the approach of optimising reactor. Therefore, an appropriate framework is required to define the range of operating conditions in a biodiesel reactor, where the significance of each parameter can be evaluated. There are research gaps in the study of kinetic model of batch type reactors, which are often limited to second-order kinetics mechanism, and does not include the kinetic rates for the intermediate reactions such as diglycerides and monoglycerides conversion. Additionally, mass transport mechanisms are not discussed extensively to provide the mass transfer coefficient which is important to provide a point of comparison for biodiesel reactors.

For microchannel reactor, the conventional flow production is inefficient due to the nature of the two phase behavior between oil and alcohol, which reduces their miscibility during the initialisation of transesterification reaction. Both the droplet and pulsating approaches in microreactor have proven to increase yield due to the enhanced surface to volume ratio. However, the physical flow pattern of the reactor is significant to the formation of biodiesel, as the contact surface between the liquid-liquid interface of methanol and oil defines the interfacial area for mass transfer. Thus, there is a research gap in the optical study of the droplets formation and interaction in microchannel reactor, which is important to characterise the physicochemical performance of the reactor. Similarly, the research gaps in kinetic models of microchannel reactor are often not integrated with its mass transport mechanism, to enable a like-to-like comparison with batch type reactor such that the advantage and disadvantage can be identified. There are also difficulties in studying the transient performance of a microchannel reactor since it is a continuous reactor, hence many analyses presented by literatures are based on the final yield point which may be misleading.

Chapter 3 Transient Transesterification for Palm Methyl Ester in a Stirred-Tank Reactor

3.1 Introduction

In this chapter, transesterification of palm methyl ester is processed through a conventional stirred tank reactor. Two main objectives were accomplished: 1) to identify the limiting stages involved in transesterification from transient to steady-state for traditional stirred-tank reactor; 2) to set a comparable benchmark for the reactor's operating condition with the biodiesel yield using a novel Pareto-Hierarchical Framework. The reaction kinetics of the batch-type reactor using the outputs from the designed framework was also conducted. The section explains the individual reaction parameters when operated under different stages during the transesterification process using a quantitative and qualitative approach.

Over the years, numerous studies on batch type biodiesel processing have been conducted [188,189]. The prevailing process of alkali transesterification has its limitations and inefficiency [190,191], and are susceptible to forming undesirable by-product such as soap, in the presence of free fatty acid within the lipid [188]. However, alkali transesterification is relatively faster than its acid counterpart with higher conversion [192] and can catalyse reaction at a lower operating temperature under atmospheric pressure [188]. Therefore, research has been conducted to compensate for the shortcomings of transesterification, from alternative catalyst [192], heterogeneous mixed oxide catalysts [193], miscibility improvement with cosolvent [194], to replacing the agitation process through different chemical reactor [195–197]. Previous research has not explicitly addressed the main problem of alkali transesterification in a batch reactor, to further optimise and improve upon the technique.

The selection of batch type reactor is due to it being the most generic type of processing technique in the biodiesel production industry, where many have to use it to represent the baseline when making a comparison with, Kouzu *et al.* [198] using a continuous stirred-tank reactor, Yasvanthrajan *et al.* [119] investigating microchannel reactors, and Chueluecha *et al.* [128] using packed-microchannel. Also, homogeneous alkali-transesterification is considered mainstream biodiesel processing technique, given that few of the important work during the development of biodiesel transesterification focuses on alkali conditioned transesterification [199–202]. Most large-scale biodiesel production has also adopted alkali and batch type processing, as they are widely accessible, simple to implement, and economically viable [203,204].

Another approach is to capitalise on the technical aspect of the transesterification process, which is often involved with a set of fixed operating conditions. Through understanding and optimising the

transesterification profile of the production process, it is possible to translate the methodological enhancement to benefit the economics of biodiesel [188,205].

Proceeding on this track, the main objective of this experimental study is to provide a methodological framework using Pareto and hierarchical analyses on the effect of key factors for biodiesel transesterification, particularly during the transient stages using the Design of Experiments methodology. Therefore, a four-factor three-level full factorial design is adopted for this experimental study, incorporating transient sampling intervals covering the initial physical-limiting, chemical-limiting and equilibrium stages of transesterification, instead of just the conventional steady-state outcomes. The use of a full factorial design allows screening of the experiments to determine which experimental variables have a real influence on the experiment results at different residence time. The orthogonal experiment design also allows like-to-like comparison of results in the other chapters with different biodiesel reactor using similar operating conditions. Thus, the analysis aims to establish an analytical guideline by incorporating the traditional final yield point analysis, with relative significance index across the entire transesterification process to allow like-to-like comparison. The indexed transesterification timeline is further clustered using supervised and unsupervised clustering algorithms based on their similarity index. The data and analyses obtained from this study are critical to support making decisions for operating conditions at a larger-scale production system, considering optimisation strategy from a technical and economical perspective.

3.2 Transesterification stages

The first mechanism suggests that the initial biphasic liquid system will eventually become a single-phase system, due to the FAME produced acting as an interface solvent for oil and methanol [57,180,206]. Noureddini and Zhu [57] proposed that the initial reaction is mass transfer controlled and transition into a faster reaction controlled regime due to the high immiscibility combined with a reaction delay that formed the sigmoidal FAME yield curve. Csernica and Hsu [206], suggested that the transition from mass transfer control to reaction control does not necessarily cause the sigmoidal production curve, but is due to a transition from a two-phase system to a single-phase system, regardless of the rate-limiting step.

However, the second proposed mechanism expects the two immiscible phases to exist throughout the methanolysis reaction, where the methanol-glycerol-FAME system is heterogeneous [207] and forms two conjugated three-component solutions. One of the phases consists of FAME-glycerol rich mixture with less than 2% methanol, while the other consists of a glycerol-methanol rich mixture with less than 3% FAME. Another study by Chiu *et al.* [208] on the distribution of methanol and catalysts between FAME and glycerine phases confirmed that the excess methanol would exist predominantly in the glycerol-methanol rich phase. Stamenković *et al.* [209] also supported this mechanism, explaining the FAME sigmoidal curve via an agitation perspective. The study suggested an intensive oil droplet breakage mechanism, led by enhancing the interfacial area of reactants through increased agitation. Thus, phase separation occurs during the reaction phase, leading to a complex multi-component system of opposing polarity.

This matches the hypothesis for transesterification mechanism, where (i) the initial rate of reaction is slow due to the immiscibility of the two-phase reactant nature, (ii) the process transitions into a higher rate of reaction as limiting factor no longer significant. As such, the optimisation for transesterification was investigated to overcome these restrictions of transesterification. For instance, Tacias-Pascacio *et al.* [210] compare RSM across four types of catalysts, namely, homogeneous alkaline, heterogeneous alkaline, homogeneous acid, and biocatalyst. The study outlines that biocatalysts are comparable to a conventional catalyst in terms of transesterification efficacy, particularly under the support of enhanced agitation method such as ultrasound. Another study from Ong *et al.* [211], combined artificial neural networks (ANN) and ant colony optimisation (ACO) as a combined optimisation strategy for the operating conditions of alkaline catalysed transesterification. The study offers a comprehensive optimisation framework that can be translated to another study, such as engine performance test and seed oil extraction. A study Nassef *et al.*[212] , optimised the lipid extraction of microalgae (*Scenesdemus quadricauda)* through the application of fuzzy modelling and Particle Swarm Optimisation (PSO). The combined strategy enables the fuzzy model to be trained and predict the lipid recovery process at a Root Mean Square Error (RMSE) of 0.0898.

The final lipid recovery from the microalgae was 62%, representing a 22% increment using the Design of Experiments methodology.

Figure 3-1 and Table 3-1 were constructed based on the observation from the understanding of the modern reaction kinetics, where transesterification no longer operates with mass transfer limitation, hence the initial slow reaction of the representative sigmoidal curve is removed. The testing parameters, particularly the agitation speed, are run at a higher speed to avoid the laminar flow regime and swirling effect, limiting mass transfer between reactants, based on the suggestion from works of literature [57,71,206,209,213]. The segregation of transesterification regime and stages allow us to present our study through the perspective of individual factor significance, with the objective to refine the current mechanism, instead of redefining the mechanism.

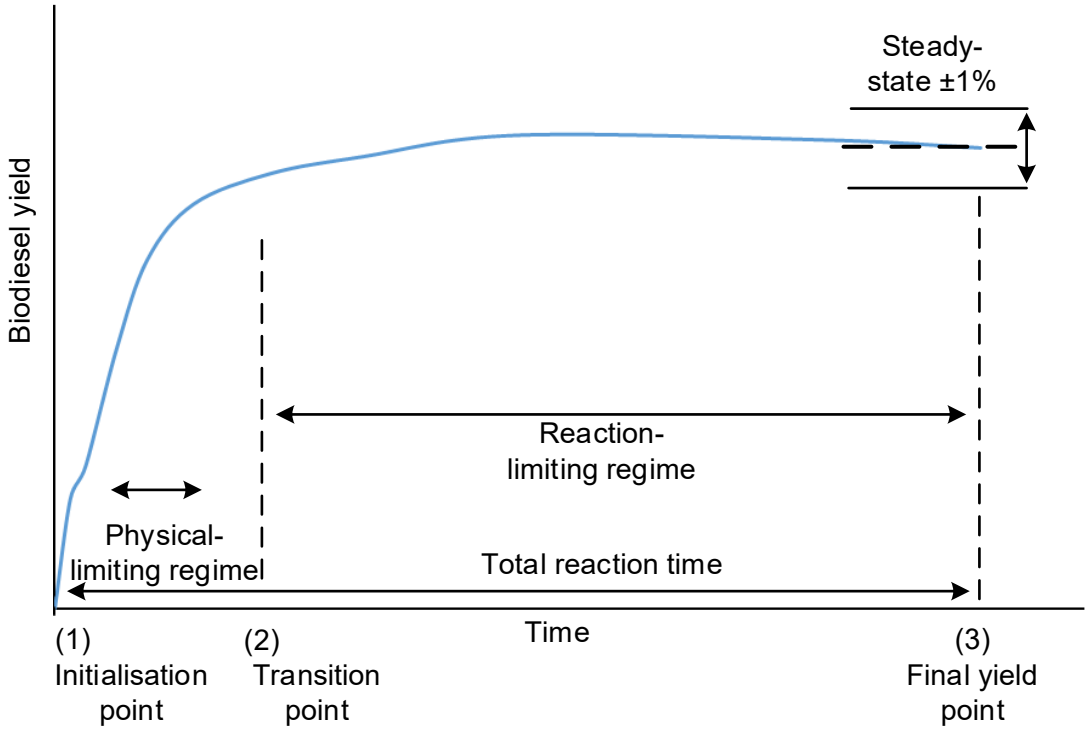

Figure 3-1. Idealised biodiesel transesterification stages.

Table 3-1. Biodiesel transesterification stages and its individual characteristic.

Phase	Transesterification Stage	Description
(1)	Initialisation point	Instantaneous contact between methanol and oil, followed by agitation.
(1) - (2)	Physical-limiting regime	Highest rate of reaction as forward reaction of transesterification dominates, also heavily dependent on homogeneous mixing from an agitator.
(2)	Transition point	When 70–80% of the oil has been converted into biodiesel, and forward transesterification reaction rapidly slows down.
(2) - (3)	Reactant-limiting regime	Rate of reaction retards as high amount of product (biodiesel and glycerol) shifts chemical equilibrium backwards. Methanol molar ratio is the main driving force to counter-shift the equilibrium forward to ensure high final yield.
(3)	Final yield point	Transesterification reaction reaches an equilibrium where the forward and backward reaction has reached steady-state, where no net product is formed.

3.3 Materials and experiment setup

The feedstock used for the experiment was commercial RBD palm olein. Analytical grade methanol 99.8 %, potassium hydroxide (KOH) >85 %, and hydrochloric acid 37 % were obtained from Qrec, Merck, and VWR, respectively. Standard analytical reagents such as methyl heptadecanoate were obtained from Sigma-Aldrich.

The transesterification reaction was conducted in a 1L cylindrical batch reactor, with a constant total reactant volume of 600 ml of, to represent methanol to oil molar ratio from 3:1 to 9:1. KOH is used as the catalyst to form potassium methoxide through the mixing of methanol. Catalyst loading ranging from 0.5–1.5 wt. % of oil. Table 3-2 shows the test factors accompanied by the lower and upper limit of each factor. Reaction time starts after the addition of potassium methoxide and initiation of the mechanical stirrer. Heat addition is done using a silicone jacket with a PID temperature controller, where the temperature is measured by a K-type thermocouple, which allows reaction temperature to be fixed in the range of 30–60 °C. Table 3-3 shows the resolution and the uncertainty for the instrument used throughout the experiment. The experiments were carried out through a full factorial test matrix design of 3^4, resulting in a total of 81 unique experiments each accompanied with ten different sampling time intervals.

Table 3-2. Design of experiments on full factorial test matrix for the 4-factor 3-level experiment.

Factor	**Unit**	**−1**	**0**	**+1**
Agitation rate	rpm	200	300	400
Catalyst loading	wt. %	0.5	1.0	1.5
Methanol to oil ratio	-	3:1	6:1	9:1
Temperature	°C	30	45	60

Table 3-3. Range, resolution and uncertainty of instruments.

Instrument	Measurement	Brand	Range	Resolution	Uncertainty
Thermocouple (K-Type)	Reagent temperature	RS Pro	−60 °C– 350 °C	0.1 °C	± 2.2 °C
Scientific oven	Temperature	Binder	25 °C– 300 °C	1 °C	± 1.0 °C
FID Gas Chromatograph	FAME Purity	Agilent	> 10^7 range with N_2 carrier and 0.29 mm id jet	-	-
Constant stirrer controller	Rotational speed	AQL	0–1000 rpm	1 rpm	± 1 rpm
Mechanical pipette	Sample volume	Dragonlab	0–10 ml	0.1 ml	± 0.3% vol.
Silicon heating jacket	Temperature	Custom fabricated	200 °C	0.1 °C	± 1.0 °C

Instead of using a conventional agitator designed for mixing, a custom baseline stirrer is made of High-density Polyethylene (HDPE). The HDPE mechanical stirrers were both constructed into the dimension of 0.09 m x 0.03 m x 0.13 m in length, width and thickness, which is then coupled to the end of the stirring rod from the AQL constant speed stirrer, with rotational agitation between 200–400 rpm. The schematic of the experimental setup is shown in Figure 3-2.

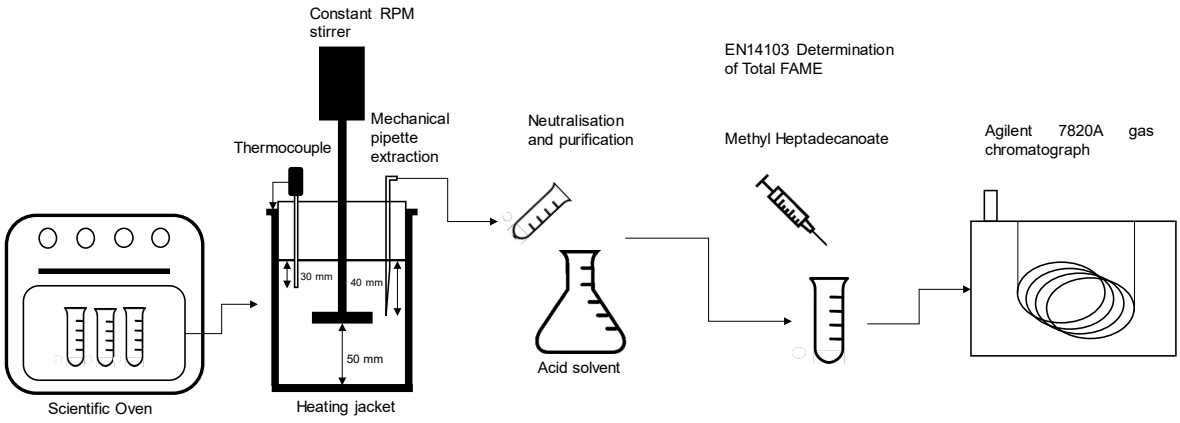

Figure 3-2. Schematic of the experimental setup using HDPE stirrer.

3.4 Sample characterisation

Sampling of transesterification (3 ml) was done using a mechanical pipette to extract ten samples between 30–1,800 s. The reaction of samples was quenched immediately using neutralisation method via diluted hydrochloric acid [214]. From it, fatty acid methyl ester (FAME) yield was determined by Agilent 7820A gas chromatograph (GC) system using a flame ionisation detector (FID), equipped with a capillary column (HP-INNOWax Column, 30 m x 0.25 mm, 0.25 µm). The GC analysis methodology follows that of the EN 14103 standard [215]. The FAME yield is defined as the conversion of vegetable lipids to biodiesel, from the gas chromatography analysis. Thus, FAME yield (%) was defined using the following equation:

$$FAME\ Yield\ (\%) = \frac{\sum A - A_{EI}}{A_{EI}} \times \frac{C_{EI} - V_{EI}}{m} \times 100 \qquad \text{Eq. 3-1}$$

where $\sum A$ is the total peak area from methyl ester in C_{14} to that in $C_{24:1}$, A_{EI} is the peak area corresponding to methyl heptadecanoate ($C_{17:0}$), C_{EI} is concentration (mg/ml) of methyl heptadecanoate solution, V_{EI} is the volume (ml) of the methyl heptadecanoate solution, and m is the mass (mg) of the sample, synthesised biodiesel .

3.5 Pareto analysis and normalisation plots

In the first part of this results, key results were interpreted using Minitab's Pareto chart of the standardised effects, shown in Figure 3-3.

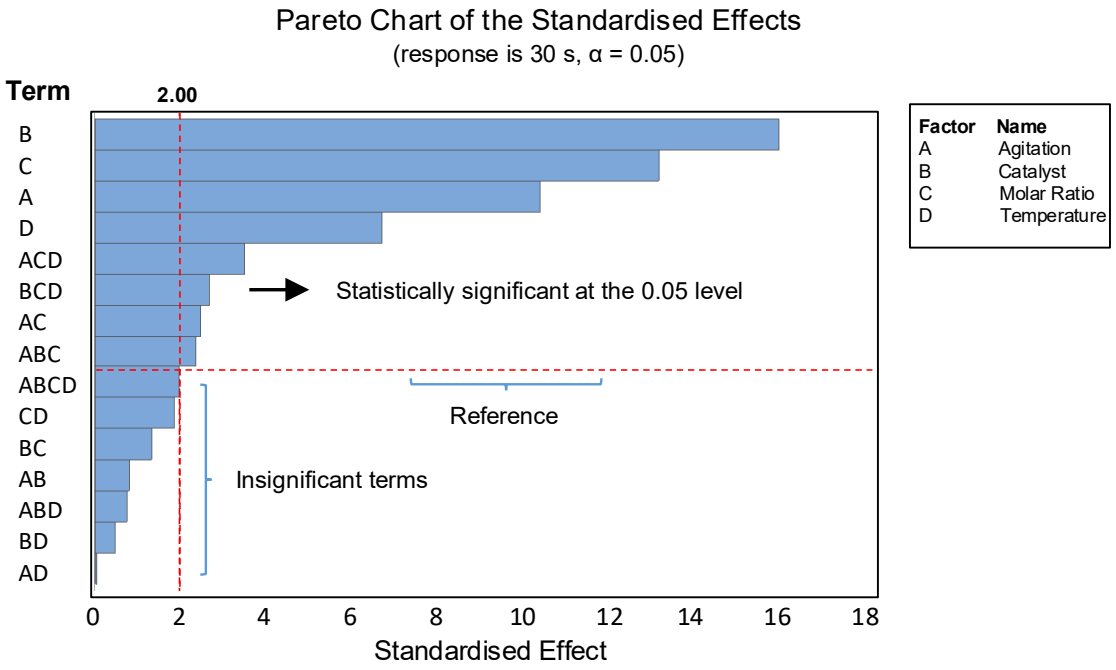

Figure 3-3. Pareto chart of the standardised effects at the 30s for biodiesel transesterification.

The four main effects of interest are namely, agitation speed (A), catalyst loading (B), methanol to oil molar ratio (C), and reaction temperature (D). The response in Figure 3-3 represents the biodiesel yield at 30 s into the transesterification process. The Pareto chart shows the standardised effect of factors when moving from a lower level (-1) to a higher level (+1), which is relative to a distribution fit line, that determines when the effects are zero. When the effect surpasses the Pareto analysis reference line, it is considered statistically significant at the 0.05 α-level with the current model terms.

The one-way interaction modelled terms are RPM, catalyst loading, methanol to oil molar ratio, and temperature as shown in Table 3-4. Additionally, one-term to four-term interactions are modelled using the maximum allowable of 15 permutations. The Pareto chart is constructed based on the degrees of freedom for the error term, the reference line is labelled at t. The quantile of a t-distribution, t is $(1-\alpha/2)$ where α is the significance level, with the degrees of freedom equal to the degrees of freedom for the error term [216].

Table 3-4. Modelled term for Pareto and normal plots.

One-term	**Two-term**	**Three-term**	**Four-term**
A = RPM	A*B	A*B*C	A*B*C*D
B = Catalyst	A*C	A*B*D	
C = Ratio	A*D	A*C*D	
D = Temperature	B*C	B*C*D	
	B*D		
	C*D		

The Pareto analysis was done across ten different yield sampling times, corresponding to 10 sets of responses. These responses are then combined to form the transient Pareto analysis, representing different independent factors for transesterification. The Pareto plots can identify which effects are large, from the absolute value provided in the form of standardised effect. However, it cannot determine if the factors influence the response, in this case, the biodiesel yield, positively or negatively.

Therefore, the analysis is followed by a discussion on the Normal plot, which also shows the standardised effect of factors relative to a distribution fit line representing zero effect. For the normal plot, positive effects will increase the response when the factor changes from a lower to an upper limit, while the converse is true for negative effect. Effects which is further away from zero on the x-axis has a larger magnitude and are more influential.

As the yield results from the full factorial test matrix are standardised in the analysis, the main focus here is to establish the key effects of the factors on the transesterification dynamically. The analysis results can provide the relevance of each factor at different stages of transesterification to better understand the limitation and potential of the factors independently.

3.6 Key results and discussion for Pareto analysis

The results and discussion section outlines the Pareto standardised effect analysis, followed by a similarity analysis via hierarchical cluster mapping, and normal distribution analysis, as described in the framework in Figure 3-4.

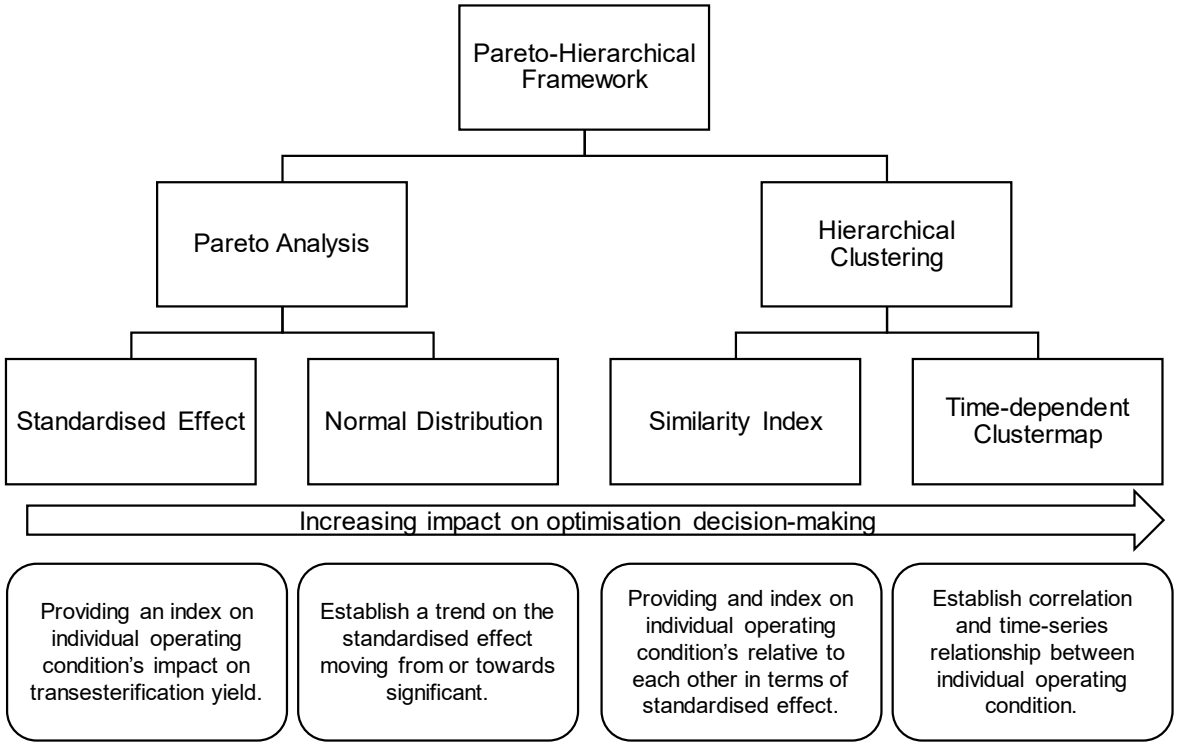

Figure 3-4. Pareto-Hierarchical Clustering Framework for biodiesel transesterification yield analysis.

3.6.1 Pareto analysis on the effect of agitation rate

Transesterification involves mixing oil and alcohol, which are naturally immiscible to each other. Agitation is required initially to initiate the reaction, as the turbulence and vortex shredding created from the agitator allows a larger contact surface between reactants. Thus, batch type reactor heavily relies on agitation, with the aid of usually an impeller to provide adequate mixing. In this experiment, 200 and 400 rpm are studied to identify its effect on the transesterification from transient to steady-state.

From the Pareto chart in Figure 3-5, the effect of high agitation is more pronounced at the physical-limiting regime. As the methanol-catalyst mixture is added to the preheated oil when the experiment commences, the high agitation rate is inevitably important for high reaction rate due to the need for homogenisation for temperature, catalyst and oil-methanol mixture. The general trend of the standardised effect for agitation rate showed a diminishing effect when agitation increased from 200 to 400 rpm. The standardised effect of agitation rate plummeted from 10.75 to 3.11, when the

transesterification process moves from the initialisation stage to the transition stage, reflecting a decrease of 3.46-fold in effect.

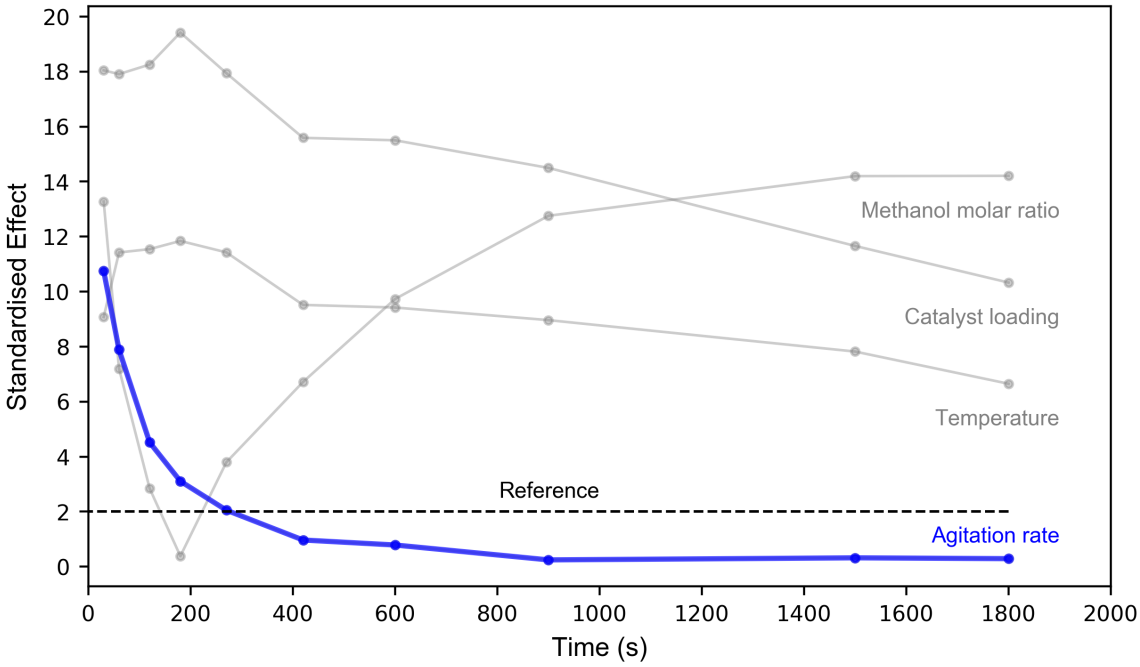

Figure 3-5. Transient Pareto analysis on the standardised effect of agitation rate.

The increasing agitation speed results in creating finer droplet size of the oil-alcohol mixture, and narrows the drop size distribution, effectively improving the specific interfacial area between the oil and methanol layers [209].

At the beginning of the reactant-limiting regime, as the mixture is achieving complete homogenisation, the role of agitation diminished in terms of maintaining an evenly distributed mixture system. Therefore, a high agitation rate is not required during the reactant-limiting regime as it does not further increase the biodiesel production rate, indicating that mass transfer becomes the least concern [217]. During the transition point of the transesterification process at about 270 s, increasing agitation produces a non-significant effect on transesterification, as the standardised effect reached the reference line. The trend continues to fall to a standardised effect of 0.30 at about 900 s into the reaction which represents the steady-state.

Similar results have been reported for increasing agitation with other feedstock, where the effect of high impeller speed will reduce the delay of biodiesel formation [57,206,213]. The use of a higher operating agitation speed has a natural limitation for improving biodiesel reaction rates. Therefore, high agitation throughout the entire transesterification stages may not be required for biodiesel production. Also, it is worth mentioning that high agitation might not be favourable throughout the entire process, especially when transesterification is coupled using a high catalytic loading condition.

This would consequently contribute to the facilitation of unwanted competing reaction such as saponification due to base-catalysed transesterification, which was observed in this experiment.

3.6.2 Pareto analysis on the effect of catalyst loading

The standardised effect of increasing catalyst loading is observed to significantly improve the biodiesel yield, as shown in Figure 3-6. During the physical limiting regime, the increase of catalyst concentration in the methanol-oil mixture increases the biodiesel yield, as more catalyst effectively increases the contact surface with a reactant, which contributed to the reduction of activation energy during the beginning of transesterification [218]. The standardised effect of catalyst loading showed an increase from 18.00 to a peak of 19.40 during the physical limiting regime, for 0.5 wt. % to 1.5 wt. % catalyst loading.

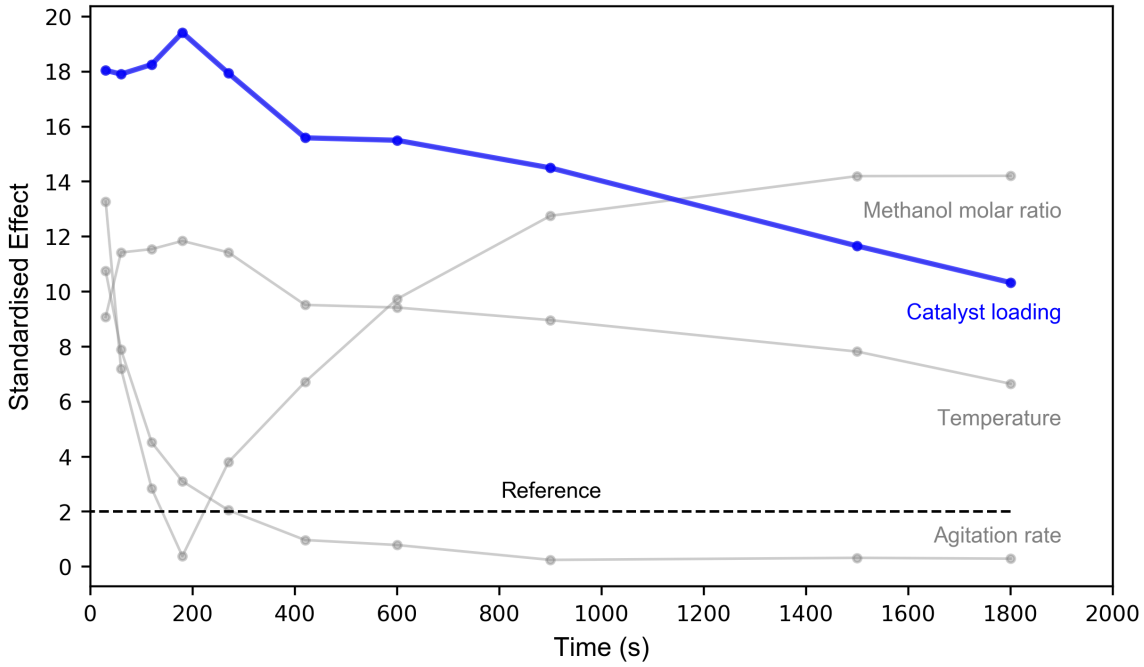

Figure 3-6. Transient Pareto analysis on the standardised effect of catalyst loading.

The result of peaking during an increased concentration of catalyst is speculated to be linked to the cascading conversion of glycerides to biodiesel and glycerol. Table 3-5 shows the base type catalysed reaction rate constants for biodiesel transesterification. From it, the forward reaction rate constants of diglyceride to monoglyceride and monoglyceride to glycerine, are observed to be higher than of triglycerides to diglyceride. Additionally, it is noticeable that the reaction rates of glycerides conversion order are independent of feedstock, catalyst, and temperature. However, since catalyst loading has the highest standardised effect in transesterification within this regime, it is evident to deduce that the elevation of catalyst concentration dominantly affects transesterification positively.

Table 3-5. Reaction kinetic constants of base-type catalysed transesterification.

Oil	Alcohol/ Molar ratio of alcohol to oil	Catalyst/ loading (wt. %)	Temperature (°C)	Reaction Mechanism; kinetics model	Triglyceride -> Diglyceride ($L \cdot mol^{-1}min^{-1}$)	Diglyceride -> Monoglyceride ($L \cdot mol^{-1}min^{-1}$)	Monoglyceride -> Glycerine ($L \cdot mol^{-1}min^{-1}$)	References
Palm	Methanol 6:1	KOH 1.0	60	Reversible reactions; second-order	0.0360 (wt. %.min)$^{-1}$	0.0700 (wt. %.min)$^{-1}$	0.1910 (wt. %.min)$^{-1}$	[71]
Palm	Methanol 6:1	KOH 1.0	60	Reversible reactions; second-order	0.0157	0.1184	0.1310	[219]
Soybean	Methanol 6:1	NaOH 0.2	50	Reversible reactions; second-order	0.0500	0.2150	0.2420	[57]
Sunflower	Methanol 6:1	KOH 0.5	25	Reversible reactions; second-order	0.6116	2.0642	2.0642	[213]

Furthermore, as the reaction exits the physical-limiting regime, the standardised effect of catalyst loading is observed to be gradually decreasing until the end of the reaction. The effect of high catalyst loading during the reactant-limiting regime is not as efficient as during the physical-limiting regime, but remains relatively important for producing high biodiesel yield when compared with the reference line.

There is also a noticeable change in the rate of reduction for the standardised effect at two different regimes, between 180 s to 420 s, and 420 s to 1800 s, with the former decreasing at a higher rate than the latter. The standardised effect for catalyst loading was observed to be 10.32 at steady-state, representing a total reduction of 1.88 times in standardised effect since the physical-limiting stage.

This reduction during the reactant-limiting regime is most likely due to reaction approaching chemical equilibrium, where the tri-, di-, monoglyceride levels are low. Thus, becoming relatively insensitive to the benefit from the lowered activation energy by using a catalyst, as compared to that of the physical-limiting regime.

3.6.3 Pareto analysis on the effect of methanol to oil molar ratio

The effect of methanol to oil molar ratio on transesterification is observed at two different ends, for the two different phases, as shown in Figure 3-7.

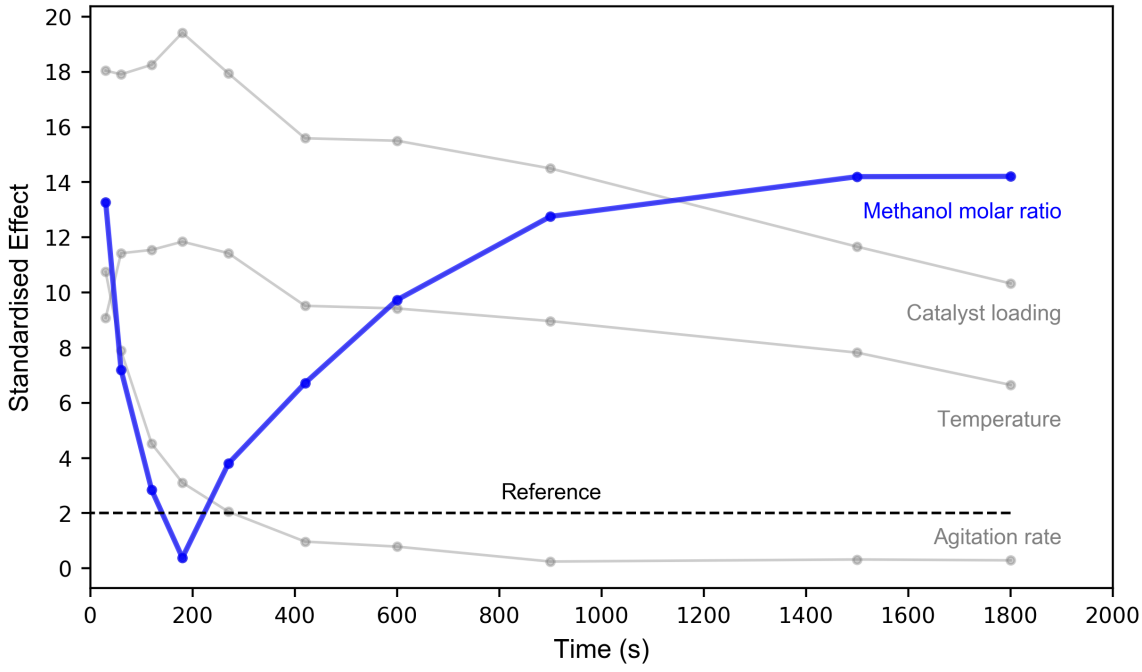

Figure 3-7. Transient Pareto analysis on the standardised effect of methanol to oil molar ratio.

For the physical-limiting regime, the standardised effect of molar ratio has shown a clear significance in the biodiesel yield from the start of the reaction, but the standardised effect undergoes declination as it transits into the reactant-limiting regime.

The high standardised effect at the beginning (13.28) can be explained by the increase in methanol quantity that increases the contact surface between oil and methanol, hence resulting in more biodiesel to be produced. The effect of methanol to oil molar ratio changes from significant to non-significant over the physical-limiting regime, where it plummeted to a standardised effect of 0.38, which is equivalent to a 35-fold reduction in total. This may seem counterintuitive as the conventional understanding of molar ratio is straightforward. The higher molar ratio should have a positive effect on the rate of reaction and biodiesel yield. However, this is only true for the final yield point, when methanol becomes a limiting factor for the chemical reaction. Thus, the use of high methanol to oil molar ratio will promote the complete conversion of oil, resulting in a greater biodiesel yield.

During the physical-limiting regime, higher methanol to oil molar ratio contributes to the inefficiency of the transesterification process. This is postulated to be related to the miscibility between oil, alcohol, and biodiesel. Methanol and oil are naturally immiscible due to alcohol being polar, while lipid being non-polar. Therefore, for a lower molar ratio setting, the biodiesel produced initially is more likely to diffuse into the oil, increasing the permeability between oil-methanol, resulting in higher biodiesel yield. On the other hand, when a higher molar ratio is used, the biodiesel formed initially will have a higher tendency to immediately diffuse into most of the methanol. Thus, oil-methanol remains to be less miscible, as a result, yield and reaction rate are low.

As the biodiesel concentration increases, the transesterification is no longer physical-limiting. Instead, the reaction rates retards, as the high concentration of biodiesel and glycerol shifts the chemical equilibrium backwards. The change in reaction rates is noticeable between the two regimes, where the reactant-limiting regime is dominantly driven by methanol to oil molar ratio, which is supported by the results in Figure 3-7.

Standardised effect of methanol to oil molar ratio increases from 0.38 to 14.21 (final yield), as higher molar ratio invariably promotes complete transesterification, reflecting an improvement of 37.4 fold in terms of standardised effect during the reactant-limiting regime.

3.6.4 Pareto analysis on the effect of reaction temperature

Temperature's role in transesterification is to provide sufficient activation energy for the reaction and improve the solubility between oil and methanol as the miscibility of liquid increases with temperature. The standardised effect of temperature is statistically significant from transient to steady-state, as shown in Figure 3-8.

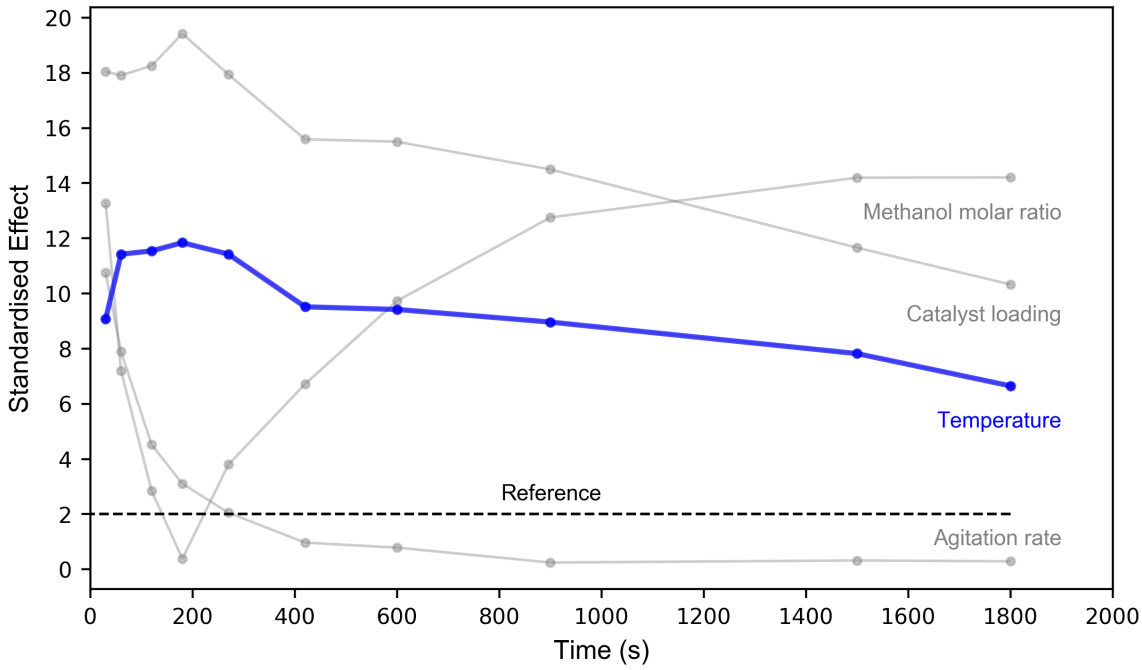

Figure 3-8. Transient Pareto analysis on the standardised effect of temperature.

The standardised effect of temperature was observed to be 9.07, followed by a steep increase between 30 s to 60 s, while maintaining the similar magnitude of standardised effect during the physical-limiting regime, arriving at the peak of 11.8, at about 180 s. The sharp increase is most likely due to the addition of methanol to the oil, causing the preheated-oil to reduce in temperature, hence the upper testing limit of 60 °C is inevitably more effective due to the larger recovery of temperature difference. Besides, the mixture also requires time for homogenisation of temperature across, where the physical-limiting regime is observed with higher standardised effect as compared to the reactant-limiting regime.

Additionally, the temperature is also responsible for providing the reactant system with enough energy, for overcoming the activation energy required for the initiation of transesterification mechanism. Therefore, the increase in temperature also exhibits similar characteristics in standardised effect compared with catalytic loading. From it, a larger improvement can be observed at the physical-limiting regime, due to a high level of glycerides acting as precursors in transesterification, which favours the forward reaction.

During the reactant-limiting regime, a relatively larger drop in effect is observed from 270 s to 420 s, from a standardised effect of 11.43 to 9.52. The trend of temperature effect is followed by a small but noticeable decrease until steady-state, remaining relatively constant throughout, achieving a standardised effect of 6.65 at the final yield. The decline in standardised effect is most likely due to the reactant no longer requiring a high demand for energy in the system, while simultaneously alleviating issue caused by immiscibility, as the system becomes dominantly single-phase liquid [220].

3.6.5 Pareto analysis across the individual main effect

The results from the Pareto analysis for each factor are independent of each other. However, comparisons can still be made to examine the relative importance between factors and draw a correlation of the main effects on transesterification during the transient stage. The heat map for the individual factor's respective standardised effect is shown in Figure 3-9.

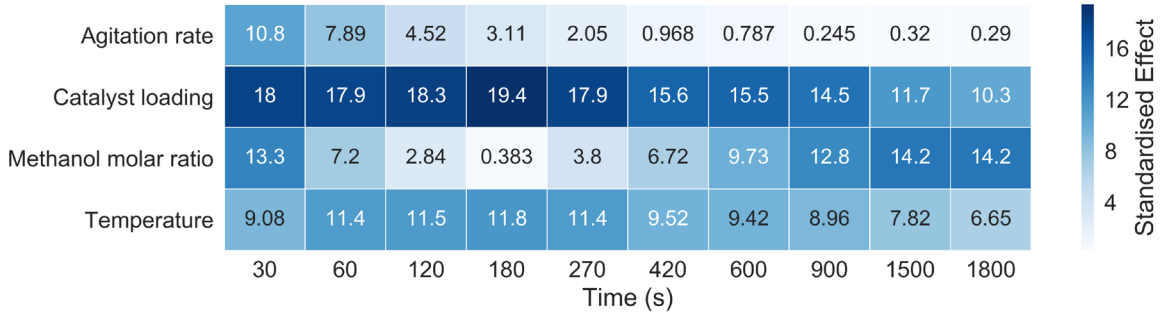

Figure 3-9. Heat map for standardised effect during transient transesterification for all factors.

From it, each of the factor's standardised effect is ranked at different stages and tabulated in Table 3-6.

Table 3-6. Standardised effect of factors at initialisation, transition, and final yield point.

Factors	Initialisation		Transition		Final Yield	
	Standardised effect	**Ranking of relative importance**	**Standardised effect**	**Ranking of relative importance**	**Standardised effect**	**Ranking of relative importance**
Agitation rate	10.75	Third	3.11	Third	0.29	Fourth
Catalyst loading	18.05	First	19.42	First	10.32	Second
Methanol molar ratio	13.28	Second	0.38	Fourth	14.21	First
Temperature	9.08	Fourth	11.84	Second	6.65	Third

During the physical-limiting regime, the higher rate of agitation is hypothesised to facilitate homogenisation, heat and catalyst to spread across the mixture. The postulation is supported by the increase in standardised effect for catalyst loading and temperature, followed by a simultaneous decline in the standardised effect for both factors as transesterification enters reactant-limiting regime.

Besides, the standardised effect for catalyst loading and temperature showed similar trends with a consistent offset. This observation reflects that excess catalyst and temperature produced a higher yield, possibly through the reduction in activation energy by the former, and provision of energy by the latter.

As transesterification reaches the reactant-limiting regime, the agitation rate increases have no significant effect on biodiesel yield. Evidently, increasing agitation does not improve mixing between methanol and oil, which suggest that the transesterification at this stage can be dominantly diffusion-driven. Here, the increase in concentration gradient by increasing methanol to oil molar ratio contributed to a higher standardised effect, resulting in a reactant-limiting regime.

Consequently, additional heat and catalyst benefit biodiesel yield during the reactant-limiting stage, but methanol to oil molar ratio surpasses their standardised effect halfway into the stage, leading it to be the most significant effect until steady-state has been achieved.

3.7 Hierarchical agglomerative clustering

The categorisation of individual factors and transesterification regimes was done using a hierarchical agglomerative clustering method. This is implemented to analyse the correlation and time-series relationship of main effects, through a bottom-up approach. Initially, each of the main effects and time intervals is treated as an individual cluster, where

(i) clusters that are the closest in a distance matrix are identified and labelled.

(ii) combining both clusters with the highest similarity.

Processes (i) and (ii) are repeated until all of the clusters are merged, hence forming elements of a dendrogram [221] leading to a clustermap [222]. For the dendrogram, the height of the dendrogram represents the order in which the clusters were joined. The length of the line from each cluster represents how close or distant related they are in their respective grouping. Overall, a dendrogram is a derivation of a distance matrix using existing data points, in this case the value of the standardised effect.

In this study, the values used in the clustering analysis are derived from the standardised effect. Therefore, the clustering of each group serves as a similarity indication, with respect to their individual influence on biodiesel yield, the classical hierarchical clustermap for standardised effect is implemented and illustrated in Figure 3-10a. Additionally, for this study, an extension of the classical hierarchical agglomerative clustering is used, with a time-dependent condition shown in Figure 3-10b. The clustering methodology follows (i) and (ii), with an additional condition to

(iii) align the clusters by time.

This modification of clustering can be applied in our study since it considers the sequence of time which is a reasonable justification for the transesterification process. Therefore, the classical hierarchical clustering is generated to benchmark against the time-dependent clustering method, allow for the comparison of individual clusters with and without the temporal dimension.

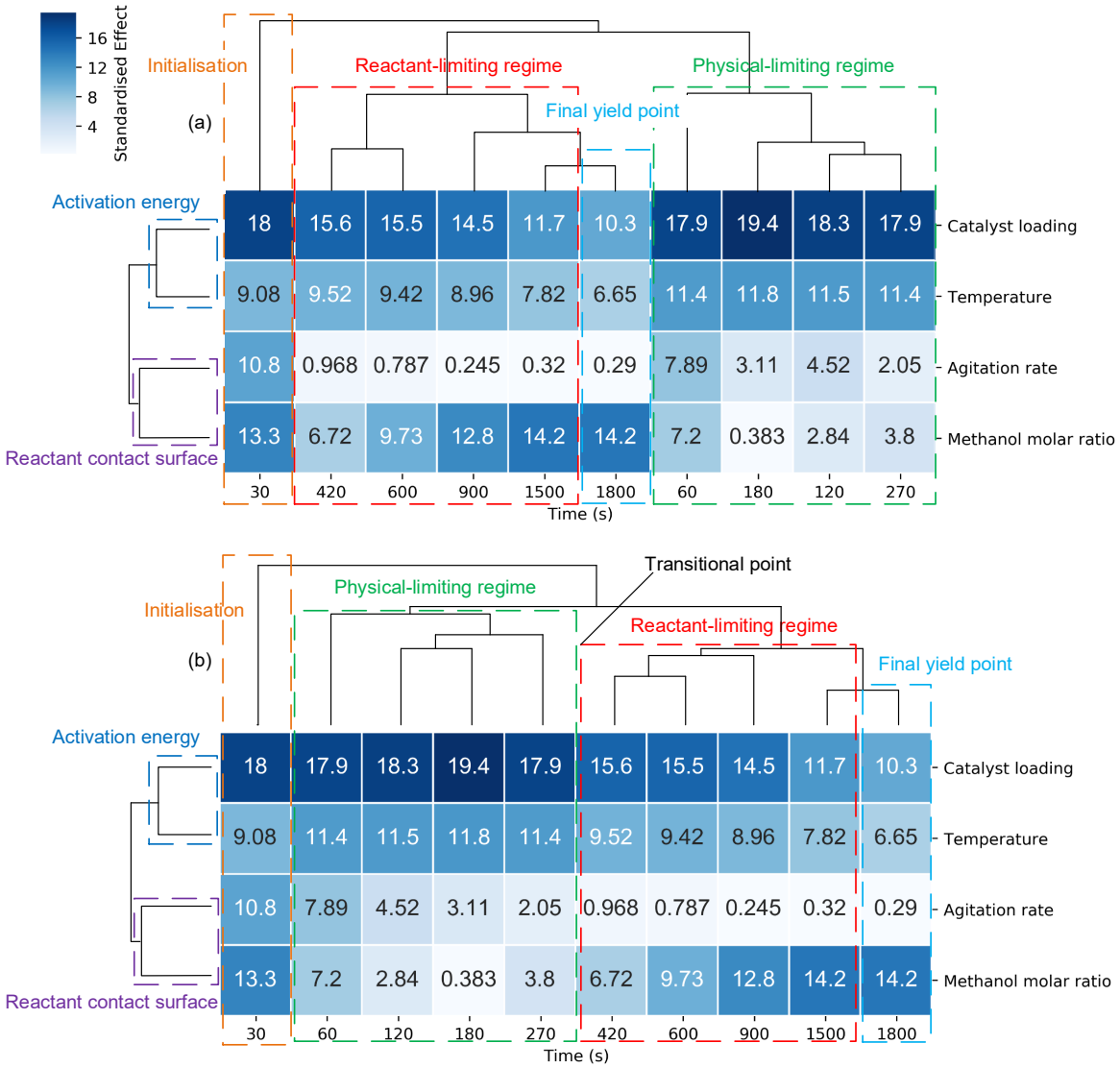

Figure 3-10. (a) Classical (b) Time-dependent hierarchical clustermap analysis for standardised effect.

The overall outcome using two different hierarchical clustering techniques in Figure 3-10, provided a noticeable difference in the lower level of clustering as compared to the higher level. However, it is important to note that although the cluster sequence in Figure 3-10 is not in ascending order, the individual elements of each cluster remain unchanged even when time-effect is considered, as shown in Figure 3-10b. This result validates the classical hierarchical clustering with the time-dependent clustering methods.

Figure 3-10 also shows the clustermaps with the higher level of clusters labelled, with their appropriate functions and regimes, in the context of the transesterification process. The labelled clusters in the main effects are activation energy and the reactant contact surface, while for the time-dependent clusters are, the initialisation, followed by physical-limiting and ending with the reactant-limiting regime.

Based on Figure 3-10, the standardised effect's averaged magnitude is in the increasing order of methanol to oil molar ratio, agitation rate, temperature, and catalyst loading for the physical-limiting stage (transient-state). For the reactant-limiting stage, the standardised effect's averaged magnitude is in the increasing order of agitation rate, temperature, methanol to oil molar ratio, and catalyst loading (steady-state).

The clustering of individual main effects, in the horizontal direction is identical, where catalyst loading and temperature falls under the same group, while the agitation rate and methanol to oil molar ratio formed the other cluster. Although the main effects are segregated into two distinct clusters, they are still moderately related judging from the length of their individual lines. This also can be interpreted by the difference of their standardised effect throughout the entire process.

It can be observed that despite the activation energy cluster has a sizable difference in standardised effect when the time interval is compared independently. Nonetheless, when the activation energy cluster is analysed as a whole, the main effects exhibit similar evolution trends for their standardised effect throughout the process, with a consistent offset.

On the contrary, the reactant contact surface cluster formed by agitation rate and methanol to oil molar ratio is slightly less related than the activation energy cluster. The main similarity for this group is the trend during the physical-limiting regime, where the standardised effects of both factors experience significant decreases. However, the cluster does not have a clear relationship in the reactant-limiting regime, which suggest the weak correlation for this particular cluster.

3.8 Normal plot analysis on one-way transient transesterification interactions

3.8.1 Normal plot on the effect of agitation rate

The effect of agitation when elevated from 200 to 400 rpm has shown significance up to 270 s, leading to a change in standardised effect from 10.75 to 2.05 from 30 s to 270s. The effects of the agitation rates from the Pareto analysis has also presented a trend which agrees with the normal plot result in terms of factor significance, shown in Figure 3-11.

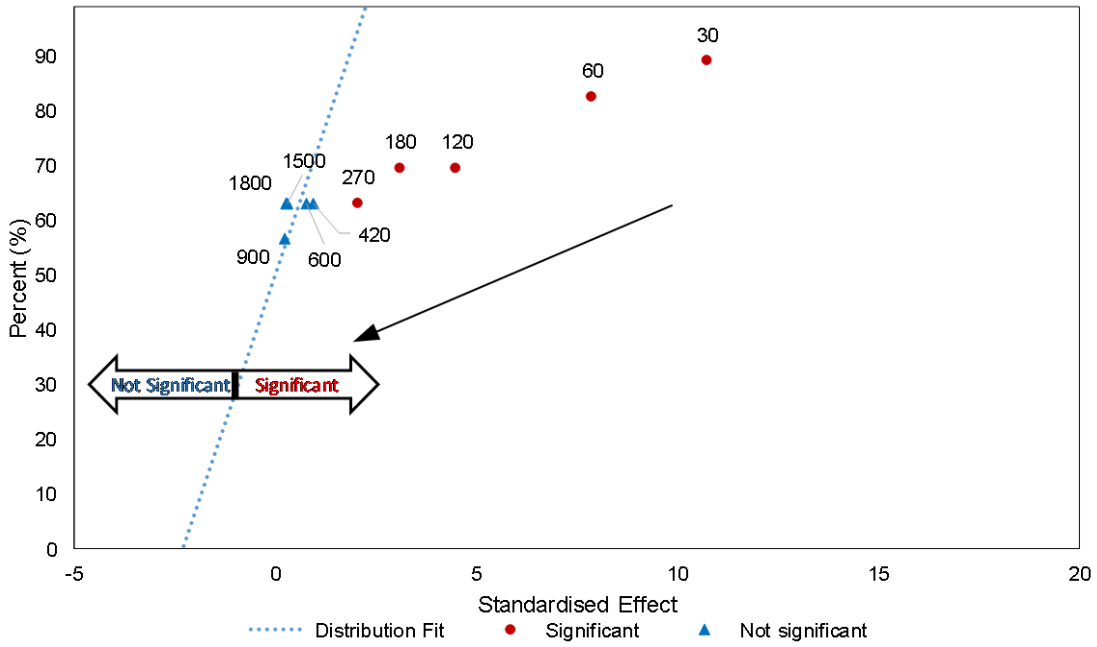

Figure 3-11. Normal plot for the effect of agitation rate from 30s to 1800s.

Increased agitation showed a more prominent effect in the first 120 s, when a high agitation rate improves homogenisation of methanol-oil mixture, temperature, and catalyst distribution. This duration is the window of transesterification where mechanical agitation can benefit the biodiesel yield the most, as the increase of contact surface between oil and methanol speeds up the reaction, resulting in the physical-limiting regime.

From the results, agitation is not significant beyond the physical-limiting regime, as the standardised effect hugs closely to the distribution fit line, representing the zero effect of a factor.

3.8.2 Normal plot on the effect of catalyst loading

The excess catalyst in this study has proved to be very important for high biodiesel transesterification yield, as the factor has contributed positive effects throughout transesterification when catalyst

loading changes from 0.5 wt. % to 1.0 wt. %. A noticeable improvement in the standardised effect was achieved at 180 s in Figure 3-12, which corresponded to the peak in the Pareto analysis.

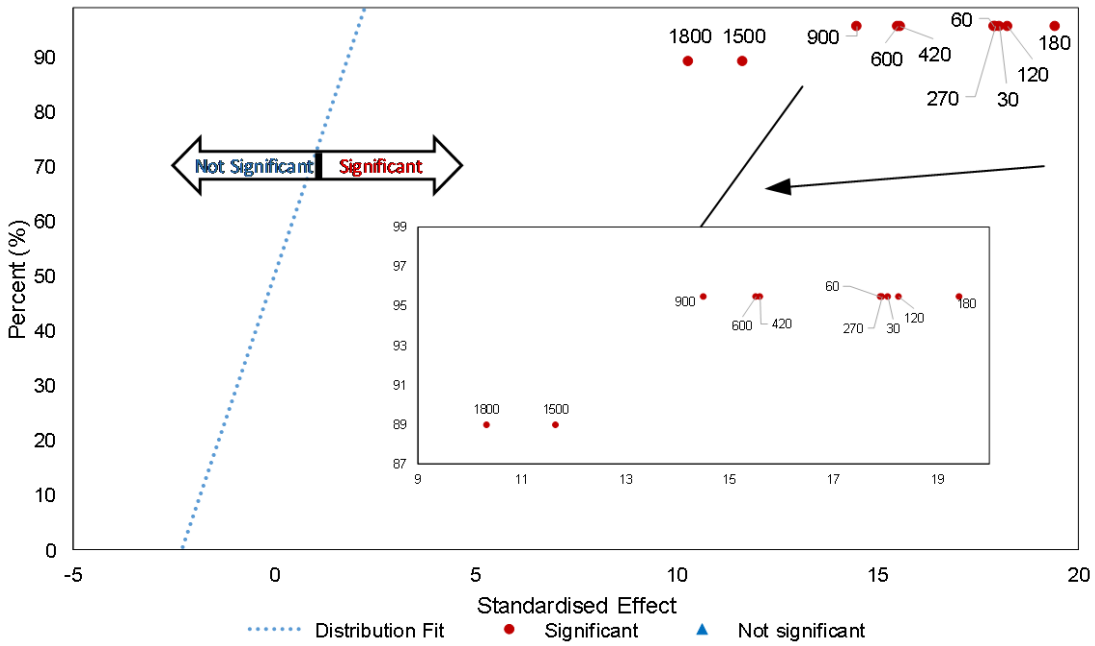

Figure 3-12. Normal plot for the effect of catalyst loading from 30s to 1800s.

The standardised effect is observed to decrease beyond 180 s, as the transesterification advances to reactant-limiting from physical-limiting, corresponding to a total reduction of 1.88-fold, from a standardised effect of 19.42 to 10.33, while remaining statistical significance.

Overall, the catalyst effect has shown limited sensitivity towards time-dependent changes in transesterification, which is reflected by a narrow distance amongst the individual data points from Figure 3-12.

3.8.3 Normal plot on the effect of methanol to oil molar ratio

The standardised effect of methanol to oil molar ratio is widely spread across transient to steady-state, which illustrate that the effect of methanol to oil molar ratio is receptive to changes over time. Figure 3-13 shows that the standardised effect for methanol to oil molar ratio increases from −13.28 to −2.84 at 30 s to 120 s. This explicitly indicates that the excess use of methanol to oil molar ratio negatively impacted biodiesel yield, particularly at the beginning of the transesterification process. This result is important as the previous analysis could not determine the direction of effect, since only the effect significance can be determined.

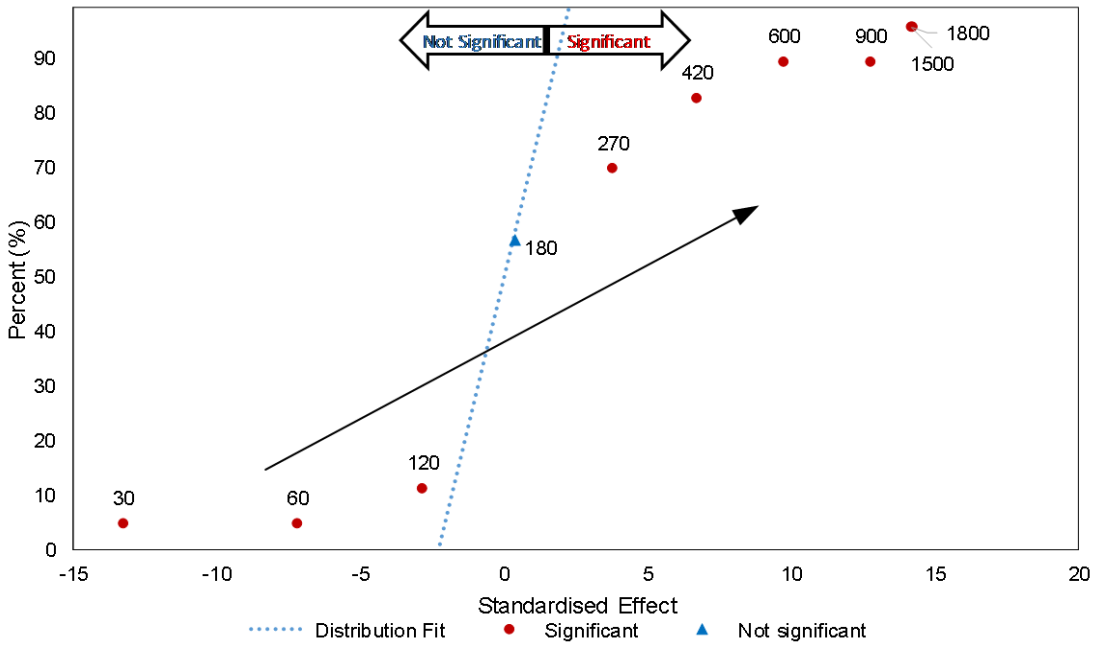

Figure 3-13. Normal plot for the effect of methanol to oil molar ratio from 30s to 1800s.

However, excess methanol has zero effect on biodiesel yield at about 180 s, which coincide with the end of the physical-limiting regime. As the reaction progresses to the reactant-limiting regime, high methanol to oil molar ratio can produce a greater magnitude of effect on biodiesel yield, reaffirming that transesterification heavily relies on the methanol to oil molar ratio for high final yield.

3.8.4 Normal plot on the effect of reaction temperature

The elevated reaction temperature produces a positive effect throughout biodiesel transesterification, as shown in Figure 3-14. The act of increasing reaction temperature from 30 °C to 60 °C is observed to provide the largest enhancement to biodiesel yield, especially at the beginning of the reaction. This is reflected when the standardised effect increases from 9.08 to 11.84 from 30 s to 180 s, which superpose the peak performance trend for catalyst loading at 180 s.

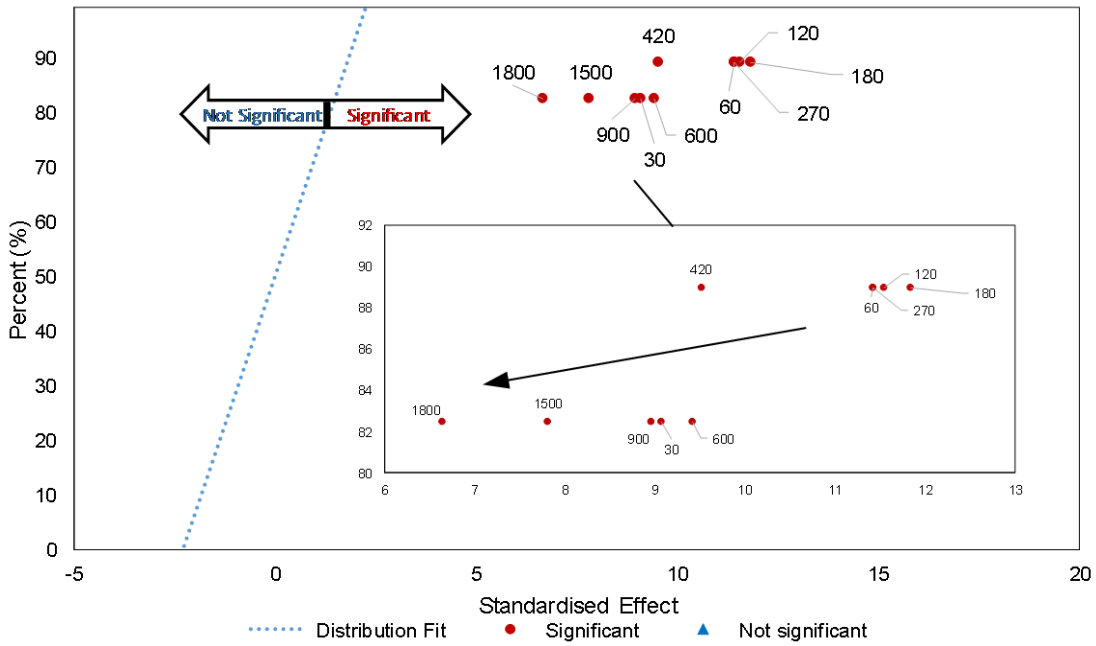

Figure 3-14 Normal plot for the effect of temperature from 30s to 1800s.

The result is then followed by a reduction in effect as it progresses from physical-limiting to reactant-limiting regime. A progressive reduction of standardised effect from 11.84 to 6.65 is shown, during the reactant-limiting to the final yield point, resulting in a 1.78-fold decrease in effect, which is relatively small compared against agitation rate and catalyst loading.

The declination of effect is most likely due to the reaction system requiring less energy for the later stages as compared to the initial stages. Also, improvement of solubility for the reactants due to heating effect has reached a threshold, resulting in a smaller improvement towards the end of the reaction. The standardised effect of temperature has a minimal fluctuation overall, which suggests that temperature is a less sensitive factor to time, but at the same time significant to the improvement of biodiesel yield.

3.8.5 Comparison of normal plot analysis across the individual main effect

The main effects were first determined with a normal plot, then compiled and tabulated as shown in Table 3-7. The '↑' sign denotes that the main effects positively influence the biodiesel yield and significant to the response. The '↔' represents not significant to the transesterification, while '↓' denotes negative effect towards the response. The values of the standardised effect for each main effect has been normalised, where every additional '↑' sign is approximately a quarter strength of the highest standardised effect

Table 3-7. Main effect's direction of significance and relative magnitudes.

Time (s)	**30**	**60**	**120**	**180**	**270**	**420**	**600**	**900**	**1500**	**1800**
Factors	**Initialisation**				**Transition**				**Final Yield**	
Agitation	↑↑↑	↑↑	↑	↑	↑	↔	↔	↔	↔	↔
Catalyst loading	↑↑↑↑	↑↑↑↑	↑↑↑↑	↑↑↑↑	↑↑↑↑	↑↑↑↑	↑↑↑↑	↑↑↑	↑↑↑	↑↑↑
Methanol to oil molar ratio	↓	↓	↓	↔	↑	↑↑	↑↑↑	↑↑↑	↑↑↑	↑↑↑
Temperature	↑↑	↑↑↑	↑↑↑	↑↑↑	↑↑↑	↑↑	↑↑	↑↑	↑↑	↑↑

To elaborate for the results from Pareto analysis, the normal plot indicates that most of the main effect showed significance toward biodiesel production, at different stages of the transesterification process. One key observation from Table 3-7 is the standardised significance of agitation rate and methanol to oil molar ratio, where the main effects impact non-overlapping stages. The only exception is 270 s, where both have relatively low influence. These results suggest that there could be counteracting synergy for both factors when increasing the level of study.

During the initialisation, the higher molar ratio used for transesterification showed significance in a negative manner, whereas increased agitation suffered from a diminishing effect. Catalyst loading and reaction temperature have relatively similar trends, with the former leading by a significant margin. For the transitional and final yield stage, all factors showed a favourable inclination towards biodiesel yield, except for agitation, where there is no improvement, nor deterioration.

3.9 Optimisation of the operating conditions

The response optimisation was then applied using the full factorial analysis results. The response optimiser identifies the multiple combinations of an input variable settings that optimise a single or a set of responses, in this case, the biodiesel yield at a different timeframe of the transesterification.

The goal was set up to maximise the response (yield) using the regression model at a different time of transesterification. The yield fit is the results calculated from the highest possible yield that is achievable from the regression model, hence the values could be overestimated due to the errors in the regression model. A 95% confidence and prediction intervals were selected to ensure the validity of the optimisation. The composite desirability outlines how likely the parameters are chosen to achieve the targeted value. Table 3-9 shows the results of optimising the operating conditions using the full factorial results.

Table 3-9. Response optimiser for operating conditions from 0 to 1800 s.

Time (s)	RPM	Catalyst (wt. %)	Molar Ratio	Temperature (°C)	Yield target	Yield fit	Composite desirability
30	400	1.5	3	60	74.1853	77.1343	1
60	400	1.5	6	60	84.8535	90.5073	1
120	400	1.5	6	60	90.1970	91.7787	1
180	400	1.5	9	60	92.9500	94.1468	1
270	400	1.5	9	60	96.1859	96.9885	1
420	–	1.5	9	60	98.1024	97.2478	0.9884
600	–	1.5	9	60	98.6559	98.1861	0.9926
900	–	1.5	9	60	98.7489	99.2869	1
1500	–	1.5	9	60	99.1414	100.067	1
1800	–	1.5	9	60	99.0232	99.4210	1

The composite desirability is a function to find the combination of levels of process parameters that can produce the maximum biodiesel yield for transesterification within the constraints. The constraints are defined by the lower level (−1) and higher level (+1) of the operating conditions in Table 3-2.

For the methanol to oil molar ratio, the optimised parameters are observed to agree with the standardised effect study via Pareto analysis, suggesting that the initialisation phase can be improved

with lesser methanol as reactants. Thus, during the initialisation phase of the transesterification, a 3:1 methanol to oil molar ratio should be used, and gradually increased to 9:1 which is in excess as indicated in the optimised results for 180 s.

The reactants require adequate mixing at the beginning of the process, hence 400 rpm was selected. As the reaction progresses to beyond 270s, the effect of agitation becomes insignificant, hence a lower rpm setting can be used to reduce the energy consumption. The indicated time where agitation is not included in the optimiser also coincides with the Pareto analysis findings in Figure 3-5.

For the 1500s into the onset of transesterification, the yield fit is above 100 due to the overestimation in the factorial regression model.

3.10 Reaction kinetics mechanism of the batch reactor

The field of physical chemistry that deals with understanding the rates of chemical reactions is chemical kinetics, also known as reaction kinetics. In contrast, reaction kinetics are different from thermodynamics, which deals with the direction in which a system takes place but does not explain about its rate in itself. Reaction kinetics involves research into how the rate of a chemical reaction is influenced by experimental conditions and offers knowledge about the mechanism and transition states of the reaction, as well as the formation of mathematical models that can also explain the characteristics of a chemical reaction.

In essence, reaction kinetics describes the rate of a transformation which the reactants convert into the product in a chemical reaction. Conventionally, the concentration of a known chemical is displayed in square brackets to denote that the system is not at equilibrium. The reaction rates, $\Delta[X]$ is calculated by subtracting the initial concentration, and the final concentration of a known chemical is calculated as shown below:

$$\Delta[X] = \Delta[X]_{final} - \Delta[X]_{initial} \quad \text{Eq. 3-2}$$

In a first-order chemical reaction, the rate of reaction is concentration-dependent. By observing the concentration of a chemical compound against time, the tangent gradient indicates the rate of reaction in any instances. Thus, the kinetics of the chemical reaction can be understood, as shown in an example in Figure 3-15.

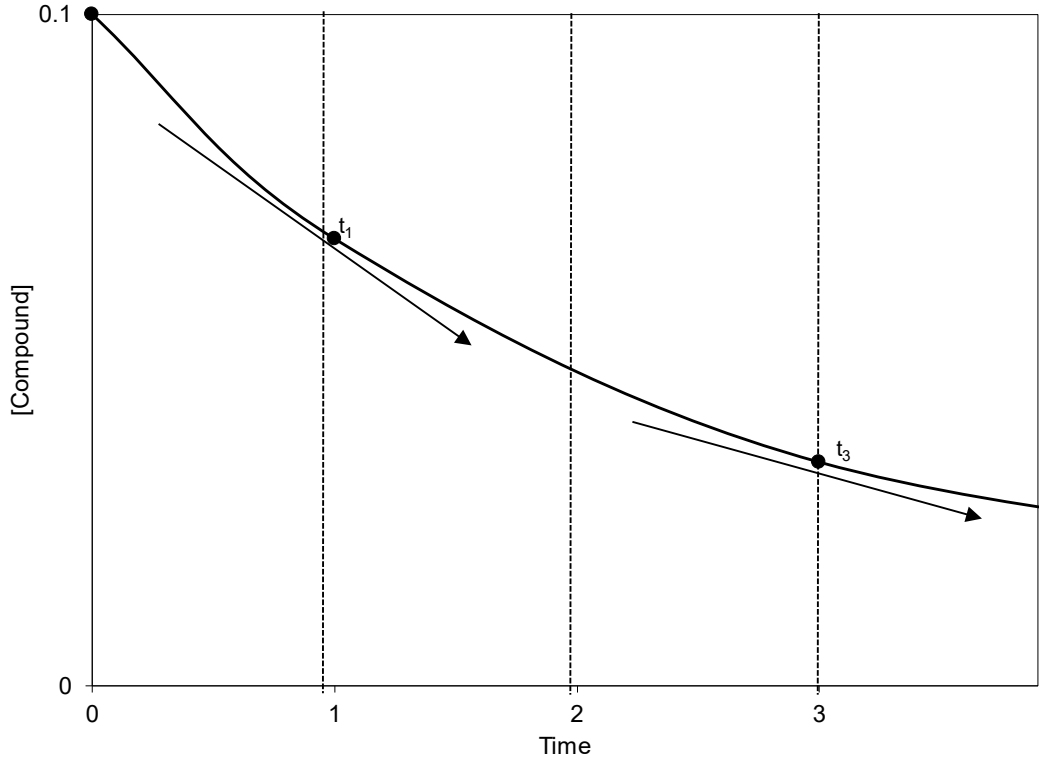

Figure 3-15. An example of a first-order chemical kinetics transformation of a chemical compound, where the rate of reactions at t_1 is greater than t_2 due to the steeper slope [223].

In the study of transesterification chemical kinetics, the reaction of the reactants, oil and alcohol yield two final products, namely, biodiesel and glycerol. The molecules of the oil and alcohol must collide for the transesterification reaction to occur. Thus, using a higher molar concentration of a reactant is more likely the increase the reaction rates. Therefore, the transesterification reaction rates must be a function of the concentrations of the oil and alcohol reacting. This function's mathematical expression is known as the "rate law". The relationship between rate law, order and the rate constant, *k* can be described as shown in Table 3-8.

Table 3-8. The relationship between rate law, order, and the rate constant in chemical kinetics [224].

Rate law	**Order**	**Units of *k***
Rate = k	Zero	M s^{-1}
Rate = k[A]	First-order with respect to A First-order overall	s^{-1}
Rate = k[A]^2	Second-order with respect to A Second-order overall	M^{-1} s^{-1}
Rate = k[A][B]	First-order with respect to A First-order with respect to B Second-order overall	s^{-1}

In transesterification reaction, the rate law can be determined experimentally by varying independent reaction conditions and measuring the yield result will compute a concentration curve.

The FAME produced by the transesterification can be modelled with three stepwise reactions starting with triglycerides (TG) and alcohol (A), followed by intermediate formation of diglycerides (DG) and monoglycerides (MG), hence resulting 3 mol of fatty acid methyl ester (FAME) and 1 mol of glycerol (GL) produced.

$$Triglycerides + 3\ Methanol \overset{Catalyst}{\Longleftrightarrow} 3\ FAME + Glycerol \quad \text{Eq. 3-3}$$

The stepwise reaction consists of a total of three consecutive reactions that are reversible,

$$TG + A \underset{k_2}{\overset{k_1}{\rightleftharpoons}} DG + FAME \quad \text{Eq. 3-4}$$

$$DG + A \underset{k_4}{\overset{k_3}{\rightleftharpoons}} MG + FAME \quad \text{Eq. 3-5}$$

$$MG + A \underset{k_6}{\overset{k_5}{\rightleftharpoons}} GL + FAME \quad \text{Eq. 3-6}$$

Thus, the rate law for the reactions mentioned above can be described as,

$$Rate_1 = k_1[TG][MeOH] \quad \text{Eq. 3-7}$$

$$Rate_2 = k_2[DG][MeOH] \quad \text{Eq. 3-8}$$

$$Rate_3 = k_3[MG][MeOH] \quad \text{Eq. 3-9}$$

Where the general form of the stepwise reactions using a differential equation as below,

$$\frac{d[TG]}{dt} = -k_1[TG][MeOH] + k_2[DG][MeOH] \quad \text{Eq. 3-10}$$

$$\frac{d[DG]}{dt} = k_1[TG][MeOH] - k_2[DG][MeOH] - k_3[DG][MeOH] + k_4[MG][FAME] \quad \text{Eq. 3-11}$$

$$\frac{d[MG]}{dt} = k_3[DG][MeOH] - k_4[MG][MeOH] - k_5[MG][MeOH] + k_6[GL][FAME] \quad \text{Eq. 3-12}$$

$$\frac{d[FAME]}{dt} = k_1[TG][MeOH] - k_2[DG][FAME] + k_3[DG][MeOH] - k_4[MG][FAME] + k_5[MG][MeOH] - k_6[GL][FAME] \quad \text{Eq. 3-13}$$

$$\frac{d[MeOH]}{dt} = -\frac{-d[FAME]}{dt} \quad \text{Eq. 3-14}$$

$$\frac{d[GL]}{dt} = k_5[MG][MeOH] - k_6[GL][FAME] \quad \text{Eq. 3-15}$$

In transesterification through an alkali catalyst, the reaction mechanism is shown in Figure 3-16. The three steps reaction mechanism for an alkali-catalysed transesterification was proposed and formulated by E.W. Eckey in 1956.

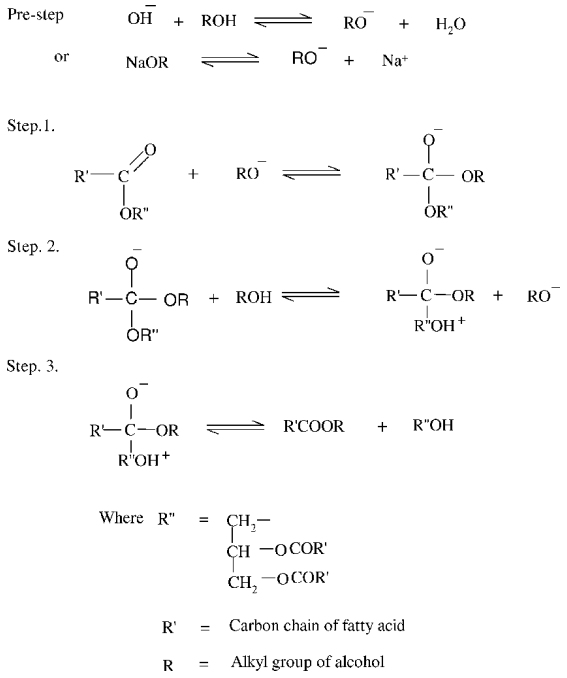

Figure 3-16. The mechanism of alkali-catalysed transesterification of triglycerides with alcohol [65].

Biodiesel production rate increases rapidly in alkaline catalysts, with the most widely used catalysts being hydroxides, alkoxides, and sodium and potassium carbonate. The first step is an attack by the alcohol anion (methoxide ion) on the electrophilic carbon in a triglyceride carbonyl community to form a tetrahedral intermediate.

The tetrahedral intermediate reacts with an alcohol (methanol) in the second step in order to regenerate the alcohol anion (methoxide ion) [65]. With another alcohol molecule, the catalyst will react, and the process is repeated until the alcohol molecule is completely depleted to form alkyl ester and glycerol in the last step. The kinetics of the alkali-catalysed transesterification has been studied the most compared to other transesterification kinetics [57,64,71,115,213,225–227].

In the experiment, low FFA feedstock such as RBD palm oil is recommended to be used with KOH catalyst in transesterification. Thus, the alkaline-catalysed pathway would be feasible without significant formation of by-product such as soap. As discussed, the soap formation would cause an emulsion complication with the biodiesel and glycerol phases, resulting in difficulty during separation.

3.11 Importance of kinetic modelling in transesterification study

The development and implementation of kinetic models for any chemical transformation processes are crucial for reactor design. In terms of transesterification where the process involves a non-linear production rate of biodiesel and separation of by-products such as glycerol, the kinetic model plays an essential role in optimising these steps. Thus, these models are studied, built, and implemented to simulate the transesterification process results.

Besides, kinetic models are also vital to aid in decision-making for the reaction operating conditions such as reaction temperature, agitation rate, reactant concentration, and reaction time. For instance, the kinetic model can be used to predict the yield of the reaction which enables the cost-efficiency study. The reactor's design and the reaction mechanism option are also a major consideration for the optimisation process.

The major difference between a kinetic model and a data-driven model is the capability to account for mass and heat-transfer characteristics of the reaction on top of thermodynamics equilibrium. The complexity of a kinetic model can vary depending on the numbers of parameter involved, which essentially affects the robustness of the model. However, deriving an accurate kinetic model with a greater predictive outcome requires the iterative revision of the mechanism involved at multiple levels of detail. Therefore, one of the essential steps in developing the kinetic model for industrial application is a well-planned design of experiment, to assess the scaling potential of the reactor model.

3.12 Material and sample analysis

The experimental setup is identical to the full-factorial analysis of the RVC study where stirred-tank batch reactor combined with RVC agitator is used. The number of sampling point was increased to eighteen in 30 minutes to improve the resolution of the results. The holding values for the operating conditions used are 6:1 methanol to oil molar ratio, 1.0 wt. % KOH catalyst loading, 300 rpm agitation rate, and an impeller from 20 ppi RVC. The standard analytical reagent to determine the free and total glycerol and mo-, di-, triglyceride contents such as tripalmitin, triolein, diolein, monoolein, methyl heptadecanoate, glycerol were sourced from Sigma-Aldrich.

The samples were analysed for the analysis procedure for triglycerides, diglycerides, monoglycerides, methyl ester, and glycerol content using the EN 14105 method. The sample was injected into the Agilent 7820A gas chromatograph system using FID detector, equipped with a stainless steel capillary column (VF-5ht Ultimetal Column, 15 m x 0.32 mm, 0.10 µm)

Four calibration solutions were prepared using the mentioned solutions accordingly, based on the internal standards of 1,2,4-Butanetriol and 1,2,3-Tricaproylglycerol (tricaprin). The derivatisation of the sample was conducted by adding 100 µl of MSTFA, 80 µl of internal standard 1, and 100 µl of internal standard 2 to 100 mg of homogenised mixture. Then, 1 µl of the reaction mixture is analysed in the GC using the column temperature of 50°C held for 1 min, programmed at 15°C/min up to 180°C, programmed at 7°C/min up to 230°C, programmed at 10°C/min up to 370°C, where the final temperature is held for 5 min. The analysed results utilise the identification of the peaks by comparison of retention times. The relative retention times corresponding to the different peaks to be integrated is shown in Table 3-9.

Table 3-9. Relative retention times of glycerol and glycerides [228].

Compounds	**Retention time for IS1**	**Retention time for IS2**
Glycerol	0.75	
1,2,4-Butanetriol (IS 1)	1.00	
Monopalmitin		0.61
Monoolein, monolinolein, monolinolenin		0.68
Monostearin		0.69
Tricaprin (IS 2)		1.00
Diglycerides		1.19 – 1.30
Triglycerides		1.56 – 1.65

3.13 Results and discussions

The concentration of glycerides content and FAME yield is calculated and presented in Figure 3-17. The operating condition used for this test is an overhead stirring batch reactor, with reaction temperature of 45°C, agitation speed of 300 rpm, methanol to oil molar ratio of 6:1, and KOH catalyst loading at 1.0 wt. %. This test aims to set a benchmark for the other reactors, which will be discussed in the following section.

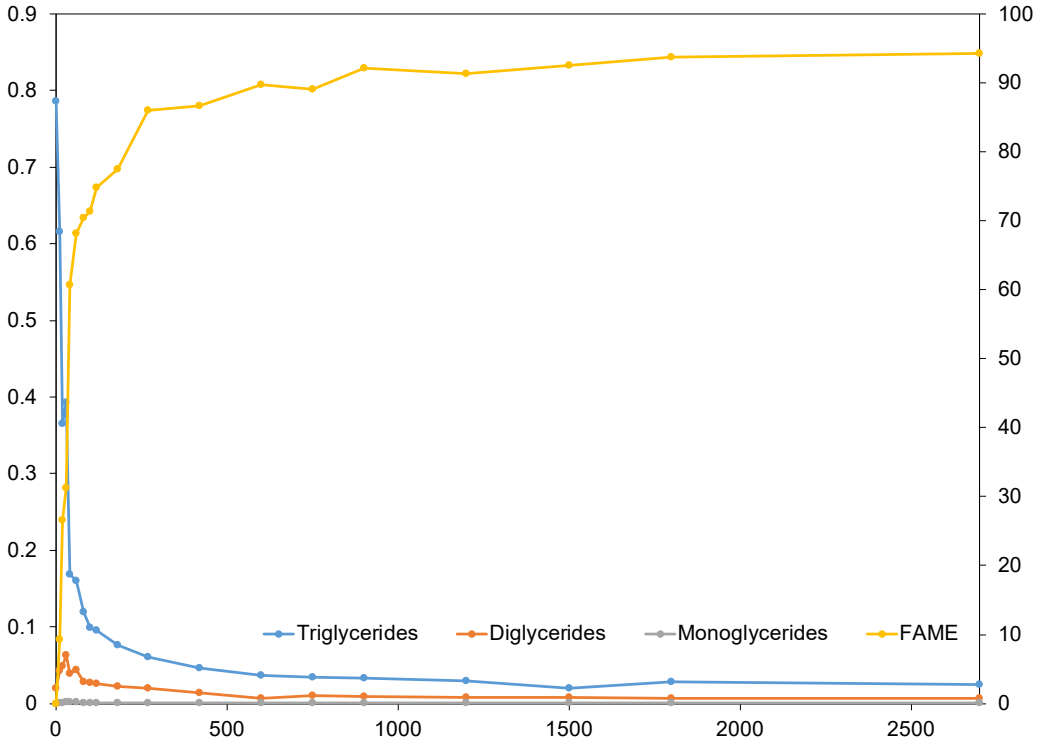

Figure 3-17. The transesterification reaction products using stirred tank batch-type reactor at 45°C, agitation speed of 300 rpm, methanol to oil molar ratio of 6, and KOH catalyst loading of 1.0 wt. %

3.13.1 Reaction kinetics calculation model assumptions

The following of model assumptions are introduced to describe the transesterification process, as shown in Table 3-10.

Table 3-10. Kinetic modelling assumptions for biodiesel transesterification in a stirred-tank batch reactor.

No.	Assumptions	Reasoning	Reference
1	The high agitation intensity is high enough the surpass the mass transfer limitation. The reaction mixture is considered as a pseudo homogeneous system as methanol has a high tendency to dissolve in the oil phase.	The preliminary test in Figure 3-5 shows that mass transfer becomes a bottleneck. Thus, in the full-factorial and glycerides study, 200–400 rpm range is used for agitation.	[57,213,225,227,229]
2	The overall process of kinetics is chemically controlled.	Based on Figure 3-1, the idealised transesterification is dominantly the chemical equilibrium stage.	[230,231]
3	The transesterification of the triglycerides is an irreversible pseudo second-order reaction during initialisation.	The initial concentration of the methanol is high, and there is an absence of biodiesel and glycerol. Thus, it is unlikely that the reversible process can occur.	[71]
4	As transesterification approaches equilibrium, the forward and reverse reactions is a second-order mechanism.	As FAME are formed, the reaction is kinetic-controlled, which gives the higher rates.	[213,227]
5	The oil and methanol is a homogeneous mixture	There should be no mass transfer limitation as the reaction approaches equilibrium.	[57,213]
6	The free fatty acid content in the oil is negligible. Diglycerides and monoglycerides concentration are low in oil.	The feedstock used is RBD palm oil which is made up of majority neutral palmitic acid.	[232]
7	The saponification branch reaction is negligible. Catalyst concentration is constant throughout.	The catalyst loading is 1.0 wt. % which accounts for less	[233]

	than 3 mol% of FAME yield lost.	

In order to determine the best fit kinetic model for the data, the first-order and second-order models are both presented to compare with each other, as shown in Table 3-11.

Table 3-11. Comparison of kinetic models used in representing transesterification of biodiesel.

Reaction Kinetics Model	**Equation**	**Ref**
First-order/Pseudo First-order	$-\ln(1-TG)$	Shahla *et al.* [234], Latchubugata *et al.* [235]
Pseudo second-order	$\frac{TG}{1-TG}$	Richard *et al.* [236]
Pseudo second-order	$\frac{1}{TG}$	Darnoko and Cheryan [71]
Irreversible pseudo second-order	$\frac{k_2 TGt}{1+k_2 TGt}$	Marjanović *et al.* [225]
Reversible pseudo second-order	$\frac{\left[-(1+3M)-\sqrt{-\Delta}\cdot exp\left(\vec{k}_2 A\sqrt{-\Delta}+C_2\right)\right]}{[6M(1-K)]-\left[1-exp\left(\vec{k}_2 A\sqrt{-\Delta}+C_2\right)\right]}$	Stamenković *et al.* [237]

3.13.2 Pseudo first-order kinetic model

For transesterification, the reaction is a second-order overall as explained using the rate law, where oil and alcohol concentration affects the entire reaction rate.

$$rate = k[Oil][Alcohol] \qquad \text{Eq. 3-16}$$

The initial reaction rate depends on the concentration of oil and alcohol when the reaction moves in the forward direction while constantly changing in concentration. Therefore, the rate will be affected to compensate for the change in reactant concentration.

In a stoichiometric scenario of the transesterification process, this explanation will hold true as one mol of oil will react with three mol of alcohol to produce three mol of biodiesel and one mol of glycerol. However, in most biodiesel transesterification cases, excess alcohol in the range of six to nine molar ratio of alcohol to oil is used to promote the complete conversion of oil. Thus, during the initial stage of the reaction the change in oil concentration will have negligible changes to the alcohol concentration [234,235].

Therefore, the triglycerides' concentration can be used as the only factor to determine the reaction kinetics, provided that the loss of alcohol is negligible [238]. This makes the initial transesterification reaction behave like a first-order reaction, hence the term, pseudo first-order. Thus, if the reaction kinetics is pseudo first-order with respect to the triglycerides and methanol for the overall transesterification, the reaction rate can be written as below,

$$-r_A = -\frac{dC_{TG}}{dt} = k[TG][MeOH] = k(constant)[TG] = k'[TG] \qquad \text{Eq. 3-17}$$

The equation Eq. 3-17 can be rearranged to represent triglycerides conversion as shown below,

$$\frac{dx_{TG}}{dt} = k_1(1 - x_{TG}), \qquad x_{TG} = \frac{[TG]_0 - [TG]}{[TG]_0} \qquad \text{Eq. 3-18}$$

Where k_1 is the kinetic rate and x_{TG} is the conversion of triglycerides concentration. The integration of first-order equation Eq. 3-18 is shown below,

$$-\ln(1 - x_{TG}) = k_1 t + C \qquad \text{Eq. 3-19}$$

Where x_{TG} is the conversion of the triglycerides. Therefore, the conformity of the transesterification can be tested with the first-order kinetic model by a linear plot using Eq. 3-19, where the slope of the plot is the kinetic rates. In order to screen and identify the range of the initial physical-limiting regime, pseudo first-order was applied to the triglycerides concentration throughout as shown in Figure 3-18.

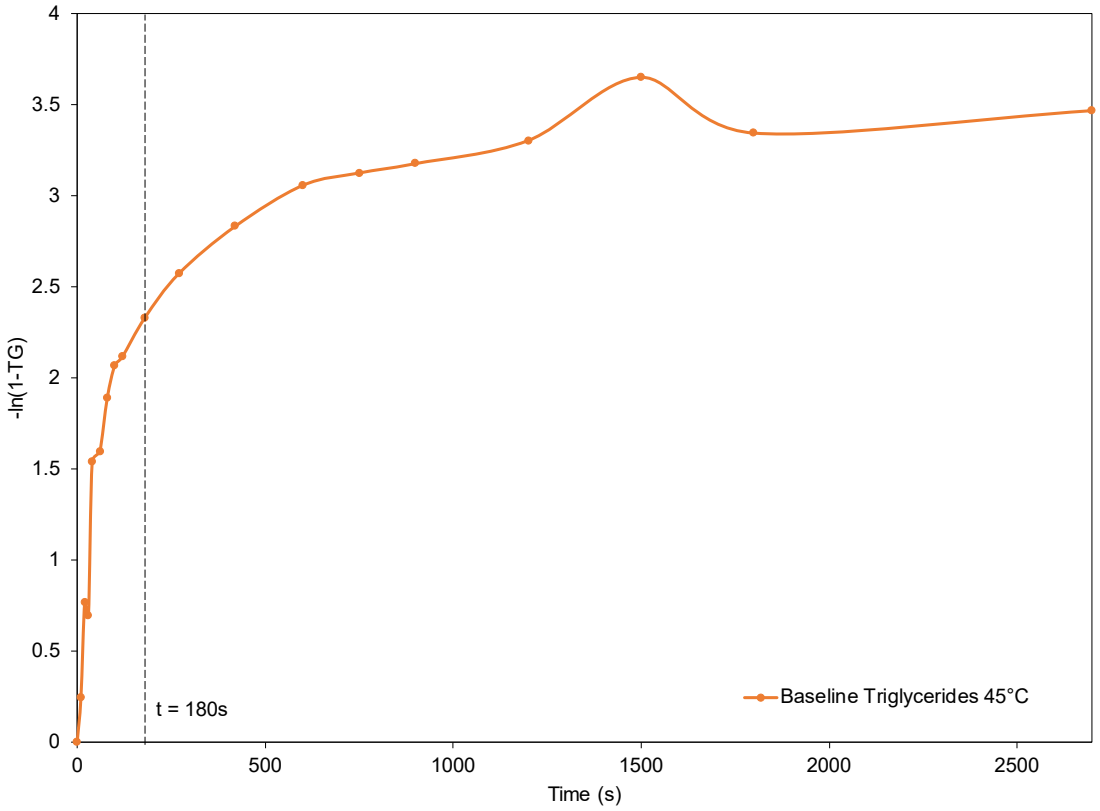

Figure 3-18. Pseudo first-order transformation of triglycerides concentration for baseline batch-type reactor.

The screening test from the Pareto study suggests that the effect of mixing showed a strong significance in the result of yield, as shown in Figure 3-5. From Figure 3-18, the pseudo first-order transformation of the triglycerides for baseline study showed high linearity from the mentioned residence time. Thus, the initial stage used for kinetic rates calculation will be isolated to 0s to 180s, as shown in Figure 3-19.

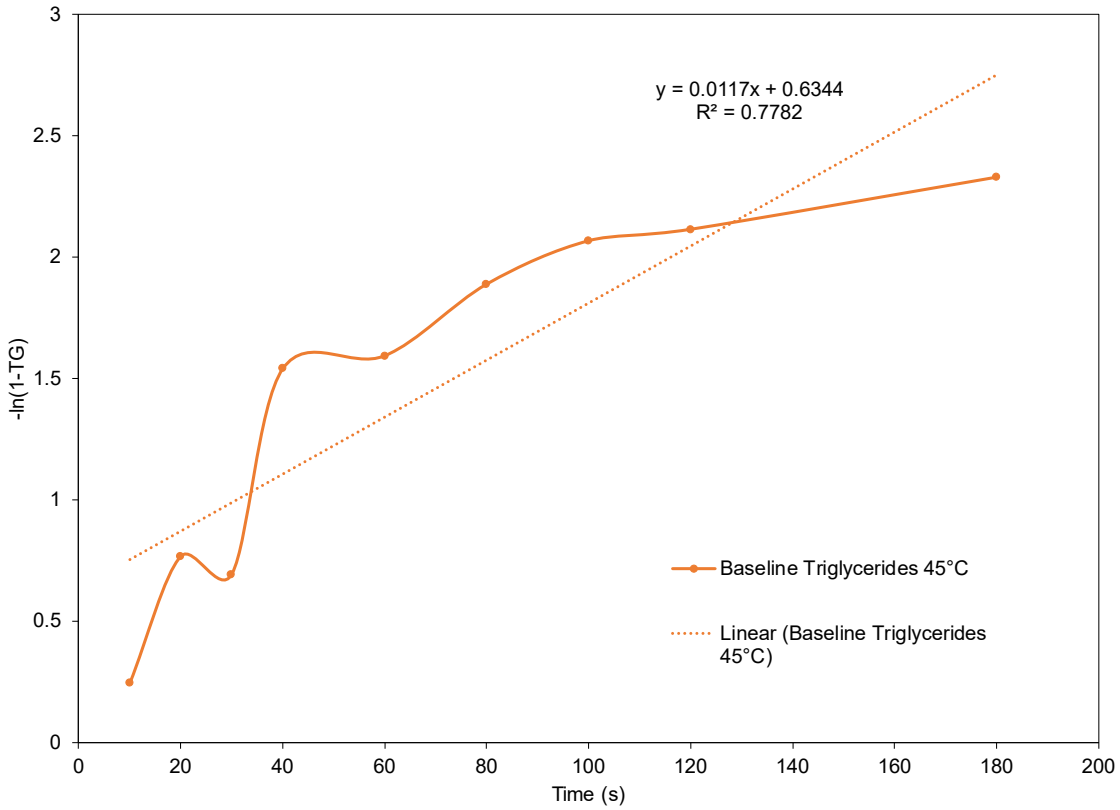

Figure 3-19. The physical-limiting regime during the initial stage of transesterification for baseline batch-type reactor.

From Figure 3-19, the kinetic rate is the gradient of the linear equation, as shown in Figure 3-19. However, to determine the maximum reaction rate, the inflection point of the triglycerides conversion curve is required. Thus, a running average slope strategy is implemented, where the slope at each interval is averaged over the time interval before and after as shown in Figure 3-20.

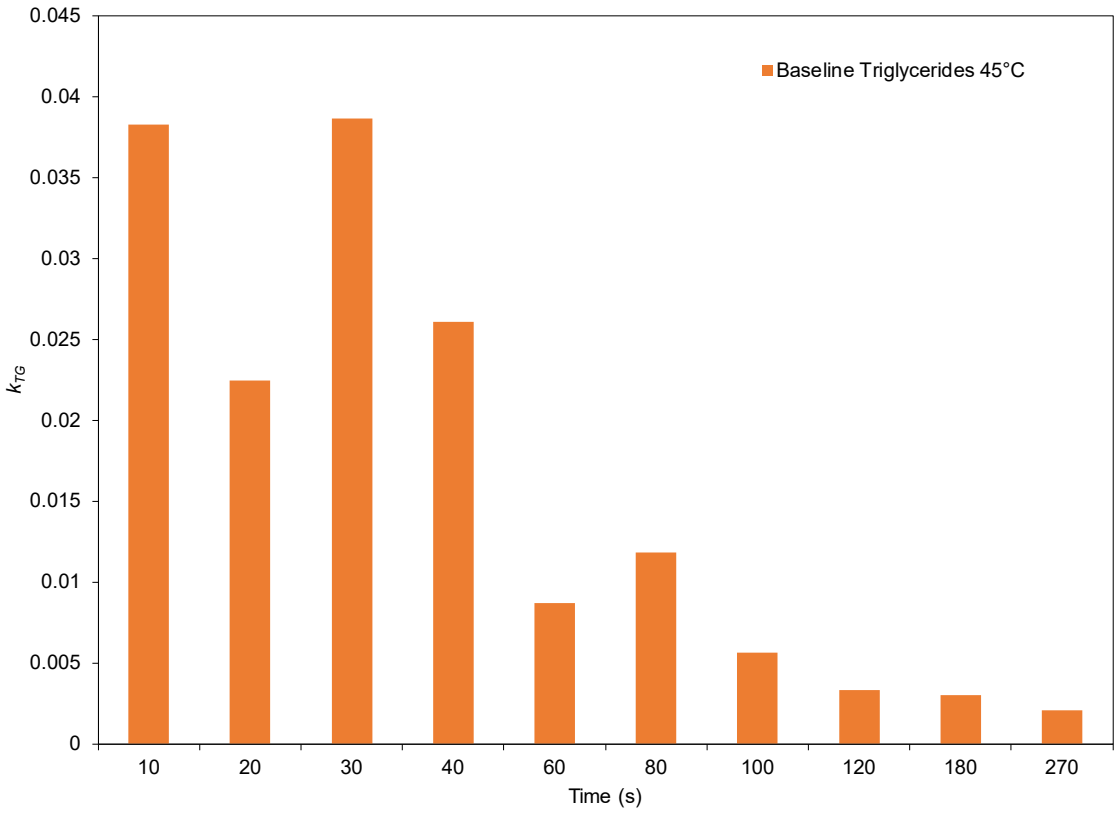

Figure 3-20. The kinetic rates of pseudo first-order baseline transesterification at the physical-limiting stage.

The presence of excess alcohol in the reaction has caused many researchers to assume that the transesterification kinetics are based on the overall reaction as the intermediates conversions of diglycerides and monoglycerides are rapidly consumed [85,225,234,236,239–241]. According to Latchubugata *et al.*[235], the same pseudo first-order kinetic model from Eq. 3-19 was implemented in their kinetic studies. However, instead of using the conversion rate of triglycerides concentration, the biodiesel yield rate was replaced. Therefore, this suggests the hypothesis of approximating kinetic rates based on the conversion of biodiesel as shown below,

$$-r_A = -\frac{dC_{TG}}{dt} \cong \frac{dC_{ME}}{dt} \qquad \text{Eq. 3-20}$$

Eq. 3-20 can be rearranged to represent methyl ester conversion as shown below,

$$\frac{dx_{ME}}{dt} = k_1(1 - x_{ME}), \qquad x_{ME} = \frac{[ME]_0 - [ME]}{[ME]_0} \qquad \text{Eq. 3-21}$$

$$-\ln(1 - x_{ME}) = k_1 t + C \qquad \text{Eq. 3-22}$$

The pseudo first-order kinetics of the methyl ester formation is illustrated in Figure 3-21.

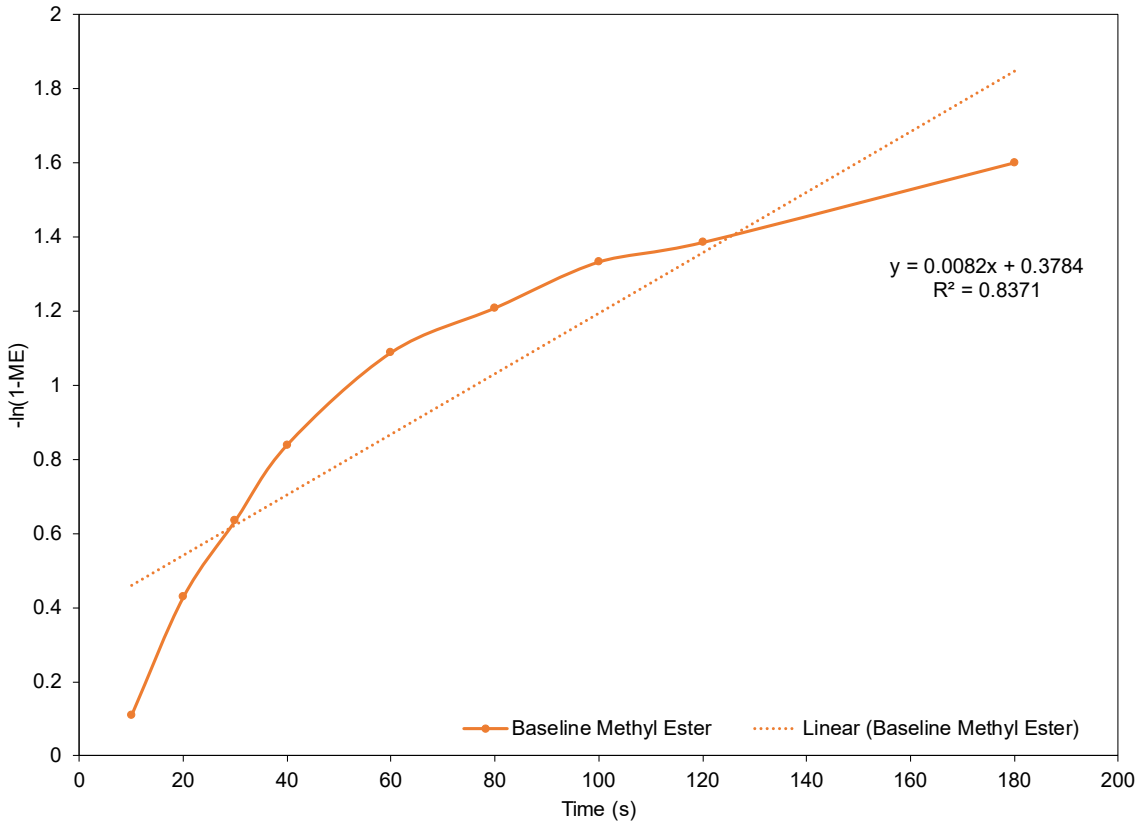

Figure 3-21. Pseudo first-order kinetics model of methyl ester formation in transesterification for baseline.

Based on Figure 3-21, the methyl ester pseudo first-order model showed a different trend than the triglycerides depletion model. The higher linearity suggests a better fit with the pseudo first-order model, with a lowered overall value on the y-axis, suggesting lowered kinetic rates. This is likely to be an outcome of the lag from the intermediate reactions such as diglycerides and monoglycerides formation and depletion, which accounts for the reduction in kinetics for methyl ester formation. Thus, the kinetic rates of methyl ester are not good approximations of the triglycerides depletions as the intermediate reaction is considerably important. The finding suggests that the development of the kinetic model based on the assumption of an overall reaction used for the pseudo first-order kinetic model should be revised.

Based on the assumption of excess methanol, equation Eq. 3-17, Eq. 3-18, and Eq. 3-19 can be applied on the diglyceride depletion and monoglyceride depletion. Therefore, the revised pseudo first-order kinetic model is shown below,

$$-\ln(1 - x_{DG}) = k_2 t + C \qquad \text{Eq. 3-23}$$

$$-\ln(1 - x_{MG}) = k_3 t + C \qquad \text{Eq. 3-24}$$

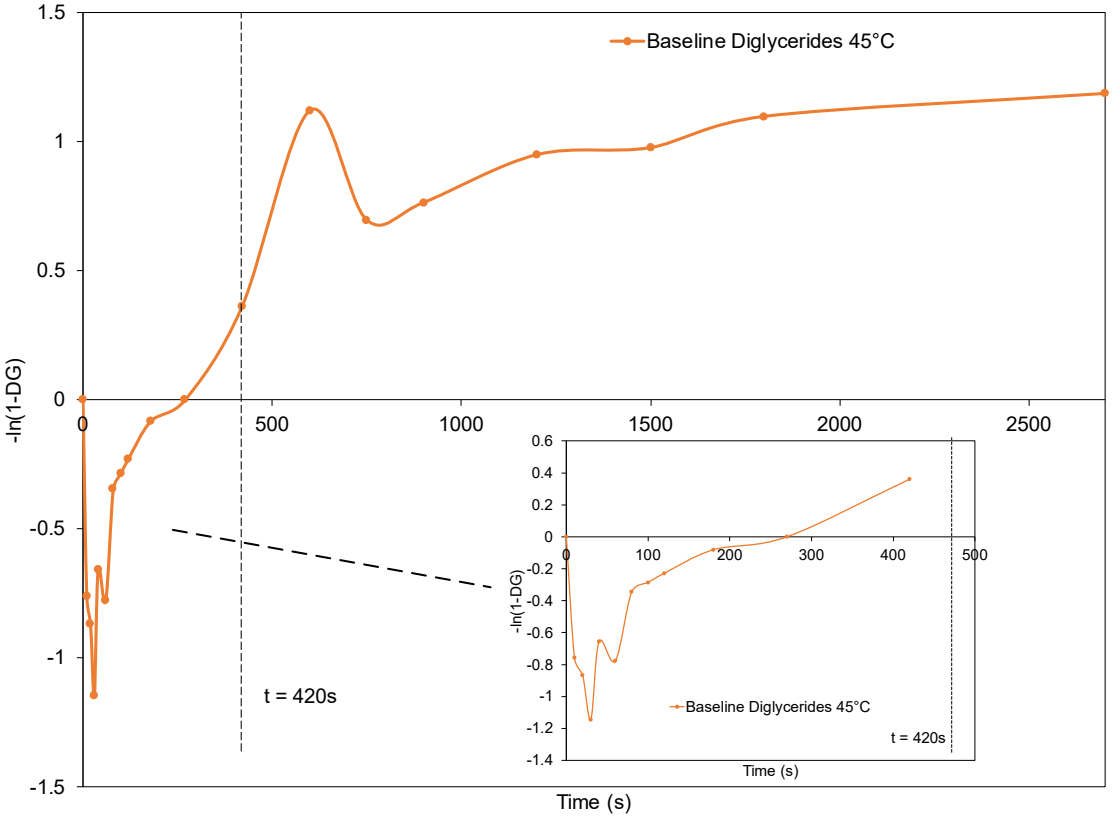

Figure 3-22. Pseudo first-order kinetic model of diglycerides formation and depletion for baseline.

Figure 3-22 shows the fluctuation of the transformation after applying the pseudo first-order model due to the high reaction rates for the formation and depletion of diglycerides. Thus, there is high volatility and inaccuracy of the results which might not reflect the actual kinetics of the glycerides. Therefore, through removing and isolating the range of uncertainty, it is possible to identify useful data to be implemented on the kinetic model which is a better representative of the whole initial part of transesterification as shown in Figure 3-23.

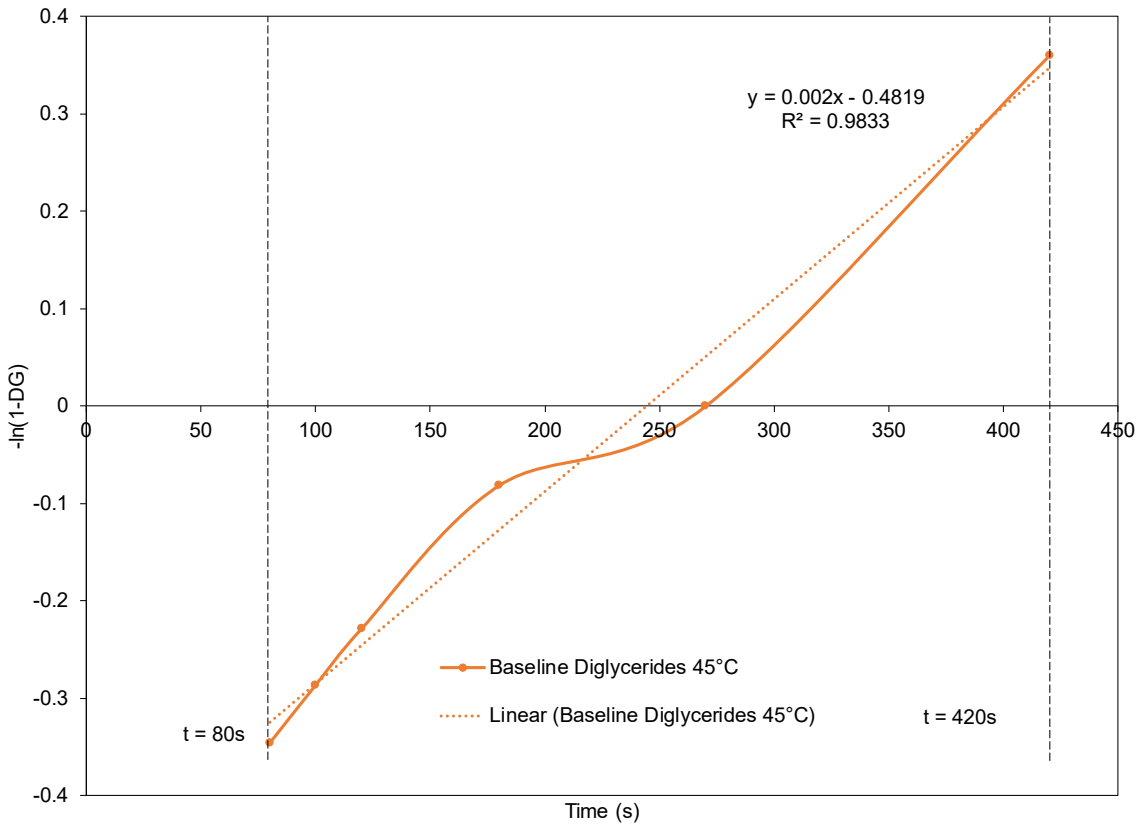

Figure 3-23. Isolated formation and depletion of diglycerides for the pseudo first-order kinetic model from 80s to 420s for baseline.

The residence time selected for diglyceride formation and depletion to be used in pseudo first-order is from 80s to 420s according to Figure 3-23. This also shows that diglyceride concentration is more likely to achieve steady-state conversion after the high depletion of triglycerides phase, where the high linearity of the model fit supports the range identified. The monoglyceride concentration results are also applied to the Eq. 3-24 to test the robustness of the kinetic model, as shown in Figure 3-24.

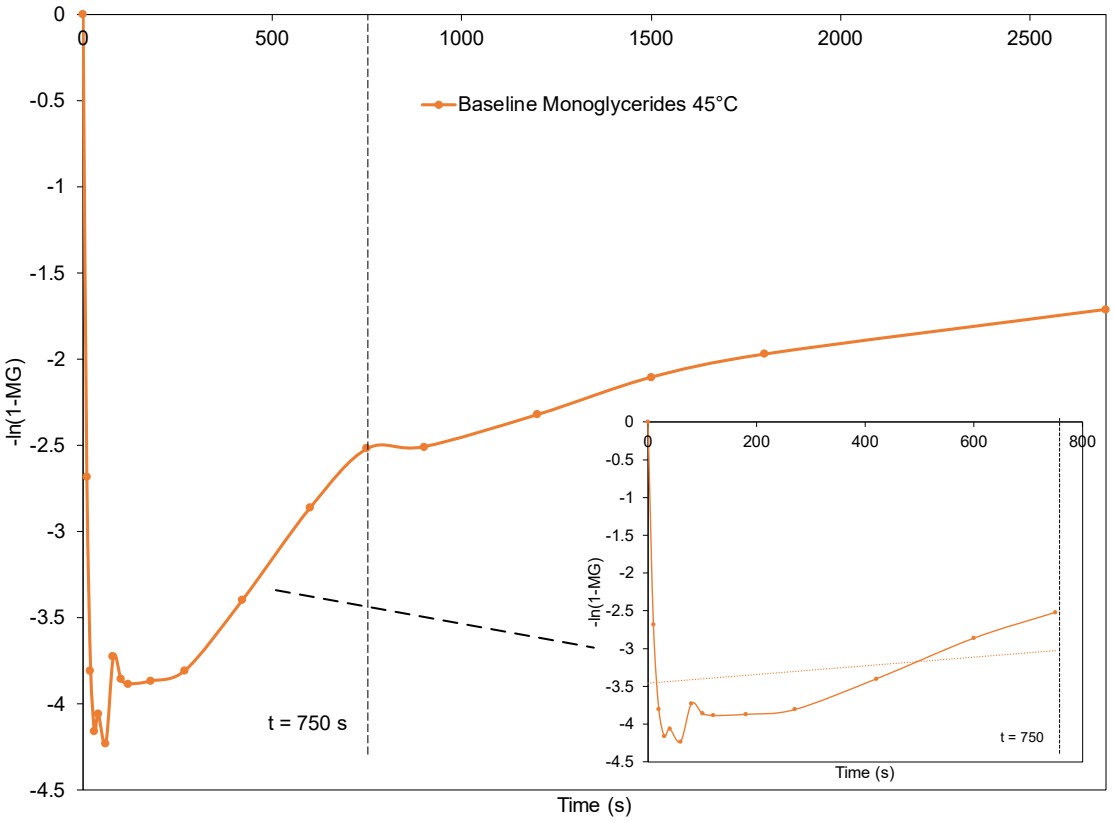

Figure 3-24. Pseudo first-order kinetic model of monoglycerides formation and depletion for baseline.

The pseudo first-order kinetic model of monoglycerides is shown above in Figure 3-24, where the initial fluctuating trend is expected as it coincides to the fast conversion phase of triglycerides and diglycerides. Thus, a similar technique is applied to the transformation to isolate the “noise” for a better representation of the kinetic mechanism, as shown in Figure 3-25.

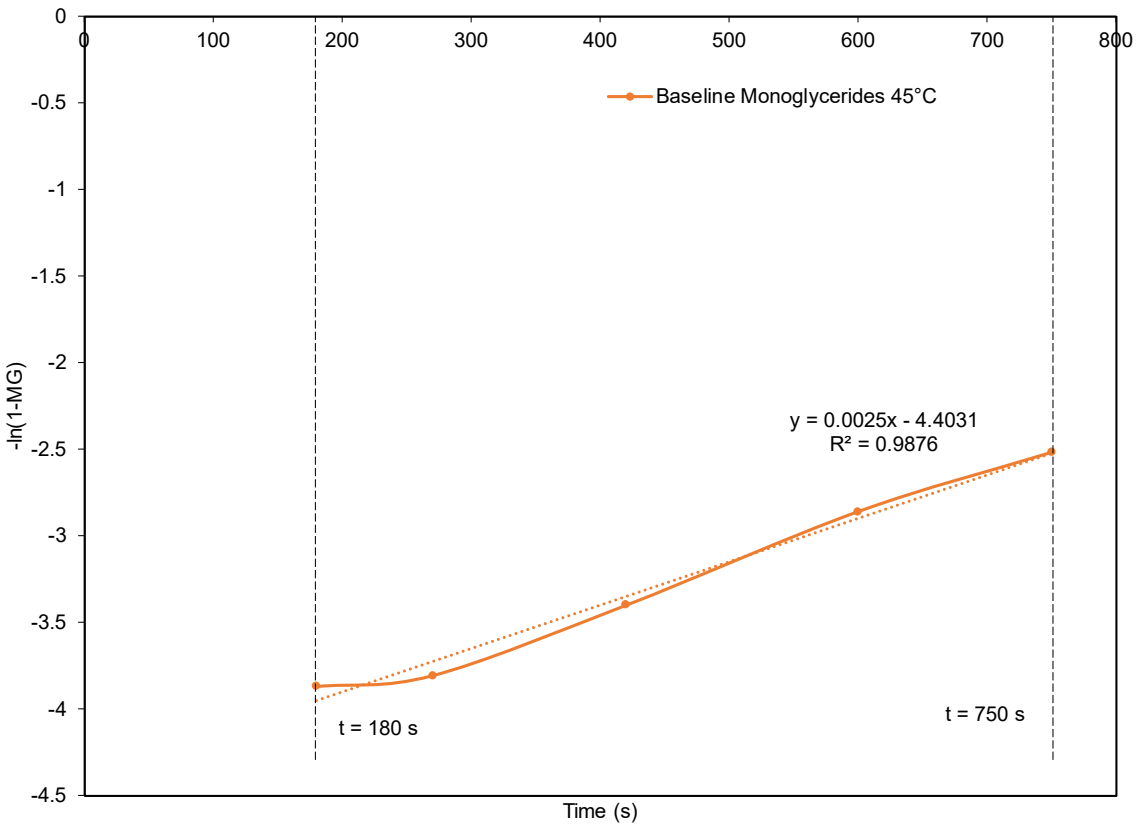

Figure 3-25. Isolated formation and depletion of monoglycerides for the pseudo first-order kinetic model from 180s to 750s for baseline.

The range identified for the conversion of monoglyceride is from 180s to 750s based on Figure 3-25. The range selected is relatively late in the residence time of the transesterification process. The reason is that two precursors are constantly converting at a high reaction rate, leading to a longer fluctuating range for monoglycerides. The selected range used in the pseudo first-order kinetic model shows good fit with equation 4-8 as reflected by the R^2 value. Furthermore, the three-point moving average kinetic constant is calculated from 0s to 750s for both diglycerides and monoglycerides to study their respective inflection point at different times, as shown in Figure 3-26.

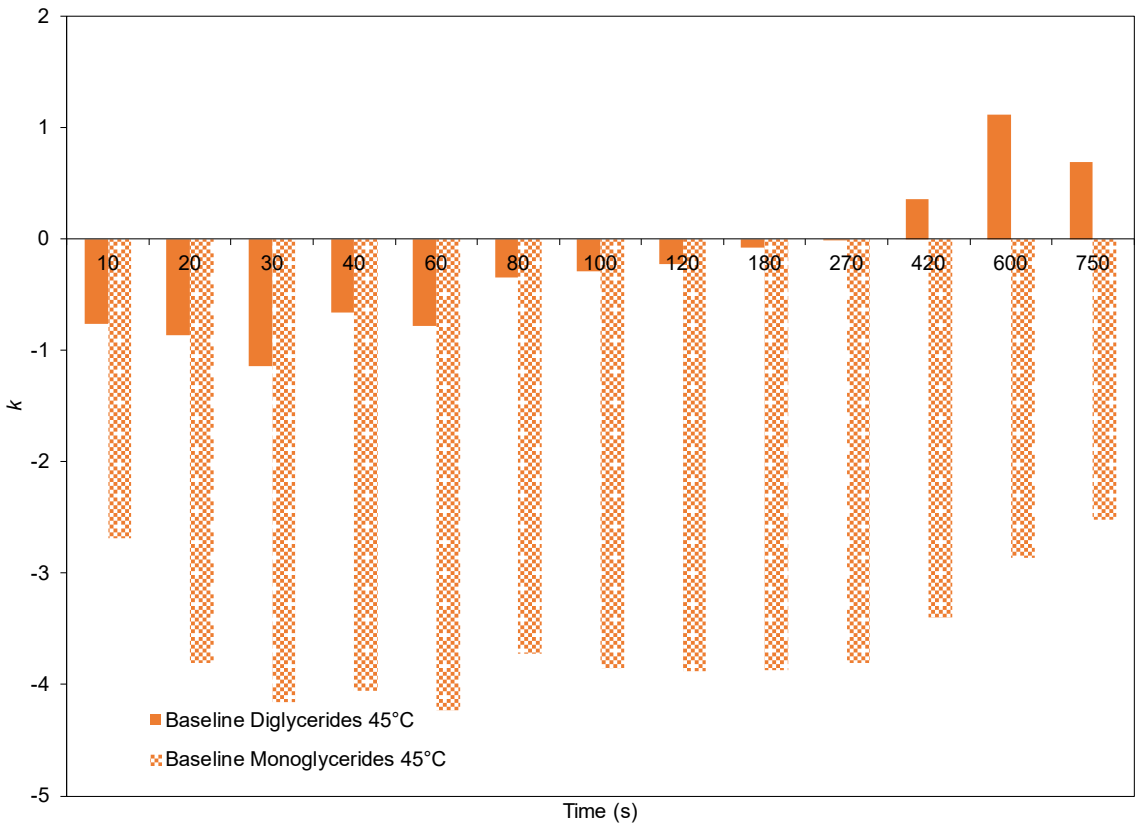

Figure 3-26. The kinetic constant of diglycerides and monoglycerides via moving average of the linear gradient for baseline.

From Figure 3-26, the evolution of the averaged kinetic rates can be observed for diglycerides and monoglycerides. The negative values in kinetic rates represent a net surplus of the particular glycerides where the effect of formation dominates the effect of depletion. Monoglycerides conversion showed a constant formation-dominant phase overall, but diglycerides conversion starts depleting at about 420s, which is logical as steady-state of triglycerides is only after 270s based on Figure 3-17. Therefore, the depletion of monoglycerides can be expected much later than 750s, where the depletion of diglycerides approaches steady-state.

3.14 Conclusion

This working chapter aims to extend the research for current batch-type biodiesel transesterification, widely practised in research and industry. Generally, the batch-type biodiesel reactor is in the form of a stirred tank, while monitoring of the reactor is based on the operating conditions such as reacting temperature, catalyst concentration, methanol to oil molar ratio, and stirring speed. However, these parameter's effects are often analysed and concluded based on the final yield point with translates to a steady-state condition. Therefore, the conclusion made is not a fair comparison, given that the transition of transesterification is not captured throughout.

The effects of the operating conditions were analysed dynamically at different stages of transesterification in batch processing. For instance, the requirement for adequate mixing is important during the initialisation for the transient-state of transesterification, but diminishes as the reaction occurs when oil and methanol become more miscible. Another observation is from the methanol to oil molar ratio, which negatively affects the transesterification process when used in excess at the physical-limiting stage, while increasing importance as the reaction approaches the steady-state of the reaction-limiting stage. The interaction between factors and yield is analysed via the hierarchical agglomerative clustering method from transient to the steady-state reaction of transesterification. Thus, the limiting factors are identified at different points of the process with the respective operating conditions, while evaluated through the standardisation and normalisation of Pareto analyses. Therefore, Pareto analysis can be applied in a transient manner to identify the dynamic effects of the operating condition in a standardised and comparable setting throughout transesterification.

In all, the framework allows the results from the Design of Experiment to be analysed in a transient manner. Thus, individual factors can be screened throughout for mass transfer limitations (reaction-based), or operating condition (design-based) limitation at different stages. Therefore, the limitations from factors are then used to analyse the process at the glyceride level, to refine and extend the mechanisms for the reaction kinetics in transesterification.

Chapter 4 Reticulated Vitreous Carbon as a Novel Agitator for Stirred Tank Reactor

4.1 Introduction

In this chapter, microturbulence-assisted transesterification is studied via the integration of Reticulated Vitreous Carbon (RVC) agitator in a stirred-tank reactor. The interaction of RVC and the mass transport of transesterification is characterised via (i) the relationship of micro-turbulence and physical agitation for biodiesel production, (ii) the mass transfer rates and reaction kinetics of the reactor, (iii) the study of operating conditions such as temperature, RVC pores per inch (ppi), the rotational speed of perturbation, catalyst loading, and methanol to oil molar ratio at different levels to understand how the use of RVC impacts high-shear for enhanced mass transport. Additionally, a conventionally stirred tank reactor is used to benchmark against the results from the RVC reactor and compare their respective performances from transient to steady-state of the transesterification process.

4.1.1 Reticulated Vitreous Carbon on its properties, structure, and applications

Porous materials can be applied in a wide range of areas in applied sciences and engineering. The study of porous media offers excellent practical applications, from biology to geoscience, chemistry to materials science and civil engineering to environmental engineering. The main goal for conventional and advanced applications, such as in the pharmaceutical, food, petroleum, gas and nuclear industries, is to understand the relationships between systems and properties.

The research of transport phenomena in porous materials has emerged as a distinct area of study thanks to their importance and prevalence. The general theories behind flow and transport in porous media are encompassed by transport phenomena, known from the microscopic scale upwards, and form the basis of deterministic and stochastic models to describe them. Porous media's role in a single and multiphase fluid flow is often assessed based on the biomolecular and chemical responses. The evaluations generally are from the studies of motions for suspending solid particles, heat transfer mechanisms (conduction, convection, and radiation), and the combination of electrical-acoustic transport.

RVC is a solid foam made up of an open-cell network consisting of vitreous carbon, with a rigid honeycomb structure. The reticulated characteristic is described as a matrix of cells and ligaments spatially connected within the skeletal strut. The material features basic properties such as exceptionally high void volume (*ca.* 97%), rigid structure, high surface area, low fluid flow resistance, high resistance to temperature and chemical stability in a non-oxidising atmosphere.

These physicochemical properties have led to a vast amount of research interest, particularly in the fuel storage and production or chemical catalyst supports in the applied electrochemistry field.

The morphological parameters, such as cell and window diameter, strut diameter and porosity, are used to define the foam structure of RVC [242,243]. The porosity of RVC is also measured in ppi, which give rise to a variety of strut morphologies, namely, cylindrical, triangular and triangular concave [244]. The timeline in Figure 4-1 shows the historical research and development of RVC from production, characterisation to application.

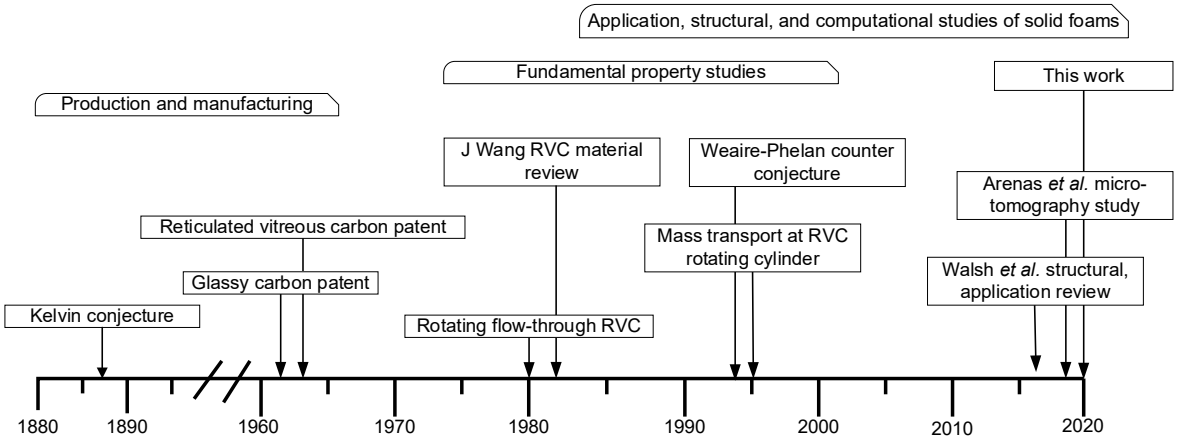

Figure 4-1. Timeline for the implementation of reticulated vitreous carbon from the critical development of its structure, characteristics and applications adapted from Walsh *et al.* [245].

In 1964, Ford's [246] first iteration of RVC was produced by the carbonisation and graphitisation of phenolic foam, a resin precursor. The manufacturing process occurs in an inert atmosphere of 540°C, followed by a second stage of heating the polymerised resin at a higher temperature of 1100-1300°C for strengthening the structure. The choice of resin precursor, solvent, carbon source soaking time, curing temperature and duration, and carbonisation rate can significantly affect the RVC properties.

In terms of application, based on Figure 4-1 majority of the RVC studies revolves around the mass transport in the area of electrochemistry [247] such as fuel cell [245,248] and tissue engineering [249]. However, many evidence from these studies are often pointed towards the huge advantage of using RVC to improve mass transport, but none has tested the material as a rotary agitator in a chemical reactor. Therefore, in this chapter RVC is integrated into the traditional batch-type stirred-tank reactor to evaluate its strength in agitating chemical reactants by introducing microturbulence and micro-level diffusion.

4.1.1.1 Structure and properties of RVC

In 1887, Kelvin proposed a space-filling structure with a limited surface area for identical cells of comparable volume. In a 14-sided truncated octahedron, the hexagonal faces with a small curvature are the natural solution to the structure. Thus, a foam based on a bitruncated cubic honeycomb is the most efficient bubble foam in partitioned equal volume cells, widely accepted as the Kelvin structure.

The Kelvin's optimal isoperimetric quotient of the uncurved truncated octahedron is given by

$$Q = \frac{36\pi V^2}{S^3} = \frac{64\pi}{3(1+2\sqrt{3})^3} \approx 0.753367 \qquad \text{Eq. 4-1}$$

A counter-conjecture only arises after 100 years as the Kelvin's conjecture is widely accepted. In 1994 Weaire and Phelan found a space-filling unit cell composed of six 14-sided polyhedral and two 12-sided polyhedral with irregular faces via computational mathematical simulations of open-foams. The improved structure shows an isoperimetric quotient of approximately 1.0 % higher than Kelvin's cell [250]. This event has led to the use of the Weaire-Phelan foam structure in constructing the Beijing Olympic Water Cube in 2008.

The RVC structure can be described as a foam with thick outer perimeters of window frames interconnected by vitreous carbon strut. The three-dimensional porous structure, combined with a large number of voids of between 90 % to 97 % enabled it to have an average volumetric surface area of 65 cm^{-1}. The RVC porosity of the range from 10–100 ppi is commercially available, which is a parameter that affects the void volume.

It is exceptionally resistant to intercalation by graphite disintegrating materials and is inert to a wide variety of acids, bases and organic solvents that are very reactive. This characteristic makes the material highly versatile in a chemically harsh environment.

Figure 4-2 presents images of 10, 20, 45, 60, 80, 100 ppi porosity grade samples of RVC taken from a digital microscope with 50x magnification. Figure 4-3 presents the SEM images of 10, 30, 60, 80, and 100 ppi grade samples of RVC. The honeycomb-like structure shown in Figure 4-2 (a)-(f) are formed by strands of carbon strut, which takes a form similar to a triangle or tetrahedron, as one of the strands are hidden behind the 2-dimensional surface. The repetition of this structure gives rise to RVC's rigidity. Additionally, four different variables are required to characterise the RVC structure, namely, pores per linear inch, the strut length, strut thickness and the surface area of the trigonal strut where the area of the strut meet [247].

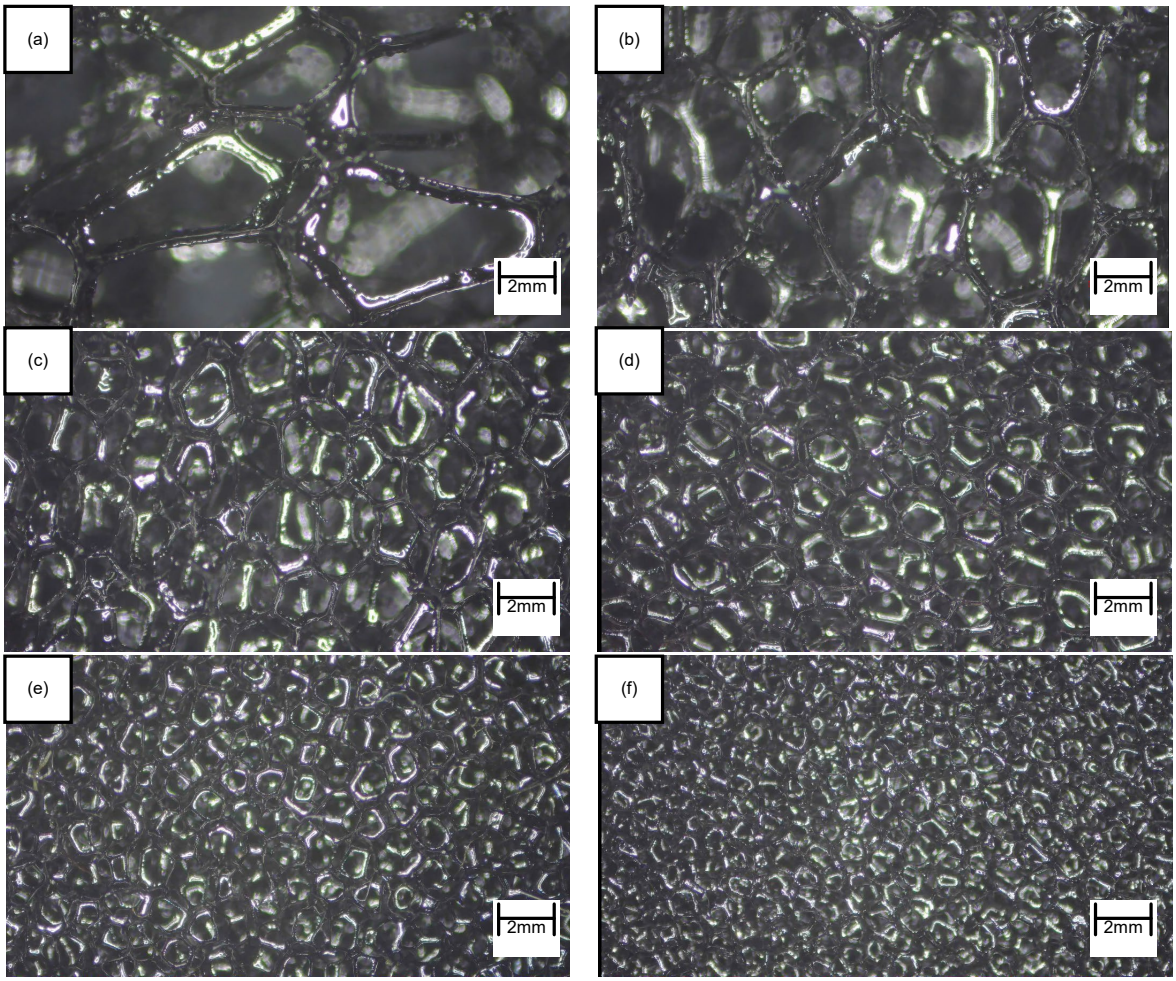

Figure 4-2. RVC of various porosity under 50x magnification using digital microscope, (a) 10 ppi, (b) 20 ppi, (c) 45 ppi, (d) 60 ppi, (e) 80 ppi, (f) 100 ppi.

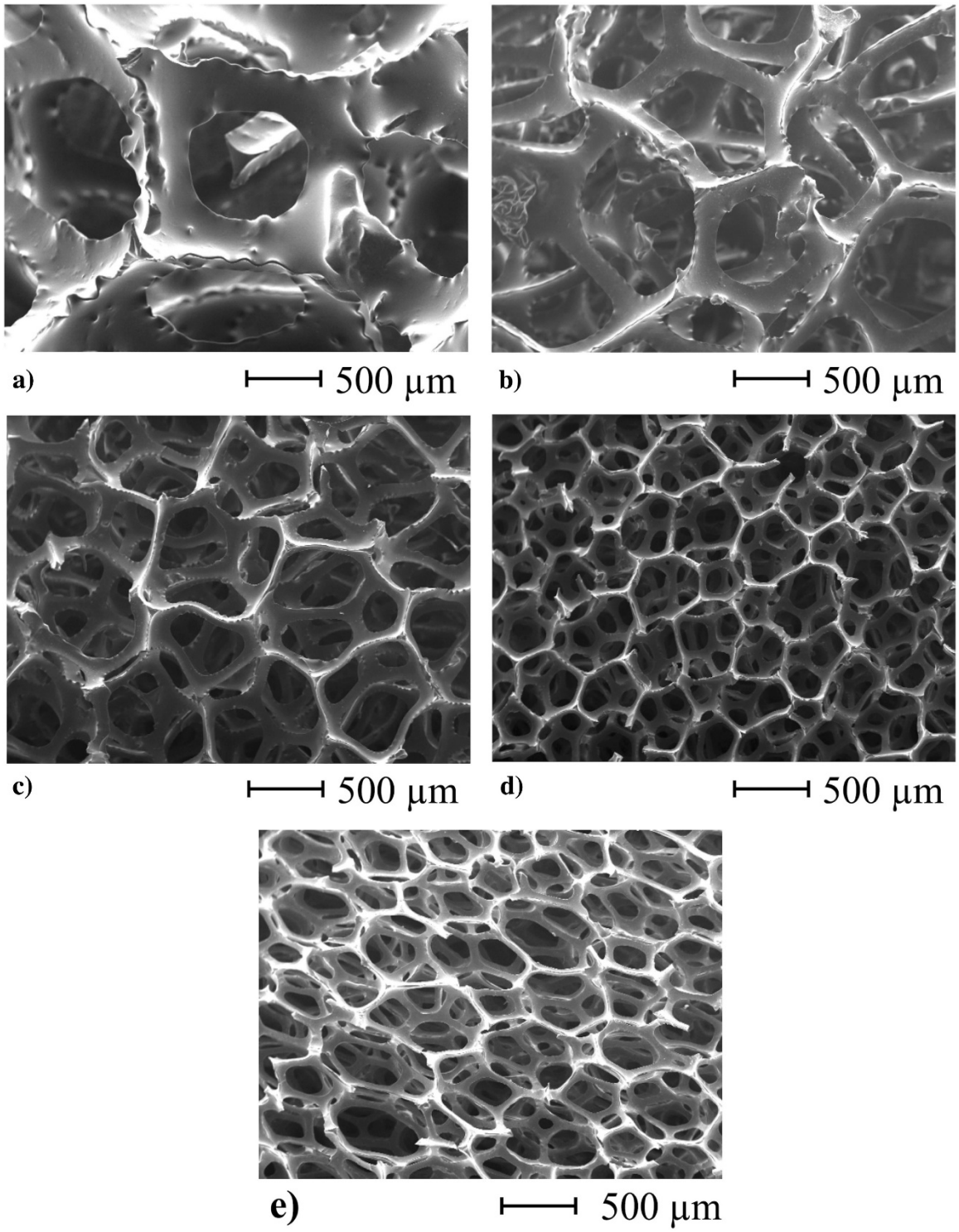

Figure 4-3.SEM micrographs of: (a) 10, (b) 30, (c) 60, (d) 80 and e) 100 ppi (nominal pores per linear inch) porosity grades of RVC [251].

The strut length was defined as the length of one end of the trigonal struts where the strands are uniform as shown in Figure 4-4, while the area is calculated from measuring the radius of the trigonal strut. All measurements were done using the digital microscopy software calibrated for RVC, averaged over ten different lengths of struts and trigonal struts radius. Table 4-1 shows the

measurements of the physical characteristics at various porosity grade of RVC. The specific surface area of a porous solid is defined as the amount of surface area over a given bulk volume of foam.

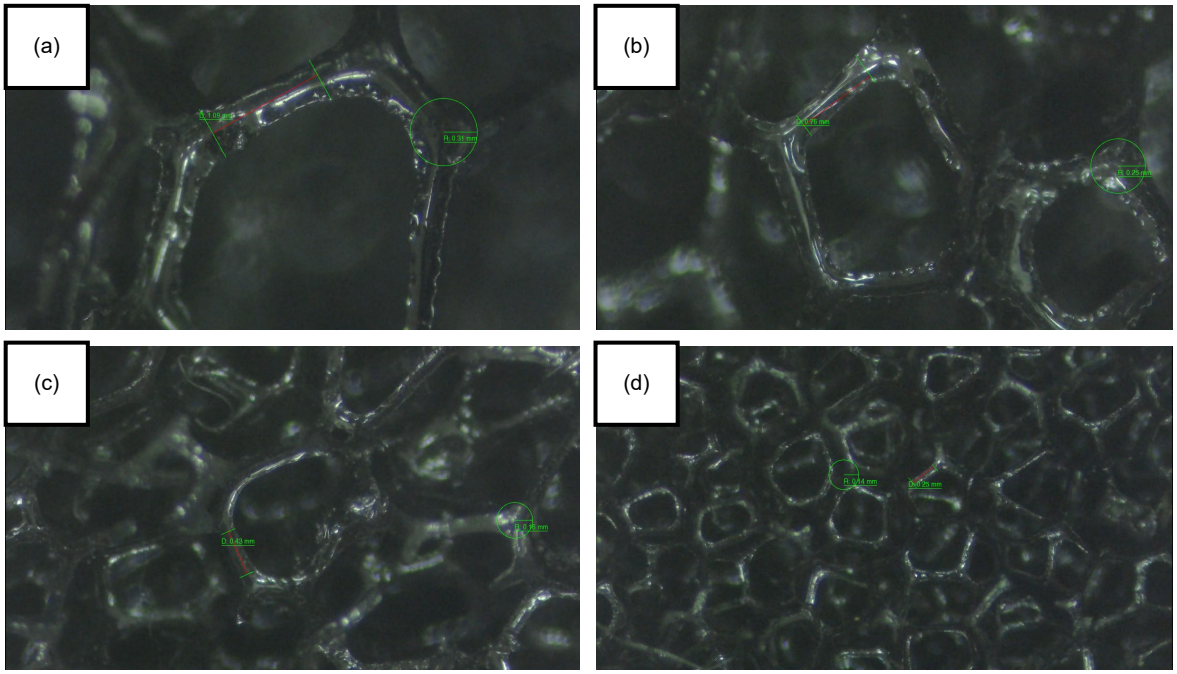

Figure 4-4. Digital microscopy of (a) 10 ppi RVC, the green parallel lines mark the end-points of length and thickness is measured from the green circular radius. (b) 20 ppi, (c) 45 ppi, (d) 100 ppi.

Table 4-1. Dimensions of the physical characteristics of four porosity grades of RVC (taken from a digital microscope at 50x magnification).

Property	**Nominal pores per linear inch (ppi)**			
	10	20	45	100
Strut length (mm)	1.055	0.364	0.320	0.322
Strut thickness (mm)	0.745	0.303	0.245	0.189
Trigonal strut circle radius (mm)	0.450	0.169	0.170	0.091
Trigonal strut area (mm^2)	0.197	0.088	0.135	0.057

The specific surface area data is shown in Figure 4-5, obtained from the manufacturer's RVC datasheet. The foam's specific surface area is calculated geometrically using the multipoint Brunauer-Emmett-Teller (BET) method via the adsorption of krypton gas at cryogenic temperature,

as shown in Figure 4-6 [252]. Based on Figure 4-6, the specific surface area increases logarithmically as pore density and relative density increases.

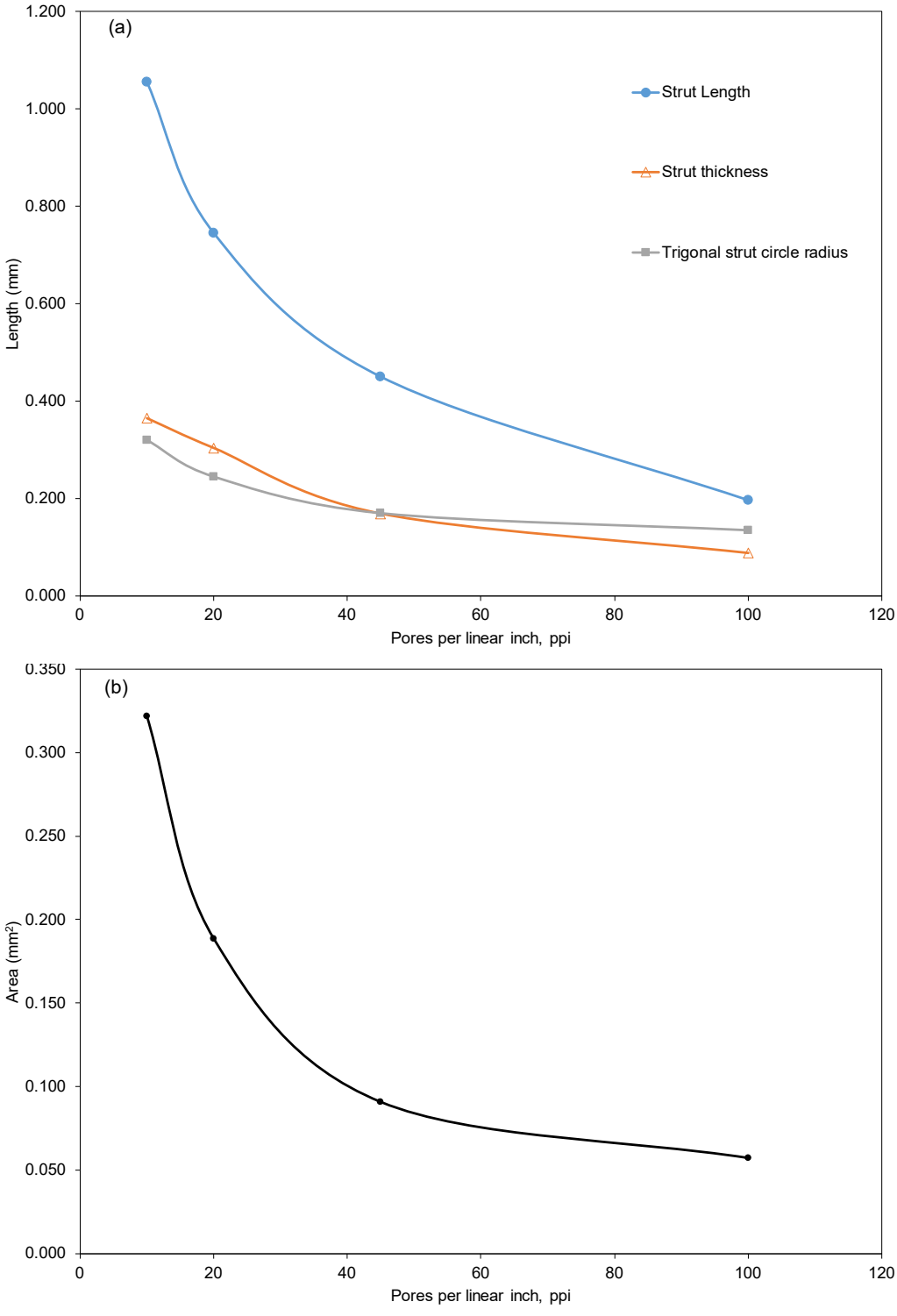

Figure 4-5. (a) Strut dimension and (b) area with pores per linear inch.

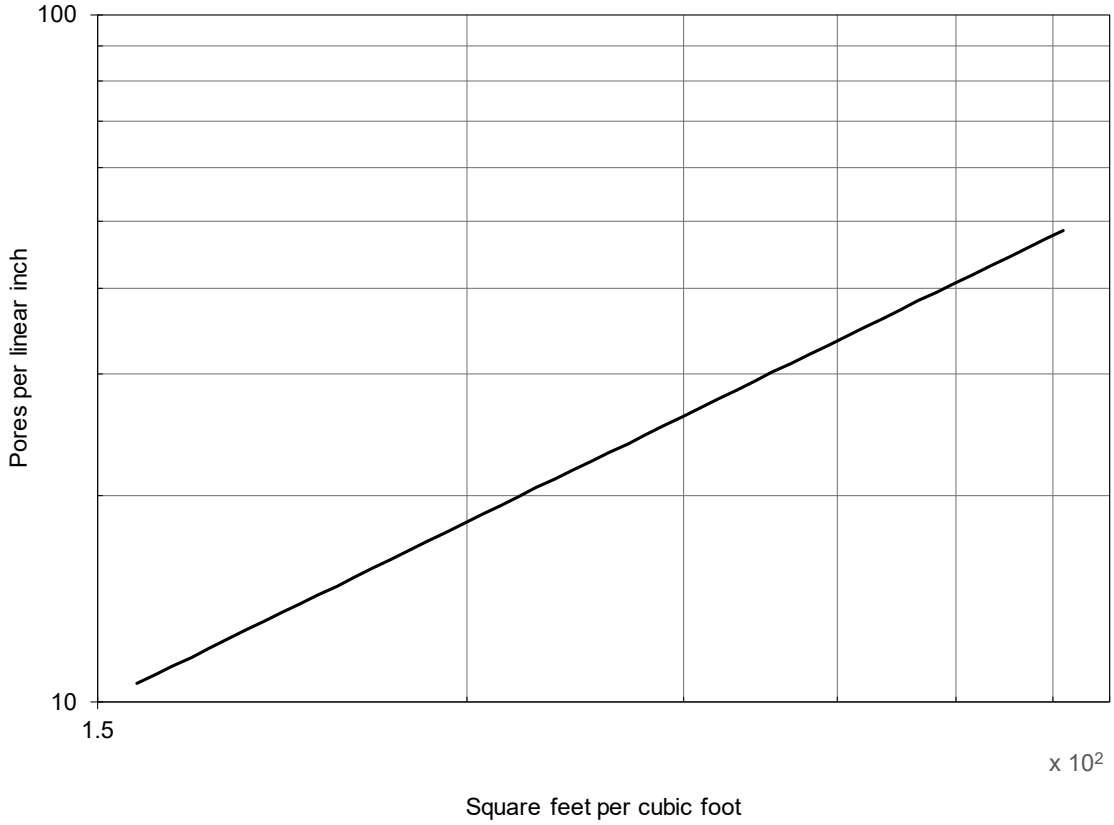

Figure 4-6. The specific surface area of RVC foam from Materials and Aerospace Corporation. Adapted from ERG Aerospace, USA [252].

4.2 Preliminary experimental studies of RVC-assisted transesterification

This study aims to identify the range of interest for a follow up experimental study involving a full factorial test matrix. Thus, the preliminary test allows a smaller subset of operating conditions for the RVC reactor to be used, for highlighting the significance of interactions between RVC and biodiesel transesterification.

4.2.1 Materials and experimental setup

The feedstock used for the experiment was commercial RBD palm olein. Analytical grade methanol 99.8 %, potassium hydroxide (KOH) >85 %, and hydrochloric acid 37 % were obtained from Qrec, Merck, and VWR. Standard analytical reagents such as methyl heptadecanoate were obtained from Sigma-Aldrich.

The RVC used in this study has 20, 45, 65, 80 ppi. Table 4-2 summarises the physical properties of the RVC. The transesterification reaction was conducted in a 1L cylindrical batch reactor, with a constant 455 g of palm oil and varying methanol volume to represent the methanol-oil ratio from 4:1 to 7:1. Potassium hydroxide (KOH) is used as the catalyst to form potassium methoxide through the addition of methanol. Catalyst loading ranging from 0.5–1.5 wt. % of oil. Reaction time starts after the addition of potassium methoxide and initiation of the mechanical stirrer. Heat addition is done using a silicone jacket with a temperature controller, where temperature measured by a K-type thermocouple, which allows reaction temperature to be fixed in the range of 40–70 °C. Table 4-3 shows the resolution and the uncertainty for the instrument used throughout the experiment.

Table 4-2. Characteristics of Duocel® Reticulated Vitreous Carbon foams at 3% nominal density [253].

Properties	**Values**	**Unit**
Compression strength	0.10-0.52	MPa
Tensile strength	0.17-0.34	MPa
Shear strength	30.3	MPa
Mohs hardness	6-7	Mohs
Modulus of Elasticity (Tension)	101.84	MPa
Shear modulus	30.3	MPa
Vickers pyramid number	35	HV
Specific heat	1.26	J/g.°C
Bulk thermal conductivity	0.033-0.050	W/m.°C
Coefficient of Thermal Expansion (0-100°C)	2.2e-6	1/°C
Coefficient of Thermal Expansion (100-1000°C)	3.2e-6	1/°C
Bulk resistivity	32.3e-2	Ohm.cm
Temperature limitations (in air)	325	°C
Temperature limitations (inert)	3499	°C

Table 4-3. Resolution and uncertainty of measuring instruments.

Instrument	Measurement	Resolution	Uncertainty
Thermocouple (K-Type)	Temperature	0.1 °C	± 2.2 °C
Constant stirrer controller	Revolution per min	1 rpm	± 1 rpm
Silicon heating jacket	Temperature	0.1 °C	± 1.0 °C
Mechanical pipette	Sample volume	0.1 ml	± 0.3% vol.

The performance of transesterification using RVC stirrer was studied by comparing with a baseline stirrer, made of High-density Polyethylene (HDPE). The RVC and HDPE mechanical stirrers were both constructed into an identical dimension of 0.09 m x 0.03 m x 0.13 m in length, width and thickness, which is then coupled to the end of the stirring rod from the AQL constant speed stirrer, with rotational agitation between 100–400 rpm. The schematic of the experimental setup is shown in Figure 4-7.

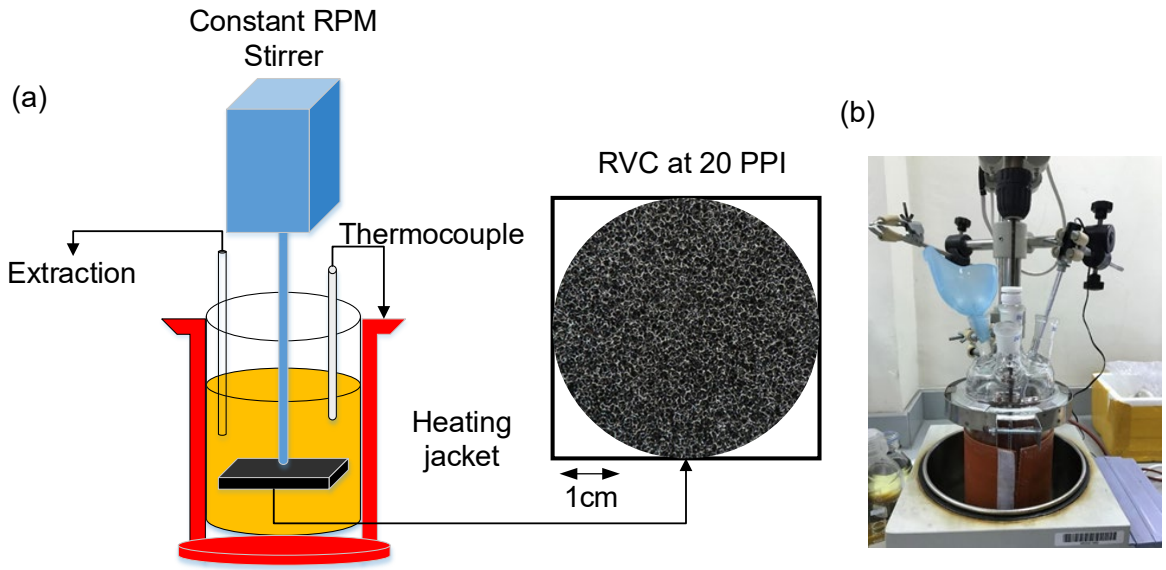

Figure 4-7. (a) Schematic of the preliminary setup using RVC mechanical stirrer. (b) Experimental setup of the batch-type transesterification with RVC stirrer.

The one-factor-at-a-time (OFAT) method is implemented for the preliminary test matrix, as shown in Table 4-4.

Table 4-4. One-factor-at-a-time (OFAT) test matrix for RVC preliminary studies and HDPE benchmark reactor.

Case No.	RPM	Temperature (°C)	Methanol to oil molar ratio	Catalyst loading (wt. %)	Ppi	Testing For
1,13,32	200	60	1 : 6	1	20	Baseline
2	100	60	1 : 6	1	20	
23	300	60	1 : 6	1	20	RPM
3	400	60	1 : 6	1	20	
19	200	60	1 : 6	0.5	20	
29	200	60	1 : 6	1.2	20	Catalyst
20	200	60	1 : 6	1.5	20	
9	200	60	1 : 4	1	20	
25	200	60	1 : 5	1	20	Methanol to oil ratio
10	200	60	1 : 7	1	20	
14	200	40	1 : 6	1	20	
28	200	50	1 : 6	1	20	Temperature
15	200	70	1 : 6	1	20	
7	200	60	1 : 6	1	45	
24	200	60	1 : 6	1	65	ppi
8	200	60	1 : 6	1	80	
4,16,33	200	60	1 : 6	1	HDPE	Baseline
5	100	60	1 : 6	1	HDPE	
26	300	60	1 : 6	1	HDPE	RPM
6	400	60	1 : 6	1	HDPE	
21	200	60	1 : 6	0.5	HDPE	
31	200	60	1 : 6	1.2	HDPE	Catalyst
22	200	60	1 : 6	1.5	HDPE	

11	200	60	1 : 4	1	HDPE	Methanol to oil ratio
27	200	60	1 : 5	1	HDPE	
12	200	60	1 : 7	1	HDPE	
17	200	40	1 : 6	1	HDPE	Temperature
30	200	50	1 : 6	1	HDPE	
18	200	70	1 : 6	1	HDPE	

4.2.2 Sample characterisation

Sampling of transesterification (3 ml) was done using mechanical pipette to extract 9 samples between 20s to 1,800 s, and reaction of samples was quenched immediately using the neutralisation method via diluted hydrochloric acid [214]. The fatty acid methyl ester (FAME) yield was determined by Agilent 7820A gas chromatograph (GC) system using a FID, equipped with a capillary column (HP-INNOWax Column, 30 m x 0.25 mm, 0.25 μm). The GC analysis parameters were adopted from EN 14103. The FAME yield is defined as the conversion of vegetable lipids to biodiesel, from the gas chromatograph analysis, FAME content (%) was defined using Eq. 3-1.

4.2.3 Results and discussion

The experiment is conducted with RVC and baseline HDPE mechanical stirrers, with default reaction conditions of 200 rpm stirring speed, 1.0 wt. % KOH catalytic loading, 60 °C reaction temperature, and 6:1 for methanol to oil molar ratio. A test matrix of five factors each with four levels was run to study the parameters of interest, with 29 unique experiments consisting of a total of 261 sample points.

4.2.3.1 Effects of pores per inch (ppi)

The use of RVC as an alternative material for mechanical agitation in biodiesel transesterification has not been approached. Thus, the geometrical characteristics of RVC are investigated to determine the optimum porosity for transesterification, one of the main parameters is pores per inch, which is essentially pore density. The ppi gives rise to the low-density characteristics of RVC, as the ppi increases, the density also increases. The experiments were conducted with RVC ranging from 20–80 ppi, then compared against the baseline, as illustrated in Figure 4-8.

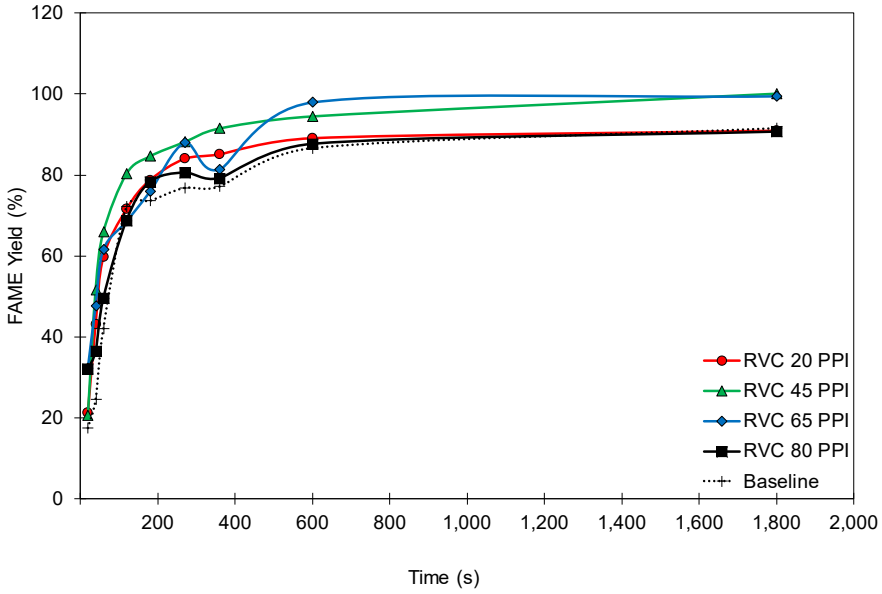

Figure 4-8. Effect of pores per inch (ppi) on FAME yield for RVC against HDPE baseline.

The RVC with 20, 45, and 65 ppi demonstrated an improvement in FAME conversion in series. Therefore, increasing ppi is an effective option to improve the overall volume to surface area ratio during intensification, which allows a higher rate of mass transfer between oil and methanol. However, 80 ppi performs the poorest amongst all the RVC. This is expected as the ppi increases, the effective surface area diminishes due to oil droplet not able to penetrate between the pores, hence RVC essentially loses its porous characteristics at high ppi. Nonetheless, it is observed that the RVC of 80 ppi is still able to outperform the baseline in the initial stage of reaction, before 600s, which indicates the microturbulence induced is still relevant to improve reaction rates from RVC.

The highest yield was obtained from the results of 45 and 65 ppi, achieving up to 99.5% conversion. In contrast, 20 and 80 ppi only slightly surpasses 90% yield, which is similar to the baseline. Thus, low ppi might not provide sufficient surface area needed for reaction, and the oil droplet size would limit the excessive level of ppi. Therefore, results indicate an optimum point for ppi, situated between RVC of 45 and 65 ppi.

4.2.3.2 Effects of agitation rate

Transesterification without mixing is a diffusion-controlled reaction, hence by using batch processing technique, physical agitation can be used to promote rates of reaction via mechanical stirrer. Thus, rpm represent the rate of rotational agitation provided to the reaction to enhance mass transfer. Adequate mixing is vital for homogeneous mixing in this experiment, the biodiesel yield is studied across a range of 100−400 rpm, for both RVC and baseline cases.

Figure 4-9 shows the influence of rpm on FAME yield for both RVC and baseline. In general, the increase in rpm leads to an overall improvement of reaction rates. However, RVC shows a greater impact for intensification at the beginning phase of mixing and provides near full conversion of

biodiesel within 200 s of mixing at 300 rpm. The result is postulated to be due to the microturbulence-induced from the edges and micropores through shearing of the reactants. During mixing, the reticulated surfaces of RVC provide a greater total volume to surface area for the transesterification reaction.

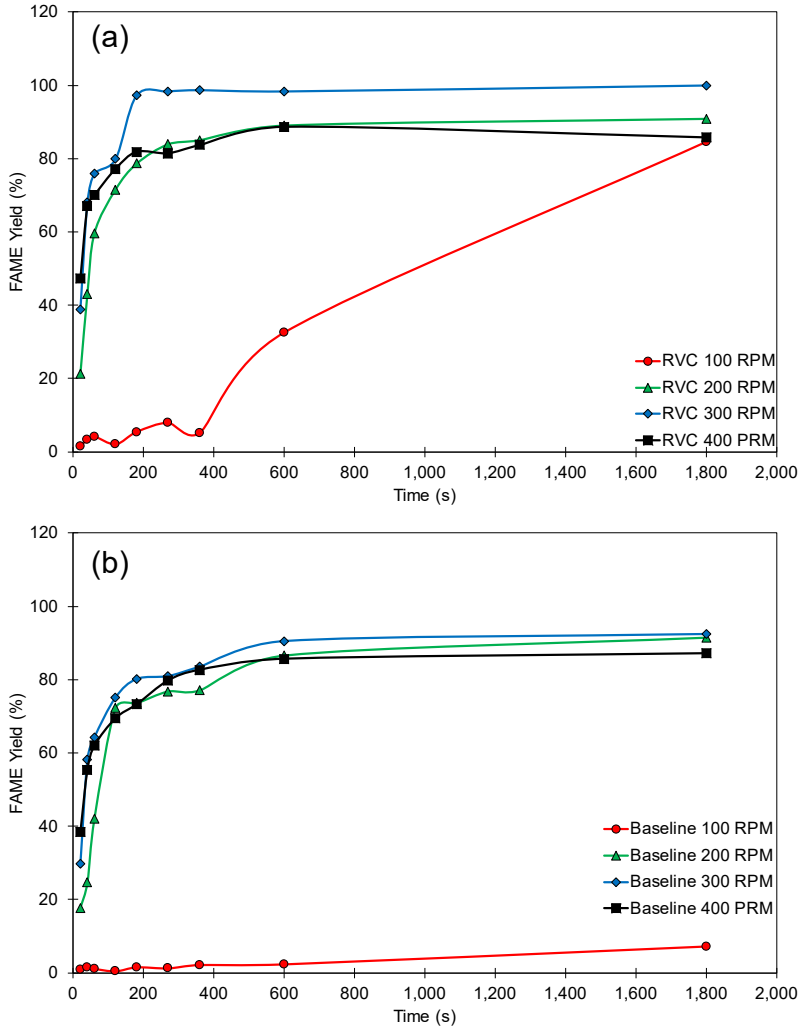

Figure 4-9. Effect of agitation rate on FAME yield for (a) RVC and (b) HDPE baseline.

For lower rpm operations, the reaction did not mix homogeneously at 100 rpm for baseline. However, RVC is still able to generate superior mixing capability to achieve high yield. This suggests that RVC facilitates physical intensification via mechanical stirring while also contributing to diffusion-based transesterification between reactants. The reactant can enter the porous structure more readily at lower rpm benefiting from the large surface area for enhanced reaction rates, due to the reticulated geometry.

At the high rpm operation of 400 rpm, vortex starts to form in the reactor, hindering homogeneous mixing of the reactants, resulting in diminishing reaction rates. The high rpm also causes the bulk

fluid to move further away from the centre of the reactor, effectively causing lesser contact area with the stirrer, substantially declining the mixing capabilities for RVC.

4.2.3.3 Effects of KOH Catalyst Loading

Base-catalysed transesterification is used in this study as it is highly effective at mild reacting conditions. The experiments were carried out using KOH with catalyst concentration at 0.5−1.5 wt. % of the palm oil. As shown in Figure 4-10, the effect of catalytic loading for RVC demonstrates a sequential improvement with increasing KOH concentration, which is also reflected for the baseline.

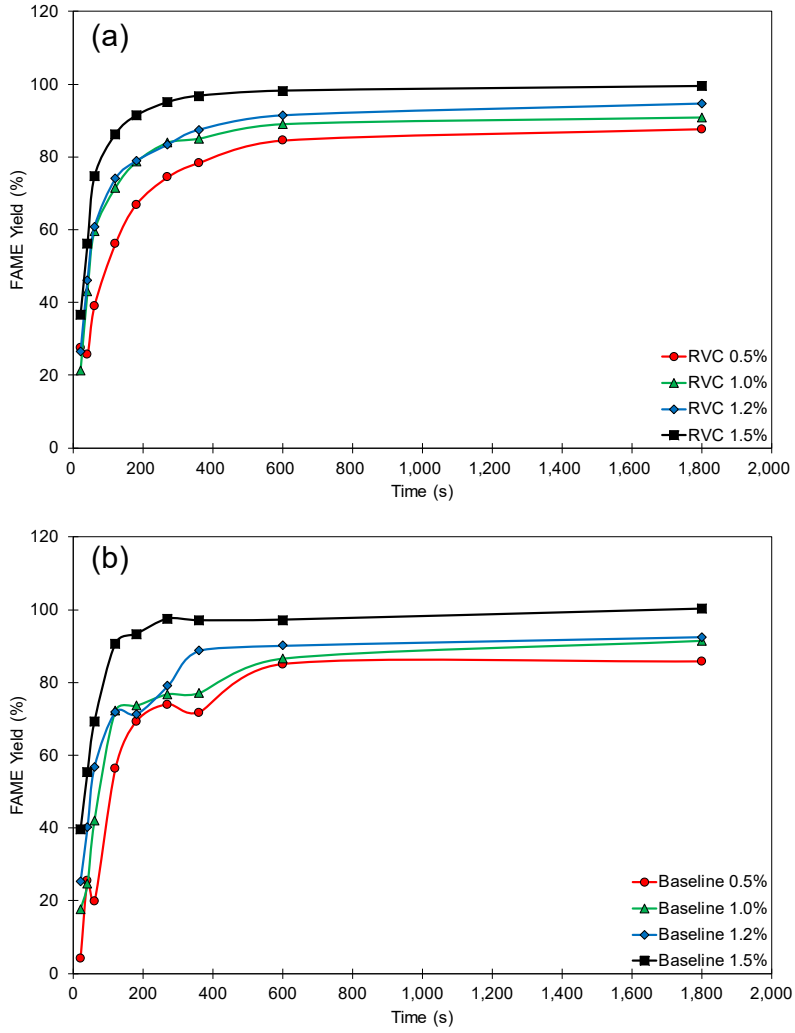

Figure 4-10. Effect of KOH catalytic loading on FAME yield for (a) RVC and (b) HDPE baseline.

Both studies showed that 1.5 wt. % catalyst provided the highest reaction rates and final yield of FAME, while the inverse is true for 0.5 wt. % catalyst. Also, enhancement in FAME conversion is observed in the initial physical-limiting stage from 0−360 s for RVC mechanical stirrer as compared to baseline. Furthermore, 99.4% and 100.0 % FAME yield are achieved by RVC and baseline, respectively at 1.5 wt. % catalytic loading.

Overall, all experimental results from RVC surpass 90% FAME yield for catalytic loading. However, baseline tested at 0.5 wt. % catalytic loading obtained a FAME yield of only 85.8%, which is the lowest in this study. Thus, RVC can still retain high yield at low catalytic conditions, likely because of microturbulence, creating a local mixing between catalyst and reactants, improving catalytic activity. Therefore, making RVC approaches potentially more financially viable for commercialisation and minimising the catalyst-polluted wastewater allows for a cleaner biodiesel processing technique.

4.2.3.4 Effect of Molar Ratio of Methanol to Oil

Methanol to oil molar ratio affects the chemical equilibrium of the transesterification, with stoichiometric defined at 3:1 molar ratio. Therefore, the range of 4:1−7:1 molar ratio is investigated, as shown in Figure 4-11.

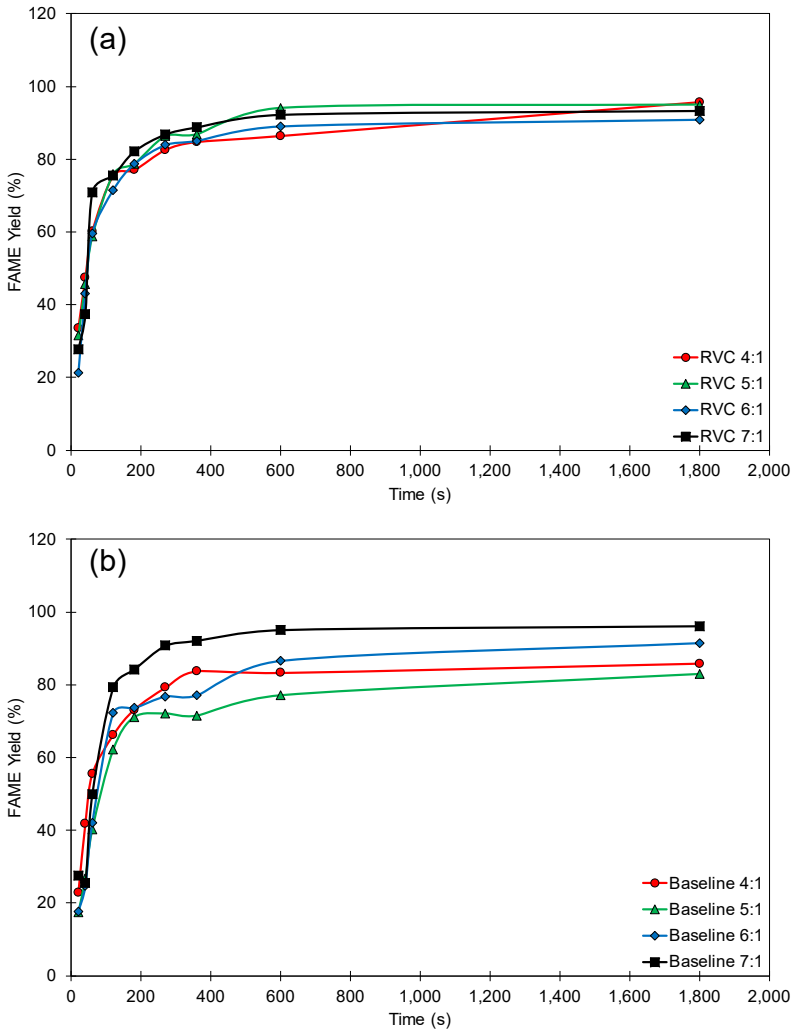

Figure 4-11. Effect of the molar ratio of methanol to oil on FAME yield for (a) RVC and (b) HDPE baseline.

Conventionally, excess methanol is used to promote reaction rates, favouring the forward reaction of transesterification. However, since the volume of oil is set as a constant, and molar ratio is varied by volume of methanol. The mixture's total volume should be considered for reaction rates since total volume to the surface area between stirrer and reactant will reduce for high molar ratio as more reactant is present.

The 7:1 molar ratio provided significant improvement for both RVC and baseline, surpassing 70% yield within 60 s. The highest yield is achieved at 96.1 % and 93.3 % by 7:1 molar ratio for baseline and RVC, respectively. However, RVC is observed to be effective at a lower range of methanol to oil molar ratio, reflected in Figure 4-11(a). Nonetheless, the reaction rates for RVC studies have less of a variation, which suggests that methanol to oil is a less sensitive factor for RVC. All results consistently achieve more than 90 % yield for RVC.

The FAME yield of baseline has a larger variation, dispersing across a final yield of 83.1−96.2 %. Therefore, this shows that the strong mixing capabilities of RVC can efficiently utilise the reactants, raising the lower limit of FAME yield compared to baseline results. The reduction in molar ratio consequently reduces the total volume of the mixture within the reactor, which adequately increases the effective total volume to surface area for the RVC. This causes an indirect effect to facilitate the reaction rates at a lower operating range of methanol to oil molar ratio, leading to low volume reacting conditions and better mixing for reactants. Microturbulence created by the RVC also enables homogeneous mixing between the palm oil and methanol, which are both immiscible and improve reaction rates and yield.

4.2.3.5 Effects of Reaction Temperature

Increase in temperature promotes reaction rates in transesterification, as biodiesel is produced via forward reaction of an endothermic process, which essentially requires the addition of heat. Raising the temperature of the mixture system allows the shift of the chemical equilibrium to favour biodiesel production. Besides, the temperature increase is associated with improved miscibility due to solubility limits between oil and methanol, which is partially soluble in nature, since oil is non-polar and methanol is a polar solvent.

In this experiment, the temperature range of 40−70°C is studied to determine the effectiveness of heat distribution for mechanical stirrers to improve reaction rates, as illustrated in Figure 4-12. RVC exhibits moderate biodiesel yield from 40−70°C, as the maximum achievable yield is from 87.5% to 90.9%. However, RVC shows improvement particularly for lower temperature experiments, such as the 40°C and 50°C cases, prior to 600 s reaction time when compared against the baseline. Similarly, in the previously examined methanol to oil molar ratio studies, the FAME yield variation is small at the final phase of the reaction. Consequently, it is possible to achieve the same yield using a lower reaction condition with RVC.

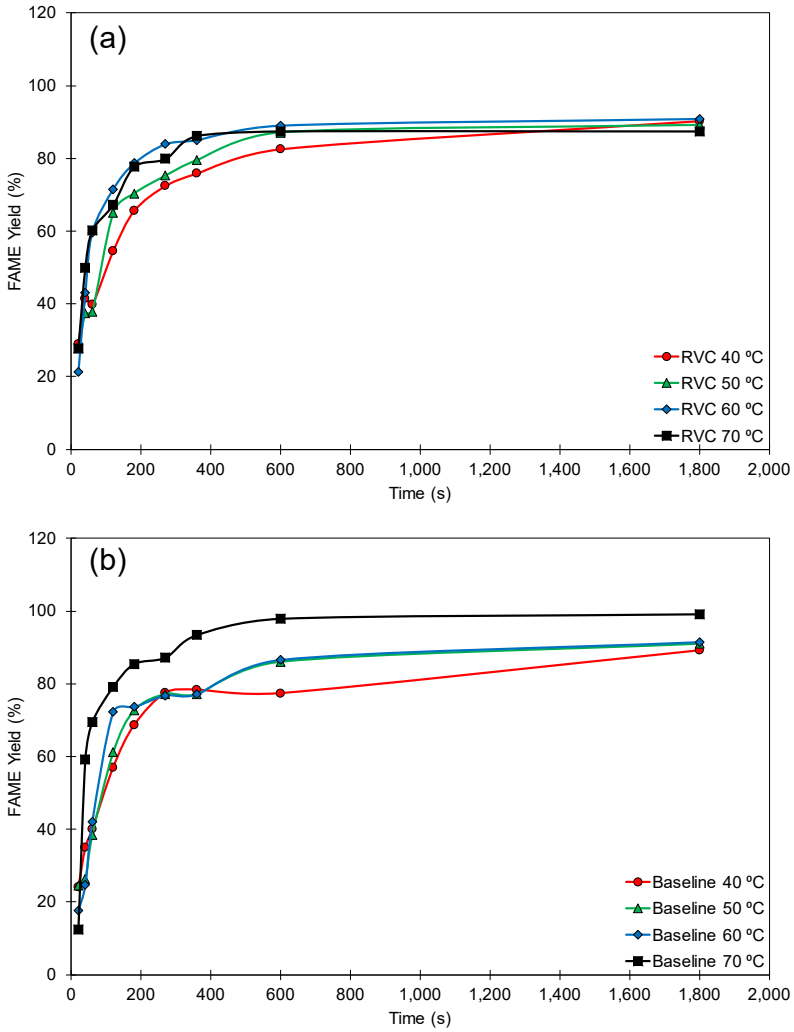

Figure 4-12. Effect of reaction temperature on FAME yield for (a) RVC and (b) HDPE baseline.

For the baseline studies, the 40 °C case takes longer time to converge to the final yield point than the other temperature, while 50 °C and 60 °C cases are virtually identical in terms of reaction rates and FAME yield. The baseline case at 70 °C can achieve a higher FAME yield of 99.2 %, as compared to RVC after 200 s.

4.2.3.6 Summary of the preliminary results for RVC transesterification

Majority of the RVC studies are reported from the field of electrochemistry to promote mass transfer by leveraging on the enhanced surface area from the reticulated characteristic. Thus, the main goal of the preliminary results is to identify the suitable range of operating condition for RVC reactor in biodiesel transesterification. Therefore, RVC as a material is tested to elucidate the feasibility of a stirred-tank agitator. As such, the range of the parameters used in this preliminary experiment mimics the conventional batch-type reactor, as discussed in Chapter 3 for benchmarking purposes.

In this experiment, RVC as a material for overhead stirrer is expected to improve the physical agitation aspect for transesterification. Therefore, studying the PPI and agitation rates provides more noticeable differences as compared to catalyst loading, methanol to oil molar ratio, and reaction temperature. This is only partially true as observed from the results using the effects of molar ratio, reaction temperature, and catalyst loading, where the use of RVC provides a smaller variance in yield, hence improving consistency.

For the agitation rate, the results of using 100 rpm highlight the mass transfer issue with transesterification, where the baseline is unable to provide adequate mixing. However, RVC is able to take advantage of its material properties to homogenise the reactants, hence a relatively higher yield is obtained at the end of the process. The increase in ppi improves the biodiesel yield, where the performance peaks at 45 ppi, followed by a plateau and negative effect using 65 and 80 ppi stirrer, respectively. In terms of catalyst loading, the trends for the yield are in the increasing order of magnitude with the amount of catalyst used. This is shown in both RVC and baseline test results, with the former observed to be more stable in yield growth than the latter. For methanol to oil molar ratio, increasing the molar ratio clearly increases biodiesel formation in the baseline. However, the RVC test shows a small effect of yield difference for using different molar ratios as the results are small in variance. The effects of reaction temperature have similar trends as the methanol to oil molar ratio. RVC is observed to be a more efficient agitator in reaction for heat distribution to obtain a high yield despite using a lower reaction temperature at 40°C. Figure 4-13 shows the FAME yield comparison of RVC and the baseline stirrer which acts as a benchmark for three different stage of transesterification, namely, the initialisation phase(20 s), the transition stage (180 s), and the final yield point (1,800 s).

		FAME Yield (%)					
		Initialisation 20 s		Transition Stage 180 s		Final Yield 1800 s	
		RVC	Baselines	RVC	Baselines	RVC	Baselines
RPM	100	1.55	0.94	5.45	1.59	84.61	7.27
	200	21.26	17.64	71.30	73.62	90.92	91.54
	300	38.93	29.80	97.29	80.16	100.00	92.42
	400	47.27	38.42	81.86	73.22	85.79	87.13
PPI	20	21.26	17.64	78.68	73.62	90.92	91.54
	45	20.62		84.60		100.11	
	60	32.29		75.87		99.49	
	80	32.01		78.20		90.65	
Catalyst loading	0.5	27.56	4.19	66.95	69.29	87.70	85.75
	1	21.26	17.64	78.68	78.68	90.92	91.54
	1.2	26.57	25.36	78.93	71.30	94.68	92.54
	1.5	36.58	39.62	91.36	93.32	99.42	100.23
Methanol to oil molar ratio	4:1	33.64	22.98	77.04	73.17	95.76	85.86
	5:1	31.65	17.37	78.72	71.19	94.96	83.09
	6:1	21.26	17.64	78.68	73.62	90.92	91.54
	7:1	27.73	27.49	82.11	84.21	93.30	96.17
Temperature	40	28.98	24.11	65.58	68.66	90.32	89.16
	50	27.76	24.58	70.37	72.69	89.16	91.01
	60	21.26	17.64	78.68	73.62	90.92	91.54
	70	27.73	12.34	77.70	85.45	87.51	99.17

Figure 4-13. Comparison of RVC and baseline stirrer across factors.

In all, the selection of operating conditions is required to be comparable with the batch reactor results, where the transesterification regime of interest determined from the full factorial test can be analysed in the RVC experiments.

4.3 Reticulated Vitreous Carbon transesterification study via the full factorial design of experiments

The preliminary results provide sufficient insights for implementing the Design of Experiments with the appropriate inputs. Thus, Minitab 19 was utilised to create the Full Factorial study using five factors (ppi, agitation rate, methanol to oil molar ratio, catalyst loading, reaction temperature) at three different levels, as shown in Table 4-5. The number of permutation in the factorial design totalled 243 (3^5) unique experiments, with ten sampling points within 30 minutes of reaction time individually. The levels of factors and time of sampling were selected based on the transesterification yield profile from the preliminary studies. Therefore, the agitation rate for RVC at 100 rpm is not considered homogeneous mixing, as shown in Figure 4-13 where the yield for baseline is significantly lower than the RVC. The 65 ppi is also eliminated since the pores start to saturate beyond 45 ppi, as shown in the small variance in yield. The molar ratio was selected based on transesterification stoichiometry in increasing order. The temperature was based on near-room temperature and in increasing order of magnitude, the 60°C upper limit is selected due to the boiling point of methanol at 64.7 °C. The KOH catalyst loading of 1.2 wt. % is removed as the difference between 1.0 wt. % and 1.5 wt. % is small.

Table 4-5. Factorial Design Parameters in Minitab 19.

Factor	**Name**	**Unit**	**Type**	**Level Values**		
				-1	0	+1
A	Agitation rate	rpm	Continuous	200	300	400
B	Pores per inch	-	Continuous	10	20	45
C	Catalyst Loading	%.wt	Continuous	0.5	1.0	1.5
D	Molar Ratio	-	Continuous	3	6	9
E	Reaction Temperature	°C	Continuous	30	45	60

4.4 Results and discussions

4.4.1 General factorial regression model assessment for RVC transesterification reaction.

General factorial regression analysis from the data was conducted to validate the biodiesel yield.

$$Y = \beta_0 + \sum_{i=1}^{k} \beta_i X_i + \sum_{i=1}^{k} \beta_{ii} X_i^2 + \sum_{i=i<j}^{k-1} \sum_{i=2}^{k} B_{ij} X_i X_j \qquad \text{Eq. 4-2}$$

Where Y is the predicted transesterification yield produced from the RVC reactor, and β_i, β_{ii}, and β_{ij} are coefficients calculated based on the general factorial stepwise regression analysis. To define a useful subset of terms stepwise eliminates and adds terms to the model. This approach begins with an empty model or includes the terms that the user has defined in the original or model models. The regression analysis terminates when all the model variables have p-values greater than the value entered by the specified alpha. All variables in the model have p-values less than or equal to the value removed by the specified alpha. In this study, the alpha to enter and remove is 0.05. The regression analysis is conducted on the ten different sampling points independently as they are considered individual responses. The model summary is shown in Table 4-6.

Table 4-6. General factorial regression model summary for 30s to 1800s using RVC.

Sampling Time (s)	S	R^2 (%)	R^2(adjusted) (%)	R^2(predicted) (%)
30	11.8193	70.86	68.51	65.68
60	12.7017	66.27	65.41	64.24
120	10.8169	75.76	72.83	69.31
180	10.2328	74.19	71.07	67.33
270	9.48577	73.48	70.27	66.42
420	8.6317	71.21	69.43	67.29
600	8.00846	71.8	70.06	67.96
900	7.41198	71.26	69.49	67.35
1500	7.28417	68.55	66.61	64.26
1800	7.75728	62.66	61.38	59.72

4.4.2 Factorial plots analysis for the RVC transesterification reaction.

The factorial plots analysis consists of an interaction plot and main effect plots for each continuous variable based on the regression model. Figure 4-14 and Figure 4-15 is the results of a factorial plot analysis at the 30s into transesterification for RVC reactor. The interaction plots in Figure 4-15 show the fitted means of transesterification yield by combining different level settings for transesterification. This plot demonstrates an apparent interaction effect. The lines are not parallel, indicating that the relationship between RPM, ppi, catalyst loading, and reaction temperature depends on the methanol to oil molar ratio at 30s. The regression analysis results imply that the interaction effect for ppi*Molar Ratio and Catalyst*Temperature are statistically significant.

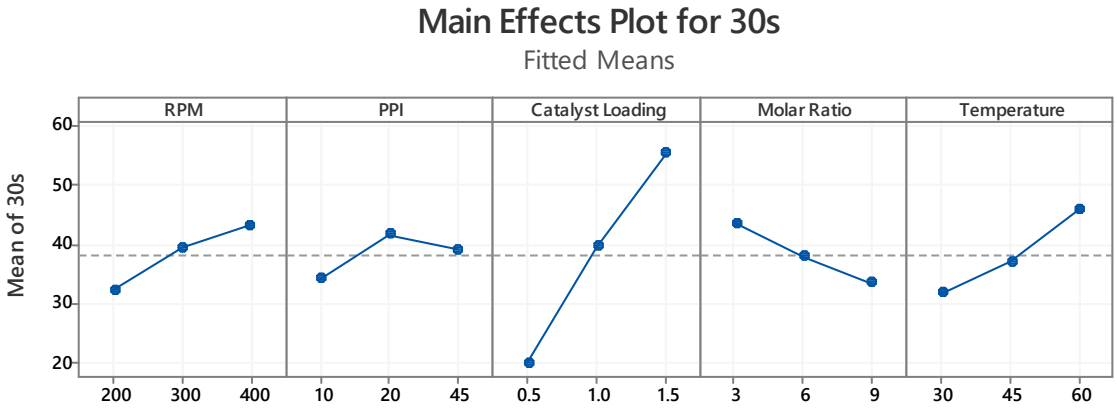

Figure 4-14. Main effects plot for 30s into RVC transesterification.

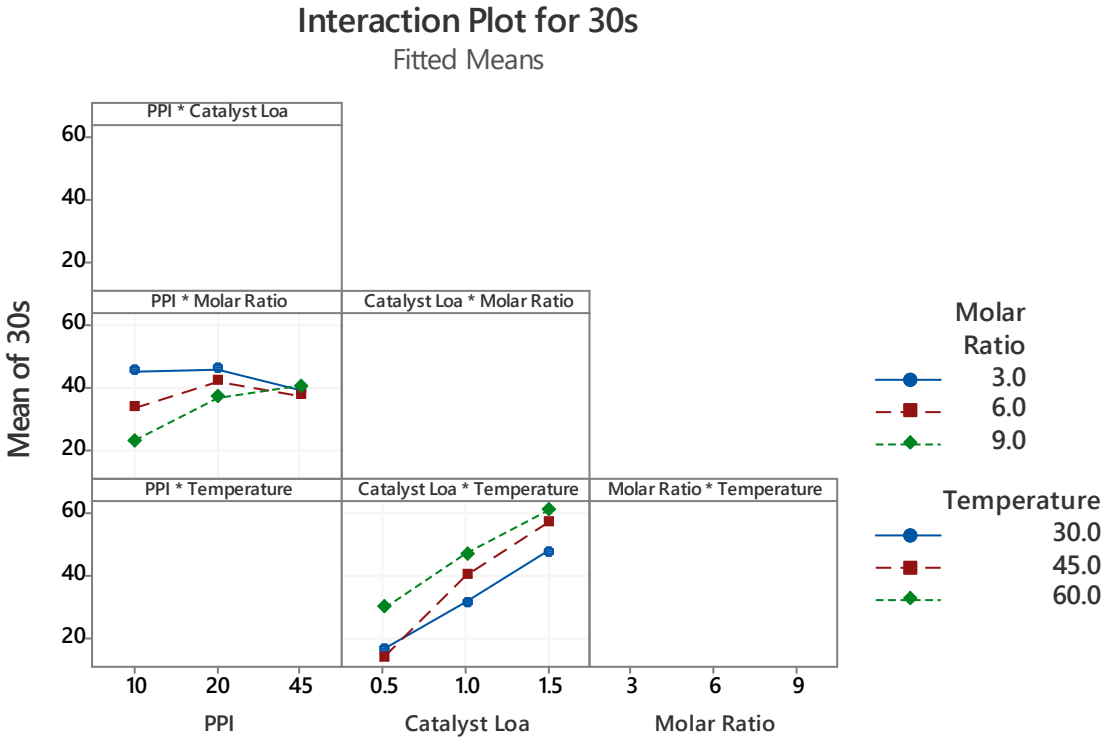

Figure 4-15. Interaction plot for 30s into RVC transesterification.

In the ppi*Molar Ratio interaction plot, the lower molar ratio has a higher mean of yield, particularly at 10 ppi, where the means of yield converges as ppi increases. The observation suggests that

methanol saving can be potentially achieved using lower molar ratio settings, without trading off biodiesel yield purely based on the surface area effect from RVC agitation. Another interesting interaction is the Catalyst*Temperature, where positive correlation is observed with the increase in both operating conditions. The effect is expected to contribute to the activation energy required to initiate the transesterification reaction.

For each continuous variable, the main effects plots display the fitted means, while the other variables in the model are kept constant, as shown in Figure 4-15. Since the lines are not horizontal, the key effects of all these factors are present. The findings of the regression analysis confirm the statistical importance of all the key effects. However, the main effects plot can be misleading because the interaction effects are statistically significant. Consequently, the main effects plots cannot be interpreted without the interaction effects plots.

For the 60s factorial analysis, there is no valid interaction plot since none of the two-way interactions is within the p-value of 0.05. Therefore, the modelled terms in the 60s sampling are RPM, catalyst loading, and temperature, as shown in the main effect plots Figure 4-16. The transesterification reaction's physical-limiting stage suggests that a higher agitation rate promotes the reactants to achieve homogeneity, resulting in greater yield. The catalyst loading and temperature are still dominant in terms of main effect strength.

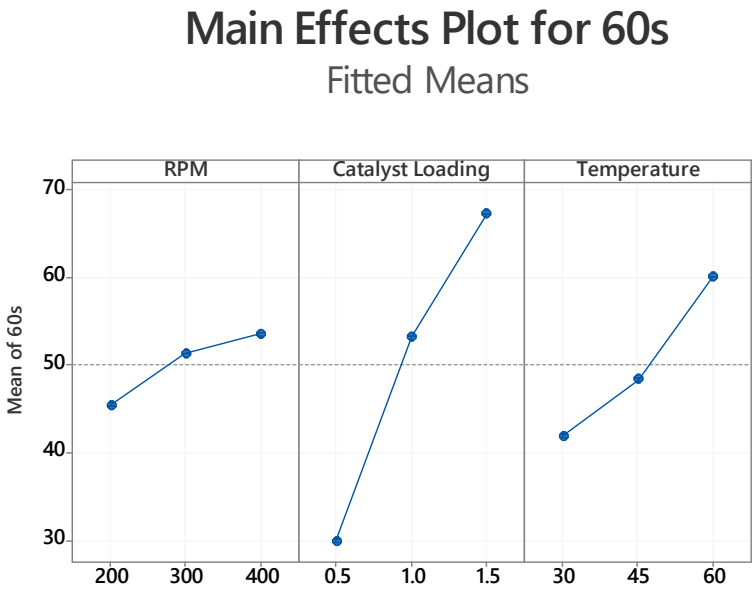

Figure 4-16. Main effects plot for 60s into RVC transesterification.

The main effects and interactions at 120s in Figure 4-17, catalyst loading, molar ratio, and temperature are statistically significant. However, the molar ratio's main effects are relatively weaker than catalyst loading and temperature, with a maximum difference in mean yield of 5%. The interaction of Molar Ratio*Temperature in Figure 4-18 shows a more considerable divergence of

means of yield moving from 3 to 9 molar ratio, with lower temperature decreasing across, while greater yield contributed by higher temperature. The relationship between the miscibility of methanol-oil and biodiesel supports the previous observation. The total volume of reactants is constant for all test cases, with the total mass having a percentage difference of 1.18% for low and high molar ratio cases. Therefore, when the molar ratio is low, the methanol becomes a bottleneck for producing biodiesel, where the higher temperature has minimal effect on the interaction between Molar Ratio*Temperature. However, at 9:1 methanol to oil molar ratio, the methanol is no longer a limiting factor for the reaction. As the volume fraction of methanol increases in the total volume, the reaction's surface area increases. Thus, the higher temperature enables higher reaction rates, producing more biodiesel as the reaction overcomes the activation energy barrier. The higher temperature also improves the miscibility between oil and methanol as the solubility of oil in methanol increases, resulting in more homogeneous mixing for the reactants. The lower temperature at the higher molar ratio, since the volume fraction of methanol increases, and miscibility of oil and methanol is low, suggesting no homogeneous mixing among reactants. Therefore, the reaction only occurs at the surface of oil and methanol, resulting in a relatively lower yield.

On the other hand, the interaction of Catalyst*Temperature is similar to the 30s factorial plot. However, the Catalyst*Molar Ratio interaction has an opposite effect at the lower catalytic loading condition. The operating conditions of 3:1 and 6:1 methanol to oil molar ratio perform better than the 9:1 by a 9% margin in yield. Since the catalyst concentration is low, this suggests that the lower molar ratio enables a higher collision rate between the catalyst and the reactants as there is an effectively higher mass of catalyst per volume of methanol (mg/ml).

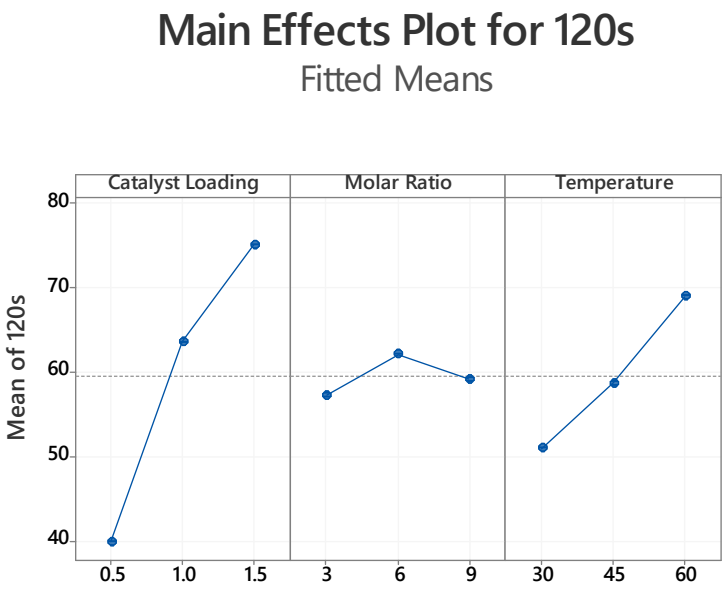

Figure 4-17. Main effects plot for 120s into RVC transesterification.

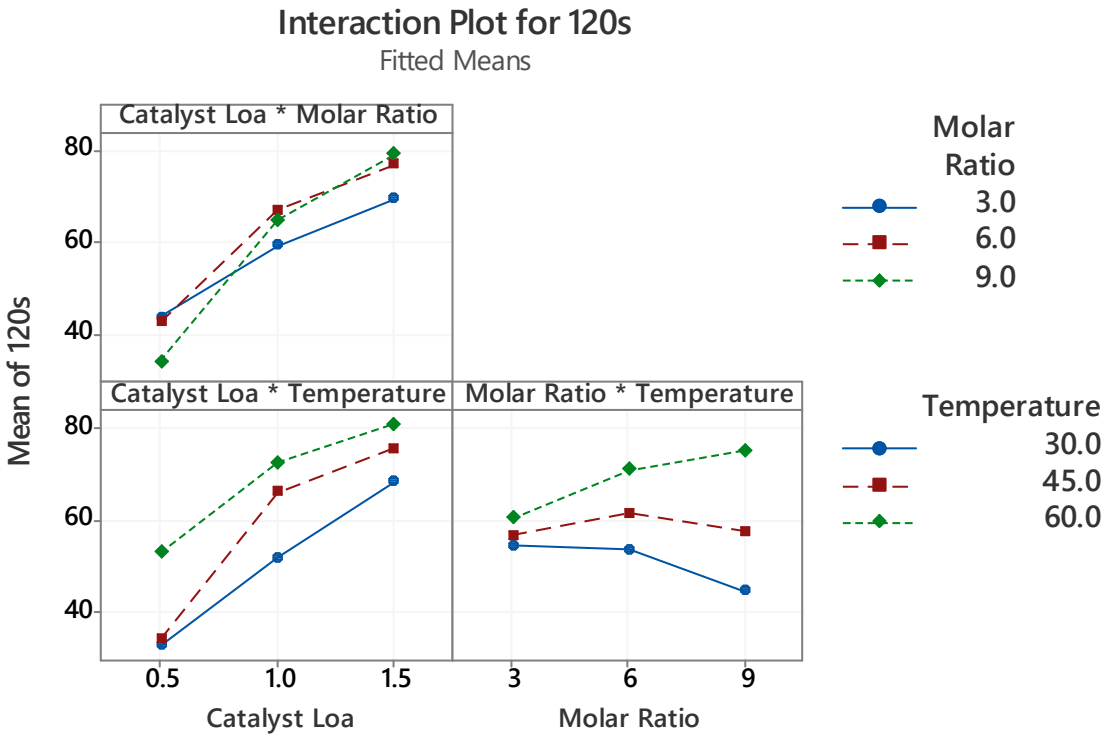

Figure 4-18. Interaction plot for 120s into RVC transesterification.

The main effects plot for biodiesel yield of 180s in Figure 4-19 are observed to be dominated by increasing catalyst loading and reaction temperature, with catalyst loading having a significant difference in mean yield of 32% moving from 0.5wt. % to 1.5wt. % of oil.

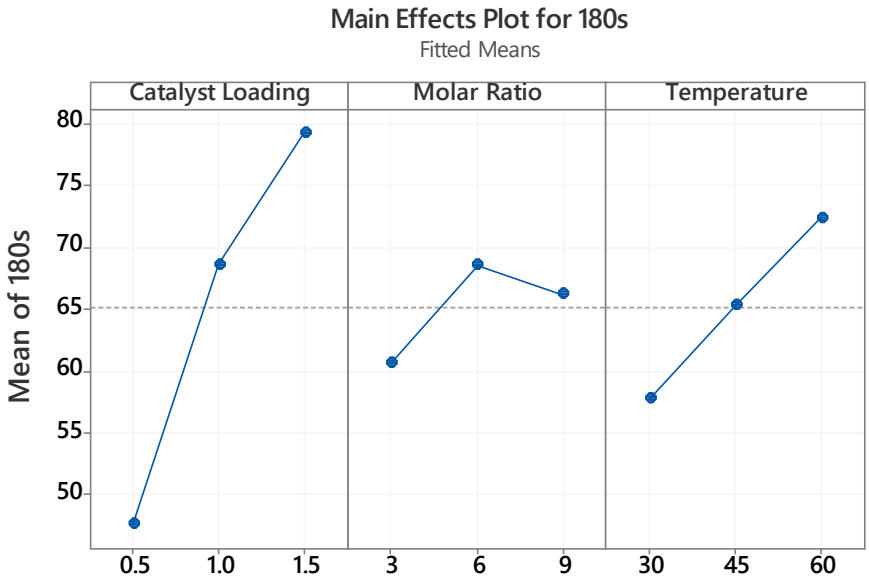

Figure 4-19. Main effects plot for 180s into RVC transesterification.

This observation is also reflected in Catalyst*Molar Ratio and Catalyst*Temperature interactions in Figure 4-20, where catalyst loading dictates the mean yield direction. The molar ratio main effect

does not follow the conventional trend of transesterification reaction of higher reactants promotes higher rates of reactions. A decrease in 2% mean yield was observed when moving from 6:1 to 9:1 methanol to oil molar ratio. The interaction plot reveals that the potential decrease in yield is associated with the Molar Ratio*Temperature interaction similar to the 120s analysis. This observation's implication enables practical application of biodiesel production, such as using dynamic and adaptive methanol to oil molar ratio for transesterification from the beginning to the end of the reaction.

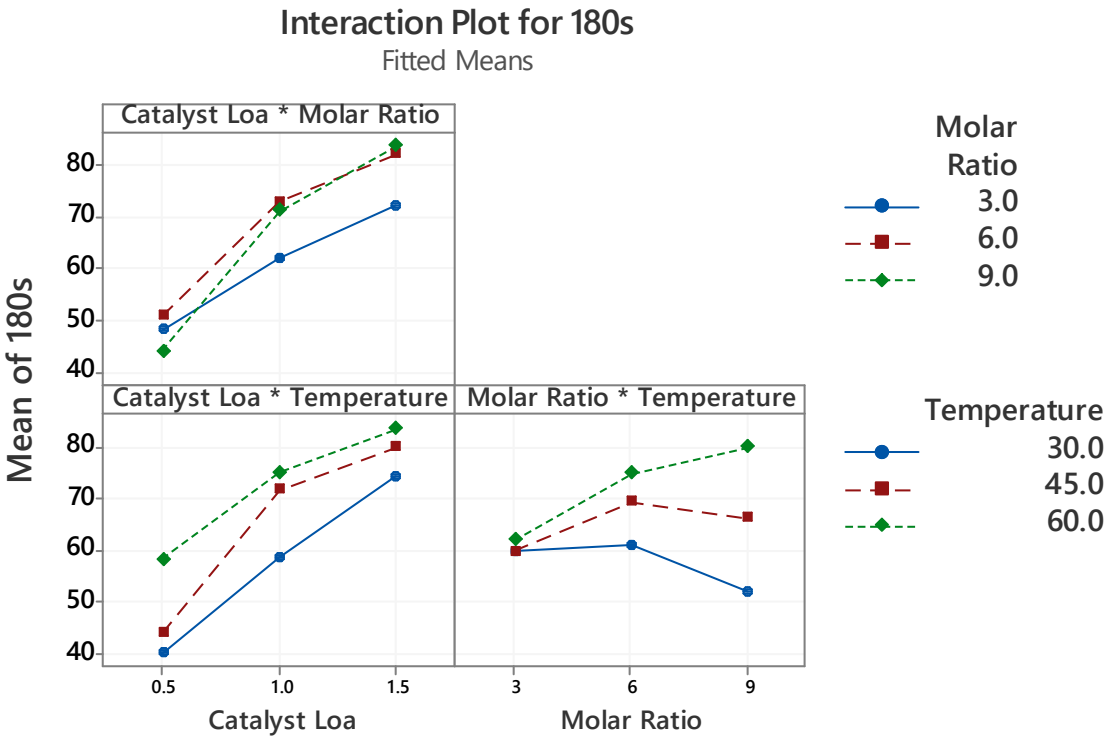

Figure 4-20. Interaction plot for 180s into RVC transesterification.

In the factorial plots for 270s as shown in Figure 4-21 and Figure 4-22, catalyst loading, methanol to oil molar ratio, and the temperature are statistically significant. The 270s study also situates between the physical-limiting and reaction-limiting regime, right at the transition point of transesterification reaction. As shown in the main effect plot, the 9:1 methanol to oil molar ratio operating condition does not enhance the reaction rate, as per how literature perceives the effect of using excess methanol. The result is consistent with the full-factorial study's findings using the baseline batch reactor, hence 6:1 methanol to oil molar ratio will be a more efficient and economical choice for the operating condition at 270s.

An in-depth analysis of the interaction plot shows that the interaction of Catalyst*Molar Ratio favours a higher yield using 6:1 methanol to oil molar ratio at 0.5 wt. % catalytic loading. However, moving towards a higher catalytic loading operating condition, the effectiveness of using a high molar ratio appears to be synergistic with the catalytic action. A small difference can be observed for Catalyst*Molar Ratio interactions, particularly at the methanol to oil molar ratio of 6:1 and 9:1 when

using 1.0 and 1.5 wt. % KOH. Therefore, the economic motivation could still outweigh the slight increase in mean yield for this scenario. The Catalyst*Temperature and Molar Ratio*Temperature interaction follows the same trend as the 180s interaction plot results.

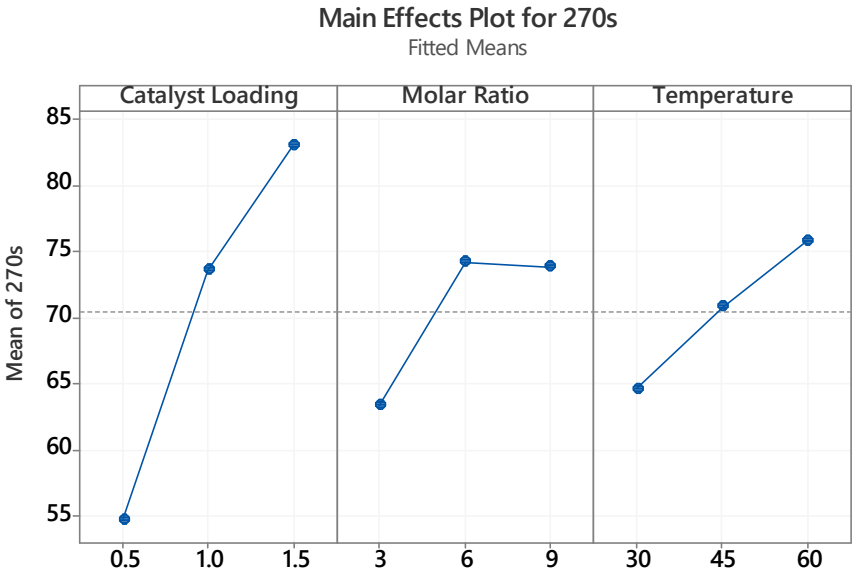

Figure 4-21. Main effects plot for 270s into RVC transesterification.

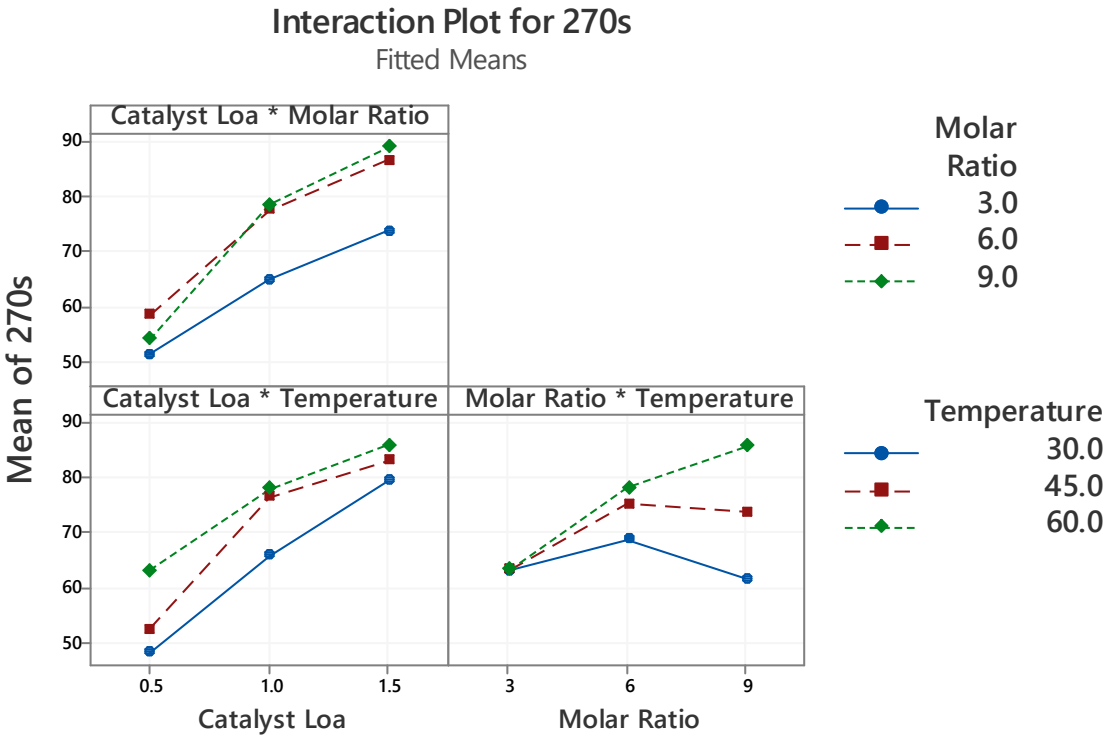

Figure 4-22. Interaction plot for 270s into RVC transesterification.

The increase in reaction temperature did not benefit transesterification in this interaction at 45 ppi, except for 30°C. When the ppi doubles from 20 to 45, the mean yield increased by 13.5% using a

30°C reaction temperature. The low reaction temperature limits the reactants' miscibility and the energy required to overcome the activation energy barrier. However, this is compensated by improving the surface area between oil and methanol from the 45 ppi agitator. The implication indicates promising use of RVC as an efficient agitator, as the effect of lowered reaction temperature can be offset by increasing ppi values.

At 420s, 600s, and 900s into the onset of transesterification in **Error! Reference source not found.**, Figure 4-24, Figure 4-25, Figure 4-26, Figure 4-27, and Figure 4-28, the reaction progresses into the reaction-limiting regime, where the reactants and products achieved homogeneous mixing. During this stage, the transesterification process relies on the effect of catalyst loading, methanol to oil molar ratio, and reaction temperature. Catalyst loading and reaction temperature are still consistently significant in the transesterification reaction. The molar ratio has an improving trend moving from 6:1 to 9:1 methanol to oil ratio, as this is the first time it showed a positive increment in mean yield. Most likely, due to the effect of excess methanol for the forward reaction outweighs the miscibility problem caused by it. At 900s, the temperature main effect plot shows negligible improvement from 45°C to 60°C, which is observed as a decreasing trend from 420s to 900s in terms of mean yield. Thus, at this point, the lower reaction temperature can be used to achieve similar results as transesterification performance is similar.

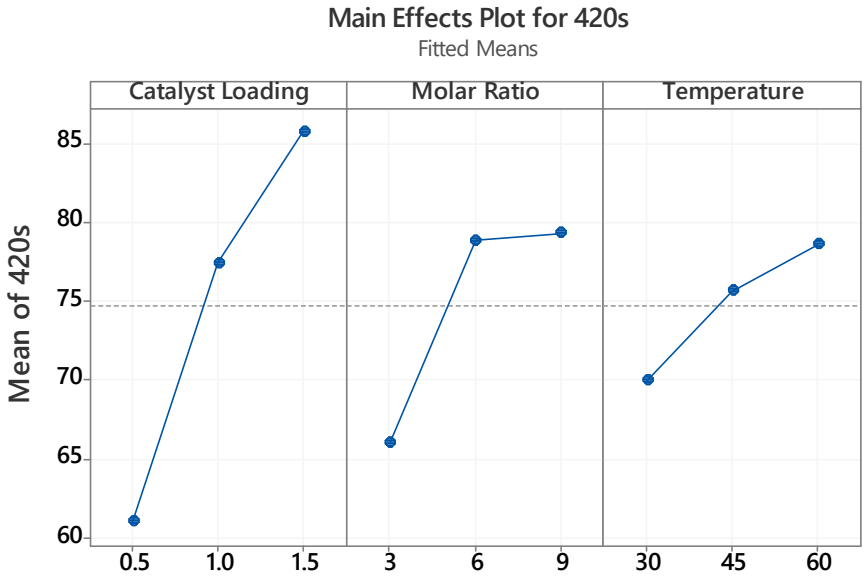

Figure 4-23. Main effects plot for 420s into RVC transesterification.

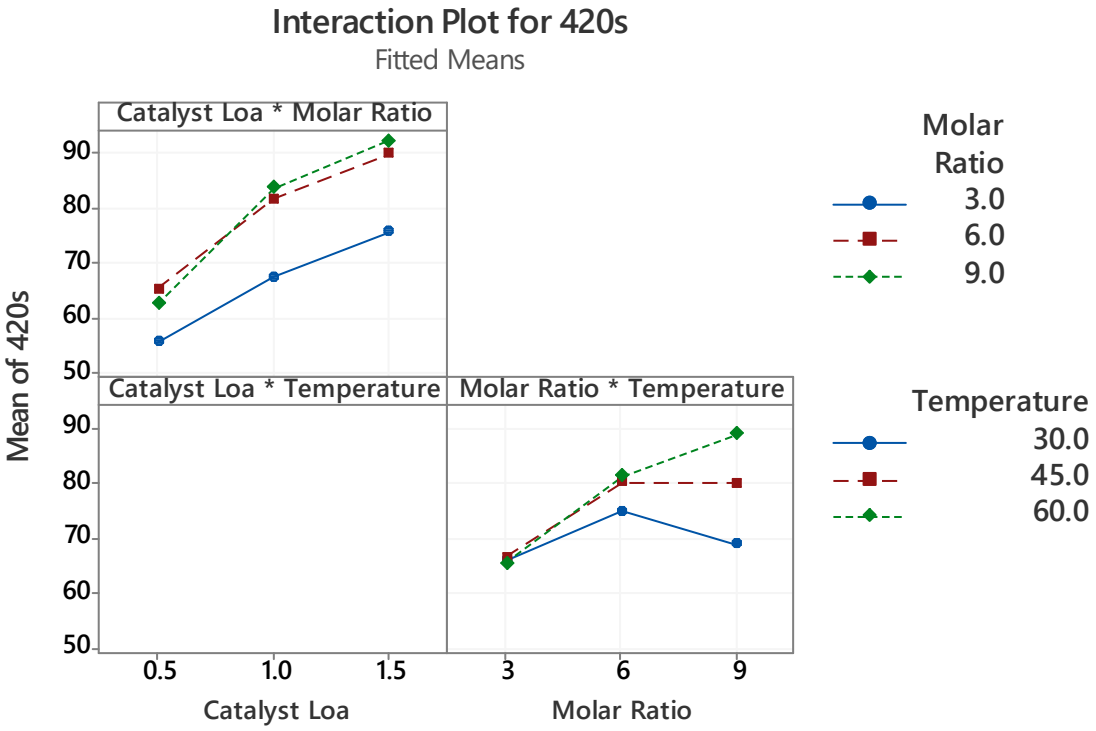

Figure 4-24. Interaction plot for 420s into RVC transesterification.

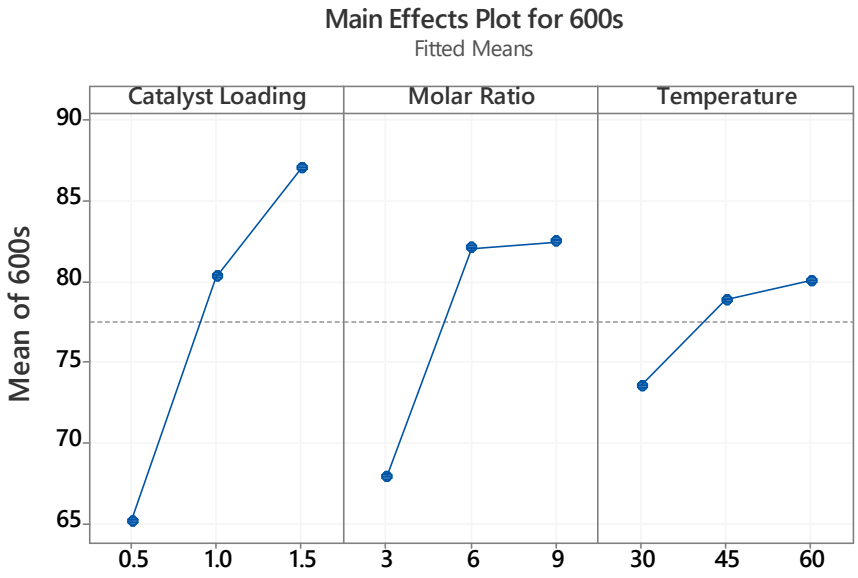

Figure 4-25. Main effects plot for 600s into RVC transesterification.

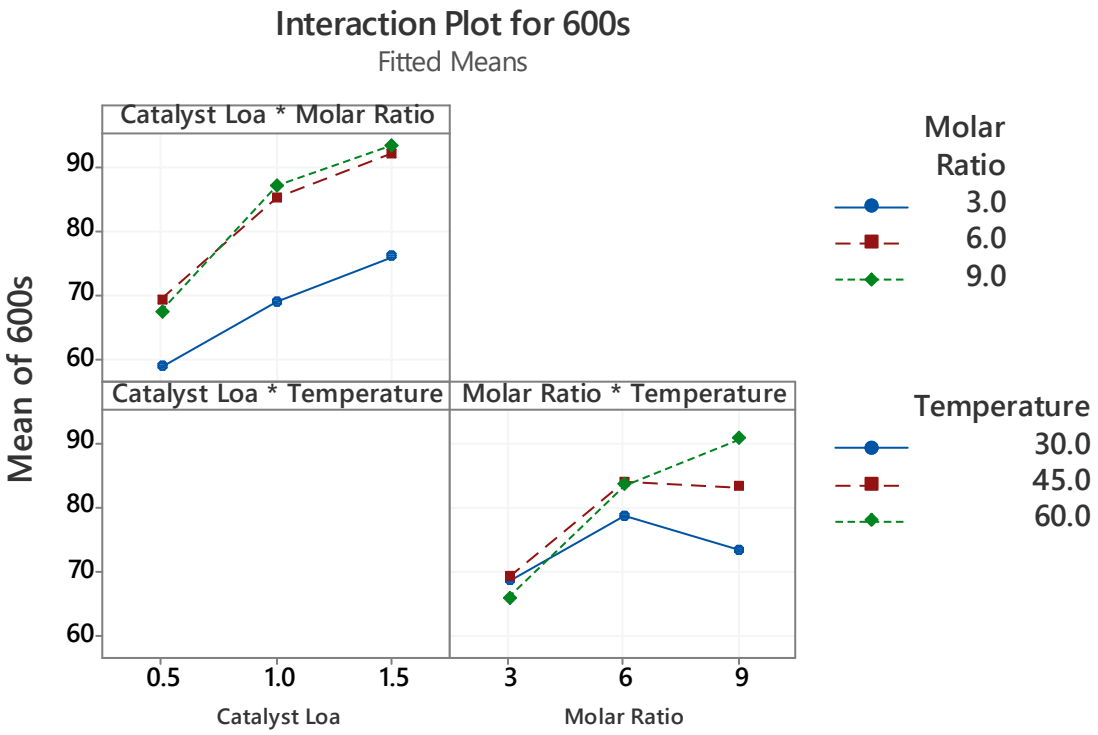

Figure 4-26. Interaction plot for 600s into RVC transesterification.

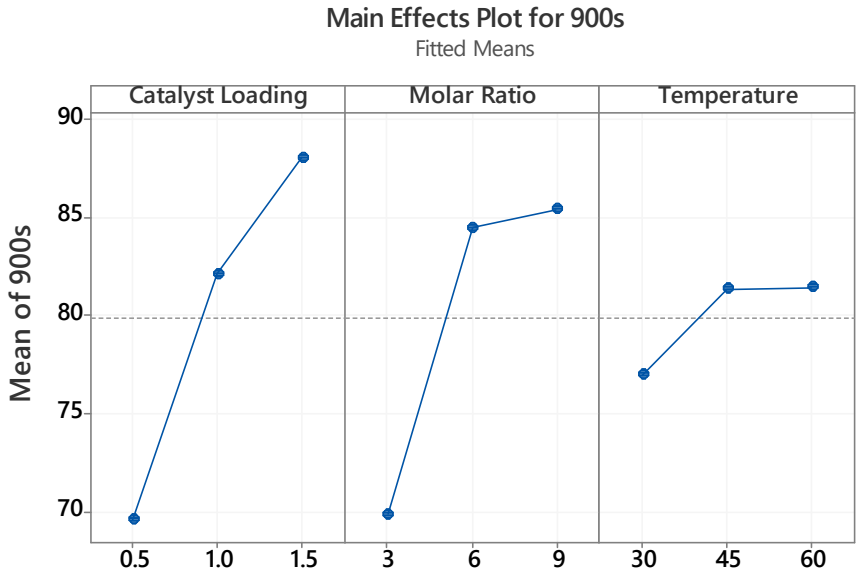

Figure 4-27. Main effects plot for 900s into RVC transesterification.

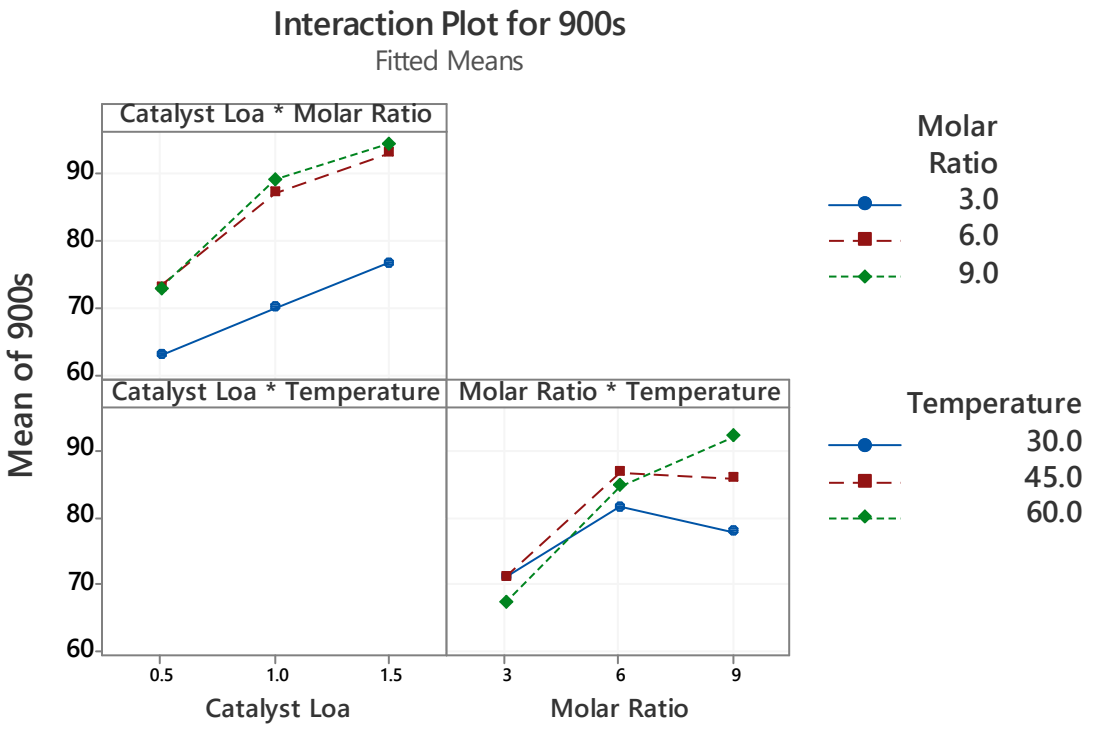

Figure 4-28. Interaction plot for 900s into RVC transesterification.

The modelled terms for the 1500s and the final yield point, 1800s are catalyst loading, molar ratio, and reaction temperature as shown in Figure 4-29, Figure 4-30, Figure 4-31, and Figure 4-32. From the Catalyst*Molar Ratio interaction, it can be observed that the gap between the stoichiometry molar ratio and beyond has increased, which suggests that methanol acting as a limiting factor for complete reaction. Additionally, the main effect plot of reaction temperature shows a negative trend moving from 45°C to 60°C, resulting in a decrease in the mean yield of 2% in both scenarios. This result is speculated to be the higher temperature evaporating some of the methanol, causing a drop in performance. The hypothesis can be supported by looking at the interaction of Molar Ratio*Temperature, where a higher temperature of 60°C performs worse than the lower temperature at 3:1 and 6:1 methanol to oil molar ratios, where methanol is not in excess. However, the 9:1 methanol to oil molar ratio can outperform in mean yield for 60°C due to the large buffer of excess methanol able to compensate for the evaporation rate, benefitting from the high temperature.

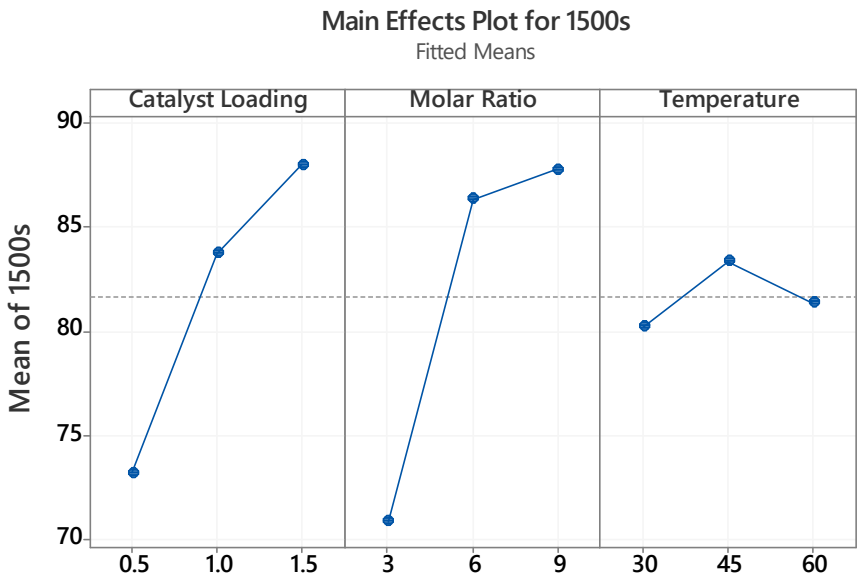

Figure 4-29. Main effects plot for 1500s into RVC transesterification.

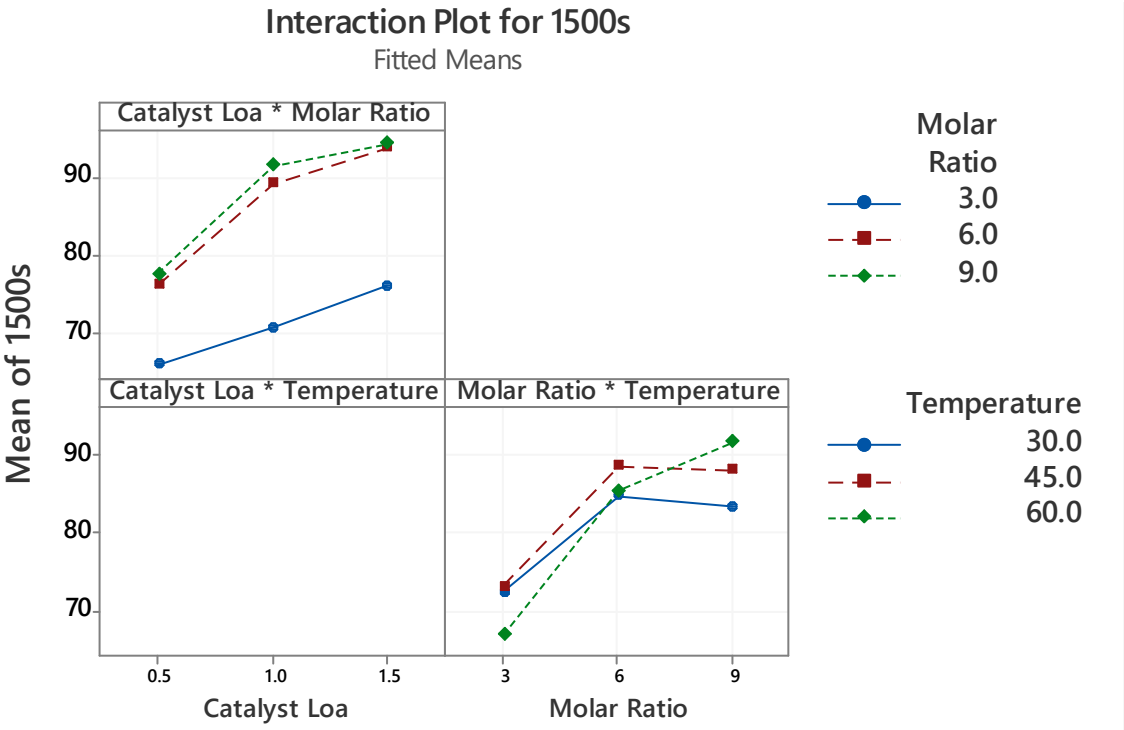

Figure 4-30. Interaction plot for 1500s into RVC transesterification.

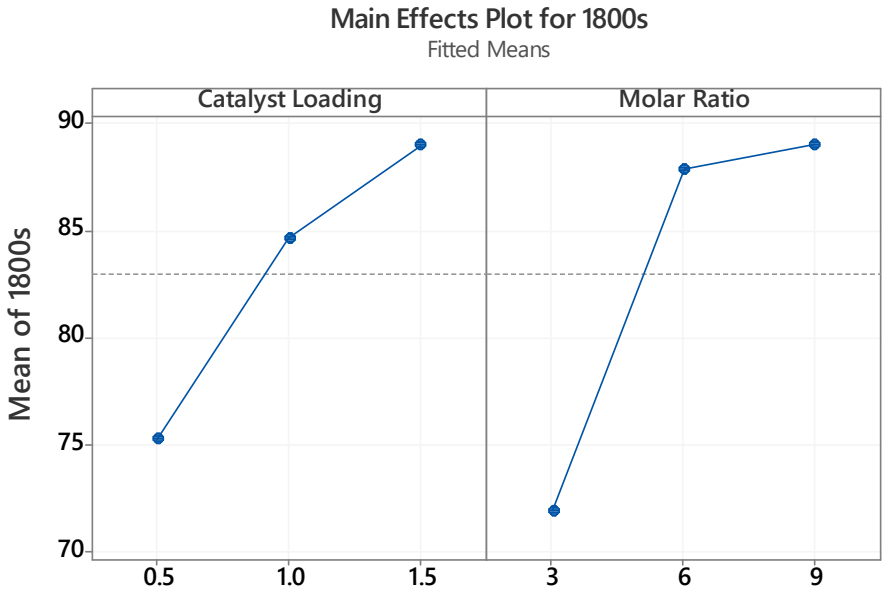

Figure 4-31. Main effects plot for 1800s into RVC transesterification.

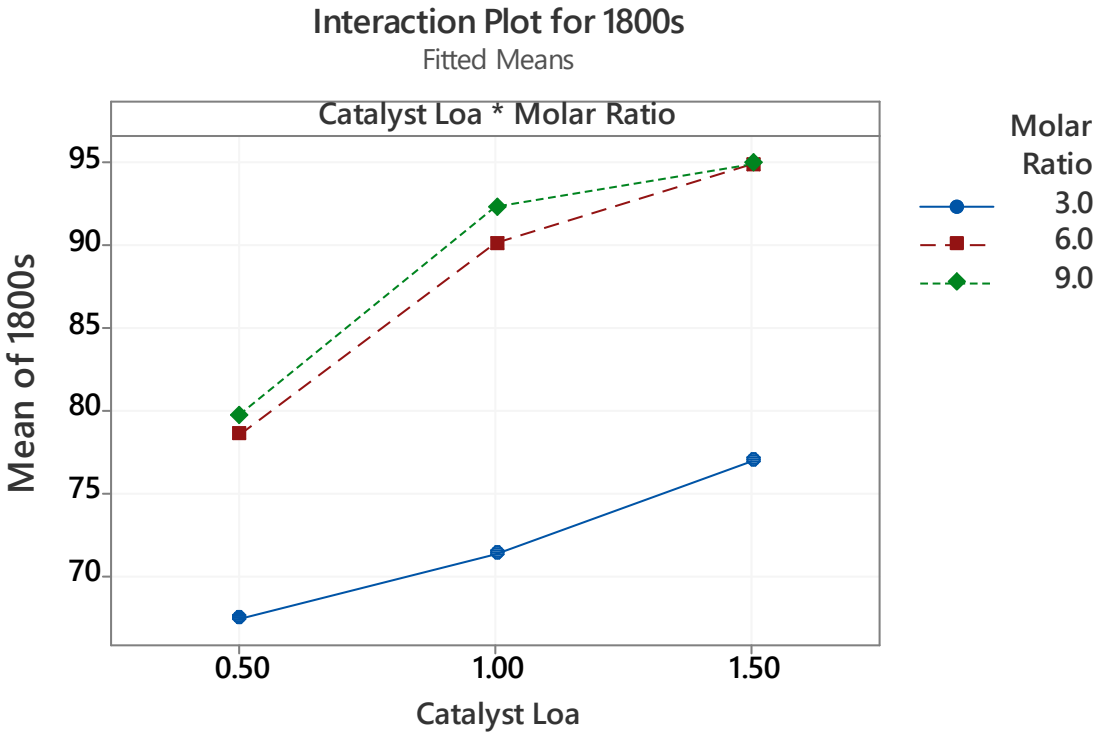

Figure 4-32. Interaction plot for 1800s into RVC transesterification.

Response optimiser is used based on the regression model with the goal set to maximise biodiesel yield, where the higher values of the response are preferable. The model used for the optimiser is from its respective regression model from the 30s to the 1800s of transesterification. The constraints for the variables are set to the lower (-1) and upper (+1) regions to ensure that it is within the range of this Design of Experiments. The confidence level for all intervals is set to 95%. As the goal is to maximise the yield response, the value setup for the target yield is only used to calculate the fit of

the model (yield fit) and the achievability (composite desirability). The composite desirability is capped at 1 when the responses are greater than the target value. Table 4-7 shows the result of the input as a function of reaction time.

Based on Table 4-7, ppi is a significant factor at the initialisation of transesterification, which complements the effect of agitation at the physical-limiting regime. Therefore, as the mixture has achieved adequate mixing, agitation with the RVC stirrer (ppi) is no longer required, which is indicated at beyond 60s. The results from the response optimiser of the benchmark batch reactor in Table 3-9 suggest that the optimised responses can only achieve adequate mixing at 270s which is four times longer than using the RVC reactor.

Low methanol to oil molar ratio (3:1) is beneficial for biodiesel production at the beginning of transesterification from 0s to 120s, essentially the physical-limiting stage. This is observed to improve the overall transesterification defined from the benchmark batch reactor, where its physical-limiting stage extends into 180s. Therefore, the use of the RVC reactor can allow the transesterification process to transition from physical-limiting stage to chemical-limiting stage sooner, through the effect of microturbulence induced by the stirrer.

Table 4-7. Response optimiser for 30s to 1800s in RVC Transesterification.

Time (s)	**RPM**	**ppi**	**Catalyst loading (wt. %)**	**Molar ratio**	**Reaction temperature**	**Yield target**	**Yield fit**	**Composite desirability**
30	400	20	1.5	3	60	79.9033	73.7566	0.9215
60	400	–	1.5	–	60	85.1057	80.7665	0.9458
120	–	–	1.5	9	60	89.7597	87.4601	0.9730
180	–	–	1.5	9	60	93.3232	90.2655	0.9619
270	–	–	1.5	9	60	97.6772	94.4837	0.9583
420	–	–	1.5	9	60	99.2307	101.721	1
600	–	–	1.5	9	60	99.4009	101.478	1
900	–	–	1.5	9	60	100	101.237	1
1500	–	–	1.5	9	60	100	98.289	0.9602
1800	–	–	1.5	9	–	100	95.0137	0.8780

4.4.3 Optimisation of Process Variables for Biodiesel Production by Transesterification via Response Surface Methodology (RSM)

A response surface design is a set of Design of Experiments (DOE) techniques that refine the experimental responses. The methodology of response surface design is often used for refining models after determining important factors using screening designs or factorial designs, particularly if the response surface is suspected of having a curvature.

The difference between the response surface equation and the equation from the regression of factorial design is the addition of the squared or quadratic terms that allows to model curvature in the responses, making them beneficial for:

1) Understanding or mapping the region of a response surface.
2) Response surface equations model how variables influence the response of interest.
3) Identifying the variable levels to optimise a set of responses.
4) Selecting an optimal operating condition to satisfy the criteria.

In this study, the central composite design (CCD) inputs are based on a subset of the full factorial study results. The CCD is either factorial or fractional factorial design with centre points, created with axial points or star points that allow the analysis to estimate curvature. A central composite design can be used for:

1) Estimating first and second-order terms effectively.
2) Model a response variable with a curvature by adding centre and axial points to previously-completed factorial design.
3) Central composite designs are particularly useful in sequential experiments, as axial and centre points can be frequently added based on prior factorial experiments.

In this RSM study, the analysis is built upon the previous factorial design, hence adding axial points to the parameters' existing levels, creating the curved surface. The initial results from the factorial design using multiple independent parameters and their corresponding responses on dependent variables were used to fit without any bias to the linear (first-order), linear and squares, linear and interactions, and full quadratic (second-order polynomial) models. The RSM model analysis presented in this study is based on a full quadratic term without using the stepwise method as it gave the best fit of the regression coefficient, R^2. The model summary is shown in Table 4-8. Response Surface Methodology Regression Model Summary for 30s to 1800s using RVC.

Table 4-8. Response Surface Methodology Regression Model Summary for 30s to 1800s using RVC.

Sampling Time (s)	S	R^2 (%)	R^2(adjusted) (%)	R^2(predicted) (%)
30	11.9678	70.31	67.63	63.97
60	11.4654	74.07	71.73	68.54
120	10.9172	74.52	72.22	68.93
180	10.2995	73.01	70.58	66.97
300	9.32457	73.55	71.16	67.45
420	7.92985	76.24	74.10	70.71
600	7.38260	76.57	74.45	71.19
900	6.78989	76.43	74.31	71.23
1500	6.62246	74.60	72.31	69.13
1800	6.75075	73.10	70.68	67.31

4.4.4 Response Surface Plots

The 3D surface plot examines the interaction between two independent variables simultaneously on biodiesel's percentage yield while constantly holding the remaining variables. The 3D surface response plots (%yield) for the interactions between the independent variables are shown in Figure 4-33 for the 30s into the transesterification reaction. The modelled plots are ppi-RPM, catalyst loading-RPM, molar ratio-RPM, temperature-RPM, catalyst loading-ppi, molar ratio-ppi, temperature-ppi, molar ratio-catalyst loading, temperature-catalytic loading, and temperature-molar ratio. Since the interaction involves two variables, the rest of the parameters are held constant as shown in Table 4-9.

Table 4-9. Hold values for surface plots of yield and interacting variables.

Variables	Unit	Hold Values
Pores per inch	-	27.5
Catalyst Loading	Wt. %	1.0
Temperature	°C	45
Molar Ratio	-	6
RPM	Rpm	300

The response surface plots are then arranged in the experimental timeline from the 30s to 1800s for individual pair of interactions. The responses are not presented using the same set of ranges to highlight the temporal effect on biodiesel yield caused by the interactions. This method can illustrate the response surfaces evolving and morphing as the reaction progress forward in time. Thus, insights can be evaluated by comparing the difference in trend and performance using the prior and latter response surfaces in time.

4.4.4.1 PPI-RPM

In Figure 4-33, the interactive effect of ppi and RPM is shown. For the 30s cases, the biodiesel yield increases with higher rpm while peaked at 20 and 30 ppi, before dropping in yield at 45 ppi. However, using higher ppi can achieve a high yield even at low RPM conditions, suggesting an enhanced mixing effect contributed by the increase in ppi for diffusive and turbulent modes of mixing due to the reticulated surface. As transesterification progresses into 120s, the response surface transitioned into an inverted form compared to 30s for the effects of increasing ppi, where lower ppi favours biodiesel production more than higher ppi. The finding can be clarified by the transformation from a heterogeneous oil and methanol phase reaction to a homogeneous methanol-oil-biodiesel mixture as transesterification occurs. Thus, the porous structure within the RVC can facilitate the mass transfer of the one-phase mixture at a larger surface area for forward transesterification reaction.

During 270s, the 200 rpm and 300 rpm cases showed the most considerable improvement at 10 ppi, as the mass transfer occurs more frequently in the porous foam. The same trend can be observed until the end of the experiment at the 1800s, where the combination of 10 ppi and 200 rpm provides the best interaction for biodiesel production.

On the other hand, higher rpm settings paired with 10 ppi peaked in performance around 900s, while the 200 rpm cases continue to improve in yield for 10 and 45 ppi. Besides, the performances of ppi

between 10 and 45 do not perform as well as when they are at both ends of the ppi spectrum (10 and 45 ppi).

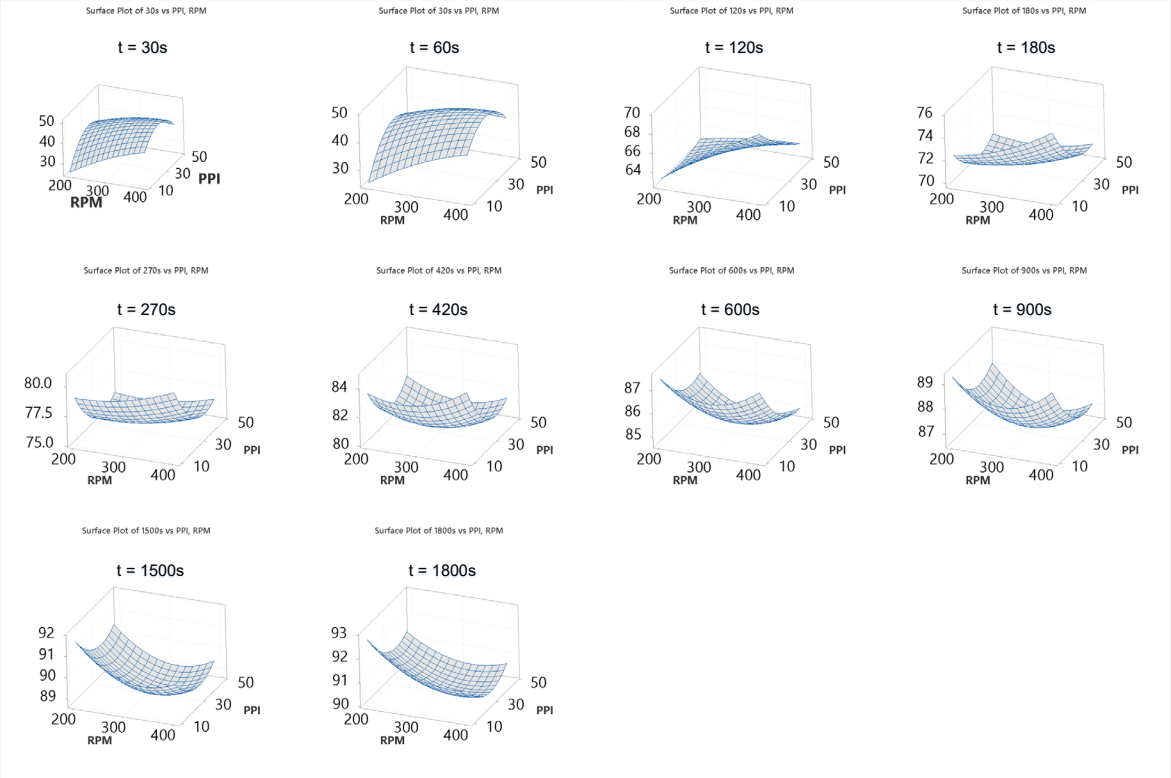

Figure 4-33. Temporal surface plot of interactions for ppi and RPM from 30s to 1800s into transesterification.

As the transesterification proceeds to 1500s and 1800s, the surface plots illustrate that higher agitation speed does not result in better performance as the effect of adequate mixing is more prominent at the beginning of the reaction. The use of higher agitation speed has led to a counter-productive result as more biodiesel and glycerol are produced.

In an ideal scenario, the agitation speed should be high at the beginning of the transesterification process using a 20–30 ppi RVC agitator. This combination provides the optimal biodiesel yield during the physical-limiting stage as mass transport between the reactants is the highest when the mass fraction of oil and methanol is high. As the transesterification progress into the reactant-limiting regime, the reactants should have achieved adequate homogeneity. Thus, intense mixing is no longer required, where the mode of reaction is generally diffusion dominant, which favours low rpm and low ppi interaction.

4.4.4.2 Catalyst Loading-RPM

In Figure 4-34 the surface response of catalyst loading and RPM interaction is observed to be increasing biodiesel yield concurrently in the direction of increasing RPM and catalyst loading.

Based on the surface plot results, increasing agitation rate and catalyst loading increase the biodiesel yield, with more substantial influence from the effect of catalyst loading. RPM is still significant as the reactants require adequate mixing at the beginning of the reaction. The lowest and highest performing interactions are of 200 rpm, 0.5wt. % catalyst loading and 400 rpm, 1.5 wt. % catalyst loading, respectively. The yield for the former and latter from the surface response is 19.9% and 65.1%, respectively, with a difference of 45.2% yield at 30s.

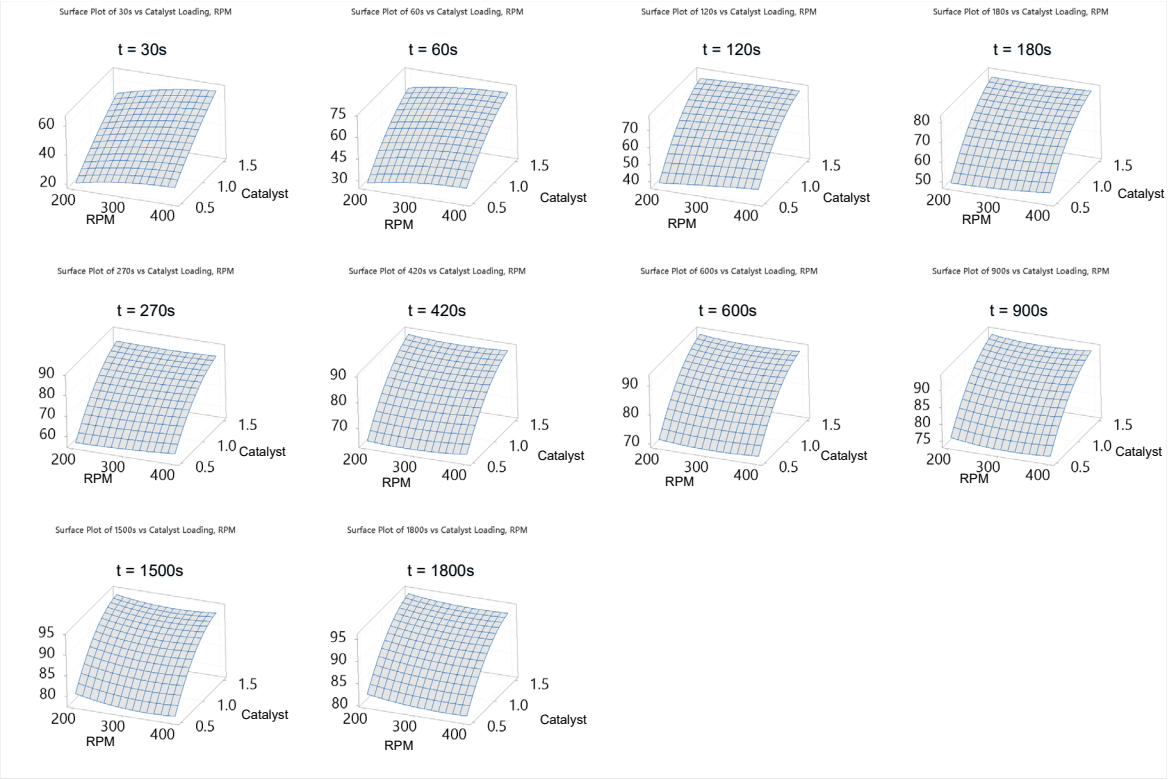

Figure 4-34. Temporal surface plot of interactions for catalyst loading and RPM from 30s to 1800s into transesterification.

As the agitation of reactant mixture reaches 120s, the effect of increasing rpm is diminished for improving biodiesel yield. However, the effect of catalyst loading remains relatively dominant in this interaction, leading to most of the increase in biodiesel yields. The difference in yield at 1.5 wt. % catalyst loading range for all rpm becomes negligible while small differences can be observed at the 0.5 wt. % catalyst loading with 400 rpm edging out. This particular interaction becomes more irrelevant in the later stage of transesterification as additional agitation speed no longer contributes to yield response. In fact, a small decline in performance at 400 rpm is detected towards the 1800s, which exhibit similar trend from the ppi-rpm interaction, further establishing the lack of need for high agitation rate for final yield stage of transesterification.

Therefore, the optimal operating condition for the RVC reactor should be a high agitation speed leading the initialisation of transesterification, combined with the use of a higher catalyst loading.

This set of inputs will ensure that the effective surface area of the catalyst is maximised during the physical-limiting stage, while a lowered rpm setting can be used at about 270s for the conserving power.

4.4.4.3 Molar Ratio-RPM

In Figure 4-35, the interaction of molar ratio and RPM is shown. Initially, with high RPM and low molar ratio, the biodiesel yield increases, which is also observed in the baseline study and the general RVC regression model. Furthermore, the lowest rpm combined with higher molar ratio shows comparatively worse output at 30s.

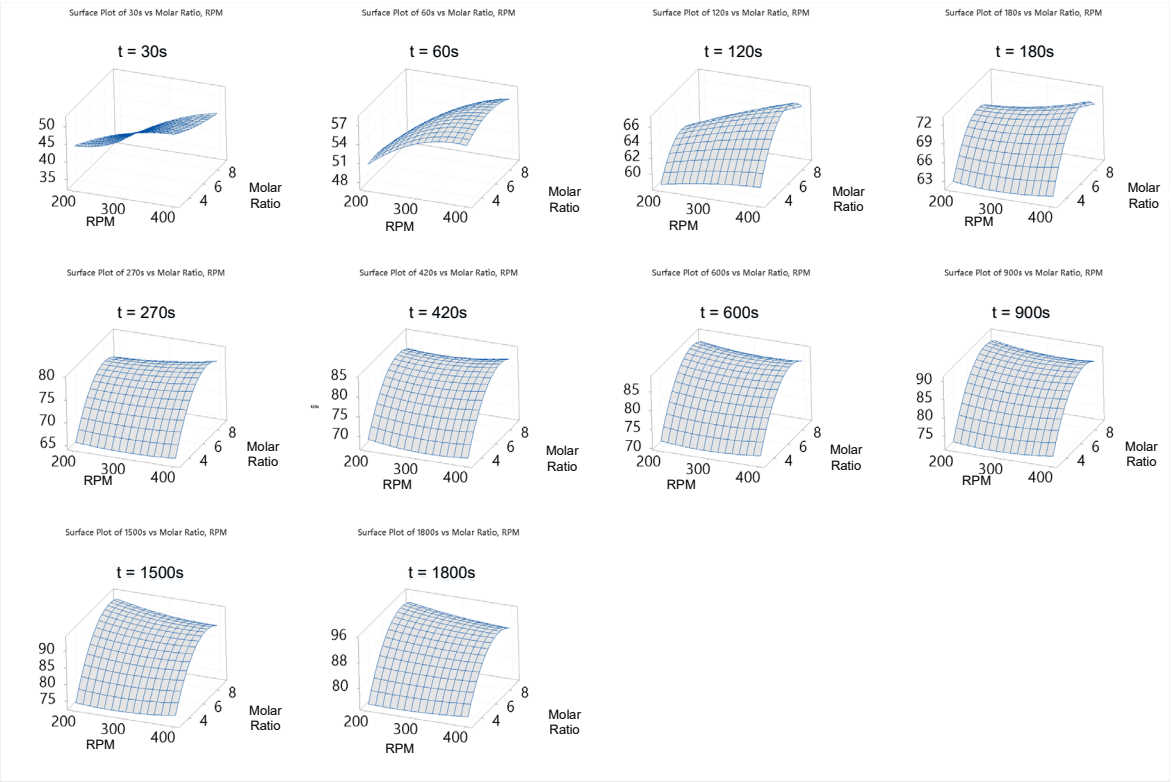

Figure 4-35. Temporal surface plot of interactions for molar ratio and RPM from 30s to 1800s into transesterification.

The catalyst loading and rpm interaction show a rapid growth from 60s to 180s in the direction of high molar ratio, as the yield growth of the low molar ratio plateaus about 180s. Simultaneously, the use of higher rpm settings shows a decreasing effect around the 180s, where there is little or no change when using a lower molar ratio setting. Similarly, the low rpm output improves on the other end of the spectrum at high molar ratio condition, and levels at 420s with the high rpm condition.

The findings indicate a comparable pattern towards the end of the 1800s experiment, where the low rpm condition performs consistently better than the high rpm condition. The best performing condition for final yield is 200 rpm at 9:1 methanol to oil molar ratio, which is expected as the molar

ratio eventually becomes a limiting factor. However, the initialisation of the transesterification should ideally start at a higher rpm and lower molar ratio and slowly adjusted for reacting conditions suitable for the final yield.

The 3:1, 6:1 and 9:1 methanol to oil molar ratio conditions resulted in a yield of 74.6%, 91.4%, and 93.3%, respectively, at the final yield point of the 1800s using 200 rpm. The stoichiometry molar ratio usage indicates a major difference from the other conditions, where an additional 16.8% yield is given by doubling the methanol and oil molar ratio to 6:1. However, the use of excess methanol is further increased with mediocre performance as shown by the 1.9% improvement from 6:1 to 9:1 methanol to oil molar ratio.

4.4.4.4 Temperature-RPM

In general, as shown in Figure 4-36, the temperature and RPM interactions increase biodiesel yield simultaneously with increasing RPM and temperature.

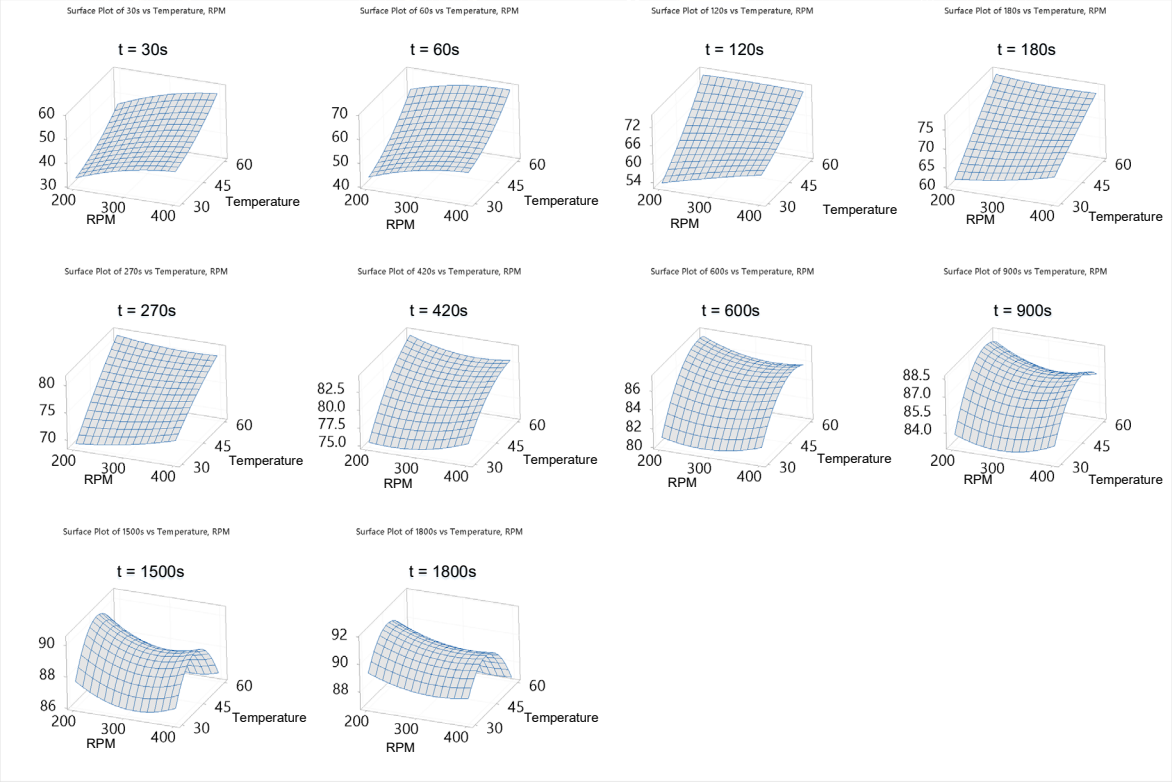

Figure 4-36. Temporal surface plot of interactions for temperature and RPM from 30s to 1800s into transesterification.

The higher reaction rate increases the yield as reactant molecules collide more frequently, increasing kinetic energy during transesterification from elevated temperature, which shifts the transesterification path favouring the forward reaction. The surface plot of interactions for PPI-RPM, catalyst loading-RPM, molar ratio-rpm, and temperature-RPM shows a consistent trend where higher

agitation favours biodiesel yield during initialisation. At the 30s, using 60°C and 400 rpm agitation speed, a yield of 70% can be expected.

Higher RPM has a more important effect in combination with temperature to increase biodiesel yield, based on the evolution of the temporal response surfaces. The 60°C cases show that a maximum yield of 70% can be achieved for agitation speed. Therefore, higher RPM should be considered to generate the best yield result when combined with lower operating reaction temperature. However, lower agitation condition of 200 rpm shows an increase in mean yield after the physical-limiting stage of transesterification, as seen when moving from 60s to 270s. On the other hand, higher agitation conditions can also be useful because at 30°C the output is consistently better than lower rpm conditions, where heat input is minimal.

The findings from 420s indicate that the use of 45°C and 60°C both enhances reaction rates, whereby the 45°C outperforms the 60°C when transitioning beyond 900s into the reaction-limiting process. For all rpms, the yield profiles from 30°C to 60 ° C shows a rapid yield growth ramp, peaking at 45°C, followed by a symmetrical negative ramp of yield drop until 60 °C. The optimum operating condition for biodiesel production is 200 rpm and 45°C at 1800s, resulting in a final yield of 91.4%.

Despite the enhanced performance of 60°C biodiesel processing at the beginning of transesterification, 45°C at the end of the reaction is optimal. This indicates that some of the excess methanol needed for a high final yield would have evaporated at the elevated temperature of 60°C, while the lower temperature of 30°C simply does not provide sufficient energy for the reaction to progress.

The results from 1500s and 1800s show that towards the end of transesterification, the 45°C reaction temperature is favoured when combined with a lower agitation speed to produce a higher yield. Fundamentally, a higher reaction temperature should enhance the reaction speed by increasing the frequency of collision from molecules, hence a higher yield is expected. However, this is only observed up to 600s where the benefit of using a higher reaction temperature slowly diminish. Therefore, the limiting factor in this case is the amount of unreacted methanol in the mixture, as they can either react to form biodiesel, or evaporate into the atmosphere. Thus, the high reaction temperature of 60°C is more likely to reduce the total mass fraction of methanol in the reactor through passive evaporation or boiling.

4.4.4.5 Catalyst Loading-PPI

In Figure 4-37, the interaction of catalyst loading and ppi is shown. In the direction of increasing catalytic loading, biodiesel yield is consistently improving. However, the biodiesel yield curvature in the ppi direction is also expected, as biodiesel yield increases moving from 10 ppi, peaked at 30 ppi, and decreases consistently at a small rate as it reaches 45 ppi.

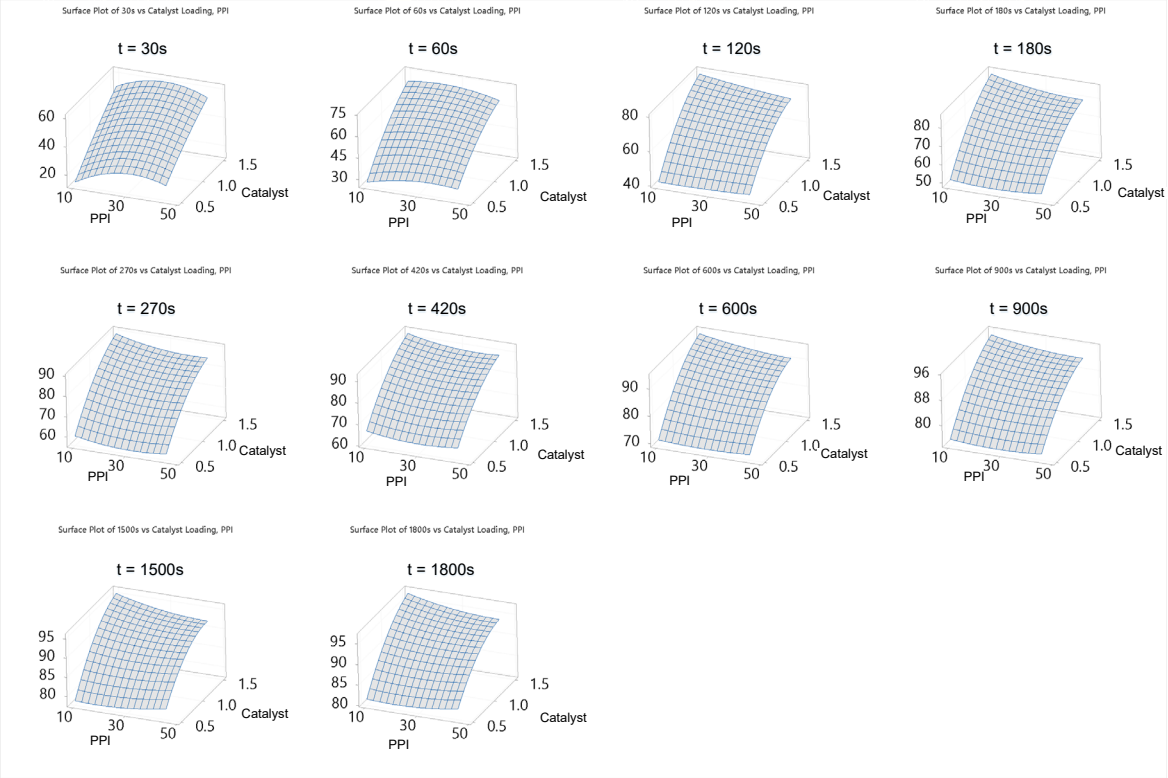

Figure 4-37. Temporal surface plot of interactions for catalyst loading and ppi from 30s to 1800s into transesterification.

A higher catalyst loading environment shows a comparatively greater increase when combined with lower ppi than higher ppi RVC from the 60s onwards. As stated, the probability of oil and potassium methoxide solution penetrating entirely within the 10 ppi RVC is greater, increasing the reactants' effective contact surface. The effect of greater catalyst loading concentration is therefore more prevalent. In addition, the use of different grade ppi at 0.5 wt. % catalyst loading has limited added benefit to the transesterification process, indicating the bottleneck of catalytic impact.

With the 10 ppi, 1.5 wt. % catalyst loading peaking at 96.6% for final yield, the pattern of the catalyst-loading-ppi interaction remains nearly similar throughout. Besides, the additional enhancement of catalyst loading indicates a lower growth rate for all ppi grades from initialisation to final yield, transitioning from a linear to a sigmoid profile.

4.4.4.6 Molar Ratio-PPI

Based on Figure 4-38, the response surfaces describe the yield relationship of molar ratio coupled with ppi in the transesterification reaction. At 30s, the yield for 3:1 methanol to oil molar ratio when paired with 10, 20, and 45 ppi is 45.4%, 49.7%, and 39.2%, respectively. On the other end, the yield of using a 9:1 methanol to oil molar ratio when paired with 10, 20, 45 ppi are 25.7%, 36.5%, and

41.8%, respectively. The observation of this interaction suggests that ppi has a stronger influence on the performance of the transesterification reaction.

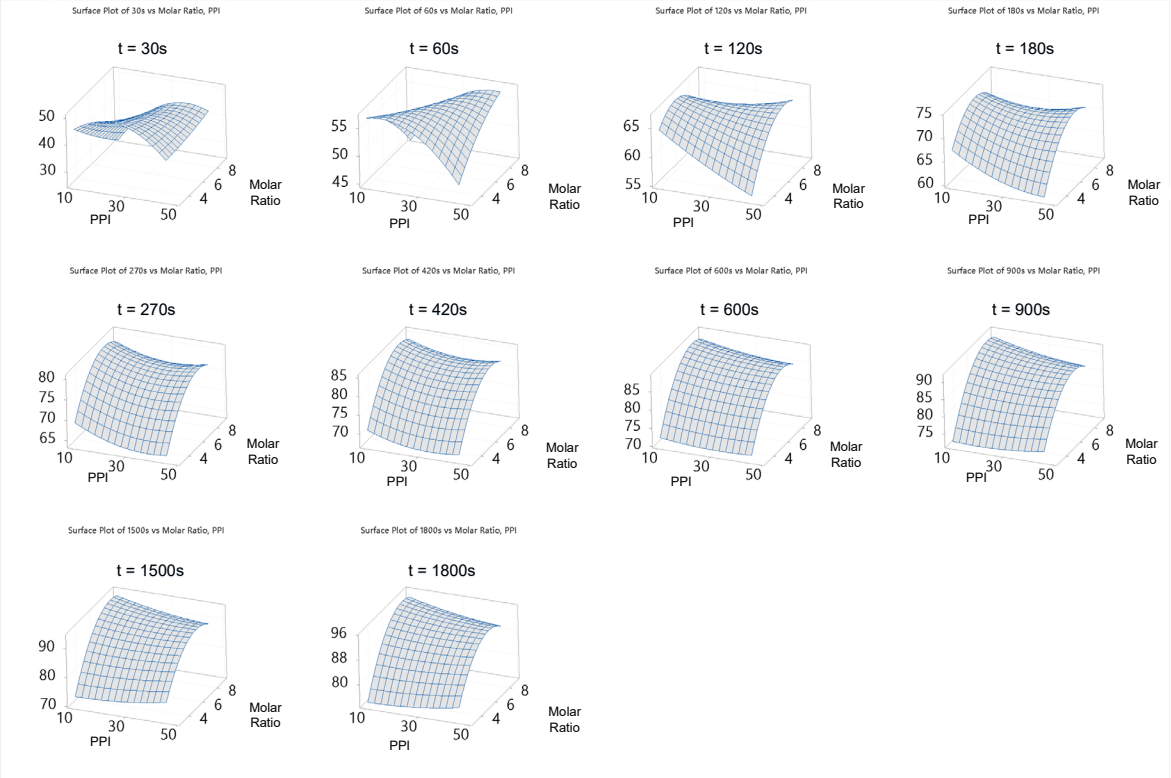

Figure 4-38. Temporal surface plot of interactions for molar ratio and ppi from 30s to 1800s into transesterification.

Yield response increases as ppi increases. The yield plateaus from 20 ppi to 30 ppi and gradually decreases as ppi increases to 45 ppi for low molar ratio cases, at 10 ppi to 20 ppi. The yield response also increases when moving from a lower molar ratio to a higher molar ratio case. RVC with smaller ppi can achieve a high mean yield by using lower methanol to oil molar ratio, whereas RVC with larger ppi is more suitable with higher methanol to oil molar ratios to obtain a high mean yield. The reticulated structure increases the contact surface area between oil and methanol at a lower ppi and molar ratio, thereby encouraging reaction rates. However, the use of low ppi has diminishing return with increasing methanol to oil molar ratio, as more reactants also lead to the higher surface area of reaction. RVC's increasing pore structure at higher ppi will also promote reaction rates at greater methanol to oil molar ratios.

The previous observations are also supported by this observation, as the lowest molar ratio coupled with high ppi shows worse yield efficiency, indicating mediocre diffusive mixing. With the increasing molar ratio for all ppi, biodiesel yield also improves consistently at 60s and beyond, as the effect of excess methanol balances the mixing effect given by the RVC. The effect of ppi diminishes in this interaction gradually up to 600s where there are no significant differences of the ppi grade between the 3:1 and 6:1 methanol to oil molar ratios. However, for the 9:1 methanol to oil molar ratio condition, slight performance improvement can be observed using 10 ppi until final yield.

The final yield of the 9:1 molar ratio for 10, 20, and 45 ppi are 94.2%, 92.3%, and 89.5%, respectively. The final yield of 3:1 molar ratio for 10, 20, and 45 ppi are 73.8%, 74.1%, and 76.8%, respectively.

4.4.4.7 Temperature-PPI

Figure 4-39 shows the curvature of response for temperature and ppi interaction. The increase in ppi showed an increasing trend for yield moving from 10 ppi, where it peaked at 30 ppi and decreases slowly in the direction of 40 ppi. The elevated temperature provides positive results for yield for all ppi in the range of 30°C to 60°C. Thus, the yield profile for increasing temperature exhibits the same trend for all ppi. At 30s into transesterification, the combination of 30 ppi and 60°C provides the highest yield of 53.8% in this interaction. Moving towards 60s, the 10 ppi ad 45 ppi cases had shown an increase in yield as compared to the 20 to 30 ppi.

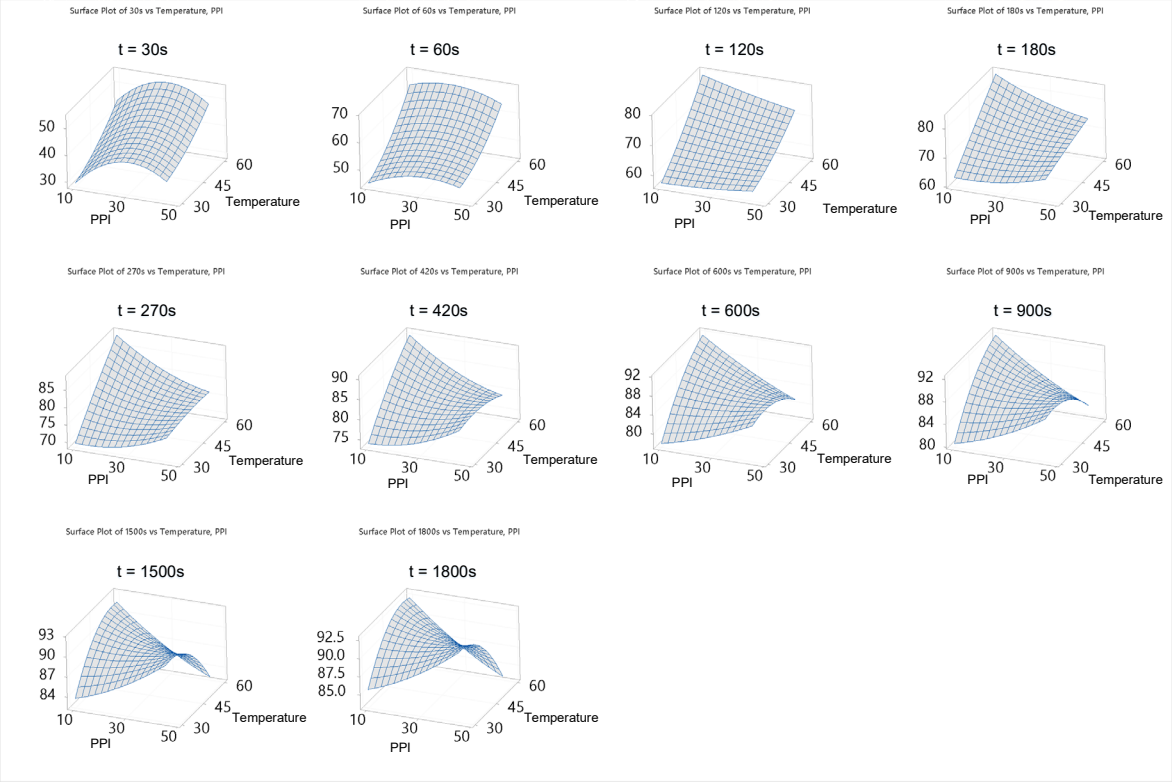

Figure 4-39. Temporal surface plot of interactions for temperature and ppi from 30s to 1800s into transesterification.

Furthermore, the interaction also shows that the increase in ppi at the lower temperature of the reaction and the increase in ppi at the higher temperature of the reaction has an opposite effect on biodiesel yield. The former shows a positive trend while the latter shows a declining trend that is more important, resulting in the curved biodiesel yield surface. The effect of rising temperatures increases biodiesel yield for all ppi. However, the 10 ppi condition offers the largest improvement as it serves to promote transesterification, comparable to a heated porous bed platform.

The observation remains consistent throughout for 10 ppi and 60°C up to the final yield point for the optimum operating environment. However, the 30°C cases improve mean yield linearly as ppi increases. The findings from both ends of the temperature condition indicate that diffusion-based reactions dominate at higher temperatures due to increased heating to decrease oil and methanol's miscibility, coupled with the 10 ppi RVC.

On the other hand, the lower temperature depends heavily on the improved shear blending from increasing ppi and reticulated surfaces. From the results, the yield growth of the 45 ppi and 60°C condition seems to be stagnant at about 180s. However, increasing ppi at high temperature conditions is not necessary counter-productive as the initial reaction rates using elevated temperature are still useful overall. The final yield for 45 ppi and 60°C can reach 83.5%, which is still considerably high as compared to other ppi interactions.

4.4.4.8 Molar Ratio-Catalyst Loading

Figure 4-40 shows the surface plot interaction for molar ratio and catalyst loading. At 30s into transesterification, biodiesel yield increases mostly with the increase of catalyst loading while increasing methanol to oil molar ratio from 3:1 to 9:1 has a slightly negative effect on the yield response. The yield of using the 3:1, 6:1 and 9:1 methanol to oil molar ratio for 1.5 wt. % catalyst loading are 65.0%, 60.5%, and 57.5%, respectively. The effective use of low molar ratio during initialisation to enhance reaction rates has been discussed and also reflected in this interaction.

From 60s to 180s, the rate of improvement from 1.5 wt. % catalyst loading reduces for the lower molar ratio conditions, while the higher molar ratio range is still growing rapidly. However, for the 0.5 wt. % catalyst loading condition, there is a small difference in response for all molar ratio range as the yield for 3:1 and 9:1 molar ratio is 45.4% and 43.7%, respectively.

From 270s to 900s, the trend of increasing catalyst loading and molar ratio remains relatively constant. The yield of 1.5 wt. % catalyst loading and 9:1 molar ratio at 270s and 900s is 88.5% and 95.4%, respectively.

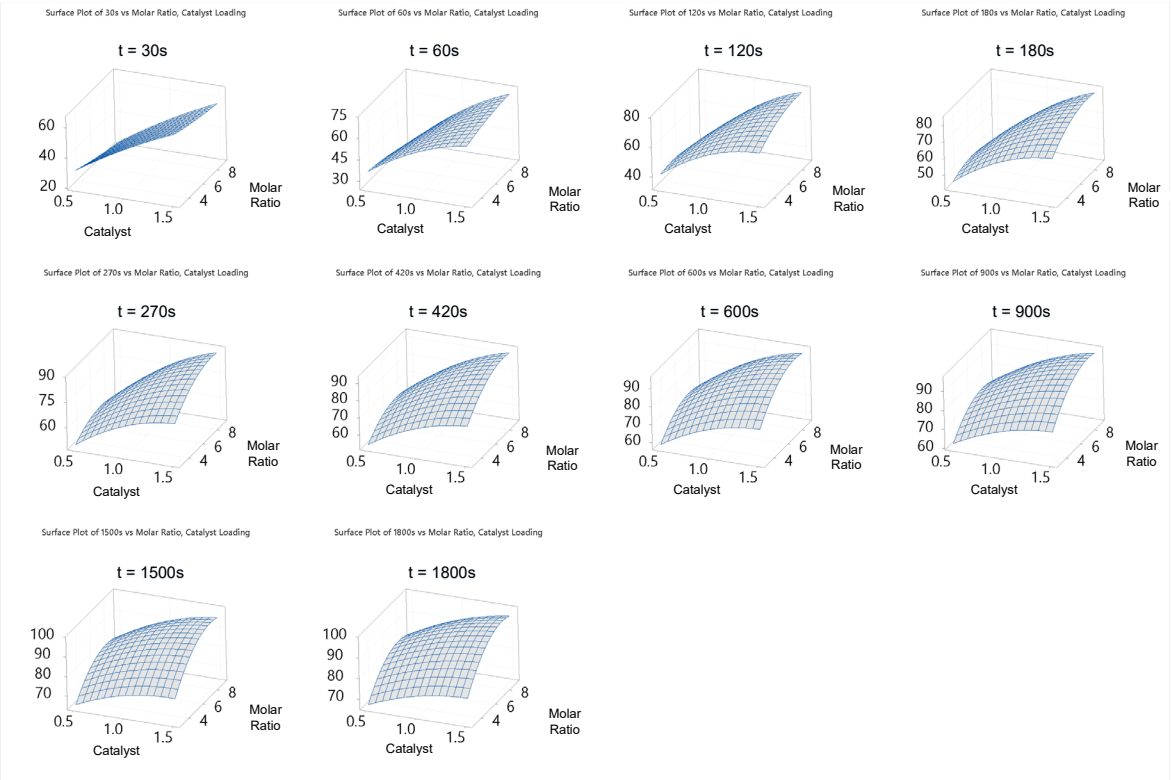

Figure 4-40. Temporal surface plot of interactions for molar ratio and catalyst loading from 30s to 1800s into transesterification.

A higher molar ratio is required for a complete reaction of biodiesel transesterification as the excess methanol facilitates to react with the oil which has a smaller mass fraction in the total reactant volume. For 1500s onset into transesterification, the final yield of the 0.5, 1.0, 1.5 wt. % catalyst loading cases for 9:1 molar ratio is 78.0%, 90.0%, and 95.8%, respectively, while 80.5%, 91.2%, and 96.8% were achieved at 1800s. The change in yield at 1500s to 1800s is consistently small for the entire catalyst range, suggesting that catalyst and methanol are not the limiting factors.

In general, catalyst loading is more important than temperature and molar ratio to promote transesterification reaction rates. The higher molar ratio coupled with lower catalyst loading setting has minimal effect on biodiesel yield. Thus, catalyst loading needs to be prioritised and optimised for the maximum interacting effect of increasing biodiesel yield.

4.4.4.9 Temperature-Catalyst Loading

The temporal surface plots of temperature and catalyst loading interaction are shown in Figure 4-41. The yield trend is consistent with the traditional transesterification theory, where biodiesel yield increases with the loading and temperature of the catalyst.

Besides, the temperature and catalyst interaction between the 30s and 60s surface plots showed a similar increase of 1.0 wt. %. 1.5 wt. % loading catalyst. The production of 1.5 wt. % catalyst loading at 30°C, 45°C, 60°C at 30s is 55.4%, 60.5%, and 69.3%, while for 60s, 63.6%, 69.7%, and 81.2%, respectively. The margin of increase in yield is relatively important, particularly if the higher temperature condition is used in the transesterification process for only one minute.

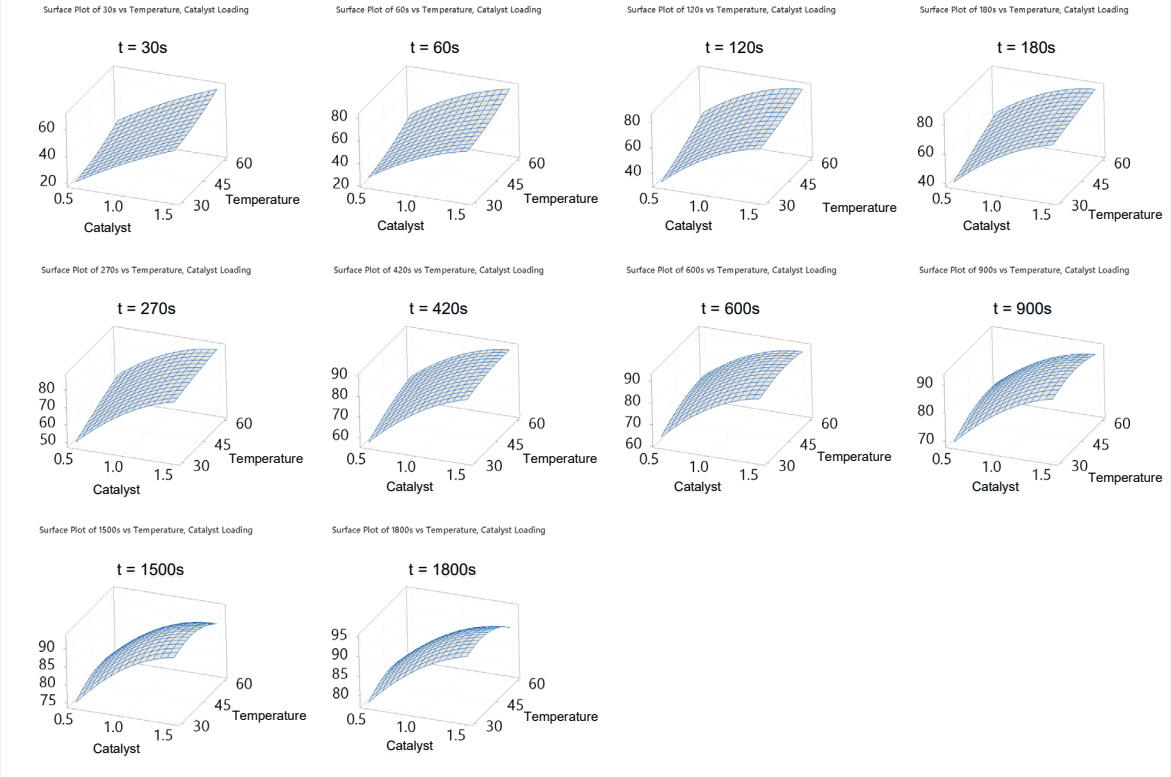

Figure 4-41. Temporal surface plot of interactions for temperature and catalyst loading from 30s to 1800s into transesterification.

While the 0.5 wt. % loading of the catalyst shows improvement with increasing reaction temperature, at the lowest reaction temperature setting, the 1.5 wt. % still outperforms all 0.5 wt. % transesterification cases at 120s. This interaction is then accompanied by a gradual reaction rate where the yield increased at 30°C and 60°C at 180s by approximately 5.0%.

The change in yield for the higher catalyst loading conditions from the 270s to 900s is almost converged as the rising temperature has a limited impact on transesterification. For the reaction temperatures of 30°C, 45°C, and 60°C, the mean yields are 90.2%, 92.6%, and 90.9%, respectively for 1.5 wt. % catalyst loading. On the other hand, the temperatures of 30°C, 45°C, 60°C, shows a maximum mean yield of 69.3%, 74.4% and 75.1%, respectively, for 0.5 wt. % catalyst loading. Evidently, to obtain similar effects, a low reaction temperature may be used along with a high catalyst loading condition. In comparison, for optimal yield response, a low catalyst loading condition must be combined with a high reaction temperature.

In all, to enhance and optimise reaction rates, the temperature and catalyst loading relationship showed that the latter has greater importance than the former. The higher molar ratio, coupled with a lower loading environment for the catalyst, has a marginal impact on biodiesel's yield. Therefore, it is vital to prioritise and optimise catalyst loading for the full interaction impact of rising biodiesel yield.

4.4.4.10 Temperature-Molar Ratio

The temporal surface plot of temperature and molar ratio is shown in Figure 4-42. The initialisation stage at 30s shows the yield increases with reaction temperature but decreases with higher molar ratio use. The low temperature combined with the high molar ratio at the beginning of transesterification has the worst performance in yield as transesterification reaction saturates during the physical-limiting regime due to high molar ratio usage. The yield of 30°C and 9:1 molar ratio at 30s is 35.8%, whereas 60°C and 3:1 molar ratio at 30s is 58.3%, a difference in 22.5% in yield.

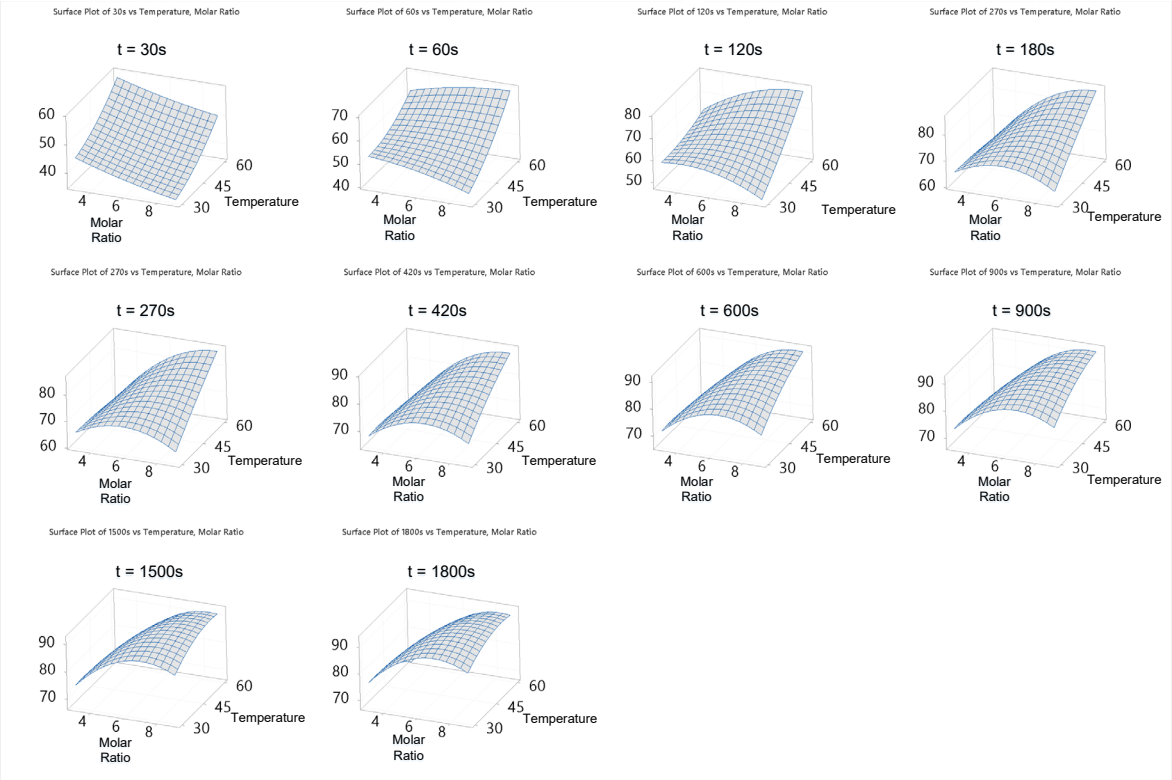

Figure 4-42. Temporal surface plot of interactions for temperature and molar ratio from 30s to 1800s into transesterification.

In comparison, the increase in the molar ratio at a higher temperature of the operating reaction contributed to increased yield. At 60s, the 60°C case combined with 3:1 molar ratio plummeted when compared with the same interaction from the surface plot at 30s, which would suggest methanol lost due to evaporation resulting in a performance drop.

From 60s to 180s, the reaction rates of the high molar ratio condition improved significantly with temperature. In contrast, reaction rates for the lower reaction temperature at 30°C is a curved profile peaked at 6:1 molar ratio. At 180s, the yield for 60°C at 3:1, 6:1, and 9:1 molar ratio is 62.4%, 77.1%, and 81.6%, respectively. The yield for 30°C combined with 3:1, 6:1, 9:1 molar ratio is 61.8%, 63.5%, and 55.0%, respectively. Therefore, the 60°C is optimal as it outperforms all other conditions in this interaction.

From 180s to 900s, the trend remains relatively similar, where the higher temperature is favoured with excess use of methanol. There is a noticeable difference when excess methanol is used at 30°C around 900s as the performance showed improvement over the low molar ratio. However, the 6:1 methanol to oil ratio is still marginally better, with a yield of 83.0%.

As the reaction approaches final yield, the 30°C reaction temperature paired with 6:1 and 9:1 molar ratio condition levels off closely with the 60°C reaction conditions. The yield of 30°C with 6:1 and 9:1 molar ratio is 88.4% and 85.8%, while 60°C is 87.2% and 91.6%, respectively.

4.4.4.11 Summary of the response surface plots for RVC

In the context of transesterification response surface methodology, many studies have used it as a tool to optimise the process of biodiesel production quantitatively. However, there is a lack of qualitative results generated to understand the dynamic interactions of factors and yield. Biodiesel transesterification is a complex process that involves multiple operating factors in the reactor system, hence the ability to highlight the interrelationship between factors and yield respond is crucial to optimising the process.

Therefore, the response surface plots are useful to identify the two-way interactions between factors and yield response in transesterification. To reiterate, the results compiled in this section emphasises on the evolution of the yield responses in the onset of transesterification, using multiple surface plots at different time intervals of the experiment. The yield range (y-axis) of the surface plots is not fixed by design to highlight and magnify the interactions' strength.

The general trend can be observed to be divided into two groups, (i) reactant contact surface type enhancement, mostly at the physical-limiting regime and (ii) activation energy type enhancement, throughout the entire process, where they complement the reaction-limiting regime well. For instance, PPI-RPM interactions, Molar Ratio-RPM, Temperature-RPM, and Molar Ratio-PPI, significantly impacted the response surface from 0s to 120s. This is the region where the oil, methanol, and catalyst are first physically mixed through the RVC agitator to ensure homogeneity. The use of a higher rpm maximises the microturbulence and shearing effect of the RVC for micro-level mixing. At 45 ppi, it is optimal for promoting surface contact of the liquid-liquid two-phase of oil and alcohol during the physical-limiting regime. The use of a 3:1 methanol to oil molar ratio also ensures that biodiesel can be rapidly produced to act as a cosolvent to facilitate solubility of methanol and oil at the beginning.

In contrast, Catalyst Loading-RPM, Temperature-PPI, Catalyst Loading-PPI, Molar Ratio-Catalyst Loading, Temperature-Catalyst Loading, and Temperature-Molar Ratio are observed to be fairly consistent throughout with their trends. The main function of these interactions is to provide energy to the system for transesterification reaction to occur, hence they play a significant for the role to achieve a complete reaction.

Without the adequate mixing provided by the enhancement in the physical-limiting regime, the reaction will delay transitioning into the equilibrium phase, where the chemical-limiting regime situates. On the other hand, without the providing enough energy into the system, the reaction kinetics of the transesterification will be low, hence the two types of interactions are vital for a holistic optimisation to be achieved.

4.5 Reaction kinetics mechanism of RVC reactor

4.5.1 Results and discussions

The concentration of glycerides content and FAME yield is calculated and presented in Figure 4-43. The concentration of tri-, di-, monoglycerides changes dynamically as transesterification progress, where biodiesel is formed through reacting with the glycerides and methanol. For instance, the depletion of triglycerides will simultaneously form FAME and also diglycerides, hence Figure 4-43 is able to elucidate both the formation and depletion of glycerides and FAME concentration. The evaluation of the Arrhenius energy of activation requires the results of different reaction temperature. Therefore, the effect of temperature is incorporated in this study using reaction temperature of 30°C, 45°C, and 60°C, which is the same testing range for the full factorial study in the previous chapter. The effects of temperature on the concentration of trigly-, digly-, monoglycerides, and FAME yield are also presented in Figure 4-44, Figure 4-45, Figure 4-46, and Figure 4-47, respectively.

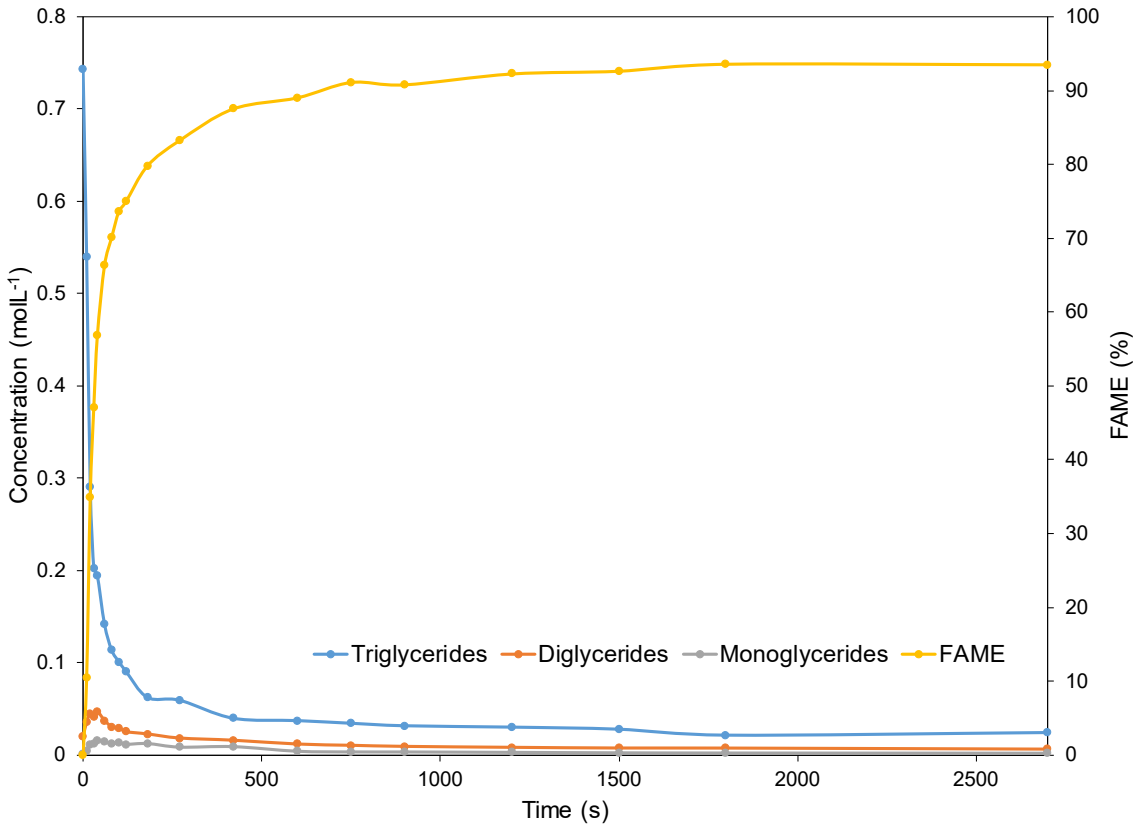

Figure 4-43. The transesterification reaction products using 20 ppi RVC reactor at 45°C, agitation speed of 300 rpm, methanol to oil molar ratio of 6, and KOH catalyst loading of 1.0 wt. %.

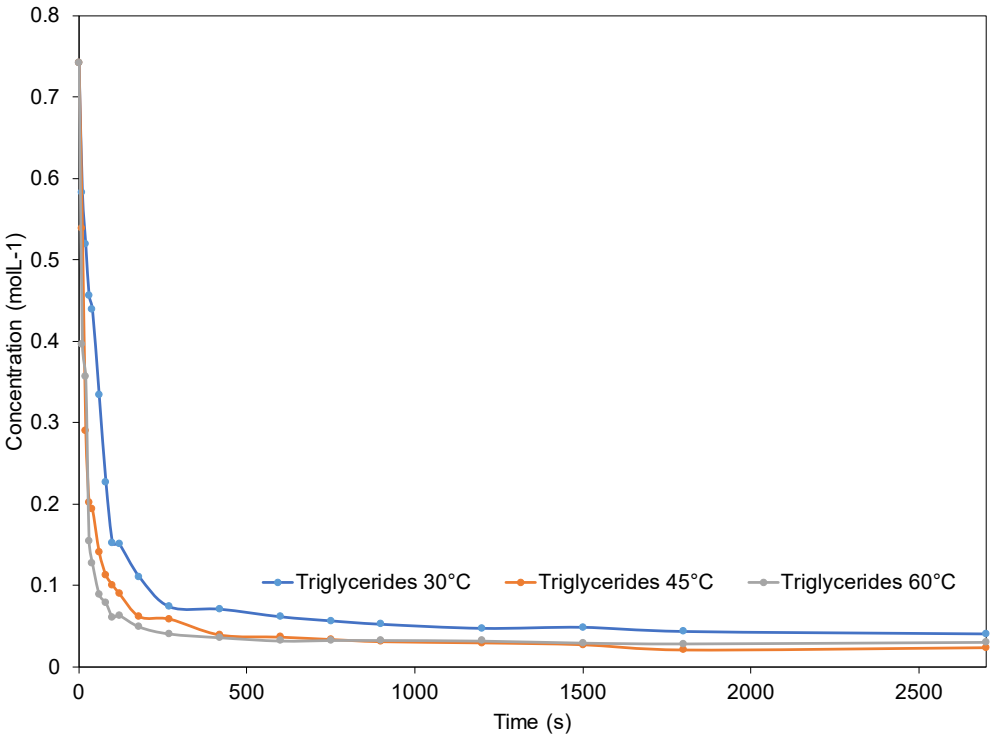

Figure 4-44. The concentration of triglycerides from 0s to 2700s at 30, 45, and 60°C using RVC reactor.

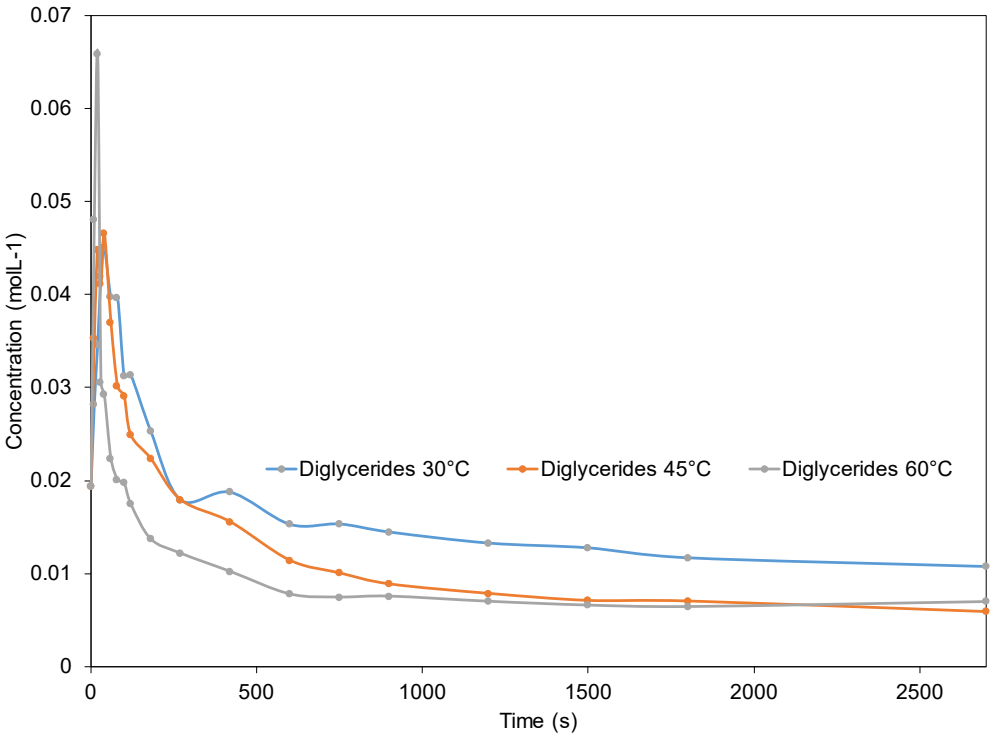

Figure 4-45. The concentration of diglycerides from 0s to 2700s at 30, 45, and 60°C using RVC reactor.

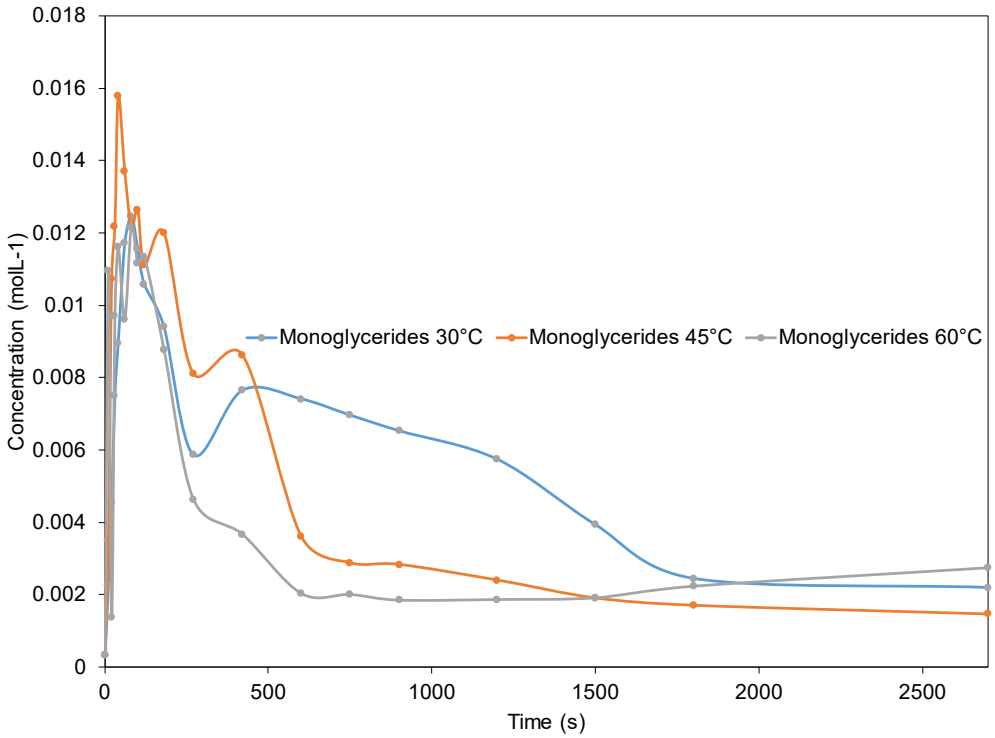

Figure 4-46. The concentration of monoglycerides from 0s to 2700s at 30, 45, and 60°C using RVC reactor.

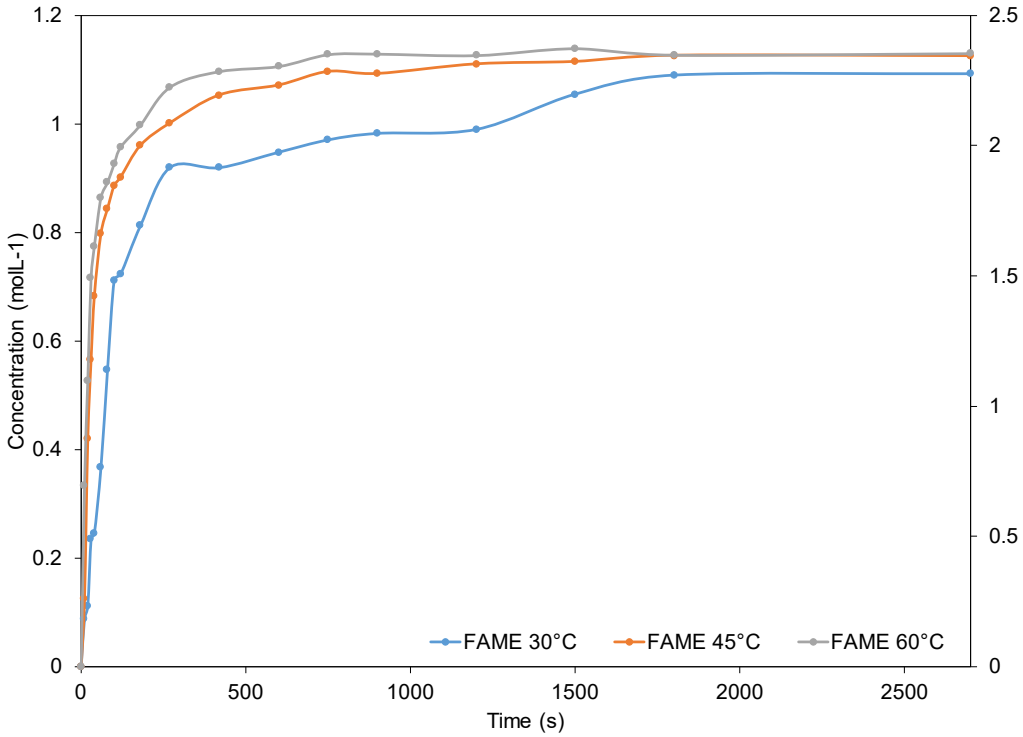

Figure 4-47. The yield of FAME from 0s to 2700s at 30, 45, and 60°C using RVC reactor.

4.5.1.1 Pseudo first-order kinetic model for RVC

The triglycerides concentration is applied using the same equation in Eq. 3-19 to produce the pseudo first-order transformation as shown in Figure 4-48. Similarly, the pseudo first-order model derived in the batch reactor kinetic model is applied to the RVC reactor.

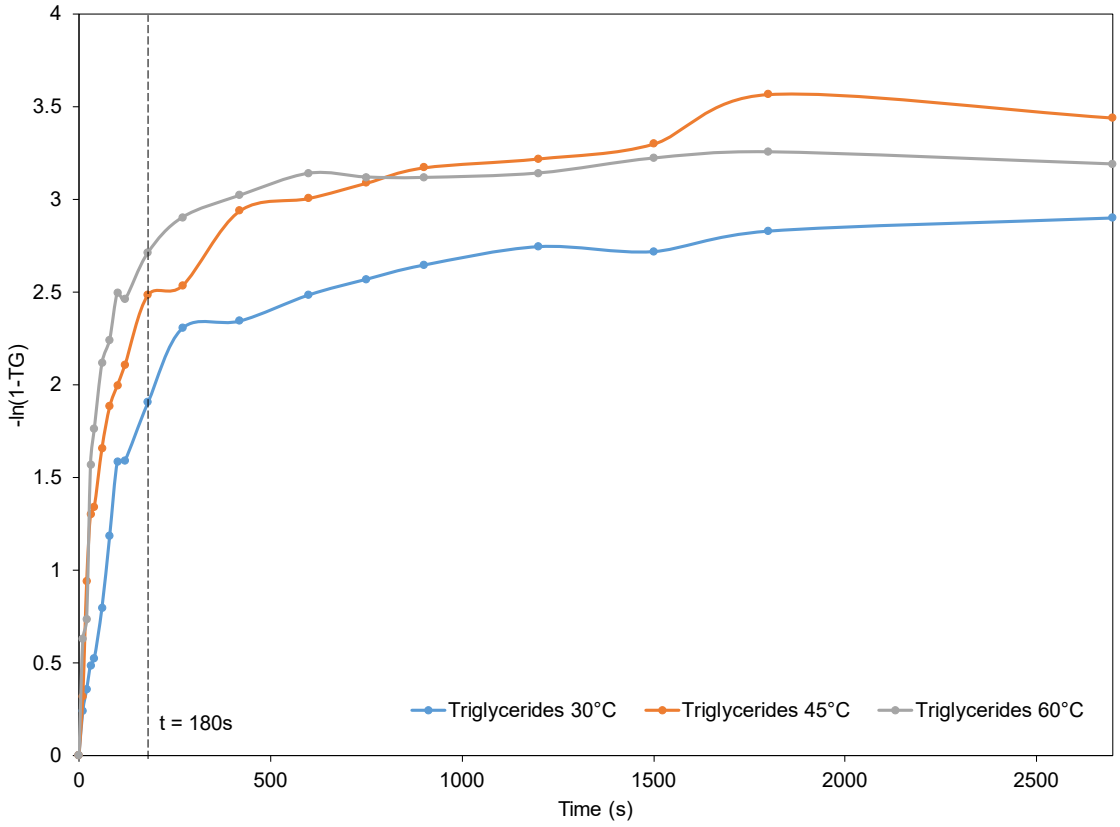

Figure 4-48. Pseudo first-order transformation of triglycerides concentration for RVC batch-type reactor.

From the response surface study, the surface plot of PPI-RPM in Figure 4-33 shows that the main fast forming of biodiesel occurs at the range of 0s to 180s, hence the effect of mixing is relevant. Additionally, the Pareto analysis for the effect of agitation rate in Figure 3-5 also supports that the physical-limiting regime of the batch reactor from 0s to 270s. Thus, Figure 4-49 shows consistency with the findings where the transition point situates between 120s and 180s. Therefore, the initial stage for the pseudo first-order is defined from 0s to 180s in this study as shown in Figure 4-49.

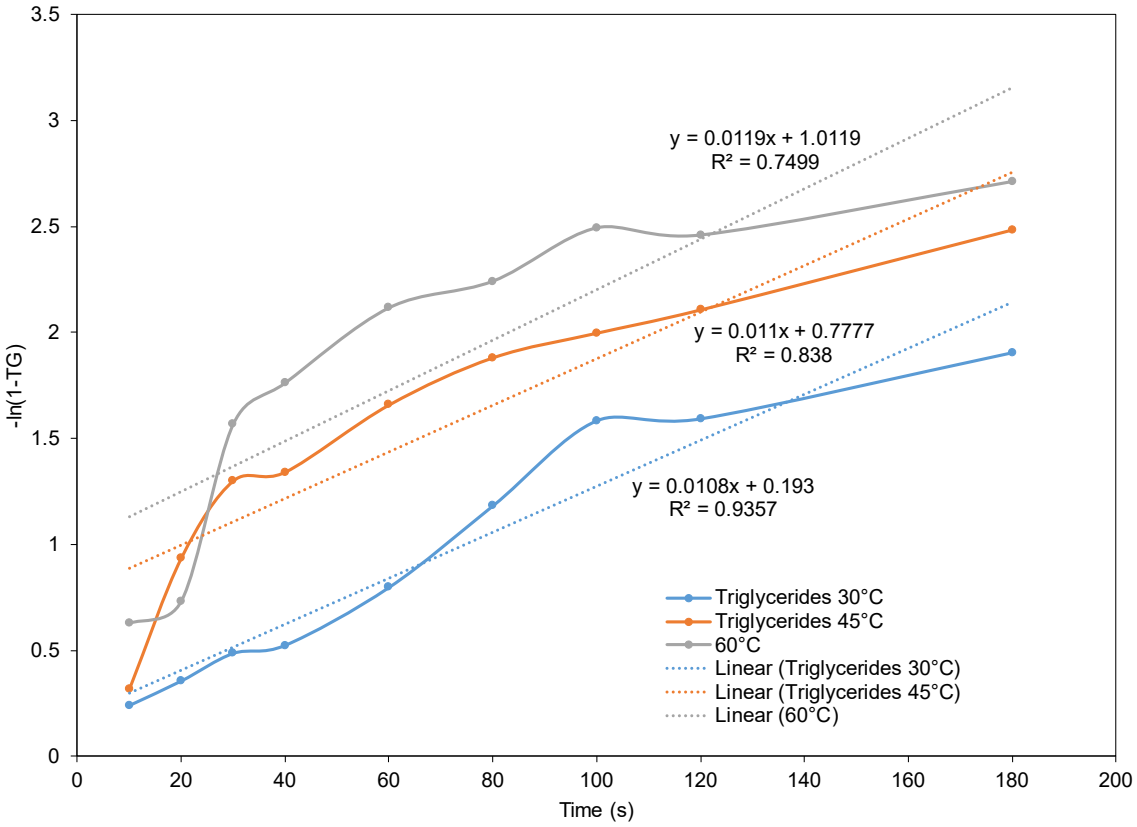

Figure 4-49. The physical-limiting regime during the initial stage of transesterification.

From the linear relationship in Eq. 3-19, the reaction's kinetic rate is the slope of the equation. However, as mentioned previously, the inflection point of the triglycerides conversion curve is required to determine the maximum kinetic reaction rate. Thus, the same running average slope strategy is implemented, where the slope at each interval is averaged over the time interval before and after as shown in Figure 4-50.

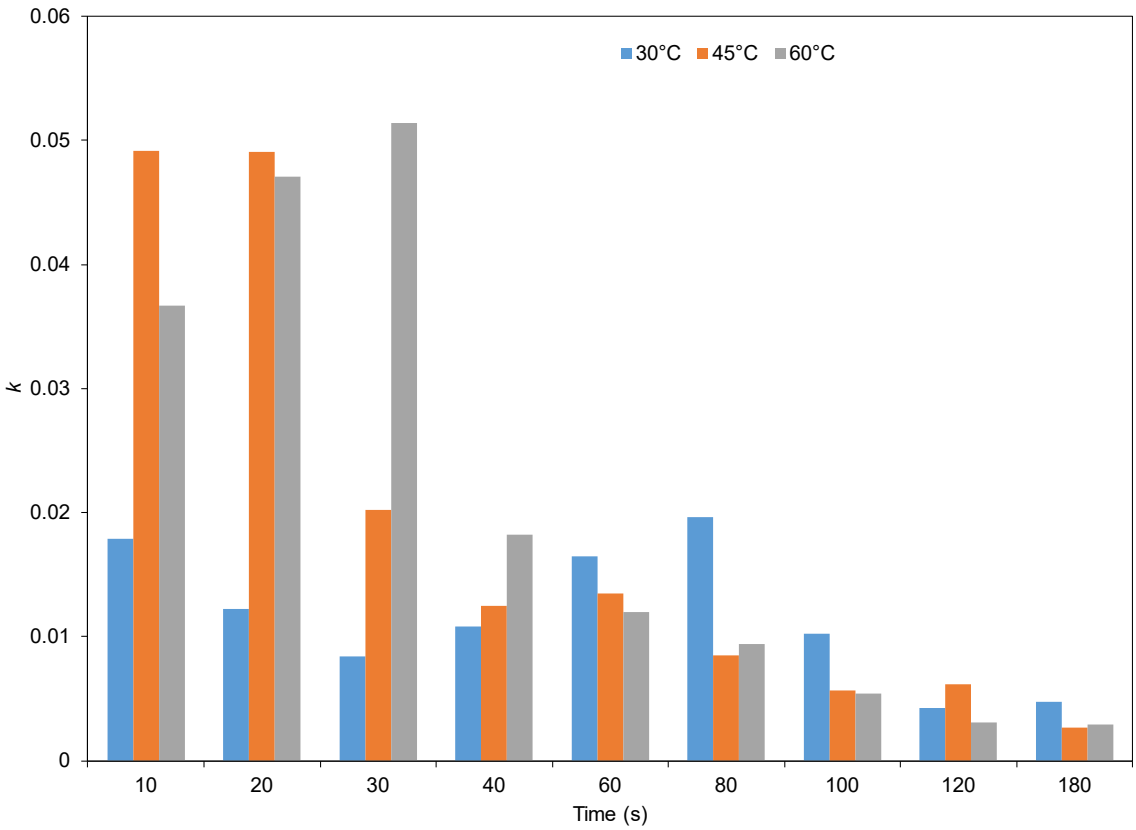

Figure 4-50. The kinetic rates of pseudo first-order RVC transesterification at the physical-limiting stage.

The methyl ester model is also implemented and tested for the RVC reactor to ensure cross reactor reliability and consistency. Additionally, this would be another validation point to support if the intermediate glycerides conversion is important to contribute to the overall transesterification kinetics. Therefore, Eq. 3-20 and Eq. 3-21 is applied to the methyl ester formation data in RVC reactor for the pseudo first-order kinetic model, as shown in Figure 4-51.

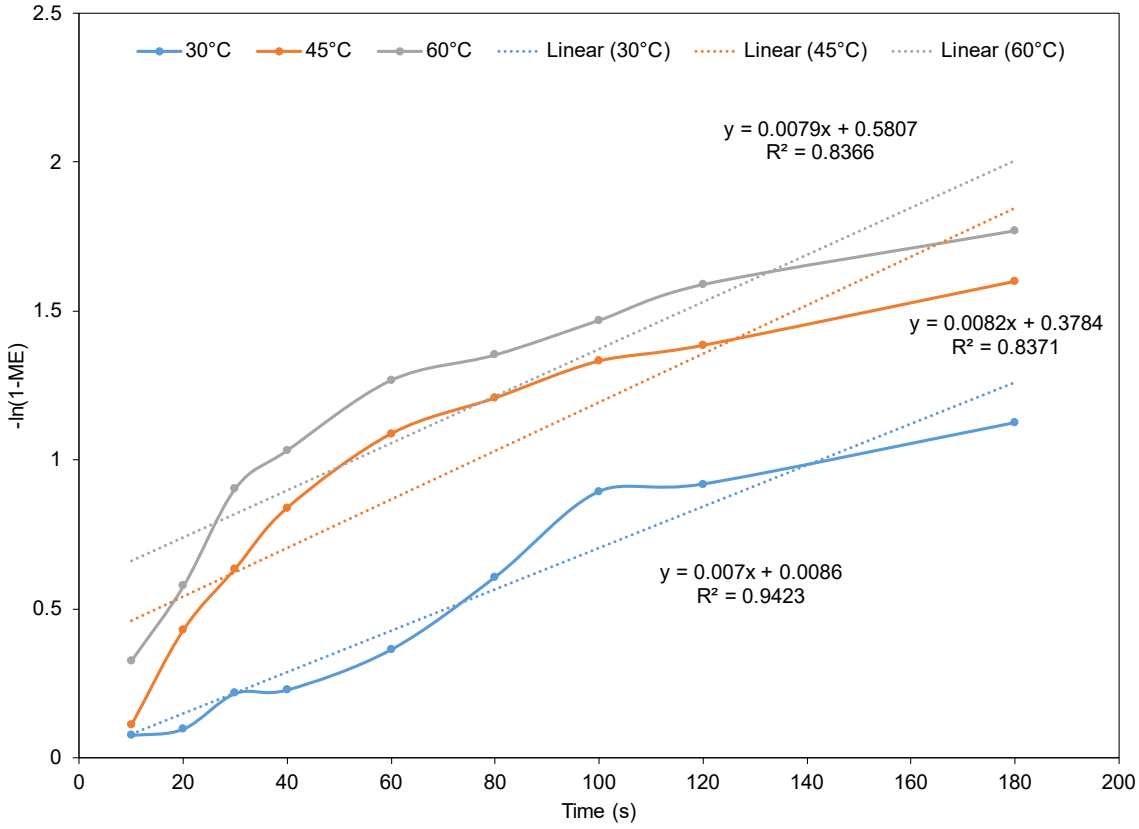

Figure 4-51. Pseudo first-order kinetics model of methyl ester formation in transesterification.

The pseudo first-order triglycerides depletion kinetic model and methyl ester formation kinetic model are compared against each other after determining their individual kinetic rates, as shown in Table 4-10.

Table 4-10. Kinetic constants and R^2 values for conformity of transesterification with the pseudo first-order kinetic models.

Pseudo First-order Kinetic Model	**Reaction Temperature (°C)**	**Max. Kinetic Constant (dm^3/mol.min)**	**R^2 of linear trend lines**
Triglycerides depletion	30	1.1779	0.9357
Triglycerides depletion	45	2.9432	0.8380
Triglycerides depletion	60	3.0850	0.7499
Methyl ester formation	30	0.7952	0.9423
Methyl ester formation	45	1.5763	0.8371
Methyl ester formation	60	1.7373	0.8366

The methyl ester formation model is always lagging behind the triglycerides depletion model in kinetic constant rates for all temperature. The percentage difference for the methyl ester formation and triglycerides depletion for 30°C, 45°C, 60°C is 38.79%, 60.49%, and 55.89%, respectively. Thus, this proves that although the methyl ester model is relatively different from the traditional triglyceride depletion modelling for first-order, it is still capable of providing qualitative representation of the kinetic trends for transesterification for both batch-type and RVC reactor.

The diglycerides conversion is implemented again to extend the pseudo first-order model to test its viability and consistency to represent intermediate reactions through Eq. 3-17, Eq. 3-18, and Eq. 3-23 as shown in Figure 4-52.

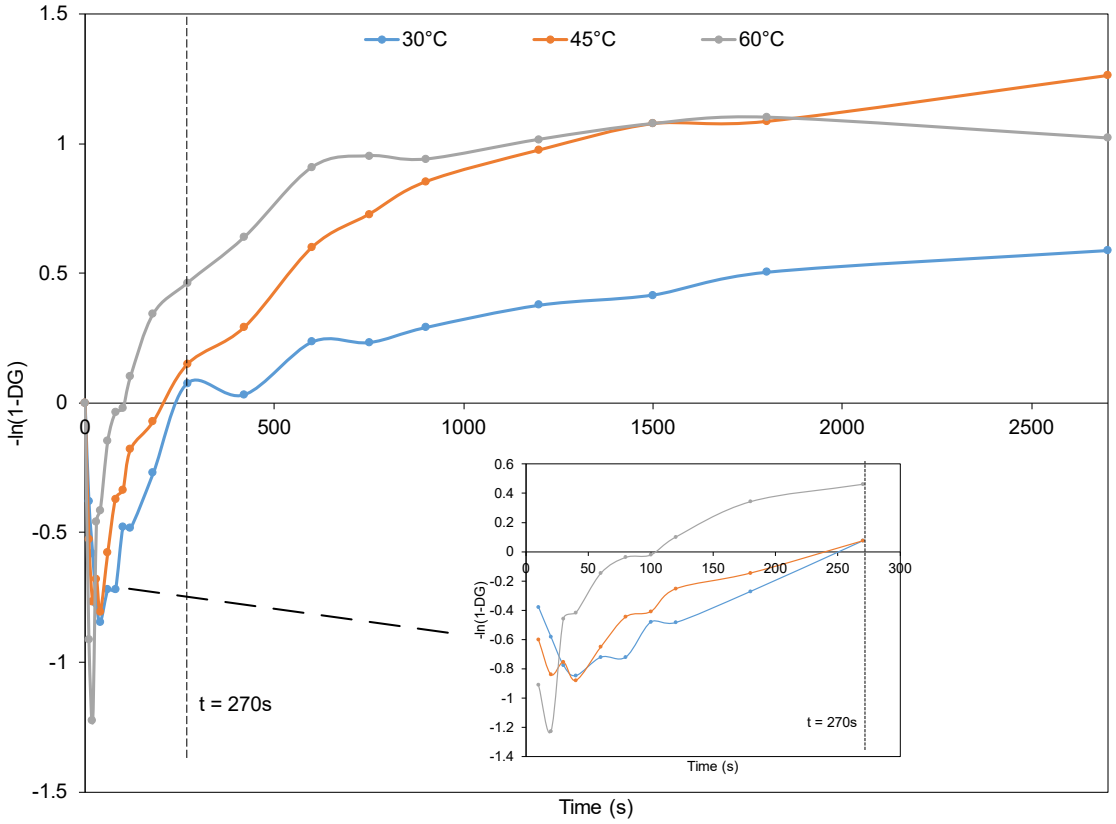

Figure 4-52. Pseudo first-order kinetic model of diglycerides formation and depletion.

Based on Figure 4-52, the initial stage of formation and depletion of diglycerides which fit the linear kinetic model equation is from 40s to 270s. Thus, this timeline is isolated to represent the kinetics of the diglycerides as shown in Figure 4-53. The range for the reaction is selected to avoid the inclusion of high formation rate of diglycerides, leading to a less accurate representation of the diglyceride depletion. Here, the assumption made is that the diglyceride formation reaction rate is much lower than the depletion in the specified range.

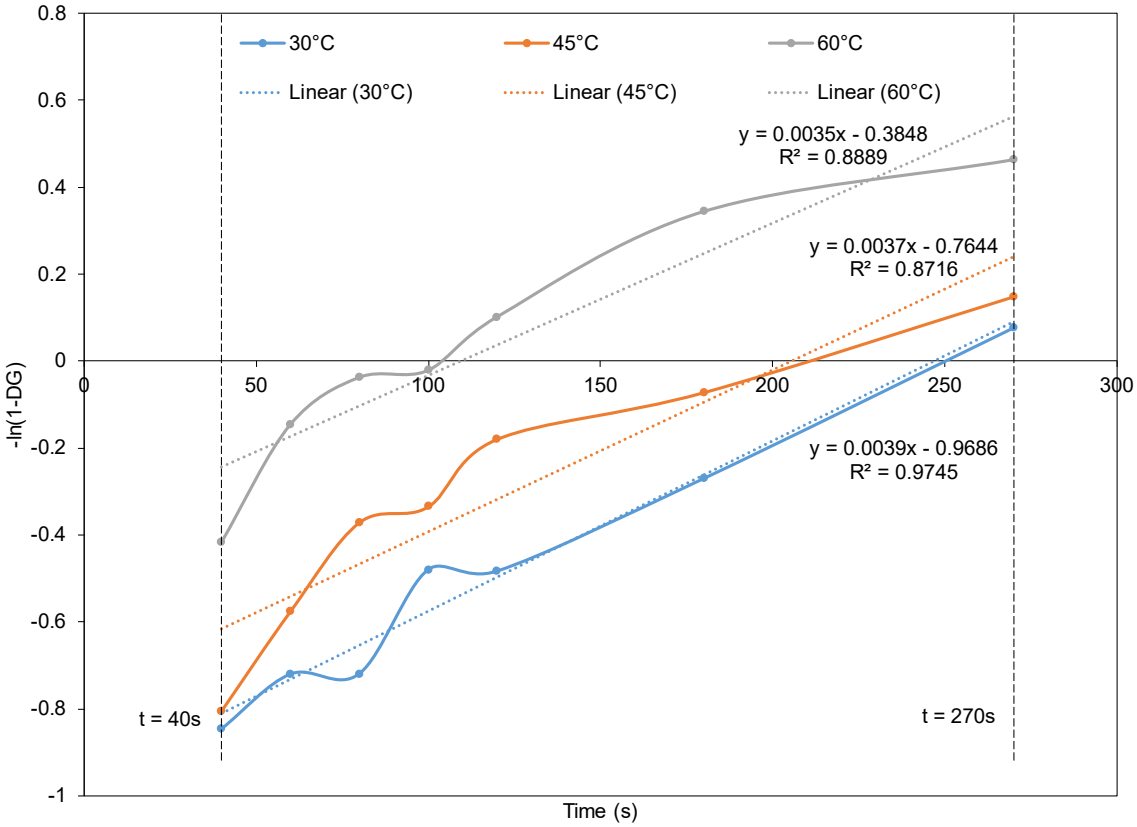

Figure 4-53. Isolated formation and depletion of diglycerides for the pseudo first-order kinetic model from 40s to 270s.

For the monoglycerides, pseudo first-order formation and depletion, the full and isolated kinetic model is shown in Figure 4-54 and Figure 4-55 using Eq. 3-17, Eq. 3-18, and Eq. 3-24, where the isolated timeline for the conversion of monoglycerides starts from 80s to 270s during transesterification.

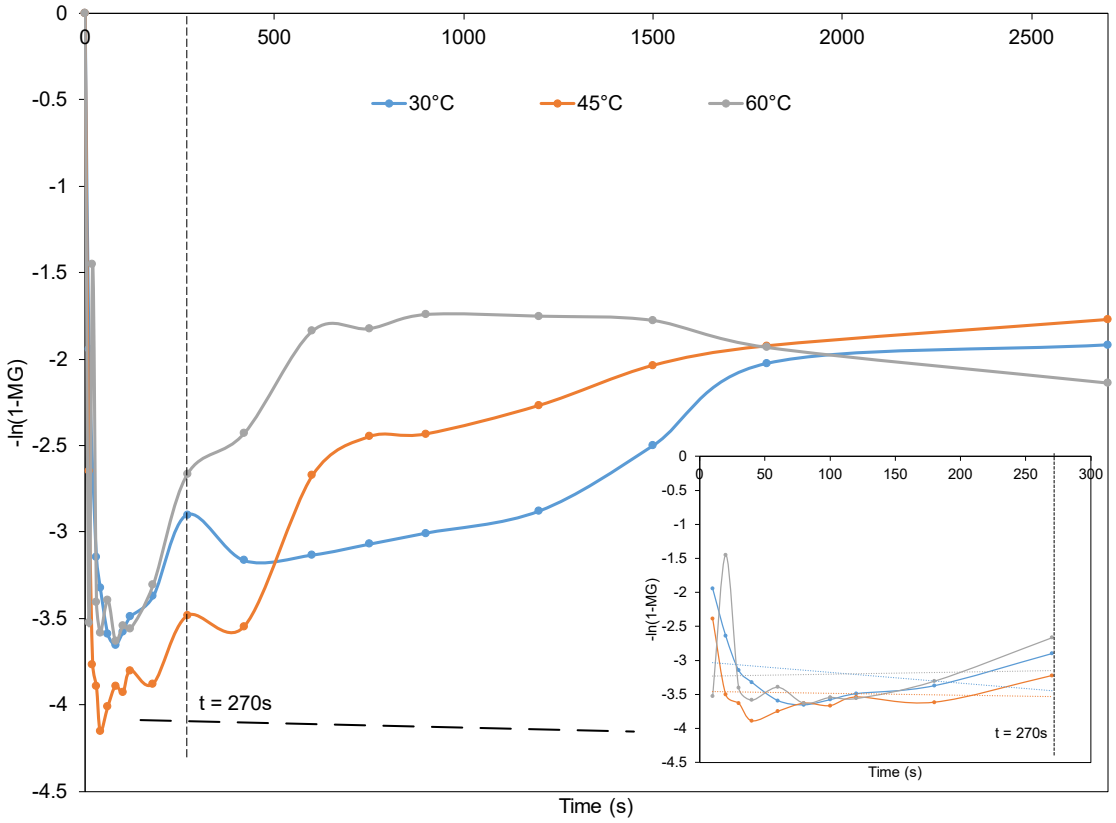

Figure 4-54. The full formation and depletion of monoglycerides using pseudo first-order kinetic model.

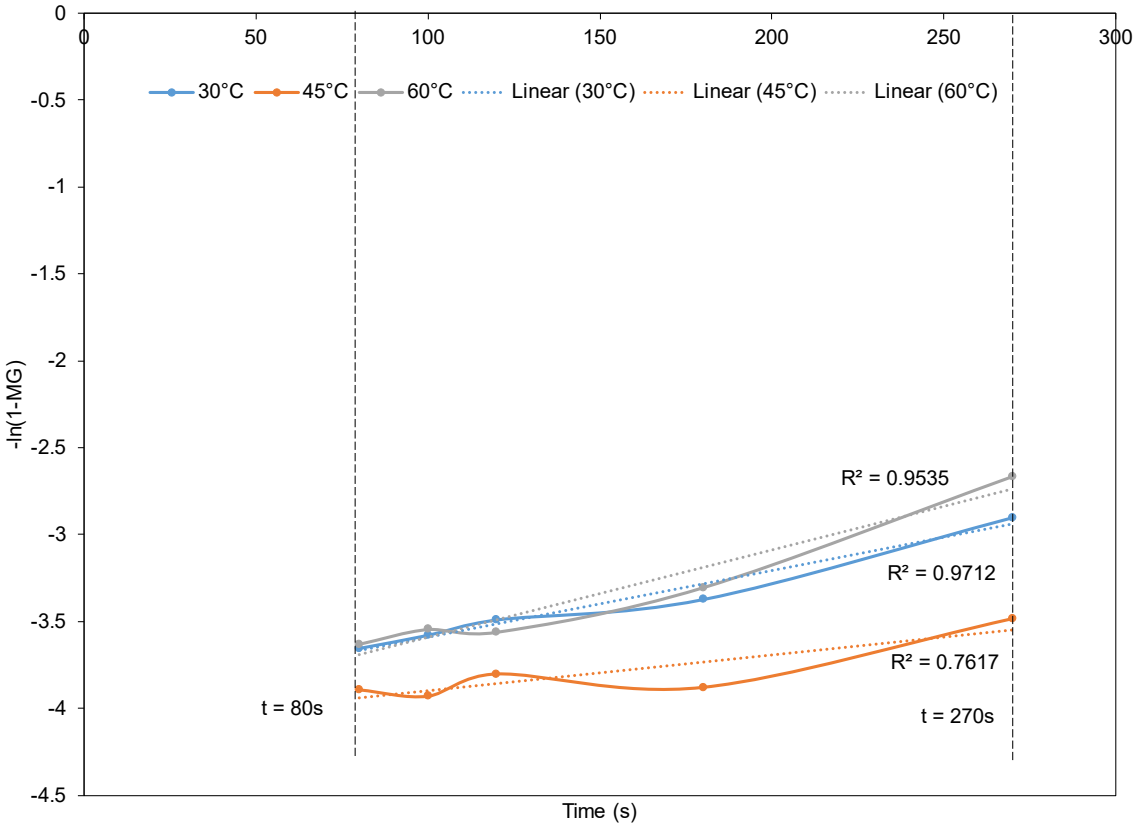

Figure 4-55. Isolated conversion of monoglyceride for the pseudo first-order kinetic model from 80s to 270s.

The moving-average strategy to identify the maximum kinetic rate for the depletion of diglycerides and monoglycerides were implemented, as shown in Figure 4-56.

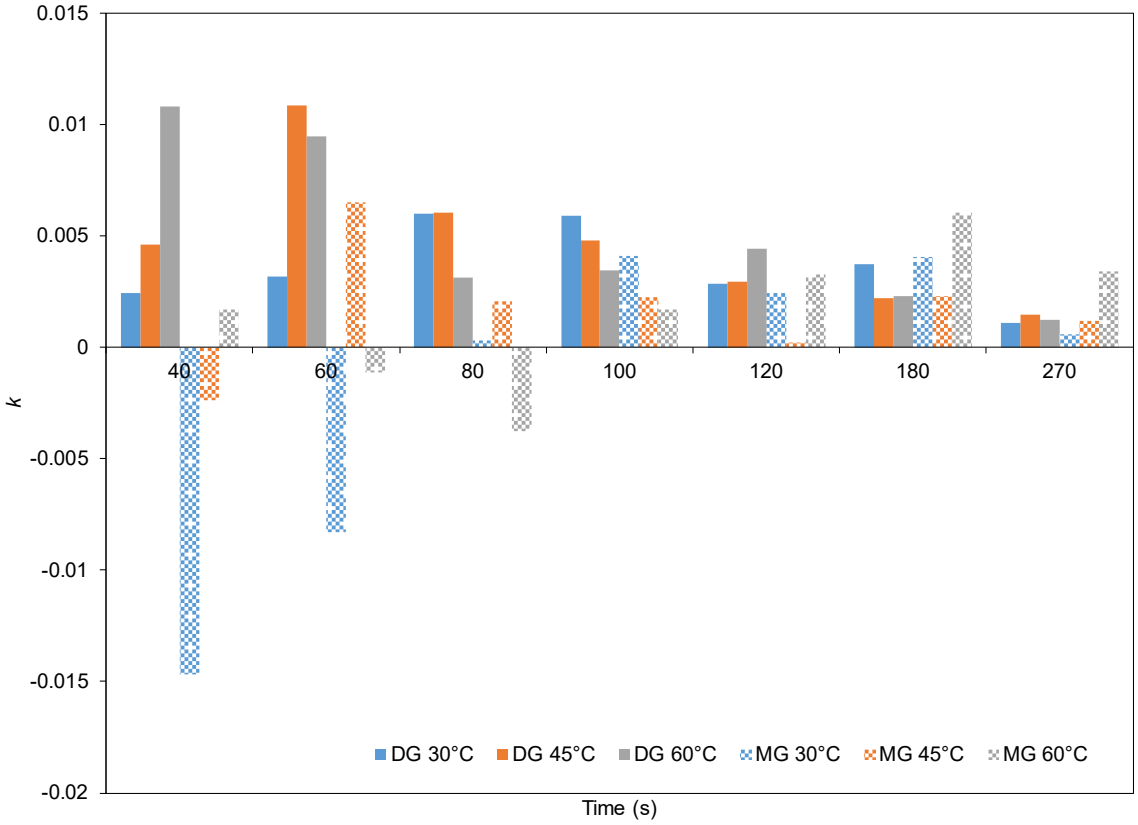

Figure 4-56. The kinetic constant of diglycerides and monoglycerides via moving average of the linear gradient.

The kinetic rates of the triglycerides, diglycerides, monoglycerides, and methyl ester with their respectively improved model were calculated and tabulated as below in Table 4-11.

Table 4-11. The kinetic rates of triglycerides, diglycerides, and monoglycerides depletion with methyl ester formation using a pseudo first-order kinetic model.

Pseudo First-order Kinetic Model	**Reaction Temperature (°C)**	**Moving Average Max. Kinetic Constant (dm^3/mol.min)**	**Linear Trend Gradient Kinetic Constant (dm^3/mol.min)**	**R^2 of linear trend lines**
Triglycerides depletion	30	1.1779	0.648	0.9357
	45	2.9432	0.660	0.8380
	60	3.0850	0.714	0.7499
Diglycerides depletion	30	0.3604	0.234	0.9745
	45	0.6508	0.222	0.8716
	60	0.6489	0.210	0.8889
Monoglycerides depletion	30	0.2464	0.126	0.7617
	45	0.1373	0.228	0.9712
	60	0.3629	0.300	0.9535
Methyl ester formation	30	0.7952	0.420	0.9423
	45	1.5763	0.492	0.8371
	60	1.7373	0.474	0.8366

Based on Table 4-11 the moving average maximum kinetic constants of the diglycerides and monoglycerides depletion rates are relatively low as compared to triglycerides depletion. However, the general trends of the kinetic rates are cohesive with the theory where rates are in the decreasing order of triglycerides, diglycerides, and monoglycerides. The other observation is the kinetic rates for 45°C and 60°C are similar for triglycerides and diglycerides, which suggest that saturation occurs about 45°C for these two compounds. On the other hand, monoglycerides kinetics are more inconsistent as at 45°C the kinetic seems to be lower than 30°C and 60°C.

The linear trend line fit was used to obtain the gradient to represent the kinetic rates. This is then compared with the calculation of the kinetic rate via the moving average method. The kinetic rates calculated from this method has a smaller variance for different reaction temperature, as the averaging of the kinetic occurs when it is linearly fitted. Generally, the kinetic rates obtained from the linear fit is lower than the moving average. The largest and smallest percentage difference is 126.73% and 18.98% between both methods, which suggest that the kinetic constants can have

differences in the order of magnitude depending on the method used. The moving average method provides the maximum kinetic rates using the average of three values, which mimics the instantaneous kinetic rates whereas the linear fit provides a more holistic description of the reaction kinetic through curve fitting of the depletion process.

4.5.1.2 Arrhenius energy of activation

The data from above were used to determine the Arrhenius activation energy using the relationship of the kinetic rate constant and the reciprocal of absolute temperature as shown in the Arrhenius equation below,

$$k = Ae^{\frac{-E_a}{RT}} \qquad \text{Eq. 4-3}$$

Where k is the kinetic rate constant, E_a is the activation energy, R is the universal gas constant, A is the pre-exponential factor, T is the absolute temperature. The Eq. 4-3 can be rearranged into the relationship mentioned to compute the activation energy of the reaction.

$$\log_{10} k = \frac{-E_a}{R} T + C \qquad \text{Eq. 4-4}$$

Figure 4-57 represents the Arrhenius plot using the linear relationship derived from Eq. 4-4.

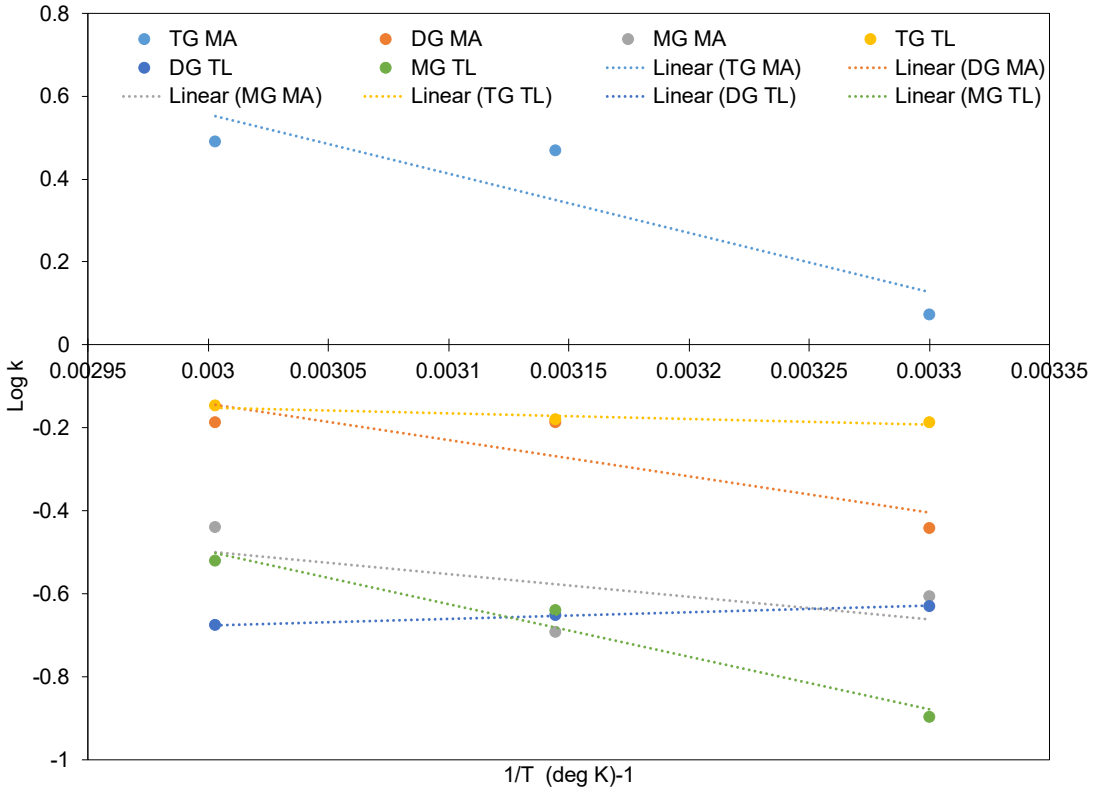

Figure 4-57. Pseudo first-order Arrhenius plot of kinetic reaction constant against reaction temperature of RVC transesterification using moving average and linear fit.

The activation energy was then calculated using the linear relationship of the logarithmic plot for both moving average and linear fit method of kinetic reaction constant, as shown in Table 4-12.

Table 4-12. Pseudo first-order Arrhenius activation energy for moving average and linear fit.

Pseudo First-order Kinetic Model	**Moving Average Activation Energy (kcal/mol)**	**R^2**	**Linear Trend Activation Energy Constant (kcal/mol)**	**R^2**
TG + MeOH → DG + ME	11.85	0.8084	13.23	0.8680
DG + MeOH → MG + ME	13.48	0.7696	14.51	0.9982
MG + MeOH → G + ME	14.45	0.1374	14.58	0.9673

Table 4-12 shows the activation energy for transesterification of triglycerides, diglycerides, and monoglycerides is all in the same order of magnitude. The activation energy value shows an increasing order of trend when going from triglycerides to monoglycerides. The linear trend fit method has consistently larger activation energy when compared with the moving average method.

The results are expected as the moving average uses the instantaneous maximum rate of reaction of each compound. However, the activation energy calculation of monoglycerides transesterification is not a good fit with the Arrhenius relationship, as shown in the moving average method's regression values. In contrast, the linear trend method shows a better regression fit for the activation energy calculation. Nonetheless, the difference in the activation energy of monoglycerides hydrolysis using two methods are relatively small, at only 0.87% of percentage difference.

The trend suggests that the exothermic reaction of transesterification would favour the conversion of triglycerides more than the diglycerides and monoglycerides from the calculated activation energy. Therefore, the initial increase in methyl ester would be substantial due to the high concentration of triglycerides, followed by a sharp increase of diglycerides and monoglycerides as the precursors are forming. The results are aligned with the sigmoidal trend of transesterification reaction as the initial depletion of triglycerides to form methyl ester quickly transition to a slower reaction rate with the surplus of diglycerides and monoglycerides reaction route of higher activation energy.

Therefore, the initial kinetic model which only uses triglycerides conversion to simulate the overall reaction of transesterification is not ideal. The subsequent conversion of diglycerides and monoglycerides requires higher activation energy during the initialisation phase of transesterification. The sudden increase in the concentration of diglycerides, monoglycerides, and methyl ester also meant that the exothermic reaction would need to compensate for the equilibrium by lowering the reaction rates of triglycerides conversion. Also, estimating methyl ester formation using pseudo first-order kinetic to represent the overall reaction is also not reliable since at the initial transesterification the methyl ester will have a higher tendency to dissolve in the excess methanol upon formation. The improved approximation of the pseudo first-order kinetic model for transesterification would be a closer representation after accounting for the intermediate reactions while remaining relatively straightforward.

4.5.1.3 Pseudo first-order kinetic prediction model

The kinetic rates from the depletion of triglycerides, diglycerides, and monoglycerides can be applied in a prediction model based on the pseudo first-order mechanism. The majority of the transesterification kinetics study involved using the homogeneous base as the catalyst. Freedman *et al.* [64] reported the transesterification of soybean oil using butanol and methanol with base and acid type catalyst. The results showed that the homogeneous base-type catalyst exhibit relatively higher reaction rates than the acid counterpart. The pseudo first-order kinetics for the base and acid catalyst is in agreement with the forward reaction. Stemanković *et al.* [254], also studied the transesterification kinetics of sunflower oil at a moderate temperature of 60°C, which involve a fast initial triglyceride mass transfer controlled region, followed by a chemical reaction controlled

environment. The overall transesterification reaction follows the pseudo first-order reaction kinetics described predominantly by the depletion of triglycerides.

In this study, the pseudo first-order kinetic model will demonstrate the triglycerides depletion, diglycerides and monoglycerides formation and depletion kinetics. Thus, the inclusion of the intermediate reaction will enhance the description of the overall transesterification process as these steps are equally important at the beginning of the reaction.

4.5.1.4 Triglycerides depletion kinetic model

Based on Table 4-12, the highest kinetic rate can be determined by locating the moving average of three points consecutively along the timeline, whereby the maximum value indicates the inflection point. The single maximum constant is used to implement the first-order concentration-time equation, as shown below in Eq. 4-5.

$$\ln A_0 - \ln A = kt \qquad \text{Eq. 4-5}$$

Where A_0 is the initial concentration of the reactant, A is the concentration of the reactant at the specified time, k is the kinetic rate of the reaction at the specified time, and t is the specified time. From Eq. 4-5, the kinetic prediction model of triglycerides depletion is implemented using (a) single maximum kinetic rate, (b) adaptive moving average kinetic rate, and (c) adaptive interpolated moving average kinetic rate. The moving average kinetic rate is used due to the inadequate description of the fast-changing reaction at the beginning of the transesterification if only a single kinetic rate is used. For the adaptive moving average kinetic model, the kinetic rate at the specified experimental point is determined via moving average of the three-point kinetic constant, which simulates an instantaneous tangent at the specified time. This is repeated for all experimental points resulting in a total of 17 pseudo instantaneous kinetic constants. These kinetic constants are then used repeatedly with their specified time for the concentration-time equation until the next known calculated kinetic rates. Therefore, the kinetic model is adaptable to its respective change in kinetic rates. The interpolated moving average is an extension of the moving average model, where the kinetic constant used at the specified time is interpolated from the known kinetic rates calculated from before and after the specified time.

Figure 4-58, Figure 4-59, and Figure 4-60 show the triglycerides depletion models using three different modelling approaches which rely on the first-order concentration-time equation from 0s to 270s. The time-step used for the moving average and interpolated moving average to calculate the concentration is 5s resulting in a total of 55 calculation points from 0s to 270s.

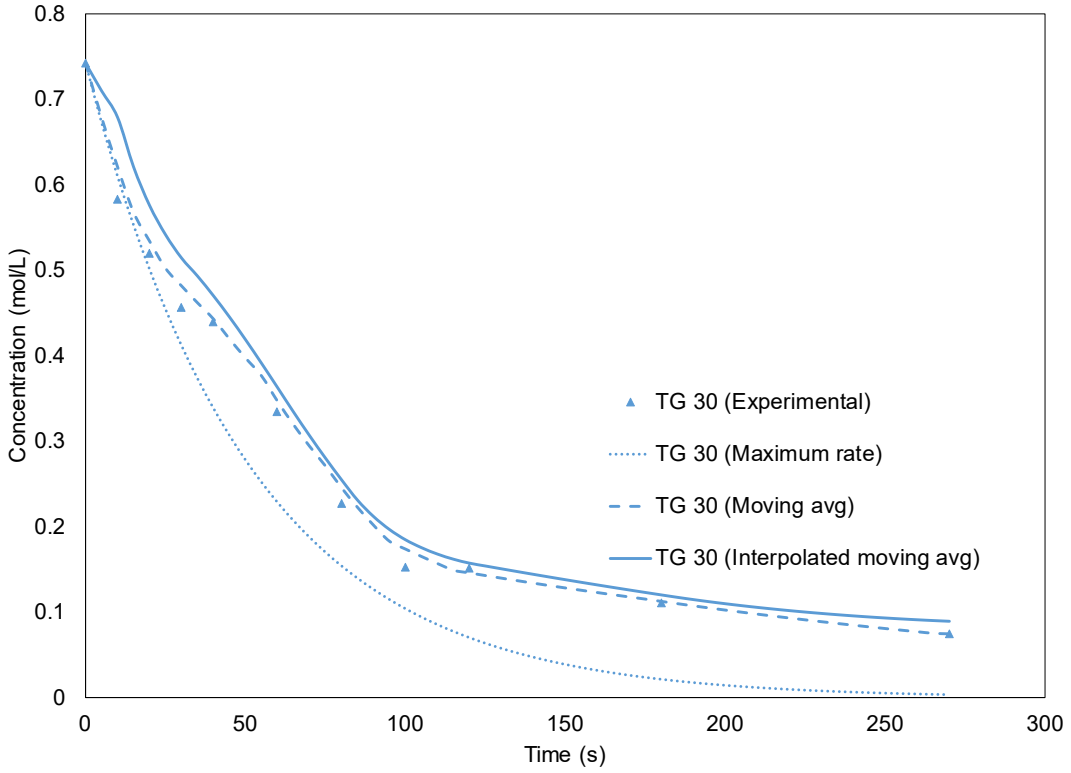

Figure 4-58. Pseudo first-order triglycerides depletion kinetic model using single maximum rate, moving average rates, and interpolated moving average rates at 30°C.

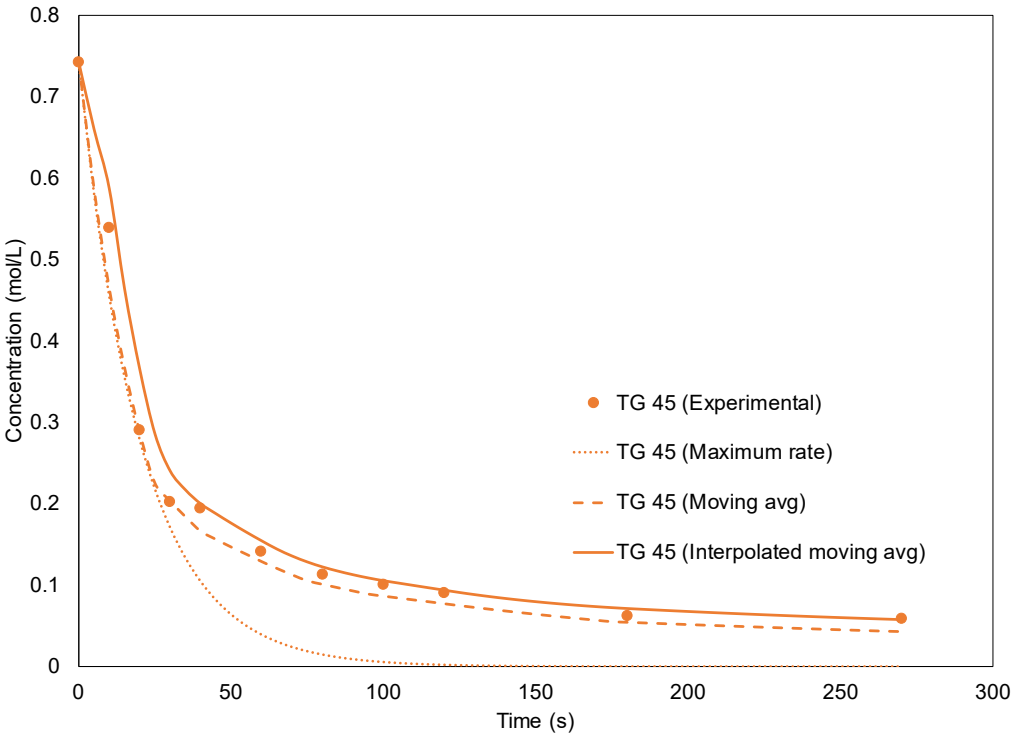

Figure 4-59. Pseudo first-order triglycerides depletion kinetic model using single maximum rate, moving average rates, and interpolated moving average rates at 45°C.

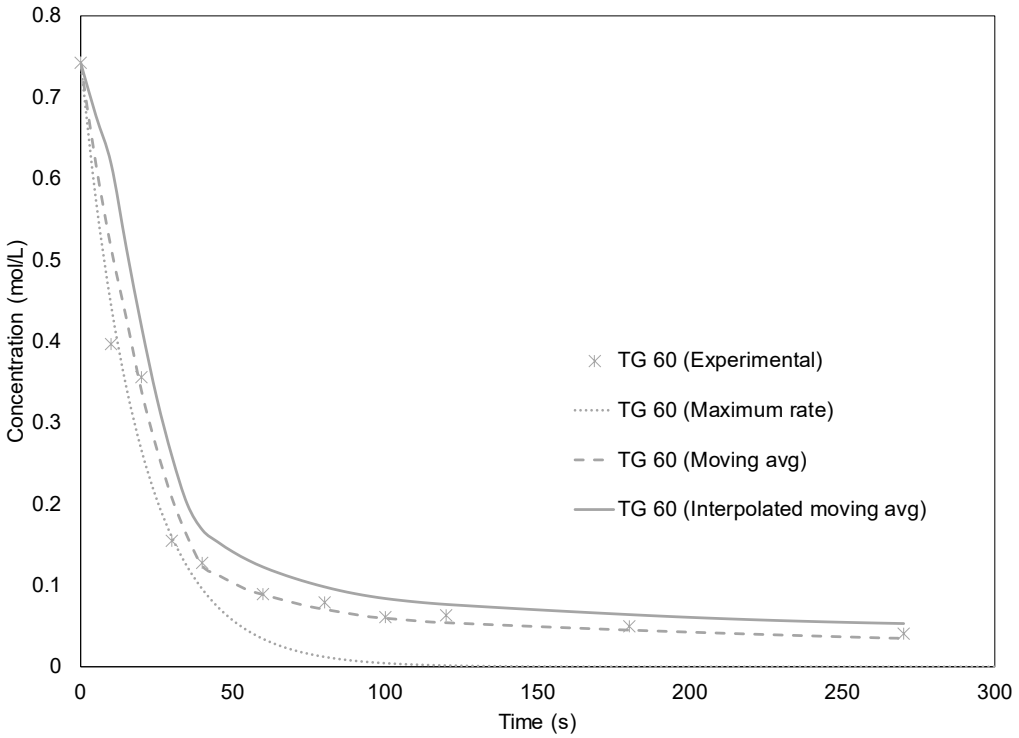

Figure 4-60. Pseudo first-order triglycerides depletion kinetic model using a single maximum rate, moving average rates, and interpolated moving average rates at 60°C.

The figures from the pseudo first-order kinetic model of triglyceride depletion show that a single maximum constant model cannot predict the depletion accurately, as shown in the constant overestimation of depletion for all reaction temperature range. However, the general trend of single constant modelling can describe the transesterification process in a qualitative manner. In contrast, the moving average and the interpolated moving average model shows good agreement with the experimental data for all reaction temperatures, which suggest that the adaptable kinetic model is more suitable for a high reaction rate chemical process like transesterification. The primary factor of the sharp decrease in the triglyceride depletion rate is likely to be the formation of diglycerides, monoglycerides, methyl ester molecules saturating the reaction mixture, combining with the lower concentration of triglycerides, resulting lesser molecule collision for the triglycerides to be reacted.

The interpolated moving average model is observed to consistently underestimate the triglyceride concentration, which suggests the compensation mechanism from the linear-interpolation to obtain a “smoothened” kinetic rates diminishes the predicted reaction rates due to the effects of averaging.

The pseudo first-order kinetic model is constructed based on the initial physical-limiting phase of the transesterification process. In kinetic theory, as transesterification progress towards equilibrium, the rate law will also transition away from first-order [231]. However, the kinetic model was also used to simulate the equilibrium stage of the transesterification process which is reaction-limiting, shown in Figure 4-61.

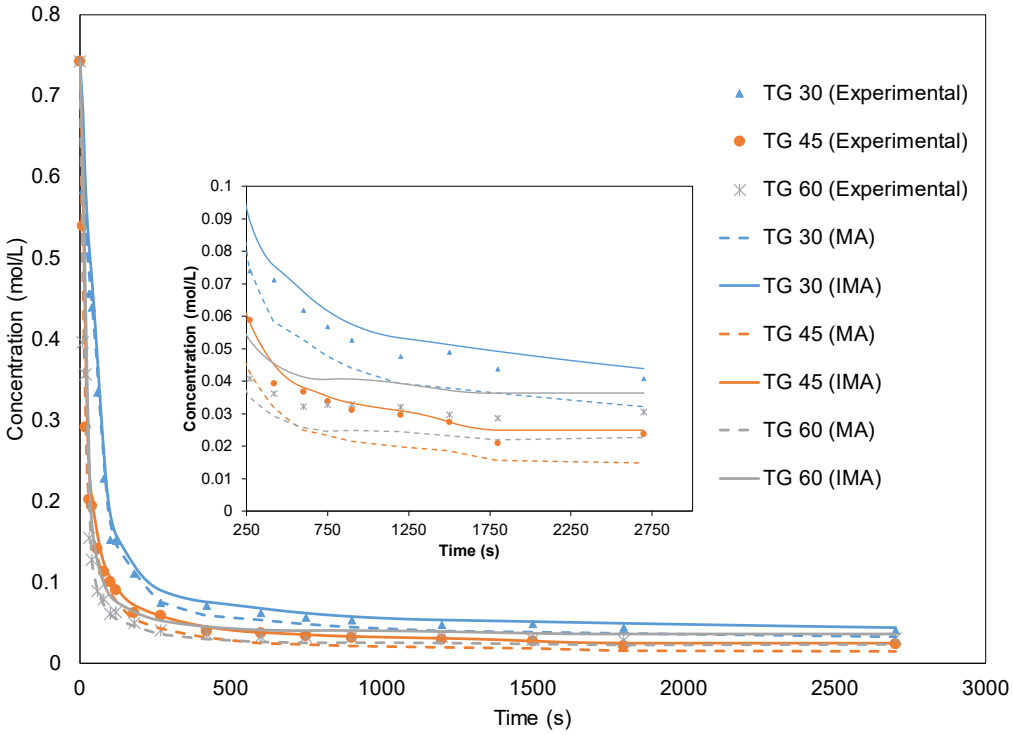

Figure 4-61. Pseudo first-order triglycerides depletion kinetic model using moving average rates and interpolated moving average rates at 30°C, 45°C, 60°C from 0s to 2700s.

Based on Figure 4-61, the results simulated from the prediction model exhibit close agreement of the transesterification kinetics, from the initial phase to the final yield point of the studies. Furthermore, relative errors are calculated to measure the precision of the prediction model, which is the ratio of the absolute error for the predicted concentration, to the experimental concentration. The table of relative errors is generated in Table 4-13 and Table 4-14 for both models.

Table 4-13. The relative errors of the predicted triglyceride concentrations via pseudo first-order kinetic model using moving average kinetic constants.

	Concentration (mol/L)								
Temperature (°C)	30			45			60		
	Experimental	Simulated	RelErr	Experimental	Simulated	RelErr	Experimental	Simulated	RelErr
Time (s)									
0	0.7425	0.7425	0.00%	0.7769	0.7769	0.00%	0.7425	0.7425	0.00%
10	0.5831	0.6211	6.51%	0.5392	0.4861	9.86%	0.3962	0.5145	29.83%
20	0.5195	0.5342	2.83%	0.2907	0.3009	3.51%	0.3565	0.3385	5.05%
30	0.4562	0.4818	5.61%	0.2022	0.2128	5.25%	0.1546	0.2069	33.78%
40	0.4392	0.4430	0.86%	0.1940	0.1738	10.39%	0.1275	0.1237	2.95%
60	0.3343	0.3468	3.75%	0.1413	0.1347	4.65%	0.0894	0.0887	0.81%
80	0.2276	0.2457	7.97%	0.1131	0.1055	6.74%	0.0789	0.0707	10.39%
100	0.1524	0.1739	14.07%	0.1007	0.0903	10.32%	0.0613	0.0597	2.64%
120	0.1511	0.1460	3.39%	0.0902	0.0805	10.81%	0.0634	0.0542	14.60%
180	0.1106	0.1127	1.83%	0.0619	0.0567	8.42%	0.0493	0.0451	8.49%
270	0.0740	0.0747	0.91%	0.0588	0.0447	24.00%	0.0407	0.0351	13.91%
420	0.0712	0.0584	17.91%	0.0393	0.0334	15.11%	0.0362	0.0292	19.27%
600	0.0618	0.0529	14.53%	0.0367	0.0261	28.99%	0.0321	0.0257	19.94%
750	0.0568	0.0477	16.02%	0.0338	0.0244	28.00%	0.0328	0.0246	24.97%
900	0.0526	0.0441	16.29%	0.0311	0.0225	27.85%	0.0329	0.0249	24.35%
1200	0.0477	0.0393	17.45%	0.0297	0.0207	30.22%	0.0321	0.0245	23.77%
1500	0.0489	0.0379	22.52%	0.0274	0.0194	29.26%	0.0296	0.0232	21.59%
1800	0.0438	0.0364	17.01%	0.0210	0.0163	22.06%	0.0286	0.0220	23.31%
2700	0.0408	0.0322	21.06%	0.0238	0.0155	34.83%	0.0306	0.0227	25.73%

When the simulated results are compared with the experimental points at the sampling intervals, a consistent trend can be observed for both models' accuracy. For the moving average model, the prediction is well within 15% relative error from 0s to 270s which defines the initial transesterification process. The model accuracy is in the decreasing order of 30°C, 45°C, and 60°C. Thus, the experimental conditions with lower reaction temperature, which translate to a slower rate of change in kinetic constants are relatively easier to be simulated. As the simulated model moves toward the equilibrium phase and final yield, the mean of errors for all reaction temperature increases, with a mean of errors of 17.85%, 27.04%, and 22.87% for 30°C, 45°C, and 60°C, respectively. The

model consistently overestimates the depletion of triglycerides, especially towards the final yield point for all reaction temperatures.

Table 4-14. The relative errors of the predicted triglyceride concentrations via the pseudo first-order kinetic model using interpolated moving average kinetic constants.

Concentration (mol/L)									
Temperature (°C)	30			45			60		
	Experimental	Simulated	RelErr	Experimental	Simulated	RelErr	Experimental	Simulated	RelErr
Time (s)									
0	0.7425	0.7425	0.00%	0.7769	0.7769	0.00%	0.7425	0.7425	0.00%
10	0.5831	0.6791	16.46%	0.5392	0.6145	13.96%	0.3962	0.6181	55.98%
20	0.5195	0.5760	10.88%	0.2907	0.3824	31.57%	0.3565	0.4173	17.07%
30	0.4562	0.5145	12.77%	0.2022	0.2517	24.48%	0.1546	0.2578	66.75%
40	0.4392	0.4702	7.05%	0.1940	0.2096	8.05%	0.1275	0.1675	31.44%
60	0.3343	0.3630	8.58%	0.1413	0.1620	14.68%	0.0894	0.1220	36.43%
80	0.2276	0.2551	12.10%	0.1131	0.1285	13.58%	0.0789	0.0978	24.05%
100	0.1524	0.1848	21.25%	0.1007	0.1108	10.00%	0.0613	0.0835	36.13%
120	0.1511	0.1575	4.23%	0.0902	0.0986	9.27%	0.0634	0.0762	20.12%
180	0.1106	0.1203	8.75%	0.0619	0.0750	21.29%	0.0493	0.0637	29.25%
270	0.0740	0.0895	20.86%	0.0588	0.0608	3.32%	0.0407	0.0527	29.35%
420	0.0712	0.0755	6.05%	0.0393	0.0472	20.01%	0.0362	0.0455	25.62%
600	0.0618	0.0676	9.23%	0.0367	0.0399	8.51%	0.0321	0.0414	28.83%
750	0.0568	0.0616	8.40%	0.0338	0.0370	9.29%	0.0328	0.0406	23.92%
900	0.0526	0.0575	9.19%	0.0311	0.0347	11.57%	0.0329	0.0407	23.88%
1200	0.0477	0.0533	11.76%	0.0297	0.0323	8.84%	0.0321	0.0394	22.68%
1500	0.0489	0.0512	4.63%	0.0274	0.0287	4.73%	0.0296	0.0373	25.89%
1800	0.0438	0.0492	12.15%	0.0210	0.0261	24.28%	0.0286	0.0364	27.19%
2700	0.0408	0.0438	7.37%	0.0238	0.0260	9.46%	0.0306	0.0364	19.18%

In contrast, the interpolated moving average kinetic model shows a reversed trend as compared to the aforementioned model, which is likely caused by insufficient data intervals. As the prediction model calculates forward in time, the sum of error over time becomes larger, hence the interpolation contributes to the prediction overshooting from the experimental point due to the lack of intervals for correction. The accuracy of prediction at the initial transesterification phase (0s to 270s) is lower

as compared to the equilibrium phase (270s to 2700s). However, the higher reaction rates simulated concentration are observed to be much worse in terms of accuracy. The mean of relative errors for 30°C, 45°C, and 60°C are 12.29%, 15.02%, and 34.66% initially, and they are 8.60%, 12.09%, and 24.65% towards the end. The interpolated method has a slower rate of change in kinetic constant due to the adjustment between known moving average constants, every 5s interval. Thus, the rate of change in triglycerides concentration is a function of the time in the concentration-time function. The selection of time interval will be emphasised in the next section for the diglycerides kinetic model.

4.5.1.5 Diglycerides formation and depletion kinetic model

In this section, the pseudo first-order kinetic modelling is implemented to simulate diglyceride's formation and depletion using Eq. 3-23 and Eq. 4-5. Figure 4-62**Error! Reference source not found.** shows the formation and depletion of diglycerides from for the initial transesterification process at 60°C using five-seconds and one-second intervals for the concentration-time equation.

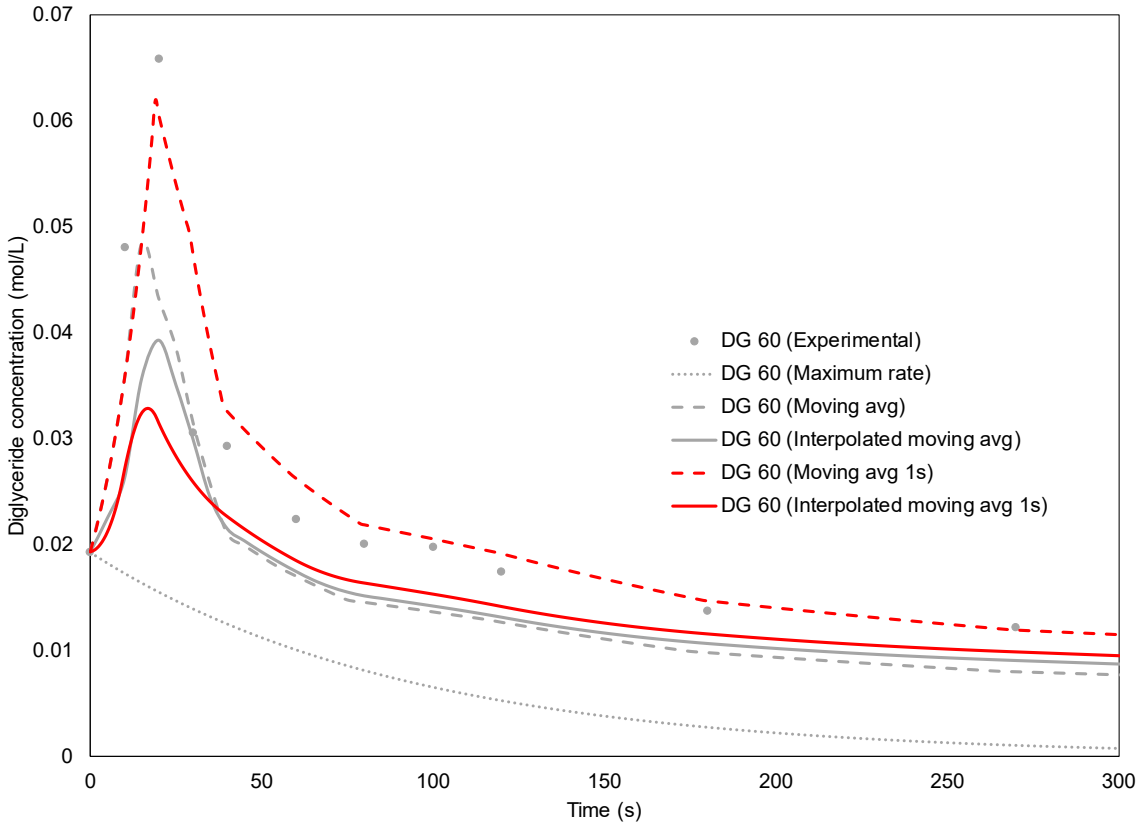

Figure 4-62. Pseudo first-order diglycerides formation and depletion kinetic model using a single maximum rate, moving average rates, and interpolated moving average rates at 60°C simulated at 5s and 1s intervals.

The simulated diglyceride concentrations using five seconds intervals are consistently underestimating the actual experimental results from the figure. The accuracy of the kinetic model is in the increasing order of single maximum kinetic constant, interpolated moving average kinetic constants, and moving average kinetic constants. The single maximum rate is unable to reflect the

large formation of diglyceride at the beginning, when triglycerides are reacted with the methanol to produce methyl ester and diglycerides. However, as mentioned for triglycerides model, the rate of change of kinetics can be improved by reducing the time interval of the concentration-time equation to overcome the fluctuating reaction rates. Thus, the one-second time interval simulation is tested as illustrated.

Based on Figure 4-62, the one-second interval showed improvement for the moving average kinetic model, while becomes less accurate for the interpolated moving average model. Fundamentally, using a smaller time-step size allows better resolution of the simulation even with just the pseudo first-order kinetic model. However, since the number of actual kinetic rates known is limited, there is also a bottleneck for how much it can improve. The moving average method benefitted from smaller step size due to the higher kinetic constant used as compared to the interpolated values which are reduced because of averaging.

Additionally, the formation and depletion of diglycerides occur simultaneously throughout the transesterification process. Thus, the kinetic constants used to describe at the specified time is the sum of both values which would cancel out the effect depending on their individual strength. For instance, from 0s to 20s a sharp increase in diglycerides concentration can be seen as more triglycerides are reacted. Therefore, the net result is the formation of diglycerides in the form of negative kinetic rates, dominating the model. Moving forward the kinetic model simulated via the one-second time-step concentration-time equation will be included in the monoglyceride concentration prediction model.

Figure 4-63 shows the diglycerides formation and depletion modelled at a reaction temperature of 45°C, using the maximum rate, moving average, interpolated moving average with 1s and 5s time-step. The overall model accuracy follows the same sequence as the 60°C diglycerides, with increasing order of accuracy from maximum rate, interpolated moving average (1s time-step), interpolated moving average (5s time-step), moving average (5s time-step), model moving average (1s time-step). As per the previous discussion, the moving average model simulated with one-second time-step has an excellent agreement (maximum difference of 9.12%) throughout the entire process. The moving average model simulated with five-second time-step also showed great representation from 0s to 270s (maximum difference of 6.72%). The smaller simulation time-step has a better overall effect in the model from the initialisation until the final yield while there are slight overestimations after the peak formation of diglycerides after 100s. The interpolated kinetic model in diglyceride prediction did not perform as well as compared to the triglycerides prediction model mainly due to the effect of averaging for formation and depletion kinetic rates.

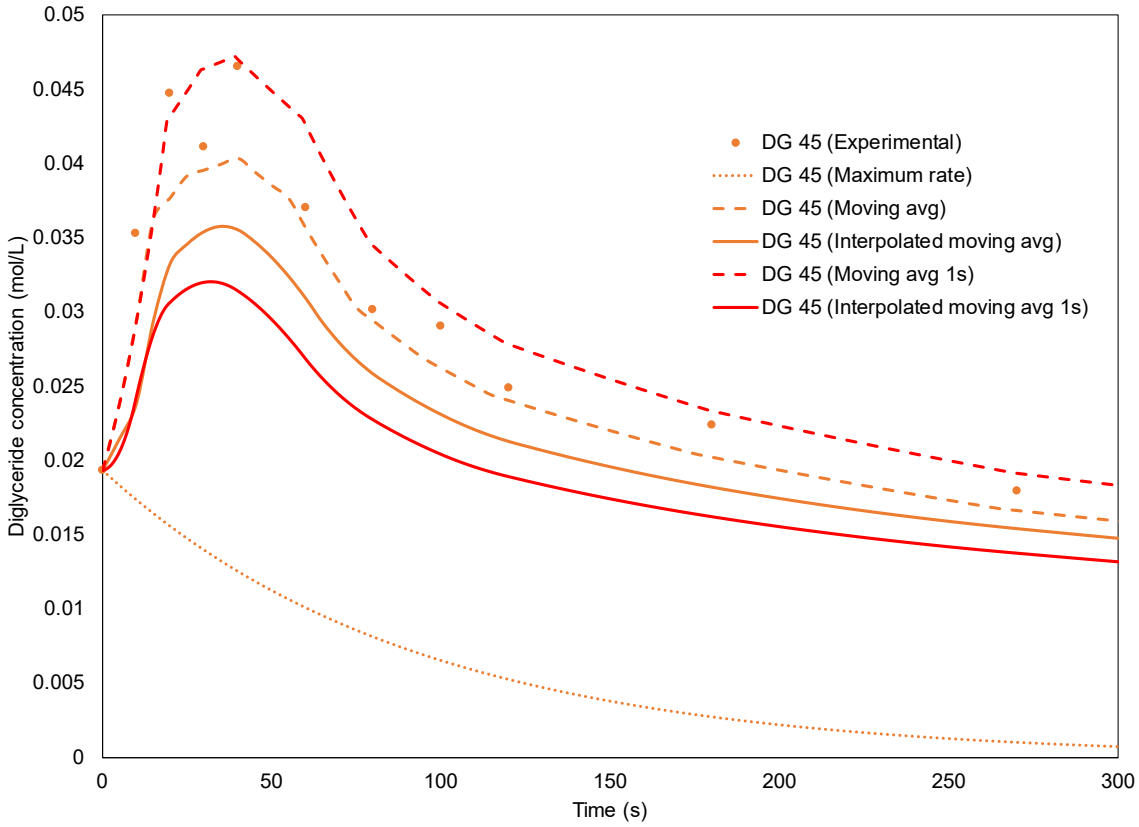

Figure 4-63. Pseudo first-order diglycerides formation and depletion kinetic model using a single maximum rate, moving average rates, and interpolated moving average rates at 45°C simulated at 5s and 1s intervals.

Figure 4-64 shows the pseudo first-order diglycerides modelled at 30°C for the formation and depletion kinetics. The difference between the moving averages model simulated at one second and five-second time-step is noticeably small. The main factor is possibly due to the lowered kinetic rates at the beginning of transesterification using a lower reaction temperature, leading to slower depletion of triglycerides. Thus, the kinetic model has ample buffer to react to the changes in reaction rates. The formation of diglycerides at 30°C dominated from 0s to 40s, coinciding with the sharp depletion of triglycerides from Figure 4-45. The depletion rate is greater than the rate of formation from 40s onwards hence the negative gradient in the concentration. In terms of model accuracy, the moving average kinetic model is closely aligned with the experimental values. The maximum percentage differences for both one second and five-second time-step model at the equilibrium phase toward the final yield is negligible, both at about 10%. However, the five seconds time-step model edges out by a small margin when compared from 0s to 270s, with a maximum percentage difference of 5.00% against the one-second time-step at 7.27%.

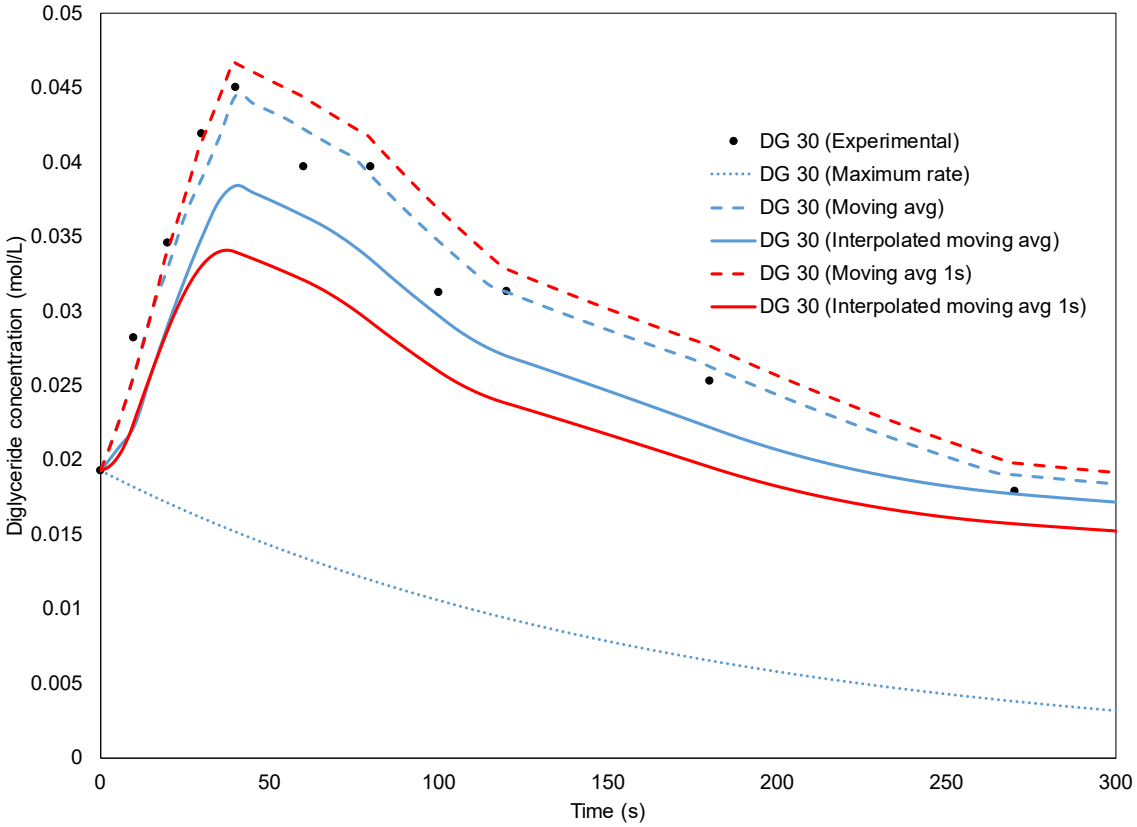

Figure 4-64. Pseudo first-order diglycerides formation and depletion kinetic model using a single maximum rate, moving average rates, and interpolated moving average rates at 30°C simulated at 5s and 1s interval.

Figure 4-65 shows the diglycerides depletion and formation modelled at all reaction temperature using the moving average kinetic rates from 0s to 2700s. The predicted concentration for diglycerides at the final yield point is in close agreement with the actual experimental data, with the one-second time-step simulation having consistently greater accuracy. The moving average models are also always underestimating the actual concentration of diglycerides during the equilibrium phase, in the order of the one second time-step followed by the five-second time-step simulation.

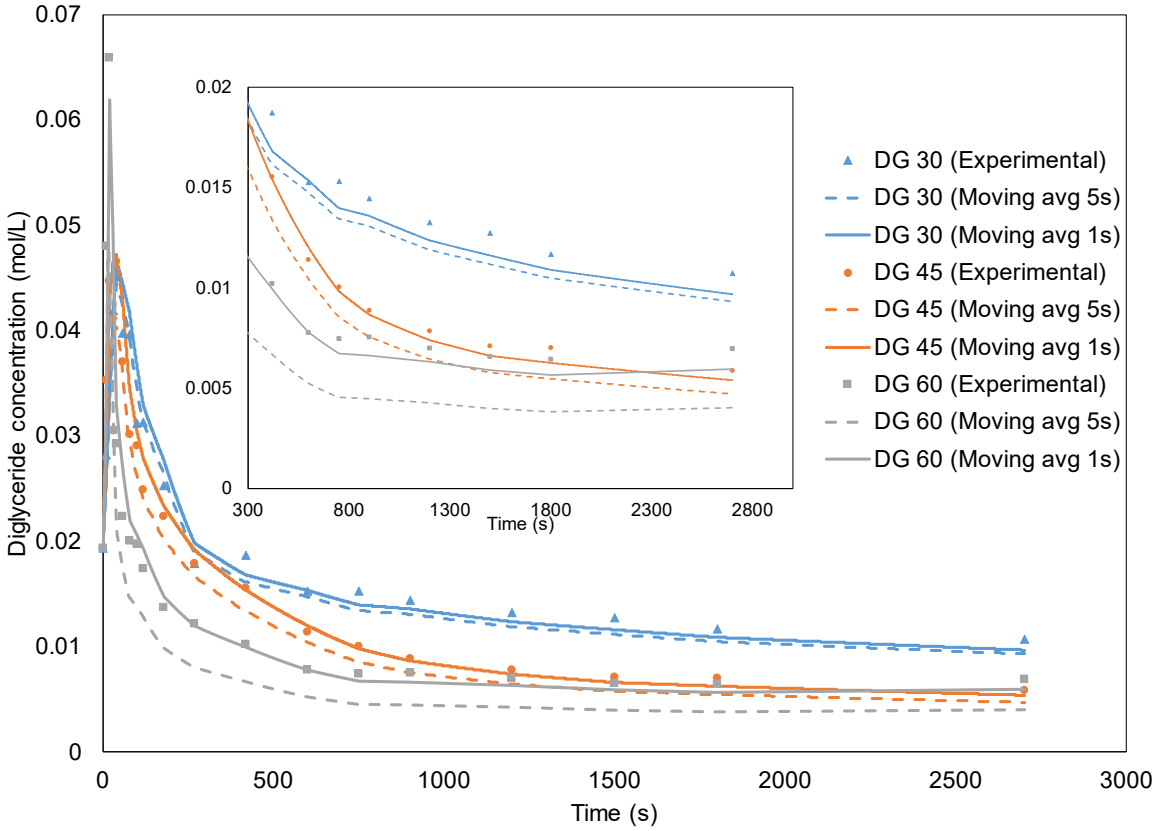

Figure 4-65. The pseudo first-order diglycerides kinetic model via moving average kinetic constant simulated at 1s and 5s intervals for 30°C, 45°C, and 60°C from 0s to 2700s.

Table 4-15 and Table 4-16 shows the relative errors of the moving average model simulated at one second and five-second time-step at all known concentration. The mean relative error from 0s to 270s for the one-second time-step model is 7.27%, 9.12%, and 14.97%, for 30°C, 45°C, and 60°C, respectively. On the other hand, the mean relative error from 0s to 270s for five seconds time-step model is 5.00%, 6.72%, and 26.32%, for 30°C, 45°C, and 60°C, respectively. There is a noticeable trend for the relative error as it is proportionate the increasing reaction temperature. Although the five-second model has better accuracy at a lower reaction temperature of 30°C and 45°C for the initial transesterification process, the inaccuracy for the 60°C model is relatively large, at about five times more. However, the one-second model showed a smaller variance overall across reaction temperature, as all models are well within 15% mean relative errors. This observation is also true compared with the equilibrium stage of transesterification for both models, where there is a small margin of error for the one-second time-step, with a maximum of 8.8% mean error at 60°C reaction temperature. The five-second time-step moving average model shows an increase in mean relative error most likely due to the carry-forward effect.

Table 4-15. The relative errors of the predicted diglyceride concentrations via the pseudo first-order kinetic model using moving average kinetic constants simulated at five-second time-step.

	Concentration (mol/L)								
Temperature (°C)	30			45			60		
	Experimental	Simulated	RelErr	Experimental	Simulated	RelErr	Experimental	Simulated	RelErr
Time (s)									
0	0.0193	0.0193	0.00%	0.0208	0.0208	0.00%	0.0193	0.0193	0.00%
10	0.0282	0.0258	8.33%	0.0353	0.0305	13.48%	0.0480	0.0357	25.77%
20	0.0346	0.0330	4.51%	0.0447	0.0384	14.20%	0.0658	0.0433	34.30%
30	0.0419	0.0389	7.13%	0.0411	0.0403	1.99%	0.0305	0.0315	3.36%
40	0.0450	0.0445	1.29%	0.0465	0.0411	11.72%	0.0293	0.0210	28.19%
60	0.0397	0.0422	6.22%	0.0370	0.0363	1.91%	0.0224	0.0171	23.69%
80	0.0397	0.0390	1.64%	0.0302	0.0299	0.74%	0.0201	0.0146	27.36%
100	0.0312	0.0346	10.89%	0.0291	0.0267	8.18%	0.0197	0.0137	30.76%
120	0.0313	0.0313	0.27%	0.0249	0.0245	1.65%	0.0175	0.0127	27.31%
180	0.0253	0.0262	3.63%	0.0224	0.0206	7.86%	0.0137	0.0098	28.30%
270	0.0179	0.0190	6.06%	0.0179	0.0169	5.47%	0.0122	0.0080	34.11%
420	0.0187	0.0162	13.73%	0.0155	0.0136	12.35%	0.0102	0.0067	34.64%
600	0.0153	0.0147	3.45%	0.0114	0.0106	6.81%	0.0078	0.0052	32.78%
750	0.0153	0.0134	12.15%	0.0100	0.0087	13.20%	0.0075	0.0045	39.06%
900	0.0144	0.0131	9.51%	0.0089	0.0077	13.14%	0.0075	0.0045	40.75%
1200	0.0133	0.0119	10.24%	0.0078	0.0066	16.19%	0.0070	0.0043	39.03%
1500	0.0127	0.0112	12.31%	0.0071	0.0059	17.00%	0.0066	0.0040	39.47%
1800	0.0117	0.0105	10.13%	0.0070	0.0056	20.75%	0.0064	0.0038	40.50%
2700	0.0107	0.0093	13.17%	0.0059	0.0048	18.41%	0.0070	0.0040	42.23%

Table 4-16. The relative errors of the predicted diglyceride concentrations via pseudo first-order kinetic model using moving average kinetic constants simulated at one-second time-step.

	Concentration (mol/L)								
Temperature (°C)	30			45			60		
	Experimental	Simulated	RelErr	Experimental	Simulated	RelErr	Experimental	Simulated	RelErr
Time (s)									
0	0.0193	0.0193	0.00%	0.0208	0.0208	0.00%	0.0193	0.0193	0.00%
10	0.0282	0.0258	8.33%	0.0353	0.0305	13.48%	0.0480	0.0357	25.77%
20	0.0346	0.0342	0.92%	0.0447	0.0434	3.02%	0.0658	0.0605	8.06%
30	0.0419	0.0415	1.06%	0.0411	0.0466	13.32%	0.0305	0.0474	55.31%
40	0.0450	0.0466	3.52%	0.0465	0.0472	1.41%	0.0293	0.0326	11.15%
60	0.0397	0.0444	11.71%	0.0370	0.0427	15.51%	0.0224	0.0263	17.47%
80	0.0397	0.0415	4.63%	0.0302	0.0346	14.66%	0.0201	0.0219	9.02%
100	0.0312	0.0368	17.91%	0.0291	0.0307	5.54%	0.0197	0.0205	4.08%
120	0.0313	0.0328	4.75%	0.0249	0.0279	12.21%	0.0175	0.0191	9.67%
180	0.0253	0.0277	9.24%	0.0224	0.0234	4.81%	0.0137	0.0147	7.26%
270	0.0179	0.0198	10.63%	0.0179	0.0192	7.21%	0.0122	0.0119	1.85%
420	0.0187	0.0168	10.23%	0.0155	0.0155	0.62%	0.0102	0.0099	2.59%
600	0.0153	0.0154	0.52%	0.0114	0.0121	5.64%	0.0078	0.0078	0.03%
750	0.0153	0.0140	8.70%	0.0100	0.0099	1.80%	0.0075	0.0067	9.64%
900	0.0144	0.0136	5.90%	0.0089	0.0087	1.85%	0.0075	0.0066	12.11%
1200	0.0133	0.0124	6.71%	0.0078	0.0074	5.36%	0.0070	0.0063	9.54%
1500	0.0127	0.0116	8.86%	0.0071	0.0066	6.34%	0.0066	0.0059	10.23%
1800	0.0117	0.0109	6.62%	0.0070	0.0063	10.58%	0.0064	0.0057	11.83%
2700	0.0107	0.0097	9.78%	0.0059	0.0054	7.94%	0.0070	0.0060	14.39%

4.5.1.6 Monoglycerides formation and depletion kinetic model

Figure 4-66 shows that the full formation and depletion of monoglycerides through the pseudo first-order kinetics is presented for various reaction temperatures. The initial transesterification of monoglycerides from 0s to 60s is highly non-linear as opposed to the first-order assumptions. Therefore, the fluctuating kinetics would lead to underestimation and overestimation of the concentrations, as shown in Figure 4-66.

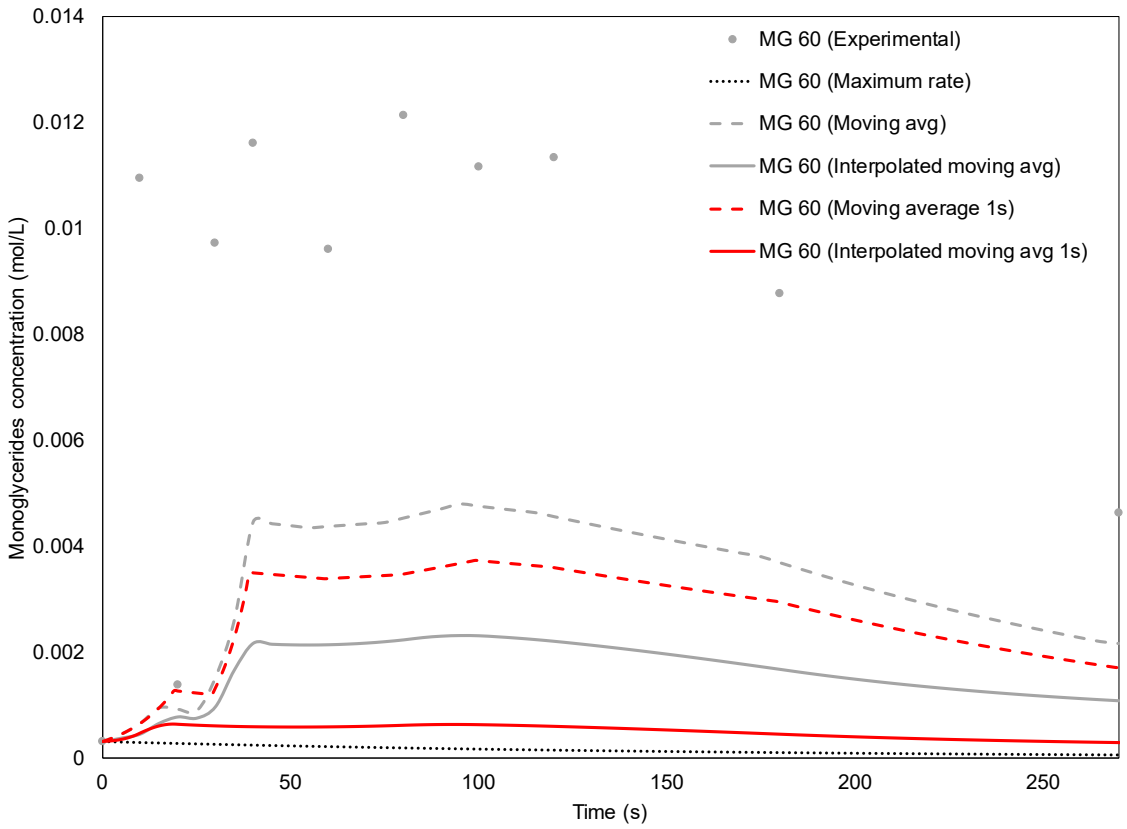

Figure 4-66. Monoglycerides formation and depletion simulation for 0s to 270s using pseudo first-order kinetics model underestimation due to fluctuation kinetic rates.

Thus, the initial region is omitted from the prediction as the variance in the moving average kinetics will lead to overcompensation in the predictor model. Figure 4-67 shows the monoglycerides predictor model from 80s and onwards using the pseudo first-order kinetics, which is a good fit with the linear relationship.

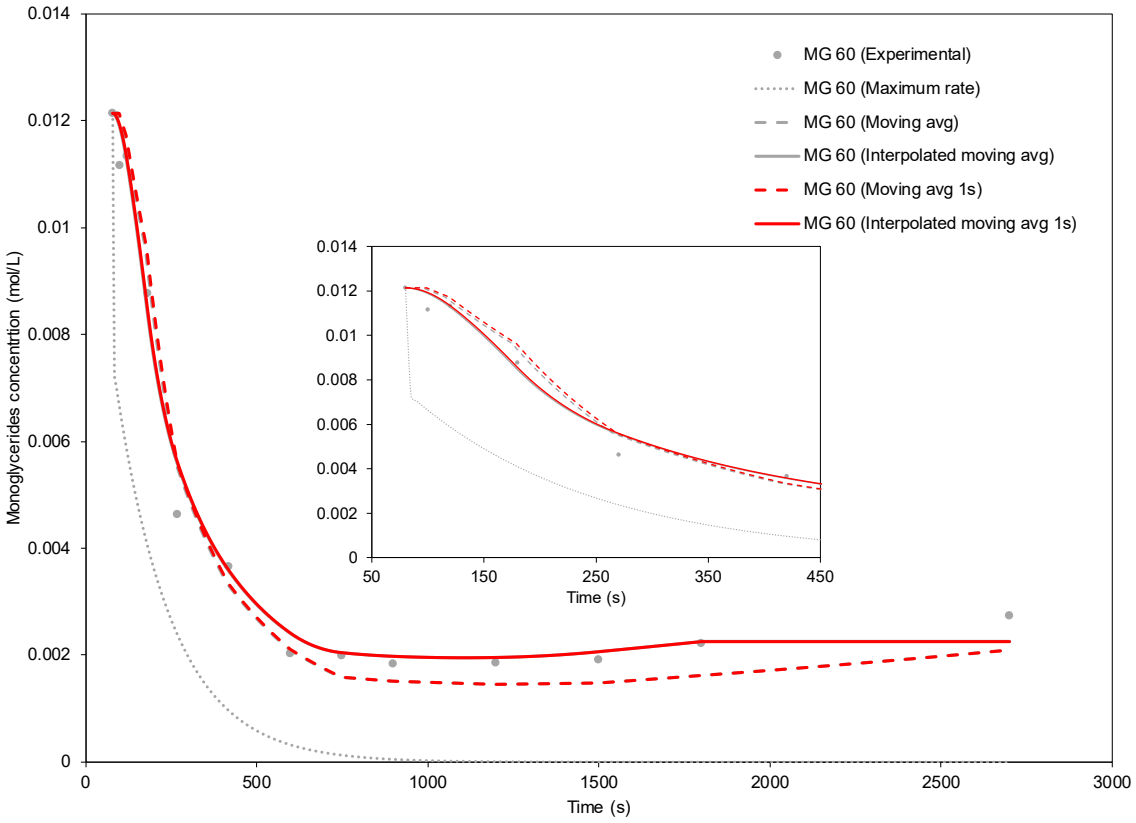

Figure 4-67. Pseudo first-order monoglycerides formation and depletion kinetic model using single maximum rate, moving average rates, and interpolated moving average rates at 60°C simulated at 5s and 1s intervals from 80s to 2700s, (a) enlarged concentration profile from 80s to 450s.

Based on Figure 4-67, the difference is significant as compared to modelling the initial monoglycerides formation and depletion in Figure 4-66. From it, the moving average kinetic model for five and one-second time-step are almost identical in trend, as both would underestimate the concentration of monoglyceride beyond 600s to the final yield point. However, the interpolated moving average simulations both show good agreement with the experiment data from 80s to final yield, where there is slight underestimation at the final yield point. Figure 4-68 shows the monoglycerides formation and depletion simulation at 45°C.

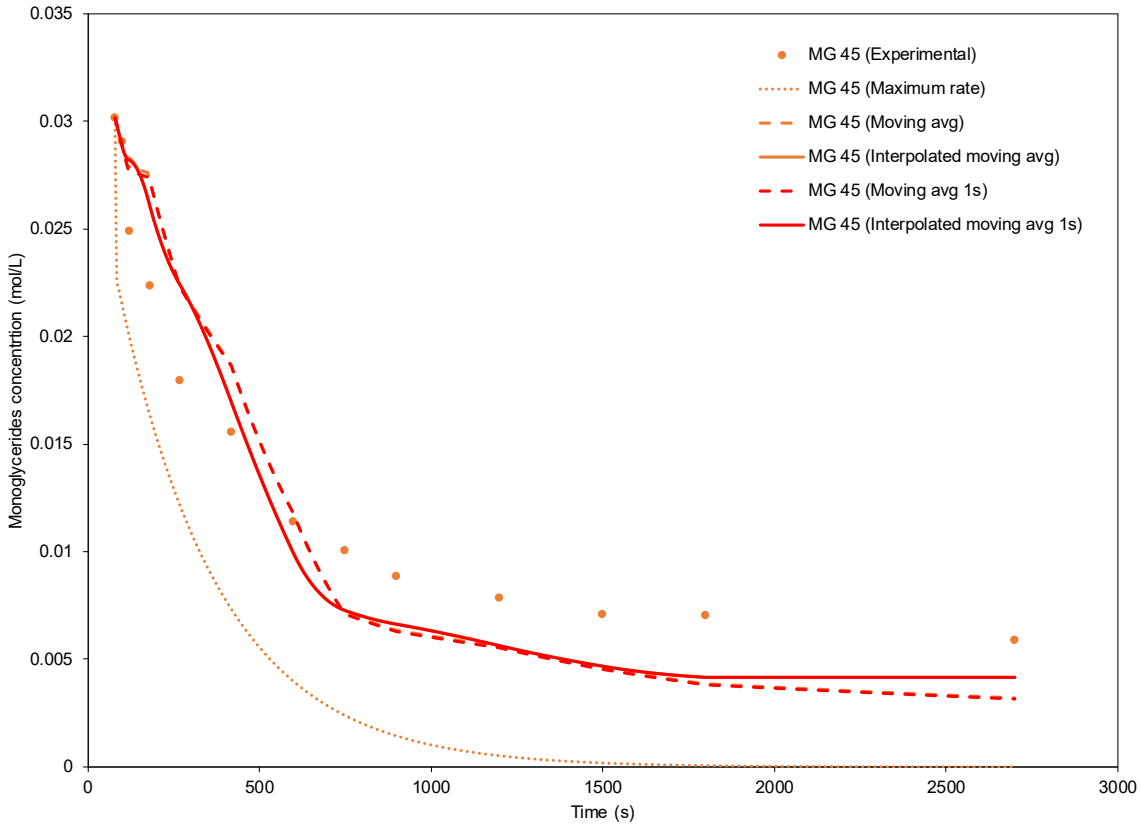

Figure 4-68. Pseudo first-order monoglycerides formation and depletion kinetic model using a single maximum rate, moving average rates, and interpolated moving average rates at 45°C simulated at 5s and 1s intervals from 80s to 2700s.

Based on Figure 4-68, the simulated concentration of monoglycerides at 45°C showed a more gradual decrease as compared to the 60°C which is expected when a lower reaction temperature is used. The accuracy of the simulation from the moving average method is relatively poor, as compared to the triglycerides and diglycerides simulation at 45°C. From 120s onward, the simulated monoglycerides concentrations are overestimating, where the depletion trend seems to be more linear than the supposed exponential decay trend. Thus, beyond 600s, the predicted concentration overshoots, resulting in an overestimation of the monoglycerides observed in the moving average and interpolated moving average model. Figure 4-69 shows the monoglycerides formation and depletion simulation at 30°C.

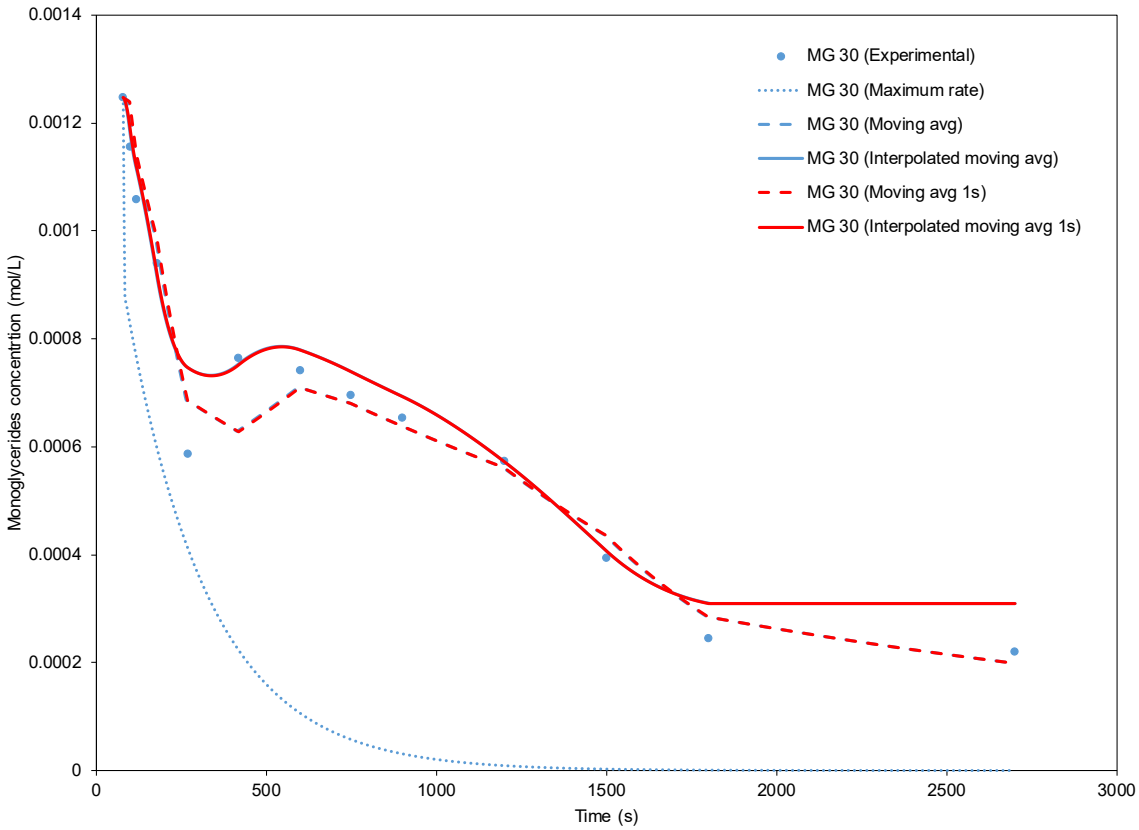

Figure 4-69. Pseudo first-order monoglycerides formation and depletion kinetic model using a single maximum rate, moving average rates, and interpolated moving average rates at 30°C simulated at 5s and 1s interval from 80s to 2700s.

From the simulation, the general trend of the moving average models fits well with the experimental data. From 270s to 420s, there is an increase in monoglycerides concentration in the actual data point. The simulated model can predict the rapid change in concentration with reasonable accuracy, as shown by both moving average and interpolated moving average model. Since the one-second time-step model has minimal differences from the five seconds time-step, this suggests that the kinetics of the monoglycerides are less affected by the effect from time. As the simulation progress into the final yield point, the moving average model can predict the final yield point with relatively high accuracy at 9.87% difference as opposed to the interpolated moving average model at 40.89% difference. The mean percentage differences from the 80s to 270s region is at 7.87%, 9.41%, 8.91%, and 9.56% for the moving average (5s), interpolated moving average (5s), moving average (1s) and interpolated moving average (1s), respectively.

Table 4-17 and Table 4-18 shows the relative errors of the moving average model and interpolated moving average model simulated at five-second time-step at all known concentration. The moving average simulation at one-second time-step shows a better accuracy from the mean relative error observed at 0s to 270s, as compared to the interpolated model. In general, the monoglycerides kinetic model can predict well for the high and low reaction temperature of 60°C and 30°C. However, the

mid-range reaction temperature at 45°C shows relatively higher errors for the initial and the final yield point using both the simulation method.

Table 4-17. The relative errors of the predicted monoglycerides concentrations via the pseudo first-order kinetic model using moving average kinetic constants simulated at five-second time-step.

	Concentration (mol/L)								
Temperature (°C)	30			45			60		
	Experimental	Simulated	RelErr	Experimental	Simulated	RelErr	Experimental	Simulated	RelErr
Time (s)									
0	0.001246	0.001246	0.00%	0.030155	0.030155	0.00%	0.001214	0.001214	0.00%
10	0.001155	0.001215	5.14%	0.029077	0.028908	0.58%	0.001116	0.001204	7.91%
20	0.001057	0.001128	6.71%	0.024892	0.027911	12.13%	0.001134	0.001154	1.81%
30	0.000940	0.000967	2.89%	0.022354	0.027297	22.11%	0.000878	0.000934	6.45%
40	0.000586	0.000684	16.74%	0.017927	0.022337	24.60%	0.000464	0.000549	18.46%
60	0.000765	0.000630	17.61%	0.015549	0.018550	19.30%	0.000366	0.000330	9.95%
80	0.000741	0.000709	4.32%	0.011409	0.011705	2.60%	0.000203	0.000210	3.46%
100	0.000696	0.000679	2.42%	0.010050	0.007145	28.91%	0.000200	0.000159	20.29%
120	0.000652	0.000637	2.35%	0.008867	0.006346	28.43%	0.000184	0.000152	17.45%
180	0.000574	0.000559	2.55%	0.007846	0.005579	28.89%	0.000186	0.000146	21.37%
270	0.000393	0.000432	10.11%	0.007091	0.004576	35.47%	0.000191	0.000149	21.87%
420	0.000244	0.000284	16.10%	0.007030	0.003861	45.08%	0.000223	0.000163	26.83%
600	0.000219	0.000198	9.87%	0.005889	0.003199	45.67%	0.000274	0.000211	23.05%
750	0.001246	0.001246	0.00%	0.030155	0.030155	0.00%	0.001214	0.001214	0.00%
900	0.001155	0.001215	5.14%	0.029077	0.028908	0.58%	0.001116	0.001204	7.91%
1200	0.001057	0.001128	6.71%	0.024892	0.027911	12.13%	0.001134	0.001154	1.81%
1500	0.000940	0.000967	2.89%	0.022354	0.027297	22.11%	0.000878	0.000934	6.45%
1800	0.000586	0.000684	16.74%	0.017927	0.022337	24.60%	0.000464	0.000549	18.46%
2700	0.000765	0.000630	17.61%	0.015549	0.018550	19.30%	0.000366	0.000330	9.95%

Table 4-18. The relative errors of the predicted diglyceride concentrations via the pseudo first-order kinetic model using interpolated moving average kinetic constants simulated at five-second time-step.

	Concentration (mol/L)								
Temperature (°C)	30			45			60		
	Experimental	Simulated	RelErr	Experimental	Simulated	RelErr	Experimental	Simulated	RelErr
Time (s)									
0	0.001246	0.001246	0.00%	0.030155	0.030155	0.00%	0.001214	0.001214	0.00%
10	0.001155	0.001181	2.21%	0.029077	0.028861	0.74%	0.001116	0.001188	6.52%
20	0.001057	0.001111	5.04%	0.024892	0.028303	13.70%	0.001134	0.001126	0.67%
30	0.000940	0.000911	3.09%	0.022354	0.026133	16.91%	0.000878	0.000845	3.73%
40	0.000586	0.000746	27.32%	0.017927	0.022403	24.97%	0.000464	0.000555	19.73%
60	0.000765	0.000753	1.47%	0.015549	0.016881	8.57%	0.000366	0.000356	2.86%
80	0.000741	0.000779	5.17%	0.011409	0.009895	13.26%	0.000203	0.000239	18.15%
100	0.000696	0.000739	6.17%	0.010050	0.007279	27.56%	0.000200	0.000204	1.96%
120	0.000652	0.000693	6.20%	0.008867	0.006645	25.06%	0.000184	0.000197	7.02%
180	0.000574	0.000572	0.33%	0.007846	0.005641	28.10%	0.000186	0.000195	4.85%
270	0.000393	0.000406	3.43%	0.007091	0.004689	33.87%	0.000191	0.000206	7.99%
420	0.000244	0.000310	26.81%	0.007030	0.004174	40.63%	0.000223	0.000225	0.89%
600	0.000219	0.000309	40.89%	0.005889	0.004170	29.19%	0.000274	0.000225	17.78%
750	0.001246	0.001246	0.00%	0.030155	0.030155	0.00%	0.001214	0.001214	0.00%
900	0.001155	0.001181	2.21%	0.029077	0.028861	0.74%	0.001116	0.001188	6.52%
1200	0.001057	0.001111	5.04%	0.024892	0.028303	13.70%	0.001134	0.001126	0.67%
1500	0.000940	0.000911	3.09%	0.022354	0.026133	16.91%	0.000878	0.000845	3.73%
1800	0.000586	0.000746	27.32%	0.017927	0.022403	24.97%	0.000464	0.000555	19.73%
2700	0.000765	0.000753	1.47%	0.015549	0.016881	8.57%	0.000366	0.000356	2.86%

4.5.1.7 RVC mass transfer

In the batch-type stirred-tank reactor, the reaction system can be described as a pseudo homogeneous phase without restrictions on its mass transfer [225]. Nevertheless, the transesterification kinetics mechanism is proposed to consist of an initial mass transfer-regulated region accompanied by a kinetically-controlled region, then the equilibrium stage [57,225,255].

In this study, the suggested mechanisms are similar as mentioned in Section 3.2, where the mass transfer limited region is relatively small as it is eliminated during preliminary studies of RVC

operating conditions as shown in Section 4.2.3.2. The lack of significant mass-transfer region is also reflected in the overall shape of the methyl ester yield results, where two out of three features of the proposed sigmoidal kinetics were observed. However, the mass-transfer limited region will still exist due to the immiscible nature of the two reactants as the transesterification reaction occurs initially.

The change in the oil-alcohol miscibility can be an effect of increased reaction temperature, which increases the solubility of the two reactants with each other, or the presence of methyl ester which acts as a cosolvent between oil and alcohol. In the case of methyl ester acting as a mutual solvent, the factors such as catalyst loading and alcohol to oil molar ratio that would affect the formation of methyl ester will have a greater impact.

In essence, when the triglycerides are in contact with the alcohol initially, the main reason of the bottleneck for triglyceride mass transfer is due to the limited availability of an active specific catalyst surface, largely covered by adsorbed alcohol molecule. Additionally, the initial formation of methyl ester would more likely be dissolved in the methanol phase, reducing the cosolvent capability to enhance miscibility. As the reaction progresses, the concentration of the adsorbed alcohol reduces, allowing both the available active site of catalyst to bind with the triglycerides, resulting in a net increase in mass transfer rate and reduction in kinetic rates [256].

Many biodiesel reactors are designed specifically to address the mass-transfer issue as discussed. For instance, ultrasonic irradiation which promotes micro-emulsion due to the cavitation effect were studied to enhance biodiesel yield [257]. The cavitation implosion would lead to a micro-turbulent effect in the reactor which directly promotes mass transfer. In the case of using the RVC reactor, the high shear strength of the material combined with the reticulated surface would also produce micro-turbulence when used as an agitator. The high porosity of the material would have an added benefit of secondary effect as the mesh-like structure effectively increases the total surface area in the reactor, promoting simple diffusion between oil and alcohol.

Therefore, the transesterification process occurs simultaneously with several side mechanisms in this study, including saponification and neutralisation of free fatty acids due to the use of base catalyst. However, in the following mass transfer model, these side reactions will be ignored as the free fatty acid content is negligible as virgin oil is used. The saponification reaction would also be insignificant as studies showed that methyl ester yield loss is less than three molar percentages at 1 wt. % KOH catalyst loading, 6:1 methanol to oil molar ratio, and a reaction temperature of 65°C [233]. Additionally, as triglycerides react with the methanol during the initial heterogeneous phase, then transition into a pseudo homogeneous phase as more methyl ester is being produced (mutual solvent). The kinetics mechanism will be mainly controlled by mass transfer briefly initially (physical-limiting), followed by chemical equilibrium (reaction-limiting) [57,209,213,237,258].

Therefore, according to the assumptions made, the rate of triglyceride depletion must total to the rate of triglyceride mass transfer from the oil phase into the emulsified methanol initially as presented below [237,259,260],

$$-r_A = -\frac{dC_a}{dt} = k_c a\left(C_A - C_{A,S}\right) = k' C_A \quad \text{Eq. 4-6}$$

Where the k_c is the triglycerides mass transfer coefficient, a is the specific interfacial area, C_a and $C_{A,s}$ is the triglycerides concentrations in the oil phase and on the interfacial area, respectively. The $C_{A,s}$ would be zero as the chemical reaction is relatively faster than the mass transfer rate at the interfacial area. Therefore, the triglyceride concentration in bulk, C_A can be simplified in terms of conversions as below,

$$C_A = C_{A_0}(1 - x_A) \quad \text{Eq. 4-7}$$

$$x_A = 1 - \frac{C_A}{C_{A_0}} \quad \text{Eq. 4-8}$$

Where x_A is the conversion of triglyceride and C_{A0} is the initial triglyceride concentration. Therefore, using the Eq. 4-7 and Eq. 4-8, the following expression can be obtained,

$$\frac{dx_A}{dt} = k'_c(1 - x_A) \quad \text{Eq. 4-9}$$

The integral form of Eq. 4-9 can be rewritten with respect to the conversion of triglycerides, x_A as below,

$$\int_0^{x_A} \frac{1}{1 - x_A} dx_A = f(x_1) = k'_c t \quad \text{Eq. 4-10}$$

The function in Eq. 4-10 can be expressed as a linear equation where k'_c is the gradient of the equation. Thus, the overall volumetric triglyceride mass transfer coefficient can be determined by the slope of the equation with the RVC reactor at the various reaction temperature.

The mass transfer-controlled regime is described as the beginning section of a sigmoidal profile where the “S” starts. To determine the mass transfer region in the RVC study, the conversion of triglycerides data was fitted based on the Boltzmann function [237,254,259]. Figure 4-69 shows the Boltzmann function sigmoidal fit of the triglyceride conversion at the mass-transfer region of transesterification for RVC at reaction temperatures of 30°C, 45°C, and 60°C.

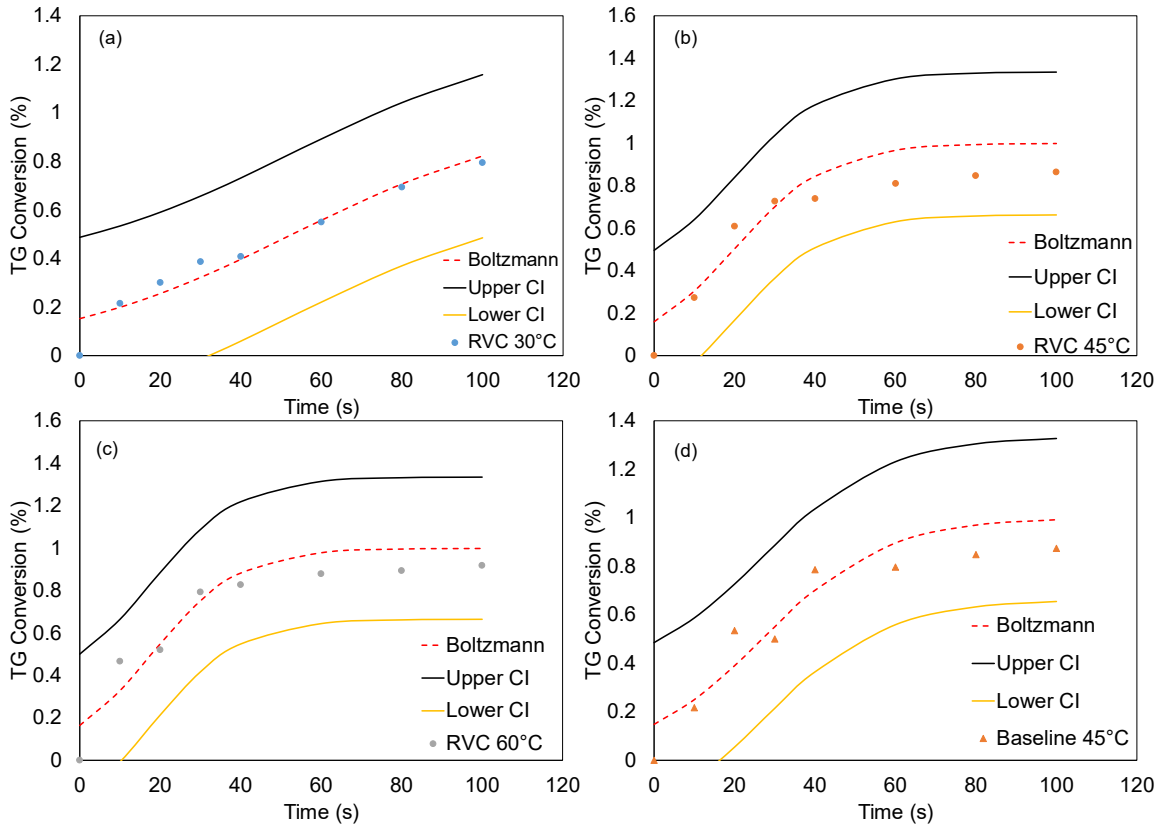

Figure 4-70. The Boltzmann function of sigmoidal fit at the mass-transfer limiting region of (a) RVC 30°C, (b) RVC 45°C, (c) RVC 60°C, (d) Baseline 45°C.

Based on Figure 4-69, the sigmoidal profile for the conversion of triglycerides is more pronounced at the lower reaction temperature of 30°C, while at an elevated reaction temperature the reaction accelerates past the mass-limiting phase in the initial stage of transesterification. Thus, upon verifying the mass transfer regime of the RVC transesterification reaction, the mass transfer coefficient is determined by plotting Eq. 4-10 with respect to time, as shown in Figure 4-70.

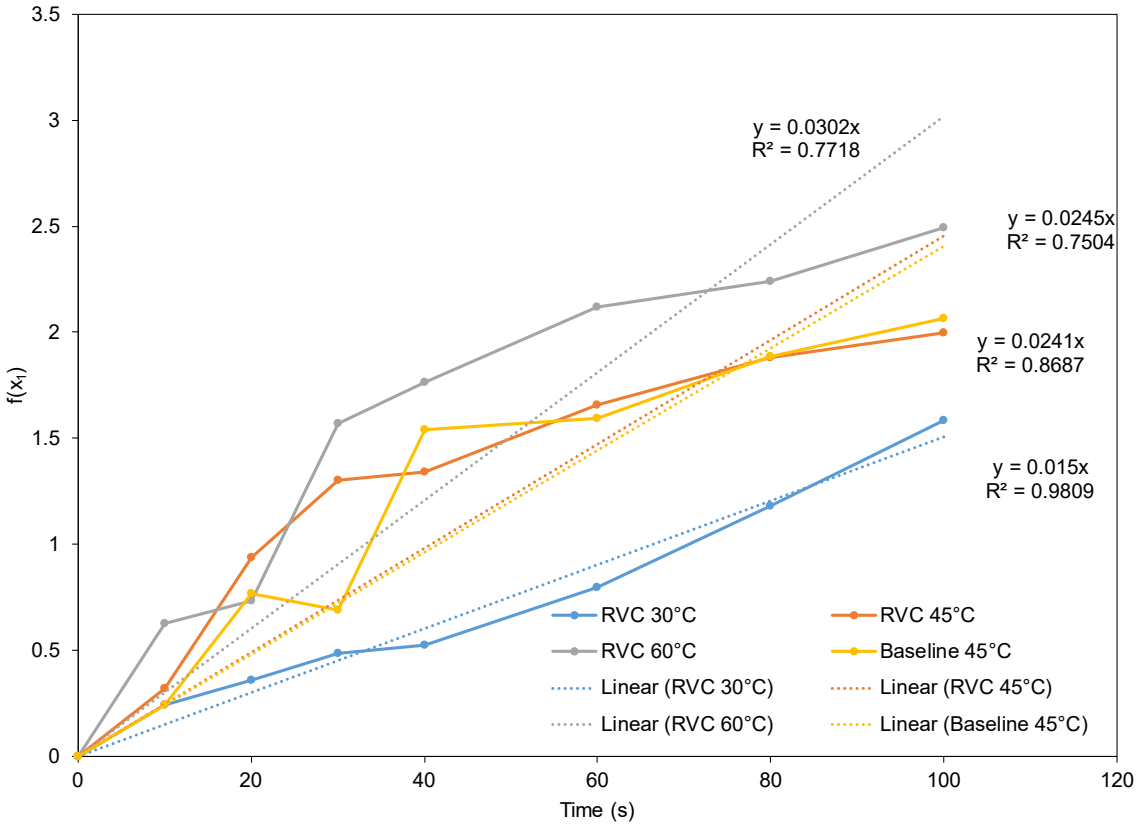

Figure 4-71. The time-averaged triglycerides mass transfer coefficient at 30°C, 45°C, and 60°C of RVC reaction and baseline.

Based on Figure 4-70, the mass transfer of RVC reactor increases as reaction temperature increases. From 0s to 30s at 45°C, the figure shows that the RVC reactor has a higher increase in mass transfer than the baseline case during the initialisation phase. This is likely due to the result of the RVC material to shear the reactants more effectively causing micro-turbulence to increase the effective surface area, leading to a higher mass transfer rate. However, the baseline case shows a sudden increase in mass transfer at 40s, followed by a decrease to slightly below the mass transfer of RVC reactor at 60s.

Table 4-19 shows the calculated mass transfer and pseudo first-order kinetic constant of RVC and baseline case. The RVC reactor has a higher mass transfer coefficient and pseudo first-order kinetic constant than the baseline case at 45°C. The difference between RVC and baseline reactor in the mass transfer is relatively small at 1.73%, while a larger difference can be observed for the kinetic rates at 23.69%. The higher kinetic rates would also mean that the triglycerides can be converted faster, where the overall transesterification reaction can take a shorter amount of time to achieve a complete reaction. In contrast, a higher mass transfer coefficient suggests that the glycerides react with the methanol at the liquid-liquid interface more efficiently. The increase in reaction temperature also improves the mass transfer and kinetic rates for the RVC reactor.

Table 4-19. Mass transfer coefficient and maximum kinetic constant from the pseudo first-order kinetic model with RVC reactor and baseline study.

Reactor	**Reaction Temperature (°C)**	**Volumetric mass transfer coefficient, k_c (1/min)**	**Maximum pseudo first-order kinetic constant, k (1/mol.min)**
RVC	30	0.90	1.1779
	45	1.47	2.9432
	60	1.81	3.0850
Baseline	45	1.45	2.3197

4.5.1.8 Pseudo second-order kinetic model

In the context of the reaction mechanism, second-order reactions have more limitations in theory as compared to first-order. This is largely due to the transesterification reaction's bimolecular steps, which involves the oil and alcohol molecules. Therefore, the consequence is a reaction that is second-order overall, where one is first-order in comparison to two separate reactants. However, in the case of transesterification, the overall reaction of the process is also modelled with respect to a single reactant, which is the triglycerides. According to Freedman *et al.*, Boocock *et. al*, Noureddini and Zhu, Darnoko and Cheryan [57,64,71,261], the 6:1 methanol to oil molar ratio is proposed to be a second-order kinetic model as the excess alcohol is only twice of the stoichiometry. Thus, the following integrated rate law can be written,

$$rate = k[Oil]^2 \qquad \text{Eq. 4-11}$$

Rewriting Eq. 4-11 with respect to transesterification yields the following,

$$-r_A = -\frac{dC_{TG}}{dt} = k[TG]^2 \qquad \text{Eq. 4-12}$$

Integrating the above equation will produce the concentration-time equation for transesterification kinetics,

$$k_{TG}t = \frac{1}{[TG]} - \frac{1}{[TG_0]} \qquad \text{Eq. 4-13}$$

where k_{TG} is the kinetic rates at the specified time, t is the specified time, [TG] is the concentration of triglycerides at the specified time, and [TG_0] is the initial concentration of the triglycerides. Therefore, rearranging the Eq. 4-13 with respect to 1/[TG] will result in a straight line equation. The gradient is positive as the concentration of the triglycerides is decreasing, the rate constant can also be determined by the gradient.

Freedman *et al.* [64] studied the transesterification of soybean oil with butanol and methanol using a second-order consecutive combined with a fourth-order shunt reaction kinetic model. The operating conditions for the transesterification is a 6:1 methanol to oil molar ratio, a catalyst loading of 0.5 wt. % using NaOH, and reaction temperature in the range of 20 to 60°C. The shunt-reaction scheme was introduced to accommodate biodiesel's formation without factoring the formation of diglycerides and monoglycerides. Three mol of methanol is used to directly reacting with one mol of triglycerides.

Noureddini and Zhu [57] expanded the work from Freedman *et al.* [64]. The second-order kinetic model derived from the three consecutive reactions is proposed to be adequate in terms of describing the soybean transesterification process, where the shunt-reaction scheme is excluded from the model. The observation from the initial step where the reaction is diffusion controlled has led to the presumption that the mass-limiting phase exist, followed by a reaction-controlled region. However, the initial stage of the reaction which is mass transfer-controlled was not included as it is deemed to be short and is minimised at the reaction temperatures combined with mixing intensities.

Darnoko and Cheryan [71] suggested that the transesterification kinetic model of triglycerides, diglycerides, and monoglycerides hydrolysis is a pseudo second-order for the first 30 minutes of the reaction. The study reported an operating condition of 1.0 wt. % KOH catalyst loading, with a 6:1 methanol to oil molar ratio, and a reaction temperature in the range of 50 to 60°C. This was also the first implementation of a second-order kinetic model on the intermediate steps of transesterification, disregarding the effects of diglycerides and monoglycerides formation.

In order to identify the range of the initial physical-limiting regime, the pseudo second-order transformation was applied to the triglycerides concentration from 0s to 2700s for 30°C, 40°C, and 60°C as shown in Figure 4-71.

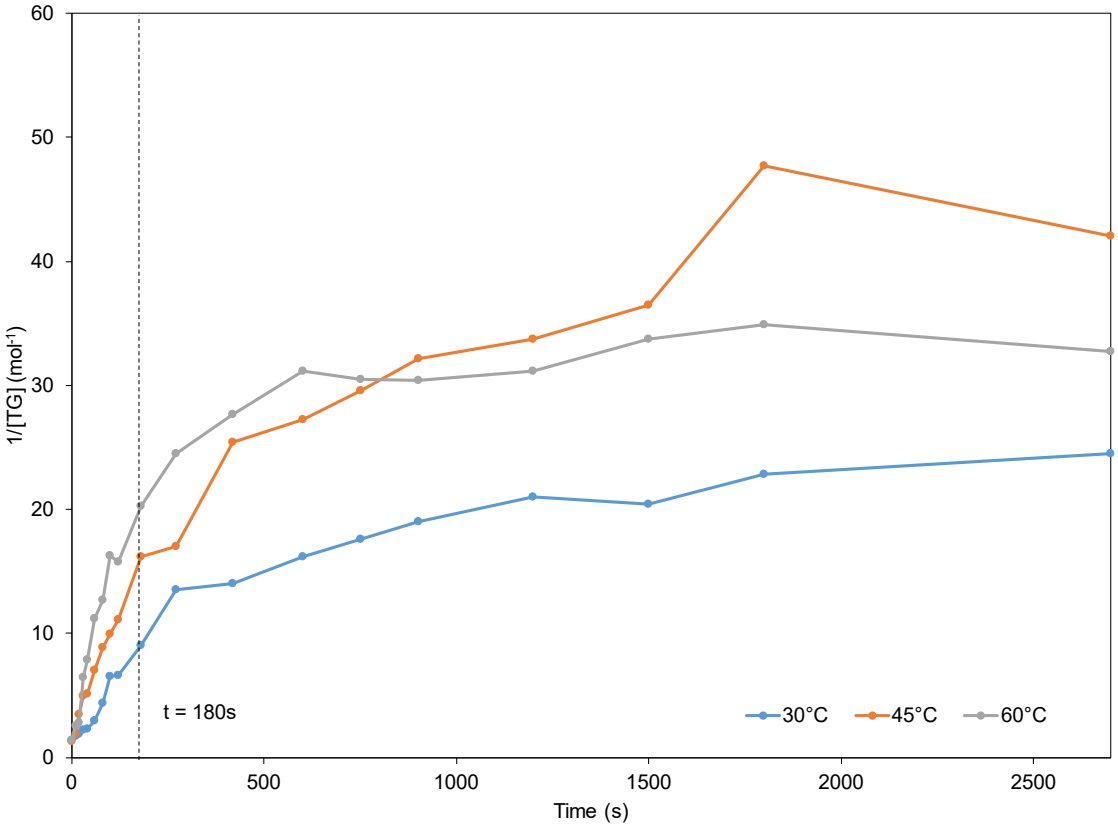

Figure 4-72. Pseudo second-order transformation of triglycerides concentration from 0s to 2700 for 30°C, 45°C, and 60°C.

Based on Figure 4-71, the linear portion of the plot can be identified from 0s to 180s, consistent with the pseudo first-order counterpart's findings. This is likely due to the influence from the physical-limiting stage as the beginning of the transesterification as explained in pseudo first-order transformation results. For the 30°C reaction temperature, the transition point and reactant-limiting stage from the Pareto analysis can be observed from the 180–270s and beyond, whereas the 45°C and 60°C are less prominent as the fluctuations are larger. The second-order transformation of the 45°C case shows a higher rate than the 60°C case beyond 750s, which suggest that more triglycerides are being hydrolysed into methyl ester and diglycerides. The overall transformation of triglycerides concentration is isolated to the initial reaction of the reaction, as shown in Figure 4-72.

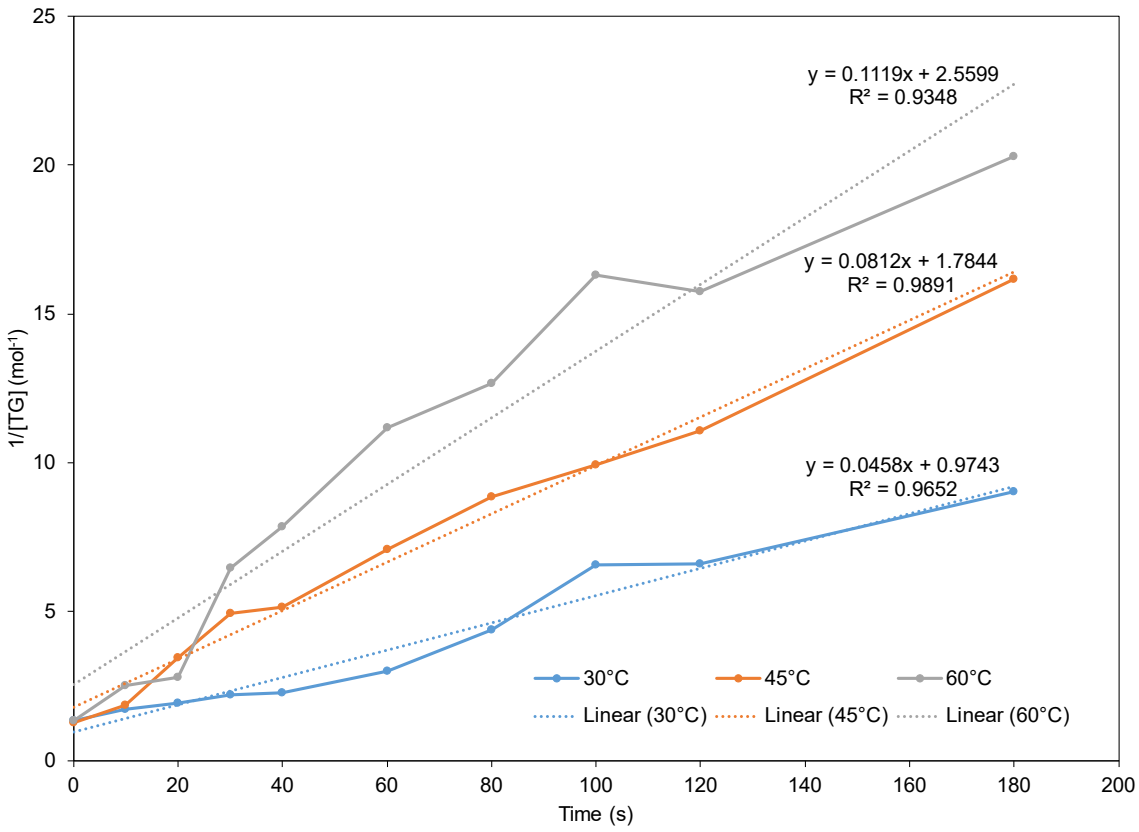

Figure 4-73. The physical-limiting regime during the initial stage of transesterification using a pseudo second-order kinetic model.

Figure 4-72 shows that the hydrolysis of triglycerides for various temperatures is well represented by the pseudo second-order kinetic model as reflected by the high linearity of the results. The kinetic rates for the initial transesterification can be determined from the gradient, where the rates of reaction are in the increasing order of k_{30}, k_{45}, and k_{60}, respectively. The three-point moving average method is also implemented to determine the instantaneous kinetic rates and inflection point of the plot, as shown in Figure 4-73.

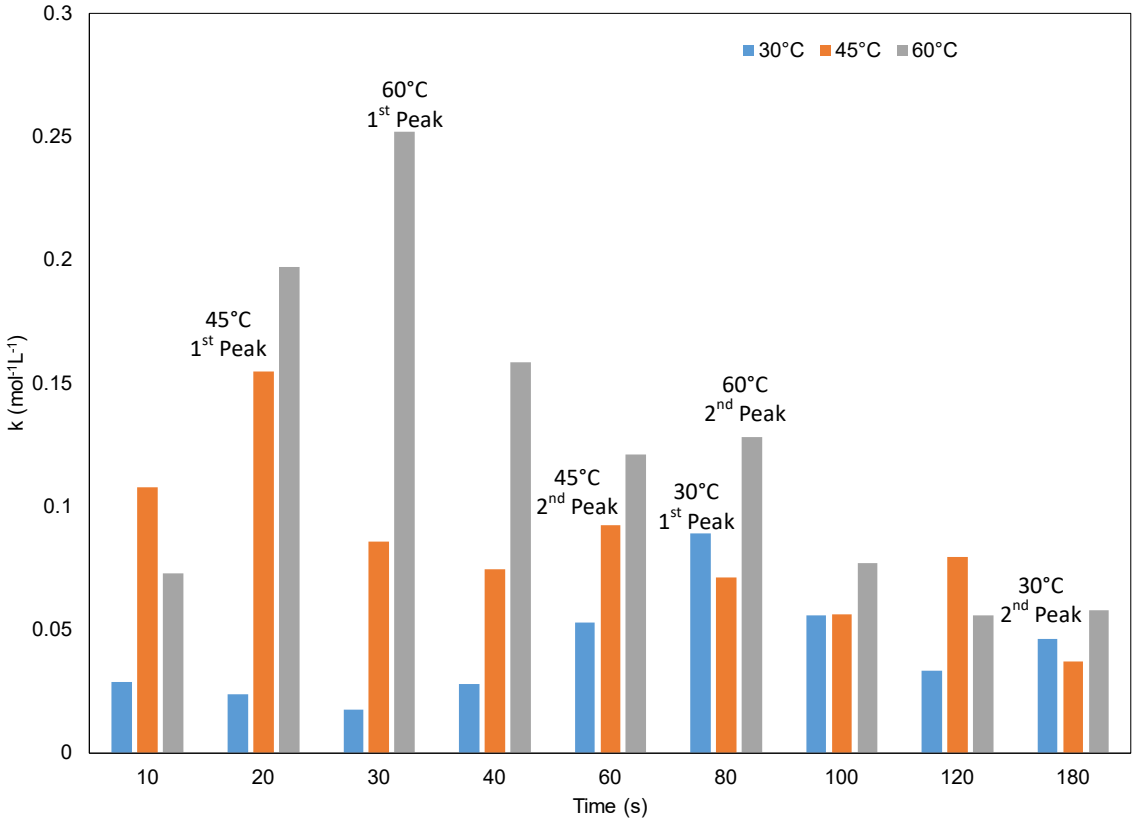

Figure 4-74. The pseudo second-order kinetic rates of triglycerides for RVC transesterification at physical-limiting stage using three-point moving average.

Based on Figure 4-73, the general trend for all reaction temperatures shows increasing kinetic rates, which 45°C reaching its peak, followed by 60°C and 30°C lagging behind. However, the magnitude of the kinetic rates for the 60°C reaction temperature is still the highest among, followed by 45°C and 30°C. Additionally, a gradual decrease in kinetic rates is observed after the peaking, followed by a secondary peak, consistent for all reaction temperature.

The methyl ester formation was also tested with the pseudo second-order kinetic model using Eq. 3-22 to study the feasibility of this reaction mechanism as an additional comparative point with the pseudo first-order methyl ester model. In theory, the equation can only hold true if the intermediate steps are negligible, meaning that diglycerides and monoglycerides are immediately hydrolysed into methyl ester, as if one mol of triglycerides molecule is reacting with three mol of methanol molecule. The initial value at 0s will be omitted as there is no methyl ester present in the reaction. The slope would be negative as the formation of methyl ester will lead to a decreasing value using the inverse function of the pseudo second-order model, as shown in Figure 4-74.

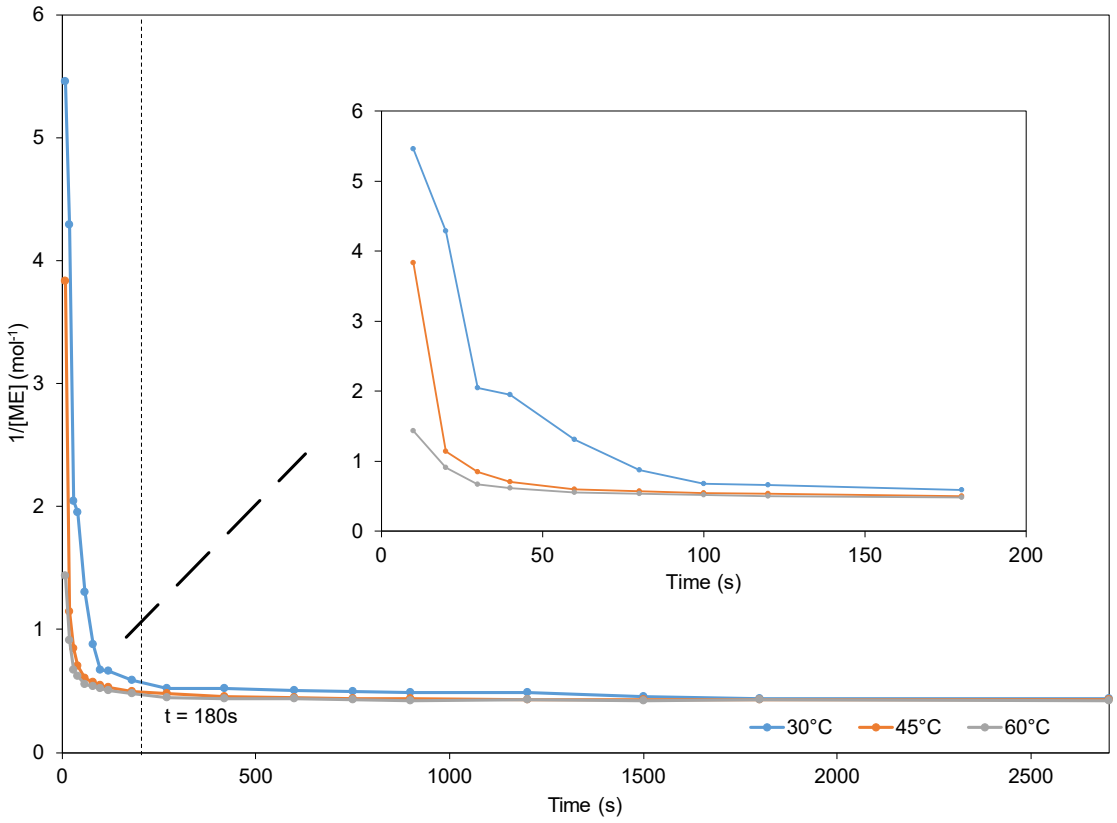

Figure 4-75. Pseudo second-order kinetics model of methyl ester formation in transesterification.

Based on Figure 4-74, the formation of methyl ester can be broken into three sections using the pseudo second-order kinetics, the initial fast converting region at the beginning, followed by a transitional mid-section which is still high in kinetic rates, and finally plateau into the equilibrium phase. As observed, the linearity of the transformation is poor which suggest that the second-order kinetics mechanism is not a good representation of the methyl ester formation. This is especially pronounced at the lower reaction temperature experiment which multiple sections can be clearly identified, followed by a diminishing characteristic with increasing reaction temperature. Additionally, the results suggest that the presumption is made where intermediate steps involving the hydrolysis of diglycerides and monoglycerides are not negligible. Therefore, the intermediate steps are incorporated into the overall equation using the equations below,

$$k_{DG}t = \frac{1}{[DG]} - \frac{1}{[DG_0]} \qquad \text{Eq. 4-14}$$

$$k_{MG}t = \frac{1}{[MG]} - \frac{1}{[MG_0]} \qquad \text{Eq. 4-15}$$

The pseudo second-order transformation is applied onto the diglycerides in Figure 4-75, using Eq. 4-14.

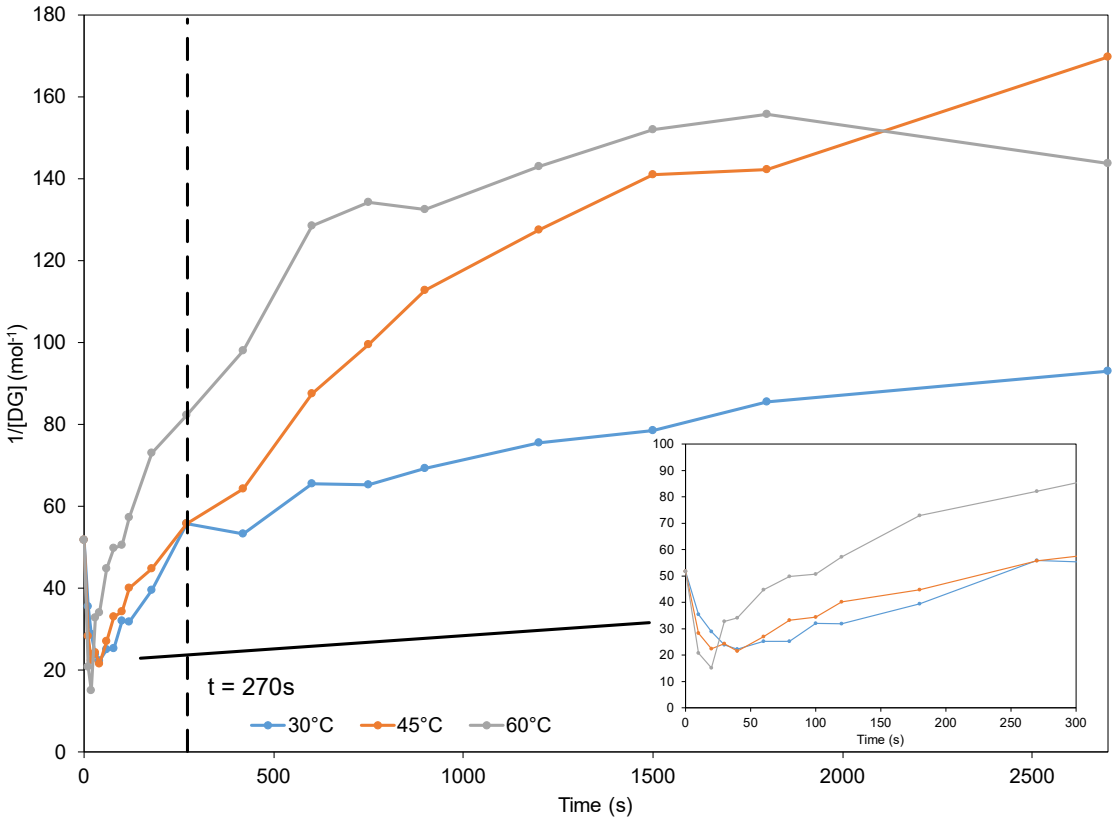

Figure 4-76. Pseudo second-order transformation of diglycerides concentration from 0s to 2700 for 30°C, 45°C, and 60°C.

Figure 4-75 shows that the formation of diglycerides can be seen from 0s to 40s which will be omitted from the kinetic model. The highlighted region is simultaneously forming and depleting diglycerides at a high rate, hence the actual rate of depletion of diglycerides will not be able to be determined. The initial stage that satisfies the pseudo order kinetic model's linear profile will be isolated from 40s to 270s. Thus, this timeline is then used to represent diglycerides' conversion as shown in Figure 4-76.

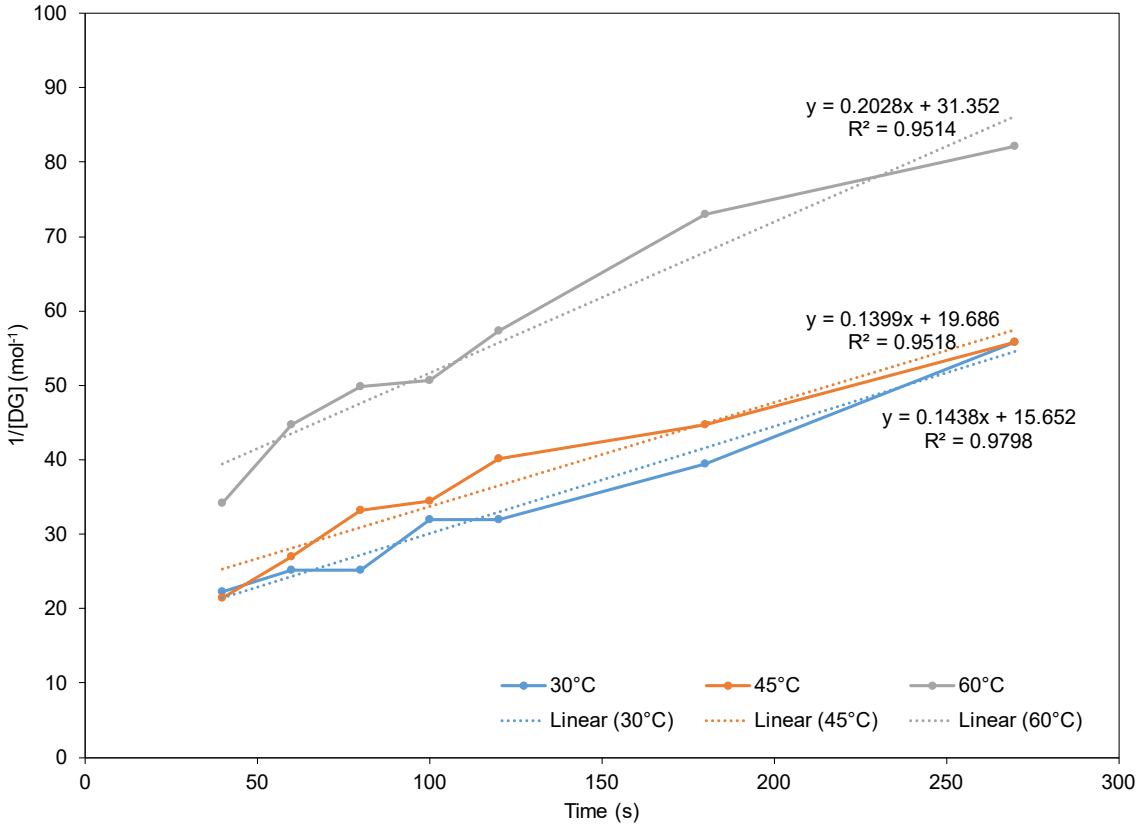

Figure 4-77. Pseudo second-order transformation of diglycerides concentration from 40s to 270 for 30°C, 45°C, and 60°C.

The overall equation of the linear fit is determined with its R^2 for each reaction temperature as shown in Figure 4-76. The results showed that the conversion of diglycerides could be a better fit using a pseudo second-order model as the R^2 is higher than the pseudo first-order counterpart. As for the kinetics rates, the general trends are similar in terms of the order of magnitude when compared with pseudo first-order. However, in the pseudo second-order kinetic model, the kinetic rate of the 30°C case is clearly higher than the 45°C. The instantaneous kinetics rates are determined using the three-point moving average for diglycerides conversion as shown in Figure 4-77.

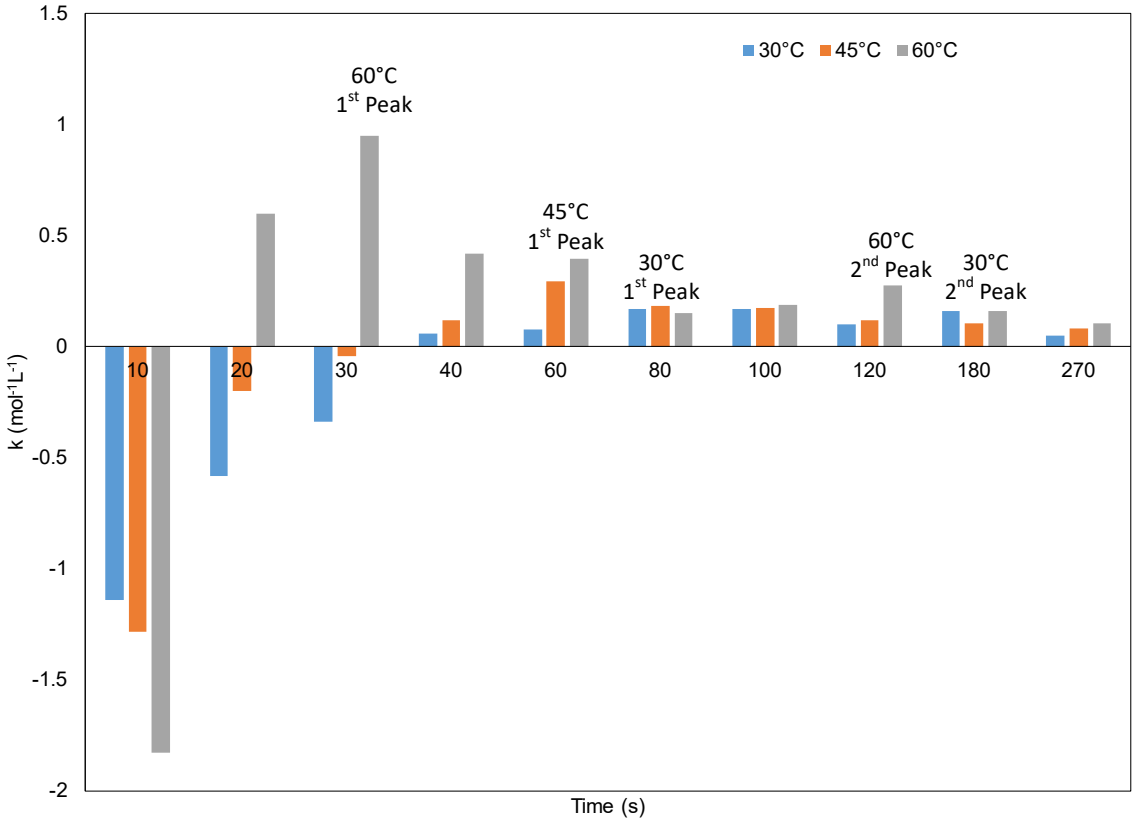

Figure 4-78. The pseudo second-order kinetic rates of diglycerides for RVC transesterification at physical-limiting stage using three-point moving average.

Based on Figure 4-77, the trend is expected as the higher reaction temperature has a faster tendency to exit the diglyceride formation dominant region due to the higher kinetic rates. At 80s, the kinetic rates for all reaction temperature were observed to stabilise. However, this is just an overlapping effect of the 60°C reduces in kinetic rate after peaking, followed by 45°C and then the peaking of 30°C, which all coincidentally aligned to a similar magnitude of kinetic rates. The second peaking of the 45°C diglycerides kinetic rate is not observed.

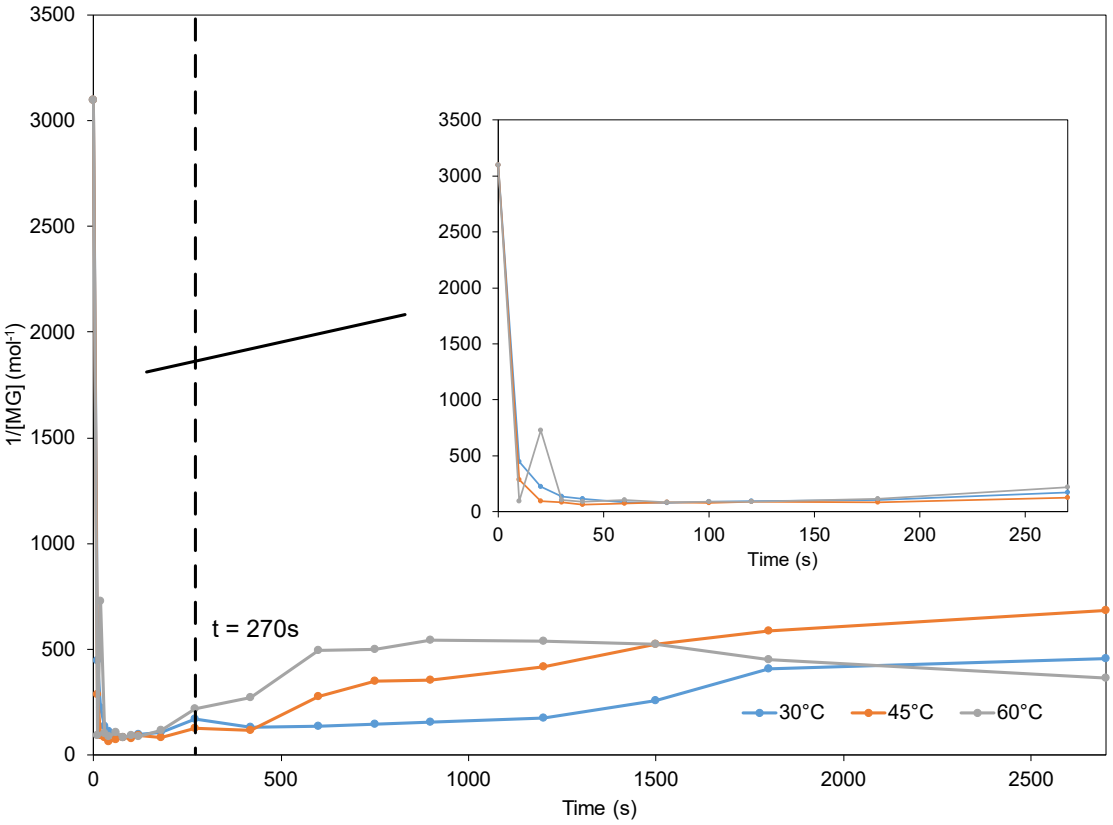

Figure 4-79. Pseudo second-order transformation of monoglycerides concentration from 0s to 2700 for 30°C, 45°C, and 60°C.

From Figure 4-78, the initial magnitude of the transformation of monoglycerides concentration is relatively large as compared to triglycerides and diglycerides, as the concentration of monoglyceride is low. Upon examining the second-order kinetics model at a small range from 0s to 270s, it can be observed that the large change in magnitude is only a small duration. Thus, this section of the results is selectively removed to improve the accuracy to model the kinetic rates of monoglycerides, as shown in Figure 4-79.

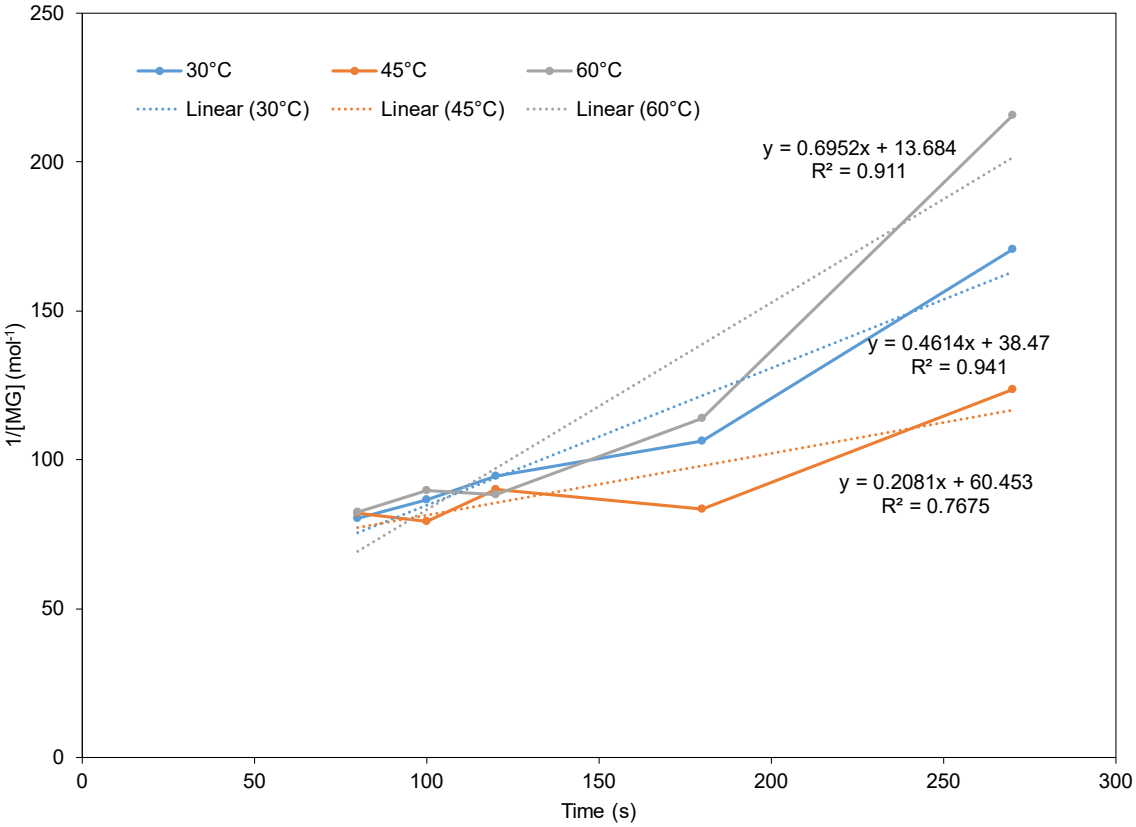

Figure 4-80. Pseudo second-order transformation of monoglycerides concentration from 80s to 270 for 30°C, 45°C, and 60°C.

The results from Figure 4-79 provides a good linear fit for the 30°C and the 60°C, while the 45°C seems to be relatively linear at first glance. The low R^2 value for the 45°C is likely due to the error being more sensitive at smaller magnitude as shown. The kinetic rates are in the increasing magnitude of 60°C, 30°C, and 45°C, which is consistent with the diglycerides conversion results. However, the 30°C shows a higher magnitude not only for the kinetic rates, but also the inverse of the monoglycerides concentration. The initial instantaneous kinetic rates of monoglycerides conversion, as shown in Figure 4-80, show a similar observation as the pseudo second-order transformation where the 45°C case has a very low kinetic rate compared to the 30°C and 60°C beyond 80s.

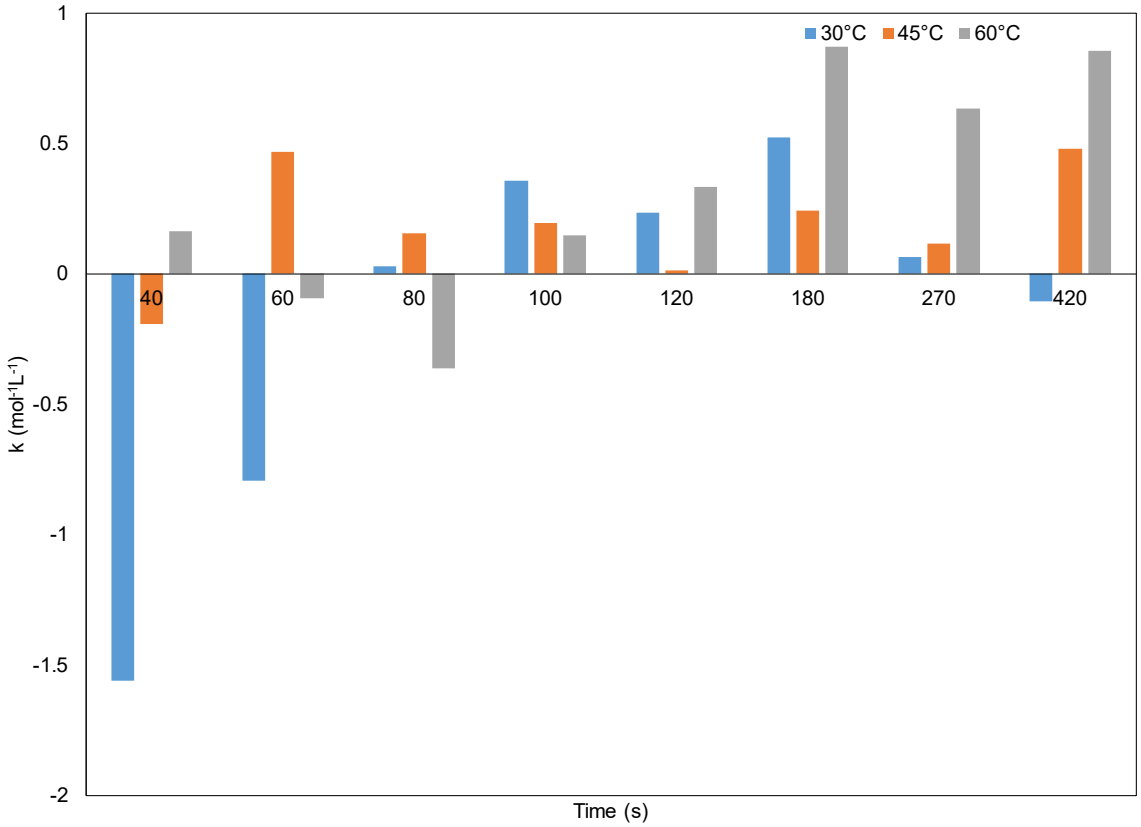

Figure 4-81. The pseudo second-order kinetic rates of monoglycerides for RVC transesterification at physical-limiting stage using three-point moving average.

The higher conversion rate of monoglycerides at 60°C results in an overall depletion of monoglycerides at 40s, which is the only operating condition with a positive kinetic rate. However, another interesting observation is that the formation of monoglycerides at 30°C and 60°C reaction temperatures have a longer delay until 80s before the depletion rate caught up, resulting in a larger change in rates. The 30°C and 60°C reaction temperature cases both peaks at 180s, before gradually dropping in kinetic rates, while peaking of 45°C reaction temperature was observed as early as 60s.

The pseudo second-order kinetic rates of the triglycerides, diglycerides, monoglycerides, and methyl ester with their respective improved model were calculated and tabulated below in Table 4-20.

Table 4-20. The kinetic rates of triglycerides, diglycerides, and monoglycerides depletion with methyl ester formation using the pseudo second-order kinetic model.

Pseudo Second-Order Kinetic Model	**Reaction Temperature (°C)**	**Moving Average Max. Kinetic Constant (dm^3/mol.min)**	**Linear Trend Gradient Kinetic Constant (dm^3/mol.min)**	**R^2 of linear trend lines**
Triglycerides depletion	30	5.353	2.748	0.9652
	45	9.276	4.872	0.9891
	60	15.119	6.714	0.9348
Diglycerides depletion	30	10.259	8.22	0.969
	45	17.509	8.352	0.9587
	60	25.036	12.66	0.9547
Monoglycerides depletion	30	31.418	27.684	0.941
	45	42.530	12.486	0.7675
	60	52.312	41.712	0.911
Methyl ester formation	30	-10.255	-0.102	0.8803
	45	-8.967	-0.186	0.7764
	60	-2.297	-1.026	0.9114

4.5.1.9 Arrhenius energy of activation

The pseudo second-order kinetics were used to calculate the activation energy of the glycerides study using Eq. 4-4. The results are plotted using the linear relationship between kinetic constant and reaction temperature with the moving average and linear fit data, as shown in Figure 4-82. The activation energy is then calculated and tabulated, as shown in Table 4-21 for the pseudo second-order kinetic model.

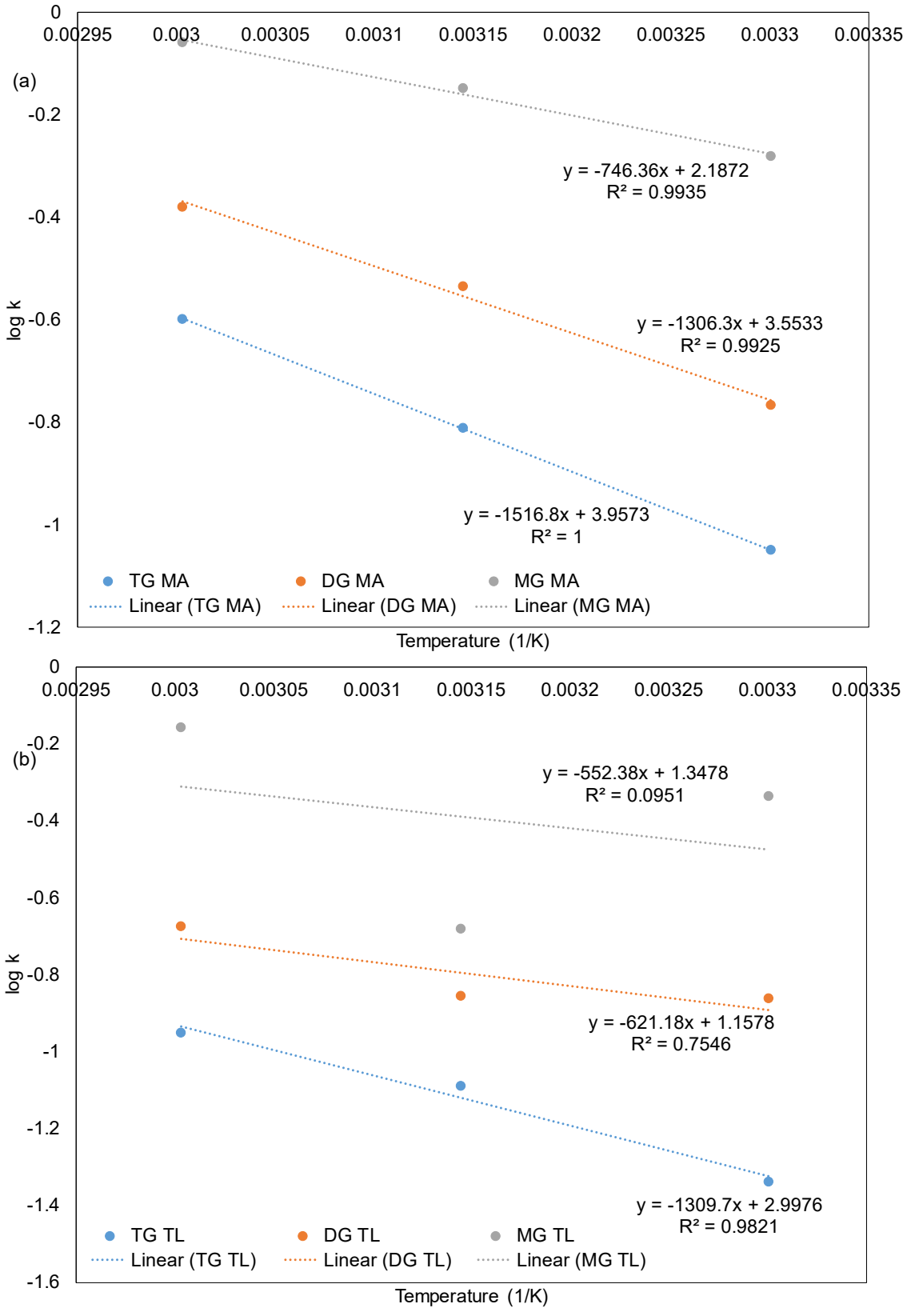

Figure 4-82. Pseudo second-order kinetic Arrhenius plot of kinetic reaction constant against reaction temperature of RVC transesterification using (a) moving average and (b) linear fit.

Table 4-21. Pseudo second-order Arrhenius activation energy for moving average and linear fit.

Pseudo First-order Kinetic Model	**Moving Average Activation Energy (kcal/mol)**	**R^2**	**Linear Trend Activation Energy Constant (kcal/mol)**	**R^2**
TG + MeOH → DG + ME	10.22	1.0000	11.04	0.9821
DG + MeOH → MG + ME	9.54	0.9925	10.18	0.7546
MG + MeOH → G + ME	8.50	0.9935	9.10	0.0951

Figure 4-82 shows a similar order in terms of magnitude for each different temperature across the methods of approach. However, the Arrhenius equation from the monoglycerides extracted using the linear trend line (MG TL) showed relatively poor linearity, most likely due to the 45°C cases being an outlier. The moving average calculation in this case shows better consistency across the glycerides Arrhenius equation at different temperatures, hence this is the favoured methodology for second-order kinetics. The activation energy was determined based on the figures, where both methods show a similar trend. The activation energy is in the descending order of magnitude of triglycerides, diglycerides, and monoglycerides in terms of the conversion reaction. Table 4-22 shows the activation energy of triglycerides, diglycerides, and monoglycerides conversion from other similar experiments, using homogeneous base-type transesterification.

Table 4-22. The activation energy of homogeneous base-type catalysed transesterification.

Feedstock	**Alcohol**	**Catalyst Loading (wt. %)**	**Molar Ratio**	**Temperature (°C)**	**Reaction Mechanism; Kinetic model**	**Activation energy (kJ/mol)**	**Ref.**
Palm	Methanol	KOH 1.0	6	55−65	Reversible second-order	TG: 14.7 DG: 14.2 MG: 6.4	[71]
Palm	Ethanol	NaOH 1.0	12	25–55	Irreversible second-order	TG: 42.36	[234]
Soybean	Butanol	NaOBu 1.0	6	20−60	Reversible second-order	TG: 15.7 DG: 13.1 MG: 13.4	[64]

Soybean	Methanol	NaOH 0.2	6	30–70	Reversible second-order		[57]
Sunflower	Methanol	KOH 0.5–1.5	6	25–65	Reversible second-order	TG: 31.6 DG: 41.6 MG: 5.96	[213]
Sunflower	Methanol	KOH 1.0	6	10–30	Irreversible Pseudo second-order	TG: 53.5 DG: 33.2 MG: 34.2	[237]
Sunflower	Ethanol	KOH 0.75–1.25	6–12	25–75	Irreversible pseudo second-order	8.3 – 35.1	[225]
Canola	Ethanol	MgCoAl-LDH 2.0		140–200	Pseudo first-order	TG: 60.5	[240]
Castor	Ethanol	NaOH 1.0	12	30–70	Pseudo first-order	TG: 70.6	[241]
Palm	Methanol	KOH 1.0	6	30–60	Irreversible pseudo second-order	TG: 10.22 DG: 9.54 MG: 8.50	This work
Palm	Methanol	KOH 1.0	6	30–60	Irreversible pseudo first-order	TG: 13.23 DG: 14.51 MG: 14.58	This work

According to Table 4-22, the activation energies found in this work for pseudo first-order and pseudo second-order are in the same order of magnitude and agrees well with the other reported glycerides studies. The pseudo second-order decreases in activation energy as conversion occurs, while the pseudo first-order has increasing activation energy values. The decreasing trend in the order of magnitude for activation energy found in the second-order model is consistent with the other activation energy studies.

For the pseudo second-order model, when compared with other reported studies that calculate for all glycerides (triglycerides, diglycerides, and monoglycerides), the activation energy in this work is significantly lower, except for the monoglyceride activation energy reported by Darnoko and

Cheryan [71], Vicente et al. [213] at 6.4 kJ/mol. This suggests that among the similar experiments of using batch reactor at comparable operating conditions, the RVC reactor would perform more efficient for biodiesel transesterification as reflected by the results.

Another noticeable trend from Table 4-22 is that the studies that do not include modelling the intermediates such as diglycerides and monoglycerides tend to have higher activation energy to convert triglycerides. These studies use the assumption of fast converting intermediates, where the kinetic rates are negligible. However, the kinetic rates are relatively significant for the intermediates, particularly for the physical-limiting stage as it would define how quick the reaction transition into chemical equilibrium.

Based on Table 4-22, there is a lack of pseudo first-order kinetic model which involves all three glycerides, hence no complete transesterification activation energies were reported in the available literature. The activation energy values are vital to the foundation of developing a kinetic model, as it provides information on how the connections exist among particle kinetic energy, temperature, and energy required for the reaction [262]. Therefore, in this study, the extension of the pseudo first-order kinetic model which integrates the intermediate reactions allows the individual activation energy to be calculated, which is important to understand the transesterification reaction kinetic model as a whole. The reported values in this study are also relatively lower than the other activation energies, when compared only using triglycerides conversion results. This would suggest that the overall kinetics of transesterification is greater with the aid of RVC microturbulence agitation. In all, the linear trend method is suitable for the pseudo first-order kinetic model, while the moving average method is more feasible for the pseudo second-order kinetic model to calculate the activation energy.

4.5.1.10 RVC reaction kinetics compared with baseline

The baseline test was conducted to determine the glycerides content through the EN14105 methodology, where 19 samples were taken between 0s to 2700s. The concentration of the glycerides was processed and analysed to form a benchmark against the RVC study. The pseudo first-order kinetic model was applied to the tri-, di-, monoglycerides to obtain the kinetic rates, as the baseline study can also be modelled via the first-order mechanism using assumptions from Eq. 3-18 and Eq. 3-19. Figure 4-83 shows the pseudo first-order transformation of the triglycerides for RVC and baseline at 45°C throughout the transesterification process.

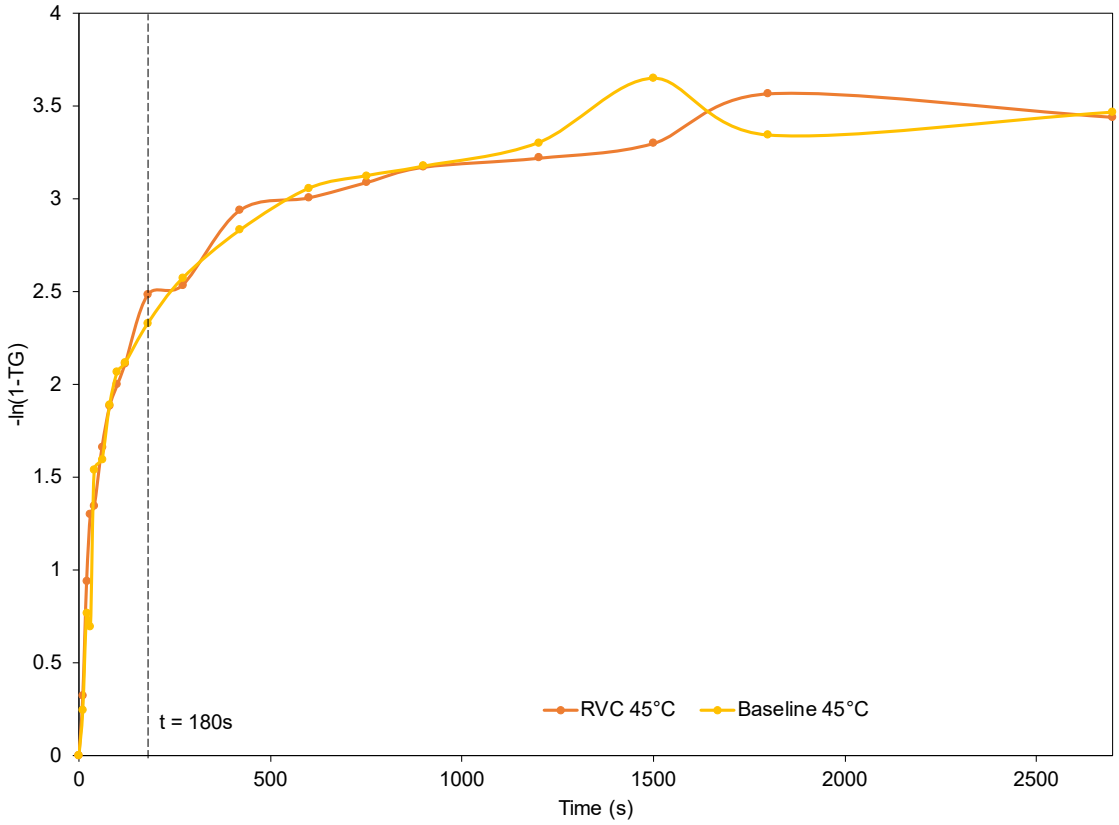

Figure 4-83. Pseudo first-order transformation of triglycerides concentration of RVC and baseline at 45°C.

The RVC and baseline study at 45°C shows a similar trend via the first-order mechanism for both the fast reacting physical-limiting regime and the slow reacting equilibrium phase. However, the main benefit of using a high surface area porous material like RVC is the ability to enhance mixing between reactants, particularly where the effect of agitation is the most significant for transesterification. Therefore, according to the Pareto analysis on the effect of agitation conducted in Figure 3-5 and RPM response surface methodology study in Figure 4-33, the timeframe of interest is located at the initialisation phase which is physical-limiting as presented in Figure 4-84.

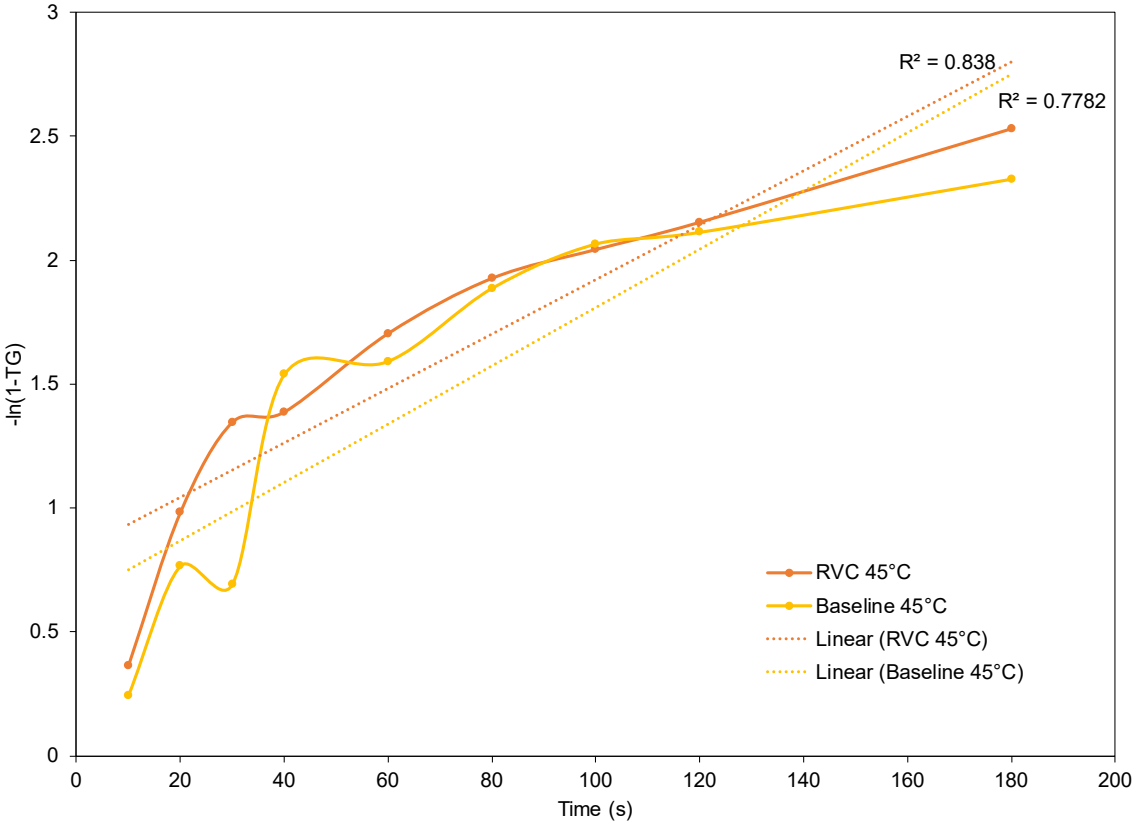

Figure 4-84. The physical-limiting regime during the initial stage of transesterification of RVC and baseline at 45°C.

Based on Figure 4-84, the RVC kinetic model shows a better fit with the linear relationship of the pseudo first-order kinetic model as compared to the baseline, represented through the R^2 of the linear trend line. In terms of kinetic rate, the RVC reactor shows slightly higher reaction rates from 0s to 30s, suggesting an adequate mixing for the heterogeneous phase of oil and methanol during initialisation. In contrast, the baseline case shows a larger gradient as compared to the RVC, but this could be due to propagated error as suggested by the weak linearity of the pseudo first-order. The results here supported the findings from the previous study on using RVC and compared with baseline in the preliminary experiments where the 20 ppi RVC has a greater effect on methyl ester yield. The faster depletion of triglycerides would also accelerate the transesterification to transition from the physical-limiting to reaction-limiting where the final yield can be achieved earlier. The kinetics of triglycerides depletion should be investigated and calculated to validate the previous statement. Thus, Figure 4-85 shows the kinetic constant of the triglyceride depletion kinetic model using the three-point moving average technique which simulates an instantaneous reaction rate. The gradient is obtained from the line formed by the three consecutive sampling point.

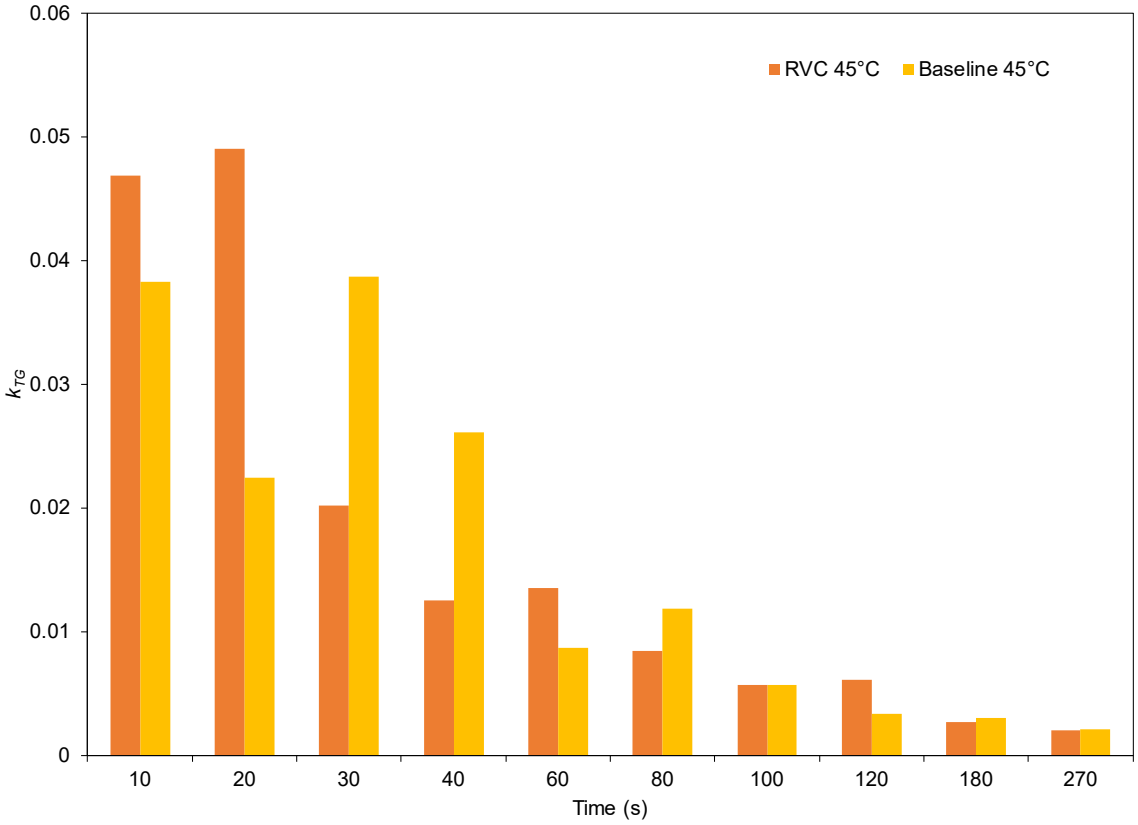

Figure 4-85. The three-point moving average triglycerides kinetic rates of pseudo first-order transesterification at the physical-limiting stage of RVC and baseline at 45°C.

From the kinetic constants of RVC and baseline as presented in Figure 4-85, the results are consistent with the observations of the pseudo first-order plot, where the RVC reactor performs better during initialisation. The higher depletion rate of triglyceride is most likely due to the combined effects of micro-turbulence generated and the enhanced surface area due to the porous nature of RVC. When compared along the timeline from 0s to 270s, the baseline case has a consistent lower kinetic rate at about 10–20s based on directly comparing the evolution of the kinetic rates. The maximum kinetic rate for RVC is 0.4916 $dm^3mols^{-1}s^{-1}$ at 10s, while the baseline is 0.03861 $dm^3mols^{-1}s^{-1}$ at 30s, where RVC shows a 24% greater performance in the beginning. Figure 4-86 shows the diglycerides kinetic rates for RVC and baseline from 10s to 270s at 45°C.

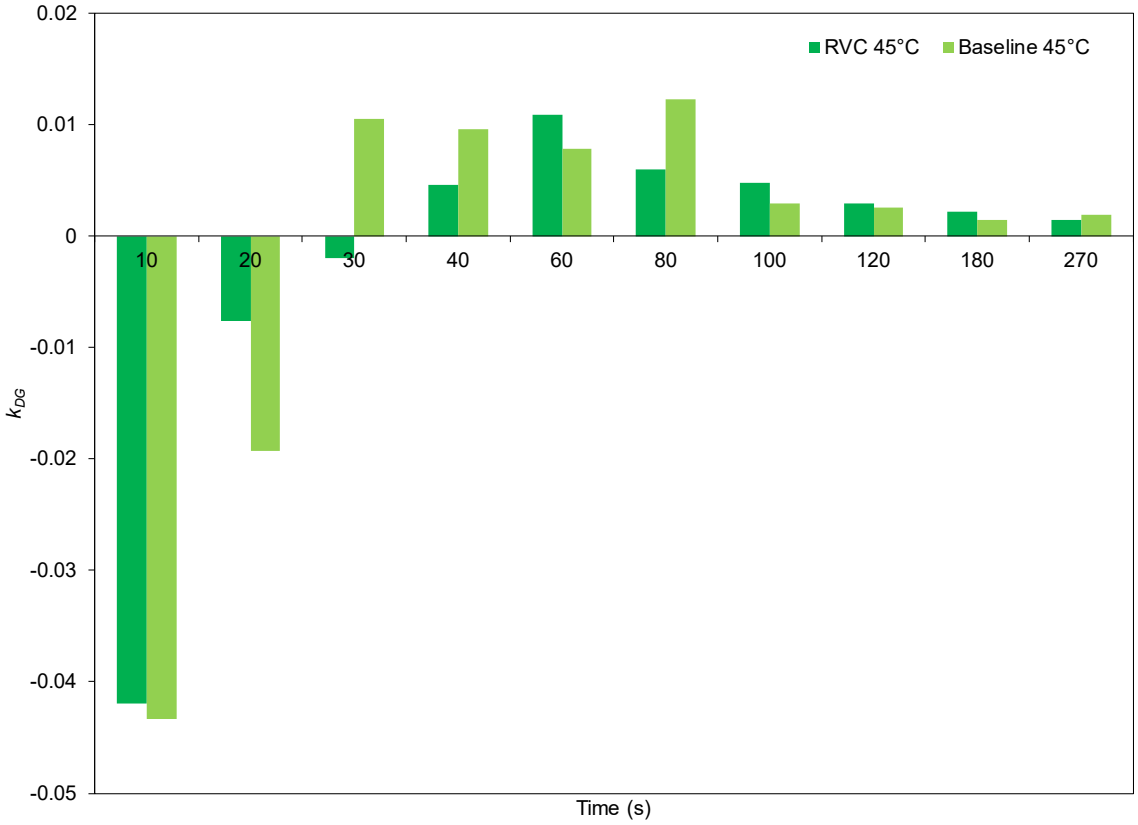

Figure 4-86. The three-point moving average diglycerides kinetic rates of pseudo first-order transesterification at the physical-limiting stage of RVC and baseline at 45°C.

The kinetic rates calculated above are a net effect of the formation and depletion kinetic rates of diglyceride. Therefore, the lower negative kinetic constants of RVC would suggest that the depletion of diglycerides is higher than the baseline, resulting in a more positive kinetic constant. As expected, RVC outperforms the baseline during the initialisation phase by a margin of 3.2% and 86.33% at 10s and 20s, respectively. However, as the mixing progresses, the baseline case would surpass in reaction rates as shown at 30s where the RVC's kinetic constant remains to be a negative value, while the baseline study for diglyceride has already transitioned to depletion dominant. As the transesterification progresses, RVC kinetic rates can be seen to peaked at 60s, followed by a gradual decrease towards 270s. In the case of baseline, the kinetic rates of diglycerides are more consistent without a significant peak, where the trend is then followed by a sharp decrease from 80s to 100s, leading to a plateau as it approaches equilibrium. The maximum kinetic rate for RVC is 0.0109 $dm^3mols^{-1}s^{-1}$ at 60s, while the baseline is 0.0122 $dm^3mols^{-1}s^{-1}$ at 80s, where baseline shows an 11.9% greater performance at its peak. Figure 4-87 shows the monoglycerides kinetic rates using the pseudo first-order model for transesterification of RVC and baseline at 45°C.

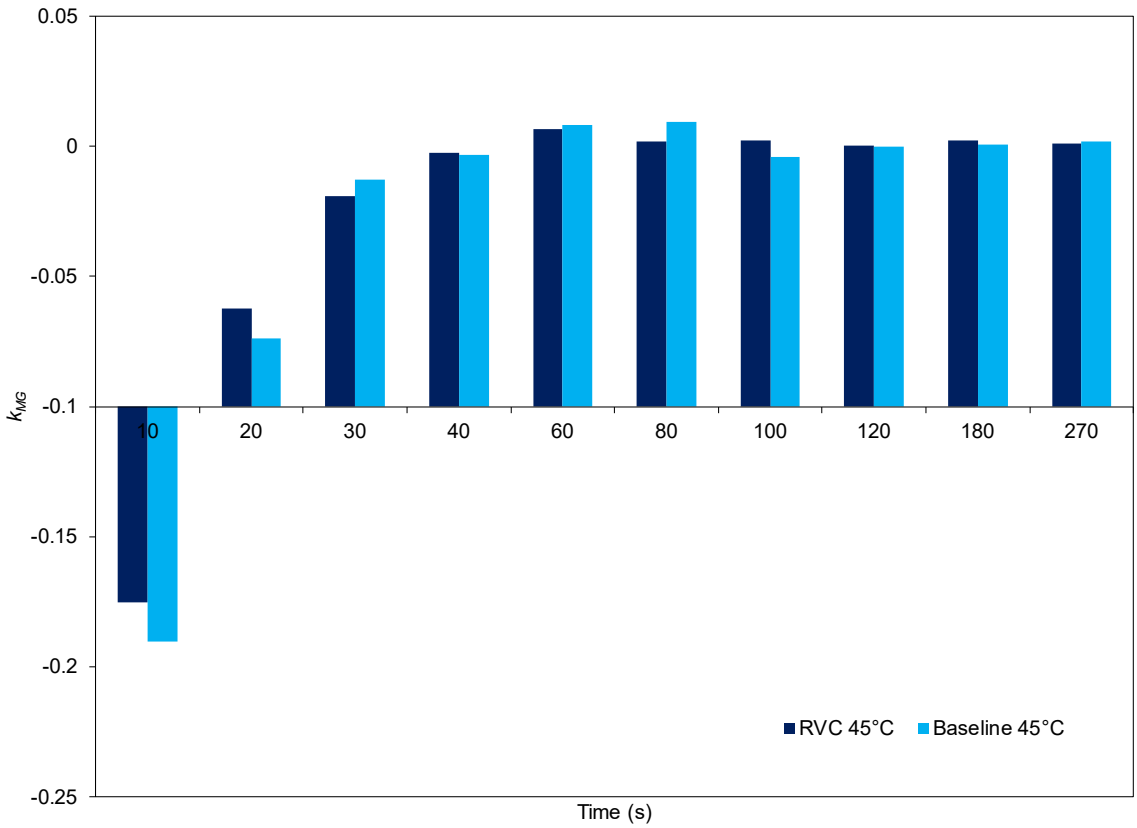

Figure 4-87. The three-point moving average monoglycerides kinetic rates of pseudo first-order transesterification at the physical-limiting stage of RVC and baseline at 45°C.

For the monoglycerides kinetic rates, the horizontal axis is adjusted to cross at −0.1 $dm^3mol^{-1}s^{-1}$ to allow better representation from the bar plots. From the analysis of triglycerides and diglycerides kinetic rates, at initialisation, a sharp increase in monoglycerides concentration is expected, which results in the negative kinetic constant shown in 10s. As expected, the higher depletion rate of triglycerides and diglycerides from the RVC reactor will consequently lead to a higher depletion rate of monoglycerides, reflected from 10s to 20s where RVC is consistently more positive than baseline. The increase in kinetic rates of the baseline study from 20s to 30s is consistent with the results from large changes in diglycerides kinetic rates. The maximum kinetic rate for RVC is 0.0065 $dm^3mols^{-1}s^{-1}$ at 60s, while the baseline is 0.0094 $dm^3mols^{-1}s^{-1}$ at 80s, where baseline shows a 36.7% greater performance with peak-to-peak behind RVC by 20s. The kinetic rates of RVC and baseline increase in a gradual trend from 30s to 60s with very small differences, where the kinetic rates plateau with minimal fluctuations from 60s onwards. Evidently, the difference in kinetic constants trend for RVC and baseline is well explained and consistent as monoglycerides' changes are a trickle effect from the precursors, diglycerides, and triglycerides.

To summarise, RVC shows faster increase in kinetic rates during the initialisation phase and peaks earlier in performance during mixing than the baseline reactor. This is consistently observed in the first-order transformation plot, triglycerides depletion kinetic rates, diglycerides conversion kinetic rates, and monoglycerides conversion kinetic rates. The result is a faster homogenisation of methanol

and oil, leading to earlier formation of biodiesel. The overall transesterification yield curve will shift as the chemical equilibrium and final yield point can be achieved sooner. Therefore, the reaction kinetics of the glycerides test are in agreement with the factorial and surface analysis, where better homogeneous mixing will have a positive impact on the final yield.

4.5.1.11 Thermal image analysis

The heat addition mechanism in the experiment is done using a heating jacket, surrounding the glass reactor controlled by a temperature controller monitoring the reactant temperature via a thermocouple probe, as illustrated in Figure 4-88. The digital images were captured by a thermal imaging unit (HT-18,) with the equipment's specifications tabulated in Table 4-23.

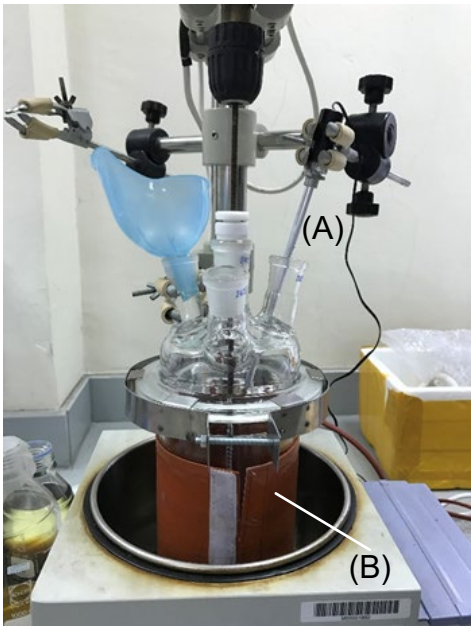

Figure 4-88. The glass reactor setup with the heating mechanism, (a) Thermocouple, (b) Heating jacket.

Table 4-23. Specification of the Thermal Imaging Unit (HT-18)

Specifications	**Value**
Temperature range	−20°C to +300°C
Maximum operating distance	2.0 m
Sensitivity	±0.07°C
Accuracy	±2.0°C or 2.0%
Acquisition refresh rate	9 Hz
Wavelength	8 to 14µm

The thermal imaging unit was setup 10cm above the surface of the reactor, and the surface temperature of the reactants was captured at different intervals for the reaction temperature of 30°C, 45°C, and 60°C. The images were later processed in MATLAB using the image processing package. Figure 4-89 shows the glyceride experiment at the reaction temperature of 45°C from 0s to 1899s.

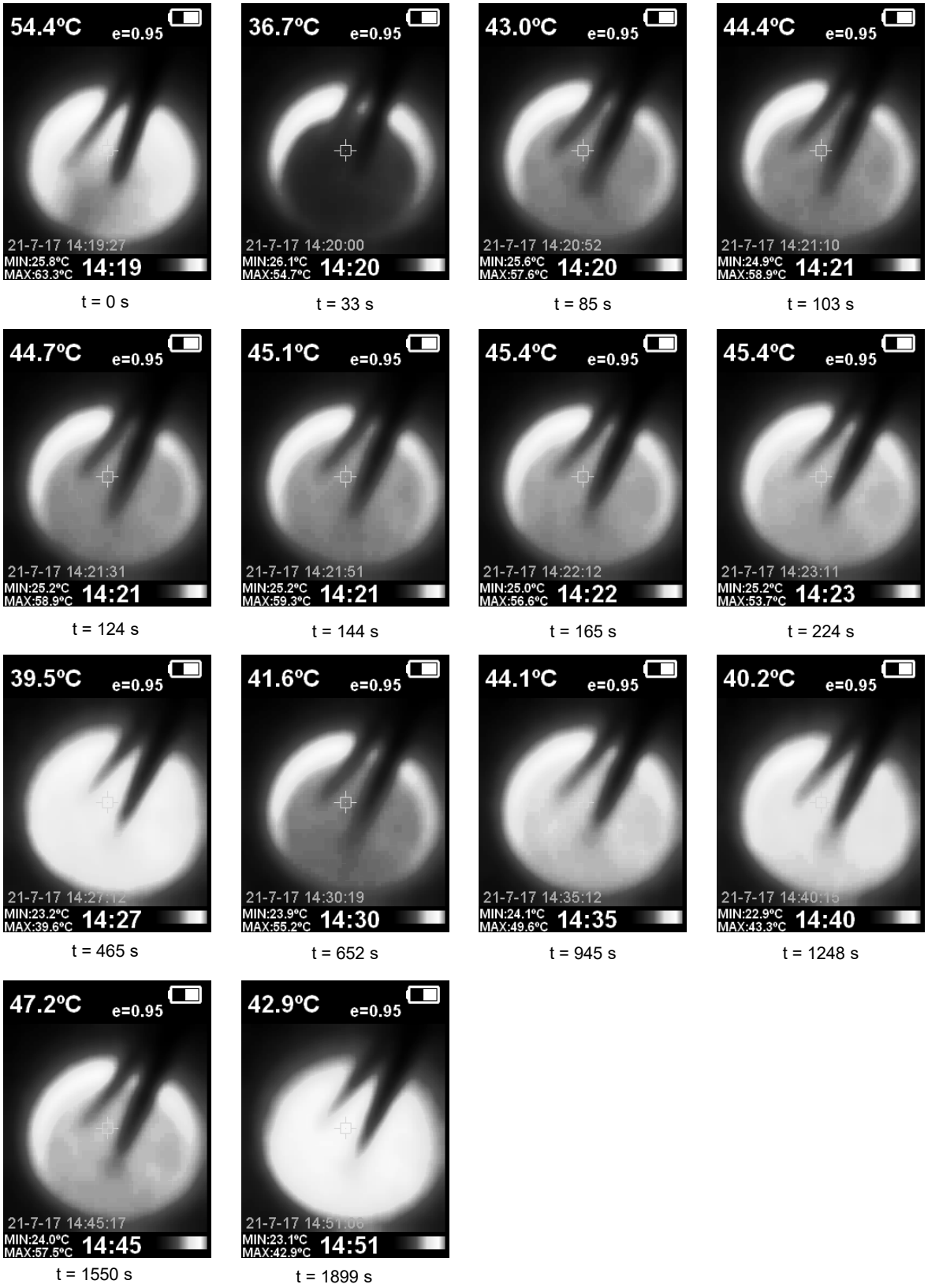

Figure 4-89. Thermal images of the RVC reactor for the glycerides experiments from 0s to 1899s, operating using 20 ppi, 45°C reaction temperature, 1wt. % catalyst loading, 300 rpm agitation speed, and 6:1 methanol to oil molar ratio.

The temperature indicated from the top left is the rectangular pointer temperature located at the centre, with the minimum and maximum temperatures of the frame located at the bottom left corner, while the colour bar (monochrome) located on the right bottom corner. From the figure, the initial temperature at 0s is 54.4°C, which is much higher than the intended 45°C to compensate for the addition of methanol when the transesterification process begins. As the methanol is added and stirring initiated, the reactant's overall temperature falls rapidly to 36.7°C as shown in 33s. The temperature controller adapts to the drop in reaction temperature from the thermocouple (black shadow in the centre), increasing the power output for the heating jacket. Thus, over time the reaction temperature slowly increases back to the set point of 45°C as illustrated in 85s onwards. The agitation speed is set at 300 rpm, where the reactants can be adequately mixed. The hot zone surrounding the sides of the reactant is the heating jacket while the colder centre zone depicts the reactants in the reactor. Moreover, the maximum temperature indicates the heating jacket's temperature, which is heating the reactants to their set point. From 144s onwards, the surface temperature of the reactants at the centre has achieved the set reaction temperature of 45°C.

The homogeneity of the heat transfer in the reactor can be visualised by implementing a series of image processing and analysis using MATLAB R2020a. Colour thresholder was implemented on the original thermal images taken in Figure 4-89, where the colorspace and range for each channel of the colorspace (RGB) were set to the temperature of interest. Thus, a masked image was produced to filter and highlight the point of interest based on the digital data of the thermal signal as shown in Figure 4-90. The red dotted circle shows the reactor's circumference, while the two yellow ellipses are the thermocouple and the overhead stirrer.

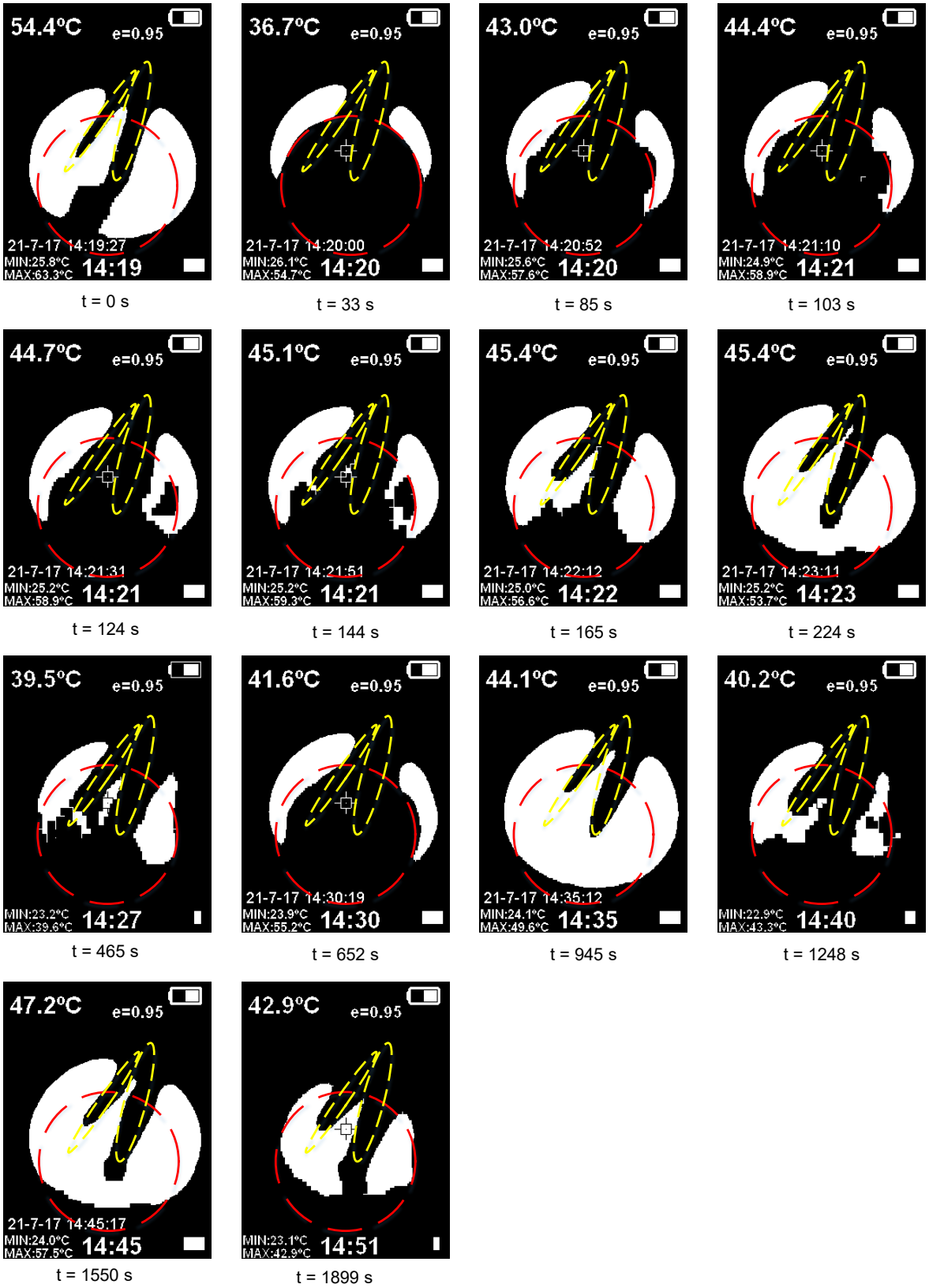

Figure 4-90. Masked thermal images of the RVC reactor for the glycerides experiments from 0s to 1899s, with the colour threshold at 45°C.

Based on the masked images, the white area shows the temperature above 45°C. Therefore, it can be observed from 144s that the area in the centre has a small spot heated to the desired temperature, while the other locations are still relatively cool. The heat can be observed to be transferred directly from the wall of the reactor, where the heating jacket is located, as the white section can be seen to engulf inwards from the outer section from 124s to 465s. A sudden drop in temperature is observed at 652s. This is then followed by compensation in heat addition via the heating jacket which is noticeable from 945s in Figure 4-90, where the surface temperature of the reactor reaches above 45°C as indicated by the white patches. As the transesterification continues at the chemical equilibrium stage, biodiesel production rate quickly falls since the triglyceride concentration is low, hence excess methanol is required for complete reaction. During the reaction-limiting stage, the fluctuations of temperature also reduce relative to the physical-limiting stage as shown from 945s to 1899s, where more than 50% of the reactor surface is at the target temperature of 45°C.

In all, the thermal image analysis can be used to identify hot and cold spots of the batch reactor, as the even distribution of heat is key to a well-designed reactor and experiment. The decrease in temperature is due to mixing a large volume of methanol which has a cooling effect. This observation is vital for understanding how transesterification kinetics reacts to the temperature change, while the kinetic rates are at its highest during the physical-limiting stage. Therefore, more accurate kinetic models can be built using the actual temperature of the reaction as captured by the thermal camera rather than assuming a uniform temperature system.

4.6 Conclusion

The idea of using a porous material as an overhead stirrer in a batch reactor is presented in this study, where the RVC reactor has proven to be a viable solution. The reactor's design takes full advantage of the material properties from RVC, to provide chemical reaction enhancement through physical agitation. The improvement in the mass transfer can also be observed using the RVC reactor, as the microturbulence induced from the reticulated surfaces of RVC improves mixing, combined with the increased surface area of reaction from the matrix of open pores.

The results from the main effects and interaction plots using factorial analysis shows that catalyst, molar ratio and temperatures have significant relevance to ensure the complete reaction of transesterification as the process approaches chemical equilibrium. The effect of agitation and ppi shows a decreasing level of importance after 60s, where adequate mixing is achieved in the reaction. The response surface analysis shows how two operating conditions interact to alter the yield. The effects of these interactions are identified to facilitate overcoming the activation energy of transesterification and the physical intensification of the reactants. For instance, the PPI-RPM surface plot shows that homogeneous mixing can be achieved as soon as 60s, where vigorous agitation is no longer required beyond 120s. This suggests that the RVC reactor can transition out of the physical-limiting stage sooner than the benchmark with a physical-limiting range from 0s to 270s. The Catalyst Loading-RPM, Temperature-PPI, Catalyst-PPI, Molar Ratio-Catalyst Loading, and Temperature-Molar Ratio interactions significantly contribute to achieving a high final yield during the reaction-limiting stage, as they are essential for overcoming the activation energy of transesterification.

Reaction kinetics of the RVC was also studied using pseudo first-order and pseudo second-order kinetic models. The results show that the RVC reactor has a higher kinetic rate than the benchmark batch reactor during the physical-limiting stage, where homogeneous mixing is significant to promote the kinetic rates. The kinetic rate of RVC reactor is 2.94 $mol \cdot min^{-1}$ while the mass transfer coefficient is 408×10^6 min^{-1}, as compared with the benchmark case at 2.32 $mol \cdot min^{-1}$ and 401×10^6 min^{-1}, respectively.

The prediction model for the glycerides concentration was also built using the two kinetic models, where the simulated results show a good fit with the experimental data. The approach involves modelling the intermediate glycerides, as they are assumed not to be immediately depleted during the physical-limiting stage, where kinetic rates are high. This is also due to the excess methanol used inhibiting the formation of biodiesel at the beginning of transesterification, hence kinetic rates are not as fast as assumed prior to achieving reactant homogeneity.

In all, the use of RVC in a batch reactor was studied to expand the practical implementation of the material in the chemical intensification category. The reactor was proven to improve

transesterification by allowing better mixing of reactants, where the reaction reaches equilibrium phase sooner. The evolving importance of factor interaction was also explored through the qualitative analysis in surface plots, to reduce the research gap in time-sensitive factor analysis.

Chapter 5 Optical and Reaction Characterisation of Microchannel Reactor in Transesterification

5.1 Introduction

In this study, the performance of microchannel reactor is characterised by (i) the physico-chemical interactions of the microchannel reactor using an integrated optical and yield analysis methods, (ii) the transient interaction of the flow patterns and chemical kinetics of the reactor during the initialisation, intermediate, and equilibrium stages of the transesterification. Microchannel reactor has emerged as a promising alternative when compared with batch-type reactor due to its unique advantages. The major attraction of using the microchannel reactor is the continuous flow capability, made possible by the highly energy-efficient system. The internal characteristic dimensions of 1,000 µm to 10 µm provides an enhanced surface area to volume ratio at the scale of 10,000 to 50,000 m^2m^{-3} [263]. Thus, these characteristics allow a shorter diffusion length between the oil and alcohol during reaction, leading to a higher heat and mass transfer rates. As a result, the microchannel reactor can overcome some of the design limitations from the batch reactor technique.

As discussed in the literature review, many microtubular reactor studies have been tailored to study the reactor's design, accompanied by the operating conditions. These studies can demonstrate comparable results on a laboratory-scale that a shorter residence time of transesterification can be achieved by using microtubular systems [97,124,126,181].

In the context of reactor geometry, microtubular reactor is often equipped with a microchannel reaction tubing, where the oil and alcohol pass and react. In general, an external heat source is required to ensure that the transesterification process can overcome the initial activation energy of conversion. The presence of a micromixer is also used to enable active or passive mixing in the system. Thus, the main mode of reaction between the reactants is usually diffusive rather than convective. Additionally, the geometrical parameters of the microchannel system will affect the droplet formation of methanol and oil in the channel. Thus, this should also be monitored to study the flow patterns of the reactants based on the liquid-liquid two-phase flow.

The general mode of mixing in microchannel reactors are the passive mixers using T-type or Y-type junction, as they are relatively inexpensive. Therefore, the main mixing method is restricted by uniting the flow of fluid streams [263].

5.2 Flow and droplet size effect

The sizing of the channel is crucial in determining the types of flow achieved throughout the microchannel system. Therefore, the decrease in the hydraulic diameter of the channel will alter the physical phenomena relevant in the context of chemical reactions.

5.2.1 Surface-to-volume ratio

As mentioned in the introduction, the microchannel system offers an enhanced specific surface area for the flow, with an inversely proportional relationship to the length scale of the channel's cross-section [264]. The narrow channel enables a high surface-to-volume ratio transesterification process, which effectively decreases the diffusion length of reactants, hence increasing the mass transfer to promote reaction rates. Microreactors are quoted to be 10−50 and 100−500 times greater in terms of total surface-to-volume ratio than conventional laboratory vessels of 1,000 m^2/m^3 and production vessel of 100 m^2/m^3, respectively [120]. Thus, microchannel reactors are often selectively operated under milder conditions, since they have superior reaction rates, which reduce the energy requirement for the transesterification process.

5.2.2 Surface forces

In flow systems, several phase distributions and flow patterns are responsible for the dynamic interplay between interfacial, gravitational, viscous and inertial forces. The laminar nature of the flow combined with the prevailing interfacial forces enables the formation of gas-liquid and liquid-liquid interfaces typical of multiphase microflows. Depending on the length-scale, the body or surface forces control the physical phenomenon in a microchannel.

These body forces can be characterised in experiments to help predict the multiphase flow behaviour in a microchannel system. The results are essential in planning out the design of the reactor as the interaction of the fluids can be manipulated. The microfluidic flow in a multiphase scenario can be characterised by the ratio of the viscous to surface forces, multiplied by the capillary number (Ca) and by the ratio of the fluid viscosities as shown,

$$Ca = \frac{\mu U_d}{\sigma}\frac{\mu}{\mu_d} \qquad \text{Eq. 5-1}$$

Where μ and μ_d are the viscosity of the fluids at the continuous and the dispersed phases, respectively [265]. The σ is defined as the surface tension or interracial tension between the two fluid phases, while U_d is the characteristic velocity of the fluids. Besides, the Weber number is defined by the ratio of inertia to surface forces as shown,

$$We = \frac{\rho U_d^2 d_h}{\sigma} \qquad \text{Eq. 5-2}$$

The Weber number is often used to analyse the fluid flows' interface with a system involving two different fluids. Table 5-1 summarises the non-dimensional numbers that are used to characterise the multiphase flow in a microchannel.

Table 5-1. Non-dimensional numbers used in characterising multiphase flow in a microchannel [264].

Non-dimensional number	**Formula**	**Definition**
Reynolds number	$\frac{\rho v d}{\mu}$	$\frac{\text{Inertial force}}{\text{Viscous force}}$
Froude number	$\frac{\rho v^2}{\Delta \rho g d}$	$\frac{\text{Inertial force}}{\text{Gravitational force}}$
Bond/ Eötvös number	$\frac{\Delta \rho d^2 g}{\sigma}$	$\frac{\text{Gravitational force}}{\text{Surface tension force}}$
Capillary number	$\frac{\mu v}{\sigma}$	$\frac{\text{Viscous force}}{\text{Surface tension force}}$
Weber number	$\frac{\rho v^2 d}{\sigma}$	$\frac{\text{Inertial force}}{\text{Surface tension force}}$

5.2.3 Surface characteristics and wall wettability

Wall wettability is a particularly important effect in fluid modelling for microchannel with the multiphase flow. However, the solid surfaces are characterised by their roughness and wettability, defined by the three-phase contact angle in a continuous liquid phase. For instance, the balanced interaction between the adhesive and cohesive forces can be used to determine the three-phase contact angle, as the attraction force between liquid, solid wall, and liquid-gas molecule; attraction among liquid molecules work in a microchannel [264,266,267]. Alternatively, the implementation of chemical reactions in a microchannel system can alter the wetting behaviour of the fluids on a micro- or nano-level by introducing surface roughness elements [268,269]. The sub-micro scale roughness elements are periodically included in the design of the reactor as it can be useful depending on the application. For instance, the heat transfer and nucleation of boiling of a multiphase flow would be altered depending on the surface roughness of the microchannel [270].

In general, the flow in a microchannel is almost always laminar in a single-phase condition. However, in a multiphase scenario, the flow patterns will be relatively different as the surface tension of the

different fluid would exhibit different physical characteristics. Figure 5-1 shows the type of flow that would normally be expected in a multiphase flow. Figure 5-2 shows the flow pattern map from Triplett *et al.* [271] developed characterised for two-phase flow in a microchannel tubing of 1.45 mm internal diameter, which a gas superficial velocity (U_G) versus the liquid superficial velocity (U_L) coordinates.

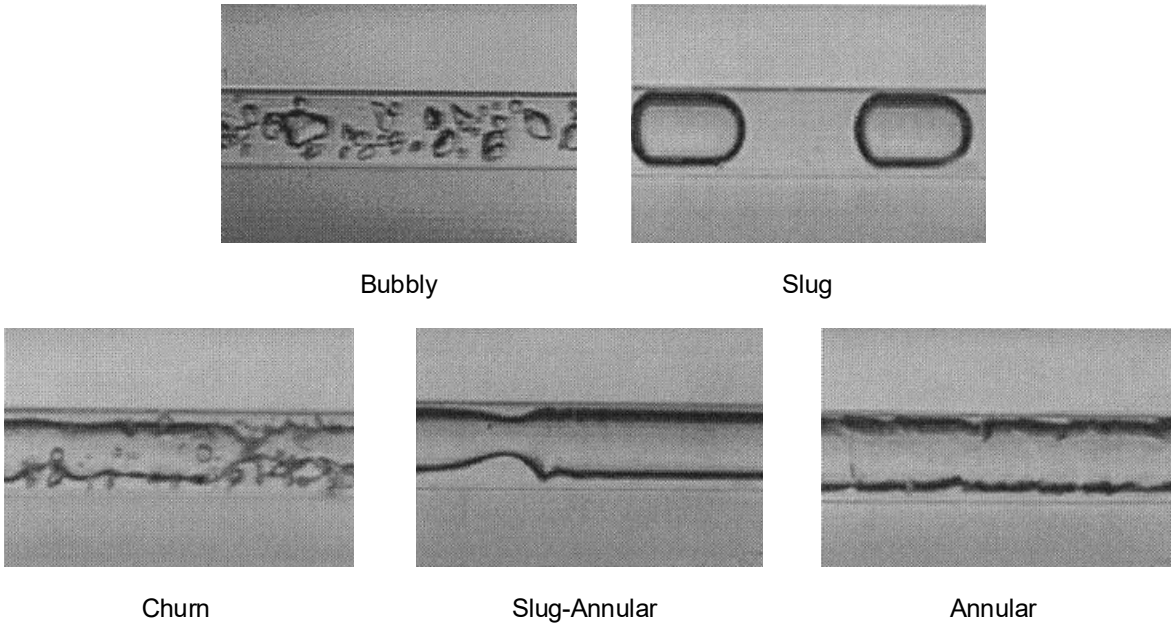

Figure 5-1. The air-water flow patterns characterised in a 1 mm internal diameter microchannel tubing. Adapted from [272].

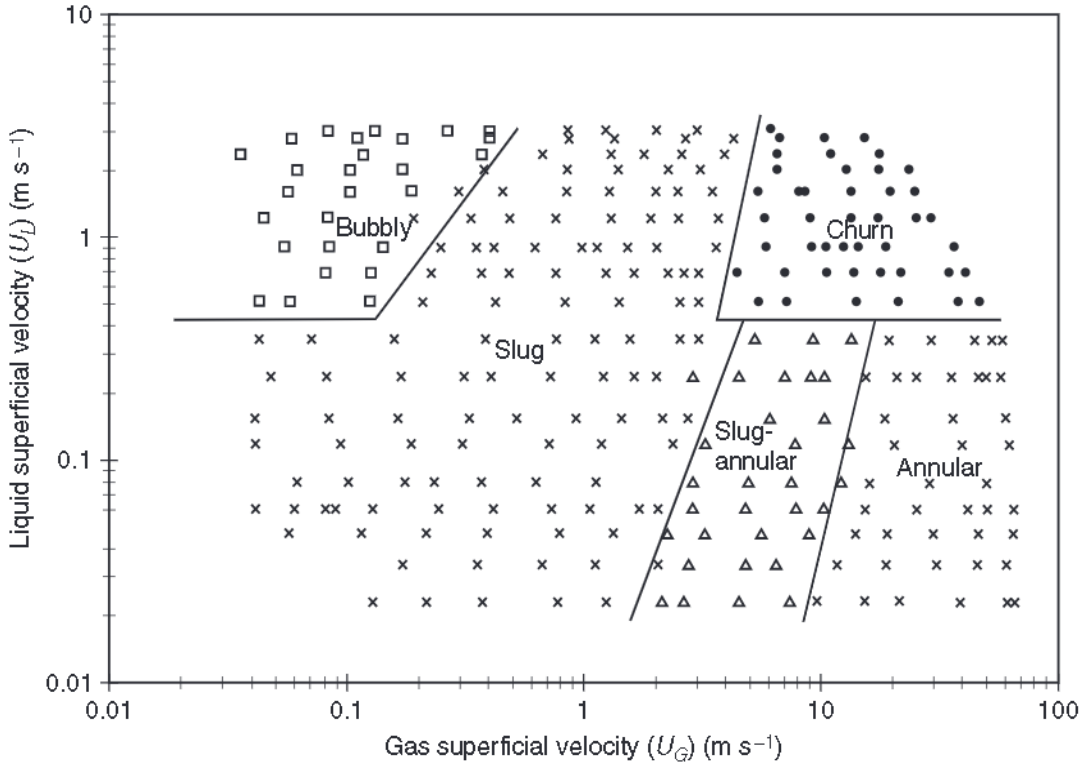

Figure 5-2. Flow patterns and flow pattern transition lines for the 1.45 mm diameter circular test observed by Triplett *et al.* [271,272]. Adapted from Gupta *et al.* [264].

5.3 Materials and experimental setup

The RDB palm olein used were sourced locally (purity 99.8%, Saji, Malaysia) with FFA (Palmitic acid) at a maximum of 0.1 wt. %, moisture and impurities at a maximum of 0.1 wt. %. The potassium methoxide solutions were prepared by dissolving KOH pellets (purity >85%, Qrec, Malaysia) at 1.0 wt. % of the feedstocks into the analytical grade methanol (purity 99.8%, Qrec, Malaysia).

The system consists of two micro peristaltic pumps with stepper motors controlled by an Arduino microcontroller. The pumps are connected to a microchannel tubing with an internal diameter of 0.8 mm varying in length depending on the residence time required. The dry surface area to volume ratio of this configuration is calculated to be at 5,002 m^2m^{-3} using the equation as follow,

$$\frac{Dry\ surface\ area}{Total\ hydraulic\ volume} = \frac{\pi d_H l + 0.5\pi d_H^2}{0.25\pi d_H^2 l} \qquad \text{Eq. 5-3}$$

Where d_H is the hydraulic diameter of the microtube, and l is the length of the microtube. However, the formation of droplets would further increase the wet surface area to volume ratio. The Y-type mixing junction was used to combine the oil flow and the methanol flow before entering the reaction

channel which is heated to within ±1.0°C of the desired temperature by a silicon jacket equipped with a temperature controller.

Additionally, the feedstock is pre-heated using a heating mantle to the desired temperature, as the mixing with methoxide will significantly lower the overall temperature. The product produced at the end of the microchannel system is immediately added to a diluted hydrochloric acid solution to quench the reaction, which also removed the excess methanol from the product. Two distinct layers were formed, the oil phase at the top and the methanol phase at the bottom. The top layer was extracted as samples, then treated and characterised in a gas chromatograph. The flow pattern is optically examined for different conditions using a digital microscope, to study the correlation between oil and alcohol droplet size, biodiesel yield, and reaction kinetics. The microchannel system used in this experimental work is schematically presented in Figure 5-3.

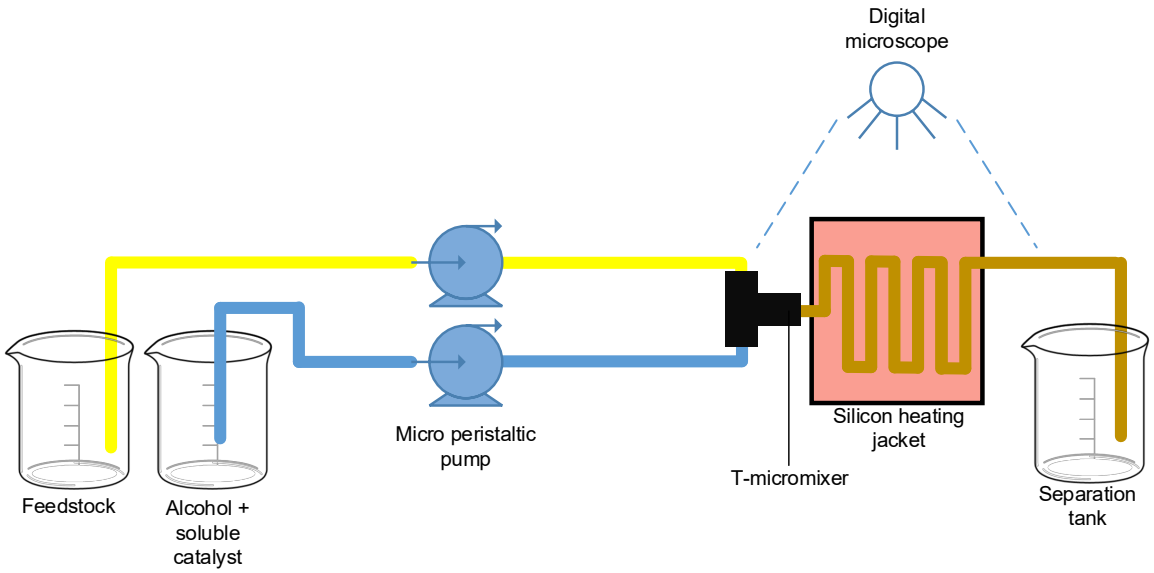

Figure 5-3. The schematic diagram of the microchannel experimental setup.

A sampling of 8 different time intervals from 0s to 450s was conducted using a different length of microchannel tubing to determine the transient to steady-state transesterification reaction using this system. The optical results are integrated into the mass transfer analysis to provide an additional perspective in determining a microchannel reactor's kinetics.

Similarly, the determination of the Arrhenius energy of activation requires to test the glycerides result through a range of elevated reaction temperature. Thus, the identical range of testing is designed to allow comparable analysis for the microchannel reactor with the RVC batch-type reactor and baseline reactor. Additionally, the effect of temperature for glycerides also enables the implementation of kinetic models which includes the prediction of glycerides.

5.4 Theoretical considerations

The stepper peristaltic pumps control the flow rates and methanol to oil molar ratio. Therefore, the range of the peristaltic pump is calibrated to identify the limitations of the experiment. The calibration was done with the fluid used in the peristaltic pumps to eliminate fluid density and compressibility errors. Thus, the flow rate range was determined, as shown in Figure 5-4. The methanol to oil molar ratio for the glycerides test is fixed at 6:1. Therefore, the flow rate is adjusted for both pumps to remain a relatively identical flow velocity and residence time for the target molar ratio. The calibration is also essential to identify the quantity of KOH required to be dissolved in the methanol to achieve 1.0 wt. % of the oil with regards to the mass flow rate of the oil. The mass of KOH required to be dissolved in the methanol can be expressed as,

$$KOH_{req} = \frac{[KOH] \cdot \dot{m}_{oil}}{\dot{m}_{MeOH}} \qquad \text{Eq. 5-4}$$

where the *[KOH]* is the catalytic loading, and $\dot{m}$ is the respective mass flow rate of the reactants.

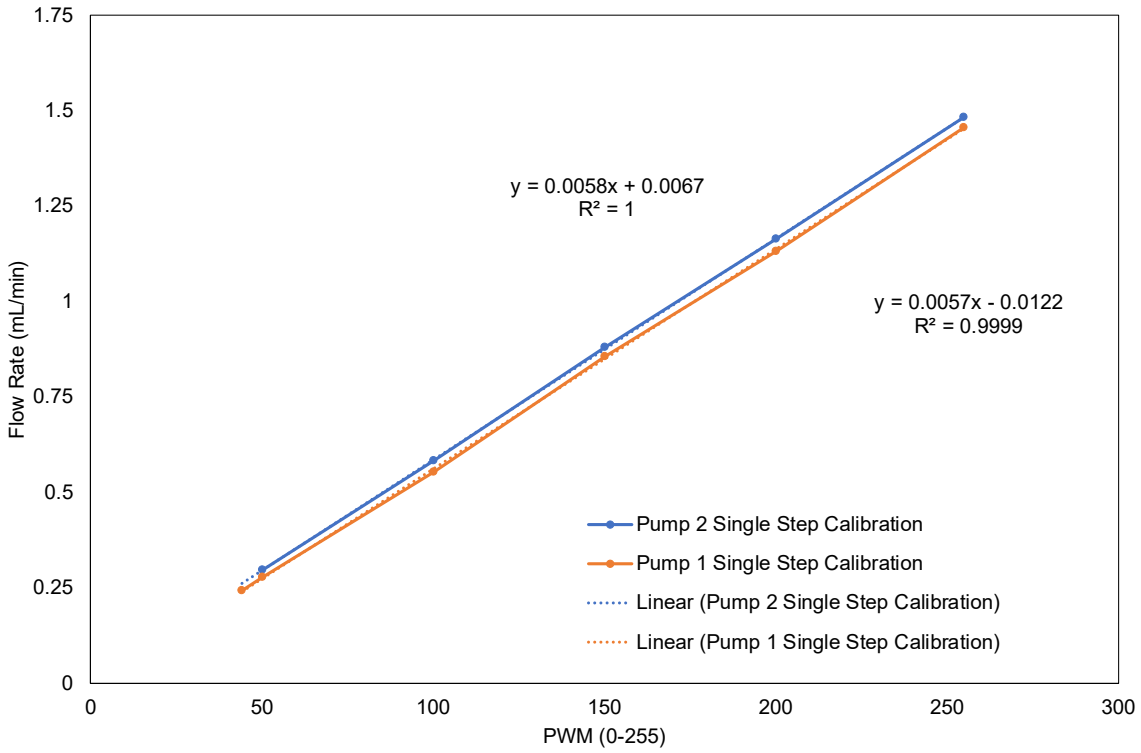

Figure 5-4. Effective range of flow rate for the sets of stepper peristaltic pumps.

In this liquid-liquid flow system, the flow patterns are also considered in this experiment where the stable flow pattern is required to be established, by calculating the capillary number (viscous stresses relative to the interfacial tension) and Weber number (fluid's inertia to the interfacial tension). Eq. 5-1 and Eq. 5-2 are summarised in Table 5-2 below.

Table 5-2. The characterisation of the multiphase flow system in the microchannel reactor.

Dimensionless number	**Equation**	**Calculated value**	**Implication**
Cavitation number, *Ca*	$Ca = \frac{\mu U_d}{\sigma}\frac{\mu}{\mu_d}$	0.004759	Low capillary numbers (Ca < 0.01), the interfacial forces are more dominant than the shear stresses. Dominantly slug flow.
Weber number, *We*	$We = \frac{\rho U_d^2 d_h}{\sigma}$	$1.352e^{-10}$	Low Weber numbers indicate that there is a higher tendency for the coalescence of the second phase. Methanol droplets are combining.

Based on Table 5-2, slug flow can be formed reliably by the microchannel reactor as indicated by the low *Ca* number (<0.01) [273,274]. By definition, slug flow is a series of slugs of the methanol phase separated by the oil phase. Within individual slug, it can be considered as an independent processing sub-volume, hence the oil acts as a continuous phase while the methanol is a discrete phase [263]. Additionally, slug flow provides an intensity of internal circulations which increases with the flow, hence diffusive penetration can be achieved by the immiscible liquid-liquid two-phase of methanol and oil, as shown in Figure 5-5.

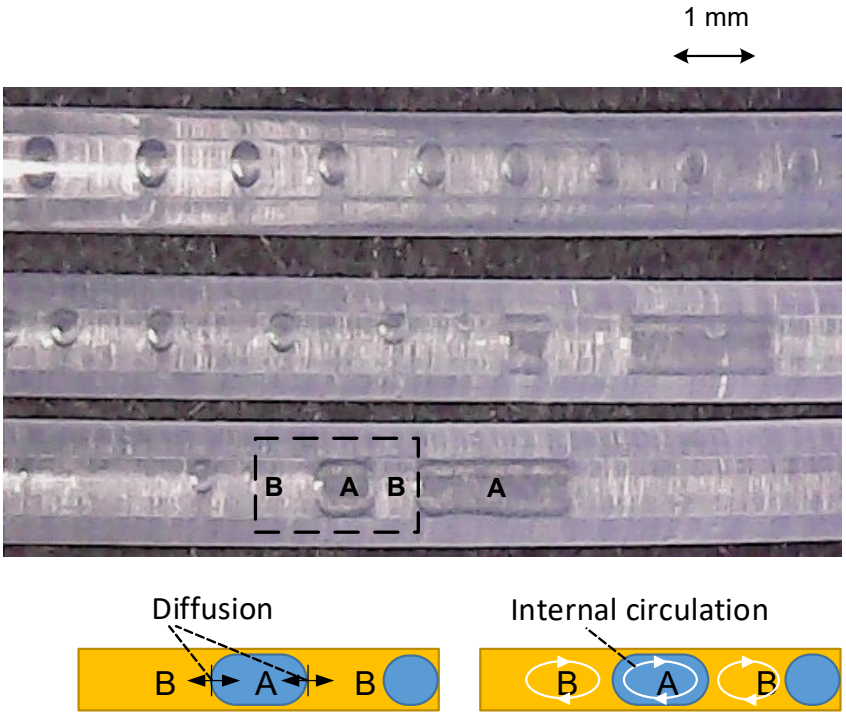

Figure 5-5. The multiphase system where the reaction occurs at (i) the forefront and interphase between [A] and [B], and (ii) within the recirculation of [A] at each flow segment, which is achieved by the formation of slug flow.

Figure 5-5 shows that slug flow is advantageous in reaction flow due to the high interfacial area that it provides, which can be manipulated by changing the flow rates. Furthermore, the high reaction rate at the fluid interface and the internal circulation within the slugs provide additional reaction planes [265]. The internal circulation also causes the hydrodynamic boundary layer to reduce in the slug flow, which essentially promotes the effect of the homogeneous catalyst in the methanol phase as diffusive resistance is negligible [275].

5.5 Results and discussions

5.5.1 Glycerides analysis

The concentration of glycerides content and FAME yield for 45°C reaction temperature was determined via EN14105 and presented in Figure 5-6.

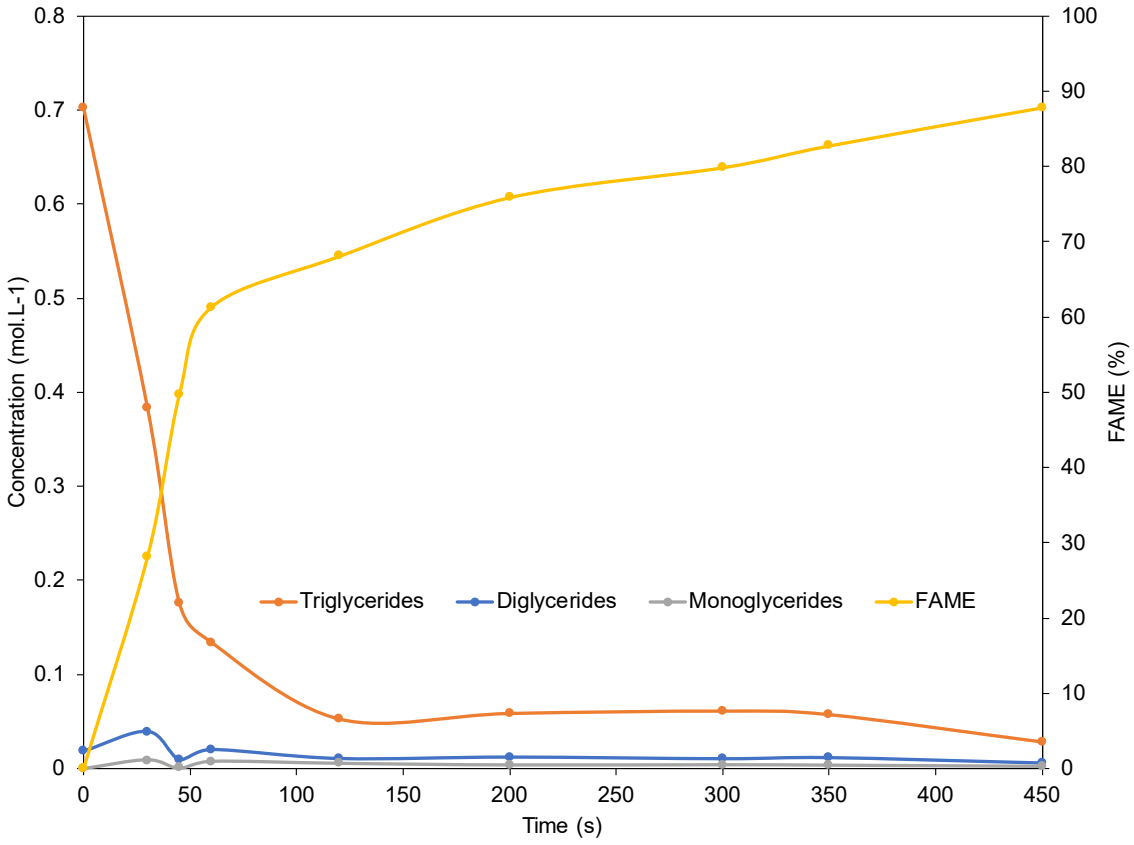

Figure 5-6. The glycerides and yield results from microchannel reactor at 45°C, the internal diameter of 1.0 mm, methanol to oil molar ratio of 6, and KOH catalyst loading of 1.0 wt. %

The effects of temperature on the concentration of trigly-, digly-, monoglycerides, and FAME yield are also presented in Figure 5-7, Figure 5-8, Figure 5-9, and Figure 5-10, respectively.

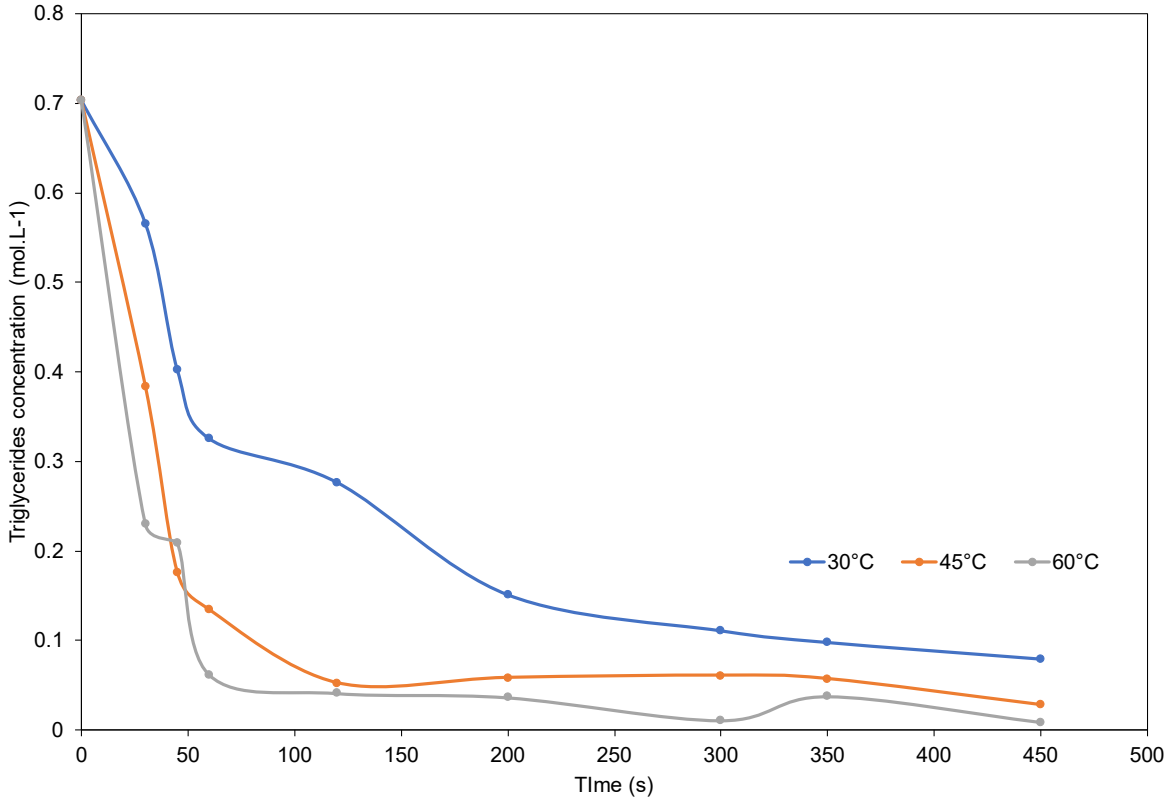

Figure 5-7. The effect of temperature for triglycerides depletion from 0s to 450s at 30, 45, and 60°C using microchannel reactor.

Based on Figure 5-7, the use of different reaction temperatures affects the rate of depletion for triglycerides in the transesterification reaction. In general, the higher temperature has a greater conversion rate for triglycerides as the kinetic rates are improved. The increase in temperature from 30°C to 45°C is more impactful in terms of triglycerides conversion, than the increase in temperature from 45°C to 60°C. This suggests that the effect of increasing reaction temperature has an observable diminishing return for the conversion of triglycerides in the microchannel reactor. The final conversion of triglycerides is measured at 88.7%, 96.0%, and 98.7% for the case of 30°C, 45°C and 60°C, respectively.

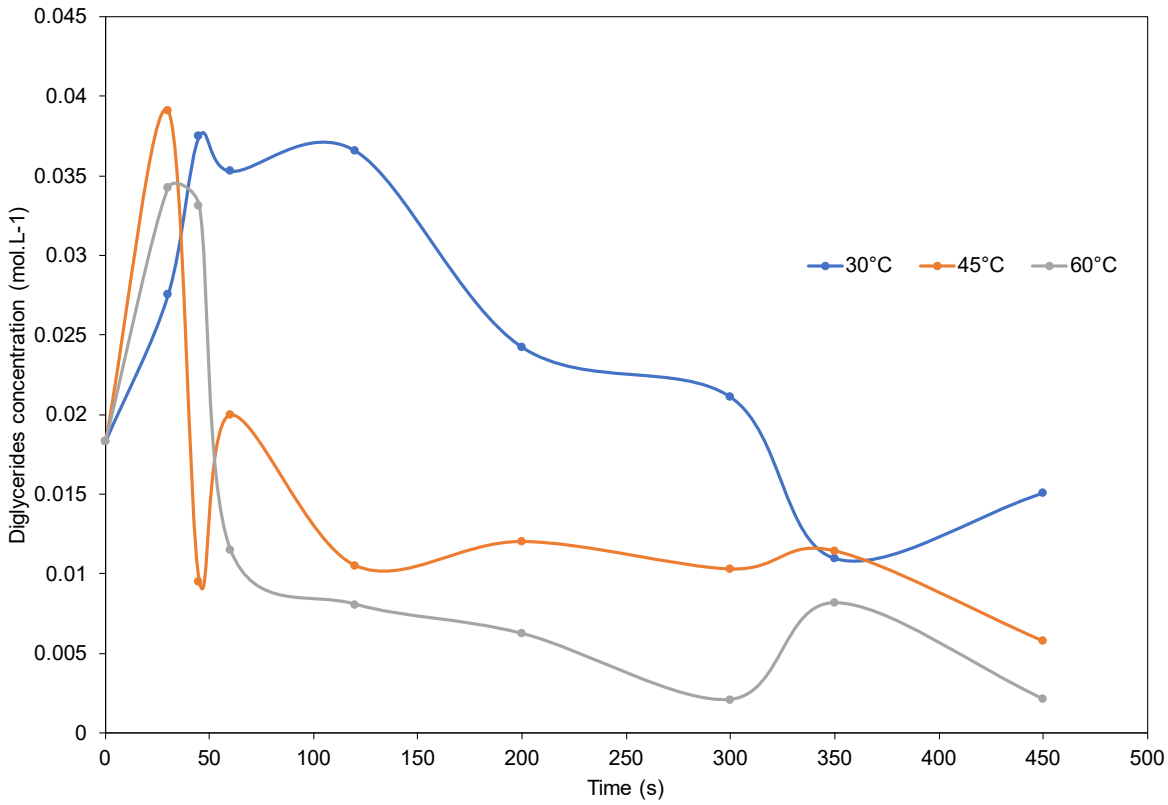

Figure 5-8. The effect of temperature for diglycerides formation and depletion from 0s to 450s at 30, 45, and 60°C using microchannel reactor.

Figure 5-8 shows the diglycerides conversion in the microchannel reactor, which is influenced heavily by the triglycerides depletion. The high depletion rate of triglycerides causes the initial increase in diglycerides, hence there is a net formation in diglycerides. As the reaction progress beyond 30s, the high concentration of diglycerides promotes the conversion of the intermediate in transesterification. Therefore, rapid decrease in concentration was observed in the reaction temperatures of 45°C and 60°C at about 30s. However, the 30°C shows a delay in diglycerides depletion, which is likely caused by insufficient energy in the system to overcome the activation energy of diglycerides reacting with methanol.

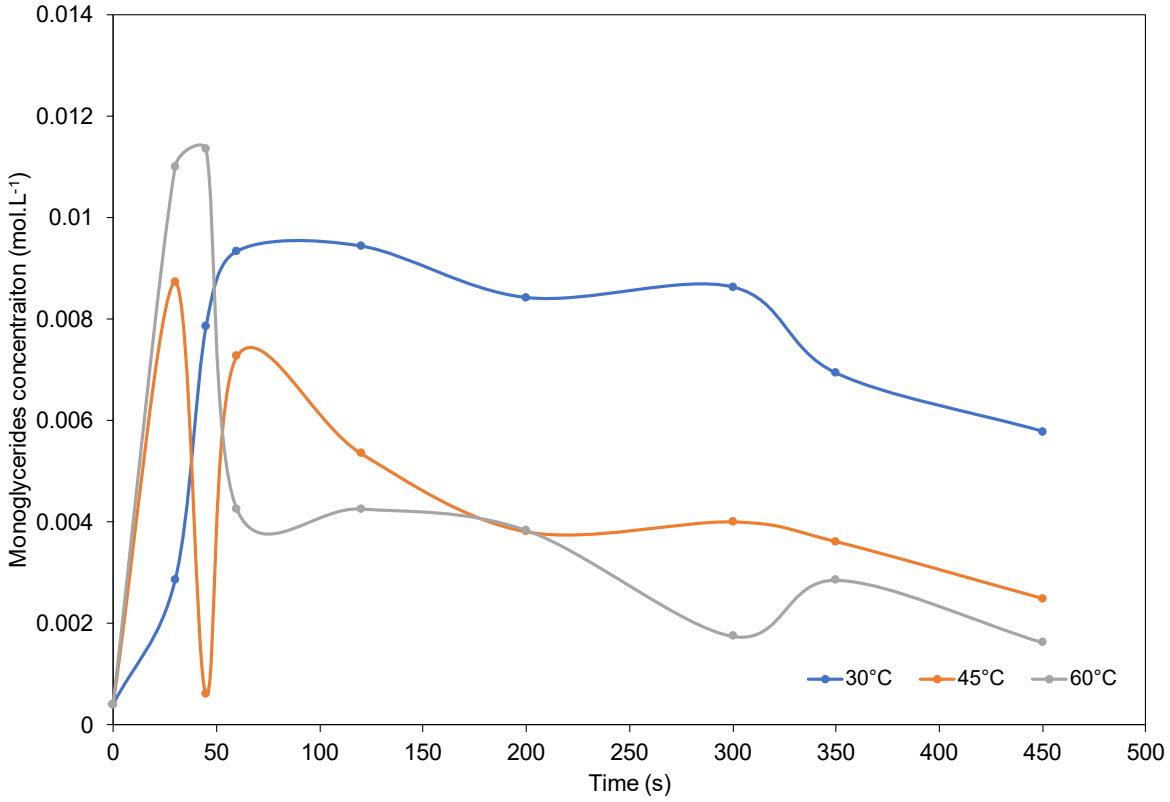

Figure 5-9. The effect of temperature for monoglycerides formation and depletion from 0s to 450s at 30, 45, and 60°C using microchannel reactor.

From Figure 5-9, the main trend of the monoglycerides conversion is similar to the diglyceride conversion. The reaction temperature of 45°C shows a more responsive conversion than 60°C at the beginning of the transesterification, as it achieves a net depletion rate sooner. The 30°C shows a relatively poor conversion towards the end of the experiment, as the resistance in the reaction is likely due to the low temperature used.

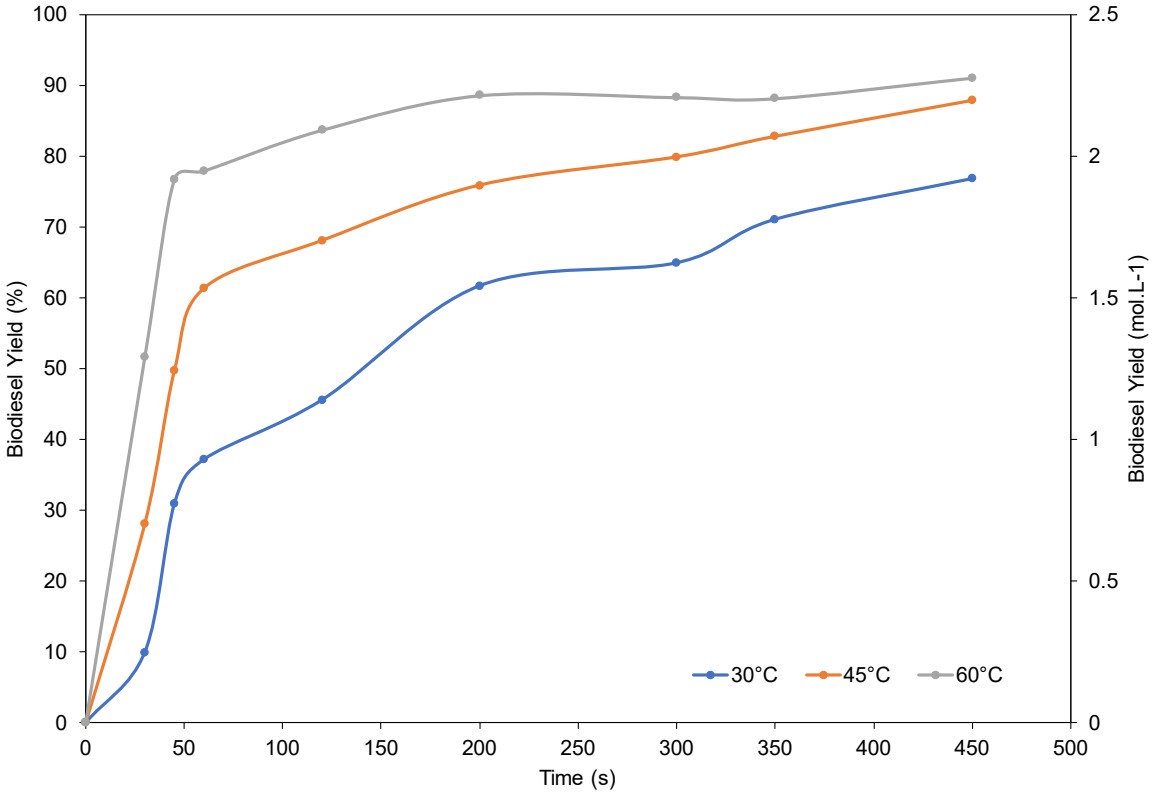

Figure 5-10. The yield of biodiesel in percentage and molar concentration from 0s to 450s at 30, 45, and 60°C using microchannel reactor.

Based on Figure 5-10, the evolution in the biodiesel yield is expected from studying the conversion of the glycerides. The effect of increasing temperature has a significant impact on how fast the reaction changes from the fast forming region initially, to the slower chemical equilibrium region. The figure shows an observable region at about 45s residence time of the microchannel reactor, where the biodiesel rate of formation starts to decrease, which is more obvious for 45°C and 60°C. The final yield achieved by the microchannel reactor using 30°C, 45°C, and 60°C is 76.8%, 87.9%, and 91.1%, respectively.

5.5.2 Pseudo first-order kinetic mechanism

The microchannel reactor utilises a homogeneous catalyst transesterification system which consists of the oil, methanol, and glycerol three-phase. Besides the main transesterification reaction, there is also saponification, a competing reaction where glycerides and methyl ester will react with the base catalyst and water molecule to form soap. Additionally, neutralisation of base can also occur with the free fatty acids. Thus, several assumptions are required to ensure that the kinetic mechanism can be well defined as below:

1. The flow of fluid from the two reactants of methanol and oil is governed by the annular type flow represented by a biphasic medium from the oil and methanol phase [231].

2. The mass transfer of the triglycerides and the intermediates, namely, diglycerides and monoglycerides, is in the oil phase's direction to the methanol phase [231].
3. The use of a homogeneous base-type transesterification reaction ensures a high rate of reaction which takes place in the methanol phase, leading to the faster conversion of triglycerides [254,256].
4. The first-order reaction is more favoured in a microchannel system as oil and methanol are used up along the channel, to produce FAME and glycerol. The mass concentration of the catalyst is an increasing function of the residence time or microchannel length since the catalyst is regenerated into the system [276].
5. Transesterification is only considered for the forward reaction as the reaction of triglycerides, diglycerides, and monoglycerides are in equilibrium. Also, triglyceride concentration approaches zero, where the reversible rate constant of the primary kinetic, k_{-1} will be relatively low to others [276].
6. The competing reactions such as neutralisation of base and saponification are neglected as the effect is relatively low as compared to the main transesterification [232,233].

The above assumptions enable the kinetic mechanism to be established for pseudo first-order with Eq. 3-16, Eq. 3-18, and Eq. 3-19. Therefore, the pseudo first-order was applied to determine the range which obeys the mechanism as shown in Figure 5-11.

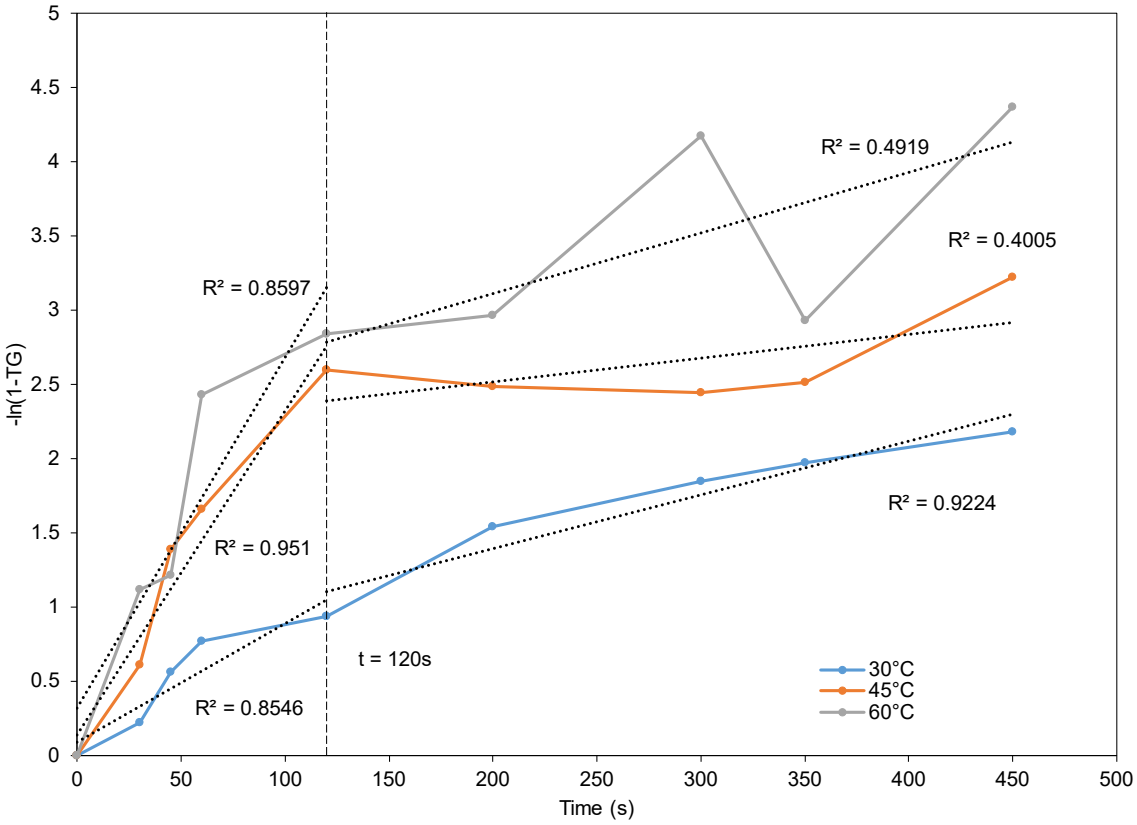

Figure 5-11. The pseudo first-order kinetic mechanism of the microchannel reactor from 0s to 450s for the reaction temperature of 30°C, 45°C, and 60°C.

Figure 5-11 shows that the linear range of the microchannel pseudo first-order can be determined from 0s to 120s, which is earlier than the batch type system. This should be reasonable as the overall scale of the entire reaction chamber is significantly smaller than the batch system, while the high throughput combined with high triglyceride conversion rate is the result of faster kinetic rates. The pseudo first-order kinetic model is often recommended to be applied at the initial transesterification region, where reaction rates are high. Thus, the two regions identified from Figure 5-11 also supports the kinetic model's limitation, where the low linear region beyond 120s is not included in the reaction kinetic study. The maximum kinetic reaction rate is determined through the three-point running average of the triglyceride conversion, as shown in Figure 5-12.

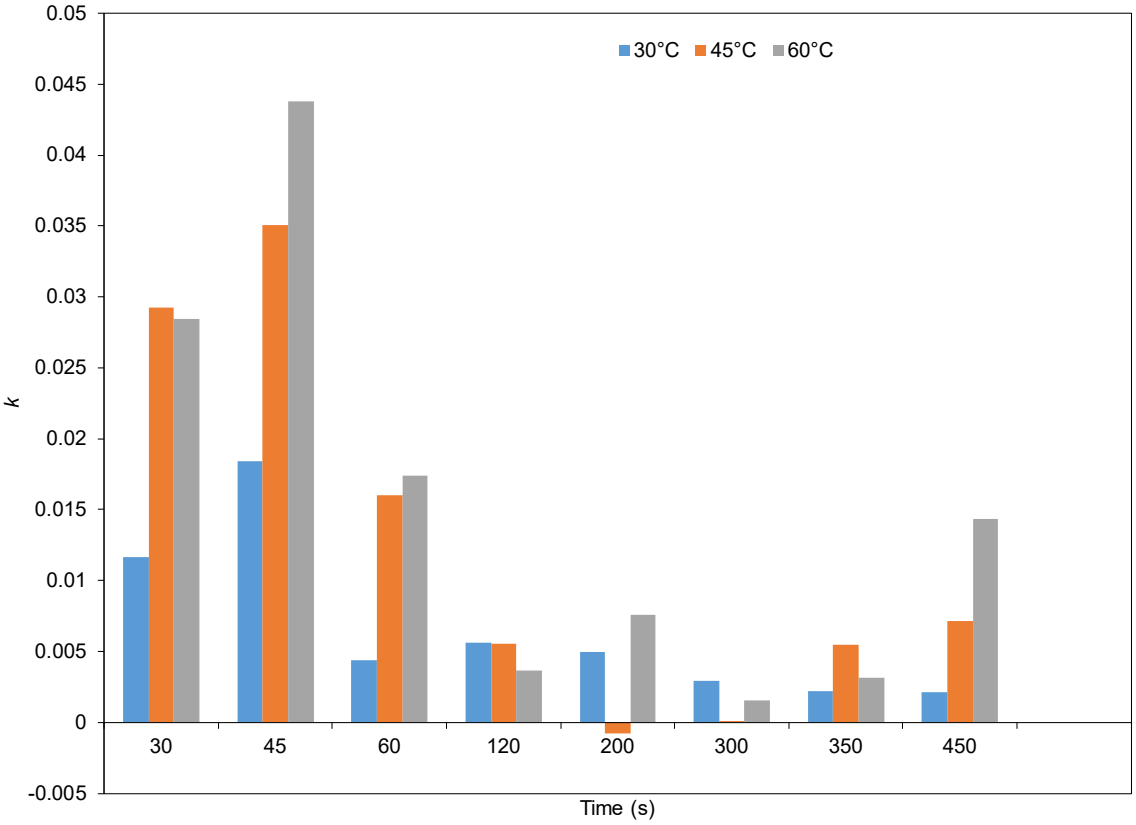

Figure 5-12. The three-point running average of the pseudo first-order microchannel transesterification of triglycerides depletion from 0s to 450s.

Based on Figure 5-12, the highest instantaneous kinetic rates are observed from 30s to 60s, which is in the order with respect to the increase in reaction temperature. This is expected from transesterification as the transesterification reaction is exothermic. The three-point running average can also be described as the rate of change in kinetics with respect to time, hence it can be used to determine the inflection point by finding the highest peak. The inflection point occurs at about 45s into the reaction, followed by a sharp decline.

The methyl ester yield results are also used to determine the pseudo first-order kinetic mechanism to test the results' consistency as compared to the batch-type system. This is done using the conversion and formation of methyl ester data with Eq. 3-22, as shown in Figure 5-13.

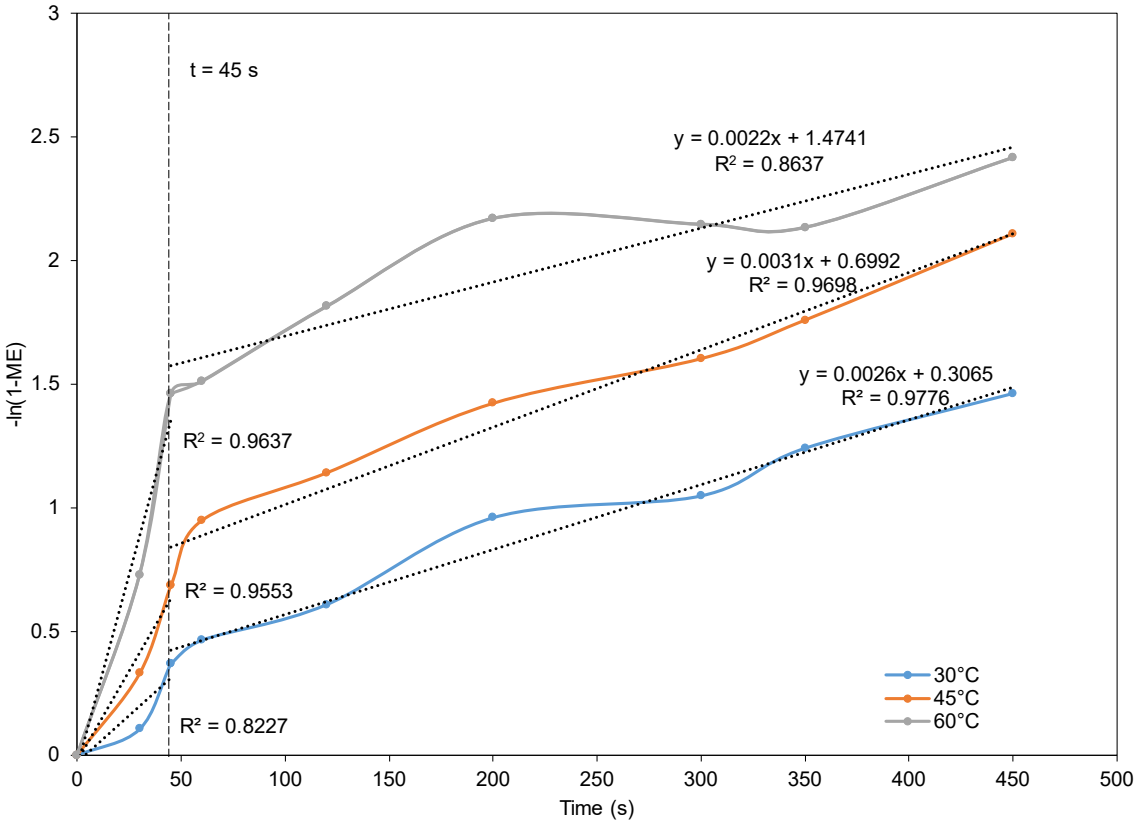

Figure 5-13. The pseudo first-order kinetic model of methyl ester formation in transesterification using microchannel system.

Based on Figure 5-13, the methyl ester pseudo first-order kinetic model can be well represented by the linear trend if the model is intersected at 45s residence time. The identified intersection also coincide with the findings for the biodiesel yield results from Figure 5-10. However, for the microchannel system, the kinetic rates seem to be leading as compared to the depletion of triglycerides. This can be further examined in the three-point running average of the pseudo first-order kinetic model, to determine the inflection point, as shown in Figure 5-14.

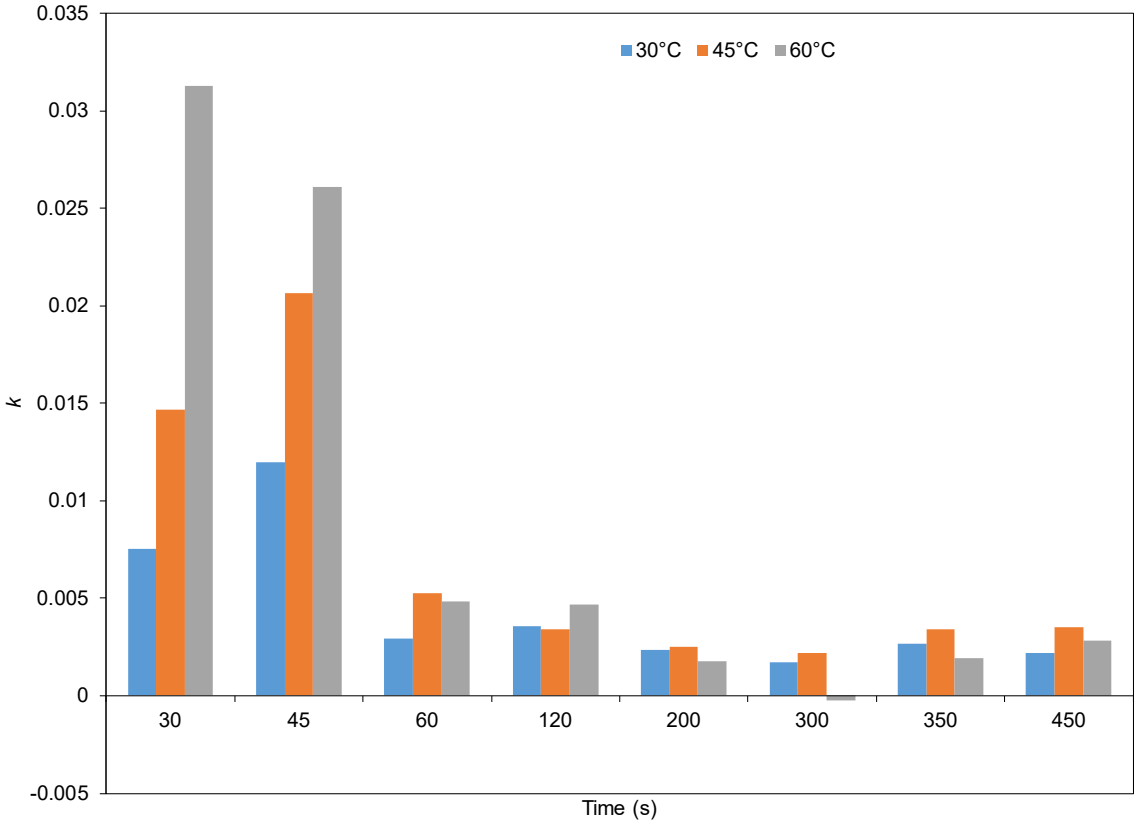

Figure 5-14. The three-point running average of the pseudo first-order microchannel transesterification of methyl ester formation from 0s to 450s.

Figure 5-14 shows the highest kinetic rate occurs at 45s for 30°C and 45°C, while 30s for 60°C. This is not expected as the highest kinetic rate of triglycerides conversion for 60°C occurred at 45s. Although the methyl ester formation first-order is not typically used in kinetic studies, the model's high linearity from three distinct reaction temperatures suggests a good representation of the transesterification kinetics qualitatively. The same model has also been tested by Latchubugata *et al.* [235], where pseudo first-order is implemented by modelling methyl ester formation, with good approximation. However, the methyl ester formation kinetic model suggests that the intermediate reactions which involve the formation and depletion of diglycerides and monoglycerides are not negligible, since they are not immediately converted into methyl ester. To investigate the previous statement, pseudo first-order is carried out for the kinetics of diglycerides and monoglycerides, as the assumption of excess methanol justifies the implementation for the intermediate reactions. Therefore, by applying Eq. 3-23 and Eq. 3-24 to the intermediate glycerides of transesterification, results are shown in Figure 5-15 and Figure 5-16.

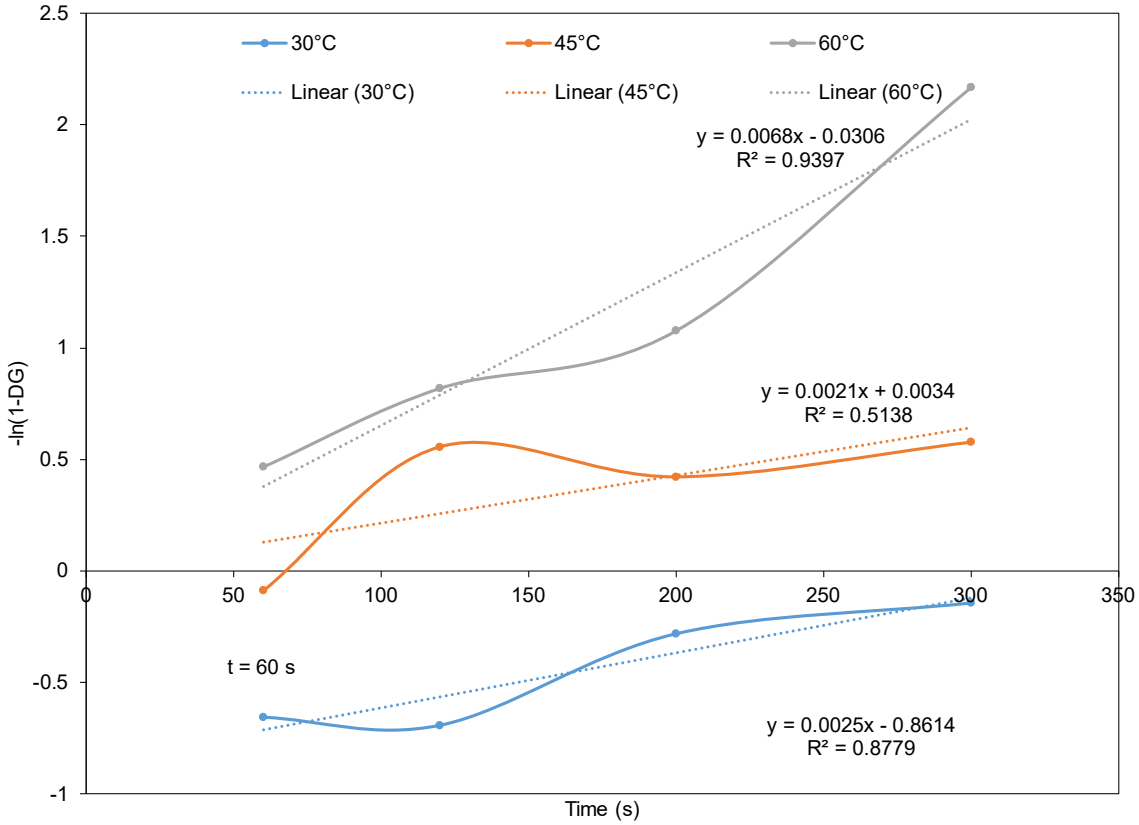

Figure 5-15. The pseudo first-order kinetic model of diglycerides formation and depletion in transesterification using microchannel system.

According to Figure 5-15, the kinetic model shows a good fit with the linear relationship for 30°C and 60°C reaction temperature, while the 45°C case does not show high linearity. The abnormalities from the 45°C are likely due to the formation rate greater than the depletion, leading to an excess diglyceride accumulation. The range of results chosen is from 60s to 300s, representing 53.3% of the total residence time. This range is selected based on the linear region where the kinetic model conforms to the conversion of diglycerides, as shown in the method used in other literature [235,237]. The 0s to 60s residence time are not included because the rate of formation is higher than the rate of depletion for diglycerides, which can introduce errors in estimating the actual kinetic rates.

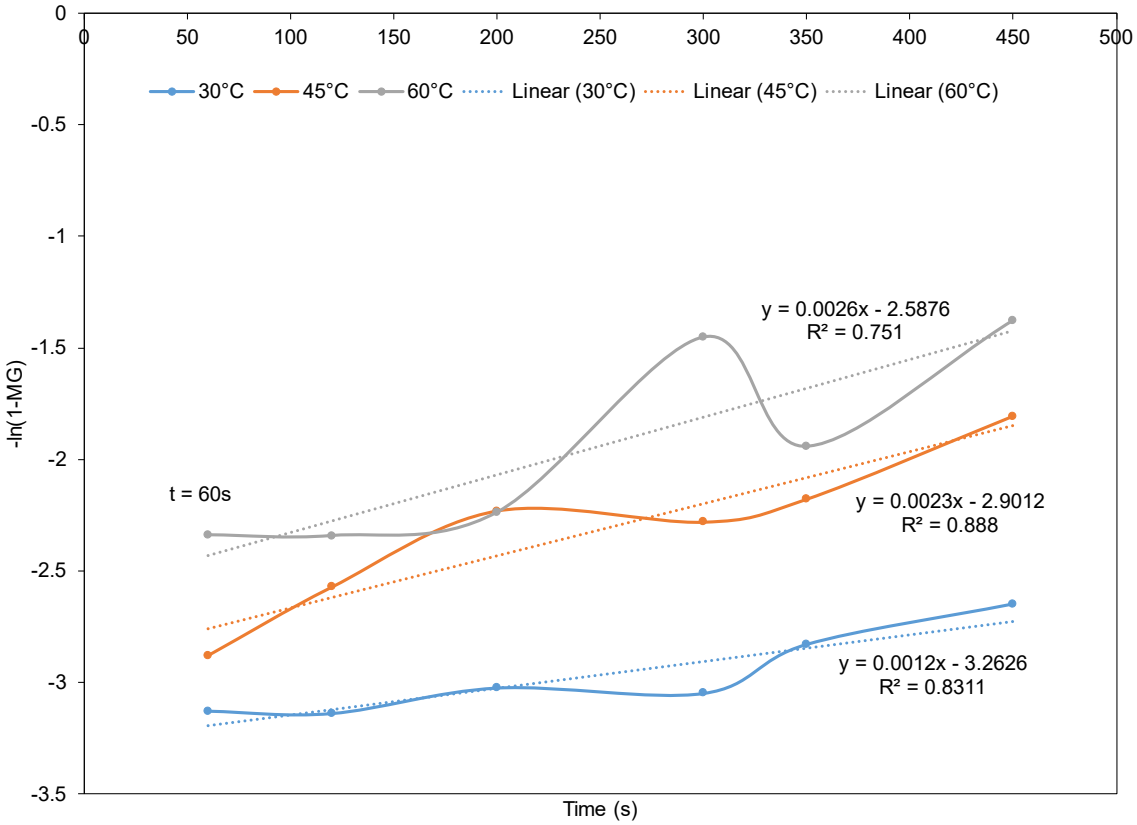

Figure 5-16. The pseudo first-order kinetic model of monoglycerides formation and depletion in transesterification using microchannel system.

Figure 5-16 shows that the pseudo first-order monoglyceride kinetic model exhibits a relatively good fit for first-order reaction, given that the intermediate concentration is constantly fluctuating. The results from the glycerides concentration based on Figure 5-7, Figure 5-8, and Figure 5-9 all suggest that beyond 60s, the concentrations are a better representative set of result to be used in kinetic modelling, as the fluctuation is lesser due to the reaction approaching equilibrium state. Thus, this is also reflected in selecting the range of the concentration results used in the pseudo first-order kinetic model for the glycerides and coinciding with the split for the methyl ester model. Table 5-3 tabulates and compares the kinetic rates from the linear trend line and the running average calculation.

Table 5-3. The kinetic rates of triglycerides, diglycerides, and monoglycerides depletion with methyl ester formation using the pseudo first-order kinetic model for microchannel reactor.

Pseudo First-order Kinetic Model	**Reaction Temperature (°C)**	**Moving Average Max. Kinetic Constant (dm^3/mol.min)**	**Linear Trend Gradient Kinetic Constant (dm^3/mol.min)**	**R^2 of linear trend lines**	**Applicable region (s)**
Triglycerides depletion	30	1.1059	0.4800	0.8546	0–120
	45	2.1017	1.3080	0.9510	
	60	2.6292	1.4160	0.8597	
Diglycerides depletion	30	0.2832	0.1500	0.8779	60–300
	45	0.4102	0.1260	0.5138	
	60	0.8070	0.4080	0.9397	
Monoglycerides depletion	30	0.1524	0.0720	0.8311	60–450
	45	0.2230	0.1380	0.8880	
	60	0.3384	0.1560	0.7510	
Methyl ester formation	30	0.7190	0.1560	0.9776	0–450
	45	1.2400	0.1860	0.9698	
	60	1.8764	0.1320	0.8637	

5.5.2.1 Arrhenius energy of activation

The pseudo first-order kinetic model is used to generate the Arrhenius activation energy calculation input based on Eq. 4-3 and Eq. 4-4. The results are represented in Figure 5-17 using the linear fit and moving average, while the activation energy value is calculated in Table 5-4.

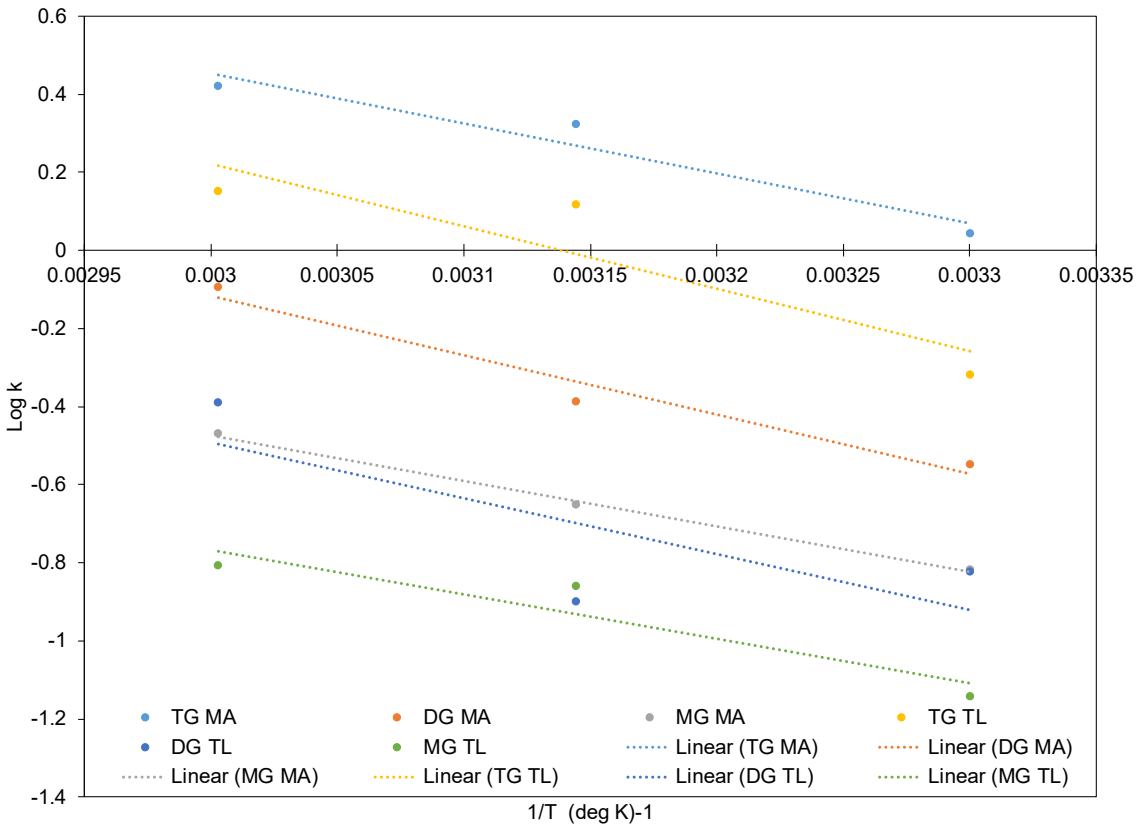

Figure 5-17. Pseudo first-order Arrhenius plot of kinetic reaction constant against reaction temperature of microchannel transesterification using moving average and trend line linear fit.

Table 5-4. Pseudo first-order Arrhenius activation energy using moving average and linear fit for microchannel reactor.

Pseudo First-Order Kinetic Model	**Moving Average Activation Energy (kcal/mol)**	**R^2**	**Linear Trend Activation Energy Constant (kcal/mol)**	**R^2**
TG + MeOH → DG + ME	12.07	0.9413	12.08	0.8258
DG + MeOH → MG + ME	13.66	0.9626	14.62	0.5960
MG + MeOH → G + ME	14.47	0.9971	15.24	0.8835

Based on Figure 5-17 and Table 5-4, the activation energies are in the ascending order of triglycerides, diglycerides, and monoglycerides conversions. This is consistent for both the moving average and linear trend line calculation methods. The moving average and linear trend calculations show nearly identical values for triglycerides depletion mechanism in terms of the magnitude.

However, the moving average calculation shows lower activation energy for the subsequent conversions from diglycerides to glycerol, as compared to the linear trend activation energy values. The Arrhenius equation's linearity is also examined, where moving average method shows a higher accuracy when fitted with Eq. 4-4. In the microchannel reactor context, these values will be further evaluated by comparing to the batch-type counterpart to examine the differences in the later section.

5.5.3 Pseudo first-order kinetic prediction model for microchannel reactor

In general, the transesterification prediction model can be implemented either via the first or second-order, which are usually not significantly different [236,276]. However, there is a lack of published studies on the glycerides simulation via the first-order mechanism in the microchannel reactor. The pseudo first-order transformation from the previous section suggests that this mechanism could be a good representation to simulate transesterification.

5.5.3.1 Triglycerides depletion kinetic prediction model for microchannel reactor

The triglycerides depletion model of the batch reactor and RVC reactor, the triglycerides depletion model has been tested with the three-point moving average and interpolated moving average method. Thus, in this prediction model for the microchannel reactor, a similar approach will be implemented using Eq. 3-19 to ensure that a like-to-like comparison can be made. Therefore, the pseudo first-order microchannel reactor kinetic prediction models for 30°C, 45°C, and 60°C is illustrated in Figure 5-18, Figure 5-19, and Figure 5-20, respectively.

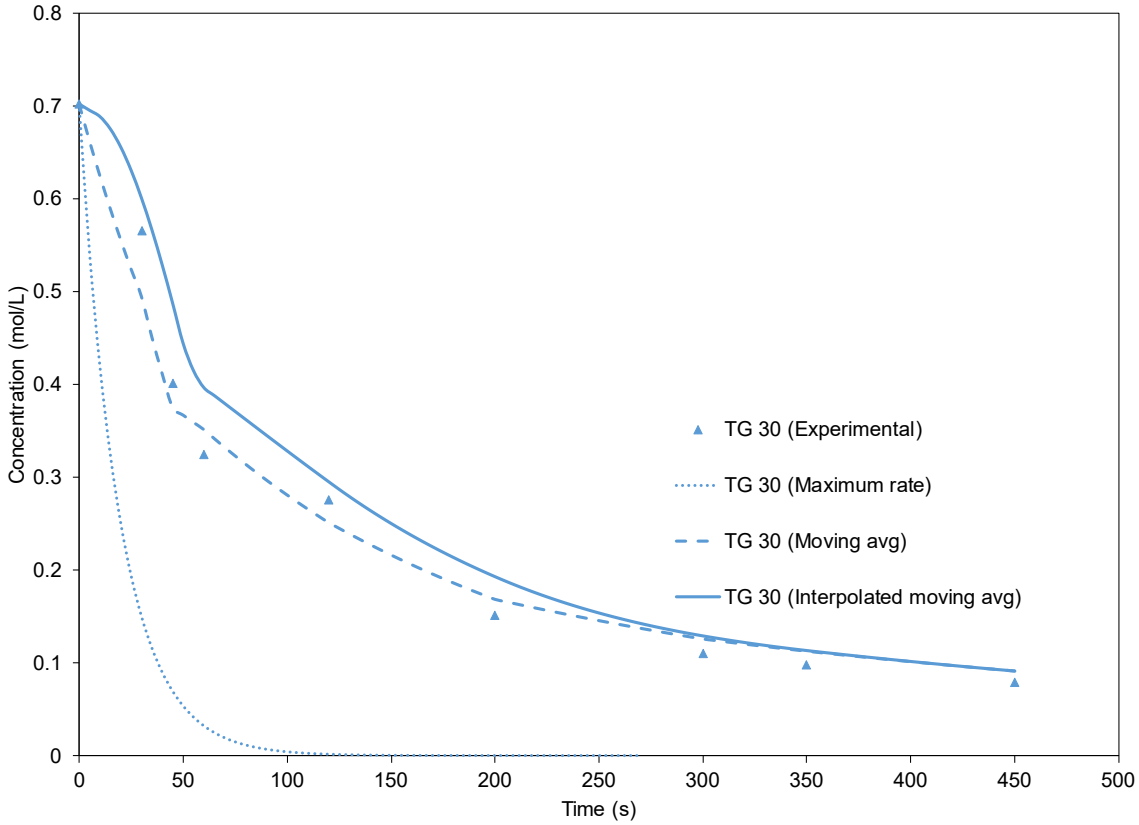

Figure 5-18. Pseudo first-order triglycerides depletion kinetic model of microchannel reactor using a single maximum rate, moving average rates, and interpolated moving average rates at 30°C.

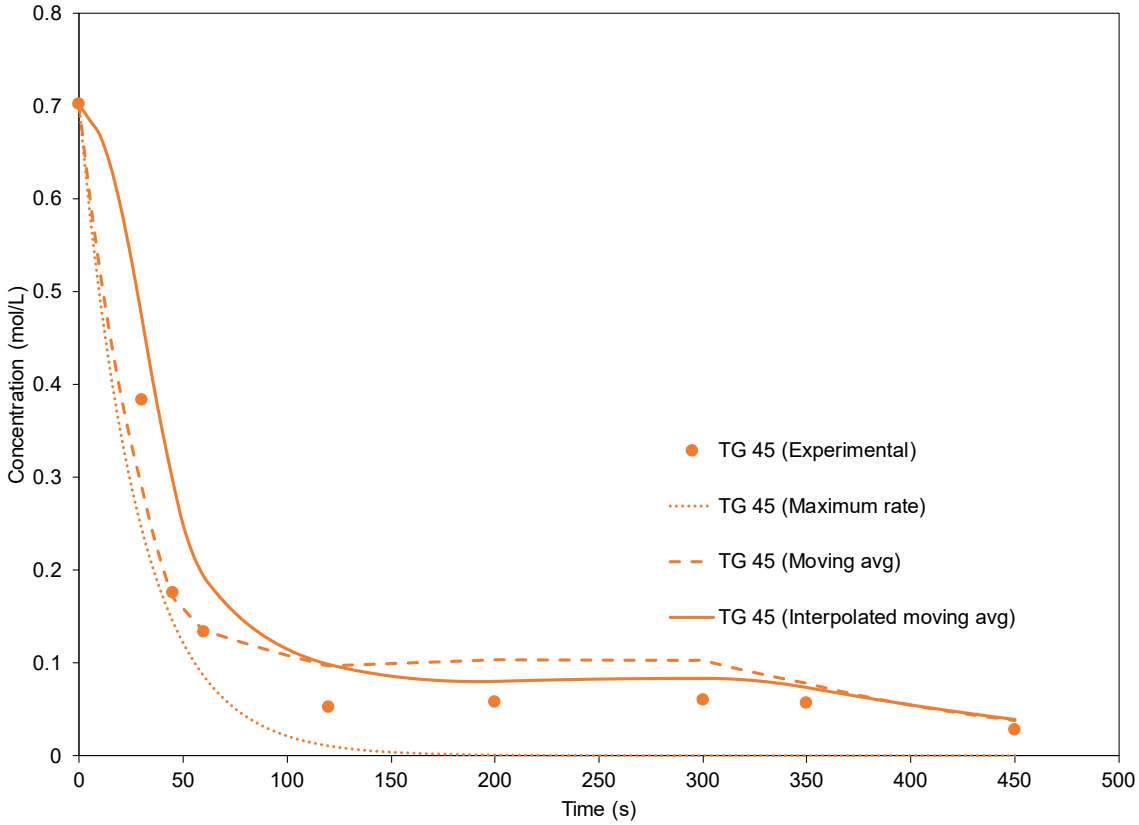

Figure 5-19. Pseudo first-order triglycerides depletion kinetic model of microchannel reactor using a single maximum rate, moving average rates, and interpolated moving average rates at 45°C.

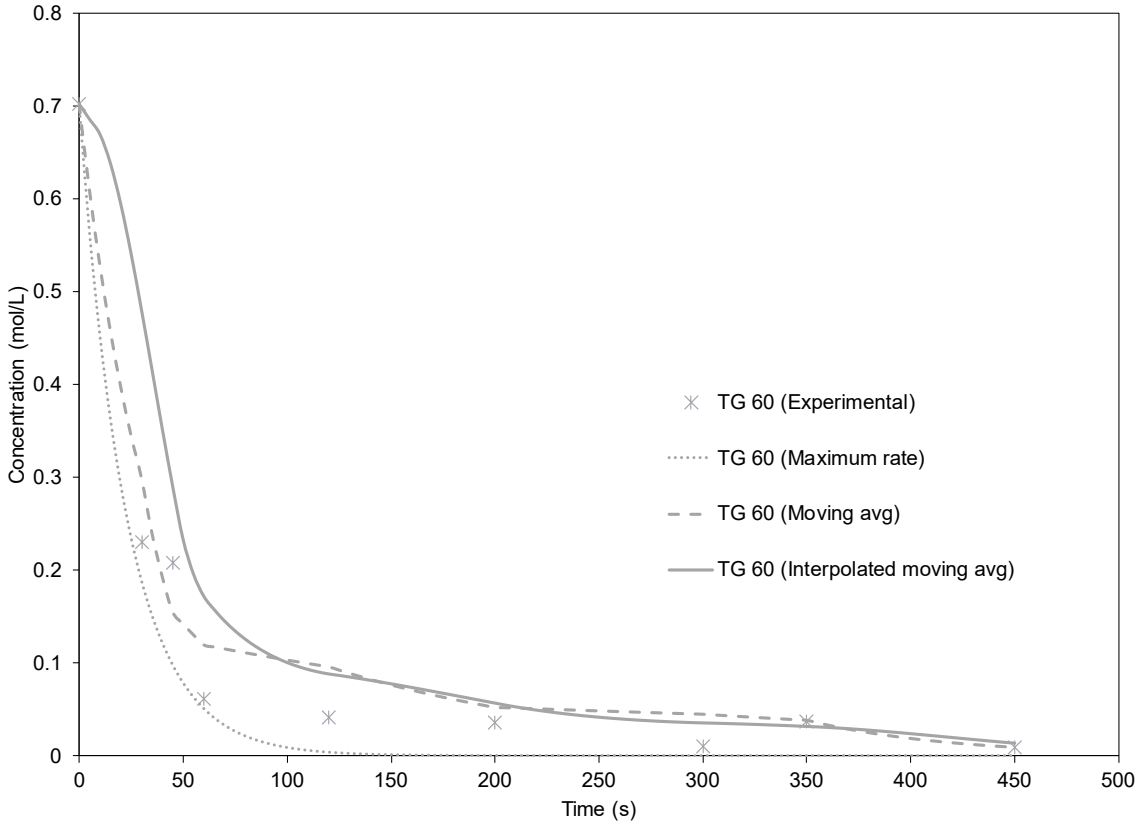

Figure 5-20. Pseudo first-order triglycerides depletion kinetic model of microchannel reactor using a single maximum rate, moving average rates, and interpolated moving average rates at 60°C.

The prediction models showed high reliability and repeatability across different reaction temperatures based on Figure 5-18, Figure 5-19, and Figure 5-20. This is observable from the beginning to the final yield point of the transesterification as compared to the batch-type counterpart, where the initial phase is usually modelled. Therefore, the modelled range illustrates the compatibility of the first-order kinetic mechanism with the microchannel system.

The 30°C reaction temperature case shows relatively good fit throughout the entire reaction, while the other two prediction model showed lower accuracy particularly at the transition point to the equilibrium of the reaction. The lower reaction temperature has a smaller rate of change in kinetic constant, hence the model can adjust adequately to the fluctuations. Similarly, using a single maximum kinetic constant to model the entire transesterification does not work in the microchannel reactor, consistent with batch and RVC reactor. The interpolated moving average prediction model tends to under-predict the concentration for all reaction temperature. The moving average prediction model shows a relatively good fit to the experimental data from 0s to 60s, followed by an underestimation towards the final yield similar to the interpolated counterpart.

In general, the moving average simulation showed the best fit as compared to the interpolated version which is observable in the initial part of the reaction. The notable trend of increasing relative error of the simulation with increasing reaction temperature was also repeated in the microchannel kinetic model. The relative errors of the simulated glyceride values are calculated in Table 5-5 and Table 5-6 for both models. The general trend suggests that the lower reaction temperature of 30°C has higher accuracy than 45°C and 60°C.

Table 5-5. The relative errors of the predicted triglyceride concentrations via the pseudo first-order kinetic model using moving average kinetic constants for microchannel reactor.

	Concentration (mol/L)								
Temperature (°C)	30			45			60		
	Experimental	Simulated	Relative Error	Experimental	Simulated	Relative Error	Experimental	Simulated	Relative Error
Time (s)									
0	0.7029	0.7029	0.00%	0.7029	0.7029	0.00%	0.7029	0.7029	0.00%
30	0.5654	0.4951	12.44%	0.3836	0.2920	23.88%	0.2298	0.2994	30.25%
45	0.4019	0.3755	6.58%	0.1758	0.1727	1.79%	0.2087	0.1552	25.67%
60	0.3252	0.3518	8.17%	0.1341	0.1359	1.30%	0.0617	0.1195	93.54%
120	0.2764	0.2516	8.96%	0.0525	0.0974	85.61%	0.0411	0.0959	133.50%
200	0.1511	0.1688	11.69%	0.0584	0.1040	77.95%	0.0364	0.0522	43.61%
300	0.1109	0.1260	13.61%	0.0609	0.1032	69.46%	0.0108	0.0448	313.62%
350	0.0979	0.1128	15.25%	0.0571	0.0786	37.58%	0.0376	0.0382	1.70%
450	0.0794	0.0915	15.25%	0.0280	0.0385	37.58%	0.0089	0.0091	1.70%

Table 5-5 compares the concentrations of the prediction models and experimental data across different reaction temperatures using the three-point moving average method. As mentioned above, the 30°C reaction temperature showed a closer fit to the experiment, where the maximum relative error is 15.25% at the yield point. The increase in reaction temperature increases relative error, as shown in the 45°C and 60°C prediction model. The cause of the inaccuracy is likely due to the higher rate of change in kinetic rates where the three-point moving average model is unable to keep up, causing the accumulation of propagated error. Besides, the cause for the larger relative error can be explained by the faster depletion of triglycerides, where the concentration falls to a lower value. The small deviation in the prediction model's concentration is likely to give rise to a larger relative error. Besides, the pseudo first-order kinetic model is a better presentation at the physical-limiting stage of the transesterification in microchannel reactor, as shown in Figure 5-11. Therefore, the prediction accuracy for the reaction-limiting stage is inevitably poorer in relative to the physical-limiting stage.

Table 5-6. The relative errors of the predicted triglyceride concentrations via the pseudo first-order kinetic model using interpolated moving average kinetic constants for microchannel reactor.

Concentration (mol/L)									
Temperature (°C)	30			45			60		
	Experimental	Simulated	Relative Error	Experimental	Simulated	Relative Error	Experimental	Simulated	Relative Error
Time (s)									
0	0.7029	0.7029	0.00%	0.7029	0.7029	0.00%	0.7029	0.7029	0.00%
30	0.5654	0.6015	6.38%	0.3836	0.4757	24.01%	0.2298	0.4810	109.27%
45	0.4019	0.4881	21.43%	0.1758	0.2979	69.45%	0.2087	0.2907	39.26%
60	0.3252	0.3972	22.12%	0.1341	0.1938	44.47%	0.0617	0.1719	178.48%
120	0.2764	0.2958	7.03%	0.0525	0.0990	88.56%	0.0411	0.0882	114.82%
200	0.1511	0.1934	28.01%	0.0584	0.0806	38.00%	0.0364	0.0568	56.22%
300	0.1109	0.1296	16.81%	0.0609	0.0838	37.63%	0.0108	0.0354	227.26%
350	0.0979	0.1138	16.19%	0.0571	0.0740	29.59%	0.0376	0.0316	15.89%
450	0.0794	0.0917	15.50%	0.0280	0.0396	41.44%	0.0089	0.0135	51.62%

Based on Table 5-6, the relative error is tabulated for the interpolated moving average prediction model for different reaction temperature. A similar trend is observed for the accuracy of the model, when compared against the three-point moving average model where lower reaction temperature shows a higher accuracy for the prediction of triglyceride concentrations. The interpolated model should mathematically accommodate the high rate of change in concentration better than the three-point moving average model. However, the relative error calculations showed that there is higher deviation in simulating the higher reaction temperature accurately. Nevertheless, the interpolated prediction model's consistent underestimation can be proven useful to provide qualitative concentration simulation conservatively.

5.5.4 Microchannel reactor optical image and mass transfer analysis

The flow behaviour between methanol and oil is better studied to understand biodiesel formation's flow distribution effects. Optical images are taken by a digital microscope with 20x magnification, taken from 100 mm (12.5D) from the point of mixing at the Y-junction to minimise the effect from the change in flow direction due to the mixing. An LED lamp was set to illuminate the microtubes in the frame to provide an additional light source. No colour agent was used on the methanol as the difference in phase for the oil and methanol is apparent. From the experiments, the small droplets

tend to coalesce to form a larger slug and annular flow. Thus, the methanol droplets and the coalesced methanol slug's size can be represented as an ellipsoid due to a cylinder with two end caps. Therefore, the volume of the slug flow can be modelled using the equation as below [277],

$$V = \pi r^2 l + \frac{4}{3}\pi r \left(\frac{l_0}{2}\right)^2 \quad \text{Eq. 5-5}$$

where r is the internal diameter of the microchannel tubing, l is the length of the cylinder, and l_0 is the length of the ellipsoid. When modelling smaller spheroid-shaped droplets, the length of the cylinder, l, is assumed to be zero. From Eq. 5-5, the interfacial area between the oil phase and methanol phase can then be represented by the following equation [277],

$$A = \frac{4}{3}\pi \left[r l_0 + \left(\frac{l_0}{2}\right)^2 \right] + 2\pi r l \quad \text{Eq. 5-6}$$

With the specific interfacial area, $a = V/A$. The specific interfacial area is evaluated with the averaged optical results using Eq. 5-5 and Eq. 5-6 presented along in the optical analysis.

5.5.4.1 Initialisation phase

The superficial velocity of oil and methanol feed is fixed to $3.236e^{-4}$ m/s and $7.911e^{-5}$ m/s, respectively, to ensure that the methanol to oil molar ratio is 6:1 at all point of the experiment. The mixing of oil and methanol resulted in a liquid-liquid two-phase stream with oil being the continuous phase, while methanol droplets exist in the form of a slug flow as shown in Figure 5-21, Figure 5-22, and Figure 5-23 for the reaction temperature of 30°C, 45°C, and 60°C, respectively.

Also, the methanol droplets are dispersed in an even manner with the droplet size less than the diameter of the microchannel when the residence time was less than 30s for reaction temperature, 30°C and 60°C. Similarly, the methanol droplets then coalesced into a slug droplet in varying length as they developed from 5s to 30s. The increase in temperature for the microchannel led to a tighter packing of the methanol droplets in the continuous oil phase as shown in Figure 5-22 and Figure 5-23, at a residence time of 20s to 30s. The medium and high heat fluxes can intensify the internal circulation, as shown in Figure 5-5. The convective flow at the oil region between adjacent slugs occurs at a higher magnitude, leading to a smaller distance that separates slugs [278].

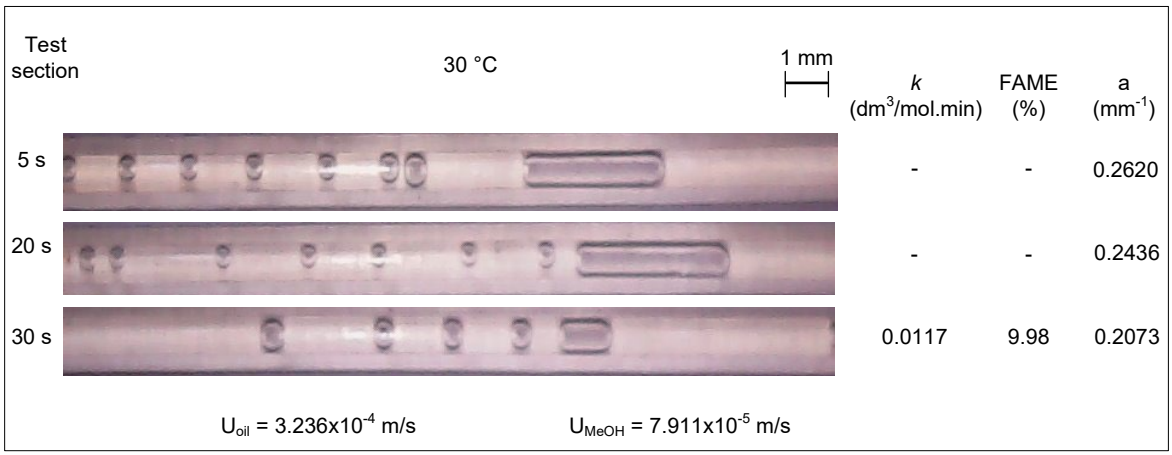

Figure 5-21. The initialisation phase of microchannel tubing upon mixing oil and methanol at a reaction temperature of 30°C.

Figure 5-21 shows that the biodiesel yield data available is at a residence time of 30s after the micromixer. The kinetic rates from the first-order analysis using triglycerides conversion are shown along with the images. The specific interfacial area is also presented using the method explained above. The coalescence of the methanol phase can be observed as early as 5s after exiting the Y-junction due to the effect of a pulsating flow. The flow patterns are expected and should not cause anomalies in the results since this phenomenon is consistent throughout the experiment. The reduction in specific interfacial area is a result of more spaced out methanol droplets and low biodiesel conversion. As the methanol phase reacts slower with the oil phase, the miscibility of the two phases are not improved from 5s to 30s.

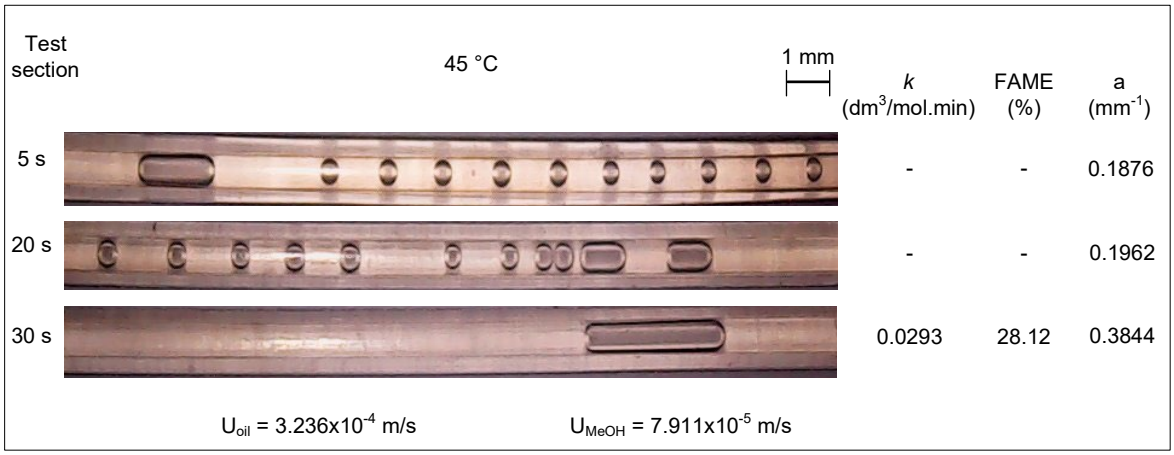

Figure 5-22. The initialisation phase of microchannel tubing upon mixing of oil and methanol at a reaction temperature of 45°C.

Based on Figure 5-22, the specific interfacial area showed a positive correlation with residence time. The methanol droplets have smaller gaps in this oil phase when moving from 5s to 20s, causing slugs to form more often. The increase in specific interfacial area is caused by the higher amount of slugs

formed, which increases the effective surface area in the oil phase. The biodiesel yield increases by more than three times from 30°C reaction temperature at 30s residence time as specific interfacial area doubles from 20s.

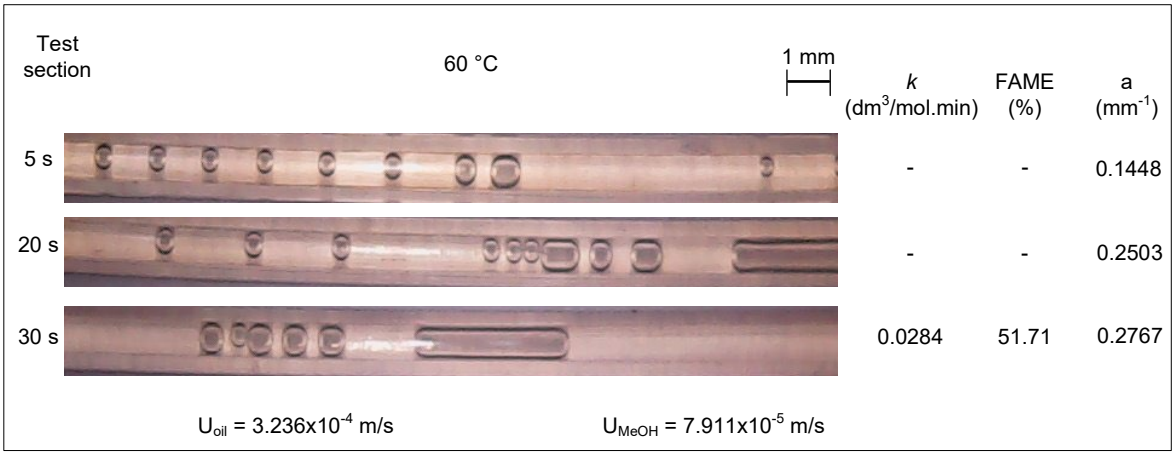

Figure 5-23. The initialisation phase of microchannel tubing upon mixing of oil and methanol at a reaction temperature of 60°C.

From Figure 5-23, methanol droplets are evenly spaced at the beginning, followed by the formation of slugs as the droplet reduces in distance and merges. The specific interfacial area also increases with the residence time as larger droplets and slugs are formed, resulting in more effective contact with the oil phase. The higher reaction temperature also positively impacts biodiesel conversion, where 51.7% yield is achieved at 30s. The slug-annular flow is observed at 30s residence time at this reaction temperature as compared to the other two test cases, mainly slug flow.

5.5.4.2 Intermediate phase

The intermediate phase for the microreactor is defined as the flow approaches the residence time of 42s to 78s in Figure 5-24, Figure 5-25, and Figure 5-26.

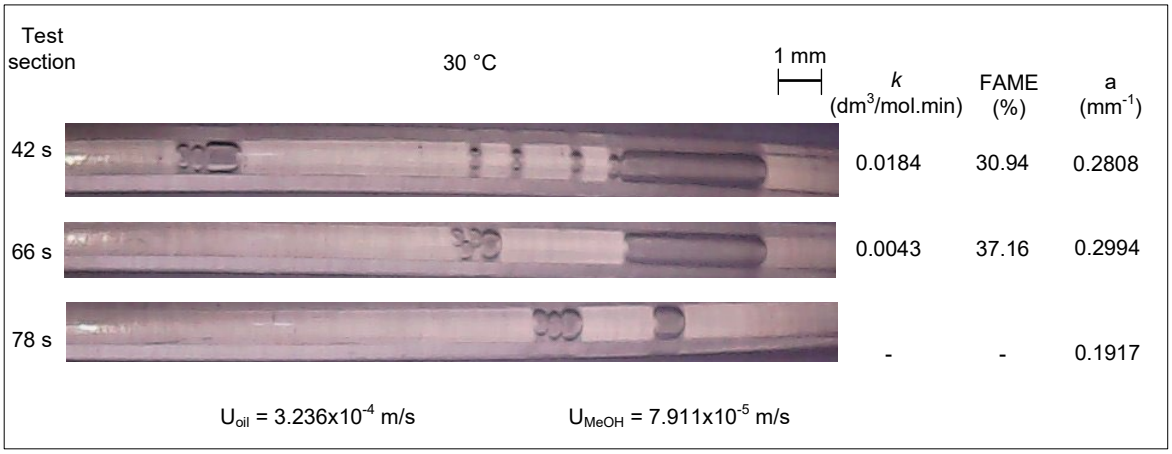

Figure 5-24. The intermediate phase of microchannel tubing upon mixing oil and methanol at a reaction temperature of 30°C.

Figure 5-24 shows that the specific interfacial area is observed to increase slightly from 42s to 66s, followed by a decline at 78s. The flow pattern also transforms from slug-annular to slug flow at 78s, which is likely to reduce the effective surface area. The coalescence of the disperse phase occurs as slugs travel away from the inlet, driven by the difference of Laplace pressure between neighbouring slugs [279].

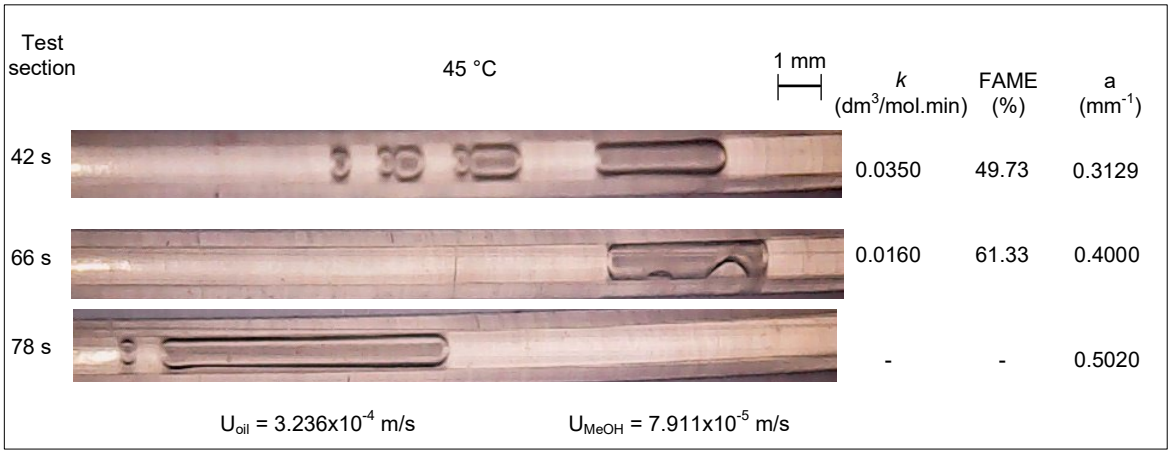

Figure 5-25. The intermediate phase of microchannel tubing upon mixing oil and methanol at a temperature of 45°C.

In Figure 5-25, the flow pattern evolved from slug-annular to annular flow is explained by using a higher heat flux, leading to tighter packing of slugs which essentially promotes coalescence. The result is an increase in the specific interfacial area with residence time, as the volume of the methanol phase is larger than the total surface area. The increase in biodiesel yield from 42s to 66s also gives rise to higher miscibility of the methanol phase in the oil phase, which results in the change in the flow pattern.

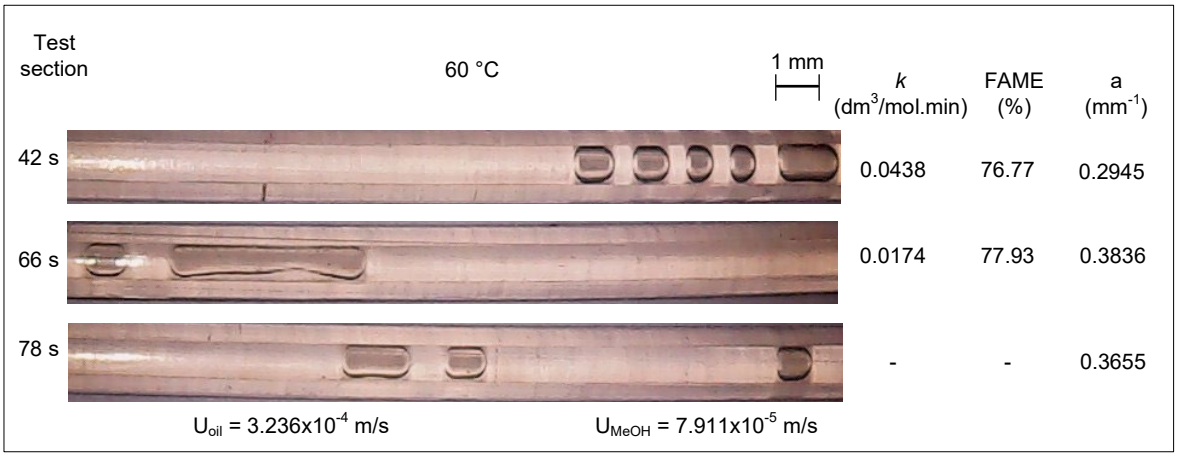

Figure 5-26. The intermediate phase of microchannel tubing upon mixing oil and methanol at a reaction temperature of 60°C.

Based on Figure 5-24, Figure 5-25, and Figure 5-26, the droplets are observed to be combined and transform into a slug-annular flow. The slug-annular flow pattern is more pronounced in the reaction temperature of 45°C and 60°C, at the residence time beyond 66s. This also coincides with the transitional point (60s) of the biodiesel yield formation profile, where the initial physical-limiting phase is approaching the equilibrium phase, as shown in Figure 5-6.

As for the 30°C reaction temperature, the flow pattern is still largely made up from smaller droplets observed going through coalescence to form larger slugs, but yet to form a consistent annular flow. This delay is also reflected in the biodiesel yield, which is consistently lower than the higher reaction temperature experiments.

The explanation for the higher biodiesel yield in the microchannel reactor is likely to be associated with the solubility of methanol in the continuous oil phase as the transesterification is majority diffusion and convective driven. The slug flow promotes the mixing process in various ways, where the contact surface between the continuous and dispersed phase increased. Additionally, the droplet can recirculate which subsequently enhance the mixing of methanol and oil inside the slugs. The movement from these slugs also intensifies the mixing within the droplets. The methanol droplets-channel friction resulting from the shear stresses across the wall interface, can also lead to the formation of internal flow circulation due to the increased length of methanol slug size [280]. Therefore, longer slug and annular flow are beneficial to the formation of biodiesel.

5.5.4.3 Equilibrium phase

The equilibrium phase for the microchannel reactor is defined as the flow approaches the residence time of 90s to 138s in Figure 5-27, Figure 5-28, and Figure 5-29.

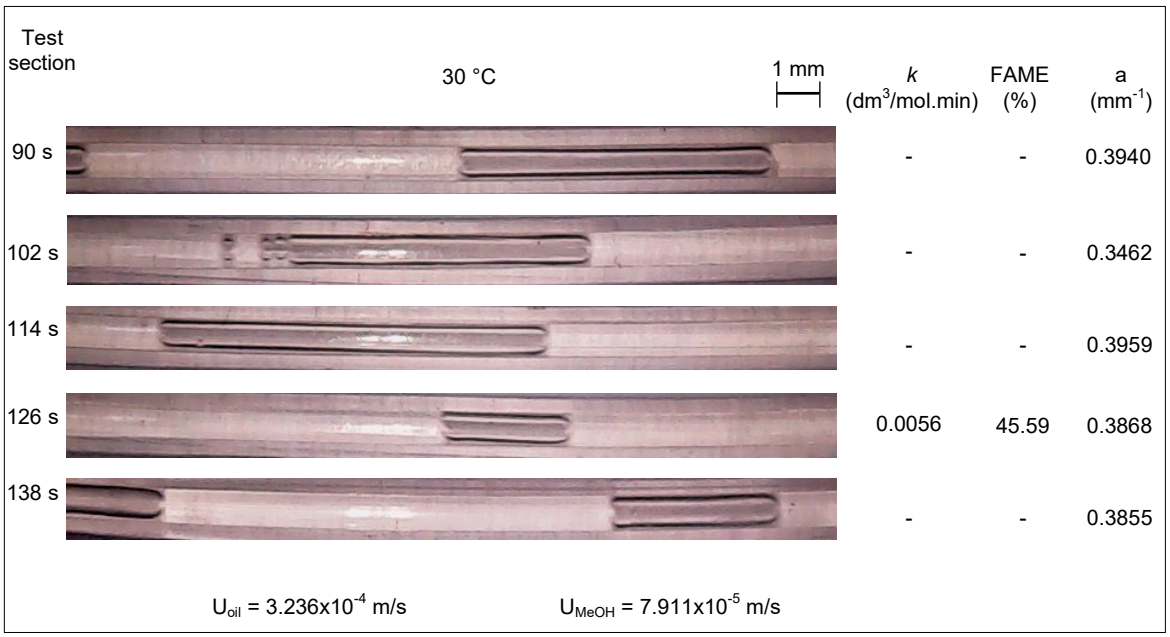

Figure 5-27. The equilibrium phase of microchannel tubing upon mixing of oil and methanol at a reaction temperature of 30°C.

In Figure 5-27, the flow is majority annular as most of the droplets have combined to form a larger volume of the second phase. The low biodiesel conversion rate is also a result of the lower reaction temperature used, combined with low kinetic rates for the triglyceride conversion. The change in specific interfacial area is low from 90s to 138s, due to a slow rate of change in miscibility for the phase interaction between methanol and oil.

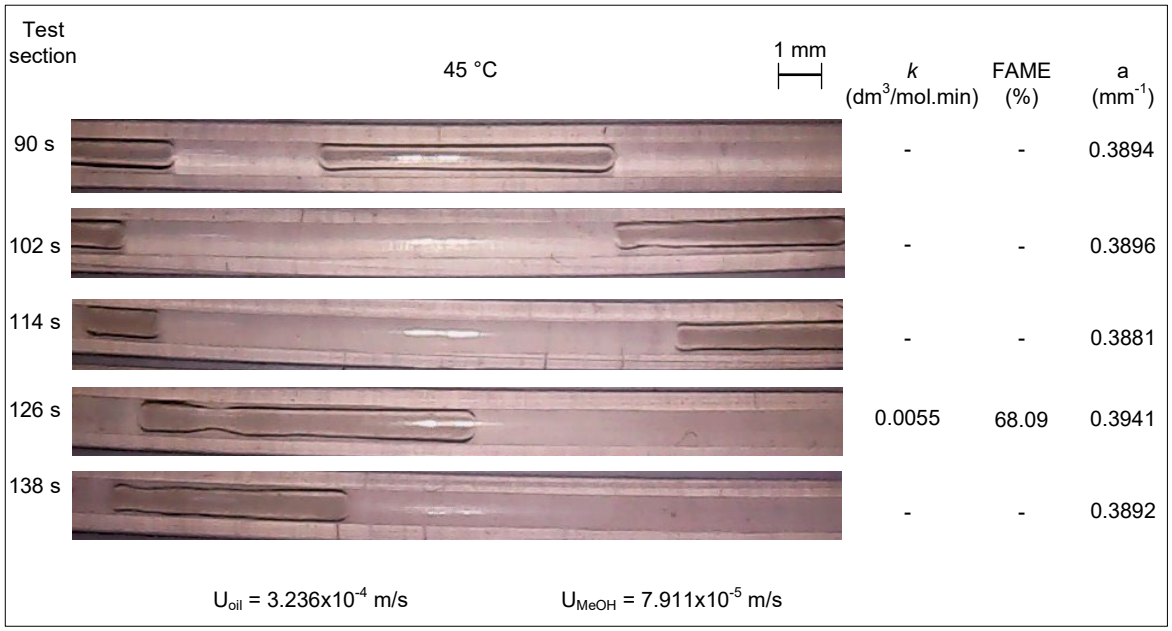

Figure 5-28. The equilibrium phase of microchannel tubing upon mixing of oil and methanol at a reaction temperature of 45°C.

For the 45°C, as shown in Figure 5-28, the flow pattern is similar to the 30°C where it is mostly annular. The consistent annular flow also has minimal influence on the specific interfacial area, since no methanol droplets are available at this section. The first-order kinetic of the triglyceride conversion in Figure 5-19 also showed minimal fluctuations, as it approaches 138s resulting in a lowered kinetic rate.

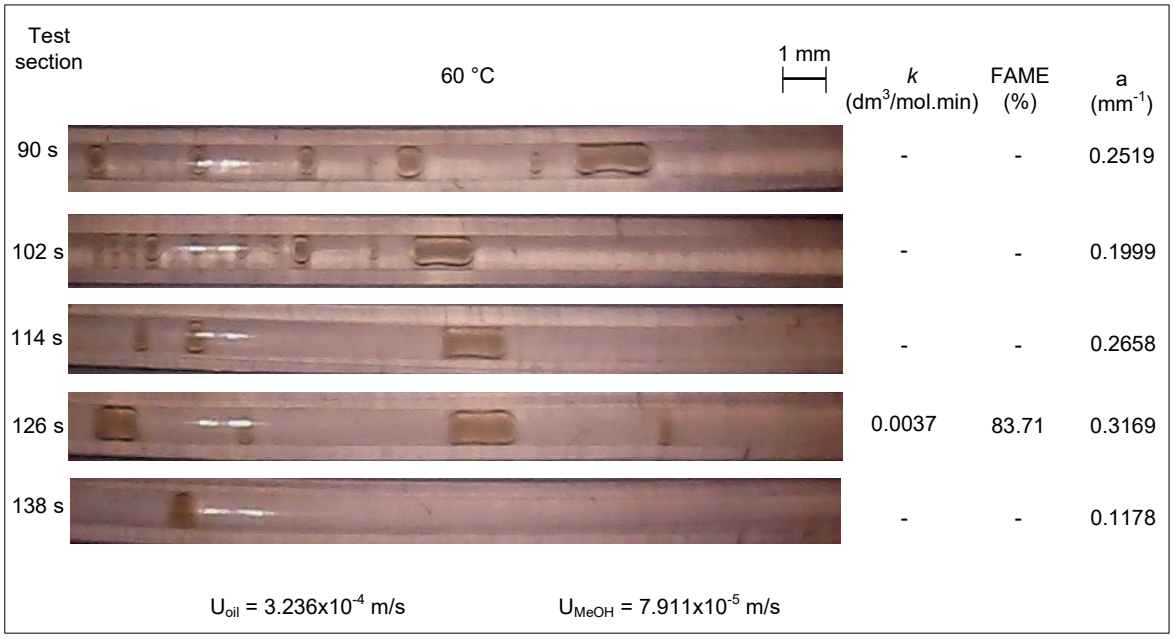

Figure 5-29. The equilibrium phase of microchannel tubing upon mixing of oil and methanol at a reaction temperature of 60°C.

At the equilibrium point of the reaction, which is defined from the yield profile in Figure 5-6, most of the oil-methanol flow pattern is observed to be annular, except for the 60°C reaction temperature. As shown in Figure 5-29, the continuous stream's droplets formation is observed to be darker in colour as compared to methanol. This is likely caused by a higher mass fraction of glycerol due to glycerol's affinity and solubility in the methanol droplets.

Methanol is very soluble in biodiesel and glycerol, but not in oil. The increase in residence time combined with the elevated temperature increases the mass fraction of biodiesel, where the solubility of methanol in the oil and biodiesel phase increases [281]. The observation of the darker coloured glycerol droplets in the methanol phase also suggests that glycerol's low solubility in the oil and biodiesel phase led to the immediate separation in the microchannel.

The high biodiesel yield from Figure 5-6 also suggests that the higher mass fraction of glycerol is formed as compared to the lower reaction temperature cases. Therefore, the diminishing of the annular flow pattern of methanol during equilibrium stage at 60°C is most likely due to the change in droplet content within the slugs-annular, whereby (i) methanol mass fraction is low as more biodiesel is produced, (ii) glycerol separates from the main continuous flow due to density differences and combines with the slugs and annular. Therefore, these interactions change the surface

tension of the slugs and annular, causing the formation of smaller droplets for the second phase. The change in flow pattern from slug-annular back to slug (droplets with low methanol content) from intermediate to equilibrium phase at 60°C also reduces the specific interfacial area of the flow. However, the specific interfacial area has diminishing importance as biodiesel yield increases, since the improved miscibility due to the cosolvent effect will reduce the effective surface area of reaction.

5.5.4.4 Mass transfer analysis

The effect of temperature on the oil and methanol flow patterns were studied and presented below, with the associated analysis on the biodiesel yield. The yield and flow pattern results are shown in Figure 5-30.

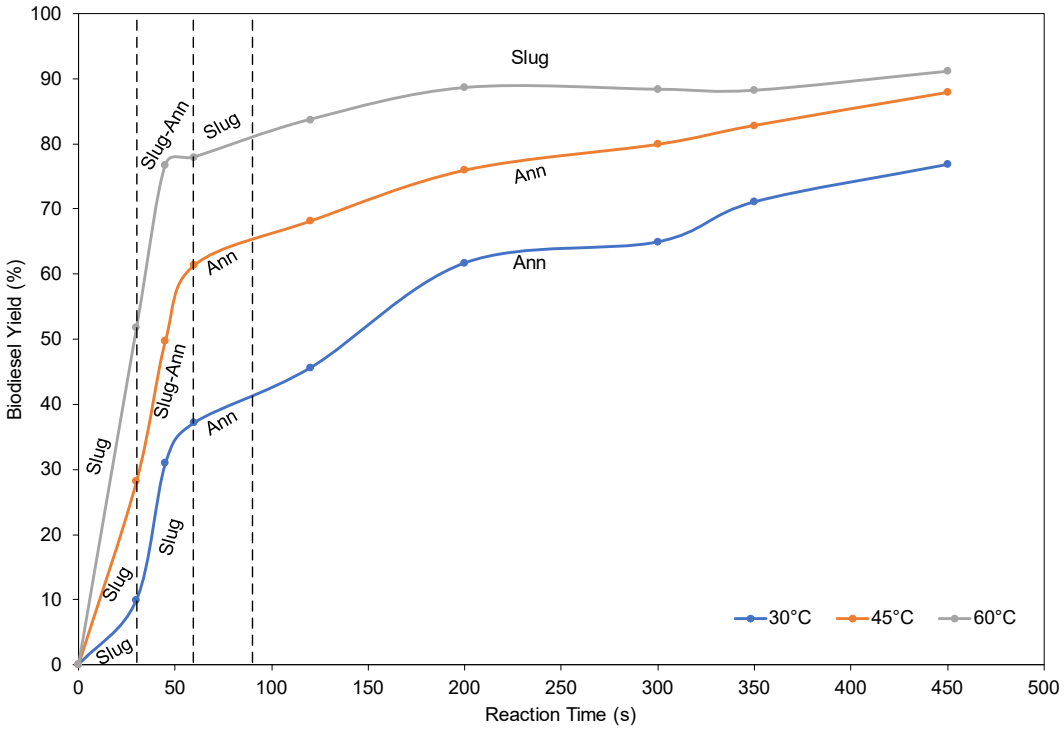

Figure 5-30. The effect of reaction temperature on biodiesel yield with the methanol to molar ratio 6:1, KOH catalyst loading 1.0%, with the flow pattern at each residence time.

The correlation between the change in the type of flow and evolution of biodiesel yield are studied to understand the microchannel reactor better. The optical analysis of the flow pattern is presented below, based on the classifications of flow in Figure 5-1, and the optical images presented from the initialisation phase in Figure 5-21 to the equilibrium phase in Figure 5-29.

Figure 5-30 shows the main types of flow in this microchannel reactor: slug flow, slug-annular, and annular flow. As the methanol and oil enter the microtube via the Y-junction, slug flow is formed for all different reaction temperatures where the droplets are spaced evenly in the continuous oil phase.

The slug flow develops into the slug-annular flow as more methanol droplets merge and coalescence into a long ellipsoid cylinder. The conversion of oil to biodiesel also reduces the two-phase behaviour of oil and methanol, hence slugs are observed again when high biodiesel yield is achieved as shown in the 60°C reaction temperature.

In general, the flow pattern remains slug from the beginning of the mixing until about 40%, where it transforms into slug-annular flow, followed by annular flow. This is observed consistently for 30°C and 45°C reaction temperature. For the higher reaction temperature of 60°C, annular flow is not observed beyond 70% yield, whereas slug and smaller droplets are observed again with a darker tone of colour, likely due to the higher conversion of oil to biodiesel. The change from annular to slug for the 60°C case is also due to the change in species mass fraction and change in miscibility in the slugs, hence the dispersed phase can no longer retain a slug flow.

For slug flows in microchannel reactor, the mass transfer occurs by two different mechanisms, (i) the convection caused by the internal circulation in slugs, (ii) the interfacial diffusion due to concentration gradients between two slugs. However, the use of the peristaltic pumps combined with the Y-junction mixer in this experiment resulted in a pulsating flow that creates droplets of methanol in the continuous stream of oil. The immiscibility of the two fluids also reduces the likelihood of a parallel flow. Therefore, the mass transfer of the system is largely dependent on the liquid-liquid two-phase interaction. Figure 5-31 shows the effect of yield with the specific interfacial area with different reaction temperature.

In all, the reaction kinetics of the microchannel reactor was studied using a transient approach, to understand the physicochemical characteristic of biodiesel transesterification by optically analysing the flow patterns. The method to determine the mass transfer coefficients of a micro-level diffusion system was also improved by integrating the physical characteristics of the flow. This will enable better reaction kinetic models of the reactor to be established based on the refined methodology.

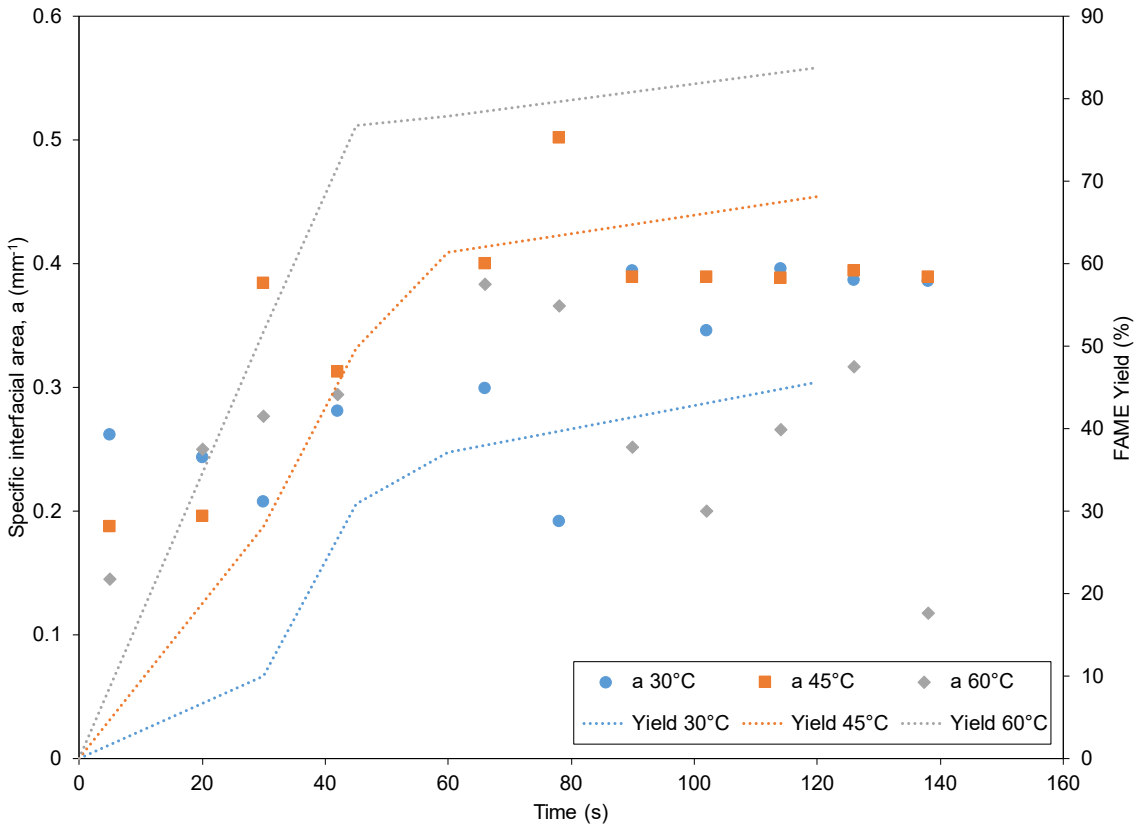

Figure 5-31. The effect of temperature on the specific interfacial area of flow pattern and yield of the microchannel reactor.

Based on Figure 5-31, the initial 0s to 30s showed a consistent range of the specific interfacial area from a minimum of 0.14 mm^{-1} to a maximum of 0.38 mm^{-1}. The flow pattern across the different reaction temperature is largely droplets and slug flow, as observed in the initialisation phase. As the flow develops into the intermediate phase, the formation of slug-annular flow becomes more frequent. This region has the highest kinetic rates of conversion from triglycerides as shown in the first-order analysis, which is observed in the steep increase for the yield profile from 30s to 60s.

The highest specific interfacial area is observed at 78s for 45°C, where the flow is annular. Simultaneously, the 60°C case shows that the specific interfacial area has peaked, where a decline is observed slightly after the intermediate phase. This might seem counterintuitive for the high biodiesel yield at first, where a reduction in the surface area has a positive effect in yield. However, the additional convection effect from the internal circulation is not accounted to promote mass transfer. Thus, a closer inspection at the optical images suggests that the second phase within the continuous oil phase is likely to be a mixture of methanol-biodiesel-glycerol due to the darker shade of colour. Therefore, these slugs and droplets can provide a higher mass transfer in the microchannel flow as they have better miscibility than a slug phase with a higher mass fraction of methanol.

The slug, slug-annular, and annular flows shows an increasing specific interfacial area, from the coalescence of the moving slugs. The microchannel reactor takes advantage of mass transfer enhancement at the fluid interface, while the series of slug trains also serve as an isolated sub-volume for transesterification.

The microchannel reactor's initialisation phase has poor mass transfer due to the heterogeneous nature of oil and methanol. The mass transfer can limit the overall transesterification process, which can be identified by curve fitting with the Boltzmann function [76,259]. The mass transfer-controlled regime in the profile of a sigmoidal shape is plotted using the Boltzmann function, also used in the RVC mass transfer calculation. The optimised Boltzmann sigmoidal plot is fitted and compared against the biodiesel yield of the respective reaction temperature, as shown in Figure 5-32.

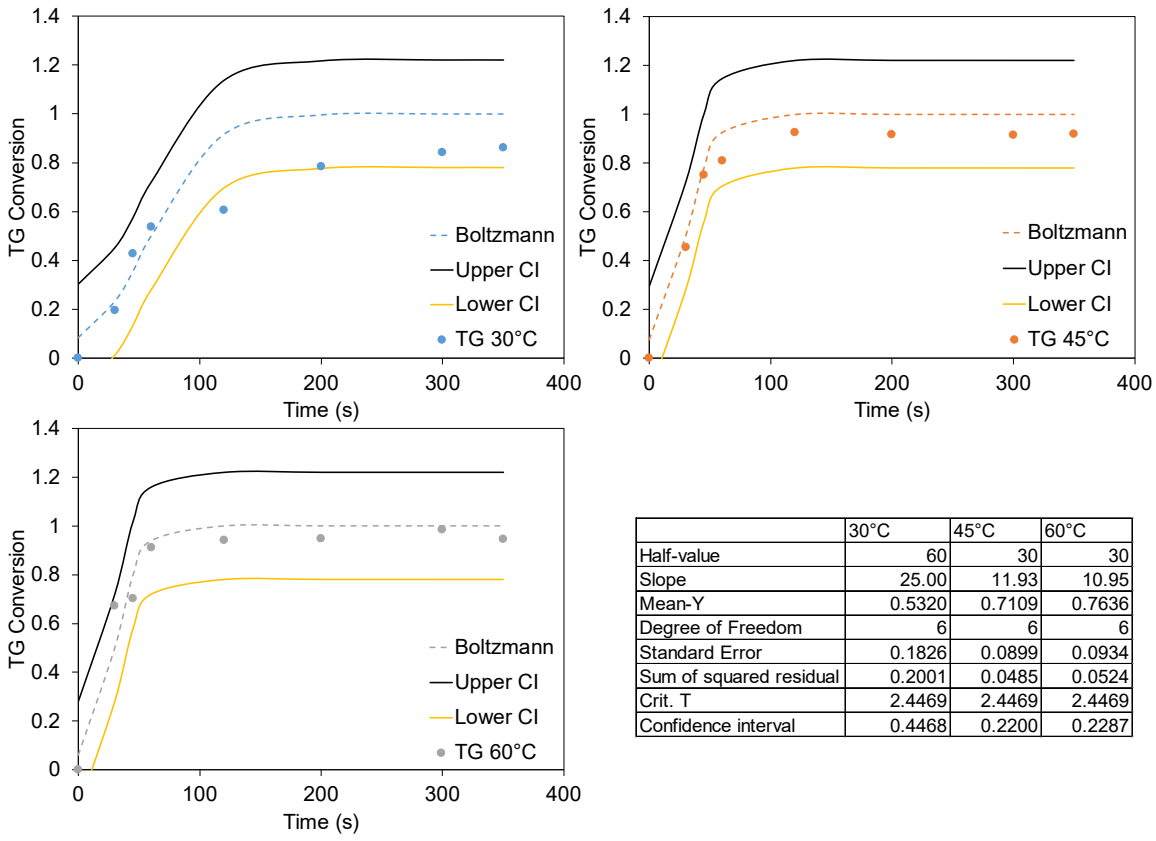

	30°C	45°C	60°C
Half-value	60	30	30
Slope	25.00	11.93	10.95
Mean-Y	0.5320	0.7109	0.7636
Degree of Freedom	6	6	6
Standard Error	0.1826	0.0899	0.0934
Sum of squared residual	0.2001	0.0485	0.0524
Crit. T	2.4469	2.4469	2.4469
Confidence interval	0.4468	0.2200	0.2287

Figure 5-32. The Boltzmann function of sigmoidal fit at the mass-transfer limiting region of the microchannel (a) 60°C, (b) 45 °C, (c) 30 °C.

Figure 5-32 shows that the half-values and slopes determine the general share of the Boltzmann sigmoid, which is optimised to be fitted as close as possible to the experimental data. The residual sum of the squared measure of the discrepancy between the data and an estimation model where a smaller value indicates a tighter fit of the model to the experimental data. The upper and lower boundaries are generated to 95 percentile of the fitted value, to ensure that the fitted value can be acceptable in the margin of error. In terms of the experimental data's sigmoidal profile, the accuracy of the fitted Boltzmann model is in the increasing order of 30°C, 60°C, and 45°C. The initial slow

rising part of the sigmoid is not observable in Figure 5-32, which is likely due to mass transfer was faster than anticipated. The 30°C reaction temperature has the highest residual sum of squared due to the low reaction kinetics as shown, where the experimental data is not within the 95 percentile boundary of the model. The mass transfer coefficient is then calculated using the linear relationship of Eq. 4-10, as shown in Figure 5-33.

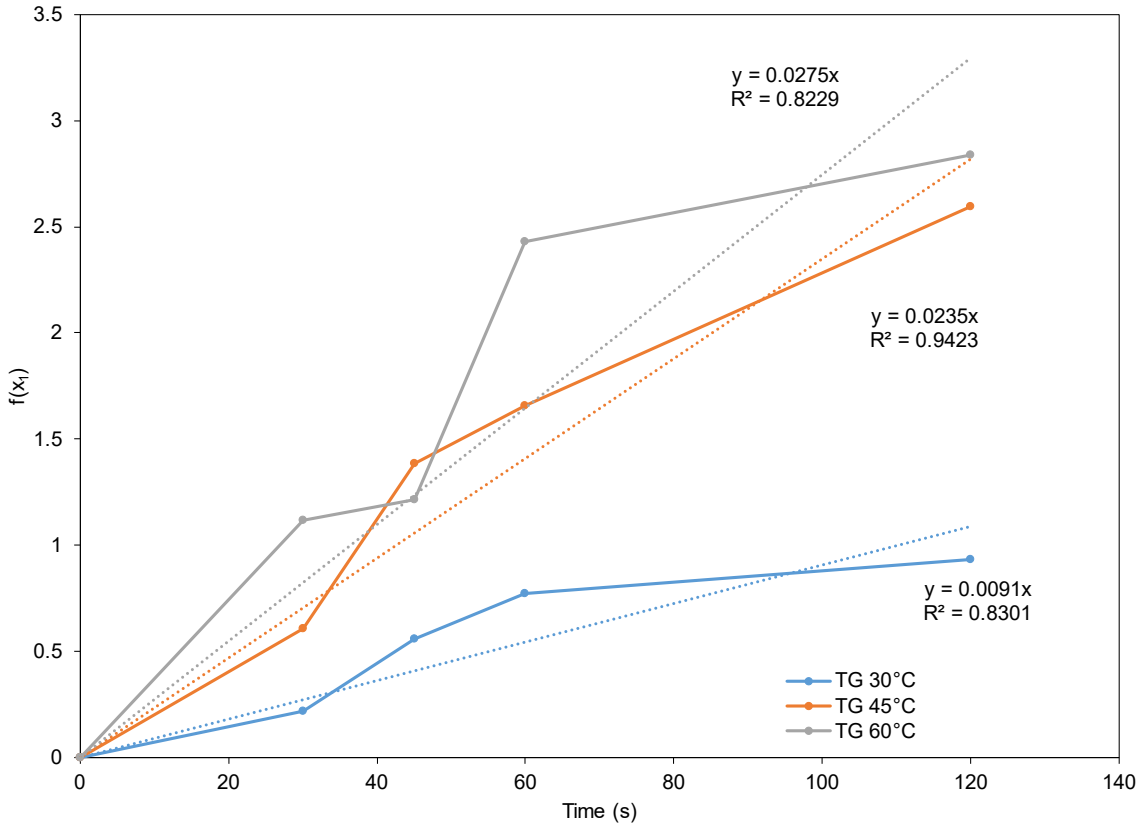

Figure 5-33. The time-averaged triglycerides mass transfer coefficient at 30°C, 45°C, and 60°C of microchannel reactor.

Based on Figure 5-33, the linear trends of the mass transfer in microchannel reactor are expected as they are in the increasing order of the reaction temperature. The mass transfer coefficient for the microchannel reactor shows a good fit with the assumptions made, where triglyceride depletion is equal to the mass transfer from the oil phase into the methanol phase, as reflected by the linear trend. At 42s residence time, a drop in mass transfer coefficient is observed for the 60°C reaction temperature. The optical analysis images for the intermediate phase in Figure 5-26 showed that the droplets are forming larger slugs as they move. The specific interfacial area results from Figure 5-31 also supports the mass transfer results, where the 60°C has a slightly lower value than the 45°C reaction temperature. However, the biodiesel yield results suggest that higher temperature is still favoured in converting triglycerides in a microchannel reactor. The microchannel reactor's mass

transfer coefficients for transesterification are compared with other microchannel systems, as shown in Table 5-7.

Table 5-7. Mass transfer survey for liquid-liquid microchannel systems.

Regime	**Reactant system**	**Conditions**	**Volumetric mass transfer coefficient**	**Reference**
Slug flow	Reacting system, Kerosene/acetic acid/water and NaOH	d_H = 380 µm $C_{acetic\ acid,org}$ = 0.65M u = 0–35 mm/s	In the 0.5 s^{-1} order of magnitude	[282]
Slug flow	Non-reacting system, Kerosene/acetic acid/water	d_H = 0.5–1 mm $C_{acetic\ acid,org}$ = 0.03M u = 10–70 mm/s	~0.4–0.8 s^{-1}	[283]
Slug flow	Reacting system, Hexane/trichloroacetic acid/water and NaOH	d_H = 400 µm $C_{acid,org}$ = 0.6M $C_{NaOH,aqu}$ = 0.15–0.3 M u = 0–20 mm/s	~0.2–0.5 s^{-1}	[275]
Parallel flow	Reacting system, Toluene/trichloroacetic acid/water and NaOH	d_H = 269 µm $C_{acid,org}$ = 0.6M $C_{NaOH,aqu}$ = 0.1–0.2 M u = 0–50 mm/s	~0.2–0.5 s^{-1}	[275]
Slug, Slug-Annular, Annular	Reacting system, Transesterification of palm oil/methanol/KOH	d_H = 8009 µm $C_{KOH,aqu}$ = 1.0 wt. % u = 0.07–0.3 mm/s	~0.0091–0.0275 s^{-1}	This work

The mass transfer coefficient of the batch type benchmark test and RVC reactor is then compared with the microchannel reactor, as shown in Table 5-8.

Table 5-8. Mass transfer coefficient and maximum kinetic constant from the pseudo first-order kinetic model with microchannel reactor, RVC reactor, baseline study.

Reactor	**Reaction Temperature (°C)**	**Volumetric mass transfer coefficient, k_c (1/min)**	**Maximum pseudo first-order kinetic constant, k (1/mol.min)**
Microchannel	30	0.546	1.1059
	45	1.41	2.1017
	60	1.65	2.6292
RVC	30	0.90	1.1779
	45	1.47	2.9432
	60	1.812	3.0850
Baseline	45	1.446	2.3197

From Table 5-8, the 30°C reaction temperature from the two reactors has a small difference in the first-order kinetic rate, with RVC reactor leading slightly. The mass transfer coefficient of RVC reactor is approximately 0.35 min^{-1} higher than the microchannel reactor at 30°C. According to literature, the mass transfer of a microreactor is often quoted as greater than that of batch type reactor in the order of magnitude as compared to similar operating conditions [126,189,284,285]. However, the actual mass transfer coefficient for the microchannel reactor should be higher, as the mass transfer for the internal circulation is not accounted for in this calculation. The current optical analysis is able to measure the diffusive-driven mass transfer at the boundary layer for slugs, while the convective mass transfer within the slugs cannot be measured using this method.

Thus, the mass transfer coefficient in Table 5-8 represents the diffusive-driven mass transfer at the interface between methanol slugs and the continuous oil phase. In the low reaction temperature transesterification, the microreactor can achieve similar kinetic rates with reduced mass transfer compared against the RVC reactor. The mass transfer difference is a physical limitation due to the reactor's design as they operate at the same parameters.

For 45°C reaction temperature, the mass transfer and kinetic rates are in the increasing order of microchannel reactor, baseline reactor, and RVC reactor. The mass transfer coefficient increases by 158% for the microchannel reactor, whereas its kinetic constant showed an increment of 90%. The

RVC reactor on the other hand shows an increase of about 63% from 30°C, while the kinetic rates improved by 150%. The increase in reaction temperature shows a greater benefit for microreactor in the mass transfer coefficient, while the RVC reactor benefits more from the kinetic rate. The RVC has less improvement in the mass transfer, which is likely due to the microturbulence induced by the RVC agitator. However, the kinetic rates are more dependent on the reaction temperature for RVC reactor, as the higher temperature input for the system allows to overcome the activation energy of transesterification reaction. In the microchannel system, since the reactants are only agitated once when they are mixed at the Y-junction, the mass transfer is largely dependent on the liquid-liquid two-phase interaction which causes micro-level diffusion to occur at the contact surfaces of the flow pattern.

Similarly, the reaction temperature at 60°C has a consistent outcome in the sequence of order for mass transfer coefficients and kinetic constants for the reactors, where RVC reactor is slightly better than the microchannel reactor. For the mass transfer coefficient, when the reaction temperature is increased from 45°C to 60°C, a 16% and 23% improvement is observed for the microchannel and RVC reactor, respectively. In terms of kinetic rates, 25% and 5% improvement is achieved by the microchannel and RVC reactor, respectively. The trends of the increases in mass transfer coefficient and kinetic rates are consistent for the reactors, where one benefits more than the other in these two parameters. However, the kinetic rates for RVC reactor also showed a minimal change, suggesting to be a bottleneck of the reactor type, while the microchannel reactor is still showing more room for improvement in both kinetic rates and mass transfer coefficient.

5.6 Conclusion

The microchannel reactor used to study the interaction of fluid flow with the transesterification. Consequently, the physical flow pattern of the reactants, in this case the methanol, palm oil, biodiesel, and glycerol are examined under the digital microscope. As the flow in the microchannel involves pulsating droplets of methanol into a continuous stream of oil, physical intensification was achieved from the pulsing flow motion combined with Y-junction's mixing effect. These droplets were measured and analysed in conjunction with the yield at the respective residence time to draw the correlation between droplet size effect and transesterification yield. The results show that the droplets are formed with slug, slug-annular, and annular flow characteristic. The flow pattern changes accordingly at different residence time due to the coalescence of methanol droplets and also chemical reaction taking place. For instance, slug flow was observed for all range of reaction temperature during initialisation stage to produce biodiesel yield up to 40%, followed by the coalescence of flow where the flow pattern transition into slug-annular where the yield can reach about 70%. The mass fraction of the slugs and annular changes as biodiesel is produced, where the biodiesel and glycerol have a higher affinity to diffuse into the second phase (droplets), which causes the flow pattern to revert to slug droplets as observed in the 60°C case during equilibrium phase. Thus, the flow droplets in the second phase will have a various level of methanol content at the different stages of the microchannel transesterification. As the methanol is being consumed, biodiesel and glycerol are being produced simultaneously.

The biodiesel yield was obtained at a different residence time of the transesterification process using a different length of microtubes, resulting in transient yield profiles. This is important to understand the effect of using different operating conditions such as reaction temperature to provide insights on the reaction kinetics of the reactor by studying the change in glycerides concentration. Similarly, the pseudo first-order kinetic model was introduced to test the feasibility of implementing using different types of glycerides. The results show that the concentration depletion profile shows a good linear fit, an important characteristic of the pseudo first-order model.

The mass transfer model in this study is also revised to integrate with the results from the flow pattern study, where the surface area of the individual droplets was calculated and used in determining the mass transfer rate. The high mass transfer rate was observed at the higher reaction temperature, where the flow pattern quickly transforms from slug flow to slug-annular, then back to a slug patterned flow. The fast formation of biodiesel has a positive compounding effect on the kinetics of transesterification in the microchannel reactor, as the design of microreactor is mainly diffusion-controlled. The presence of biodiesel reduces the resistance of miscibility between methanol and oil as it is mutually soluble. Therefore, a distinct biodiesel phase can be observed at the higher reaction temperature operating condition towards the equilibrium phase. The droplet formation of the

methanol phase increases the contact surface with the oil phase, hence mass transfer is improved in the microchannel reactor for transesterification.

Chapter 6 Conclusions

Based on the Pareto, normal, and hierarchical frameworks, the structure of transesterification in relative significance is identified for the physical-limiting and reaction limiting stages. The methanol to oil molar ratio was ineffective in excess during initialisation of transesterification, as it reduces the synergistic effect of biodiesel in the oil and methanol phase to improve miscibility. The agitation effect was identified to be more important until adequate mixing between oil and methanol is achieved. After achieving a homogeneous mixture, biodiesel production is mainly determined by factors such as the catalyst loading, reaction temperature, and methanol to oil molar ratio for complete reaction. From the hierarchical clustering, the main effects of the activation energy cluster, which consist of catalyst loading and reaction temperature outperforms the reactant contact surface cluster formed by agitation rate and methanol to oil molar ratio. A key observation from the standardised significance study in normal analysis shows that the main effects impact non-overlapping stages, which applies for agitation rate and methanol to oil molar ratio. The operating conditions were optimised using response optimiser. High-speed agitation in conjunction with increasing level of methanol to molar ratio is recommended as transesterification progress until 270s, which is the end of the physical-limiting stage.

From the RVC reactor study, the integration of the RVC agitator shows promising results in terms of mixing enhancement in transesterification. The material and structure superiority of RVC have resulted in great potential for its physical intensification function in a batch reactor. In the preliminary study of RVC transesterification experiments, the mentioned features provided added benefit towards the biodiesel formation for all the operating conditions, in terms of directly promoting yield and increasing the efficacy of the operating parameters. A notable example is the low-speed agitation test at 100 rpm, where the RVC reactor could provide adequate mixing through microturbulence and micro-level diffusion to achieve an 85.8% yield as compared to the baseline at only 7% final yield.

The preliminary study allows the determination of a sensible range to test the operating condition in the full factorial experiment, hence it is possible to conduct a like-to-like comparison with the baseline batch reactor. The factorial analysis of RVC reactor shows that agitation combined with ppi is responsible for adequately mixing the reactants at the beginning of transesterification, then followed by the cluster that facilitates reactant-limiting stage which consists of catalyst loading, temperature, and molar ratio. Further investigation of the RVC reactor was conducted using RSM where surface plots were constructed with the onset of transesterification to form a sequential surface plot timeline. The results were used to characterise the two-way interactions of operating parameters from the morphing surface plots. Interaction pairs that involves ppi, RPM, and methanol molar ratio showed a significant impact in the response surface from 0s to 120s. This observation shows that the

physical-limiting stage of RVC reactors could be shorter than the benchmark counterpart where it is in the range of 0s to 270s. Subsequently, the interaction pair that involves catalyst loading and the temperature is observed to be relatively consistent in strength throughout transesterification, focusing on promoting the complete reaction.

The reaction kinetics of the RVC reactor was also investigated using the pseudo first-order and pseudo second-order kinetic models. They are used to calculate the kinetic rates of the glycerides conversion to determine how quickly transesterification occurred throughout the experiment. Diglycerides and monoglycerides kinetic rates were able to be determined using the first-order method by identifying a suitable time range of application, which has not been tested in kinetic studies, as they were often assumed to be negligible intermediates. The results obtained suggest otherwise, where the intermediate glycerides are not recommended to be omitted as the assumption of excess methanol capable of promoting high kinetic rate at the beginning of transesterification is misleading, as supported in this work. Additionally, methyl ester formation was also used as a substitution in the triglyceride depletion model to study the viability of using methyl ester conversion. However, the results show that the calculated kinetic rates using methyl ester model are almost twice as low as compared to the triglycerides depletion. Thus, it is not an accurate representation of the overall reaction kinetics, but it is capable of providing some qualitative representation. The activation energy in the range of 8.5 to 14.58 kJ/mol was obtained using the pseudo first-order and pseudo second-order kinetic model. The calculated values are well within the range from other reported studies, where RVC transesterification has shown a relatively lower activation energies. When compared against the benchmark batch reactor in kinetic rates, RVC reactor shows outstanding performance at the initialisation phase where methanol first mixed with oil, reflected by up to 71.3% improvement for the three-point moving average triglycerides kinetic rates.

Thermal image analysis was conducted to study the heat transfer relationship with the transesterification of RVC reactor. The results suggest that temperature drop can occur during the physical-limiting regime, when the addition of methanol into preheated oil lowers the system's overall temperature. This can further reduce the kinetic rates of the reaction while oil and methanol are still relatively immiscible. Therefore, the results can provide better optimisation strategy for practical implementation in a batch reactor.

Furthermore, the microchannel reactor study was conducted to study the relationship of flow pattern and biodiesel yield. Therefore, a comprehensive flow distribution analysis was performed from the initialisation phase, to the intermediate phase, followed by the equilibrium phase. Slug flow, slug-annular flow and annular flow was observed. The effect of reaction temperature shows that biodiesel's formation can affect the flow pattern as the reaction is majority diffusion-controlled at the micron level. Higher reaction temperature forms biodiesel faster, facilitating micro-diffusion at the liquid-liquid interface as miscibility of reactants is improved. The droplet size of methanol was analysed and integrated into the mass transfer calculation to determine the specific interfacial area.

The highest specific interfacial area is observed at 78s residence time at the intermediate stage with annular flow, at a reaction temperature of 45°C. Simultaneously, the use of a higher reaction temperature at 60°C also peaked in a specific interfacial area, where a decline is observed shortly after the intermediate phase. However, this is caused by the high biodiesel mass fraction in the flow, promoting mass transfer in the reactor as mentioned. RVC reactor when compared with the microchannel reactor, shows a greater volumetric mass transfer coefficient at the same operating range of reaction temperatures. As the reaction temperature increases from 30°C to 45°C, the mass transfer coefficient increases by 158% for the microchannel reactor, whereas its kinetic constant showed an increment of 90%. The RVC reactor shows an improvement of 63% for the mass transfer coefficient, while the kinetic rates increase by 150%. Therefore, higher reaction temperatures provide greater improvement for microreactor in the mass transfer coefficient, while the RVC reactor benefits more from the kinetic rate enhancement.

Although the search for a well-rounded biodiesel reactor is often defined by the yield performance and energy efficiency in transesterification, the fact remains that reaction kinetics heavily dictates these metrics. As discussed in the previous chapters, the frameworks introduced in this study serve as a guideline to characterise the operating parameters of biodiesel reactor in a comparable manner, while the reaction kinetics governs the mass transfer mechanism of chemical reaction. Therefore, by combining the two techniques namely, frameworks and reaction kinetics, the strengths and weaknesses of different biodiesel reactor can be highlighted to improve decision making in their respective applications.

Chapter 7 Future work

7.1 Remarks on transient transesterification of the stirred-tank reactor

The recommendations for Chapter 3 with the batch-type transient and reaction kinetic analyses are as follow:

- Computational Fluid Dynamics (CFD) can be used to identify the agitation effect, particularly at the physical-limiting stage of transesterification.
- The study of the change in methanol miscibility with the formation of biodiesel applied in biodiesel reactor. The effect can be studied to understand the interactions of homogeneity and convective mixing at beginning of transesterification, that can lead to a shorter physical-limiting stage. The result directly contributes to promoting complete reaction during the reaction-limiting stage. Therefore, dynamic optimisation strategy can be used to achieve the highest yield with the shortest amount of reaction time, or in an economically feasible manner.

7.2 Remarks on the RVC reactor for biodiesel transesterification

The recommendations for Chapter 4 with the RVC reactor and reaction kinetic analyses are as follow:

- The application of RVC in other types of reactors such as plug flow reactor, continuous stirred-tank reactor, and cavitation reactor.
- Heterogeneous catalyst coating on RVC, where the large total surface-to-volume ratio of the RVC can complement the catalyst's performance.
- CFD of the RVC reactor can be used to simulate the microturbulence induced and the micro-diffusion between oil and methanol. The results from the reaction kinetics in this study can be used to support the development of the CFD to simulate chemical reactions, as the overall reaction was characterised from the physical-limiting stage to reaction-limiting stage.
- Optical study to investigate the size of the droplets caused by microturbulence during the physical-limiting stage when emulsion is being formed between oil and methanol.

7.3 Future work on the microfluidics biodiesel reactor optical analysis and reaction kinetics.

The recommendations for Chapter 5 with the microreactor optical and reaction kinetic analyses are as follow:

- Glycerides study for parameters such as catalyst loading, methanol to oil molar ratio and flow speed can provide an additional dimension to the reaction kinetics analysis.
- Thermal imaging study to identify the relationship for reaction kinetics, flow pattern and heat transfer in a microchannel reactor.
- Optimisation study based on reaction kinetics data gathered is impactful for performance enhancement or economic benefit.
- The development of a CFD model to simulate fluid pattern at different stages of transesterification. The analysis from the reaction kinetics in this study can contribute to the chemical reaction model for the CFD.

Appendices

Appendix A: Experimental procedure for the batch and RVC reactor.

Appendix B: Experimental procedure for the microchannel reactor.

Appendix C: Experimental procedure for EN14103 FAME Gas Chromatography.

Appendix A

Experimental Procedure for the Batch and RVC Reactor Experiments

EXPERIMENTAL PROCEDURE

For RVC and Baseline Test

Version: 1.5

Author: Kang Yao, WONG

Date: 15/06/2017

0. Calculation of molarity

These are the values that we will be using to calculate the molarity:

a) Density of palm oil used is 0.91 g/cm3
b) Molar mass of palm oil used is 885.5 g/mol
c) Density of methanol used is 0.792 g/cm3
d) Molar mass of methanol used is 32.04 g/mol
e) Amount of catalyst KOH used is 1 % to the amount of oil used
f) Molar ratio between oil and methanol is 1 mole oil and 6 moles methanol (1:6)

Using the supplementary excel sheet, *Figure A1* (Conversion Tables for Tests), we can calculate some useful ratios when we produce different amount of biodiesel, eg:

i) The mass ratio of oil : methanol is ~4.6 : 1

ii) The volume ratio of oil to methanol is ~4.0 : 1

Appendix A

	A	B	C	D	E	F	G	H	I	J	K	L	M
1	Example:												
2	**Properties (Subject to changes)**												
3	Type of Oil	Palm											
4	Density of Oil (g/cm3)	0.91											
5	Molar mass of Oil (g/mol)	885.5											
6													
7	Type of Alcohol	Methanol											
8	Density of Methanol (g/cm3)	0.792											
9	Molar mass of Methanol (g/mol)	32.04											
10													
11	**Inputs:**												
12	Oil volume required (ml)	500											
13	Molar ratio Alcohol:Oil	6											
14	Catalyst loading (% wt.)	1											
15													
16	**Outputs:**												
17	Mass ratio of Oil:Alcohol	4.606221											
18	Volume ratio of Oil:Alcohol	4.008931											
19	Total Volume of Oil and Methanol (mL)	624.7215											
20	Oil required (g)	455	*Use digital scale										
21	Alcohol required (g)	99	*Use digital scale										
22	Catalyst required (g)	4.55	*Use high precision Shimadzu scale										
23													
24													

Conversion Table | RPM correction

Figure A1. Conversion tables for calculating the reagents required for different case.

*In this experiment, all numbers given are based on the usage of 455g of oil. *

1) Preparation of methanol and KOH

a. Measure 4.55g of KOH with a 25ml beaker with electronic balance in *Figure A2* and *Figure A3*. (amount of KOH to be 1% the mass of oil to be used)

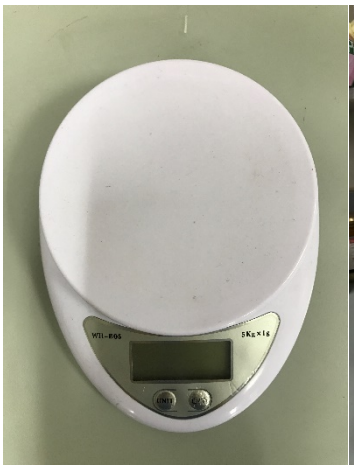

Figure A2. Digital Scale

Figure A3. Electronic Balance

b. Measure 100g of methanol into a 500ml beaker with digital scale. (If excess methanol is poured into beaker, remove using pipette.)

c. Pour all of the solid KOH into the 500ml beaker filled with methanol.

d. Use a parafilm and completely seal the top of the beaker. Reference to *Figure A4.*

Figure A4.KOH in methanol, sealed with parafilm.

e. Leave the mixture in the fume hood while waiting the KOH to dissolve completely in methanol.

Reminder:

Do not leave the methanol + KOH mixture overnight as KOH crystal will form causing the mixture to be not usable.

#Do not leave methanol in open air as it will absorb moisture from the air, making it less pure and ineffective.

2) <u>Preparation of oil</u>

a) Measure 457g of oil into a 500ml beaker with digital scale. (Extra 2g is for transfer errors, as not all the oil in the beaker will be transferred completely into the cylindrical reactor.)
b) Transfer the oil from beaker into the reactor kettle. Ensure that the reactor kettle is dry before pouring water into it by drying it with a paper towel or leaving it in the oven for a few minutes.
c) Put the (RVC or baseline) impeller into the kettle before securing the lid on the top. Reference to *Figure A5*.

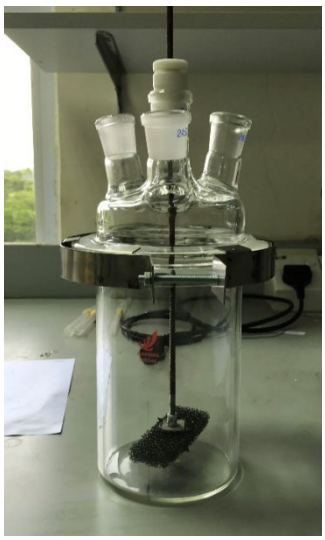

Figure A5. Reactor with lid and impeller installed.

d) Insert the impeller holder to ensure the impeller is secured.

e) Install the heating jacket onto the reactor flask, ensure that the jacket covers entirely from bottom. Reference to *Figure A6*.

Figure A6. Installing the heating jacket onto the reactor.

f) Take the reactor kettle with the impeller and holder placed and clamp it to the reactor. Refer to *Figure A7*.

Figure A7. Installing the reactor system with the impeller clamped to the overhead motor.

g) Adjust the position of the clamp with Allen key so that the impeller can be inserted into the motor spinner.
h) Insert the impeller into the motor spinner and tighten its position.
i) Set the position of the impeller about 1cm above the maximum submerged distance of the impeller in the kettle.
j) Turn on the motor spinner and set the actual rpm to 100 according to supplementary excel sheet, RPM correction in *Figure A8*.

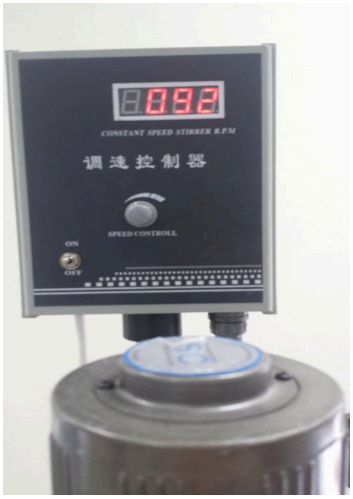

Figure A8. RPM controller with indicator.

Appendix B

Experimental Procedure for Microchannel Reactor

EXPERIMANTAL PROCEDURE

For Microchannel Reactor Experiment

Version: 1.0

Author: Kang Yao, WONG

Date: 15/06/2019

0. Calculation of Molarity

These are the values that we will be using to calculate the molarity:

a) Density of palm oil used is 0.91 g/cm3
b) Molar mass of palm oil used is 885.5 g/mol
c) Density of methanol used is 0.792 g/cm3
d) Molar mass of methanol used is 32.04 g/mol
e) Amount of catalyst KOH used is 1 % to the amount of oil used
f) Molar ratio between oil and methanol is 1 mole oil and 6 moles methanol (1:6)

Using the supplementary excel sheet, as shown in *Figure B1* (Microtubular Pipe Length Calibration), we can calculate some useful ratios when we produce different amount of biodiesel, eg:

i) The mass ratio of oil : methanol is ~4.6 : 1

ii) The volume ratio of oil to methanol is ~4.0 : 1

Flow Rate Calculator										
Step	Methan	Oil Pump							meoh	oil
88	0.4894	0.5249	ml/min		0.4894	1.935484	2.4248839		0.009967	0.0362
	0.0008	5.02655E-07				3.95481			3.632067	
Molar Ratio	Volume	Mass Ratio	Methanol P	Oil Pump S	Choosing Speed		2min			
3	8	9.2	44	350	8.001174		8.86			
6	4	4.6	44	170	4.034312		6.3			
9	2.7	3.1	44	112	2.715585		3.56			
For 6 molar ratio flow rate										
Catalytic Loadin	Methan	Oil Vol. (ml/mi	Methanol M	Oil Mass(g	Catalyst M	Dissolve in 100g Methanol				
0.5	0.2386	0.9759	0.1889712	0.888069	0.00444	2.349747			3.24E-04	0.3236
1	0.2386	0.9759	0.1889712	0.888069	0.008881	4.699494			7.91E-05	0.07911
1.5	0.2386	0.9759	0.1889712	0.888069	0.013321	7.049241				
1.2	0.1931	0.398230088	0.1529614	0.362389	0.004349	2.842987				
	Temp	Total FlowRate (ml/min)								
	30	1.165048544								
	45	1.066666667								
	60	1.121495327								
		1.117736846								

Processed Data | Raw Data (actual) | Raw Data (Test) | Volumetric Ratio | pump calibration | **Motor Calculator**

Figure B1. Conversion table for calculating the flow rate, catalyst loading required.

1) Preparation of methanol and KOH

a) The procedures can be referred from Appendix A steps 1a to 1e.

2) Preparation of oil

a) Measure 500g of palm oil into a 500 mL beaker using a digital scale as shown in *Figure B2*.

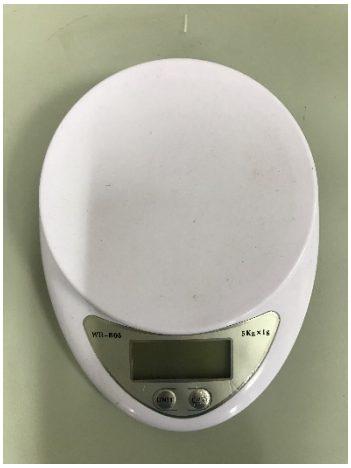

Figure B2. Digital scale used to measure mass of oil.

b) Transfer the beaker to the heating mantle and insert the thermocouple as shown in *Figure B3*.

Figure B3. Heating mantle and thermocouple used to heat up the oil. Image on the left is for illustrative purposes only.

3) <u>Setting up the microchannel reactor rig</u>

a) The peristaltic pumps used in this study is the Kamoer 12V KPP as shown in *Figure B4*.

Figure B4. Kamoer DC 12V KPP used in the microchannel reactor.

b) The peristaltic pumps are then connected to a Y-junction where the oil and methanol will be mixed as shown in *Figure B5*.

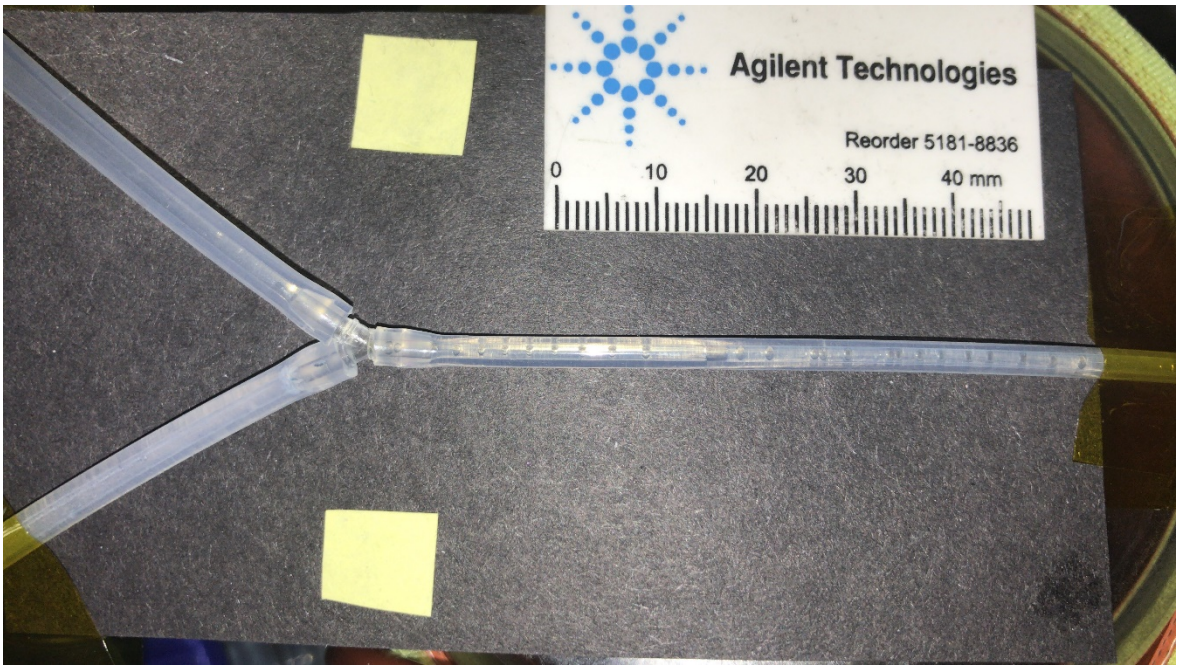

Figure B5. The Y-junction setup where oil continuous phase and methanol droplets are formed.

c) Heating jacket is wrapped around a beaker to act as a heating platform for the microtube primarily through heat conduction.
d) The microtube used in this experiment is 0.8 mm in internal diameter, which is then coiled around the heating jacket to the desired length to represent the appropriate residence time.
e) The setup from 3c and 3d is shown in *Figure B6*.

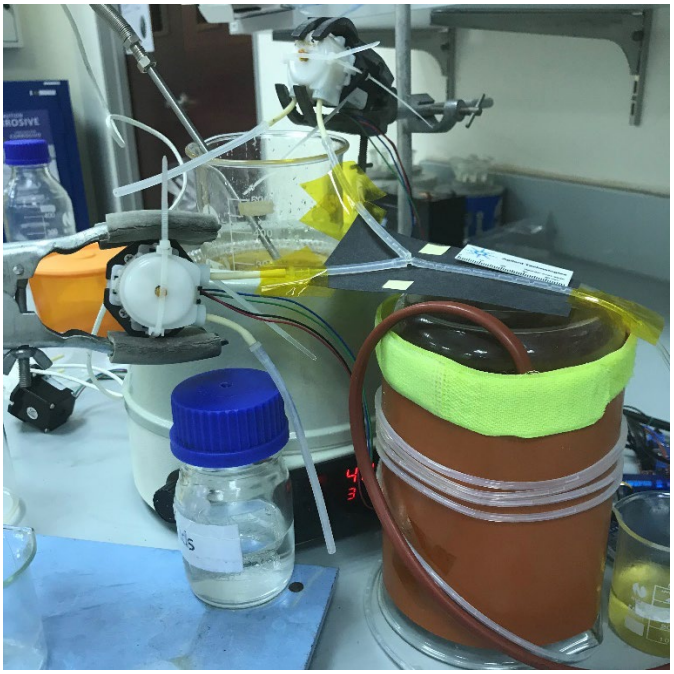

Figure B6. The experimental setup of microchannel reactor with the peristaltic pump, oil reservoir heated by the heating mantle, methanol reservoir, the Y-junction, and heating jacket.

f) Place the digital microscope as shown in *Figure B7* in front of the microtubes to capture the flow pattern.

Figure B7. Digital microscope used for recording the flow pattern.

g) Adjust the focus of the digital microscope to scale by turning the focal knob, and visually inspecting the images from the computer.

h) The calibration is done on the microtube and flow pattern as shown in *Figure B8*.

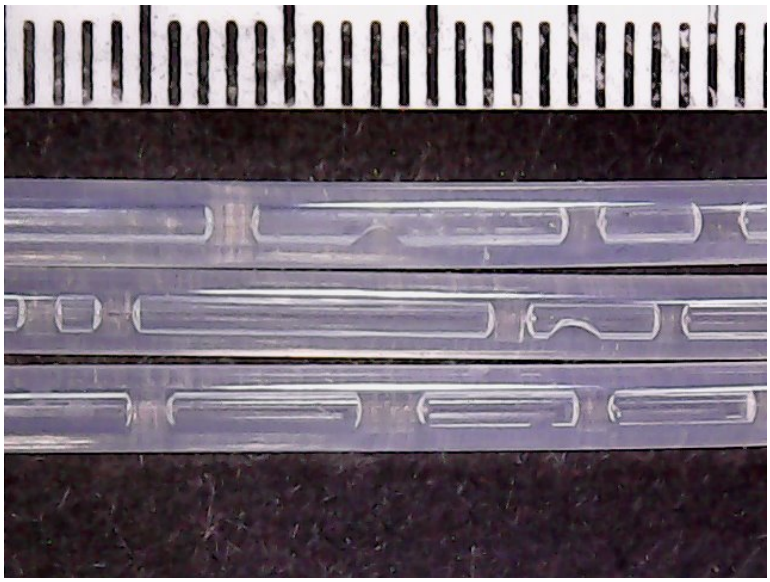

Figure B8. Calibrating the frame of the images from the digital microscope using a microscale.

Appendix C

Experimental Procedure for EN14103 FAME Gas Chromatography

EXPERIMANTAL PROCEDURE

For FAME GC Analysis

Version: 1.0

Author: Kang Yao, WONG

Date: 19/06/2017

Materials:

1. 10 mL vial and cap
2. 10 µL syringe
3. 100 µL syringe
4. 500 µL syringe
5. C17 internal standards
6. Sample (3 mL minimum)
7. N-Heptane

1) Sample preparations

a) Prepare an empty 10 mL vial (can be either amber or transparent).

b) Weigh the 10 mL vial using Shimadzu high sensitivity electronic balance.

   i) Ensure all three sides of glass door are closed, and allow measurement to stabilised.

c) Re-zero the 10 mL vial by pressing the green "-> 0/T -<" icon at the centre.

d) Using a 100 µL syringe as shown in *Figure C1*, draw 80 µL sample, discard into a beaker labelled "waste".

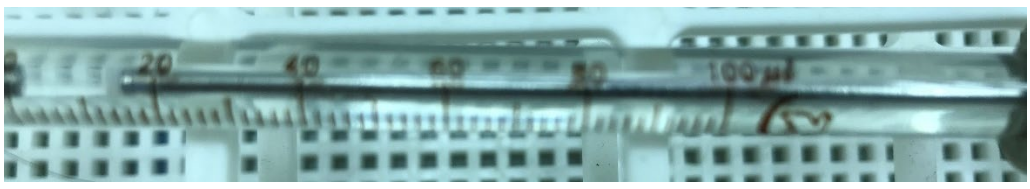

Figure C1. The 100 µl syringe for measuring sample.

e) Repeat rinsing process from step d once more.

f) Draw 70 µL of sample.

g) Dispense 50 mg ±3 into the 10 mL vial slowly. Ensure most of the sample are dispensed directly into the bottom of the vial. Carefully removing the syringe without touching the vial wall (Don't wet the vial wall). You may take out the vial and adjust the amount of sample by dispensing or drawing outside the electronic balance, then reweigh it. Hold the vial with one hand, and the syringe with the other as shown in *Figure C2.*

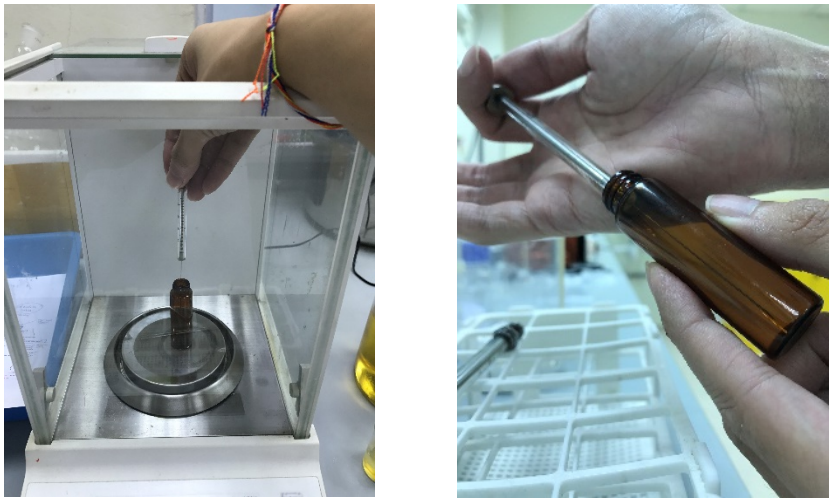

Figure C2.The measurement of 50mg of sample on the analytical balance.

1) Discard excess sample in the syringe into "waste".

2) Once the sample is within the mass range, Using the 500 µL syringe as shown in *Figure C3*, draw 250 µL of internal standard, C17.

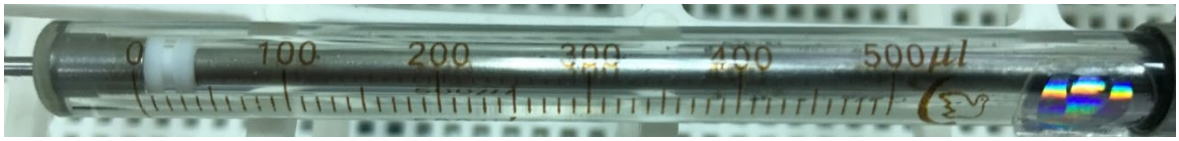

Figure C3. The 500 µl syringe for measuring internal standard C17..

h) Ensure the 250 µL internal standard is free from bubble when drawing with syringe.

i) Lower the syringe into the 10 mL sample vial, without touching the sample, then dispense the internal standards gently.

j) Close the 10 mL sample vial with its respective cap. (White for amber vial, black for transparent vial)

2) **<u>Analysis in GC</u>**. (proceed towards the GC station)

a) Using a 5 µL syringe as shown in *Figure C4*, rinse the syringe with n-heptane solvent, 10mL vial labelled Qrec, and dispense into "waste" vial. Repeat this twice.

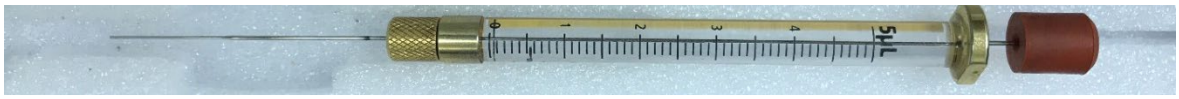

Figure C4. The 500 µl syringe for measuring internal standard C17.

b) Using 5 µL syringe, draw 1µL from 10 mL sample vial.

c) On the PC, switch on the software on the desktop, “GC (online)” and “GC (offline)” as shown in *Figure C5*.

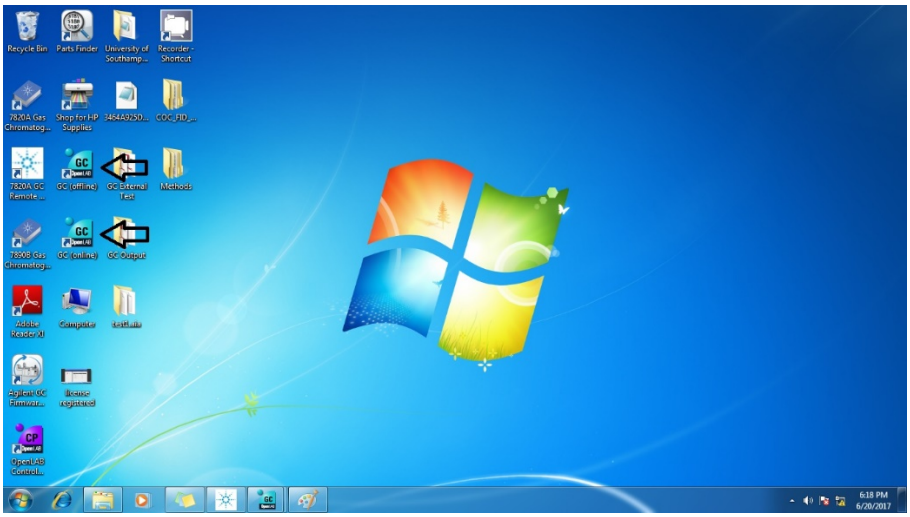

Figure C5. The GC (online) and GC (offline) software.

d) Double click to load the correct methodology, for the respective sample as shown in *Figure C6* and *Figure C7*.

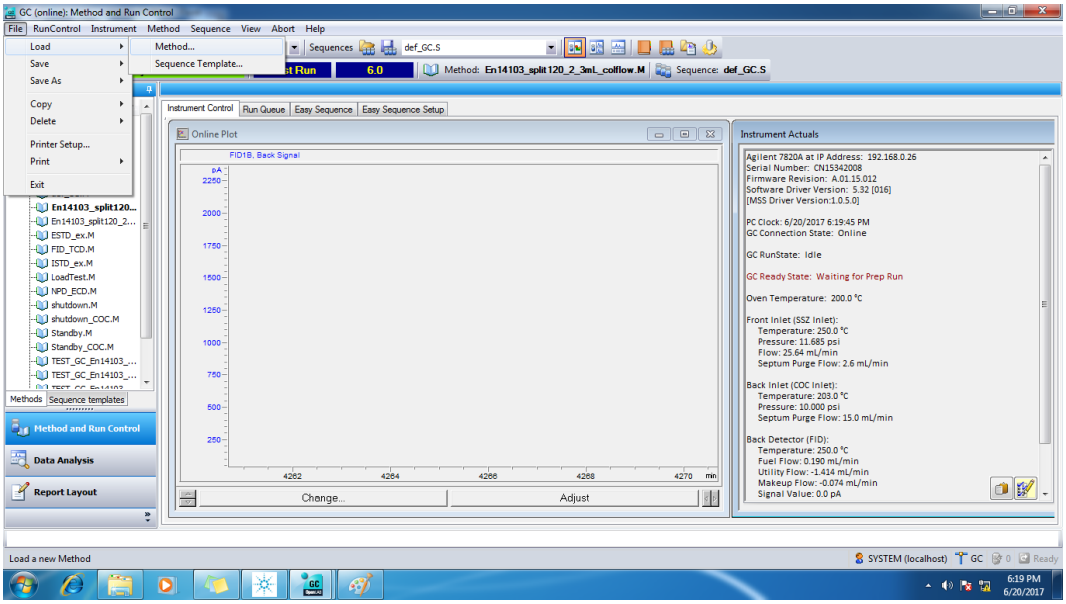

Figure C6. Part 1: Loading the methodology for analysing sample in the GC.

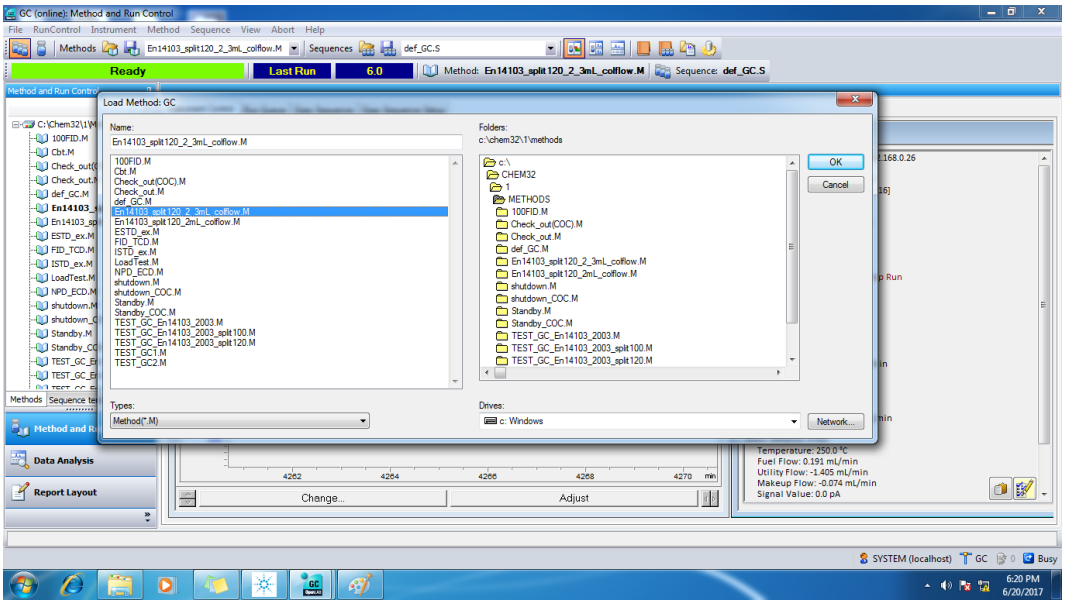

Figure C7. Part 2: Loading the methodology for analysing sample in the GC.

e) Allow the GC status to turn "**Ready**". Ensure the online signal is stabilised, before proceeding as shown in *Figure C8.*

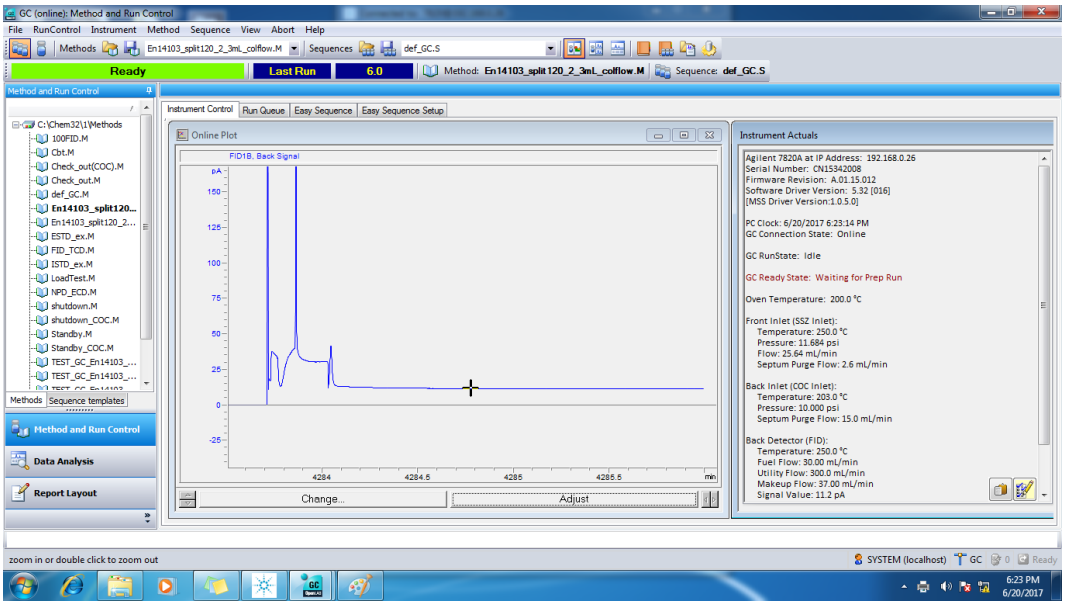

Figure C8. GC indicating ready on the top left corner after warming up.

f) On the GC, press the "**prep run**" button, and wait until the PC screen shows the "**Ready**" status.

g) On the GC, wait until only the yellow light is lit.

h) Using the 5 µL syringe with sample insert the syringe tip fully into the inlet port for FID as shown in *Figure C9*.

i) Check the volume on the syringe, if it is premature dispensed, press the “Stop” button on GC, remove the syringe and restart from step 2.a.

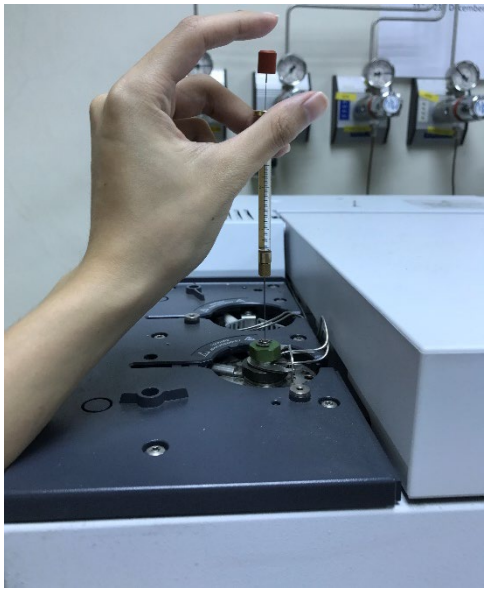

Figure C9. Injecting the sample into the GC.

j) Simultaneously inject the sample and press ‘**Start’** button on the GC.

3) <u>Post-processing of sampling data</u>

a) Test is complete, when the GC status indicates “**Ready**”.

b) On the PC screen, switch to software, GC (offline).

c) File->Load Signal-> Corresponding test name. (Usually on the bottom end of the selection) as shown in *Figure C10* and *Figure C11*.

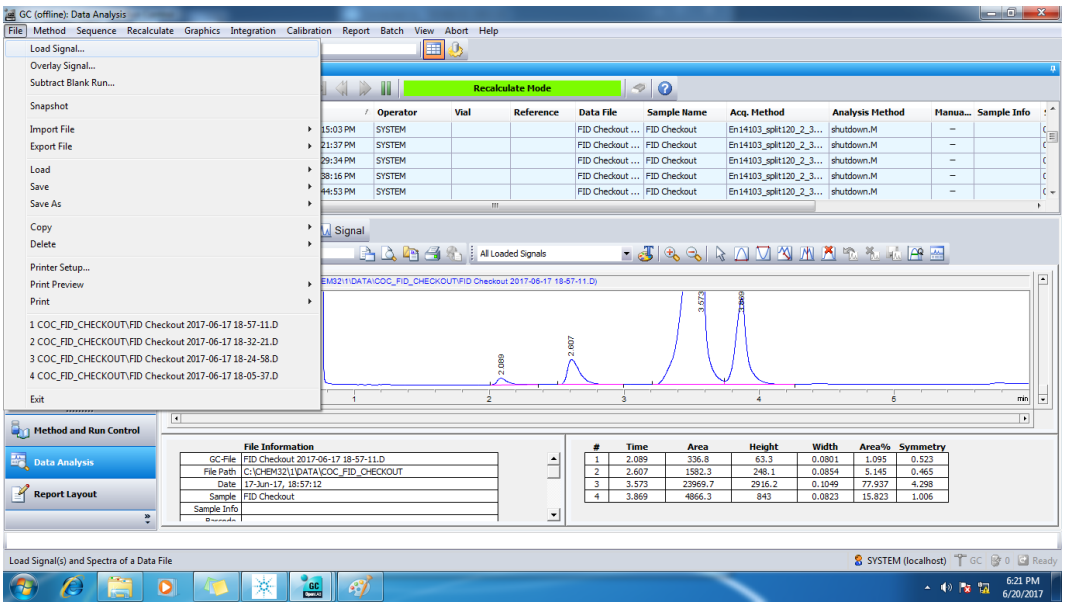

Figure C10. Part 1: Loading the results from the analysis.

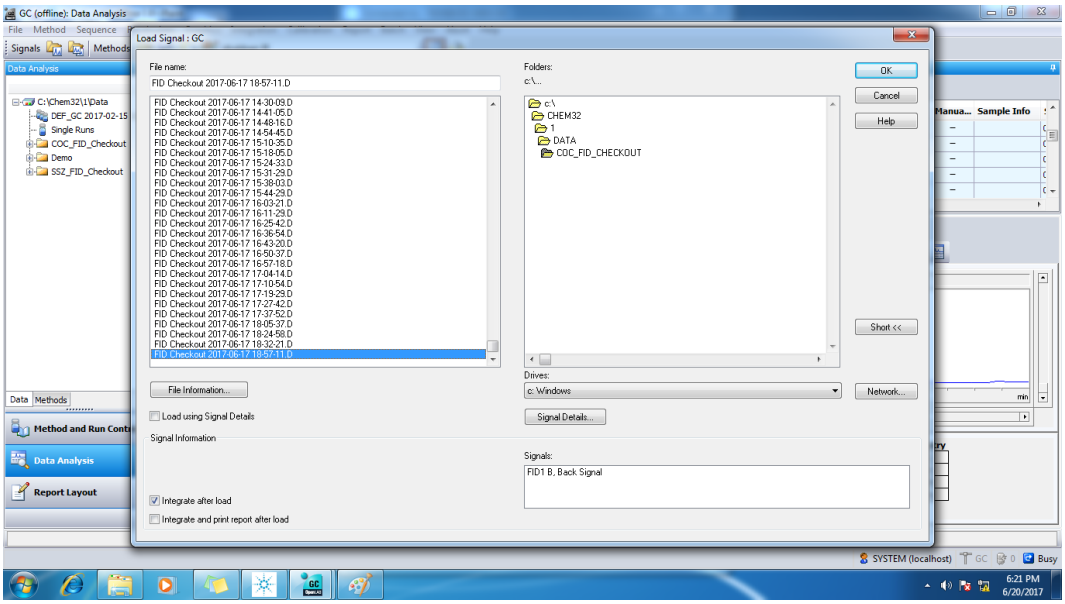

Figure C11. Part 2: Selecting the appropriate analysis from the repository.

d) Select the "Data Analysis" tab, then "Integration" tab as shown in *Figure C12*.

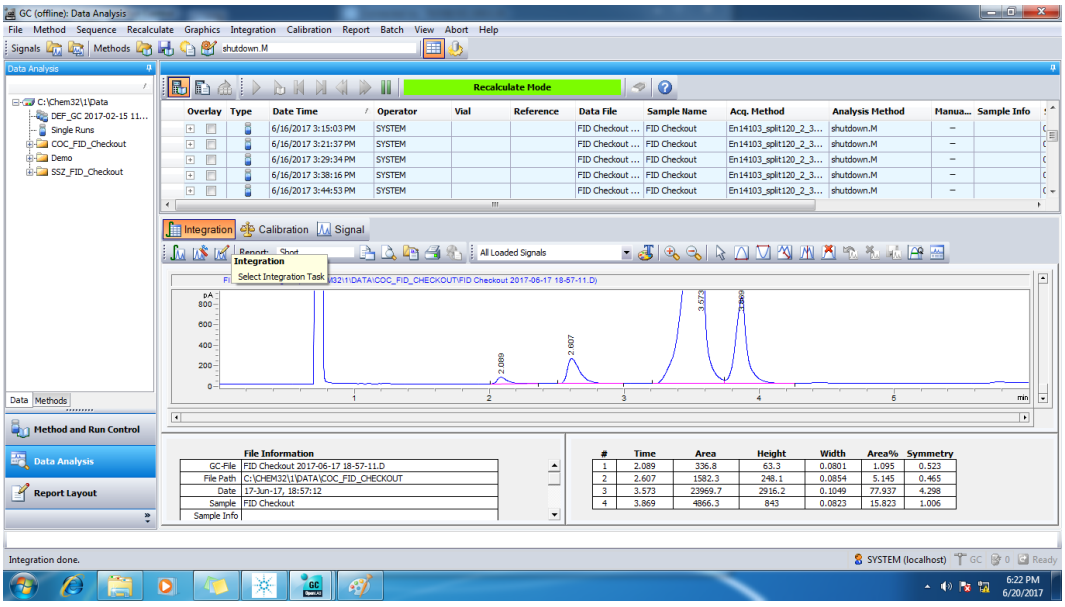

Figure C12. Selecting the analysis peaks from the sample.

e) Press the "Identify peaks, calculate and preview results" button as shown in *Figure C13*.

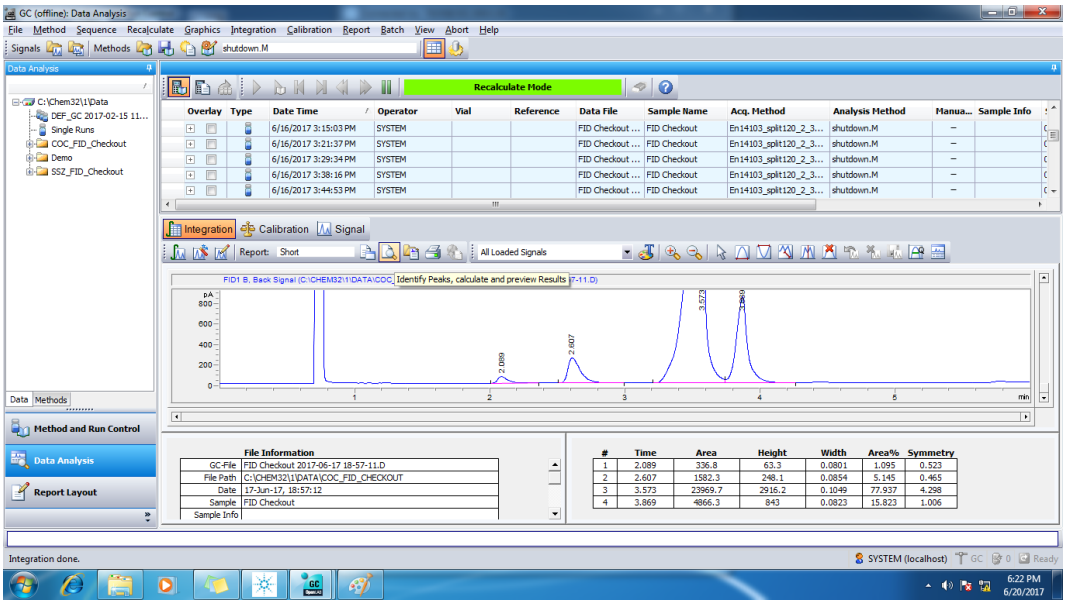

Figure C13. Integrating the analysis peaks from the sample.

f) Switch on printer, and print the result as shown in *Figure C14*.

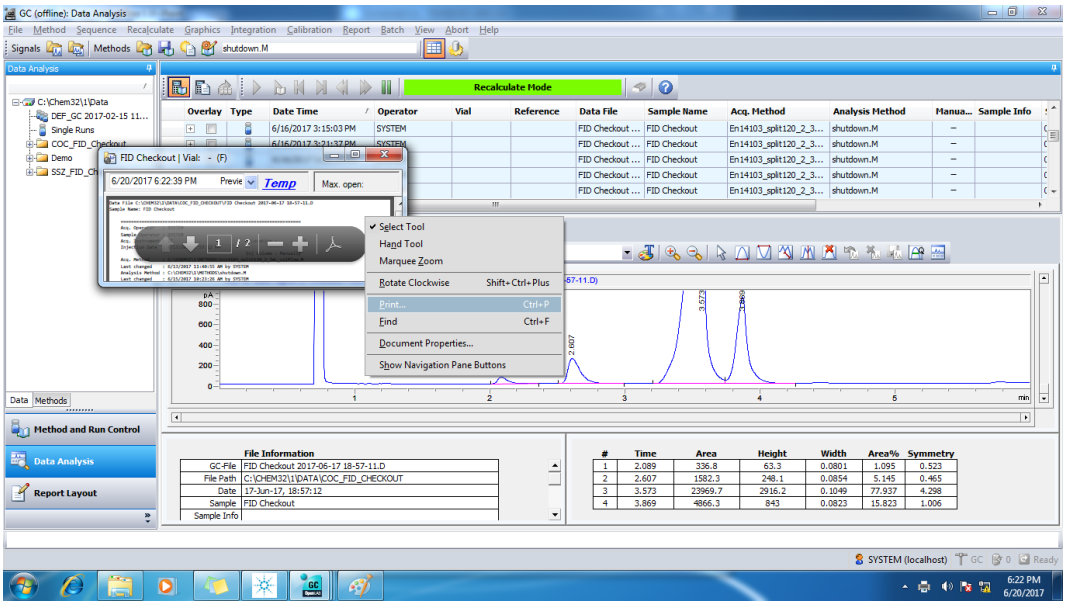

Figure C14. Printing the analysis report.

List of References

[1] U.S. Energy Information Adminisatration, Short-Term Energy Outlook (STEO), 2020. https://www.eia.gov/outlooks/steo/pdf/steo_full.pdf (accessed June 6, 2020).

[2] U.S. Energy Information Administration, International Energy Outlook, 2017. www.eia.gov/ieo (accessed February 12, 2019).

[3] UNFCCC, Katowice Climate Change Conference, (2018). https://unfccc.int/katowice (accessed January 14, 2019).

[4] A. Demirbas, Progress and recent trends in biodiesel fuels, Energy Convers. Manag. 50 (2009) 14–34. https://doi.org/10.1016/j.enconman.2008.09.001.

[5] I.B. Banković-Ilić, O.S. Stamenković, V.B. Veljković, Biodiesel production from non-edible plant oils, Renew. Sustain. Energy Rev. 16 (2012) 3621–3647. https://doi.org/10.1016/j.rser.2012.03.002.

[6] ASTM International, ASTM D975-18a, Standard Specification for Diesel Fuel Oils, West Conshohocken, PA, 2018. https://doi.org/10.1520/D0975-18A.

[7] J. Jeon, S. Park, Effect of injection pressure on soot formation/oxidation characteristics using a two-color photometric method in a compression-ignition engine fueled with biodiesel blend (B20), Appl. Therm. Eng. 131 (2018) 284–294. https://doi.org/10.1016/J.APPLTHERMALENG.2017.12.005.

[8] ASTM International, ASTM D7467-18b, Standard Specification for Diesel Fuel Oil, Biodiesel Blend (B6 to B20), West Conshohocken, PA, 2018. https://doi.org/10.1520/D7467-18B.

[9] J.H. Ng, H.K. Ng, S. Gan, Advances in biodiesel fuel for application in compression ignition engines, Clean Technol. Environ. Policy. 12 (2010) 459–493. https://doi.org/10.1007/s10098-009-0268-6.

[10] J.-H.H. Ng, H.K. Ng, S. Gan, Characterisation of engine-out responses from a light-duty diesel engine fuelled with palm methyl ester (PME), Appl. Energy. 90 (2012) 58–67. https://doi.org/10.1016/j.apenergy.2011.01.028.

[11] J.H. Ng, H.K. Ng, S. Gan, Recent trends in policies, socioeconomy and future directions of the biodiesel industry, Clean Technol. Environ. Policy. 12 (2010) 213–238. https://doi.org/10.1007/s10098-009-0235-2.

[12] M.M. Gui, K.T. Lee, S. Bhatia, Feasibility of edible oil vs. non-edible oil vs. waste edible oil as biodiesel feedstock, Energy. 33 (2008) 1646–1653. https://doi.org/10.1016/j.energy.2008.06.002.

[13] J.C. Escobar, E.S. Lora, O.J. Venturini, E.E. Yáñez, E.F. Castillo, O. Almazan, Biofuels: Environment, technology and food security, Renew. Sustain. Energy Rev. 13 (2009) 1275–1287. https://doi.org/10.1016/j.rser.2008.08.014.

[14] A.E. Atabani, A.S. Silitonga, H.C. Ong, T.M.I. Mahlia, H.H. Masjuki, I.A. Badruddin, H. Fayaz, Non-edible vegetable oils: A critical evaluation of oil extraction, fatty acid compositions, biodiesel production, characteristics, engine performance and emissions production, (2012). https://doi.org/10.1016/j.rser.2012.10.013.

[15] M.M.K. Bhuiya, M.G. Rasul, M.M.K. Khan, N. Ashwath, A.K. Azad, M.A. Hazrat, Second generation biodiesel: Potential alternative to-edible oil-derived biodiesel, Energy Procedia. 61 (2014) 1969–1972. https://doi.org/10.1016/j.egypro.2014.12.054.

[16] M.M.K. Bhuiya, M.G. Rasul, M.M.K. Khan, N. Ashwath, A.K. Azad, Prospects of 2nd generation biodiesel as a sustainable fuel - Part: 1 Selection of feedstocks, oil extraction techniques and conversion technologies, Renew. Sustain. Energy Rev. 55 (2016) 1109–1128. https://doi.org/10.1016/j.rser.2015.04.163.

[17] Food and Agriculture Organization of the United Nations, FAOSTAT, (2016). http://www.fao.org/faostat/en/#data (accessed November 25, 2016).

[18] T. Johnson, W. Brown, J. Brown, D. Harridge, C. Johnson, A Bio-energy Roadmap for South Australia, 2015.

[19] I. Suckling, Scion, Opportunities for biofuels in New Zealand, 2014.

[20] Y.C. Sharma, B. Singh, Development of biodiesel from karanja, a tree found in rural India, Fuel. 87 (2008) 1740–1742. https://doi.org/10.1016/j.fuel.2007.08.001.

[21] Y.C. Sharma, B. Singh, S.N. Upadhyay, Advancements in development and characterization of biodiesel: A review, Fuel. 87 (2008) 2355–2373. https://doi.org/10.1016/j.fuel.2008.01.014.

[22] D.Y.C. Leung, X. Wu, M.K.H. Leung, A review on biodiesel production using catalyzed transesterification, Appl. Energy. 87 (2010) 1083–1095. https://doi.org/10.1016/j.apenergy.2009.10.006.

[23] M.J. Ramos, C.M. Fernández, A. Casas, L. Rodríguez, Á. Pérez, Influence of fatty acid composition of raw materials on biodiesel properties, Bioresour. Technol. 100 (2009) 261–268. https://doi.org/10.1016/j.biortech.2008.06.039.

[24] U.S Department of Energy, Biodiesel handling and Use Guide Fifth Edition, (2016) 5th Ed. https://doi.org/10.2172/938562.

[25] European Standards, EN 590 - Automotive fuels - Diesel - Requirements and test methods, (2009) 1–12.

[26] C. Mei Mei, Malaysia to delay nationwide rollout of B20 biodiesel mandate due to coronavirus curbs, Reuters. (2020). https://www.reuters.com/article/us-health-coronavirus-malaysia-palmoil/malaysia-to-delay-nationwide-rollout-of-b20-biodiesel-mandate-due-to-coronavirus-curbs-idUSKCN21Y0AX.

[27] Ministry of Finance Malaysia, Budget 2019, 2018. www.treasury.gov.my (accessed February 14, 2019).

[28] American Society for Testing and Materials, ASTM D6751-02 Standard Specification for Biodiesel Fuel (B100) Blend Stock for Distillate Fuels, (2011).

[29] European Committee for Standardization, EN 14214 - Fatty acid methyl esters (FAME) for use in diesel engines and heating applications, (2008).

[30] Department of Standards Malaysia, Automotive fuels - Palm Methyl Esters (PME) for diesel engines - Requirements and test methods (First revision), (2014).

[31] Bureau of Indian Standards, IS 15607:2005 Bio-diesel (B100) Blend Stock for Diesel Fuel - Specification, (2005).

[32] Federal Register of Legislative Inststuments, Fuel Standard (Biodiesel) Determination 2003, 2009 (2009) 1–7.

[33] Japan Industrial Standards, JIS K2390:2016 Automotive fuels-Fatty acid methyl ester (FAME)

as blend stock, (2016) 1–8.

[34] AGÊNCIA NACIONAL DO PETRÓLEO, ANP42 - Brazilian Biodiesel Standard, (2005).

[35] South African National Standard, SANS 1935 Automotive biodiesel — Fatty Acid Methyl Esters (FAME) for diesel engines — Requirements and test methods, (2011).

[36] M. Elsayed, R. Matthews, N. Mortimer, Carbon and energy balances for a range of biofuels options, 2003. http://airburners.com/PUB/Sheffield-studie-mei2003.pdf.

[37] A.S. Ramadhas, C. Muraleedharan, S. Jayaraj, Performance and emission evaluation of a diesel engine fueled with methyl esters of rubber seed oil, Renew. Energy. 30 (2005) 1789–1800. https://doi.org/10.1016/j.renene.2005.01.009.

[38] D. Babu, R. Karvembu, R. Anand, Impact of split injection strategy on combustion, performance and emissions characteristics of biodiesel fuelled common rail direct injection assisted diesel engine, Energy. 165 (2018) 577–592. https://doi.org/10.1016/J.ENERGY.2018.09.193.

[39] M.K. Yesilyurt, The effects of the fuel injection pressure on the performance and emission characteristics of a diesel engine fuelled with waste cooking oil biodiesel-diesel blends, Renew. Energy. 132 (2019) 649–666. https://doi.org/10.1016/J.RENENE.2018.08.024.

[40] A.E. Atabani, A.S. Silitonga, I.A. Badruddin, T.M.I. Mahlia, H.H. Masjuki, S. Mekhilef, A comprehensive review on biodiesel as an alternative energy resource and its characteristics, Renew. Sustain. Energy Rev. 16 (2012) 2070–2093. https://doi.org/10.1016/j.rser.2012.01.003.

[41] G. Knothe, K.R. Steidley, Kinematic viscosity of biodiesel fuel components and related compounds. Influence of compound structure and comparison to petrodiesel fuel components, Fuel. 84 (2005) 1059–1065. https://doi.org/10.1016/j.fuel.2005.01.016.

[42] P. Mohamed Shameer, K. Ramesh, R. Sakthivel, R. Purnachandran, Effects of fuel injection parameters on emission characteristics of diesel engines operating on various biodiesel: A review, Renew. Sustain. Energy Rev. 67 (2017) 1267–1281. https://doi.org/10.1016/j.rser.2016.09.117.

[43] A. Datta, B.K. Mandal, A comprehensive review of biodiesel as an alternative fuel for compression ignition engine, Renew. Sustain. Energy Rev. 57 (2016) 799–821. https://doi.org/10.1016/j.rser.2015.12.170.

[44] R. Li, Z. Wang, P. Ni, Y. Zhao, M. Li, L. Li, Effects of cetane number improvers on the performance of diesel engine fuelled with methanol/biodiesel blend, Fuel. 128 (2014) 180–187. https://doi.org/10.1016/J.FUEL.2014.03.011.

[45] E. Automobile, WORLDWIDE FUEL CHARTER Fifth Edition, n.d. www.japanauto.com (accessed January 19, 2019).

[46] E.U.& U.S. of A. Tripartite Task Force Brazil, White Paper on International Compatible Biofuel Standards, 2007. https://www.nist.gov/sites/default/files/documents/2017/05/09/biofuels_report.pdf (accessed January 19, 2019).

[47] M. Lapuerta, J. Rodríguez-Fernández, E.F. de Mora, Correlation for the estimation of the cetane number of biodiesel fuels and implications on the iodine number, Energy Policy. 37 (2009) 4337–4344. https://doi.org/10.1016/j.enpol.2009.05.049.

[48] J. Pullen, K. Saeed, Experimental study of the factors affecting the oxidation stability of biodiesel FAME fuels, Fuel Process. Technol. 125 (2014) 223–235. https://doi.org/10.1016/j.fuproc.2014.03.032.

[49] R.L. McCormick, M. Ratcliff, L. Moens, R. Lawrence, Several factors affecting the stability of biodiesel in standard accelerated tests, Fuel Process. Technol. 88 (2007) 651–657. https://doi.org/10.1016/j.fuproc.2007.01.006.

[50] M. Tubino, J.A. Aricetti, A green potentiometric method for the determination of the iodine number of biodiesel, Fuel. 103 (2013) 1158–1163. https://doi.org/10.1016/j.fuel.2012.10.011.

[51] G. Knothe, A.C. Matheaus, T.W. Ryan, Cetane numbers of branched and straight-chain fatty esters determined in an ignition quality tester, Fuel. 82 (2003) 971–975. https://doi.org/10.1016/S0016-2361(02)00382-4.

[52] A. Serdari, E. Lois, S. Stournas, Impact of Esters of Mono- and Dicarboxylic Acids on Diesel Fuel Quality, Ind. Eng. Chem. Res. 38 (1999) 3543–3548. https://doi.org/10.1021/ie9900115.

[53] M.J. Murphy, J.D. Taylor, R.L. Mccormick, Compendium of Experimental Cetane Number Data, Natl. Renew. Energy Lab. (2004) 1–48. https://doi.org/10.2172/1086353.

[54] E.G. Giakoumis, A statistical investigation of biodiesel physical and chemical properties, and their correlation with the degree of unsaturation, Renew. Energy. 50 (2013) 858–878. https://doi.org/10.1016/J.RENENE.2012.07.040.

[55] L.F. Chuah, J.J. Klemeš, S. Yusup, A. Bokhari, M.M. Akbar, J. Rí, J. Kleme S C, S. Yusup, A. Bokhari, M.M. Akbar, J.J. Klemeš, S. Yusup, A. Bokhari, M.M. Akbar, A review of cleaner intensification technologies in biodiesel production, J. Clean. Prod. 146 (2016) 181–193. https://doi.org/10.1016/j.jclepro.2016.05.017.

[56] R. Shan, L. Lu, Y. Shi, H. Yuan, J. Shi, Catalysts from renewable resources for biodiesel production, Energy Convers. Manag. 178 (2018) 277–289. https://doi.org/10.1016/J.ENCONMAN.2018.10.032.

[57] H. Noureddini, D. Zhu, Kinetics of transesterification of soybean oil, J. Am. Oil Chem. Soc. 74 (1997) 1457–1463. https://doi.org/10.1007/s11746-997-0254-2.

[58] M. Kee Lam, K. Teong Lee, A. Rahman Mohamed, M.K. Lam, K.T. Lee, A.R. Mohamed, Homogeneous, heterogeneous and enzymatic catalysis for transesterification of high free fatty acid oil (waste cooking oil) to biodiesel: A review, Biotechnol. Adv. 28 (2010) 500–518. https://doi.org/10.1016/j.biotechadv.2010.03.002.

[59] M.K. Lam, K.T. Lee, A.R. Mohamed, Homogeneous, heterogeneous and enzymatic catalysis for transesterification of high free fatty acid oil (waste cooking oil) to biodiesel: A review, Biotechnol. Adv. 28 (2010) 500–518. https://doi.org/10.1016/J.BIOTECHADV.2010.03.002.

[60] V.C. Eze, A.N. Phan, A.P. Harvey, A more robust model of the biodiesel reaction, allowing identification of process conditions for significantly enhanced rate and water tolerance, Bioresour. Technol. 156 (2014) 222–231. https://doi.org/10.1016/j.biortech.2014.01.028.

[61] V.C. Eze, A.N. Phan, A.P. Harvey, Intensified one-step biodiesel production from high water and free fatty acid waste cooking oils, Fuel. 220 (2018) 567–574. https://doi.org/10.1016/J.FUEL.2018.02.050.

[62] A.S.S. Ramadhas, S. Jayaraj, C. Muraleedharan, Biodiesel production from high FFA rubber seed oil, Fuel. 84 (2005) 335–340. https://doi.org/10.1016/j.fuel.2004.09.016.

[63] P.K. Sahoo, L.M. Das, M.K.G. Babu, S.N. Naik, Biodiesel development from high acid value polanga seed oil and performance evaluation in a CI engine, Fuel. 86 (2007) 448–454. https://doi.org/10.1016/J.FUEL.2006.07.025.

[64] B. Freedman, R.O. Butterfield, E.H. Pryde, Transesterification kinetics of soybean oil, J. Am.

Oil Chem. Soc. 63 (1986) 1375–1380. https://doi.org/10.1007/BF02679606.

[65] F. Ma, M.A. Hanna, Biodiesel production: A review, Bioresour. Technol. 70 (1999) 1–15. https://doi.org/10.1016/S0960-8524(99)00025-5.

[66] M. Canakci, J. Van Gerpen, Biodiesel production from oils and fats with high free fatty acids, Trans. ASAE. 44 (2001) 1429–1436. http://biodieseleducation.org/Literature/Journal/2001_Canakci_Biodiesel_production.pdf (accessed May 7, 2018).

[67] Y. Zhang, M.. Dubé, D.. McLean, M. Kates, Biodiesel production from waste cooking oil: 1. Process design and technological assessment, Bioresour. Technol. 89 (2003) 1–16. https://doi.org/10.1016/S0960-8524(03)00040-3.

[68] A. Kumar Tiwari, A. Kumar, H. Raheman, Biodiesel production from jatropha oil (Jatropha curcas) with high free fatty acids: An optimized process, Biomass and Bioenergy. 31 (2007) 569–575. https://doi.org/10.1016/J.BIOMBIOE.2007.03.003.

[69] Y.C. Sharma, B. Singh, Development of biodiesel: Current scenario, Renew. Sustain. Energy Rev. 13 (2009) 1646–1651. https://doi.org/10.1016/j.rser.2008.08.009.

[70] H.C. Ong, H.H. Masjuki, T.M.I. Mahlia, A.S. Silitonga, W.T. Chong, K.Y. Leong, Optimization of biodiesel production and engine performance from high free fatty acid Calophyllum inophyllum oil in CI diesel engine, Energy Convers. Manag. 81 (2014) 30–40. https://doi.org/10.1016/J.ENCONMAN.2014.01.065.

[71] D. Darnoko, M. Cheryan, Kinetics of palm oil transesterification in a batch reactor, J. Am. Oil Chem. Soc. 77 (2000) 1263–1267. https://doi.org/10.1007/s11746-000-0198-y.

[72] J.M. Dias, M.C.M.M. Alvim-Ferraz, M.F. Almeida, Comparison of the performance of different homogeneous alkali catalysts during transesterification of waste and virgin oils and evaluation of biodiesel quality, Fuel. 87 (2008) 3572–3578. https://doi.org/10.1016/j.fuel.2008.06.014.

[73] K.H. Chung, J. Kim, K.Y. Lee, Biodiesel production by transesterification of duck tallow with methanol on alkali catalysts, Biomass and Bioenergy. 33 (2009) 155–158. https://doi.org/10.1016/j.biombioe.2008.04.014.

[74] C.S. Foon, C.Y. May, M.A. Ngan, C.C. Hock, C. Sit Foon, C. Yuen May, M.A. Ngan, C. Cheng Hock, Kinetics Study on Transesterification of Palm Oil, J. Oil Palm Res. 16 (2004) 19–29. http://palmoilis.mpob.gov.my/publications/joprv16n2-cheng.pdf (accessed February 26, 2018).

[75] U. Rashid, F. Anwar, Production of biodiesel through optimized alkaline-catalyzed transesterification of rapeseed oil, Fuel. 87 (2008) 265–273. https://doi.org/10.1016/j.fuel.2007.05.003.

[76] L. Zhang, B. Sheng, Z. Xin, Q. Liu, S. Sun, Kinetics of transesterification of palm oil and dimethyl carbonate for biodiesel production at the catalysis of heterogeneous base catalyst, Bioresour. Technol. 101 (2010) 8144–8150. https://doi.org/10.1016/j.biortech.2010.05.069.

[77] Z. Wan, B.H.H. Hameed, Transesterification of palm oil to methyl ester on activated carbon supported calcium oxide catalyst, Bioresour. Technol. 102 (2011) 2659–2664. https://doi.org/10.1016/j.biortech.2010.10.119.

[78] B.B. Uzun, M. Kiliç, N. Özbay, A.E. Pütün, E. Pütün, Biodiesel production from waste frying oils: Optimization of reaction parameters and determination of fuel properties, Energy. 44 (2012) 347–351. https://doi.org/10.1016/j.energy.2012.06.024.

[79] A.B. Fadhil, L.H. Ali, Alkaline-catalyzed transesterification of Silurus triostegus Heckel fish

oil: Optimization of transesterification parameters, Renew. Energy. 60 (2013) 481–488. https://doi.org/10.1016/j.renene.2013.04.018.

[80] D.N. Thoai, C. Tongurai, K. Prasertsit, A. Kumar, A novel two-step transesterification process catalyzed by homogeneous base catalyst in the first step and heterogeneous acid catalyst in the second step, Fuel Process. Technol. 168 (2017) 97–104. https://doi.org/10.1016/J.FUPROC.2017.08.014.

[81] S.N. Gebremariam, J.M. Marchetti, Biodiesel production through sulfuric acid catalyzed transesterification of acidic oil: Techno economic feasibility of different process alternatives, Energy Convers. Manag. 174 (2018) 639–648. https://doi.org/10.1016/J.ENCONMAN.2018.08.078.

[82] Y.-T. Wang, Z. Fang, X.-X. Yang, Y.-T. Yang, J. Luo, K. Xu, G.-R. Bao, One-step production of biodiesel from Jatropha oils with high acid value at low temperature by magnetic acid-base amphoteric nanoparticles, Chem. Eng. J. 348 (2018) 929–939. https://doi.org/10.1016/J.CEJ.2018.05.039.

[83] K.V. Thiruvengadaravi, J. Nandagopal, P. Baskaralingam, V. Sathya Selva Bala, S. Sivanesan, Acid-catalyzed esterification of karanja (Pongamia pinnata) oil with high free fatty acids for biodiesel production, Fuel. 98 (2012) 1–4. https://doi.org/10.1016/J.FUEL.2012.02.047.

[84] H.A. Farag, A. El-maghraby, N.A. Taha, Optimization of factors affecting esterification of mixed oil with high percentage of free fatty acid, Fuel Process. Technol. 92 (2011) 507–510. https://doi.org/10.1016/j.fuproc.2010.11.004.

[85] D.A.G. Aranda, R.T.P. Santos, N.C.O. Tapanes, A.L.D. Ramos, O.A.C. Antunes, Acid-catalyzed homogeneous esterification reaction for biodiesel production from palm fatty acids, Catal. Letters. 122 (2008) 20–25. https://doi.org/10.1007/s10562-007-9318-z.

[86] A.H. Mohammad Fauzi, N.A. Saidina Amin, Optimization of oleic acid esterification catalyzed by ionic liquid for green biodiesel synthesis, Energy Convers. Manag. 76 (2013) 818–827. https://doi.org/10.1016/j.enconman.2013.08.029.

[87] M.A. Khan, S. Yusup, M.M. Ahmad, Acid esterification of a high free fatty acid crude palm oil and crude rubber seed oil blend: Optimization and parametric analysis, Biomass and Bioenergy. 34 (2010) 1751–1756. https://doi.org/10.1016/j.biombioe.2010.07.006.

[88] K. Jacobson, R. Gopinath, L.C. Meher, A.K. Dalai, Solid acid catalyzed biodiesel production from waste cooking oil, Appl. Catal. B Environ. 85 (2008) 86–91. https://doi.org/10.1016/J.APCATB.2008.07.005.

[89] N. Mansir, Y. Hin Taufiq-Yap, U. Rashid, I.M. Lokman, Investigation of heterogeneous solid acid catalyst performance on low grade feedstocks for biodiesel production: A review, Energy Convers. Manag. 141 (2017) 171–182. https://doi.org/10.1016/j.enconman.2016.07.037.

[90] M.R. Avhad, J.M. Marchetti, A review on recent advancement in catalytic materials for biodiesel production, Renew. Sustain. Energy Rev. 50 (2015) 696–718. https://doi.org/10.1016/j.rser.2015.05.038.

[91] M. Kouzu, J.S. Hidaka, Transesterification of vegetable oil into biodiesel catalyzed by CaO: A review, Fuel. 93 (2012) 1–12. https://doi.org/10.1016/j.fuel.2011.09.015.

[92] M. Kouzu, S. ya Yamanaka, J. suke Hidaka, M. Tsunomori, Heterogeneous catalysis of calcium oxide used for transesterification of soybean oil with refluxing methanol, Appl. Catal. A Gen. 355 (2009) 94–99. https://doi.org/10.1016/j.apcata.2008.12.003.

[93] M.L. Granados, M.D.Z. Poves, D.M. Alonso, R. Mariscal, F.C. Galisteo, R. Moreno-Tost, J.

Santamaría, J.L.G. Fierro, Biodiesel from sunflower oil by using activated calcium oxide, Appl. Catal. B Environ. 73 (2007) 317–326. https://doi.org/10.1016/j.apcatb.2006.12.017.

[94] H. Jeon, D.J. Kim, S.J. Kim, J.H. Kim, Synthesis of mesoporous MgO catalyst templated by a PDMS-PEO comb-like copolymer for biodiesel production, Fuel Process. Technol. 116 (2013) 325–331. https://doi.org/10.1016/j.fuproc.2013.07.013.

[95] M. Kouzu, T. Kasuno, M. Tajika, Y. Sugimoto, S. Yamanaka, J. Hidaka, Calcium oxide as a solid base catalyst for transesterification of soybean oil and its application to biodiesel production, Fuel. 87 (2008) 2798–2806. https://doi.org/10.1016/j.fuel.2007.10.019.

[96] M. Koberg, R. Abu-Much, A. Gedanken, Optimization of bio-diesel production from soybean and wastes of cooked oil: Combining dielectric microwave irradiation and a SrO catalyst, Bioresour. Technol. 102 (2011) 1073–1078. https://doi.org/10.1016/j.biortech.2010.08.055.

[97] E. Martinez-Guerra, V.G. Gude, Transesterification of used vegetable oil catalyzed by barium oxide under simultaneous microwave and ultrasound irradiations, Energy Convers. Manag. 88 (2014) 633–640. https://doi.org/10.1016/j.enconman.2014.08.060.

[98] Y.H. Taufiq-Yap, S.H. Teo, U. Rashid, A. Islam, M.Z. Hussien, K.T. Lee, Transesterification of Jatropha curcas crude oil to biodiesel on calcium lanthanum mixed oxide catalyst: Effect of stoichiometric composition, Energy Convers. Manag. 88 (2014) 1290–1296. https://doi.org/10.1016/J.ENCONMAN.2013.12.075.

[99] H.H. Mardhiah, H.C. Ong, H.H.H. Masjuki, S. Lim, H.V. V Lee, A review on latest developments and future prospects of heterogeneous catalyst in biodiesel production from non-edible oils, Renew. Sustain. Energy Rev. 67 (2017) 1225–1236. https://doi.org/10.1016/j.rser.2016.09.036.

[100] F. Su, Y. Guo, Advancements in solid acid catalysts for biodiesel production, Green Chem. 16 (2014) 2934–2957. https://doi.org/10.1039/C3GC42333F.

[101] B. Fu, L. Gao, L. Niu, R. Wei, G. Xiao, Biodiesel from waste cooking oil via heterogeneous superacid catalyst SO4\n2-/ZrO2, Energy and Fuels. 23 (2009) 569–572. https://doi.org/10.1021/ef800751z.

[102] G.J. Suppes, M.A. Dasari, E.J. Doskocil, P.J. Mankidy, M.J. Goff, Transesterification of soybean oil with zeolite and metal catalysts, Appl. Catal. A Gen. 257 (2004) 213–223. https://doi.org/10.1016/j.apcata.2003.07.010.

[103] N. Özbay, N. Oktar, N.A. Tapan, Esterification of free fatty acids in waste cooking oils (WCO): Role of ion-exchange resins, Fuel. 87 (2008) 1789–1798. https://doi.org/10.1016/j.fuel.2007.12.010.

[104] M.K. Lam, K.T. Lee, A.R. Mohamed, Sulfated tin oxide as solid superacid catalyst for transesterification of waste cooking oil: An optimization study, Appl. Catal. B Environ. 93 (2009) 134–139. https://doi.org/10.1016/j.apcatb.2009.09.022.

[105] O. Babajide, N. Musyoka, L. Petrik, F. Ameer, Novel zeolite Na-X synthesized from fly ash as a heterogeneous catalyst in biodiesel production, Catal. Today. 190 (2012) 54–60. https://doi.org/10.1016/j.cattod.2012.04.044.

[106] R.I. Kusuma, J.P. Hadinoto, A. Ayucitra, F.E. Soetaredjo, S. Ismadji, Natural zeolite from Pacitan Indonesia, as catalyst support for transesterification of palm oil, Appl. Clay Sci. 74 (2013) 121–126. https://doi.org/10.1016/j.clay.2012.04.021.

[107] A. Patel, V. Brahmkhatri, N. Singh, Biodiesel production by esterification of free fatty acid over sulfated zirconia, Renew. Energy. 51 (2013) 227–233. https://doi.org/10.1016/j.renene.2012.09.040.

[108] J. Fu, L. Chen, P. Lv, L. Yang, Z. Yuan, Free fatty acids esterification for biodiesel production using self-synthesized macroporous cation exchange resin as solid acid catalyst, Fuel. 154 (2015) 1–8. https://doi.org/10.1016/j.fuel.2015.03.048.

[109] A.M. Doyle, T.M. Albayati, A.S. Abbas, Z.T. Alismaeel, Biodiesel production by esterification of oleic acid over zeolite Y prepared from kaolin, Renew. Energy. 97 (2016) 19–23. https://doi.org/10.1016/j.renene.2016.05.067.

[110] Y. Liu, T.J. Pinnavaia, Assembly of wormhole aluminosilicate mesostructures from zeolite seeds, J. Mater. Chem. 14 (2004) 1099–1103. https://doi.org/10.1039/b315193j.

[111] C. Belviso, F. Cavalcante, A. Lettino, S. Fiore, A and X-type zeolites synthesised from kaolinite at low temperature, Appl. Clay Sci. 80–81 (2013) 162–168. https://doi.org/10.1016/j.clay.2013.02.003.

[112] R. Tesser, L. Casale, D. Verde, M. Di Serio, E. Santacesaria, Kinetics and modeling of fatty acids esterification on acid exchange resins, Chem. Eng. J. 157 (2010) 539–550. https://doi.org/10.1016/j.cej.2009.12.050.

[113] M.L. Honkela, A. Root, M. Lindblad, A.O.I. Krause, Comparison of ion-exchange resin catalysts in the dimerisation of isobutene, Appl. Catal. A Gen. 295 (2005) 216–223. https://doi.org/10.1016/j.apcata.2005.08.023.

[114] N. Shibasaki-Kitakawa, K. Hiromori, T. Ihara, K. Nakashima, T. Yonemoto, Production of high quality biodiesel from waste acid oil obtained during edible oil refining using ion-exchange resin catalysts, Fuel. 139 (2015) 11–17. https://doi.org/10.1016/j.fuel.2014.08.024.

[115] D. Darnoko, M. Cheryan, Continuous production of palm methyl esters, J. Am. Oil Chem. Soc. 77 (2000) 1269–1272. https://doi.org/10.1007/s11746-000-0199-x.

[116] T. Leevijit, C. Tongurai, G. Prateepchaikul, W. Wisutmethangoon, Performance test of a 6-stage continuous reactor for palm methyl ester production, Bioresour. Technol. 99 (2008) 214–221. https://doi.org/10.1016/j.biortech.2006.11.052.

[117] G. Prateepchaikul, K. Somnuk, M. Allen, Design and testing of continuous acid-catalyzed esterification reactor for high free fatty acid mixed crude palm oil, Fuel Process. Technol. 90 (2009) 784–789. https://doi.org/10.1016/j.fuproc.2009.03.008.

[118] M. Ilmi, A. Kloekhorst, J.G.M. Winkelman, G.J.W. Euverink, C. Hidayat, H.J. Heeres, Process intensification of catalytic liquid-liquid solid processes: Continuous biodiesel production using an immobilized lipase in a centrifugal contactor separator, Chem. Eng. J. 321 (2017) 76–85. https://doi.org/10.1016/J.CEJ.2017.03.070.

[119] N. Yasvanthrajan, A. Nabera, S. Salike, D.T. Valan, P. Sivakumar, K. Muthukumar, A. Arunagiri, An overview on the process intensification of microchannel reactors for biodiesel production, Chem. Eng. Process. - Process Intensif. (2018). https://doi.org/10.1016/J.CEP.2018.12.008.

[120] G.L. Maddikeri, A.B. Pandit, P.R. Gogate, Intensification approaches for biodiesel synthesis from waste cooking oil: A review, Ind. Eng. Chem. Res. 51 (2012) 14610–14628. https://doi.org/10.1021/ie301675j.

[121] H.S. Santana, J.L. Silva, O.P. Taranto, Numerical simulation of mixing and reaction of Jatropha curcas oil and ethanol for synthesis of biodiesel in micromixers, Chem. Eng. Sci. 132 (2015) 159–168. https://doi.org/10.1016/j.ces.2015.04.014.

[122] E.A. Mansur, M. YE, Y. WANG, Y. DAI, A State-of-the-Art Review of Mixing in Microfluidic Mixers, Chinese J. Chem. Eng. 16 (2008) 503–516.

https://doi.org/10.1016/S1004-9541(08)60114-7.

[123] Z. Wen, X. Yu, S.T. Tu, J. Yan, E. Dahlquist, Intensification of biodiesel synthesis using zigzag micro-channel reactors, Bioresour. Technol. 100 (2009) 3054–3060. https://doi.org/10.1016/j.biortech.2009.01.022.

[124] P. Sun, B. Wang, J. Yao, L. Zhang, N. Xu, Fast synthesis of biodiesel at high throughput in microstructured reactors, Ind. Eng. Chem. Res. 49 (2010) 1259–1264. https://doi.org/10.1021/ie901320s.

[125] Y. Tanawannapong, A. Kaewchada, A. Jaree, Biodiesel production from waste cooking oil in a microtube reactor, J. Ind. Eng. Chem. 19 (2013) 37–41. https://doi.org/10.1016/j.jiec.2012.07.007.

[126] B. Aghel, M. Rahimi, A. Sepahvand, M. Alitabar, H.R. Ghasempour, Using a wire coil insert for biodiesel production enhancement in a microreactor, Energy Convers. Manag. 84 (2014) 541–549. https://doi.org/10.1016/j.enconman.2014.05.009.

[127] A. Kaewchada, S. Pungchaicharn, A. Jaree, Transesterification of palm oil in a microtube reactor, Can. J. Chem. Eng. 94 (2016) 859–864. https://doi.org/10.1002/cjce.22464.

[128] N. Chueluecha, A. Kaewchada, A. Jaree, Biodiesel synthesis using heterogeneous catalyst in a packed-microchannel, Energy Convers. Manag. 141 (2016) 145–154. https://doi.org/10.1016/j.enconman.2016.07.020.

[129] V. Hessel, S. Hardt, H. Löwe, F. Schönfeld, Laminar mixing in different interdigital micromixers: I. Experimental characterization, AIChE J. 49 (2003) 566–577. https://doi.org/10.1002/aic.690490304.

[130] R. Alford, M. Burns, N. Burns, Dixon rings - A revolutionary random column packing, Filtration. 11 (2011) 218–223.

[131] C.E. Brennen, N.Y. Oxford, Cavitation and Bubble Dynamics, 1995. https://authors.library.caltech.edu/25017/5/BUBBOOK.pdf (accessed January 22, 2019).

[132] P. Wu, L. Bai, W. Lin, X. Wang, Mechanism and dynamics of hydrodynamic-acoustic cavitation (HAC), Ultrason. Sonochem. 49 (2018) 89–96. https://doi.org/10.1016/J.ULTSONCH.2018.07.021.

[133] W. Lauterborn, Cavitation and Coherent Optics BT - Cavitation and Inhomogeneities in Underwater Acoustics: Proceedings of the First International Conference, Göttingen, Fed. Rep. of Germany, July 9–11, 1979, in: W. Lauterborn (Ed.), Springer Berlin Heidelberg, Berlin, Heidelberg, 1980: pp. 3–12. https://doi.org/10.1007/978-3-642-51070-0_1.

[134] P.R. Gogate, R.K. Tayal, A.B. Pandit, Cavitation: A technology on the horizon, Curr. Sci. 91 (2006) 35–46.

[135] Y. Kojima, H. Imazu, K. Nishida, Physical and chemical characteristics of ultrasonically-prepared water-in-diesel fuel: Effects of ultrasonic horn position and water content, Ultrason. Sonochem. 21 (2014) 722–728. https://doi.org/10.1016/J.ULTSONCH.2013.09.019.

[136] S.X. Tan, S. Lim, H.C. Ong, Y.L. Pang, State of the art review on development of ultrasound-assisted catalytic transesterification process for biodiesel production, 2019. https://www.sciencedirect.com/science/article/pii/S0016236118313802 (accessed January 22, 2019).

[137] K.S. Suslick, Sonochemistry, in: Kirk-Othmer Encycl. Chem. Technol., John Wiley & Sons, Inc., 2000. https://doi.org/10.1002/0471238961.1915141519211912.a01.

[138] A.S. Badday, A.Z. Abdullah, K.T. Lee, M.S. Khayoon, Intensification of biodiesel production

via ultrasonic-assisted process: A critical review on fundamentals and recent development, Renew. Sustain. Energy Rev. 16 (2012) 4574–4587. https://doi.org/10.1016/j.rser.2012.04.057.

[139] J. Ji, J. Wang, Y. Li, Y. Yu, Z. Xu, Preparation of biodiesel with the help of ultrasonic and hydrodynamic cavitation, Ultrasonics. 44 (2006) e411–e414. https://doi.org/10.1016/j.ultras.2006.05.020.

[140] C. Stavarache, M. Vinatoru, Y. Maeda, H. Bandow, Ultrasonically driven continuous process for vegetable oil transesterification, Ultrason. Sonochem. 14 (2007) 413–417. https://doi.org/10.1016/j.ultsonch.2006.09.014.

[141] N.N. Mahamuni, Y.G. Adewuyi, Optimization of the synthesis of biodiesel via ultrasound-enhanced base-catalyzed transesterification of soybean oil using a multifrequency ultrasonic reactor, Energy and Fuels. 23 (2009) 2757–2766. https://doi.org/10.1021/ef900047j.

[142] H. Mootabadi, B. Salamatinia, S. Bhatia, A.Z. Abdullah, Ultrasonic-assisted biodiesel production process from palm oil using alkaline earth metal oxides as the heterogeneous catalysts, Fuel. 89 (2010) 1818–1825. https://doi.org/10.1016/J.FUEL.2009.12.023.

[143] L.T. Thanh, K. Okitsu, Y. Sadanaga, N. Takenaka, Y. Maeda, H. Bandow, Ultrasound-assisted production of biodiesel fuel from vegetable oils in a small scale circulation process, Bioresour. Technol. 101 (2010) 639–645. https://doi.org/10.1016/J.BIORTECH.2009.08.050.

[144] N. Gharat, V.K. Rathod, Ultrasound assisted enzyme catalyzed transesterification of waste cooking oil with dimethyl carbonate, Ultrason. Sonochem. 20 (2013) 900–905. https://doi.org/10.1016/J.ULTSONCH.2012.10.011.

[145] M. Mostafaei, B. Ghobadian, M. Barzegar, A. Banakar, Optimization of ultrasonic assisted continuous production of biodiesel using response surface methodology, Ultrason. Sonochem. 27 (2015) 54–61. https://doi.org/10.1016/j.ultsonch.2015.04.036.

[146] P.B. Subhedar, P.R. Gogate, Ultrasound assisted intensification of biodiesel production using enzymatic interesterification, Ultrason. Sonochem. 29 (2016) 67–75. https://doi.org/10.1016/j.ultsonch.2015.09.006.

[147] S.K. Bhangu, S. Gupta, M. Ashokkumar, Ultrasonic enhancement of lipase-catalysed transesterification for biodiesel synthesis, Ultrason. Sonochem. 34 (2017) 305–309. https://doi.org/10.1016/J.ULTSONCH.2016.06.005.

[148] G.K. Batchelor, An Introduction to Fluid Dynamics, Cambridge University Press, Cambridge, 2000. https://doi.org/10.1017/CBO9780511800955.

[149] F.R. Young, Cavitation, World Scientific, 1999.

[150] K. Ramachandran, T. Suganya, N. Nagendra Gandhi, S. Renganathan, Recent developments for biodiesel production by ultrasonic assist transesterification using different heterogeneous catalyst: A review, Renew. Sustain. Energy Rev. 22 (2013) 410–418. https://doi.org/10.1016/J.RSER.2013.01.057.

[151] M.A. Kelkar, P.R. Gogate, A.B. Pandit, Intensification of esterification of acids for synthesis of biodiesel using acoustic and hydrodynamic cavitation, Ultrason. Sonochem. 15 (2008) 188–194. https://doi.org/10.1016/j.ultsonch.2007.04.003.

[152] A. Pal, A. Verma, S.S. Kachhwaha, S. Maji, Biodiesel production through hydrodynamic cavitation and performance testing, Renew. Energy. 35 (2010) 619–624. https://doi.org/10.1016/j.renene.2009.08.027.

[153] D. Ghayal, A.B. Pandit, V.K. Rathod, Optimization of biodiesel production in a hydrodynamic cavitation reactor using used frying oil, Ultrason. Sonochem. 20 (2013) 322–328. https://doi.org/10.1016/j.ultsonch.2012.07.009.

[154] G.L. Maddikeri, P.R. Gogate, A.B. Pandit, Intensified synthesis of biodiesel using hydrodynamic cavitation reactors based on the interesterification of waste cooking oil, Fuel. 137 (2014) 285–292. https://doi.org/10.1016/j.fuel.2014.08.013.

[155] L.F. Chuah, S. Yusup, A.R. Abd Aziz, A. Bokhari, J.J. Klemeš, M.Z. Abdullah, Intensification of biodiesel synthesis from waste cooking oil (Palm Olein) in a Hydrodynamic Cavitation Reactor: Effect of operating parameters on methyl ester conversion, Chem. Eng. Process. Process Intensif. 95 (2015) 235–240. https://doi.org/10.1016/j.cep.2015.06.018.

[156] A. Bokhari, L.F. Chuah, S. Yusup, M.M. Akbar, R.N.M. Kamil, Cleaner production of rubber seed oil methyl ester using a hydrodynamic cavitation: optimisation and parametric study, J. Clean. Prod. 136 (2016) 31–41. https://doi.org/10.1016/J.JCLEPRO.2016.04.091.

[157] Y.T. Shah, V.S. Moholkar, A.B. Pandit, Cavitation reaction engineering, 1999. https://doi.org/10.1007/978-1-4615-4787-7.

[158] K. Gunvachai, M.G. Hassan, G. Shama, K. Hellgardt, A New Solubility Model to Describe Biodiesel Formation Kinetics, Process Saf. Environ. Prot. 85 (2007) 383–389. https://doi.org/10.1205/PSEP07033.

[159] F. Motasemi, F.N.N. Ani, A review on microwave-assisted production of biodiesel, Renew. Sustain. Energy Rev. 16 (2012) 4719–4733. https://doi.org/10.1016/j.rser.2012.03.069.

[160] D. Pozar, Microwave Engineering Fourth Edition, 2005. https://doi.org/TK7876.P69 2011.

[161] Y. Groisman, A. Gedanken, Continuous flow, circulating microwave system and its application in nanoparticle fabrication and biodiesel synthesis, J. Phys. Chem. C. 112 (2008) 8802–8808. https://doi.org/10.1021/jp801409t.

[162] T.M. Barnard, N.E. Leadbeater, M.B. Boucher, L.M. Stencel, B.A. Wilhite, Continuous-flow preparation of biodiesel using microwave heating, Energy and Fuels. 21 (2007) 1777–1781. https://doi.org/10.1021/ef0606207.

[163] V. Lertsathapornsuk, R. Pairintra, K. Aryusuk, K. Krisnangkura, Microwave assisted in continuous biodiesel production from waste frying palm oil and its performance in a 100 kW diesel generator, Fuel Process. Technol. 89 (2008) 1330–1336. https://doi.org/10.1016/j.fuproc.2008.05.024.

[164] N.E. Leadbeater, T.M. Barnard, L.M. Stencel, Batch and continuous-flow preparation of biodiesel derived from butanol and facilitated by microwave heating, Energy and Fuels. 22 (2008) 2005–2008. https://doi.org/10.1021/ef700748t.

[165] H. Yuan, B.L. Yang, G.L. Zhu, Synthesis of biodiesel using microwave absorption catalysts, Energy and Fuels. 23 (2009) 548–552. https://doi.org/10.1021/ef800577j.

[166] S. Zhang, Y.G. Zu, Y.J. Fu, M. Luo, D.Y. Zhang, T. Efferth, Rapid microwave-assisted transesterification of yellow horn oil to biodiesel using a heteropolyacid solid catalyst, Bioresour. Technol. 101 (2010) 931–936. https://doi.org/10.1016/j.biortech.2009.08.069.

[167] P.D. Patil, V.G. Gude, A. Mannarswamy, P. Cooke, S. Munson-McGee, N. Nirmalakhandan, P. Lammers, S. Deng, Optimization of microwave-assisted transesterification of dry algal biomass using response surface methodology, Bioresour. Technol. 102 (2011) 1399–1405. https://doi.org/10.1016/J.BIORTECH.2010.09.046.

[168] C.-C. Liao, T.-W. Chung, Optimization of process conditions using response surface methodology for the microwave-assisted transesterification of Jatropha oil with KOH

impregnated CaO as catalyst, Chem. Eng. Res. Des. 91 (2013) 2457–2464. https://doi.org/10.1016/J.CHERD.2013.04.009.

[169] Y.-C. Lin, K.-H. Hsu, J.-F. Lin, Rapid palm-biodiesel production assisted by a microwave system and sodium methoxide catalyst, Fuel. 115 (2014) 306–311. https://doi.org/10.1016/j.fuel.2013.07.022.

[170] A. Mazubert, C. Taylor, J. Aubin, M. Poux, Key role of temperature monitoring in interpretation of microwave effect on transesterification and esterification reactions for biodiesel production, Bioresour. Technol. 161 (2014) 270–279. https://doi.org/10.1016/j.biortech.2014.03.011.

[171] I. Choedkiatsakul, K. Ngaosuwan, S. Assabumrungrat, S. Mantegna, G. Cravotto, Biodiesel production in a novel continuous flow microwave reactor, Renew. Energy. 83 (2015) 25–29. https://doi.org/10.1016/j.renene.2015.04.012.

[172] C. Gabriel, S. Gabriel, E. H. Grant, E. H. Grant, B. S. J. Halstead, D. Michael P. Mingos, Dielectric parameters relevant to microwave dielectric heating, Chem. Soc. Rev. 27 (1998) 213–224. https://doi.org/10.1039/A827213Z.

[173] G. Akerlof, DIELECTRIC CONSTANTS OF SOME ORGANIC SOLVENT-WATER MIXTURES AT VARIOUS TEMPERATURES, J. Am. Chem. Soc. 54 (1932) 4125–4139. https://doi.org/10.1021/ja01350a001.

[174] T.C. Loong, A. Idris, T. Chee Loong, A. Idris, One step transesterification of biodiesel production using simultaneous cooling and microwave heating, J. Clean. Prod. (2016). https://doi.org/10.1016/j.jclepro.2016.03.155.

[175] P.D. Luu, H.T. Truong, B. Van Luu, L.N. Pham, K. Imamura, N. Takenaka, Y. Maeda, Production of biodiesel from Vietnamese Jatropha curcas oil by a co-solvent method, Bioresour. Technol. 173 (2014) 309–316. https://doi.org/10.1016/j.biortech.2014.09.114.

[176] L.T. Thanh, K. Okitsu, Y. Sadanaga, N. Takenaka, Y. Maeda, H. Bandow, A new co-solvent method for the green production of biodiesel fuel – Optimization and practical application, Fuel. 103 (2013) 742–748. https://doi.org/10.1016/J.FUEL.2012.09.029.

[177] Y. Alhassan, N. Kumar, I.M. Bugaje, H.S. Pali, P. Kathkar, Co-solvents transesterification of cotton seed oil into biodiesel: Effects of reaction conditions on quality of fatty acids methyl esters, Energy Convers. Manag. 84 (2014) 640–648. https://doi.org/10.1016/j.enconman.2014.04.080.

[178] Y. Maeda, L.T. Thanh, K. Imamura, K. Izutani, K. Okitsu, L. Van Boi, P. Ngoc Lan, N.C. Tuan, Y.E. Yoo, N. Takenaka, New technology for the production of biodiesel fuel, Green Chem. 13 (2011) 1124–1128. https://doi.org/10.1039/C1GC15049A.

[179] C. Stavarache, M. Vinatoru, R. Nishimura, Y. Maeda, Fatty acids methyl esters from vegetable oil by means of ultrasonic energy, Ultrason. Sonochem. 12 (2005) 367–372. https://doi.org/10.1016/j.ultsonch.2004.04.001.

[180] D.G.B. Boocock, S.K. Konar, V. Mao, H. Sidi, Fast one-phase oil-rich processes for the preparation of vegetable oil methyl esters, Biomass and Bioenergy. 11 (1996) 43–50. https://doi.org/10.1016/0961-9534(95)00111-5.

[181] G. Guan, K. Kusakabe, N. Sakurai, K. Moriyama, Transesterification of vegetable oil to biodiesel fuel using acid catalysts in the presence of dimethyl ether, Fuel. 88 (2009) 81–86. https://doi.org/10.1016/j.fuel.2008.07.021.

[182] J. Park, B. Kim, Y.K. Chang, J.W. Lee, Wet in situ transesterification of microalgae using

ethyl acetate as a co-solvent and reactant, Bioresour. Technol. 230 (2017) 8–14. https://doi.org/10.1016/J.BIORTECH.2017.01.027.

[183] M. Taherkhani, S.M. Sadrameli, An improvement and optimization study of biodiesel production from linseed via in-situ transesterification using a co-solvent, Renew. Energy. 119 (2018) 787–794. https://doi.org/10.1016/J.RENENE.2017.10.061.

[184] World Intellectual Property Organization, WIPO - Search International and National Patent Collections, (n.d.). https://patentscope.wipo.int/search/en/search.jsf (accessed January 17, 2019).

[185] SCOPUS, Scopus preview - Scopus - Welcome to Scopus, (n.d.). https://www.scopus.com/results/handle.uri (accessed January 18, 2019).

[186] U.S. Energy Information Administration, Spot Prices for Crude Oil and Petroleum Products, (n.d.). https://www.eia.gov/dnav/pet/pet_pri_spt_s1_a.htm (accessed January 18, 2019).

[187] The World Bank, World Bank Open Data | Data, (n.d.). https://data.worldbank.org/ (accessed January 18, 2019).

[188] K.Y. Wong, J.-H.H. Ng, C.T. Chong, S.S. Lam, W.T. Chong, Biodiesel process intensification through catalytic enhancement and emerging reactor designs: A critical review, Elsevier Ltd, 2019. https://doi.org/10.1016/j.rser.2019.109399.

[189] M. Tabatabaei, M. Aghbashlo, M. Dehhaghi, H.K.S. Panahi, A. Mollahosseini, M. Hosseini, M.M. Soufiyan, Reactor technologies for biodiesel production and processing: A review, Prog. Energy Combust. Sci. 74 (2019) 239–303. https://doi.org/10.1016/j.pecs.2019.06.001.

[190] M.A. Sedghamiz, S. Raeissi, F. Attar, M. Salimi, K. Mehrabi, In-situ transesterification of residual vegetable oil in spent bleaching clay with alkali catalysts using CCD-RSM design of experiment, Fuel. 237 (2019) 515–521. https://doi.org/10.1016/j.fuel.2018.09.116.

[191] T.M.I. Mahlia, Z.A.H.S. Syazmi, M. Mofijur, A.E.P. Abas, M.R. Bilad, H.C. Ong, A.S. Silitonga, Patent landscape review on biodiesel production: Technology updates, Renew. Sustain. Energy Rev. 118 (2020) 109526. https://doi.org/10.1016/j.rser.2019.109526.

[192] X. Li, D. Tong, C. Hu, Efficient production of biodiesel from both esterification and transesterification over supported SO42--MoO3-ZrO2-Nd2O3/SiO2 catalysts, J. Energy Chem. 24 (2015) 463–471. https://doi.org/10.1016/j.jechem.2015.06.010.

[193] D. Salinas, C. Sepúlveda, N. Escalona, J.L. GFierro, G. Pecchi, Sol–gel La2O3–ZrO2 mixed oxide catalysts for biodiesel production, J. Energy Chem. 27 (2018) 565–572. https://doi.org/10.1016/j.jechem.2017.11.003.

[194] Z.B. Todorović, D.Z. Troter, D.R. Đokić-Stojanović, A. V. Veličković, J.M. Avramović, O.S. Stamenković, L.M. Veselinović, V.B. Veljković, Optimization of CaO-catalyzed sunflower oil methanolysis with crude biodiesel as a cosolvent, Fuel. 237 (2019) 903–910. https://doi.org/10.1016/J.FUEL.2018.10.056.

[195] A.S.S. Silitonga, A.H.H. Shamsuddin, T.M.I.M.I. Mahlia, J. Milano, F. Kusumo, J. Siswantoro, S. Dharma, A.H.H. Sebayang, H.H.H. Masjuki, H.C. Ong, Biodiesel synthesis from Ceiba pentandra oil by microwave irradiation-assisted transesterification: ELM modeling and optimization, Renew. Energy. 146 (2020) 1278–1291. https://doi.org/10.1016/j.renene.2019.07.065.

[196] G. Murillo, S.S. Ali, J. Sun, Y. Yan, P. Bartocci, N. El-Zawawy, M. Azab, Y. He, F. Fantozzi, Ultrasonic emulsification assisted immobilized Burkholderia cepacia lipase catalyzed transesterification of soybean oil for biodiesel production in a novel reactor design, Renew. Energy. 135 (2019) 1025–1034. https://doi.org/10.1016/J.RENENE.2018.12.080.

[197] J. Gupta, M. Agarwal, A.K. Dalai, Intensified transesterification of mixture of edible and nonedible oils in reverse flow helical coil reactor for biodiesel production, Renew. Energy. 134 (2019) 509–525. https://doi.org/10.1016/J.RENENE.2018.11.057.

[198] M. Kouzu, A. Fujimori, R. Fukakusa, N. Satomi, S. Yahagi, Continuous production of biodiesel by the CaO-catalyzed transesterification operated with continuously stirred tank reactor, Fuel Process. Technol. 181 (2018) 311–317. https://doi.org/10.1016/J.FUPROC.2018.10.008.

[199] P. Chhabra, S. Mosbach, I.A. Karimi, M. Kraft, Practically Useful Models for Kinetics of Biodiesel Production, ACS Sustain. Chem. Eng. 7 (2019) 4983–4992. https://doi.org/10.1021/acssuschemeng.8b05636.

[200] Y. Gao, Y. Chen, J. Gu, Z. Xin, S. Sun, Butyl-biodiesel production from waste cooking oil: Kinetics, fuel properties and emission performance, Fuel. 236 (2019) 1489–1495. https://doi.org/10.1016/j.fuel.2018.09.015.

[201] G. Knothe, J.J. Krahl, J.H. Van Gerpen, The biodiesel handbook, Elsevier, 2015.

[202] W. Ahmed, M.F. Nazar, S.D. Ali, U.A. Rana, S.U.D. Khan, Detailed investigation of optimized alkali catalyzed transesterification of Jatropha oil for biodiesel production, J. Energy Chem. 24 (2015) 331–336. https://doi.org/10.1016/S2095-4956(15)60319-9.

[203] S.N. Gebremariam, T. Hvoslef-Eide, M.T. Terfa, J.M. Marchetti, Techno-Economic Performance of Different Technological Based Bio-Refineries for Biofuel Production, Energies. 12 (2019) 3916. https://doi.org/10.3390/en12203916.

[204] S.B. Glisic, J.M. Pajnik, A.M. Orlović, Process and techno-economic analysis of green diesel production from waste vegetable oil and the comparison with ester type biodiesel production, Appl. Energy. 170 (2016) 176–185. https://doi.org/10.1016/j.apenergy.2016.02.102.

[205] M.A.A. Farid, A.M. Roslan, M.A. Hassan, M.Y. Hasan, M.R. Othman, Y. Shirai, Net energy and techno-economic assessment of biodiesel production from waste cooking oil using a semi-industrial plant: A Malaysia perspective, Sustain. Energy Technol. Assessments. 39 (2020) 100700. https://doi.org/10.1016/j.seta.2020.100700.

[206] S.N. Csernica, J.T. Hsu, The phase behavior effect on the kinetics of transesterification reactions for biodiesel production, Ind. Eng. Chem. Res. 51 (2012) 6340–6349. https://doi.org/10.1021/ie300116p.

[207] A. Asoodeh, F. Eslami, S.M. Sadrameli, Liquid–liquid equilibria of systems containing linseed oil biodiesel + methanol + glycerol: Experimental data and thermodynamic modeling, Fuel. 253 (2019) 460–473. https://doi.org/10.1016/j.fuel.2019.04.170.

[208] C.W. Chiu, M.J. Goff, G.J. Suppes, Distribution of methanol and catalysts between biodiesel and glycerin phases, AIChE J. 51 (2005) 1274–1278. https://doi.org/10.1002/aic.10385.

[209] O.S. Stamenković, M.L. Lazić, Z.B. Todorović, V.B. Veljković, D.U. Skala, The effect of agitation intensity on alkali-catalyzed methanolysis of sunflower oil, Bioresour. Technol. 98 (2007) 2688–2699. https://doi.org/10.1016/J.BIORTECH.2006.09.024.

[210] V.G. Tacias-Pascacio, B. Torrestiana-Sánchez, L. Dal Magro, J.J. Virgen-Ortíz, F.J. Suárez-Ruíz, R.C. Rodrigues, R. Fernandez-Lafuente, Comparison of acid, basic and enzymatic catalysis on the production of biodiesel after RSM optimization, Renew. Energy. 135 (2019) 1–9. https://doi.org/10.1016/j.renene.2018.11.107.

[211] H.C. Ong, J. Milano, A.S. Silitonga, M.H. Hassan, A.H. Shamsuddin, C.T. Wang, T.M. Indra Mahlia, J. Siswantoro, F. Kusumo, J. Sutrisno, Biodiesel production from Calophyllum

inophyllum-Ceiba pentandra oil mixture: Optimization and characterization, J. Clean. Prod. 219 (2019) 183–198. https://doi.org/10.1016/j.jclepro.2019.02.048.

[212] A.M. Nassef, H. Rezk, M.A. Abdelkareem, A. Alaswad, A. Olabi, Application of fuzzy modelling and Particle Swarm Optimization to enhance lipid extraction from microalgae, Sustain. Energy Technol. Assessments. 35 (2019) 73–79. https://doi.org/10.1016/j.seta.2019.06.003.

[213] G. Vicente, M. Martínez, J. Aracil, A. Esteban, Gemma Vicente, Mercedes Martínez, * and José Aracil, A. Esteban, Kinetics of Sunflower Oil Methanolysis, Ind. Eng. Chem. Res. 44 (2005) 5447–5454. https://pubs.acs.org/doi/abs/10.1021/ie040208j (accessed March 26, 2018).

[214] B. Likozar, A. Pohar, J. Levec, Transesterification of oil to biodiesel in a continuous tubular reactor with static mixers: Modelling reaction kinetics, mass transfer, scale-up and optimization considering fatty acid composition, Fuel Process. Technol. 142 (2016) 326–336. https://doi.org/10.1016/j.fuproc.2015.10.035 Research article.

[215] T. Ruppel, T. Huybrighs, C. Shelton, Fatty acid methyl esters in B100 biodiesel by gas chromatography (Modified EN 14103), Perkin Elmer's Appl. …. (2008) 1–4. http://www.perkinelmer.com/PH/CMSResources/Images/44-74116APP_FAMEbyGCinB100Biodiesel.pdf.

[216] Y. Cao, B.J. Smucker, T.J. Robinson, A hybrid elitist pareto-based coordinate exchange algorithm for constructing multi-criteria optimal experimental designs, Stat. Comput. 27 (2017) 423–437. https://doi.org/10.1007/s11222-016-9630-9.

[217] G. Vicente, A. Coteron, M. Martinez, J. Aracil, Application of the factorial design of experiments and response surface methodology to optimize biodiesel production, Ind. Crops Prod. 8 (1998) 29–35. https://doi.org/10.1016/S0926-6690(97)10003-6.

[218] M.D.G. de Luna, J.L. Cuasay, N.C. Tolosa, T.W. Chung, Transesterification of soybean oil using a novel heterogeneous base catalyst: Synthesis and characterization of Na-pumice catalyst, optimization of transesterification conditions, studies on reaction kinetics and catalyst reusability, Fuel. 209 (2017) 246–253. https://doi.org/10.1016/j.fuel.2017.07.086.

[219] T. Leevijit, A second order kinetics of palm oil transesterification, Jt. Int. Conf. "Sustainable Energy Environ. (SEE)." 025 (2004) 277–281. http://www.aseanenergy.info/Abstract/33004664.pdf.

[220] J.-Y. Park, D.-K. Kim, Z.-M. Wang, J.-S. Lee, Fast Biodiesel Production with One-Phase Reaction, Appl. Biochem. Biotechnol. 154 (2009) 67–73. https://doi.org/10.1007/s12010-008-8421-y.

[221] D. Müllner, Modern hierarchical, agglomerative clustering algorithms, (2011). http://arxiv.org/abs/1109.2378 (accessed January 9, 2019).

[222] Seaborn, seaborn.clustermap - seaborn 0.9.0 documentation, (2019). https://seaborn.pydata.org/generated/seaborn.clustermap.html# (accessed January 11, 2019).

[223] D.A. Vallero, Environmental Biotechnology-A Biosystems Approach, 2010. https://doi.org/https://doi.org/10.1016/C2009-0-01984-9.

[224] T.K. Harris, M.M. Keshwani, Chapter 7 Measurement of Enzyme Activity, in: Methods Enzymol., Academic Press Inc., 2009: pp. 57–71. https://doi.org/10.1016/S0076-6879(09)63007-X.

[225] A. V. Marjanović, O.S. Stamenković, Z.B. Todorović, M.L. Lazić, V.B. Veljković, Kinetics of the base-catalyzed sunflower oil ethanolysis, Fuel. 89 (2010) 665–671. https://doi.org/10.1016/j.fuel.2009.09.025.

[226] K. Karel, S. František, S. Radek, M. Jaroslav, Kinetics and mechanism of the KOH — catalyzed methanolysis of rapeseed oil for biodiesel production, Eur. J. Lipid Sci. Technol. 104 (2002) 728–737. https://doi.org/10.1002/1438-9312(200211)104:11<728::AID-EJLT728>3.0.CO;2-J.

[227] G. Vicente, M. Martínez, J. Aracil, Kinetics of Brassica carinata oil methanolysis, Energy and Fuels. 20 (2006) 1722–1726. https://doi.org/10.1021/ef060047r.

[228] British Standards Institution, BS EN 14105:2003 Fat and oil derivatives - FAME - Determination of free and total glycerol and mono-, di-, triglyceride content, (2003) 20.

[229] J.M. Encinar, J.F. González, J.J. Rodríguez, A. Tejedor, Biodiesel fuels from vegetable oils: Transesterification of Cynara cardunculus L. Oils with ethanol, Energy and Fuels. 16 (2002) 443–450. https://doi.org/10.1021/ef010174h.

[230] B. Likozar, J. Levec, Transesterification of canola, palm, peanut, soybean and sunflower oil with methanol, ethanol, isopropanol, butanol and tert-butanol to biodiesel: Modelling of chemical equilibrium, reaction kinetics and mass transfer based on fatty acid composition, Appl. Energy. 123 (2014) 108–120. https://doi.org/10.1016/j.apenergy.2014.02.046.

[231] I. Poljanšek, B. Likozar, Influence of Mass Transfer and Kinetics on Biodiesel Production Process, (n.d.).

[232] Y.B. Che Man, M.H. Moh, F.R. Van De Voort, Determination of free fatty acids in crude palm oil and refined-bleached-deodorized palm olein using Fourier transform infrared spectroscopy, JAOCS, J. Am. Oil Chem. Soc. 76 (1999) 485–490. https://doi.org/10.1007/s11746-999-0029-z.

[233] G. Vicente, M. Martínez, J. Aracil, Integrated biodiesel production: A comparison of different homogeneous catalysts systems, Bioresour. Technol. 92 (2004) 297–305. https://doi.org/10.1016/j.biortech.2003.08.014.

[234] S. Shahla, G.C. Ngoh, R. Yusoff, The evaluation of various kinetic models for base-catalyzed ethanolysis of palm oil, Bioresour. Technol. 104 (2012) 1–5. https://doi.org/10.1016/j.biortech.2011.11.010.

[235] C.S. Latchubugata, R.V. Kondapaneni, K.K. Patluri, U. Virendra, S. Vedantam, Kinetics and optimization studies using Response Surface Methodology in biodiesel production using heterogeneous catalyst, Chem. Eng. Res. Des. 135 (2018) 129–139. https://doi.org/10.1016/j.cherd.2018.05.022.

[236] R. Richard, Y. Li, B. Dubreuil, S. Thiebaud-Roux, L. Prat, On-line monitoring of the transesterification reaction between triglycerides and ethanol using near infrared spectroscopy combined with gas chromatography, Bioresour. Technol. 102 (2011) 6702–6709. https://doi.org/10.1016/j.biortech.2011.03.111.

[237] O.S. Stamenković, Z.B. Todorović, M.L. Lazić, V.B. Veljković, D.U. Skala, Kinetics of sunflower oil methanolysis at low temperatures, Bioresour. Technol. 99 (2008) 1131–1140. https://doi.org/10.1016/j.biortech.2007.02.028.

[238] Joelianingsih, H. Maeda, S. Hagiwara, H. Nabetani, Y. Sagara, T.H. Soerawidjaya, A.H. Tambunan, K. Abdullah, Biodiesel fuels from palm oil via the non-catalytic transesterification in a bubble column reactor at atmospheric pressure: A kinetic study, Renew. Energy. 33 (2008) 1629–1636. https://doi.org/10.1016/j.renene.2007.08.011.

[239] K.G. Georgogianni, M.G. Kontominas, P.J. Pomonis, D. Avlonitis, V. Gergis, Alkaline conventional and in situ transesterification of cottonseed oil for the production of biodiesel,

Energy and Fuels. 22 (2008) 2110–2115. https://doi.org/10.1021/ef700784j.

[240] E. Li, Z.P. Xu, V. Rudolph, MgCoAl-LDH derived heterogeneous catalysts for the ethanol transesterification of canola oil to biodiesel, Appl. Catal. B Environ. 88 (2009) 42–49. https://doi.org/10.1016/j.apcatb.2008.09.022.

[241] N. De Lima Da Silva, Ć.B. Batistella, R.M. Filho, M.R.W. Maciel, Biodiesel production from castor oil: Optimization of alkaline ethanolysis, Energy and Fuels. 23 (2009) 5636–5642. https://doi.org/10.1021/ef900403j.

[242] M. V. Twigg, J.T. Richardson, Fundamentals and applications of structured ceramic foam catalysts, Ind. Eng. Chem. Res. 46 (2007) 4166–4177. https://doi.org/10.1021/ie061122o.

[243] D. Edouard, M. Lacroix, C.P. Huu, F. Luck, Pressure drop modeling on solid foam: State-of-the art correlation, Chem. Eng. J. 144 (2008) 299–311. https://doi.org/10.1016/j.cej.2008.06.007.

[244] A. Inayat, H. Freund, T. Zeiser, W. Schwieger, Determining the specific surface area of ceramic foams: The tetrakaidecahedra model revisited, Chem. Eng. Sci. 66 (2011) 1179–1188. https://doi.org/10.1016/j.ces.2010.12.031.

[245] F.C. Walsh, L.F. Arenas, C. Ponce de León, G.W. Reade, I. Whyte, B.G. Mellor, The continued development of reticulated vitreous carbon as a versatile electrode material: Structure, properties and applications, Electrochim. Acta. 215 (2016) 566–591. https://doi.org/10.1016/j.electacta.2016.08.103.

[246] W.D. Ford, Method of making cellular refractory thermal insulating material, 1964. https://doi.org/10.1145/178951.178972.

[247] J.M. Friedrich, C. Ponce-de-León, G.W. Reade, F.C. Walsh, Reticulated vitreous carbon as an electrode material, J. Electroanal. Chem. 561 (2004) 203–217. https://doi.org/10.1016/j.jelechem.2003.07.019.

[248] Y. Yuan, S. Kim, Polypyrrole-coated reticulated vitreous carbon as anode in microbial fuel cell for higher energy output, Bull. Korean Chem. Soc. 29 (2008) 168–172. https://doi.org/10.5012/bkcs.2008.29.1.168.

[249] M.K. Pec, R. Reyes, E. Sánchez, D. Carballar, A. Delgado, J. Santamaría, M. Arruebo, C. Evora, Reticulated vitreous carbon: A useful material for cell adhesion and tissue invasion, Eur. Cells Mater. 20 (2010) 282–294. https://doi.org/10.22203/eCM.v020a23.

[250] D. Weaire, R. Phelan, A counter-example to Kelvin's conjecture on minimal surfaces, Philos. Mag. Lett. 69 (1994) 107–110. https://doi.org/10.1080/09500839408241577.

[251] J.M. Friedrich, Characterisation of electrode materials for electrochemical reactors, 2006.

[252] ERG Aerospace, Surface Area of Duocel® Foam, (n.d.). https://ergaerospace.com/technical-data/surface-area-of-duocel-foam/#tab-f027f83bf84a985f8b7.

[253] ERG Aerospace Corporation, ERG: Duocel® - RVC, Reticulated Vitreous Carbon Foam Properties, (n.d.). http://www.ergaerospace.com/RVC-properties.htm (accessed February 26, 2017).

[254] O.S. Stamenković, V.B. Veljković, Z.B. Todorović, M.L. Lazić, I.B. Banković-Ilić, D.U. Skala, Modeling the kinetics of calcium hydroxide catalyzed methanolysis of sunflower oil, Bioresour. Technol. 101 (2010) 4423–4430. https://doi.org/10.1016/j.biortech.2010.01.109.

[255] Z.B. Todorovic, O.S. Stamenkovic, I.S. Stamenkovic, J.M. Avramovic, A. V. Velickovic, I.B. Bankovic-Ilic, V.B. Veljkovic, The effects of cosolvents on homogeneously and heterogeneously base-catalyzed methanolysis of sunflower oil, Fuel. 107 (2013) 493–502.

https://doi.org/10.1016/j.fuel.2012.11.049.

[256] O.S. Stamenkovic, Z.B. Todorovic, M.L. Lazic, V.B. Veljkovic, Kinetics of sunflower oil methanolysis catalyzed by calcium oxide, 88 (2009) 1554–1562. https://doi.org/10.1016/j.fuel.2009.02.013.

[257] A. Sharma, P. Kodgire, S.S. Kachhwaha, Investigation of ultrasound-assisted KOH and CaO catalyzed transesterification for biodiesel production from waste cotton-seed cooking oil: Process optimization and conversion rate evaluation, J. Clean. Prod. 259 (2020) 120982. https://doi.org/10.1016/j.jclepro.2020.120982.

[258] I.C.P. Tschoeke, J.P. Silva, J.G.A. Pacheco, J.M.F. Silva, Kinetic modeling of cottonseed oil transesterification with ethanol, React. Kinet. Mech. Catal. 128 (2019) 707–722. https://doi.org/10.1007/s11144-019-01661-2.

[259] V.K. Aniya, R.K. Muktham, K. Alka, B. Satyavathi, Modeling and simulation of batch kinetics of non-edible karanja oil for biodiesel production : A mass transfer study, Fuel. 161 (2015) 137–145. https://doi.org/10.1016/j.fuel.2015.08.042.

[260] D. Galvan, H. Cremasco, A. Carolina, G. Mantovani, E. Bona, Kinetic study of the transesterification reaction by artificial neural networks and parametric particle swarm optimization, Fuel. 267 (2020) 117221. https://doi.org/10.1016/j.fuel.2020.117221.

[261] D.G.B. Boocock, S.K. Konar, V. Mao, C. Lee, S. Buligan, Fast Formation of High-Purity Methyl Esters from Vegetable Oils, 1998. http://citeseerx.ist.psu.edu/viewdoc/download?doi=10.1.1.475.58&rep=rep1&type=pdf (accessed February 24, 2019).

[262] A. Di Vincenzo, M.A. Floriano, Elucidating the Influence of the Activation Energy on Reaction Rates by Simulations Based on a Simple Particle Model, (2020). https://doi.org/10.1021/acs.jchemed.0c00463.

[263] M.N. Kashid, L. Kiwi-minsker, Microstructured Reactors for Multiphase Reactions : State of the Art, (2009) 6465–6485. https://doi.org/10.1021/ie8017912.

[264] R. Gupta, D.F. Fletcher, B.S. Haynes, Taylor Flow in Microchannels : A Review of Experimental and Computational Work, (2010).

[265] A. Günther, M.T. Kreutzer, Multiphase Flow, Micro Process Eng. (2013) 1–40. https://doi.org/https://doi.org/10.1002/9783527631445.ch1.

[266] S. Afkhami, S. Zaleski, M. Bussmann, A mesh-dependent model for applying dynamic contact angles to VOF simulations, J. Comput. Phys. 228 (2009) 5370–5389. https://doi.org/10.1016/j.jcp.2009.04.027.

[267] V.S. Ajaev, G.M. Homsy, Modeling Shapes and Dynamics of Confined Bubbles, (2006). https://doi.org/10.1146/annurev.fluid.38.050304.092033.

[268] A. Lafuma, D. Quéré, Superhydrophobic states, Nat. Mater. 2 (2003) 457–460. https://doi.org/10.1038/nmat924.

[269] D. Bartolo, F. Bouamrirene, E. Verneuil, A. Bugun, P. Silberzan, S. Moulinet, Bouncing or sticky droplets : Impalement transitions on superhydrophobic micropatterned surfaces Bouncing or sticky droplets : Impalement transitions on superhydrophobic micropatterned surfaces, (2006). https://doi.org/10.1209/epl/i2005-10522-3.

[270] J.R. Thome, V. Dupont, A.M. Jacobi, Heat transfer model for evaporation in microchannels . Part I : presentation of the model, 47 (2004) 3375–3385.

https://doi.org/10.1016/j.ijheatmasstransfer.2004.01.006.

[271] K.A. Triplett, S.M. Ghiaasiaan, A. Lemouel, B.N. Mccord, Gas ± liquid two-phase ¯ ow in microchannels Part II : void fraction and pressure drop, 25 (1999) 395–410.

[272] K.A. Triplett, S.M. Ghiaasiaan, D.L. Sadowski, Gas ± liquid two-phase ¯ ow in microchannels Part I : two-phase ¯ ow patterns, 25 (1999) 377–394.

[273] P. Garstecki, M.J. Fuerstman, A. Stone, G.M. Whitesides, Formation of droplets and bubbles in a microfluidic T-junction — scaling and mechanism of break-up, (2006) 437–446. https://doi.org/10.1039/b510841a.

[274] A. Gavriilidis, P. Angeli, Mixing and Contacting of Heterogeneous Systems, 2009.

[275] A. Dessimoz, L. Cavin, A. Renken, L. Kiwi-minsker, Liquid – liquid two-phase flow patterns and mass transfer characteristics in rectangular glass microreactors, 63 (2008) 4035–4044. https://doi.org/10.1016/j.ces.2008.05.005.

[276] R. Richard, S. Thiebaud-Roux, L. Prat, Modelling the kinetics of transesterification reaction of sunflower oil with ethanol in microreactors, Chem. Eng. Sci. 87 (2013) 258–269. https://doi.org/10.1016/j.ces.2012.10.014.

[277] X. Wang, X. Xu, Q. Wang, Z. Huang, J. He, T. Qiu, Fatty Acid Methyl Ester Synthesis through Transesteri fi cation of Palm Oil with Methanol in Microchannels : Flow Pattern and Reaction Kinetics, (2020). https://doi.org/10.1021/acs.energyfuels.9b03365.

[278] V. Hessel, A. Renken, J.C. Schouten, J. Yoshida, Micro Process Engineering: A comprehensive handbook, Wiley-VCH, 2009.

[279] S.L. Anna, N. Bontoux, H.A. Stone, Formation of dispersions using " flow focusing " in microchannels, 364 (2009) 10–13. https://doi.org/10.1063/1.1537519.

[280] S. Ma, J.M. Sherwood, W.T.S. Huck, S. Balabani, On the flow topology inside droplets moving in rectangular microchannels, Lab Chip. 14 (2014) 3611–3620. https://doi.org/10.1039/c4lc00671b.

[281] H. Zhou, H. Lu, B. Liang, Solubility of Multicomponent Systems in the Biodiesel Production by Transesterification of Jatropha curcas L . Oil with Methanol, (2006) 1130–1135. https://doi.org/10.1021/je0600294.

[282] J.R. Burns, C. Ramshaw, U.K. Ne, The intensification of rapid reactions in multiphase systems using slug flow in capillaries, (2001) 10–15. https://doi.org/10.1039/b102818a.

[283] M.N. Kashid, Y.M. Harshe, D.W. Agar, Liquid - Liquid Slug Flow in a Capillary : An Alternative to Suspended Drop or Film Contactors, (2007) 8420–8430. https://doi.org/10.1021/ie070077x.

[284] H.S. Santana, D.S. Tortola, É.M. Reis, J.L. Silva, O.P. Taranto, Transesterification reaction of sunflower oil and ethanol for biodiesel synthesis in microchannel reactor: Experimental and simulation studies, Chem. Eng. J. 302 (2016) 752–762. https://doi.org/10.1016/J.CEJ.2016.05.122.

[285] R. Kumar, V. Ravi, P. Ankur, M. Sumana, Biodiesel production in a serpentine minireactor — Effect of flow distribution, (2019) 3461–3474. https://doi.org/10.1002/er.4488.